Indirect probes to constrain the $\mathcal{CP}$ nature of the Higgs boson

Dissertation
zur
Erlangung des Doktorgrades (Dr. rer. nat.)
der
Mathematisch-Naturwissenschaftlichen Fakultät
der
Rheinischen Friedrich-Wilhelms-Universität Bonn

von
Tobias Klingl
aus
Göppingen

Bonn, 04.05.2021

Angefertigt mit Genehmigung der Mathematisch-Naturwissenschaftlichen Fakultät der Rheinischen Friedrich-Wilhelms-Universität Bonn

1. Gutachter:	Prof. Dr. Klaus Desch
2. Gutachter:	Prof. Dr. Florian Bernlochner
Tag der Promotion:	08.07.2021
Erscheinungsjahr:	2021

Abstract

The measurements of the coupling, spin, and charge-parity ($C\mathcal{P}$) properties of the Higgs boson are consistent with the Standard Model (SM) predictions. However, the corresponding uncertainties are still large, and alternative theories of electroweak symmetry breaking (EWSB) also fit the data. While the pure $C\mathcal{P}$-odd hypothesis is already ruled out, general $C\mathcal{P}$ admixtures are still possible. This thesis studies the scope of possible $C\mathcal{P}$ violation in the Higgs sector using different Higgs boson interpretation frameworks.

The tensor structure of the Higgs boson couplings to weak gauge bosons, gluons, and top quarks is measured in Higgs boson decays into four leptons, $H \to ZZ^* \to 4\ell$ ($\ell = e, \mu$), using 139 fb^{-1} of proton-proton collision data with a center-of-mass energy of 13 TeV recorded with the ATLAS detector at the Large Hadron Collider (LHC). Beyond the SM (BSM) effects in the Higgs couplings are measured at particle level and are interpreted in the Standard Model Effective Field Theory (SMEFT). Constraints have been derived on the $C\mathcal{P}$-even and $C\mathcal{P}$-odd BSM coupling parameters describing the Hgg (c_{HG} and $c_{H\widetilde{G}}$), Htt (c_{uH} and $c_{\widetilde{u}H}$), and HVV (c_{HW}, c_{HB}, c_{HWB}, and $c_{H\widetilde{W}}$, $c_{H\widetilde{B}}$, $c_{H\widetilde{W}B}$) interaction vertices. The most stringent constraints at 95 % C. L. are $-0.0083 < c_{HG} < 0.0068$ and $|c_{H\widetilde{G}}| < 0.029$. The limits on the $C\mathcal{P}$-even parameter are stronger since the linear terms dominate in this case. The constraints on the $C\mathcal{P}$-even coupling parameters to weak vector bosons are $-3.4 < c_{HW} < 2.1$, $-0.62 < c_{HB} < 0.59$, and $-1.06 < c_{HWB} < 0.99$, while the $C\mathcal{P}$-odd ones are $|c_{H\widetilde{W}}| < 2.4$, $|c_{H\widetilde{B}}| < 0.56$, and $|c_{H\widetilde{W}B}| < 1.03$.

The $C\mathcal{P}$ nature of the Higgs boson is also probed by fitting $C\mathcal{P}$-violating models to all inclusive and differential Higgs boson measurements provided by the ATLAS and CMS collaborations. This is done with the public computer code `HiggsSignals`. The first model targets the $C\mathcal{P}$ properties of the top-Yukawa interaction. The upper limit on a $C\mathcal{P}$-violating phase is found to be $\alpha_{tt} \leq 72°$, which implies that the Higgs-top coupling is at last 25 % $C\mathcal{P}$-even. The second model describes the Higgs boson, $\phi = H \cos\alpha + A \sin\alpha$, as an admixture of $C\mathcal{P}$-even (H) and $C\mathcal{P}$-odd (A) components as described by the 2HDM. In this kind of models, A does not couple to weak gauge bosons, $V = W, Z$, at tree-level. For the $C\mathcal{P}$-even component, no significant differences between the couplings to W and Z bosons are found. Therefore, a common coupling modifier $\kappa_V^s \equiv \kappa_W^s = \kappa_Z^s$ is used. Constraints on the mixing parameter α are set in case $\kappa_V^s \leq 1$, which is a valid assumption in 2HDM-type models. Effective couplings of the $C\mathcal{P}$-odd state to SM gauge bosons are considered in an effective field theory (EFT) approach. Since AVV couplings can only be realized through loop corrections of heavy new fields, they are strongly suppressed. By requiring that the EFT is perturbative, their impact is found to be marginal, and possible $C\mathcal{P}$ admixtures are constrained to $\alpha \leq 27.4°$. This means that in the context of 2HDM-type models, the Higgs boson is at most 34 % $C\mathcal{P}$-odd. In addition to these studies, several performance tests of `HiggsSignals` with LHC Run-1 and Run-2 data are presented.

The $H \to \tau\tau$ channel is one of the most promising candidates for a direct $C\mathcal{P}$ measurement of a Higgs boson coupling. This measurement relies on the precise reconstruction of the tau decay products. For Run-2 of the LHC, the tau-lepton reconstruction at ATLAS has been significantly improved using the particle-flow concept. In this thesis, a new energy reconstruction method for hadronically decaying tau leptons has been developed, which improves the resolution of low-energetic taus by up to 25 % (70 %) in decays with (without) neutral pions. In addition, an energy correction of neutral pions in 1p1n, 1pXn, and 3pXn decays has been developed. The corresponding improvement of the neutral pion transverse momentum is about 20 %, 30 %, and 60 %, respectively.

Contents

1 Introduction **1**

2 Theory **3**
2.1 The Standard Model of Particle Physics . . . 3
2.1.1 The Electroweak Interaction . . . 5
2.1.1.1 Quantum Electrodynamics (QED) . . . 5
2.1.1.2 Electroweak Unification . . . 6
2.1.2 The Strong Interaction . . . 8
2.1.3 The Higgs Mechanism . . . 9
2.1.4 Higgs Boson Phenomenology in the Standard Model . . . 13
2.1.4.1 Higgs Boson Production in Proton-Proton Collisions . . . 14
2.1.4.2 Higgs Boson Decays . . . 17
2.1.5 Shortcomings of the Standard Model . . . 18
2.2 $\mathcal{CP}$ Violation in Extended Higgs Sectors . . . 23
2.2.1 The Two-Higgs-Doublet Model . . . 23
2.2.2 The Minimal Supersymmetric Standard Model . . . 26
2.3 Experimental Constraints on the $\mathcal{CP}$ Nature of the Higgs Boson . . . 30
2.3.1 Measurements Targeting the Higgs Boson Couplings to Gauge Bosons . . . 30
2.3.2 Studies Targeting the Higgs Boson Couplings to Fermions . . . 30
2.3.3 Measurements of Electric Dipole Moments . . . 31
2.3.4 Conclusion . . . 32
2.4 Higgs Boson Interpretation Frameworks . . . 32
2.4.1 The κ-Framework for the Analysis of Higgs Boson Couplings . . . 32
2.4.2 Effective Field Theory Frameworks . . . 33
2.4.2.1 The Standard Model Effective Field Theory (SMEFT) . . . 35
2.4.2.2 Framework for Probing Higgs $\mathcal{CP}$ Admixtures . . . 38
2.4.2.3 The Higgs Characterization Model . . . 43

3 The Experimental Setup **45**
3.1 The Large Hadron Collider . . . 45
3.2 The ATLAS Experiment . . . 48
3.2.1 The Coordinate System at ATLAS . . . 49
3.2.2 The Trigger System . . . 50
3.2.3 The Inner Detector (ID) . . . 50
3.2.4 The Calorimeter System . . . 51
3.2.5 The Muon System (MS) . . . 54
3.3 Event Reconstruction and Particle Identification . . . 54
3.3.1 Electrons and Photons . . . 55
3.3.2 Muons . . . 57
3.3.3 Jets . . . 58

3.3.4 Tau Leptons . . . 59
3.4 The Particle-Flow (PFlow) Method . . . 61
3.4.1 Particle Flow for Jets . . . 62
3.4.2 Particle Flow for Tau Leptons . . . 62
3.5 Improved Energy Reconstruction of Hadronic Tau Leptons . . . 64
3.5.1 Weighted Average of TauRec and CellBased+PanTau . . . 66
3.5.2 Treatment of Non-Gaussian Tails . . . 69
3.5.3 The MVA Tau Energy Scale . . . 70
3.5.4 Neutral Pion Correction at the MVA TES . . . 71
3.5.4.1 Correction for 1P1N Decays . . . 72
3.5.4.2 Correction for 1PXN and 3PXN Decays . . . 76
3.5.4.3 Neutral Pion ΔR Correction for 1PXN Decays . . . 77

4 The HiggsSignals Tool 79
4.1 Introduction to HiggsBounds and HiggsSignals . . . 79
4.2 HiggsBounds-5: Updated Effective Coupling Approximations . . . 80
4.3 HiggsSignals-2: Basic Concepts and New Developments . . . 81
4.3.1 Higgs Signals in Collider Experiments . . . 81
4.3.2 The Peak-Centered χ^2 Method . . . 82
4.3.3 The χ^2 Contribution from the LHC Run-1 Combination . . . 83
4.3.4 The χ^2 Contribution from STXS Measurements . . . 83
4.4 Statistical Interpretation in HiggsSignals . . . 84
4.5 Performance Tests . . . 86
4.5.1 Reproduction of the ATLAS and CMS Run-1 Combination . . . 86
4.5.1.1 Parameterization through Coupling Scale Factors . . . 87
4.5.1.2 Parameterization using Ratios of Coupling Scale Factors . . . 88
4.5.1.3 Parameterization using Ratios of Cross-Sections and Branching Fractions 89
4.5.2 Examples for Run 2 Analyses in HiggsSignals-2 . . . 90
4.5.2.1 Input given in Terms of Signal Strength Modifiers . . . 91
4.5.2.2 Input given in Terms of Simplified Template Cross-Sections . . . 93
4.6 Summary . . . 96

5 Higgs Boson Cross-Section Measurement in the $H \to ZZ^* \to 4\ell$ Decay Channel at ATLAS 97
5.1 Signal and Background Processes . . . 97
5.1.1 The $H \to ZZ^* \to 4\ell$ Signal . . . 97
5.1.2 Background Contributions . . . 98
5.1.2.1 Irreducible Background . . . 98
5.1.2.2 Reducible Background . . . 99
5.2 Event Samples . . . 100
5.2.1 The ATLAS Run-2 Data Set . . . 100
5.2.2 Monte Carlo Event Simulation . . . 101
5.2.2.1 The Higgs Boson Signal Model . . . 101
5.2.2.2 The Background Model . . . 102
5.3 Event Selection . . . 103
5.4 Event Categorization . . . 105
5.5 Performance Studies for PFlow Jets . . . 107
5.6 Systematic Uncertainties . . . 110
5.6.1 Experimental Uncertainties . . . 110

5.6.2 Theoretical Uncertainties . . . 111
5.7 Statistical Treatment . . . 112
5.8 Results . . . 113

6 EFT Interpretation in the $H \to ZZ^* \to 4\ell$ Decay Channel at ATLAS 115
6.1 Parameterization of the Higgs Boson Production Cross-Section . . . 116
6.1.1 Parameterization in gg2H Production . . . 120
6.1.2 Parameterization in qq2Hqq Production . . . 123
6.1.3 Parameterization in VH-Lep Production . . . 126
6.1.4 Parameterization in ttH Production . . . 128
6.2 Parameterization of the Higgs Boson Decay . . . 129
6.3 Parameterization of the Acceptance . . . 134
6.3.1 Signal Acceptance in the $H \to 4\ell$ Channel . . . 136
6.3.2 Interference between $\mathcal{CP}$-Even and $\mathcal{CP}$-Odd Operators . . . 139
6.4 The Complete EFT Signal Model . . . 142
6.5 Validation of the EFT Signal Model . . . 148
6.5.1 Validation of the Acceptance Model . . . 148
6.5.2 Validation of the Production Cross-Section Parameterization . . . 149
6.5.3 BSM Dependence of the Reconstruction Efficiency . . . 150
6.6 Systematic Uncertainties . . . 153
6.7 Statistical Treatment . . . 154
6.8 Results . . . 155
6.9 Comparison to other Decay Channels . . . 159

7 Indirect Constraints on Possible $\mathcal{CP}$ Admixtures from Rate Measurements 165
7.1 Constraints on $\mathcal{CP}$-Mixing in the Top-Yukawa Coupling . . . 165
7.2 $\mathcal{CP}$-Mixing Constraints in Global Interpretations . . . 167
7.2.1 Common Pseudoscalar Coupling Scale Factor for Fermions . . . 167
7.2.2 Probing Custodial Symmetry . . . 168
7.2.3 Probing the Yukawa Couplings and the Effects of Dimension-Five Operators . . . 170
7.2.4 Summary . . . 173
7.3 Constraints from the $H \to 4\ell$ Decay Channel at ATLAS . . . 173
7.3.1 Statistical Treatment . . . 174
7.3.2 Common Pseudoscalar Coupling Parameter for Fermions . . . 174
7.3.3 General Parameterization Including $\mathcal{CP}$-odd Dimension-Five Operators . . . 174

8 Summary and Conclusion 177

Bibliography 179

A Energy Reconstruction of Hadronic Tau Leptons 209
A.1 Gaussian fits to the Core Energy Resolutions . . . 209
A.1.1 Extracted Mean Values of Core Resolutions . . . 210
A.1.2 Extracted Widths of Core Resolutions . . . 216
A.2 Compatibility Condition . . . 221
A.3 Summary of Energy Resolution Plots . . . 222
A.3.1 1p0n Decays . . . 222
A.3.2 1p1n Decays . . . 224

A.3.3 1pXn Decays . . . 226
A.3.4 3p0n Decays . . . 228
A.3.5 3pXn Decays . . . 230
A.4 Neutral Pion Correction . . . 232
A.4.1 True==Reco 1p1n decay . . . 232
A.4.2 True==Reco 1PXN Decays . . . 233
A.4.3 True==Reco 3PXN decay . . . 234

B Experimental Input in `HiggsSignals` 235

C Higgs Boson Cross-section Measurement in the $H \to ZZ^* \to 4\ell$ Decay Channel at ATLAS 237
C.1 Event Selection . . . 237
C.2 Performance Studies for PFlow Jets . . . 239
C.2.1 Checks on the Reduced Jet Phase Space . . . 239
C.3 Results . . . 248

D EFT Interpretation in the $H \to ZZ^* \to 4\ell$ Decay Channel at ATLAS 249
D.1 Generated BSM Signal Samples . . . 249
D.2 Particle-level Production Processes . . . 252
D.2.1 gg2H Production . . . 252
D.2.2 qq2Hqq Production . . . 253
D.2.3 VH Production . . . 256
D.2.4 ttH+tH Production . . . 257
D.2.5 Validation of the Production Cross-Section Parameterization . . . 259
D.3 Generated BSM Samples for the Acceptance Parameterization . . . 261
D.3.1 gg2H Production . . . 261
D.3.2 qq2Hqq Production . . . 262
D.4 Projections of the $\mathcal{CP}$-Odd Signal Model . . . 265
D.5 EFT Parameterization with $\mathcal{CP}$-Even Operators . . . 271
D.5.1 The Complete EFT Signal Model . . . 271
D.5.2 Projections of the $\mathcal{CP}$-Even Signal Model . . . 272
D.6 Systematic Uncertainties . . . 280
D.6.1 QCD Scale Variations . . . 280
D.6.2 PDF Variations . . . 282

E Indirect Constraints on Possible $\mathcal{CP}$ Admixtures from Rate Measurements 285
E.1 Constraints on $\mathcal{CP}$-Mixing in the Top-Yukawa Coupling . . . 285
E.2 Constraints from Global Fits . . . 286
E.3 Model II . . . 286
E.4 Model III and Model IV . . . 289
E.5 Constraints from the $H \to 4\ell$ Decay Channel at ATLAS . . . 292

List of Figures 295

List of Tables 301

Acknowledgements 303

CHAPTER 1

Introduction

Over the course of the 20th century, particle physics unraveled many mysteries about the fundamental building blocks of nature and their interactions. All known matter is composed of elementary particles interacting via four fundamental forces. With the exception of gravity, the relations between the interactions and the constituents of matter are described by the Standard Model (SM) of elementary particles. Its current formulation has been finalized in the mid-1970s, and it has demonstrated ever since huge successes in describing experimental findings in particle physics. Until recently, the Higgs boson was the last missing particle predicted by the SM [1–3]. It is the quantum manifestation of the Higgs field – a scalar field with a non-zero constant value in vacuum – and it arises as a consequence of *electroweak symmetry breaking* (EWSB) via the so-called *Higgs mechanism*. This mechanism gives mass to the weak vector bosons and fermions without violating the gauge invariance of the electroweak symmetry.

Despite its tremendous success, the SM is not a complete theory of nature since it does not incorporate gravity. In addition, some evident shortcomings, like the lack of a suitable dark matter candidate, provide very strong hints that the SM is only an approximation of a more profound underlying theory and will not successfully describe phenomena at the highest energies. Moreover, the amount of $\mathcal{CP}$[1] violation provided by the SM is too small to explain the observed baryon asymmetry of the universe (BAU).

In 2012, the ATLAS and CMS collaborations at the Large Hadron Collider (LHC) discovered a new spin-0 particle with a mass of about 125 GeV [4, 5]. The observed particle is electrically neutral, and its $\mathcal{CP}$ quantum numbers are – within the current theoretical and experimental uncertainties – compatible with the SM Higgs boson. However, while no conclusive signs for beyond the SM (BSM) physics have been found so far at the LHC, the properties of the observed particle are also consistent with the predictions of a large variety of alternative theories of EWSB.

Many BSM theories that provide solutions to some of the SM shortcomings have been proposed. Alternative models of EWSB typically feature new particles at the electroweak scale in reach of current collider experiments. For instance, additional Higgs states may be present in models with extended Higgs sectors. In addition, they may also provide a new source of $\mathcal{CP}$ violation, which might help to explain the BAU. If the parameters of the scalar potential lead to a mixing of $\mathcal{CP}$-even and $\mathcal{CP}$-odd eigenstates, the resulting Higgs mass eigenstate will feature $\mathcal{CP}$-violating couplings. One prominent example describing this scenario is the *two-Higgs-doublet model* (2HDM).

Precision measurements of the Higgs boson couplings are essential to test the nature of EWSB. The observation of deviations from the SM prediction would be an indication of new physics and might hint at an extended Higgs sector. Since the uncertainties on the measured Higgs boson couplings and $\mathcal{CP}$ quantum numbers are still large, small $\mathcal{CP}$-even or $\mathcal{CP}$-odd admixtures to the SM Higgs boson, and general $\mathcal{CP}$-mixed states with sizable $\mathcal{CP}$-odd components are still possible. Currently, the strongest

[1] $\mathcal{CP}$ is the combination of the C-symmetry (charge conjugation) and $\mathcal{P}$-symmetry (parity). If $\mathcal{CP}$ is conserved, the laws of physics do not change if a particle is interchanged with its antiparticle (C), while its spatial coordinates are inverted ($\mathcal{P}$).

constraints on $\mathcal{CP}$-violating Yukawa couplings are obtained from electric dipole moments (EDMs). However, these are typically only valid in the context of specific BSM models and will become less severe or even evaporate in more general models.

The $\mathcal{CP}$ quantum numbers of a spin-0 particle can be probed either *directly* by constructing a $\mathcal{CP}$-odd observable or *indirectly* by fitting a $\mathcal{CP}$-violating model to a $\mathcal{CP}$-even observable. In this thesis, the latter approach is used to investigate scope of possible $\mathcal{CP}$ violation in the Higgs sector. For this purpose, several Higgs boson interpretation frameworks and models with different complexity are explored.

Structure of this Thesis

In Chapter 2, the theoretical basis for the studies presented in this thesis is provided. First, a brief overview of the SM with particular emphasis on the Higgs sector is given. This is followed by the discussion of several shortcomings of the SM. Some of them can be resolved in SM extensions. The Higgs boson phenomenology in two well-motivated BSM theories, the 2HDM and the minimal supersymmetric extension of the SM (MSSM) is discussed in detail. In addition, different Higgs boson interpretation frameworks for probing deviations from the SM Higgs boson are presented.

The LHC accelerator complex and the ATLAS experiment are described in Chapter 3. The sub-systems of the ATLAS detector and the methods to reconstruct the various particles are discussed. In addition, an improved energy reconstruction of hadronically decaying tau leptons in the $H \to \tau\tau$ decay channel at ATLAS is presented.

The basic concepts of the public computer code `HiggsSignals` and its latest developments are discussed in Chapter 4. Moreover, several performance tests of `HiggsSignals` using different Run-1 and Run-2 Higgs signal measurements – provided by ATLAS and CMS – are presented.

Chapter 5 describes the Higgs boson cross-section measurement in the $H \to ZZ^* \to 4\ell$ decay channel at ATLAS with an integrated luminosity of 139 fb^{-1} of proton-proton collisions at a center-of-mass energy of 13 TeV. It covers all essential steps from the relevant signal and background processes to the statistical treatment of the measurement.

Chapter 6 presents the measurement of the tensor structure of the Higgs boson couplings to weak vector bosons, gluons, and top quarks. The cross-sections are measured in exclusive regions of phase space, and the results are interpreted in terms of $\mathcal{CP}$-even and $\mathcal{CP}$-odd BSM coupling parameters within the Standard Model Effective Field Theory (SMEFT). This is done by parameterizing the production cross-sections, the $H \to 4\ell$ decay branching ratio, and the detector acceptance in terms of BSM coupling parameters on particle level.

Chapter 7 encompasses different studies probing the allowed scope of possible $\mathcal{CP}$-mixing in the Higgs sector. The studies presented in the first two sections are performed with `HiggsSignals` using all relevant inclusive and differential Higgs boson measurements provided by the ATLAS and CMS collaborations. The first study targets the $\mathcal{CP}$ nature of the top-Yukawa interaction, while the second one constraints the size of a general $\mathcal{CP}$ admixture in the context of 2HDM-type models. In addition, the same model is probed in the context of the $H \to ZZ^* \to 4\ell$ decay channel at ATLAS. The corresponding studies are presented in the third section of this chapter.

The results and conclusions of this thesis are summarized in Chapter 8.

CHAPTER 2

Theory

The Standard Model (SM) of particle physics [6–9] classifies all known elementary particles and describes three of the four known fundamental forces. It is a quantum field theory (QFT) based on $\mathrm{SU}(3)_c \otimes \mathrm{SU}(2)_L \otimes \mathrm{U}(1)_Y$ gauge invariance that describes the strong, weak, and electromagnetic interactions among a set of particles. Within this theory, each interaction has an associated particle, the force carrier, and both the particles and the force carriers are described in terms of fields. The fourth fundamental force, gravity, is not included in the SM. It is by far the weakest interaction, and it is best described by the classical theory of General Relativity [10]. The SM is the result of many ingenious contributions with a special emphasis on the works of Glashow [11], Weinberg [12], and Salam [13], which provided an approach for unifying the weak and electromagnetic interaction into one force called the electroweak interaction. Up to now, nearly all experimental results obtained in collider experiments and, more generally, most of the high energy data agree with the SM prediction. However, there are a few shortcomings, like the absence of neutrino oscillations in the basic theory and the hierarchy problem of the Higgs mass. Due to these shortcomings, it is generally believed to be a low-energy approximation, also called an effective field theory (EFT), of a more profound underlying theory.

This chapter presents the theoretical basis for the studies performed in this thesis. Section 2.1 provides an introduction to the SM and a short overview of its foundations, features, and shortcomings. A special emphasis is laid on the Higgs mechanism and the concept of *electroweak symmetry breaking* (EWSB). A short overview of the Higgs boson phenomenology in some of the beyond the SM (BSM) theories is given in Section 2.2. This is followed by the discussion of current experimental constraints on the $\mathcal{CP}$ nature of the Higgs boson in Section 2.3. The chapter closes off with the presentation of different Higgs boson interpretation frameworks in Section 2.4.2.

2.1 The Standard Model of Particle Physics

All known matter in the universe is made of fundamental building blocks that interact with each other. These building blocks are spin-$1/2$ particles, called *fermions*, while the interactions are mediated by spin-1 particles, called *gauge bosons*. The names of these particles are coined by Paul Dirac to commemorate the contributions of Enrico Fermi and Satyendranath Bose in developing the statistical models that describe the behavior of fermions [14] and bosons [15], respectively.

The particle content of the SM and some of the particles' properties are summarized in Figure 2.1. Fermions are grouped into three generations with increasing mass from the first to the third generation. Each generation consists of a pair of up-type and down-type quarks and a pair of leptons. All quarks carry color charge and participate in the strong interaction. The up-type (down-type) quarks have electromagnetic charge $+2/3$ ($-1/3$) and a weak isospin of $+1/2$ ($-1/2$). Thus, they also take part in the electromagnetic and weak interactions. However, the latter statement is only true for left-chiral and not for

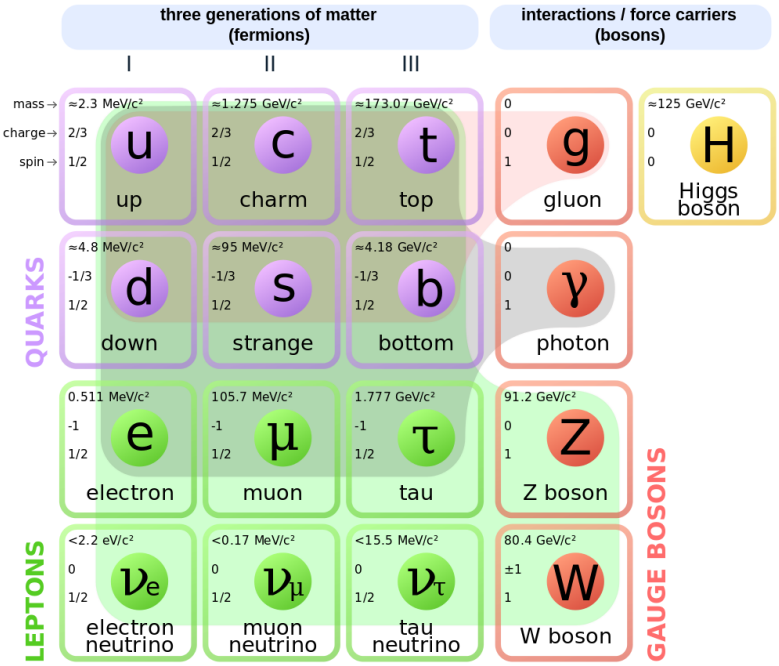

Figure 2.1: The particle content of the SM grouped into fermions (leptons and quarks) and bosons. The overview provides the mass, electric charge, and spin of each fundamental particle in the SM and highlights the interactions they participate in. Modified version of Reference [16].

right-chiral components. The lepton pair consists of an electromagnetically charged (-1) lepton with weak isospin $-1/2$ and a neutral neutrino with isospin $+1/2$. Only the former participates in the electromagnetic interaction. Due to their weak isospin, all left-chiral leptons interact weakly. Since leptons do not carry color charge, they don't interact via strong interaction. The individual generations are shown in the first three columns of Figure 2.1. While the stable matter is made out of the first-generation particles, their heavier counterparts have to be produced in high-energy experiments and are short-lived. Each fermion has a corresponding antifermion with the same mass but opposite electric charge and parity (not shown).

The force carriers are summarized in the fourth column. The strongest known fundamental interaction, called the strong interaction, is described by the theory of *quantum chromodynamics* (QCD) [17–21] and mediated by eight spin-1 gauge fields in the adjoint representation called gluons (g). Gluons carry combinations of color quantum numbers that allow them to interact with each other. The second strongest force is the electromagnetic interaction. It is described by *quantum electrodynamics* (QED) and mediated by the photon (γ), which does not carry electromagnetic charge itself. Thus, there is no self-interaction of the photon. The weakest fundamental force described by the SM is called the weak interaction. It is mediated by two electrically charged and one neutral boson, called $W^{\pm}$ and Z. While the latter acts on all fermionic particles, the former are restricted to left-chiral components. In contrast to the gluon and the photon, which are both massless, the force carriers of the weak interaction are massive.

The most recently discovered particle of the SM is the Higgs boson. It is colorless, electrically neutral, and the only known fundamental scalar (spin-0) particle. It was discovered in 2012 by the ATLAS [4] and CMS [5] collaborations at the Large Hadron Collider (LHC) almost 50 years after its prediction in 1964 by Françoise Englert, Robert Brout [1] and Peter Higgs [2, 3]. It plays an important role in the understanding of electroweak gauge symmetry breaking, which introduces masses for the weak gauge bosons and the charged fermions.

In the SM, fermionic particles are described by fields Ψ with field components Ψ_μ. Their kinematics are determined by the Lagrangian density $\mathcal{L}$, which is constructed from kinetic and potential energies, and obey the Euler-Lagrange differential equation

$$\frac{\partial \mathcal{L}}{\partial \Psi} - \partial_\mu \frac{\mathcal{L}}{\partial(\partial_\mu \Psi)} = 0\,, \tag{2.1}$$

where ∂_μ is a short-hand notation for the partial derivative with respect to the coordinate x^μ. The Lagrangian density has to be renormalizable and invariant under local gauge and Poincaré transformations. The requirement that the Lagrangian has to be invariant under local gauge transformations leads to the inclusion of additional gauge fields that couple to the fermion fields. This is a direct result of the gauge principle, which is a procedure to obtain a Lagrangian that is covariant with respect to local transformations. Renormalization is a powerful technique in QFT invented to treat infinities that appear in calculated quantities, typically due to self-interactions. However, even when no infinities occur, the renormalization of masses and fields appearing in the Lagrangian is required.

2.1.1 The Electroweak Interaction

The electroweak theory provides a unified description of the electromagnetic and weak interactions. At low energies, they appear very different from each other. While electromagnetism is associated with the motion of electrically charged particles in electric and magnetic fields, the weak interaction is used to describe radioactive beta decays. In the following, QED and electroweak unification will be discussed.

2.1.1.1 Quantum Electrodynamics (QED)

In classical electrodynamics, the interaction between a charged particle q and an electromagnetic field A_μ is introduced by the principle of *minimal coupling*. This procedure is motivated because it leads to gauge invariance in the equations of motion by replacing the four-momentum p^μ with $p^\mu - qA^\mu$.

The same approach can be used to achieve local gauge invariance in QED. The Lagrangian density for a free charged fermion (Dirac) field is given by

$$\mathcal{L} = i\bar{\Psi}\gamma^\mu \partial_\mu \Psi - m\bar{\Psi}\Psi\,, \tag{2.2}$$

where the partial derivative ∂^μ replaces the classical four-momentum in position representation of quantum mechanics ($p^\mu \rightarrow \hat{p}^\mu = i\partial^\mu$), m is the mass of the Dirac particle, and γ^μ denotes the Dirac γ-matrices. In general, quantum mechanical calculations are independent of global phases $e^{i\theta q}$, i. e. the transformation $\Psi(x) \rightarrow e^{i\theta q}\Psi(x)$ does not change the free Lagrangian. However, the symmetry group of the electromagnetic interaction, called $\mathrm{U}(1)_Q$, does not consist of global but local phase transformations $\Psi(x) \rightarrow e^{i\theta(x)q}\Psi(x)$. Such transformations are not a symmetry of the free Lagrangian as they change the kinematic term. The invariance is established by minimal coupling, i. e. by replacing the derivative with the so-called *covariant derivative*

$$\partial_\mu \rightarrow D_\mu = \partial_\mu + iqA_\mu\,. \tag{2.3}$$

The gauge field A_μ now represents the quantum version of the electromagnetic field. It can be identified with the photon, and it transforms as $A_\mu \rightarrow A_\mu - \partial_\mu \theta$. The resulting Lagrange density of QED reads

$$\mathcal{L}_{QED} = i\bar{\Psi}\gamma^\mu D_\mu \Psi - m\bar{\Psi}\Psi - \frac{1}{4}F^{\mu\nu}F_{\mu\nu}\,. \tag{2.4}$$

$F_{\mu\nu} = \partial_\mu A_\nu - \partial_\nu A_\mu$ is called the *field strength tensor*.

QED was the first QFT and served as a template for all subsequent quantum field theories like QCD. Some of its early successes were the explanation of the Lamb shift [22] and the accurate prediction of the anomalous magnetic moment of the electron a_e [23]. Nowadays, a_e has been calculated up to order α^5 [24–26], with $\alpha \approx 1/137$ being the fine structure constant. However, this value only represents the asymptotic limit of the fine structure constant at zero energy. At larger energies, its effective value increases. For instance, at the mass of the Z boson ($m_Z \approx 90\,\text{GeV}$), it is $\alpha(m_Z) \approx 1/127$. This behavior is called *the running of the coupling constant*. The dependence of the coupling constant α on the renormalization scale μ is encoded in the β-function $\beta(\alpha) = \mu\partial\alpha/\partial\mu$. Note that it only depends implicitly on μ (through α). The positive sign in the beta function of QED,

$$\beta(\alpha) = +\frac{2\alpha^2}{3\pi} + O(\alpha^3)\,, \tag{2.5}$$

implies that the coupling increases with increasing energy scale. Given that the coupling constant is known at the scale μ^2, its value at a different scale q^2 can be calculated via [27]

$$\alpha(q^2) = \frac{\alpha(\mu^2)}{1 - \frac{\alpha(\mu^2)}{3\pi}\ln\left(\frac{q^2}{\mu^2}\right)}\,. \tag{2.6}$$

2.1.1.2 Electroweak Unification

Shortly after the discovery of radioactive decays by Antoine Henri Becquerel in 1896 [28, 29] it became clear that the newly discovered processes, called alpha and beta decays, involve transmutation of one element to another [30]. While George Gamow [31] explained alpha decays by quantum mechanical tunneling through a Coulomb barrier in the nucleus, beta decays could not be explained by means of the electromagnetic interaction. Enrico Fermi proposed the first description of beta decay in 1934 [32]. He modeled the neutron decay $n \to pe^-\bar{\nu}_e$ as a four-point fermion interaction involving a contact force with no range. It took another 34 years until the underlying interaction had been fully described by the Glashow-Weinberg-Salam (GWS) theory [11–13]. This theory explains the electromagnetic and the weak interactions as two aspects of a single force called the *electroweak interaction*. Despite its simplicity, Fermi's four-fermion theory describes the weak interaction remarkably well at low energies. This is related to the fact that it represents a low energy approximation of the weak interaction and can be derived using the machinery of effective field theories as shown in Section 2.4.2 for educative purposes.

The GWS theory is a Yang-Mills theory [33] based on the $\mathrm{SU}(2)_L \otimes \mathrm{U}(1)_Y$ gauge group. The conserved charge of the $\mathrm{U}(1)_Y$ symmetry is the hypercharge Y, which is related to the electric charge Q and the third component of the weak isospin T_3 of a particle via

$$Y = 2(Q - T_3)\,. \tag{2.7}$$

Like the photon field in QED, it is connected to a gauge field B^μ. The $\mathrm{SU}(2)_L$ symmetry transformations

$$\Psi_L(x) \to e^{i\boldsymbol{\theta}(x)\cdot\frac{\boldsymbol{\tau}}{2}}\Psi_L(x)\,, \tag{2.8}$$

with $\boldsymbol{\tau}$ being the generators given by the Pauli-Matrices, act on the weak isospin of left-handed chirality eigenstates $\Psi_L(x) = 1/2(1-\gamma^5)\Psi(x)$ of fermions. They form weak isospin doublets with $T_3 = \pm 1/2$. On the other hand, right-handed fermion states $\Psi_R(x) = 1/2(1+\gamma^5)\Psi(x)$ do not participate in the weak interaction and they form singlets with $T_3 = 0$. Due to its more complex gauge structure, the $\mathrm{SU}(2)_L$

Table 2.1: The electroweak multiplets and the quantum numbers of their left- and right-handed components. Listed are the electric charge Q, the third component of the weak isospin T_3 and the weak hypercharge Y of the fermions.

$\mathrm{SU}(2)_L$ eigenstates	quantum number		
	Q	T_3	Y
$\boldsymbol{L}_L = \left[\begin{pmatrix}\nu_{e,L}\\ e_L\end{pmatrix}, \begin{pmatrix}\nu_{\mu,L}\\ \mu_L\end{pmatrix}, \begin{pmatrix}\nu_{\tau,L}\\ \tau_L\end{pmatrix}\right]$	0 -1	$+1/2$ $-1/2$	-1 -1
$\boldsymbol{\ell}_R = \left[e_R, \mu_R, \tau_R\right]$	-1	0	2
$\boldsymbol{Q}_L = \left[\begin{pmatrix}u_L\\ d_L\end{pmatrix}, \begin{pmatrix}c_L\\ s_L\end{pmatrix}, \begin{pmatrix}t_L\\ b_L\end{pmatrix}\right]$	$+2/3$ $-1/3$	$+1/2$ $-1/2$	$+1/3$ $+1/3$
$\boldsymbol{u}_R = \left[u_R, c_R, t_R\right]$	$+2/3$	0	$+4/3$
$\boldsymbol{d}_R = \left[d_R, s_R, b_R\right]$	$-1/3$	0	$-2/3$

symmetry has three gauge bosons W^1, W^2, and W^3, given in the infinitesimal form by

$$W^i_\mu \to W^i_\mu - \partial_\mu \theta^i + g_2 \epsilon^{ijk} W^j_\mu \theta^k \,. \tag{2.9}$$

The gauge coupling of the $\mathrm{SU}(2)_L$ symmetry is given by g_2, and ϵ^{ijk} is the totally antisymmetric tensor. The electroweak quantum numbers of the fermions are summarized in Table 2.1.

Before electroweak symmetry breaking the electroweak Lagrangian for N fermion fields reads

$$\mathcal{L}_{ew} = i \sum_{n=1}^{N} \left(\bar{\Psi}^n_L \gamma^\mu D_{\mu,L} \Psi^n_L + \bar{\Psi}^n_R \gamma^\mu D_{\mu,R} \Psi^n_R \right) - \frac{1}{4} \boldsymbol{W}_{\mu\nu} \cdot \boldsymbol{W}^{\mu\nu} - \frac{1}{4} B_{\mu\nu} B^{\mu\nu} \,, \tag{2.10}$$

where Ψ^n_L (Ψ^n_R) represents a left-handed (right-handed) fermion doublet (singlet) and

$$B_{\mu\nu} = \partial_\mu B_\nu - \partial_\nu B_\mu \qquad \text{and} \qquad W^i_{\mu\nu} = \partial_\mu W^i_\nu - \partial_\nu W^i_\mu + g_2 \epsilon^{ijk} W^j_\mu W^k_\nu \tag{2.11}$$

are the field strength tensors of the $\mathrm{U}(1)_Y$ and $\mathrm{SU}(2)_L$ gauge fields. The operators

$$D_{\mu,L} = \partial_\mu + i g_Y \frac{Y}{2} B_\mu + i g_2 \frac{\boldsymbol{\tau}}{2} \cdot \boldsymbol{W}_\mu \tag{2.12}$$

and

$$D_{\mu,R} = \partial_\mu + i g_Y \frac{Y}{2} B_\mu \tag{2.13}$$

are the covariant derivatives for left-handed and right-handed fields, respectively, and g_Y refers to the coupling constant of the $\mathrm{U}(1)_Y$ symmetry. The non-abelian nature of the $\mathrm{SU}(2)_L$ gauge group introduces triple and quartic self-interactions between the W^i_μ fields. However, the gauge fields introduced so far do not correspond to the observed gauge bosons $W^\pm$, Z, and γ. Moreover, the particles in the electroweak theory are all massless, and invariance under local gauge transformations forbids all mass terms. For instance, any gauge boson mass (GBM) term $\mathcal{L}_{\mathrm{GBM}} = \frac{1}{2} m_B^2 B_\mu B^\mu$ and Dirac fermion mass (DFM) term $\mathcal{L}_{\mathrm{DFM}} = -m_\Psi \bar{\Psi}\Psi$ would break the $\mathrm{SU}(2)_L \otimes \mathrm{U}(1)_Y$ gauge symmetries. However, it is an experimental fact that fermions and weak gauge bosons are massive [34, 35]. This can be reconciled without *violating* the $\mathrm{SU}(2)_L \otimes \mathrm{U}(1)_Y$ gauge invariance by spontaneous breaking of the electroweak symmetry as demonstrated in Section 2.1.3.

2.1.2 The Strong Interaction

Although Gamow was able to explain the alpha decay, the nature of the attractive force that holds the nucleus together in the first place was unknown at that time. In 1935 Hideki Yukawa suggested that the nucleons are bound together by a "strong force" mediated by a new massive boson of about 100 GeV [36], which he called the *meson*. Twelve years later, the pi meson (pion) was discovered in cosmic rays [37]. It has a mass of approximately 140 GeV, comes in three states, and fulfills the criteria of the proposed force carrier. However, shortly after the discovery of the pions, four new mesons with about 500 GeV, called *kaons*, were discovered [38]. They also carry this "strong force" and decay into nucleons and pions. In addition, at the same time, new nucleon-like particles, called *baryons*, were discovered [39, 40].

Until the late 1960s, an extensive amount of particles had been discovered, and all these particles have been believed to be fundamental in their own right ("particle zoo"). In 1964, it was proposed that they were actually composites of a few elementary particles [21, 41]. By introducing their eightfold way [42], Murray Gell-Mann and Juval Ne'eman could relate the zoo of particles to three underlying quarks, as they called them. For example, the proton consists of two up and one down quark and the neutron of one up and two down quarks. It was clear that a powerful force is required to bind these quarks. Strong enough that even its residual – the nuclear force – can bind protons and neutrons together, hence the name *strong interaction*. From experimental observations, it is concluded that the quarks can take on three different charges under the strong interaction [43] called "red" (r), "green" (g), and "blue" (b).

The strong interaction is described by QCD [17] and invariant under $\mathrm{SU}(3)_c$ gauge transformations. The index c in the name of the (non-abelian) gauge group refers to the above-mentioned color charge. It comes with eight generators, $\lambda^{1,\dots,8}$, given by the Gell-Mann matrices in the fundamental representation and hence eight gluon fields $G_\mu^{1,\dots,8}$. The Lagrangian for N quark fields q^n ($n = 1, \dots, N$) is given by

$$\mathcal{L}_{\mathrm{QCD}} = i \sum_{n=1}^{N} \bar{q}^n \gamma^\mu D_\mu q^n - \frac{1}{4} \boldsymbol{G}_{\mu\nu} \cdot \boldsymbol{G}^{\mu\nu} \,, \tag{2.14}$$

with the covariant derivative and the gluon field strength tensor being

$$D_\mu = \partial_\mu + i g_s \frac{\lambda^a}{2} G_\mu^a \qquad \text{and} \qquad G_{\mu\nu}^a = \partial_\mu G_\nu^a - \partial_\nu G_\mu^a + g_s f^{abc} G_\mu^b G_\nu^c \,, \tag{2.15}$$

respectively, and g_s is the coupling strength of the strong interaction. $\mathcal{L}_{\mathrm{QCD}}$ is invariant under the $\mathrm{SU}(3)_c$ symmetry transformations

$$q(x) \to e^{i\boldsymbol{\theta}(x)\cdot\frac{\boldsymbol{\lambda}}{2}} q(x) \,, \tag{2.16}$$

and the infinitesimal form of the gauge fields G_μ^a is given by

$$G_\mu^a \to G_\mu^a - \partial_\mu \theta^a + g_s f^{abc} G_\mu^b \theta^c \,, \tag{2.17}$$

where f^{abc} refers to the structure constants of the Lie algebra

$$\left[\lambda^a, \lambda^b\right] = i f^{abc} \lambda^c \,. \tag{2.18}$$

Note that while quarks transform as triplets under the $\mathrm{SU}(3)_c$ group, leptons transform as singlets, i. e. they do not interact via strong interaction. This avoids the appearance of chiral anomalies and preserves the renormalizability of the electroweak theory [44].

Since gluons carry color charge, they interact among themselves allowing for three- and four-point

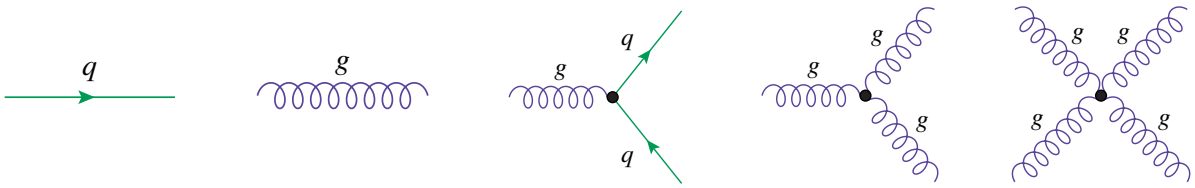

(a) "$\bar{q}q$" (b) "G^2" (c) g_s"$\bar{q}qG$" (d) g_s"G^3" (e) g_s^2"G^4"

Figure 2.2: The Feynman diagrams for the terms in the simplified QCD Lagrangian illustrating (a) the propagation of quarks and (b) gluons, (c) the gluon-quark coupling, (d) the triple and (e) the quartic gluon self-coupling.

self-interactions. This may be deduced by considering a simplified version of the QCD Lagrangian:

$$\mathcal{L}_{\text{QCD}}^{(\text{sim})} = \text{"}\bar{q}q\text{"} + \text{"}G^2\text{"} + g_s\text{"}\bar{q}qG\text{"} + g_s\text{"}G^3\text{"} + g_s^2\text{"}G^4\text{"} \tag{2.19}$$

The corresponding Feynman diagrams are shown in Figure 2.2. The first two terms represent the propagation of quarks and gluons, the third one the gluon-quark coupling, and the last two terms the gluon self-couplings. In 1973, David Politzer [19], David Gross, and Frank Wilczek [20] discovered that the gluons' self-coupling leads to asymptotic freedom. This feature describes the fact that the coupling constant of the strong force, α_s, becomes weaker as the energy scale increases. This behavior is opposite to the running coupling in QED and reflected by the negative sign in the beta-function of QCD,

$$\beta(\alpha_s) = -\left(11 - \frac{2}{3}n_f\right)\frac{\alpha_s^2}{2\pi} + O(\alpha_s^3)\,. \tag{2.20}$$

The one-loop approximation for the running of the strong coupling constant is described by [45]

$$\alpha_s(q^2) = \frac{\alpha_s(\mu^2)}{1 + \alpha_s(\mu^2)\frac{11n_c - 2n_f}{12\pi}\ln\left(\frac{q^2}{\mu^2}\right)}\,, \tag{2.21}$$

where n_f refers to the number of quark flavors and n_c to the number of colors.

Despite the gluons being massless, the strong force is very short-ranged (effectively a few femtometers). If two quarks are separated, the self-interaction between gluons leads to an attractive force that increases with the distance between the quarks. Figuratively speaking, the gluon field lines are squeezed into a flux tube with constant energy density. Eventually, the total binding energy surpasses the threshold for quark-antiquark pair production, and the additional particles bind with the separated quarks. Thus, no non-zero color charge state can exist freely, and quarks are confined. In hadron collider experiments, this process is referred to as *hadronization*.

2.1.3 The Higgs Mechanism

Except for QED, none of the above Lagrangians contain any mass terms, since the introduction of explicit mass terms for fermions ($\mathcal{L}_{\text{DFM}}$) and gauge bosons ($\mathcal{L}_{\text{GBM}}$) would break the gauge symmetries. In 1964 Françoise Englert, Robert Brout [1] and Peter Higgs [2, 3] proposed a mechanism which came to be called *the Higgs mechanism* and which explains the non-zero masses by spontaneous breaking of the electroweak symmetry. The term spontaneous refers to the fact that the symmetry is not broken by explicit terms in the Lagrangian, but by the ground state (vacuum) of the theory.

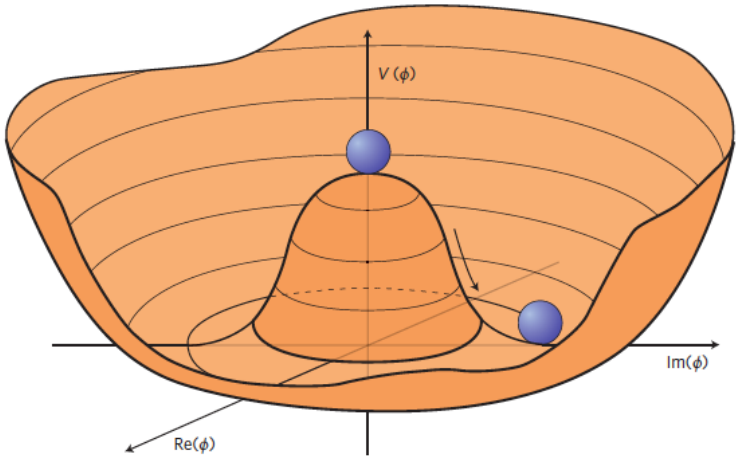

Figure 2.3: Illustration of the Higgs potential $V(\Phi)$ in the case of $\mu^2 < 0$ and $\lambda > 0$. Taken from Reference [46].

In the SM, the Higgs mechanism introduces a complex $\mathrm{SU}(2)_L$ doublet of scalar (i. e. spin-0) fields

$$\Phi = \begin{pmatrix} \phi^+ \\ \phi^0 \end{pmatrix} = \frac{1}{\sqrt{2}} \begin{pmatrix} \phi_1 + i\phi_2 \\ \phi_3 + i\phi_4 \end{pmatrix} \quad \text{with hypercharge} \quad Y = +1\,. \tag{2.22}$$

Note that the doublet's upper component has to have an electric charge +1 and the lower component has to be neutral to fulfill the hypercharge requirement of $Y = +1$. The SM Lagrangian, which so far consists of the electroweak and QCD terms, $\mathcal{L}_{\mathrm{ew}}$ (Equation 2.10) and $\mathcal{L}_{\mathrm{QCD}}$ (Equation 2.14), respectively, needs to be extended by the gauge-invariant terms of the scalar field

$$\mathcal{L}_{\mathrm{scalar}} = (D_L^\mu \Phi)^\dagger (D_{\mu,L} \Phi) - V(\Phi)\,. \tag{2.23}$$

The covariant derivative is given by Equation 2.12 and the scalar potential by

$$V(\Phi) = \mu^2 \Phi^\dagger \Phi + \lambda (\Phi^\dagger \Phi)^2, \qquad (\mu, \lambda \in \mathbb{R})\,. \tag{2.24}$$

According to the general model of the Big Bang, right after the creation of the universe, the Higgs field started in the origin of the "Mexican hat" potential depicted in Figure 2.3. The form of this potential corresponds to $\mu^2 < 0$ and $\lambda > 0$, and it features an infinite number of degenerate states with minimum energy satisfying $|\Phi|^2 = -\mu^2/2\lambda$. About one microsecond after the Big Bang, the universe cooled down far enough and underwent a phase transition that broke the electroweak $\mathrm{SU}(2)_L \otimes \mathrm{U}(1)_Y$ symmetry into the two distinct forces observed today. This process, called *electroweak symmetry breaking* (EWSB), corresponds to the ball moving downwards from the center of the Mexican hat and choosing a random position in the valley. Initially, all positions in the valley are equivalent, but choosing one fixes the gauge. Since the potential depends only on the combination $\Phi^\dagger \Phi$, the vacuum state can be arbitrarily chosen,

$$\langle \Phi \rangle = \langle 0 | \Phi | 0 \rangle = \frac{1}{\sqrt{2}} \begin{pmatrix} 0 \\ v \end{pmatrix}\,, \tag{2.25}$$

where $v = (-\mu^2/\lambda)^{1/2}$ is the vacuum expectation value (vev). While the ground state is no longer invariant under $\mathrm{SU}(2)_L \otimes \mathrm{U}(1)_Y$, it preserves the $\mathrm{U}(1)_Q$ gauge group of the electromagnetic interaction. This can be

seen explicitly by considering the infinitesimal versions of the corresponding symmetry transformations:

$$\theta_i \tau_i \langle \Phi \rangle \neq 0 \quad \text{for} \quad i = 1,2,3\,; \quad \theta Y \langle \Phi \rangle \neq 0\,; \quad \theta Q \langle \Phi \rangle = \theta(T_3 + Y/2) \langle \Phi \rangle = 0\,. \tag{2.26}$$

Thus, the $\mathrm{SU}(2)_L \otimes \mathrm{U}(1)_Y$ symmetry is broken, and the existence of one massless gauge boson, the photon, is ensured. Fluctuations around the minimum can be parameterized by introducing four new fields

$$\Phi(x) = e^{\frac{i}{2v}\boldsymbol{\theta}(x)\cdot\boldsymbol{\tau}} \frac{1}{\sqrt{2}} \begin{pmatrix} 0 \\ v + H(x) \end{pmatrix} \approx \frac{1}{2\sqrt{2}} \begin{pmatrix} \theta_2 + i\theta_1 \\ 2(v + H) - i\theta_3 \end{pmatrix}, \tag{2.27}$$

which are referred to as the Higgs boson $H(x)$ and the Goldstone bosons $\theta_{1,2,3}(x)$. The latter are a direct result of the *Goldstone theorem* [47–50] and can be gauged away by the following $\mathrm{SU}(2)_L$ transformation on the scalar, gauge, and matter fields, respectively (Unitary gauge):

$$\Phi \to e^{-\frac{i}{2v}\boldsymbol{\theta}\cdot\boldsymbol{\tau}}\Phi = \frac{1}{\sqrt{2}} \begin{pmatrix} 0 \\ v + H \end{pmatrix}, \quad \boldsymbol{\tau}\cdot\boldsymbol{W_\mu} \to \boldsymbol{\tau}\cdot\boldsymbol{W'_\mu}, \quad L \to e^{-\frac{i}{2v}\boldsymbol{\theta}\cdot\boldsymbol{\tau}} L \tag{2.28}$$

The matter fields $L = L_{iL}, Q_{iL}$, for $i = 1,2,3$, are given in Table 2.1. In this gauge, $\mathcal{L}_{\text{scalar}}$ reads

$$\begin{aligned} \mathcal{L}_{\text{scalar}} =& \frac{1}{2}(\partial_\mu H)(\partial^\mu H) - \lambda v^2 H^2 - \lambda v H^3 - \frac{1}{4}\lambda H^4 + \frac{1}{4}\lambda v^4 \\ &+ \frac{1}{8}\left(v^2 + 2vH + H^2\right)\left[g_2^2 \left|W_\mu^1 - iW_\mu^2\right|^2 + (g_2 W_\mu^3 - g_Y B_\mu)^2\right]. \end{aligned} \tag{2.29}$$

The first two terms in this equation represent the kinetic term and the mass term of the physical Higgs boson, respectively. The Higgs mass is given by $m_H = \sqrt{2\lambda v^2} = \sqrt{-2\mu^2}$. Since μ is not constrained by any SM parameter, there is no a priori prediction for m_H. The third (fourth) term describes the three-point (four-point) self-interaction. The terms in the second row encode the Higgs-gauge boson interactions and the mass terms of the weak gauge bosons. The mass eigenstates of the gauge fields are given by specific linear combinations of the original fields. The charged and neutral weak gauge boson fields are

$$W_\mu^\pm = \frac{1}{\sqrt{2}}\left(W_\mu^1 \mp iW_\mu^2\right) \quad \text{and} \quad Z_\mu = \frac{g_2 W_\mu^3 - g_Y B_\mu}{\sqrt{g_2^2 + g_Y^2}} = \cos\theta_W W_\mu^3 - \sin\theta_W B_\mu\,, \tag{2.30}$$

respectively, while the photon field is given by

$$A_\mu = \frac{g_Y W_\mu^3 + g_2 B_\mu}{\sqrt{g_2^2 + g_Y^2}} = \sin\theta_W W_\mu^3 + \cos\theta_W B_\mu\,. \tag{2.31}$$

In these equations, θ_W describes the weak mixing (or Weinberg) angle. It is defined by

$$\sin\theta_W = \frac{g_Y}{\sqrt{g_2^2 + g_Y^2}} = \frac{e}{g_2} \qquad \text{and} \qquad \cos\theta_W = \frac{g_2}{\sqrt{g_Y^2 + g_2^2}}\,. \tag{2.32}$$

Using these definitions, the second row of $\mathcal{L}_{\text{scalar}}$ (Equation 2.29) becomes

$$\frac{g_2^2 v^2}{4} W_\mu^+ W^{-\mu} + \frac{g_2^2 v^2}{8\cos^2\theta_W} Z_\mu Z^\mu + \left(H^2 + 2Hv\right)\left[\frac{g_2^2}{4} W_\mu^+ W^{-\mu} + \frac{g_2^2 v^2}{8\cos^2\theta_W} Z_\mu Z^\mu\right], \tag{2.33}$$

and the weak gauge boson masses can be identified with

$$m_{W^\pm} = \frac{g_2 v}{2} \qquad \text{and} \qquad m_Z = \frac{g_2 v}{2\cos\theta_W} = \frac{m_{W^\pm}}{\cos\theta_W} \,. \tag{2.34}$$

The mass of the W boson is related to the Fermi constant[1] [54], $G_F = 1.166\times10^{-5}\,\text{GeV}^{-2}$, via $\frac{G_F}{\sqrt{2}} = \frac{g_2^2}{8m_W^2}$. This relation fixes the Higgs vev to

$$v = \frac{1}{\sqrt{2}G_F} \approx 246.2\,\text{GeV} \,. \tag{2.35}$$

To recap, by using the Unitary gauge (Equation 2.28), the three Goldstone bosons have been absorbed by the $W^\pm$ and Z bosons to make them massive. While a massless spin-1 boson has two transverse polarization states if it satisfies the equations of motion (on-shell), a massive one can also be longitudinally polarized. The number of degrees of freedom (ndf) before and after EWSB remains the same. The scalar field Φ features four degrees of freedom, and each of the gauge fields, $W_\mu^{1,2,3}$ and B_μ, features two (transverse polarizations). This amounts to ndf = 12. After EWSB, the physical Higgs field H has one degree of freedom, the $W^\pm$ and Z have three each (two transverse and one longitudinal polarization), and the massless photon field A_μ has two, yielding again ndf = 12.

Beyond that, the same field Φ can generate the masses for charged leptons and down type quarks. However, in order to generate the masses for up-type quarks, a different representation of the field Φ is needed. Since up-type quarks appear in the first component of left-handed weak isospin doublets (in contrast to leptons and down-type quarks), no term of the form $\bar{Q}_{iL}\Phi u_{jR} \propto \bar{d}_{iL}(v+H)u_{jR}$ will generate their masses[2]. The issue can be resolved by choosing a different isospin doublet

$$\widetilde{\Phi} = i\tau_2\Phi^* = \begin{pmatrix} \phi^{0*} \\ -\phi^- \end{pmatrix} \qquad \text{with hypercharge} \quad Y = -1 \,. \tag{2.36}$$

The gauge-invariant coupling terms between the scalar and Dirac fields are given by the *Yukawa Lagrangian*

$$\mathcal{L}_{\text{Yukawa}} = -Y_{ij}^{(l)}\bar{L}_{iL}\Phi\ell_{jR} - Y_{ij}^{(d)}\bar{Q}_{iL}\Phi d_{jR} - Y_{ij}^{(u)}\bar{Q}_{iL}\widetilde{\Phi}u_{jR} + \text{h. c.}\,, \tag{2.37}$$

where $Y_{ij}^{(f)}$ are 3×3 complex matrices encoding the so-called *Yukawa couplings* for leptons ($f = \ell$), down-type ($f = d$) and up-type ($f = u$) quarks. After EWSB, the mass terms for up-type quarks will be of the form $\bar{Q}_{iL}\widetilde{\Phi}u_{jR} \propto \bar{u}_{iL}(v+H)u_{jR}$, as anticipated. Using the Unitary gauge (Equation 2.28) again, the Yukawa Lagrangian becomes

$$\mathcal{L}_{\text{Yukawa}} = -\frac{v+H}{\sqrt{2}}\left[Y_{ij}^{(l)}\bar{\ell}_{iL}\ell_{jR} + Y_{ij}^{(d)}\bar{d}_{iL}d_{jR} + Y_{ij}^{(u)}\bar{u}_{iL}u_{jR}\right] + \text{h. c.} \tag{2.38}$$

after EWSB. In this equation the following abbreviations are used:

$$\ell_{iX} = \left[e_X, \mu_X, \tau_X\right], \quad u_{iX} = \left[u_X, c_X, t_X\right], \quad d_{iX} = \left[d_X, s_X, b_X\right] \qquad \text{with} \quad X = L, R \,. \tag{2.39}$$

The masses of the fermions f are proportional to the corresponding Yukawa couplings

$$m_{fi} = \frac{v}{\sqrt{2}}Y_{ii}^{(f)} = \frac{v}{\sqrt{2}}y_{fi}, \,, \tag{2.40}$$

[1] The Fermi constant is determined from precise measurements of the muon lifetime [51–53].

[2] Note that only the ϕ^0 component of the Higgs field acquires a non-zero vev (Equation 2.25) after EWSB.

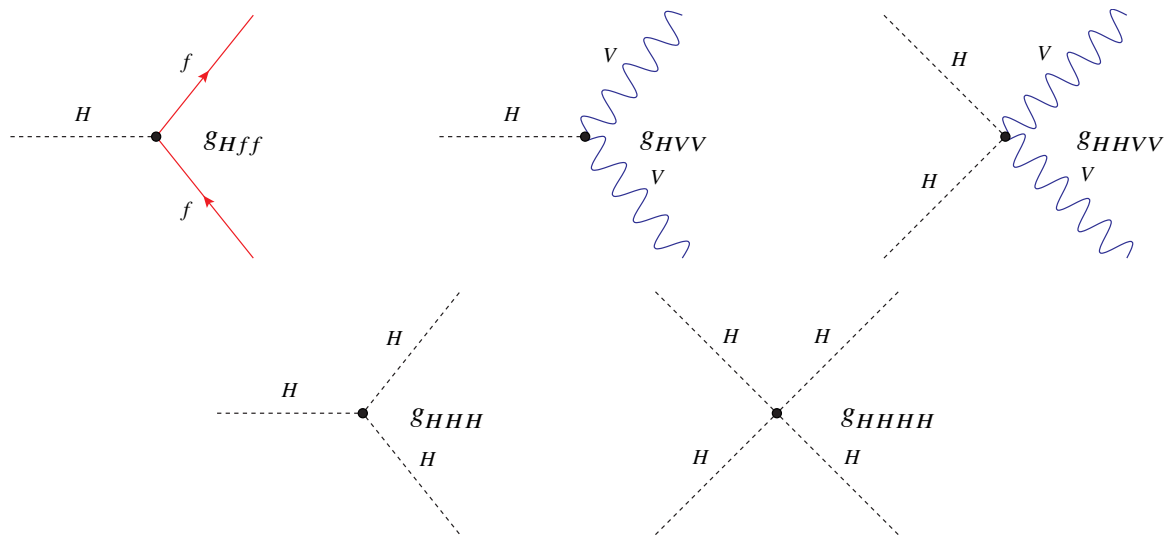

Figure 2.4: The Higgs boson couplings to fermions and gauge bosons, and the Higgs self-couplings in the SM.

and are not predicted by the SM. Here, the short-hand notation $y_{fi} \equiv Y_{ii}^{(f)}$ is introduced.

In its most general form, the Yukawa Lagrangian in Equation 2.37 will also contain mixed terms between different quark flavors. In this case, the fields do not have a well-defined mass. However, by diagonalizing the matrices, it is possible to rewrite them in terms of mixed fields with well-defined mass. This means that the eigenstates of the weak interaction (flavor eigenstates) are different from the mass eigenstates. For quarks, this misalignment is described by the unitary *Cabibbo-Kobayashi-Maskawa* [55, 56] (CKM) mixing matrix, V_{CKM}. It is parameterized by three real angles and one complex $\mathcal{CP}$-violating phase. In the case of massive neutrinos, a similar formulation can be used to describe the lepton sector. The corresponding matrix is called the *Pontecorvo-Maki-Nakagawa-Sakata* [57–59] (PMNS) matrix.

The Feynman diagrams for the Higgs-fermion, Higgs-gauge boson and Higgs self-couplings are depicted in Figure 2.4. The coupling strengths of the former three are

$$g_{Hff} = i\frac{m_f}{v}, \quad g_{HVV} = -2i\frac{m_V^2}{v}, \quad \text{and} \quad g_{HHVV} = -2i\frac{m_V}{v^2}, \tag{2.41}$$

where $V = W^{\pm}, Z$, while the triple and quartic Higgs self-couplings are given by

$$g_{HHH} = 3i\frac{m_H}{v} \quad \text{and} \quad g_{HHHH} = 3i\frac{m_H}{v^2}. \tag{2.42}$$

2.1.4 Higgs Boson Phenomenology in the Standard Model

The SM Higgs boson is a $\mathcal{CP}$-even (i. e. scalar) spin-0 particle ($J^{PC} = 0^{++}$). The $\mathcal{CP}$ quantum numbers describe the behavior of the particle under the combined application of charge conjugation C and parity transformation $\mathcal{P}$. In contrast to a $\mathcal{CP}$-odd (pseudoscalar) eigenstate, the SM Higgs boson does not change its sign under $\mathcal{CP}$ transformations. It is electrically neutral and couples to all massive particles[1].

[1] Neutrinos are excluded from this discussion since they are massless in the SM. However, the appearance of neutrino oscillations proves that they have small masses [60–68] and the upper limit on the sum of their masses is $\sum_i m_{\nu,i} < 0.12\,\text{eV}$ [69] (at 95 % C. L.). In principle, these masses could be related to very small Yukawa couplings $< 10^{-12}$. However, since they are so tiny, some theorists prefer different approaches to explain neutrino masses, like the seesaw mechanism [70–72].

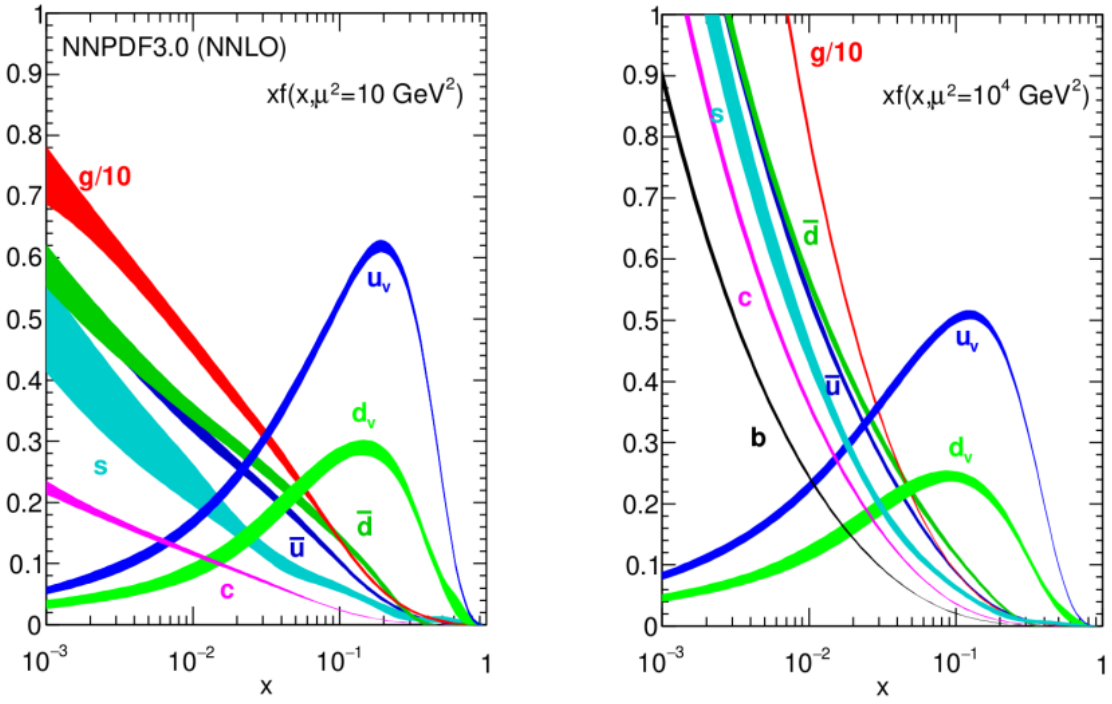

(a) $\mu^2 = 10\,\text{GeV}^2$ (b) $\mu^2 = 10^4\,\text{GeV}^2$

Figure 2.5: The PDFs for valence quarks (u_v, d_v), sea quarks ($\bar{u}$, $\bar{d}$, $s \approx \bar{s}$, $c = \bar{c}$, $b = \bar{b}$) and gluons (g) obtained in the NNLO NNPDF3.0 global analysis with $\alpha_s(M_Z^2) = 0.118$ [73]. Taken from Reference [54].

Within the SM, the Higgs boson mass is not predicted and has to be measured. However, once determined, all parameters in the scalar potential (Equation 2.24) are fixed. In 2012, the ATLAS [4] and the CMS [5] collaborations at the LHC discovered the Higgs boson in the $H \to \gamma\gamma$ and $H \to ZZ^* \to 4\ell$ decay channels. These are also the channels that provide the best mass resolution of about $1 - 2\,\%$. The Higgs boson mass is measured to be $125.10 \pm 0.14\,\text{GeV}$ [54]. Given its mass, the complete phenomenological profile of the SM Higgs boson can be deduced, and its production cross-sections and decay widths are fully determined.

2.1.4.1 Higgs Boson Production in Proton-Proton Collisions

In proton-proton (pp) collisions, only a fraction of the center-of-mass (cms) energy $\sqrt{s}$ is available to the hard scattering process of the proton's constituents called *partons*. Typically only two of the partons are actually colliding, and the other constituents remain relatively unaffected. However, protons do not only consist of the valence quarks, u_v and d_v but instead, they are embedded into a sea of virtual quark-antiquark pairs generated by the gluons which bind the quarks together. The exact structure of the proton depends on the energy scale μ of the collision and the fraction of the protons momentum carried by the struck parton x. The proton structure is described by means of *parton distribution functions* (PDFs) $f(x, \mu^2)$. They are determined from experiment, and two examples for such PDFs are shown in Figure 2.5 for two different energy scales. At large x, the number of partons decreases with μ^2, and the valence quarks dominate. At low x, the sea quarks prevail, and the number of partons increases with μ^2.

Since the SM Higgs boson couples preferentially to heavy particles, it is most likely produced in processes that involve top and bottom quarks, and weak vector bosons. In pp collisions, the main production mechanisms are gluon-gluon fusion (ggF), vector boson fusion (VBF) and the productions in

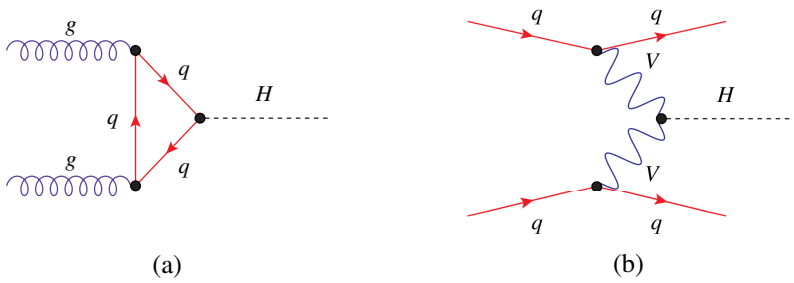

Figure 2.6: The leading-order Feynman diagrams for the SM Higgs boson production in pp collisions via (a) gluon-gluon fusion and (b) vector boson fusion.

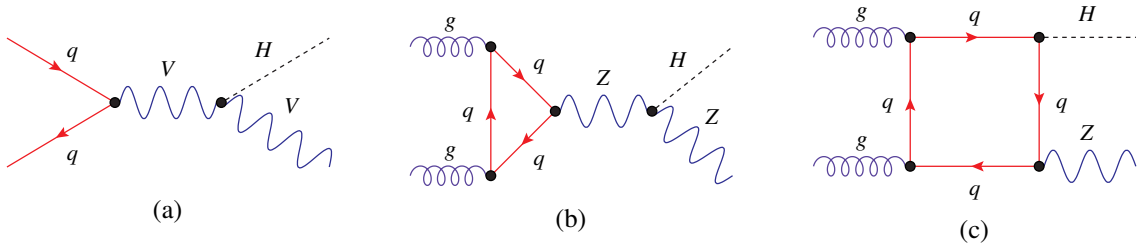

Figure 2.7: Feynman diagrams for the SM Higgs boson production in pp collisions via associated production with a weak gauge boson ($V = W^{\pm}, Z$) (a) at leading order, and (b) and (c) with loop contributions for $gg \rightarrow ZH$.

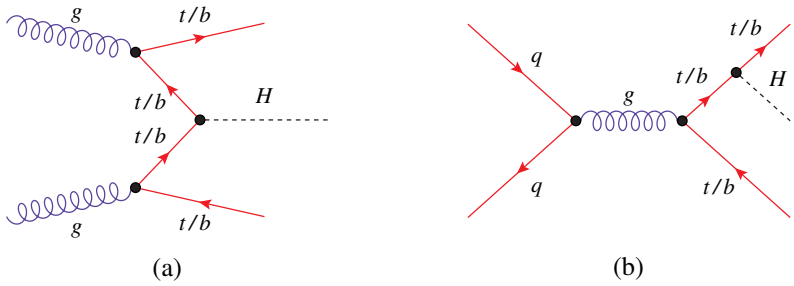

Figure 2.8: The leading-order Feynman diagrams for the SM Higgs boson production via $t\bar{t}H$ and $b\bar{b}H$ production.

association with a $W^{\pm}$ (WH) or Z (ZH) boson, or with a top ($t\bar{t}H$) or bottom ($b\bar{b}H$) quark-antiquark pair.

At the cms energy of $\sqrt{s} = 13\,\text{TeV}$ and for the Higgs boson mass of $m_H = 125\,\text{GeV}$, about 87.2 % of the generated Higgs bosons are created via ggF. Since gluons are massless, they do not couple to the Higgs boson directly. However, an effective Higgs-gluon coupling is possible via intermediate couplings to (preferentially) heavy quarks. The corresponding Feynman diagram for this process is depicted in Figure 2.6(a). The second-largest production mode is VBF with 6.8 %. In this mode, the Higgs bosons are generated by two weak gauge bosons, emitted in the scattering of the incoming quarks. Higgs bosons generated in VBF feature two accompanying jets, which are (mainly) emitted in opposite directions due to the t-channel topology of the process shown in Figure 2.6(b). Jets are narrow cones of hadrons produced by the hadronization of quarks or gluons. A special cut selection on these jets can be used to discriminate the Higgs boson signal from QCD background.

The Higgs strahlung processes, WH and ZH contribute to 4.0 % to the Higgs production cross-section. The LO diagrams are generated by quark-antiquark annihilation, as shown in Figure 2.7(a). In addition, ZH production can also be initiated by ggF via an additional quark loop (see Figures 2.7(b) and 2.7(c)).

Even smaller contributions are from the $t\bar{t}H$ and $b\bar{b}H$ production, depicted in Figure 2.8, accounting for

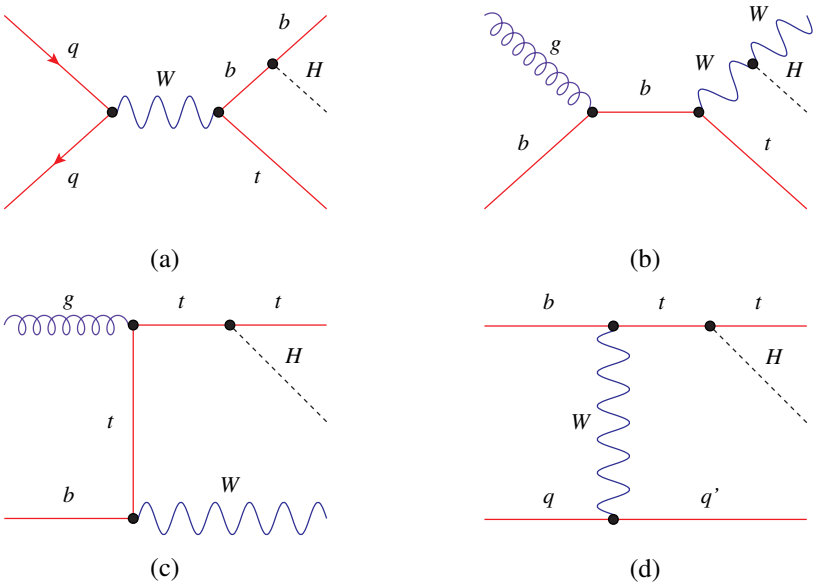

Figure 2.9: The leading-order s- and t-channel diagrams for the SM Higgs boson production via (a) tHb, (b) and (c) tHW, and (d) tHq production.

Table 2.2: The cross-sections (σ) of the dominant SM Higgs boson production modes at $\sqrt{s} = 13\,\text{TeV}$ assuming a Higgs mass of 125 GeV. The quoted theoretical uncertainties are calculated by adding in quadrature the uncertainties due to missing higher-order corrections and the QCD scale (α_s) and PDF uncertainties [74].

Production mode	process	σ [pb]
ggF	$gg \to H$	$48.6\,^{+2.7}_{-3.6}$
VBF	$qq \to Hqq$	$3.78\,^{+0.08}_{-0.08}$
WH	$qq \to WH$	$1.373\,^{+0.028}_{-0.028}$
ZH	$qq/gg \to ZH$	$0.884\,^{+0.036}_{-0.031}$
$t\bar{t}H$	$qq/gg \to t\bar{t}H$	$0.507\,^{+0.035}_{-0.05}$
$b\bar{b}H$	$qq/gg \to b\bar{b}H$	$0.488\,^{+0.099}_{-0.117}$
tH	$qq \to tHq$ (t-channel)	$0.0743\,^{+0.0056}_{-0.0114}$
	$qq \to tHb$ (s-channel)	$0.00288\,^{+0.00009}_{-0.00009}$
	$gb \to tHW$	$0.0152\,^{+0.0012}_{-0.0014}$

0.9 % of the total Higgs production cross-section each. These processes are experimentally challenging due to their low production rates and the large QCD background. However, $t\bar{t}H$ production provides an important means to probe the Yukawa coupling without relying on ggF production. The $b\bar{b}H$ processes are relevant in BSM Higgs searches, where the bottom-Yukawa coupling can be significantly increased. Figure 2.9 shows the contribution from single-top production (tH) with an additional W boson or quark jet in the final state. These processes only contribute about 0.2 % to the Higgs production cross-section.

The Higgs boson production cross-section is a function of the colliding protons' cms energy. This energy dependence is illustrated in Figure 2.10 for the various production modes. For example, the cross-section for producing a SM Higgs boson with $m_H = 125\,\text{GeV}$ at $\sqrt{s} = 13\,\text{TeV}$ is about three times as high as the corresponding cross-section at $\sqrt{s} = 7\,\text{TeV}$. The corresponding numerical values, including their theoretical uncertainties at $\sqrt{s} = 13\,\text{TeV}$ are given in Table 2.2.

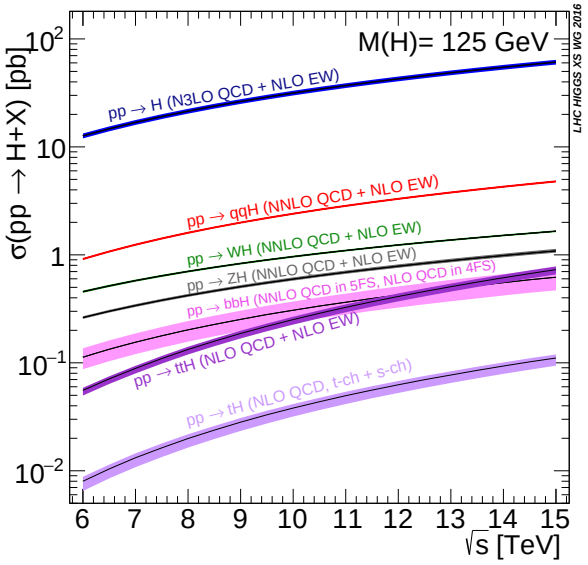

Figure 2.10: The SM Higgs boson production cross-sections for the main production modes in pp collisions as a function of the cms energy. The Higgs boson mass is assumed to be 125 GeV. Taken from Reference [74].

2.1.4.2 Higgs Boson Decays

In the Born approximation, the partial decay widths of the Higgs boson into fermionic final states is given by [75, 76]

$$\Gamma(H \to f\bar{f}) = \frac{G_F n_c}{4\sqrt{2}\pi} m_H m_f^2 \beta_f^3 \,, \tag{2.43}$$

where n_c is the color factor ($n_c = 3$ for quarks and $n_c = 1$ for leptons) and $\beta = (1 - 4m_f^2/m_H^2)^{1/2}$ is the velocity of the fermions in the final state. Note that Equation 2.43 will change in case of a pseudoscalar Higgs boson (see Equation 2.100). The ratio of the partial decay width $\Gamma(H \to X_i)$ into the final state X_i divided by the total width of the Higgs boson Γ_H^{tot} defines the *decay branching ratio*

$$\text{BR}(H \to X_i) = \frac{\Gamma(H \to X_i)}{\Gamma_H^{\text{tot}}} = \frac{\Gamma(H \to X_i)}{\sum_j \Gamma(H \to X_j)} \,. \tag{2.44}$$

The mass dependence of the total width and the decay branching ratios of the Higgs boson is shown in Figure 2.11. The Higgs boson can decay into all massive particles in the SM. Since the coupling increases with the mass of the particle, the dominant decay process for a Higgs boson mass of $m_H = 125$ GeV is into $b\bar{b}$ final states (see Figure 2.11(b)). Despite its large branching ratio of 58.2 %, this decay mode is experimentally challenging due to the large QCD background. This explains why it took more than six years to observe this channel at the LHC [77, 78]. Although the top quark is even heavier than the bottom quark, the decay into $t\bar{t}$ final states violates energy conservation and is therefore not possible. About 21.4 % of the time the Higgs boson decays into WW^*. Note that one of W bosons has to be produced off-shell (W^*) due to the mass constraint $m_H < 2m_W$. This suppresses the matrix element and explains why $H \to WW^*$ is only the second most abundant decay process. Its signature is characterized by two oppositely charged leptons and large missing energy due to the neutrinos in the final state. Note that for a slightly larger Higgs boson mass of about 135 GeV (and above), this would be the dominant decay channel. The Higgs boson's branching ratio into pairs of gluons, tau leptons, charm quarks, and Z bosons make up a couple of percent each. Due to their hadronic nature, decays into gluons and charm quarks are

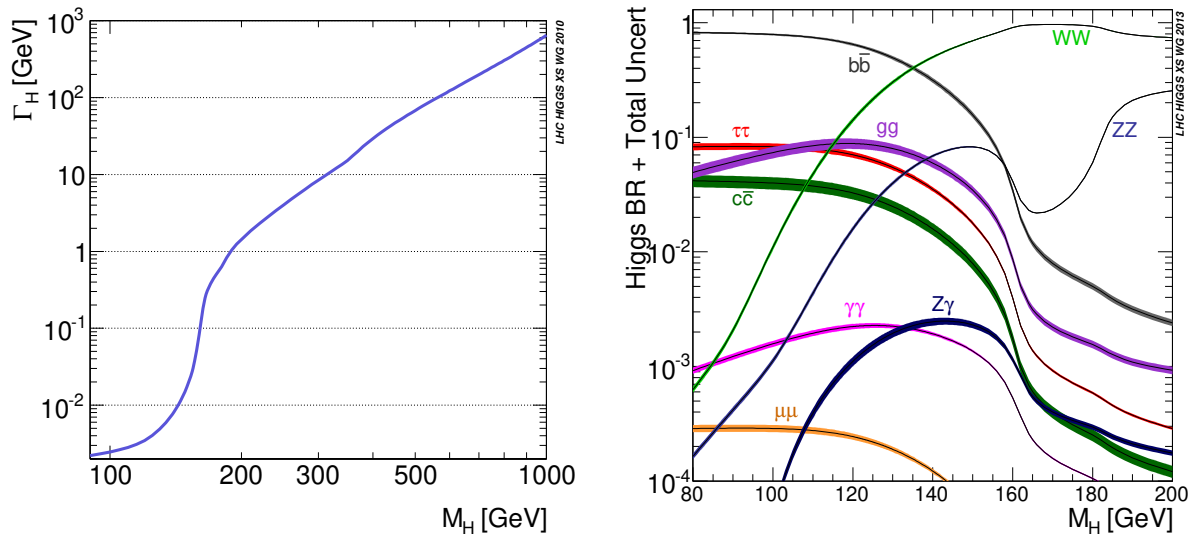

(a) (b)

Figure 2.11: The dependence of (a) the total Higgs boson decay width and (b) the decay branching ratios on the mass of the SM Higgs boson. Taken from Reference [74].

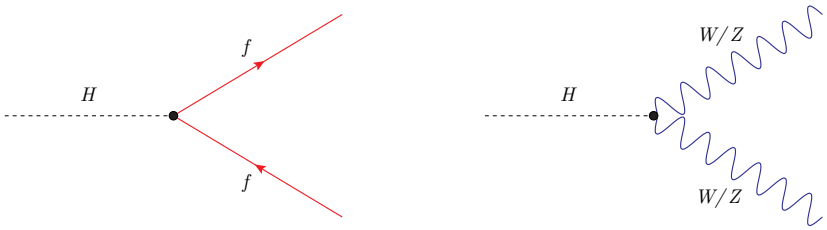

(a) (b)

Figure 2.12: Tree-level Feynman diagrams for the SM Higgs boson decays into (a) fermion-antifermion and (b) weak gauge boson final states.

experimentally inaccessible at the LHC. The smallest contributions to the Higgs boson width are from decays into photon pairs, $Z\gamma$, muon pairs, and lighter quarks like $s\bar{s}$. The largest sensitivity is achieved for decay modes with light leptons ($H \to ZZ^* \to \ell^+\ell^-\ell^+\ell^-$ with $\ell = e, \mu$) and photons ($H \to \gamma\gamma$) in the final state. Since massless particles like photons and gluons do not couple to the Higgs boson directly, the $H \to \gamma\gamma$ and $H \to gg$ decay processes are only possible via heavy-quark loops.

Figures 2.12(a) and 2.12(b) show the tree-level diagrams for Higgs boson decays into fermions and weak gauge bosons, respectively. The loop-induced decays into $\gamma\gamma$ and $Z\gamma$ final states are depicted in Figure 2.13. The branching ratios of the most prominent decay channels for a Higgs boson mass of $m_H = 125\,\text{GeV}$ are given in Table 2.3.

2.1.5 Shortcomings of the Standard Model

The SM is able to successfully explain three of the four known interactions between the fundamental particles and to predict the outcome of particle physics experiments. However, it is inherently an incomplete theory because a couple of phenomena are not (or not correctly) described by the SM. Some of the most prominent examples are:

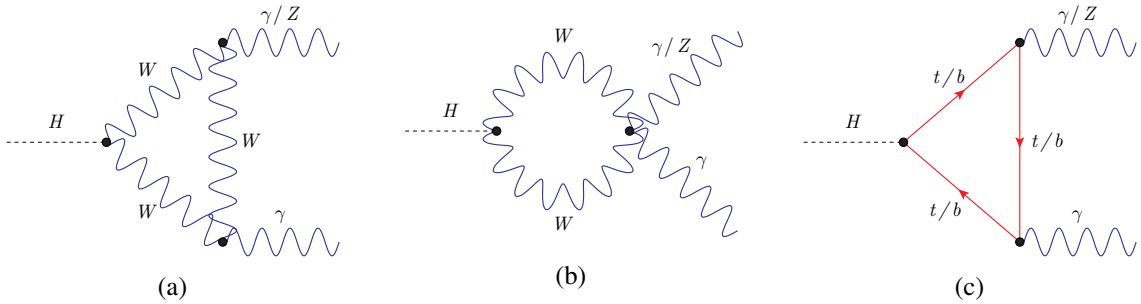

Figure 2.13: Leading-order Feynman diagrams for the SM Higgs boson decays into two photons or a Z boson and a photon via (a) and (b) a W boson, and (c) a heavy quark loop.

Table 2.3: The branching ratios (BR) of the dominant Higgs boson decay modes as predicted by the SM for a Higgs boson mass of 125 GeV. The quoted theoretical uncertainties are calculated by adding in quadrature the uncertainties due to missing higher order corrections and input parameter uncertainties (α_s and m_q with $q = c, b, t$) [74].

Decay mode	decay process	BR [%]
bb	$H \to b\bar{b}$	$58.24\,^{+0.72}_{-0.74}$
WW	$H \to WW$	$21.37\,^{+0.33}_{-0.33}$
gg	$H \to gg$	$8.19\,^{+0.42}_{-0.42}$
$\tau\tau$	$H \to \tau^+\tau^-$	$6.272\,^{+0.103}_{-0.103}$
cc	$H \to c\bar{c}$	$2.891\,^{+0.160}_{-0.058}$
ZZ	$H \to ZZ$	$2.619\,^{+0.041}_{-0.040}$
$\gamma\gamma$	$H \to \gamma\gamma$	$0.2270\,^{+0.0047}_{-0.0047}$
$Z\gamma$	$H \to Z\gamma$	$0.1533\,^{+0.0089}_{-0.0009}$
$\mu\mu$	$H \to \mu^+\mu^-$	$0.02176\,^{+0.0004}_{-0.0004}$

- **Neutrino oscillations**
  Flavor oscillations have been observed in various experiments involving neutrinos from solar, atmospheric, reactor, and fixed-target experiments [62–68, 79]. This observation implies that there is a mass difference among the neutrino generations, indicating that at least two of them are massive [80, 81]. The upper limit on the sum of the neutrino masses is constrained by cosmological observations to $\sum_i m_{\nu_i} < 0.12\,\text{eV}$ [69] (at 95 % C. L.). As demonstrated in Section 2.1.3, the generation of masses for fermions via the Higgs mechanism requires left- and right-handed fields. However, there are no right-handed neutrinos in the SM (see Table 2.1). Even if right-handed neutrinos were added to the theory by hand, the required Yukawa couplings would be tiny. Therefore, different explanations for the neutrino masses like the seesaw mechanism [70–72] or supersymmetric models that allow for lepton number violating operators [82–87] are being discussed.

- **The baryon asymmetry of the universe**
  The observable universe is almost exclusively composed of matter. One of the most promising ways to explain the observed baryon asymmetry of the universe (BAU) is called *electroweak baryogenesis* (EWBG) [88–93]. While many different versions of this mechanism have been proposed, they all satisfy the three *Sakharov conditions* [94]. These are: (1) the existence of a baryon number violating process, (2) thermal disequilibrium, and (3) C- as well as $C\mathcal{P}$ violation.

  In EWBG, the initial state is assumed to be a hot, radiation-dominated universe that fulfills the electroweak gauge symmetry $\text{SU}(2)_L \otimes \text{U}(1)_Y$ and contains equal amounts of left-handed

(right-handed) quarks q_L (q_R) and right-handed (left-handed) antiquarks $\bar{q}_R$ ($\bar{q}_L$). As the universe cooled down, it underwent a phase transition at $T \approx 100\,\text{GeV}$ in which the Higgs field acquired its vev and spontaneously broke the electroweak symmetry. This process also introduces $\mathcal{CP}$ violation in the SM as a single complex phase in the CKM quark mixing matrix. EWSB is assumed to start in small, quickly expanding bubbles with broken phase (in these bubbles, the Higgs field $H(x)$ is already present), while in the surrounding space, the initial symmetry still holds. Chiral quarks that scatter off the moving wall of the Higgs bubble are reflected. If the bubble wall is $\mathcal{CP}$ conserving, the probability for reflecting a left-handed quark into a right-handed quark will be equal to the probability for reflecting a right-handed antiquark into a left-handed antiquark and vice versa,

$$\mathcal{R}(q_L \to q_R) = \mathcal{R}(\bar{q}_R \to \bar{q}_L) \qquad \text{and} \qquad \mathcal{R}(q_R \to q_L) = \mathcal{R}(\bar{q}_L \to \bar{q}_R)\,. \tag{2.45}$$

However, for a $\mathcal{CP}$-violating bubble wall, the probabilities differ by

$$\Delta\mathcal{R}_{\mathcal{CP}} = \mathcal{R}(q_L \to q_R) - \mathcal{R}(\bar{q}_R \to \bar{q}_L) = \mathcal{R}(q_R \to q_L) - \mathcal{R}(\bar{q}_L \to \bar{q}_R) \neq 0\,. \tag{2.46}$$

This leads to asymmetries in the vicinity of the Higgs bubble[1] which are converted into a net baryon number by electroweak sphaleron transitions [96, 97]. Sphalerons have not been confirmed experimentally, and they cannot be represented by perturbative methods such as Feynman diagrams. They are unstable solutions to the electroweak field equations, and they convey transitions from one minimum of the periodic vacuum structure to another. They can act on left-handed fermions and right-handed antifermions, and they violate $B + L$ while conserving $B - L$ [95], where B is the baryon number and L the lepton number. Sphaleron transitions must change B and L by at least three units and by the same amount for each generation, e. g. $\Delta L_e = \Delta L_\mu = \Delta L_\tau = {}^{\Delta B}/_3$. The main contributions are from transition with $\Delta B = \Delta L = \pm 3$, and a possible transition could be

$$\bar{u}_R + \bar{d}_R \to d_L + 2s_L + c_L + 2b_L + t_L + \nu_e + \nu_\mu + \nu_\tau\,. \tag{2.47}$$

The expanding bubble absorbs the increased baryon density, and since sphaleron transitions are strongly suppressed within the bubble, a net baryon number remains.

Although the SM contains the requirements for EWBG, it is not possible to explain the BAU with the SM alone [98]. On the one hand, the measured Higgs mass is too large for EWBG to happen [99, 100], and on the other hand, the $\mathcal{CP}$ violating phase in the CKM matrix is far too small to explain the asymmetry [101–103]. Therefore, any viable realization of the EWBG mechanism has to incorporate BSM physics. Since the $\mathcal{CP}$ nature of the Higgs boson has not been determined with sufficient precision, it is still possible to find $\mathcal{CP}$ violating effects in the Higgs sector. A prominent example that introduces a Higgs $\mathcal{CP}$ admixture is presented in Section 2.2.1.

- **Dark Matter**
  Various astrophysical observations such as the measurement of velocity distributions of spiral galaxies and gravitational lensing caused by galaxy clusters provide evidence that the actual mass of these galaxies is much larger than the cumulated mass of their visible constituents. It is commonly believed that the missing mass is related to non-baryonic and non-luminous matter, called *Dark Matter*[2] (DM). DM does not interact electromagnetically, has no electric charge, and cannot decay

[1] Note that particles in the broken phase transmitted into the symmetric phase also contribute to the asymmetry around the Higgs bubble. The corresponding transmission probabilities are $\mathcal{T}(q_L \to q_L) = 1 - \mathcal{R}(q_R \to q_L) = 1 - \mathcal{R}(\bar{q}_L \to \bar{q}_R) = \mathcal{T}(\bar{q}_L \to \bar{q}_L)$ [95]. The same relation holds for the opposing chiral states, where $L \leftrightarrow R$.

[2] Other approaches like Modified Newtonian Dynamics [104] (MOND), entropic gravity [105] and other suitable modifications

into charged particles or photons since such processes would be detectible as some form of radiation. Interactions with neutral atoms would lead to observable ionization and excitation processes. Thus, DM is believed to mainly interact gravitationally with ordinary matter. Still, elastic interactions with energy transfers far below the excitation levels of atoms, and interactions among the DM particles are possible. While the idea of DM has first been suggested by Jacobus Kapteyn in 1922 [106], the first substantial evidence for unseen mass was provided in 1933 by Fritz Zwicky [107].

The SM does not provide a suitable candidate for DM. Technically, the neutrino is such a candidate, but due to its tiny mass, it is highly relativistic and cannot easily explain the structure formation of galaxies. However, viable candidates are easily found in many SM extensions. A very prominent example is *weakly interacting massive particles* (WIMPs) like the neutralino [108, 109] in supersymmetric models [110]. Other DM candidates are Higgs singlets [111], inert doublets [112], axions [113, 114], lightest Kaluza-Klein states [115–117] and hidden sector particles [118–121]. However, so far, no DM candidate has been experimentally discovered.

- **Dark Energy**
  In addition to the DM content in the universe, observations of Type Ia supernovae suggest the existence of an unidentified form of energy in the universe [122], called *Dark Energy*. This energy is related to the cosmological constant [123] and causes the expansion of the universe to accelerate. The SM prediction for the cosmological constant overestimates this energy by a factor of 10^{120}.

  Measurements of the anisotropies in the *Cosmic Microwave Background* (CMB) have shown that within the current Standard Model of Cosmology, only 5 % of the energy content in the universe is made out of baryonic matter, while 27 % are assigned to Dark Matter and 68 % to Dark Energy [124].

Besides these shortcomings, there are also some features that are technically allowed but unsatisfying from a theoretical point of view:

- **Grand unification and a theory of everything**
  One of the outstanding goals of theoretical physics is the unification of all known forces into one fundamental interaction. In the SM, two of the four interactions – the weak and electromagnetic interactions – are already connected. The true nature of these forces becomes apparent at the electroweak (EW) scale $\Lambda_{\mathrm{EW}} = v \approx 246\,\mathrm{GeV}$ (see Equation 2.35).

  The inclusion of the strong interaction into a common description of the forces is achievable at the energy scale $\Lambda_{\mathrm{GUT}} \approx 10^{16}\,\mathrm{GeV}$ in so-called *Grand Unified Theories* (GUTs) [125–128]. In these kinds of models the SM gauge group $\mathrm{SU}(3)_c \otimes \mathrm{SU}(2)_L \otimes \mathrm{U}(1)_Y$ is embedded in a larger group like SU(5) or SO(10). At the scale Λ_{GUT}, the running couplings of the electroweak and strong interaction converge if non-SM particles are incorporated into the theory. One prominent example that achieves this unification is the *minimal supersymmetric extension of the SM* [129, 130].

  At even higher energies near the *Planck scale* $\Lambda_{\mathrm{P}} \approx 10^{19}\,\mathrm{GeV}$, the strength of the gravitational interaction becomes comparable to the strength of the other forces. It is believed that at this point, a quantum mechanical description of gravity is necessary. However, no successful quantum theory of gravity has been formulated so far. The two most prominent candidates trying to achieve such a description are based on *string theory* [131–134] and *loop quantum gravity* [135–137].

- **The hierarchy problem**
  The *hierarchy problem* is a fine-tuning problem of the Higgs boson mass, and it is one of the most

to the general theory of relativity are competing models to explain the astrophysical observations.

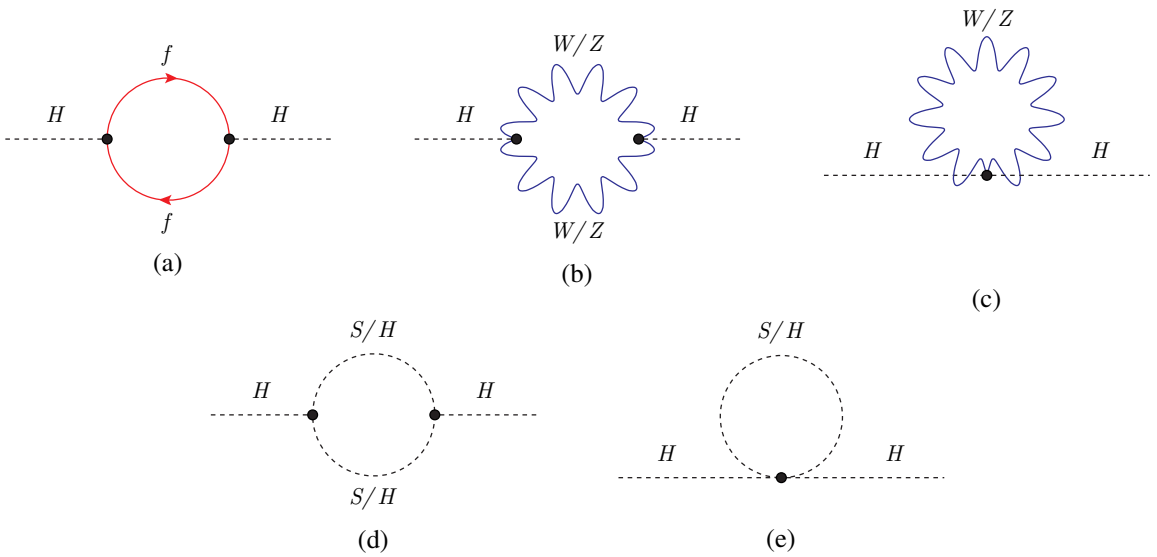

Figure 2.14: Possible one-loop corrections to the Higgs boson mass. Shown are the contributions from (a) fermions f, (b) and (c) heavy gauge bosons $W^{\pm}$ and Z, and (d) and (e) the Higgs boson H and some hypothetical scalar particle S. In the SM, these Feynman diagrams lead to quadratically divergent Higgs mass corrections.

striking theoretical arguments for expecting BSM physics at the TeV scale. The bare mass of the Higgs boson $m_{H,0}$ is subject to radiative corrections that are quadratically divergent. Figure 2.14(a) shows the Feynman diagrams for the one-loop radiative corrections from fermions.

In order to regulate the divergence, an ultraviolet momentum cut-off scale Λ_{UV} is introduced. The corresponding correction of the Higgs boson mass is given by

$$\Delta m_{H,f}^2 = -\frac{y_f^2}{8\pi^2}\left[\Lambda_{\mathrm{UV}}^2 - 6m_f^2 \ln\left(\frac{\Lambda_{\mathrm{UV}}}{m_f}\right) + \ldots\right], \tag{2.48}$$

where y_f (m_f) is the Yukawa coupling (mass) to the fermion f. If the SM was valid up to the Planck scale, the mass correction $\Delta m_{H,f}^2 >> m_{H,0}^2$ would exceed the bare Higgs mass squared by about 30 orders of magnitude. This would have to be countered by an unnatural amount of fine-tuning to keep the renormalized Higgs boson mass at the electroweak scale. Note that while this problem is only demonstrated for fermions, the same problem arises for loop contributions of heavy gauge bosons (Figures 2.14(b) and 2.14(c)) and the Higgs boson self-coupling (Figures 2.14(d) and 2.14(e)) [138].

A possible solution to this fine-tuning problem is provided by Supersymmetry. Consider the coupling terms of a scalar field S to the Higgs field $-\sqrt{2}y_S^{(1)}H|S|^2 - y_S^{(2)}|H|^2|S|^2$. In this case, the one-loop corrections, shown in Figures 2.14(d) and 2.14(e), read

$$\Delta m_{H,S}^2 = \frac{1}{16\pi^2}\left[y_S^{(2)}\Lambda_{\mathrm{UV}}^2 - \left(4(y_S^{(1)})^2 + 2y_S^{(2)}\right) m_S^2 \ln\left(\frac{\Lambda_{\mathrm{UV}}}{m_S}\right) + \ldots\right]. \tag{2.49}$$

SUSY introduces two complex scalar fields for each Dirac fermion[1] and prescribes the relation $y_S^{(2)} = y_f^2$. Thus, the quadratic terms in Equations 2.48 and 2.49 cancel exactly [139]. If SUSY were also *unbroken* by mass (i. e. $m_S = m_f$) and if $y_S^{(1)} = y_f$, the logarithmic divergences would

[1] In order to have the same number of degrees of freedom for the fermions (left-handed and right-handed) and their supersymmetric partners, two scalars have to be introduced per fermion.

cancel as well.

Alternative approaches to solving the hierarchy problem are the introduction of a new force at the TeV scale [140–142] or the existence of large extra dimensions [143–146].

2.2 $\mathcal{CP}$ Violation in Extended Higgs Sectors

As discussed in Section 2.1.5, the BAU cannot be explained with the amount of $\mathcal{CP}$ violation present in the SM. However, many SM extensions introduce additional $\mathcal{CP}$-violating phases, either by explicitly breaking the symmetry in the Lagrangian or by spontaneously breaking it by the ground state of the theory. The observable consequences of $\mathcal{CP}$ violation in the Higgs sector include the mixing of (neutral) Higgs states with even (scalar) and odd (pseudoscalar) $\mathcal{CP}$ symmetry and the existence of $\mathcal{CP}$-violating Higgs interactions.

In any BSM Higgs sector, $\mathcal{CP}$ violating effects will disappear if the potential of the scalar fields and the vevs of the neutral Higgs bosons can be described by real parameters (in some basis). For example, in the simplest SM extensions, a real (xSM) or complex (cxSM) scalar singlet field is added to the SM Higgs sector. Such pure singlet extensions are inherently theories of $\mathcal{CP}$-even scalars. In the case of a complex singlet $\mathbb{S}$, one would naively expect that Im($\mathbb{S}$) describes a pseudoscalar. Consequently, one would assume that mixing it with a scalar like the SM Higgs boson or the singlet's real component would lead to $\mathcal{CP}$ violation. However, singlets do not couple to SM particles, and thus, it is always possible to find a $\mathcal{CP}$ transformation under which both components are $\mathcal{CP}$-even [147, 148]. $\mathcal{CP}$ violation in the cxSM is only possible if additional vector-like fermions are added to the theory[1] [151–154]. In this case, a $\mathcal{CP}$-odd Yukawa coupling can be established if the vector-like fermion couples to Im($\mathbb{S}$).

The simplest SM extension that allows for $\mathcal{CP}$ violation in the Higgs sector is the two-Higgs-doublet model (2HDM) [155–159]. Because of its importance, it will be discussed in detail in Section 2.2.1. A well-motivated theoretical model is the Minimal Supersymmetric extension of the Standard Model (MSSM) [110, 159–161]. The Higgs sector in the MSSM has the form of a 2HDM. The MSSM also introduces new partners for the SM fermions and the SM gauge bosons.

2.2.1 The Two-Higgs-Doublet Model

In the 2HDM, a second $\mathrm{SU}(2)_L$ scalar doublet is added to the SM Higgs sector. In this section, the case of a scalar doublet with hypercharge $Y = +1$ is discussed. However, depending on the Yukawa coupling structure, doublets with negative hypercharge can be required. The most general gauge invariant and renormalizable potential for two $\mathrm{SU}(2)_L$ doublets Φ_1 and Φ_2 is given by [159]

$$\begin{aligned} V(\Phi_1,\Phi_2) =& m_{11}^2\Phi_1^\dagger\Phi_1 + m_{22}^2\Phi_2^\dagger\Phi_2 - \left(m_{12}^2\Phi_1^\dagger\Phi_2 + \text{h. c.}\right) \\ &+ \frac{\lambda_1}{2}(\Phi_1^\dagger\Phi_1)^2 + \frac{\lambda_2}{2}(\Phi_2^\dagger\Phi_2)^2 + \lambda_3(\Phi_1^\dagger\Phi_1)(\Phi_2^\dagger\Phi_2) + \lambda_4(\Phi_1^\dagger\Phi_2)(\Phi_2^\dagger\Phi_1) \\ &+ \left(\frac{\lambda_5}{2}(\Phi_1^\dagger\Phi_2)^2 + \lambda_6(\Phi_1^\dagger\Phi_1)(\Phi_1^\dagger\Phi_2) + \lambda_7(\Phi_1^\dagger\Phi_2)(\Phi_2^\dagger\Phi_2) + \text{h. c.}\right) . \end{aligned} \tag{2.50}$$

The parameters m_{11}^2, m_{22}^2, and $\lambda_1, ...\lambda_4$ are real, while the remaining parameters can be complex. This means that the general 2HDM scalar potential explicitly violates the $\mathcal{CP}$ symmetry. However, the last two terms (containing λ_6 and λ_7) in Equation 2.50 will introduce flavor-changing neutral currents (FCNCs) at

[1] Alternatively, one could also add another doublet in addition to the complex singlet like in the next-to-minimal supersymmetric extension of the SM [149, 150] (NMSSM).

tree level. In the SM, such processes are loop-induced, and thus, very tiny. Due to strong experimental bounds on FCNCs[1] from precision B-physics [163–165] it is reasonable to impose an additional discrete symmetry on the scalar fields to remove those terms. The most frequently used discrete symmetry is a softly broken $\mathbb{Z}_2$ symmetry $\Phi_1 \to \Phi_1$, $\Phi_2 \to -\Phi_2$ which leads to $\lambda_6 = \lambda_7 = 0$. This leaves two complex parameters λ_5 and m_{12}^2 which can have a nontrivial relative phase that allows for explicit $\mathcal{CP}$ violation in the scalar potential[2] [166, 167].

During EWSB, the scalar fields acquire non-zero vevs fulfilling the conditions

$$\left.\frac{\partial V(\Phi_1,\Phi_2)}{\partial \Phi_1}\right|_{\substack{\Phi_1=\langle\Phi_1\rangle\\ \Phi_2=\langle\Phi_2\rangle}} = 0\,, \qquad \left.\frac{\partial V(\Phi_1,\Phi_2)}{\partial \Phi_2}\right|_{\substack{\Phi_1=\langle\Phi_1\rangle\\ \Phi_2=\langle\Phi_2\rangle}} = 0\,. \tag{2.51}$$

By using appropriate $\mathrm{SU}(2)_L$ and $\mathrm{U}(1)_Y$ transformations and requiring that the minimum fulfills the $\mathrm{U}(1)_Q$ gauge symmetry, the vacuum state can be written as

$$\langle\Phi_1\rangle = \langle 0|\Phi_1|0\rangle = \frac{1}{\sqrt{2}}\begin{pmatrix}0\\ v_1\end{pmatrix}\,, \qquad \langle\Phi_2\rangle = \langle 0|\Phi_2|0\rangle = \frac{1}{\sqrt{2}}\begin{pmatrix}0\\ v_2\end{pmatrix}\,, \tag{2.52}$$

where v_1 and v_2 are real and positive parameters satisfying

$$v^2 = v_1^2 + v_2^2 = (246.2\,\mathrm{GeV})^2\,. \tag{2.53}$$

Inserting Equation 2.50 into Equations 2.51 one finds the relations

$$v_2\,\mathrm{Re}(m_{12}^2) = m_{11}^2 v_1 + \frac{\lambda_1}{2}v_1^3 + \frac{\lambda_{345}}{2}v_1 v_2^2\,, \tag{2.54}$$

$$v_1\,\mathrm{Re}(m_{12}^2) = m_{22}^2 v_2 + \frac{\lambda_2}{2}v_2^3 + \frac{\lambda_{345}}{2}v_1^2 v_2\,, \tag{2.55}$$

$$2\,\mathrm{Im}(m_{12}^2) = v_1 v_2\,\mathrm{Im}(\lambda_5)\,, \tag{2.56}$$

where $\lambda_{345} = \lambda_3 + \lambda_4 + \mathrm{Re}(\lambda_5)$. $\mathcal{CP}$ violation is ensured if the phases $\phi(m_{12}^2)$ and $\phi(\lambda_5)$ of the complex parameters

$$m_{12}^2 = |m_{12}^2|e^{i\phi(m_{12}^2)} \quad \text{and} \quad \lambda_5 = |\lambda_5|e^{i\phi(\lambda_5)} \tag{2.57}$$

fulfill the condition [168]

$$\phi(\lambda_5) \neq 2\phi(m_{12}^2)\,. \tag{2.58}$$

Otherwise, it is always possible to rephase one of the Higgs doublets $\Phi \to e^{i\xi}\Phi$ with a phase $\xi = -\phi(m_{12}^2)$ such that only one of the phases remains in Equation 2.56:

$$2|m_{12}^2|\,\mathrm{Im}\left(e^{i\phi(m_{12}^2)}\right) = v_1 v_2 |\lambda_5|\,\mathrm{Im}\left(e^{i\phi(m_{12}^2)}\right)\,. \tag{2.59}$$

Similar to Equation 2.27, the fields can be written in terms of the vacuum and small excitations around the minimum

$$\Phi_1 = \begin{pmatrix}\phi_1^+ + i\theta_1^+\\ \frac{1}{\sqrt{2}}\left(v_1 + \phi_1 + i\eta_1\right)\end{pmatrix}\,, \qquad \Phi_2 = \begin{pmatrix}\phi_2^+ + i\theta_2^+\\ \frac{1}{\sqrt{2}}\left(v_2 + \phi_2 + i\eta_2\right)\end{pmatrix}\,. \tag{2.60}$$

[1] For a review on flavor anomalies reported by BaBar, Belle, CMS and LHCb see Reference [162])

[2] Note that a fully realized $\mathbb{Z}_2$ symmetry leads to $m_{12}^2 = \lambda_6 = \lambda_7 = 0$. Thus, λ_5 is the only complex parameter, and its phase can be removed by rephasing one of the doublets. Moreover, $\mathcal{CP}$ violation cannot even arise spontaneously in this case.

However, there is an important difference. In the SM Higgs mechanism, only one physical degree of freedom remains after the would-be Goldstone bosons have been absorbed by the $W_\mu^{1,2,3}$ fields. In the case of two Higgs doublets, there are eight degrees of freedom, and three of these become Goldstone bosons, $G^\pm$ and G^0, that get absorbed by the electroweak gauge fields. To separate them from the physical degrees of freedom, the fields can be rotated by an angle $\beta = \arctan v_2/v_1$

$$\begin{pmatrix}\mathcal{H}_1\\ \mathcal{H}_2\end{pmatrix} = \begin{pmatrix}\cos\beta & \sin\beta\\ -\sin\beta & \cos\beta\end{pmatrix}\begin{pmatrix}\Phi_1\\ \Phi_2\end{pmatrix}. \tag{2.61}$$

Note that the values of v_1, v_2 and β depend on the basis chosen for Φ_1 and Φ_2. The resulting doublets in the Higgs basis are given by

$$\mathcal{H}_1 = \begin{pmatrix}G^\pm\\ \frac{1}{\sqrt{2}}\left(v + H_1^0 + iG^0\right)\end{pmatrix}, \qquad \mathcal{H}_2 = \begin{pmatrix}H^\pm\\ \frac{1}{\sqrt{2}}\left(H_2^0 + iA\right)\end{pmatrix}. \tag{2.62}$$

Thus, there are five physical degrees of freedom in the Higgs sector. Two of them correspond to charged $\mathcal{CP}$-even fields $H^\pm$, two to neutral $\mathcal{CP}$-even fields H_1^0 and H_2^0, and one to a neutral $\mathcal{CP}$-odd field A. The neutral Higgs mass eigenstates H_i with mass m_i, for $i = 1, 2, 3$, are obtained by rotation of the neutral fields,

$$\begin{pmatrix}H_1\\ H_2\\ H_3\end{pmatrix} = R\begin{pmatrix}H_1^0\\ H_2^0\\ A\end{pmatrix}. \tag{2.63}$$

This diagonalizes the 3×3 mass matrix $\mathcal{M}^2$ in the $\{H_1^0, H_2^0, A\}$ basis via

$$R\mathcal{M}^2R^T = \begin{pmatrix}m_{H_1}^2 & 0 & 0\\ 0 & m_{H_2}^2 & 0\\ 0 & 0 & m_{H_3}^2\end{pmatrix}. \tag{2.64}$$

The Higgs mass eigenstates are by definition ordered as $m_{H_1} \leq m_{H_2} \leq m_{H_3}$. The orthogonal mixing matrix $R = R_3R_2R_1$ describes rotations around three angles $\alpha_i \in (-\pi/2, \pi/2)$. It is given by

$$R = \begin{pmatrix}c_1c_2 & c_2s_1 & s_2\\ -c_3s_1 - c_1s_2s_3 & c_1c_3 - s_1s_2s_3 & c_2s_3\\ -c_1c_3s_2 + s_1s_3 & -c_1s_3 - c_3s_1s_2 & c_2c_3\end{pmatrix}, \tag{2.65}$$

where $s_i = \sin\alpha_i$ and $c_i = \cos\alpha_i$, for $i = 1, 2, 3$, is used. Consequently, the $\mathcal{CP}$ properties of the neutral Higgs sector are indefinite in the general case.

If all $\mathcal{CP}$-violating phases of the 2HDM vanish (see Equation 2.59), only the fields H_1^0 and H_2^0 will mix, while A remains unmixed. This case is called the real ($\mathcal{CP}$-conserving) 2HDM (R2HDM). In the $\mathcal{CP}$-violating 2HDM (C2HDM), Equation 2.58 is satisfied, and the scalar and pseudoscalar states mix.

Since both $\mathrm{SU}(2)_L$ doublets couple to weak gauge bosons and fermions, the 2HDM has a richer coupling structure than the SM. The couplings of H_i to weak gauge bosons $V = W^\pm, Z$ is given by

$$g_{H_iVV} = c_{H_iVV} \cdot g_{H_{\mathrm{SM}}VV}, \quad \text{for} \quad i = 1, 2, 3. \tag{2.66}$$

where $c_{H_iVV} = R_{i1}\cos\beta + R_{i2}\sin\beta$ scales the corresponding SM coupling $g_{H_{\mathrm{SM}}VV}$. Note that this coupling is identical for the R2HDM and the C2HDM since $\mathcal{CP}$-invariance forbids tree-level couplings of

Table 2.4: The effective Yukawa couplings of the Higgs boson H_i to SM fermions in the C2HDM.

$SU(2)_L$	up-type		down-type		leptons	
doublet	$c_f^s(H_i)$	$c_f^p(H_i)$	$c_f^s(H_i)$	$c_f^p(H_i)$	$c_f^s(H_i)$	$c_f^p(H_i)$
Φ_1			$+\frac{R_{i1}}{\cos\beta}$	$-R_{i3}\tan\beta$	$+\frac{R_{i1}}{\cos\beta}$	$-R_{i3}\tan\beta$
Φ_2	$+\frac{R_{i2}}{\sin\beta}$	$-\frac{R_{i3}}{\tan\beta}$	$+\frac{R_{i2}}{\sin\beta}$	$+\frac{R_{i3}}{\tan\beta}$	$+\frac{R_{i2}}{\sin\beta}$	$+\frac{R_{i3}}{\tan\beta}$

the pseudoscalar state A to the massive gauge bosons[1]. However, AVV couplings can be induced through loop corrections of heavy new fields. Since such couplings are expected to be very small, observables that target the H_iVV coupling provide limited sensitivity on a $C\mathcal{P}$-odd field. The Yukawa Lagrangian in the mass basis of the C2HDM has the form

$$\mathcal{L}_{\text{Yukawa}} \supset -\frac{m_f}{2}\bar{f}_L\left[c_f^s(H_i) + ic_f^p(H_i)\gamma_5\right] f_R H_i \,. \tag{2.67}$$

Thus, the effective fermion couplings contain scalar and pseudoscalar parts. The corresponding coefficients for the Higgs mass state H_i are given by $c_f^s(H_i)$ and $c_f^p(H_i)$, respectively. These couplings are the main source of $C\mathcal{P}$ violation in the C2HDM.

The softly broken $\mathbb{Z}_2$ symmetry allows four different realizations of the coupling structure of down-type quarks and leptons to the Higgs doublets. In all of these realizations, the up-type quarks are defined to only couple to Φ_2. The following types of 2HDMs are distinguished:

- Type I: All fermions only couple to Φ_2
- Type II: Down-type quarks and leptons only couple to Φ_1
- Type III: Down-type quarks only couple to Φ_2, while leptons only couple to Φ_1
- Type IV: Down-type quarks only couple to Φ_1, while leptons only couple to Φ_2

The coefficients c_f^s and c_f^p depend on the doublet the fermions couple to. The corresponding couplings are summarized in Table 2.4. Thus, the Yukawa couplings for down-type quarks and leptons will depend on the realization of the $\mathbb{Z}_2$ symmetry.

2.2.2 The Minimal Supersymmetric Standard Model

The supersymmetric extension of the SM (SSM) provides solutions to many of the SM shortcomings. Supersymmetry (SUSY) is the most popular and best-studied BSM theory. It is the only possible way to extend the Poincaré symmetry of space-time by relating fermions to bosons via spinorial charges [169]. A supersymmetric transformation Q transforms fermions $|F\rangle$ into bosons $|B\rangle$ and vice versa,

$$Q\,|F\rangle = |B\rangle \,, \qquad Q\,|B\rangle = |F\rangle \,. \tag{2.68}$$

In the SSM, *supermultiplets* are introduced consisting of a SM particle and its superpartner. The latter differs by spin $1/2$ from the SM particle. If SUSY were an exact symmetry, the superpartners would have the same quantum numbers and mass as the SM fields. However, since SUSY particles have not been observed yet, SUSY must be a broken symmetry if it exists in nature. Similar to EWSB, the SUSY

[1] This statement holds very generally in 2HDMs, including typical SUSY models like the MSSM. However, tree-level couplings might be possible in strongly coupled or composite Higgs models.

Table 2.5: The chiral supermultiplets of the MSSM. Given are fermion and sfermions fields as well as the two Higgs boson and higgsino doublets. The index $i = 1, 2, 3$ refers to the generation and the last column provides the representation under the SM gauge group.

Field names	superfield	spin-0	spin-1/2	$SU(3)_c$, $SU(2)_L$, $U(1)_Y$
Sleptons, leptons (3 generations)	L_i	$\tilde{\ell}_{iL} = \begin{pmatrix} \tilde{\nu}_{iL} \\ \tilde{e}_{iL} \end{pmatrix}$	$\ell_{iL} = \begin{pmatrix} \nu_{iL} \\ e_{iL} \end{pmatrix}$	$(1, \mathbf{2}, -1/2)$
	$\bar{E}_i$	$\tilde{\ell}_{iR} = \tilde{e}_{iR}$	$\ell_{iR} = e_{iR}^{\dagger}$	$(1, \mathbf{1}, +1)$
Squarks, quarks (3 generations)	Q_i	$\tilde{q}_{iL} = \begin{pmatrix} \tilde{u}_{iL} \\ \tilde{d}_{iL} \end{pmatrix}$	$q_{iL} = \begin{pmatrix} u_{iL} \\ d_{iL} \end{pmatrix}$	$(\mathbf{3}, \mathbf{2}, +1/6)$
	$\bar{U}_i$	$\tilde{u}_{iR} = \tilde{u}_{iR}$	$u_{iR} = u_{iR}^{\dagger}$,	$(\bar{\mathbf{3}}, \mathbf{1}, -2/3)$
	$\bar{D}_i$	$\tilde{d}_{iR} = \tilde{d}_{iR}$	$d_{iR} = d_{iR}^{\dagger}$,	$(\bar{\mathbf{3}}, \mathbf{1}, +1/3)$
Higgs, higgsino	Φ_1	$\boldsymbol{\phi}_1 = \begin{pmatrix} \phi_1^0 \\ \phi_1^- \end{pmatrix}$	$\tilde{\boldsymbol{\phi}}_1 = \begin{pmatrix} \tilde{\phi}_1^0 \\ \tilde{\phi}_1^- \end{pmatrix}$	$(1, \mathbf{2}, -1/2)$
	Φ_2	$\boldsymbol{\phi}_2 = \begin{pmatrix} \phi_2^+ \\ \phi_2^0 \end{pmatrix}$	$\tilde{\boldsymbol{\phi}}_2 = \begin{pmatrix} \tilde{\phi}_2^+ \\ \tilde{\phi}_2^0 \end{pmatrix}$	$(1, \mathbf{2}, +1/2)$

breaking is anticipated to be spontaneous. However, since there is no consensus on the exact dynamics of spontaneous SUSY breaking, it is useful to parameterize this ignorance by introducing additional terms in the Lagrangian that break SUSY explicitly. The corresponding couplings should be *soft* in order not to reintroduce ultraviolet divergencies in the scalar masses, which would spoil the natural solution to the hierarchy problem discussed in Section 2.1.5.

The simplest SUSY model that realizes low-energy supersymmetry is the Minimal SSM (MSSM). The chiral supermultiplets in the MSSM are given in Table 2.5. In addition to the SM particles, there are three generations of left-handed (right-handed) up-type and down-type *squarks*, $\tilde{u}_{iL}$ and $\tilde{d}_{iL}$ ($\tilde{u}_{iR}$ and $\tilde{d}_{iR}$), respectively. These are the spin-0 superpartners of the up-type and down-type quarks. There are also superpartners of the charged leptons and neutrinos called *sleptons*, $\tilde{e}_{iL}$ and $\tilde{e}_{iR}$, and *sneutrinos*, $\tilde{\nu}_{iL}$, respectively. In general, the squarks and sleptons could mix between different generations and between left- and right-handed fields after EWSB. However, this would lead to severe flavor problems of the theory [170] by introducing large FCNCs. Since these are heavily constrained by experiment [171, 172] it is usually assumed that there is no mixing between different generations. Thus, the left-right mixing is restricted to be within one generation, and the corresponding couplings are proportional to the SM Yukawa couplings. An essential SUSY feature is the necessity of having at least two $SU(2)_L$ doublet fields in order to give mass to up-type and down-type quarks. The fermionic superpartner of a single Higgs doublet ϕ_2, called the *Higgsino* $\tilde{\phi}_2$, would cause gauge anomalies of the electroweak symmetry [173, 174]. These cancel naturally if a second doublet ϕ_1 (superpartner: $\tilde{\phi}_1$) with opposite hypercharge ($Y = -1$) is introduced.

The supersymmetric partners of the SM gauge bosons are fermions, called *gauginos*. These are the *bino* field $\tilde{B}$, the three *wino* fields $\tilde{W}^{1,2,3}$ and the *gluino* fields $\tilde{g}^{1,\ldots,8}$. The gauge fields of the MSSM are listed in Table 2.6.

The MSSM is a Type-II 2HDM, which means that down-type quark and lepton superfields couple to Φ_1, while up-type quark superfields couple to Φ_2. The coupling structure is reflected in the superpotential of the MSSM. Before soft SUSY breaking, it is given by

$$V_{\text{MSSM}} = Y_{ij}^{(l)} L_i \cdot \Phi_1 \bar{E}_j + Y_{ij}^{(d)} Q_i \cdot \Phi_1 \bar{D}_j + Y_{ij}^{(u)} Q_i \cdot \Phi_2 \bar{U}_j - \mu \Phi_1 \cdot \Phi_2 + V_{\text{RV}} \,, \tag{2.69}$$

Table 2.6: The gauge supermultiplets of the MSSM.

Field names	superfield	spin-1/2	spin-1	$SU(3)_c$, $SU(2)_L$, $U(1)_Y$
Bino, B boson	V_1	$\tilde{B}$	B	$(1, 1, 0)$
Winos, W bosons	V_2	$\tilde{W}^i$	W^i	$(1, \mathbf{3}, 0)$
Gluinos, gluons	V_3	$\tilde{G}^i$	G^i	$(\mathbf{8}, 1, 0)$

where $A \cdot B = \epsilon_{ab} A^a B^b$ is the $SU(2)_L$-invariant product contracted by the total anti-symmetric tensor ϵ_{ab}. The potential contains the supersymmetric generalizations of the Yukawa couplings $Y_{ij}^{(f)}$. The parameter μ is the Higgsino mass parameter which can be complex in general. The term $V_{R\!\!\!/}$ contains baryon number (B) and lepton number (L) violating operators. Since such operators would lead to rapid proton decay, an additional discrete gauge symmetry, called *R-parity* $R_p = (-1)^{3B+L+2S}$, where S is the particle spin, is imposed. This symmetry assigns $R_p = +1$ for SM particles and $R_p = -1$ for their superpartners.

While the SUSY-conserving superpotential V_{MSSM} contains only one new parameter μ, soft SUSY breaking introduces 104 additional parameters in the most general R-parity conversing case. However, if no flavor violating interactions are present, the number of new MSSM parameters can be reduced to 41.

The Higgs Sector in the MSSM

The structure of the Higgs potential is the same as in the 2HDM. Thus, in a general SUSY model, the complex parameters in Equation 2.50 will induce $\mathcal{CP}$ violation. However, a fully realistic softly-broken supersymmetric model that satisfies all phenomenological constraints will conserve $\mathcal{CP}$ in the Higgs sector at tree level[1] [138], i. e. $\lambda_5 = \lambda_6 = \lambda_7 = 0$. In this case, the parameters of the Higgs self-interaction, $\lambda_{1,\dots,4}$, are defined by the electroweak gauge couplings and the Higgs potential[2] reads [175]

$$V(\phi_1, \phi_2) = (m_{H_1}^2 + |\mu|^2)\phi_1^\dagger \phi_1 + (m_{H_2}^2 + |\mu|^2)\phi_2^\dagger \phi_2 - m_{12}\left(\phi_1^T i\tau_2 \phi_2 + \text{h. c.}\right) \tag{2.70}$$

$$+ \frac{g_Y^2 + g_2^2}{8}(|\phi_1|^2 - |\phi_2|^2)^2 + \frac{g_2^2}{2}|\phi_1^\dagger \phi_2|^2 , \tag{2.71}$$

where $m_{H_i}^2$ $(i = 1, 2)$ and $m_{12}^2 = B\mu$ are additional soft SUSY breaking mass parameters. After EWSB the neutral components aquire non-zero vevs and the vacuum state reads

$$\left\langle \phi_1 \right\rangle = \langle 0|\phi_1|0\rangle = \frac{1}{\sqrt{2}}\begin{pmatrix} v_1 \\ 0 \end{pmatrix} , \qquad \left\langle \phi_2 \right\rangle = \langle 0|\phi_2|0\rangle = \frac{1}{\sqrt{2}}\begin{pmatrix} 0 \\ v_2 \end{pmatrix} . \tag{2.72}$$

Following the logic of the 2HDM (see Section 2.2.1), five physical degrees of freedom remain after absorption of the three Goldstone bosons. The mass eigenstates of the MSSM at tree-level are given by two charged Higgs bosons, $H^\pm$, two neutral $\mathcal{CP}$-even states, which are given by

$$\begin{pmatrix} h \\ H \end{pmatrix} = \begin{pmatrix} \cos\alpha & \sin\alpha \\ -\sin\alpha & \cos\alpha \end{pmatrix} \begin{pmatrix} \phi_1^0 \\ \phi_2^0 \end{pmatrix} , \tag{2.73}$$

after diagonalizing the $\mathcal{CP}$-even Higgs squared-mass matrix in the neutral sector, and one neutral $\mathcal{CP}$-odd state A. Thus, the scalar and pseudoscalar parts do not mix. The tree-level masses of all Higgs bosons

[1] In singlet extensions of the MSSM $\mathcal{CP}$-violating effects can already be effective at tree level.

[2] Note that the full scalar potential has a much richer structure compared to the 2HDM due to the spin-0 sfermions. In this discussion, only the Higgs sector of the scalar potential is considered because squarks and sleptons do not get vevs.

can be obtained from the scalar potential if one of the masses and $\tan\beta = v_2/v_1$ are known. However, the true masses can be significantly affected by radiative corrections resulting from incomplete cancelation between fermion and sfermion loops. An important tree-level prediction of the MSSM states

$$m_h \leq \min(m_A, m_Z)|\cos 2\beta| \leq m_Z \,. \tag{2.74}$$

If the observed Higgs boson at 125 GeV is considered a candidate for the light Higgs state h, large radiative corrections have to lift m_h to the observed value. In the *decoupling limit* of extended Higgs sectors ($m_A >> m_Z$) h behaves like the SM Higgs boson.

Another important prediction states that the Higgs couplings to the electroweak gauge bosons, $V = W^\pm, Z$, are shared between the $C\mathcal{P}$-even Higgs bosons

$$\frac{g^2_{hVV} + g^2_{HVV}}{g^2_{H_{\text{SM}}VV}} = \sin^2(\beta-\alpha) + \cos^2(\beta-\alpha) = 1 \,. \tag{2.75}$$

This sum rule generalizes to arbitrary models with extended Higgs sectors that are built out of $\text{SU}(2)_L$ doublets and singlets. In contrast, there are no tree-level couplings of the pseudoscalar A to massive gauge bosons in the MSSM. Since the MSSM is a Type-II 2HDM, the tree-level couplings of the Higgs states h, H and A are given by

$$g_{huu} = \frac{\cos\alpha}{\sin\beta} \,, \qquad g_{hdd} = g_{h\ell\ell} = -\frac{\sin\alpha}{\cos\beta} \,, \tag{2.76}$$

$$g_{Huu} = \frac{\sin\alpha}{\sin\beta} \,, \qquad g_{Hdd} = g_{H\ell\ell} = \frac{\cos\alpha}{\cos\beta} \,, \tag{2.77}$$

$$g_{Auu} = \cot\beta \,, \qquad g_{Add} = g_{A\ell\ell} = \tan\beta \,. \tag{2.78}$$

Higgs $C\mathcal{P}$ mixing in the MSSM

The flavor conserving MSSM contains 41 additional parameters. Twelve of these are possible complex phases that are found in the mass parameters of the higgsino μ, and gauginos $M_{1,2,3}$, in the bilinear mass term $m^2_{12} = B\mu$, and in the trilinear Higgs-sfermion couplings A_f ($f \in \{\tilde{e}, \tilde{\mu}, \tilde{\tau}, \tilde{u}, \tilde{d}, \tilde{c}, \tilde{s}, \tilde{t}, \tilde{b}\}$).

The complex parameters in the MSSM provide additional sources of $C\mathcal{P}$ violation beyond the single phase in the CKM matrix. Beyond tree-level, the quartic self-couplings λ_5, λ_6, and λ_7 will receive significant radiative corrections from the phases of the trilinear Yukawa couplings. The most important ones are from third-generation sfermions, $\varphi(A_{\tilde{t}})$ and $\varphi(A_{\tilde{b}})$. In addition, the phase of the gluino (higgsino) mass parameter, $\varphi(M_3)$ ($\varphi(\mu)$), affects the bottom-Yukawa coupling at one-loop level and the Higgs boson self-energies at two-loop (one-loop) level. The complex parameters in the MSSM give rise to $C\mathcal{P}$ violation in the Higgs sector which induces mixing between the tree-level mass eigenstates h, H, and A.

Experimental constraints on some of the phases are very tight. The most restrictive ones are on the phases of the trilinear couplings of Higgs Boson to the light sfermions. They are obtained from measurements of the electric dipole moment (EDM) of the electron and the neutron [176–178], heavy quarks [179, 180], and the deuteron [181]. The MSSM contributions to these EDMs are significant at one-loop level, primarily involving the first two generations of sleptons. On the other hand, the constraints on the phases of the stop and sbottom trilinear Higgs couplings are much weaker [182].

The predicted production and decay rates for a $C\mathcal{P}$-mixed Higgs boson are similar to those of a pure $C\mathcal{P}$-even Higgs boson. The measured Higgs boson mass of $m_H = 125$ GeV and the observed decay rates into massive gauge bosons impose strong constraints on the realization of the $C\mathcal{P}$-mixing scenario within the context of the MSSM and the allowed range for a pseudoscalar component is about 10 % [159].

However, in more general 2HDM models or the NMSSM, larger $C\mathcal{P}$-odd components are still possible.

2.3 Experimental Constraints on the $C\mathcal{P}$ Nature of the Higgs Boson

In order to determine the Higgs boson coupling properties, it is important to identify its spin and $C\mathcal{P}$ quantum numbers. Since it decays into two photons, it cannot be a spin-1 particle. On the other hand, a spin-2 particle features distinguishable properties in the angular distributions of its decay products in $H \to \gamma\gamma$ [183–185], $H \to ZZ^* \to 4\ell$ [185–192], $H \to WW^* \to \ell\nu\ell\nu$ [183, 184], and $H \to Z\gamma \to \ell\ell\gamma$ [185, 193, 194] decays.

The $C\mathcal{P}$ quantum numbers for the spin-0 hypothesis can be probed experimentally by using two different strategies. The *direct* approach is based on the construction of pure $C\mathcal{P}$-odd observables. These are typically obtained from angular distributions in the Higgs boson production and decay processes. $C\mathcal{P}$-sensitive observables are, for example, found in the $H \to ZZ^* \to 4\ell$ decay channel [185–191] and in $H + 2\,\text{jets}$ production [195–199]. They can also be determined from spin correlations in $H \to \tau\tau$ decays [200–202] and from measurements of the top-Yukawa coupling in tH and $t\bar{t}H$ production [203–205]. Direct measurements can be used to constrain scalar and pseudoscalar Higgs components in a model-independent way if both components couple with significant strength to the particle from which the $C\mathcal{P}$-odd observable is measured. On the other hand, the *indirect* approach is purely based on $C\mathcal{P}$-even observables. Typical examples are production cross-sections, decay rates, and p_T distributions. Constraints on the $C\mathcal{P}$ nature are derived by fitting the parameters of a $C\mathcal{P}$-violating model to the $C\mathcal{P}$-even observables. The indirect approach is investigated in this thesis. It is very powerful for studying deviations from the SM. However, significant deviations cannot be uniquely pinned down to $C\mathcal{P}$-violating effects. Therefore, both approaches are complementary in order to determine the $C\mathcal{P}$ nature of the Higgs sector. Constraints on the $C\mathcal{P}$-odd Yukawa couplings can also be inferred from EDM measurements. Besides the experimental publications, there are also phenomenological studies that focus on $C\mathcal{P}$ violation. The current constraints from the different measurements are discussed in the following.

2.3.1 Measurements Targeting the Higgs Boson Couplings to Gauge Bosons

Early studies have shown that the spin-1 and spin-2 hypotheses, as well as the pure pseudoscalar spin-0 hypothesis, are ruled out and that the observed Higgs boson is in accordance with the predictions for a SM Higgs boson [206–208]. However, a spin-0 resonance may also be a $C\mathcal{P}$-mixed state. Most of the analyses conducted so far are based on $C\mathcal{P}$-odd observables that involve the couplings of the Higgs boson to SM gauge bosons. In particular, the $H \to ZZ^* \to 4\ell$ [209, 210] and $H \to WW^* \to \ell\nu\ell\nu$ [207, 208, 211] decay channels and the Higgs boson production processes VH [211, 212] and VBF [212–214]. However, in many BSM models, the corresponding couplings of a $C\mathcal{P}$-odd Higgs boson A are loop-induced and heavily suppressed compared to the $C\mathcal{P}$-even tree-level coupling. In this case, even if the pseudoscalar component itself is large, the experimental signatures in these channels will be small. Consequently, the constraints from these analyses on a $C\mathcal{P}$ admixture are still weak. Because of this problem, it is crucial also to measure the $C\mathcal{P}$ properties of the Higgs in its couplings to fermions.

2.3.2 Studies Targeting the Higgs Boson Couplings to Fermions

Shortly after the discovery of the Higgs boson, the first weak constraints on its $C\mathcal{P}$ nature have been set either by investigating the Higgs couplings [215, 216] in a global fit or by focussing on the top-Yukawa interaction [217]. The experimental input for the former studies are the Higgs production rates in different final state channels using the data of the LHC (Run-1) and Tevatron experiments. In these studies, mixing angles up to $\alpha \approx 62° - 74°$ are compatible with the data at 95 % C. L. The differences between these

constraints mainly result from the complexity of the underlying model assumptions. In the latter study, no conclusive evidence on the $C\mathcal{P}$ nature of the top-Yukawa coupling is obtained.

Recently, the Higgs $C\mathcal{P}$ properties have been studied in its couplings to top quarks and tau leptons. Since these measurements only focus on a specific Yukawa coupling, it is useful to introduce different mixing angles for the top quark and the tau lepton-Yukawa couplings, α_{tt} and $\alpha_{\tau\tau}$, respectively.

The most stringent constraints on the $C\mathcal{P}$ nature of the Higgs-top coupling have been provided by the ATLAS [218] and CMS [219] collaborations. Both analyses target Higgs bosons that are produced in tH, tHW and $t\bar{t}H$ production and decay into a pair of photons. They combine the direct and indirect approaches by fitting the measured rates in certain kinematic regions that are sensitive to the $C\mathcal{P}$ nature of the interaction. The presence of $C\mathcal{P}$ violation in the top-Yukawa coupling would modify the decay rate because of the top quark in the loop-induced $H \to \gamma\gamma$ decay. Using the full Run-2 dataset with an integrated luminosity of 139 fb^{-1} (137 fb^{-1}) ATLAS (CMS) reports the exclusion of a pure $C\mathcal{P}$-odd state at 3.9 σ (3.2 σ). Under the assumption of a pure $C\mathcal{P}$-even coupling, the $t\bar{t}H$ signal is observed at the 5 σ level. They also report the exclusion of mixing angles $|\alpha_{tt}| > 43°$ ($|f_{C\mathcal{P}}^{Htt}| > 0.67$ which corresponds to $|\alpha_{tt}| > 55°$) at 95 % C. L. However, it is difficult to interpret the results of studies that include direct and indirect elements in a model-independent way.

CMS also published the first direct measurement of the $C\mathcal{P}$ properties of the Higgs boson in the tau-Yukawa coupling [220]. This is achieved by measuring the angle $\phi_{C\mathcal{P}}$ between the tau decay planes in various $H \to \tau\tau$ decay modes. The angle $\phi_{C\mathcal{P}}$ is sensitive to the $C\mathcal{P}$-state of the Higgs boson because of characteristic features in the transverse spin correlations between the tau lepton and its decay products. The observed exclusion limits are slightly asymmetric concerning the sign of $\alpha_{\tau\tau}$. They are found to be $\alpha_{\tau\tau} > 40°$ and $\alpha_{\tau\tau} < -32°$. Note that ATLAS is also working on a similar measurement. This measurement relies heavily on the precise reconstruction of tau leptons and their hadronic decay products. For Run-2 of the LHC, these have been significantly improved as described in Sections 3.4.2 and 3.5. Preliminary results obtained with the smaller 2015+2016 dataset (36.1 fb^{-1}) exclude $C\mathcal{P}$-mixing angles $\alpha_{\tau\tau} > 50°$ and $\alpha_{\tau\tau} < -25°$ at 68 % C. L. [221].

2.3.3 Measurements of Electric Dipole Moments

As pointed out in Section 2.2.2, there are severe constraints on the $C\mathcal{P}$-violating phases in the MSSM imposed by EDM measurements. For example, if a $C\mathcal{P}$-mixed state ϕ couples to the top quark and the electron as described by Equation 2.67, constraints on the $C\mathcal{P}$ nature of the top-Yukawa coupling can be imposed from an EDM of the electron. In typical SUSY models, there are interference terms at the two-loop level (Barr-Zee diagram) that induce an EDM for the electron

$$d_e \propto c_t^p c_e^s F_1\left(\frac{m_t^2}{m_\phi^2}\right) + c_e^p c_t^s F_2\left(\frac{m_t^2}{m_\phi^2}\right), \tag{2.79}$$

where the prefactors c_f^s and c_f^p ($f = t, e$) are defined in Equation 2.67, and $F_{1,2}$ are known loop functions [222, 223]. Under the assumption that the coupling of the Higgs boson to electrons is $C\mathcal{P}$-even, i. e. $c_e^s = 1$ and $c_e^p = 0$, very stringent constraints on c_t^p can be realized. However, if the assumptions on c_e^s and c_e^p are loosened or if there are other sources of $C\mathcal{P}$ violation, the constraint on c_t^p will become less severe or even evaporate. The same is true if the electron is replaced with the muon in this argumentation. In Reference [223], EDMs are used to set an upper limit on the $C\mathcal{P}$-odd top-Yukawa coupling of $O(0.5)$. However, since the most recent EDM measurements [224, 225] are not taken into account in this study, the actual constraint may be stronger. In the analysis of these constraints, it is assumed that the Higgs boson only couples to fermions of the third generation. If the Yukawa couplings of the first- and second-generation fermions, which are experimentally hardly accessible so far, are assumed

to be SM-like, it leads to substantially tighter bounds of order $\mathcal{O}(0.01)$. However, if there is also a $\mathcal{CP}$-odd component to these couplings, the actual $\mathcal{CP}$ constraint might be much weaker [226–228].

2.3.4 Conclusion

While the pure $\mathcal{CP}$-odd hypothesis is already ruled out by experiment, $\mathcal{CP}$ admixtures with sizable pseudoscalar components are still compatible with the current data. Most of the analyses conducted so far are based on observables that involve bosonic couplings. In many BSM models, $\mathcal{CP}$-odd contributions to these couplings only enter via higher-dimensional interaction operators which are loop-suppressed. This is not the case for the couplings to fermions. The first direct measurement of the $\mathcal{CP}$ properties of the tau-Yukawa coupling has been performed by CMS. The upper limit on the corresponding mixing angle is about 40°. There are also indirect (and semi-indirect) constraints on the $\mathcal{CP}$ nature of the Higgs boson. Such approaches are useful for exploring the $\mathcal{CP}$ structure of the Higgs boson within the constraints of certain BSM models. However, in this case, it is not possible to guarantee that deviations from the SM are due to $\mathcal{CP}$-violating effects. On the other hand, constraints from EDM measurements are strongly dependent on the underlying model. For example, in the MSSM, pseudoscalar components are restricted to about 10 %, while in more general models, the constraints are much weaker.

2.4 Higgs Boson Interpretation Frameworks

The SM makes accurate predictions about the Higgs boson couplings to all known particles once the Higgs mass is specified. These couplings affect the Higgs boson production cross-sections as well as decay widths, and hence the measured signal rates. Significant deviations from the SM predictions would indicate BSM physics. Several interpretation frameworks for the study of the Higgs boson phenomenology have been proposed. The frameworks used in this thesis will be discussed in the following.

2.4.1 The κ-Framework for the Analysis of Higgs Boson Couplings

The κ-Framework [229] is used to explore the coupling strengths of the Higgs boson. Deviations from the SM are described by multiplicative coupling scale factors $\boldsymbol{\kappa}$, assuming that there is only one narrow resonance at $m_H = 125\,\text{GeV}$. It is further assumed that the Higgs boson is SM-like which means that it is a $\mathcal{CP}$-even state with the SM tensor coupling structure. Given that the resonance is sufficiently narrow, the width of the Higgs boson can be neglected. In this case, the zero-width approximation can be used to decompose the production cross-section σ_i and the decay branching ratio $\text{BR}(H \to f)$

$$(\sigma \cdot \text{BR})(i \to H \to f) = \sigma_i \cdot \frac{\Gamma_f}{\Gamma_H}\,, \tag{2.80}$$

where Γ_f is the decay width into the final state f, and Γ_H is the total Higgs boson decay width. In the κ-Framework, the scale factors κ_i are defined in such a way that the cross-sections and partial decay widths scale with the square of the corresponding scale factor when compared to the SM prediction, i. e.

$$\kappa_i^2 = \frac{\sigma_i}{\sigma_i^{\text{SM}}} \qquad \text{and} \qquad \kappa_f^2 = \frac{\Gamma_f}{\Gamma_H^{\text{SM}}}\,. \tag{2.81}$$

The best available SM predictions, including higher-order QCD and EW corrections for all Higgs boson production cross-sections and decay branching ratios, are recovered if all scale factors equal unity. This implies that higher-order accuracy is lost for any deviation from the SM. Thus, the κ-Framework is only

applicable for small deviations from the SM. In case a firm deviation is observed, it should be replaced with a more general analysis framework like an effective field theory.

At the LHC, the total width of the Higgs boson cannot be constrained with sufficient precision in a model-independent way unless it exceeds the SM expectation ($\Gamma_H \approx 4\,\text{MeV}$) by several orders of magnitude. Therefore, only ratios of coupling scale factors can be determined without further assumptions. This can easily be seen by assuming that all Higgs boson production cross-sections σ_i and decay widths Γ_f are scaled by the common coupling modifier $\kappa_j^2 = x$. If simultaneously the total width of the Higgs boson Γ_H is scaled by x^2, all experimental signatures will be identical to the SM prediction

$$\sigma_i \cdot \frac{\Gamma_f}{\Gamma_H} = x \cdot \sigma_i^{\text{SM}} \frac{x \cdot \Gamma_f^{\text{SM}}}{x^2 \cdot \Gamma_H^{\text{SM}}} = \sigma_i^{\text{SM}} \frac{\Gamma_f^{\text{SM}}}{\Gamma_H^{\text{SM}}} \,. \tag{2.82}$$

Possible assumptions to overcome the degeneracy induced by the unknown total width are the following:

1. There are no Higgs boson decays into states of new physics (NP), i. e. $\text{BR}(H \to \text{NP}) = 0$.

2. BSM decays are allowed, i. e. $\text{BR}(H \to \text{NP}) \geq 0$, but the scale factors for the Higgs-gauge boson couplings are required to be $|\kappa_{W,Z}| \leq 1$ [230, 231]. This assumption breaks the degeneracy by limiting the VBF and VH Higgs production channels [232, 233].

3. All additional Higgs boson decays yield an invisible final state, i. e. $\text{BR}(H \to \text{NP}) = \text{BR}(H \to \text{inv.})$. Such decays can then be constrained by direct searches at the LHC, which exploit the Higgs recoil when produced in association with other objects (Z or W boson, quarks, etc.).

The second assumption is theoretically well-motivated and compatible with a wide range of BSM models. In particular, it is valid for all models that contain only singlet and doublet Higgs fields, and it is also justified in certain classes of composite Higgs models. However, it may be violated in Higgs sectors that are extended by isospin-2 scalar multiplets [234].

2.4.2 Effective Field Theory Frameworks

An *effective theory* (ET) is a type of approximation for a more profound underlying theory. It is called "effective" because it is, in many circumstances, the only viable method to investigate a physical phenomenon and to calculate the outcome of an experiment. ETs describe phenomena with an efficient set of parameters and principles, and they come into play when microscopic properties are negligible or can be averaged. The conclusions drawn from an ET are strictly limited to the domain where it is defined. This is typically some energy or length scale. ETs play an important role in many areas of physics, and their scope of application ranges from planetary orbits to particle physics. An elementary example for an ET is *Galileo's theory of falling bodies*. It states that the distance traveled by a falling object is proportional to the square of the elapsed time. This theory is effective in two ways. First, it is only valid in the limit that the density of the falling object is much higher than the density of air. Thus, the molecular interactions between the falling object and the air's molecules, i. e. friction can be neglected. Second, the gravitational constant does not vary as the object falls. Another well-known example of an effective theory is classical thermodynamics. It neglects the positions and velocities of individual atoms and molecules in a gas and considers only averaged properties like temperature and pressure.

An *effective field theory* (EFT) is an ET in which the underlying theory is described by a field. It is a physical model that is valid at some energy scale E, and it is assumed that there is no new physics up to some energy scale $\Lambda \gg E$. To a first approximation, energies above this scale are treated as infinity, and energies much smaller than E are approximated as zero. The finite effects are included by perturbative

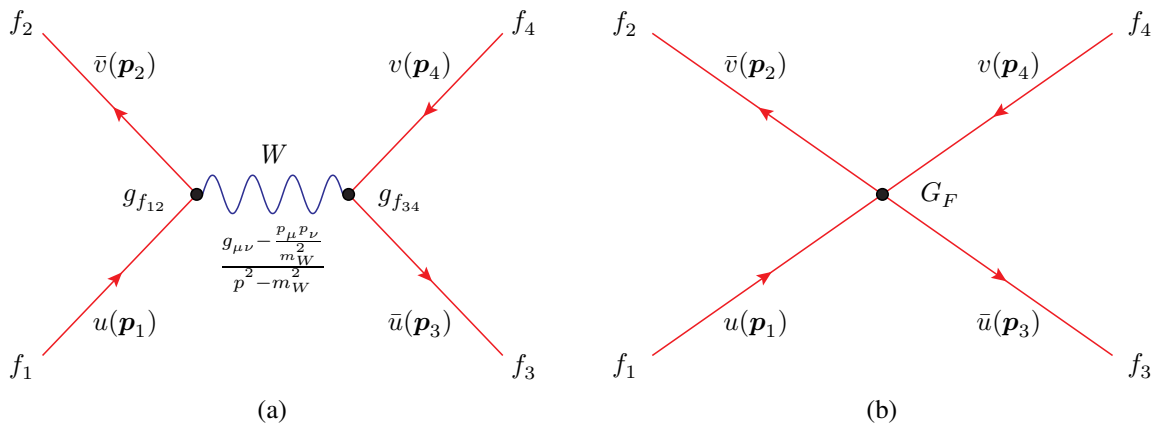

Figure 2.15: The Feynman diagram for (a) the charged current interaction in the SM and (b) the four-point fermion interaction in the Fermi theory.

expansion about this simple approximation [235]. EFTs are used in several branches of physics like particle physics, nuclear physics, condensed matter physics, and more. A famous historical example for an EFT is the *Bardeen-Cooper-Schrieffer* (BCS) theory which explains the superconductivity of metals at low temperatures [236]. The underlying theory is based on the interactions of electrons with lattice vibrations, called phonons. These phonons cause an attraction between pairs of electrons which can overcome the Coulomb repulsion. The length scale l_C of these so-called *Cooper pairs* is much larger than the characteristic wavelength of phonons l_p, which implies that the two electrons effectively interact at a single point. The hierarchy (in this case $l_C \gg l_p$) between two very different scales is a necessary requirement for any EFT.

In particle physics, fascinating phenomena occur at many different energy scales ranging from neutrino masses in the sub-eV region to the TeV region at which current collider experiments operate. At very high energies, the world might be described by a quantum theory of gravity. However, it is not required to know this underlying theory to describe physics at much lower energies. For instance, at a few hundred GeV, the Standard Model of particle physics is in excellent agreement with most measurements. However, at energies much smaller than the mass of weak gauge bosons, the details about the charged current interaction become less important, and the weak interaction can effectively be described by the Fermi theory [237]. Because of its historical importance for particle physics, it is briefly discussed in the following.

The Fermi theory is one of the best-known EFTs in particle physics. It describes the charged current interaction at low energies. The underlying theory is the SM, which was unknown when Fermi invented the theory to explain the beta decay [237]. Figure 2.15(a) shows the Feynman diagram for the charged current interaction in the SM. The incoming fermion (antifermion) f_1 (f_2) has three-momentum $\boldsymbol{p}_1$ ($\boldsymbol{p}_2$) and the outgoing fermion (antifermion) f_3 (f_4) has three-momentum $\boldsymbol{p}_3$ ($\boldsymbol{p}_4$). The corresponding kinetic factors are given by $u(\boldsymbol{p}_1)$, $\bar{v}(\boldsymbol{p}_2)$, $\bar{u}(\boldsymbol{p}_3)$ and $v(\boldsymbol{p}_4)$. The weak interaction is mediated by the exchange of a virtual W boson with mass m_W and four-momentum $p = p_1 + p_2$. The corresponding propagator is suppressed by $(p^2 - m_W^2)^{-1}$ and the couplings of the W boson to fermions is g_x, where $x = f_{12}, f_{34}$. For leptons, g_x is given by the gauge coupling of the weak interaction g_2. However, for quarks the misalignment between the mass and weak eigenstates has to be taken into account. Thus, g_2 has to be multiplied with the appropriate element in the CKM quark mixing matrix. In the following, it is assumed that the initial and final state fermions are leptons. In this case, the matrix element M_{SM} is given by

$$M_{\text{SM}} = \left(\bar{v}(\boldsymbol{p}_2)\frac{ig_2}{\sqrt{2}}\gamma^\mu\frac{1-\gamma^5}{2}u(\boldsymbol{p}_2)\right)\frac{\left(g_{\mu\nu}-\frac{p_\mu p_\nu}{m_W^2}\right)}{p^2-m_w^2}\left(\bar{u}(\boldsymbol{p}_3)\frac{ig_2}{\sqrt{2}}\gamma^\nu\frac{1-\gamma^5}{2}v(\boldsymbol{p}_4)\right)$$
$$= -\frac{g_2^2}{8}\frac{g_{\mu\nu}-\frac{p_\mu p_\nu}{m_W^2}}{p^2-m_W^2}\left(\bar{v}(\boldsymbol{p}_2)\gamma^\mu(1-\gamma^5)u(\boldsymbol{p}_2)\right)\left(\bar{u}(\boldsymbol{p}_3)\gamma^\nu(1-\gamma^5)v(\boldsymbol{p}_4)\right)\,. \tag{2.83}$$

Starting from the SM matrix element, an EFT can easily be created. The characteristic scale of the charged current interaction is the W boson mass, i. e. $\Lambda = m_W$. For much smaller energies $E^2 = p^2 \ll \Lambda^2$, the matrix element can be expanded in powers of p^2/m_W^2. One process that satisfies this requirement is the muon decay ($E = m_\mu \ll m_W$). In this case, the relevant part of Equation 2.83 simplifies to

$$\frac{g_2^2}{8}\frac{g_{\mu\nu}-\frac{p_\mu p_\nu}{m_W^2}}{p^2-m_W^2} \approx -\frac{g_2^2}{8m_W^2}g_{\mu\nu} = -\frac{G_F}{\sqrt{2}}g_{\mu\nu}\,. \tag{2.84}$$

The corresponding matrix element in the Fermi theory is then given by

$$M_{\text{Fermi}} = \frac{G_F^2}{\sqrt{2}}\left(\bar{v}(\boldsymbol{p}_2)\gamma^\mu u(\boldsymbol{p}_2)\right)\left(\bar{u}(\boldsymbol{p}_3)\gamma_\mu v(\boldsymbol{p}_4)\right)\,. \tag{2.85}$$

The projection operator $(1-\gamma^5)$ is neglected in this equation because the original Fermi theory does not know about the maximally parity-violating character of the weak interaction [238, 239]. Equation 2.85 represents a four-fermion contact interaction with the effective coupling strength $\frac{G_F}{\sqrt{2}} = \frac{g_2^2}{8m_W^2}$, where G_F is the so-called *Fermi constant*. The corresponding Feynman diagram is depicted in Figure 2.15(b).

Fermi's theory is only valid up to energies of about 100 GeV due to ultraviolet divergencies in the predicted cross-section $\sigma \approx G_F^2 E^2$. The relative error Δ_{EFT} of the EFT approach depends on the energy scales E and Λ. For the muon decay, the relative error is

$$\Delta_{\text{EFT}} \approx \frac{E^2}{\Lambda^2} = \frac{m_\mu^2}{m_W^2} \approx 10^{-6}\,. \tag{2.86}$$

The approach used to derive the Fermi theory in this section is called *top-down* because the EFT is derived from a known theory, the SM. Historically, the Fermi theory was developed without knowledge of the SM. In EFT terminology, this approach is called *bottom-up*. The Standard Model Effective Field Theory discussed in the following section is also derived using the bottom-up approach.

2.4.2.1 The Standard Model Effective Field Theory (SMEFT)

The SM is generally believed to be a low-energy approximation of a more profound underlying theory. It accurately describes processes below a certain energy scale Λ. Above this scale, new heavy particles and potentially new interactions are expected to appear. This means that at energies $E \ll \Lambda$ the SM particles are effectively "*independent* of (i. e. *decoupled* from) the new heavy states. This is described by the Appelquist-Carazzone theorem [240] and means that the effects of new physics at scale Λ can be effectively included in a low-energy approximation of the theory. Such an effective field theory can be constructed by extending the SM Lagrangian $\mathcal{L}_{\text{SM}}$ with higher-dimensional interaction operators $O_k^{(D)}$ of mass dimension $D > 4$. These operators are built out of combinations of SM fields and are suppressed by

appropriate powers of Λ. The Lagrangian of the SMEFT can be written as

$$\mathcal{L}_{\text{SMEFT}} = \mathcal{L}_{\text{SM}} + \mathcal{L}^{(5)} + \mathcal{L}^{(6)} + \dots, \quad \text{with} \quad \mathcal{L}^{(D)} = \frac{1}{\Lambda^{D-4}} \sum_i^{n_D} C_i^{(D)} O_i^{(D)} . \tag{2.87}$$

The coefficients $C_i^{(D)}$ are dimensionless coupling constants called *Wilson coefficients*. The higher-dimensional operators of the SMEFT are constructed before electroweak symmetry breaking and are known up to mass dimension nine [241–244]. The number of independent operators grows rapidly with the mass dimension. For example, while there are only 12 operators at mass dimension five, there are already 3 045 operators at dimension six and 90 456 operators at dimension nine [245].

The possible dimension-five operators that are consistent with the SM gauge symmetries create effective four-point interactions between the scalar $\text{SU}(2)_L$ doublet Φ and the fermion doublets L_{iL},

$$O_{vv}^{(5)} = (\widetilde{\Phi}^\dagger L_{pL})^T C (\Phi^\dagger L_{rL}) , \qquad \text{for} \quad p, r = 1, 2, 3 , \tag{2.88}$$

where C is the charge conjugation matrix given by $C = i\gamma^2\gamma^0$ in Dirac representation. Such operators violate lepton number conservation, and they lead to mass terms for neutrinos after EWSB [241]. Dimension-seven operators generically violate lepton and/or baryon number [242]. This statement can be generalized to all SMEFT operators of odd dimensions. Such operators are heavily suppressed and strongly constrained by experiment [246, 247]. Moreover, they cannot be observed at the LHC [248]. For that reason, they are not considered in the following. Therefore, the leading-order contributions to the SMEFT Lagrangian are from dimension-six operators

$$\mathcal{L}_{\text{SMEFT}} = \mathcal{L}_{\text{SM}} + \sum_i^{n_6} c_i O_i^{(6)} , \tag{2.89}$$

where $c_i = C_i^{(6)}/\Lambda^2$. These operators can be formulated in different basis representations. In this thesis, the so-called *Warsaw basis* is used, comprising 59 independent lepton-number and baryon-number conserving operators. They are divided into different classes depending on their field content. The bosonic operators classes are X^3, $X^2\Phi^2$, Φ^6 and $\Phi^4 D^2$ and the fermionic ones are $\Psi^2\Phi^3$, $\Psi^2 X\Phi$, $\Psi^2\Phi^2 D$ and Ψ^4. $X = G_{\mu\nu}^a, W_{\mu\nu}^i, B_{\mu\nu}$ represents the field strength tensors introduced in Equations 2.11 and 2.17, Φ the $\text{SU}(2)_L$ scalar doublet Higgs field, Ψ the fermion spinors of $\text{SU}(2)_L$ eigenstates, and $D = D_\mu$ the covariant derivative. The complete list of independent dimension-six operators is given in Reference [241].

To precisely calculate the couplings at a given energy scale using perturbation theory, the measured input parameters have to be chosen. The values of the parameters in the SM Lagrangian are extracted from experimental measurements using a specific parameter input scheme. In this thesis, the electroweak input parameter scheme $\{\hat{m}_W, \hat{m}_Z, \hat{G}_F\}$ [249] is used. In this notation, the parameters with the superscript "ˆ" are either directly measured quantities or related quantities derived from the input parameters. For example, $\hat{m}_W$ is extracted from transverse mass distributions m_W^T at hadron colliders. Using this input scheme, the parameters of the SM Lagrangian are defined as

$$\hat{e} = 2 \cdot 2^{1/4} \hat{m}_W \sqrt{\hat{G}_F} \sin\hat{\theta}_W , \qquad \hat{g}_1 = 2 \cdot 2^{1/4} \hat{m}_Z \sqrt{\hat{G}_F} \sin\hat{\theta}_W , \qquad \hat{g}_2 = 2 \cdot 2^{1/4} \hat{m}_W \sqrt{\hat{G}_F} ,$$

$$\sin\hat{\theta}_W = \sqrt{1 - \frac{\hat{m}_W^2}{\hat{m}_Z^2}} , \qquad \hat{v} = \frac{1}{2^{1/4}\sqrt{\hat{G}_F}} . \tag{2.90}$$

Historically, a different input scheme based on $\{\hat{\alpha}, \hat{m}_Z, \hat{G}_F\}$ has been more prominent. This is because

Table 2.7: The operators of the SMEFT in the $U(3)^5$ symmetry limit that contribute to the Higgs boson interactions. Operators that are sensitive to the $H \to ZZ^* \to 4\ell$ measurement are written in bold letters.

class	name	field content	class	name	field content	
$X^2\Phi^2$	$\boldsymbol{O_{\Phi G}}$	$\boldsymbol{\Phi^\dagger\Phi G^a_{\mu\nu}G^{a,\mu\nu}}$	Φ^6	O_Φ	$(\Phi^\dagger\Phi)^3$	
	$\boldsymbol{O_{\Phi\widetilde{G}}}$	$\boldsymbol{\Phi^\dagger\Phi\widetilde{G}^a_{\mu\nu}G^{a,\mu\nu}}$	Φ^4D^2	$O_{\Phi\Box}$	$(\Phi^\dagger\Phi)\Box(\Phi^\dagger\Phi)$	
	$\boldsymbol{O_{\Phi W}}$	$\boldsymbol{\Phi^\dagger\Phi W^i_{\mu\nu}W^{i,\mu\nu}}$		$O_{\Phi D}$	$(\Phi^\dagger D^\mu\Phi)^*(\Phi^\dagger D_\mu\Phi)$	
	$\boldsymbol{O_{\Phi\widetilde{W}}}$	$\boldsymbol{\Phi^\dagger\Phi\widetilde{W}^i_{\mu\nu}W^{i,\mu\nu}}$	$\Psi^2\Phi^3$ + h. c.	$O_{\ell\Phi}$	$(\Phi^\dagger\Phi)(\bar{L}_p e_r\Phi)$	
	$\boldsymbol{O_{\Phi B}}$	$\boldsymbol{\Phi^\dagger\Phi B_{\mu\nu}B^{\mu\nu}}$		$\boldsymbol{O_{u\Phi}}$	$\boldsymbol{(\Phi^\dagger\Phi)(\bar{Q}_p u_r\widetilde{\Phi})}$	
	$\boldsymbol{O_{\Phi\widetilde{B}}}$	$\boldsymbol{\Phi^\dagger\Phi\widetilde{B}_{\mu\nu}B^{\mu\nu}}$		$O_{d\Phi}$	$(\Phi^\dagger\Phi)(\bar{Q}_p d_r\Phi)$	
	$\boldsymbol{O_{\Phi WB}}$	$\boldsymbol{\Phi^\dagger\tau^i\Phi W^i_{\mu\nu}B^{\mu\nu}}$	$\Psi^2\Phi^2D$	$O^{(1)}_{\Phi F}$	$(\Phi^\dagger i\overleftrightarrow{D}_\mu\Phi)(\bar{F}_p\gamma^\mu F_r)$	for $F = L, Q, \ell, u, d$
	$\boldsymbol{O_{\Phi\widetilde{W}B}}$	$\boldsymbol{\Phi^\dagger\tau^i\Phi\widetilde{W}^i_{\mu\nu}B^{\mu\nu}}$		$O^{(3)}_{\Phi F}$	$(\Phi^\dagger i\overleftrightarrow{D}^i_\mu\Phi)(\bar{F}_p\tau^i\gamma^\mu F_r)$	for $F = L, Q$

the precise extraction of $\hat{m}_W$ happened after the operation of the Large Electron-Positron Collider (LEP). However, there are advantages in using the W boson mass over the electromagnetic coupling constant. For example, the input parameters scales are closer together, which reduces errors introduced by running $\hat{\alpha}$ up to make predictions at the LHC. A detailed comparison of the two input schemes is given in Reference [249].

In the general SMEFT, 76 hermitian operators can be constructed from the 59 independent operators if only one fermion generation is considered. For three generations, the number increases to 2499. 1350 (1149) of these operators characterize $C\mathcal{P}$-even ($C\mathcal{P}$-odd) interactions [250]. The number of operators can be reduced by requiring flavor symmetry. In this thesis, the global flavor symmetry $U(3)^5$ is assumed. In $U(3)^5$ models, the Yukawa matrices for the operator classes $\Psi^2\Phi^3$, $\Psi^2X\Phi$ and Ψ^4 are diagonal, and all Wilson coefficients are scalar parameters. However, the bosonic operators are unchanged and allow for complex Wilson coefficients and hence for $C\mathcal{P}$ violation. In the $U(3)^5$ symmetry limit, there are 52 $C\mathcal{P}$-even and 17 $C\mathcal{P}$-odd operators. More than two-thirds of these do not contribute to Higgs boson interactions and are therefore not considered.

The remaining operators are summarized in Table 2.7. The operator O_Φ is not relevant at the current stage and is therefore neglected. However, once double Higgs production can be probed, this operator will become measurable. The Higgs boson self-couplings, $O_{\Phi\Box}$ and $O_{\Phi D}$ and the Yukawa couplings of the Higgs boson to down-type quarks and leptons, $O_{\ell\Phi}$ and $O_{d\Phi}$, respectively, have minor impact on the measurement in the $H \to ZZ^* \to 4\ell$ decay channel. Thus, they are also neglected. On the other hand, the top-quark Yukawa coupling is taken into account since it can be probed in $t\bar{t}H$ production. All operators of the class $X^2\Phi^2$ are considered because they can be measured in ggF, VBF, and VH production and the HZZ decay vertex. The operators that are taken into account, i. e. that are sensitive to the $H \to ZZ^* \to 4\ell$ measurement, are written in bold letters in Table 2.7.

In total, five $C\mathcal{P}$-even (scalar) and five $C\mathcal{P}$-odd[1] operators are considered. In case of the pseudoscalar operators one of the field strength tensors $X_{\mu\nu}$, for $X = G^a, W^i, B$, is replaced by its dual tensor $\widetilde{X}_{\mu\nu} \to 1/2\,\epsilon_{\mu\nu\rho\sigma}X^{\rho\sigma}$. The Wilson coefficients for all considered operators are

$$\begin{aligned} &c_{HW},\ c_{HB},\ c_{HWB},\ c_{HG},\ c_{uH} && (C\mathcal{P}\text{-even}),\\ &c_{H\widetilde{W}},\ c_{H\widetilde{B}},\ c_{H\widetilde{W}B},\ c_{H\widetilde{G}},\ c_{\widetilde{u}H} && (C\mathcal{P}\text{-odd}), \end{aligned}$$

[1] Note that the operator $O_{u\Phi}$ is not hermitian, i. e. it has a real and an imaginary part accounting for a $C\mathcal{P}$-even and a $C\mathcal{P}$-odd coupling, respectively.

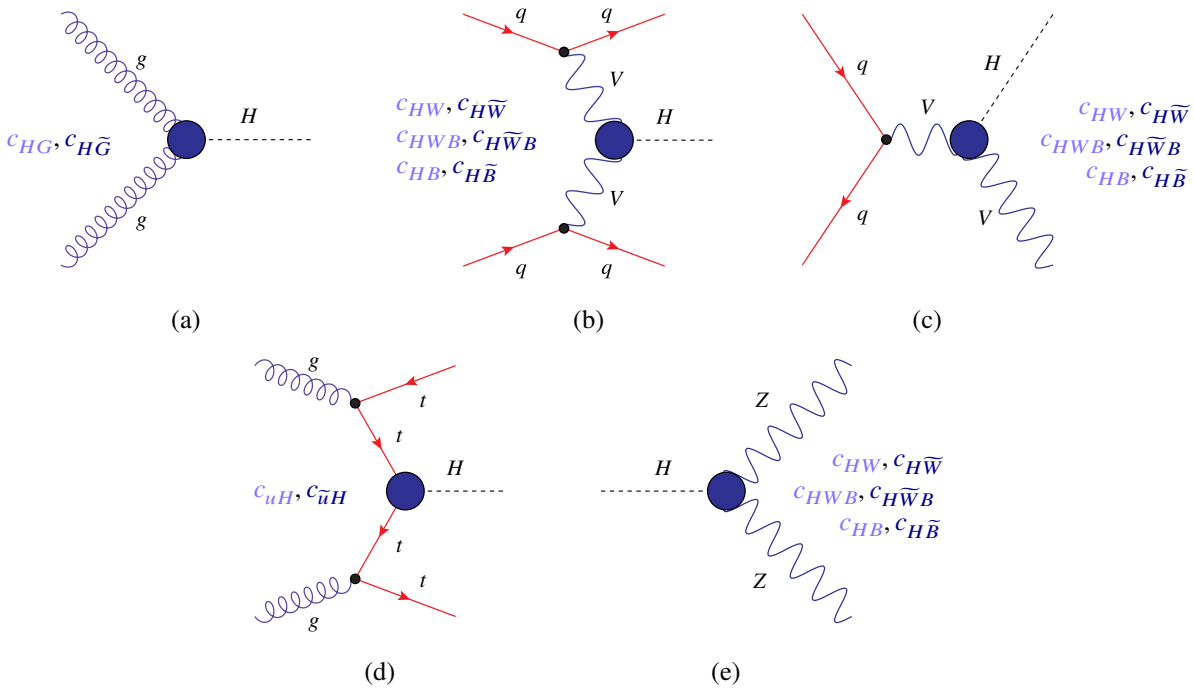

Figure 2.16: The tree-level Feynman diagrams for the Higgs boson production processes (a) ggF, (b) VBF, (c) VH, and (d) $t\bar{t}H$, and (e) the $H \to ZZ^*$ decay vertex. The vertices affected by at least one of the considered SMEFT operators are displayed as large blue circles. The corresponding $\mathcal{CP}$-even and $\mathcal{CP}$-odd BSM coupling parameters that affect these vertices are added in light and dark blue, respectively.

where the name for the Higgs doublet is replaced $\Phi \to H$ following the naming convention of Reference [249]. Figure 2.16 shows the Feynman diagrams for the relevant Higgs boson production processes and the $H \to ZZ^*$ decay vertex together with the sensitive BSM coupling coefficients. The Wilson coefficients c_{HG} and $c_{H\widetilde{G}}$ affect the ggF vertex (Figure 2.16(a)), c_{HW}, c_{HB}, c_{HWB} and $c_{H\widetilde{W}}, c_{H\widetilde{B}}, c_{H\widetilde{W}B}$ affect the VBF (Figure 2.16(b)) and VH (Figure 2.16(c)) production processes and the $H \to ZZ^*$ decay (Figure 2.16(e)), and c_{uH} and $c_{\widetilde{u}H}$ influence the $t\bar{t}H$ vertex (Figure 2.16(d)).

2.4.2.2 Framework for Probing Higgs $\mathcal{CP}$ Admixtures

In this section, a general parameterization for a $\mathcal{CP}$-mixed Higgs boson tailored to the coupling structure in 2HDM-like models is presented. The general model setup is inspired by Reference [215]. In a second step, the framework will be simplified to satisfy the requirements of the κ-framework. This implies that at LO, the Higgs boson production cross-sections and decay widths are scaled by the same effective scale factor κ_i^2 ($\sigma_i/\sigma_i^{\mathrm{SM}} = \kappa_i^2 = \Gamma_i/\Gamma_i^{\mathrm{SM}}$). Like in the κ-framework, this assumption is only valid for small deviations from the SM.

Throughout this section it will be assumed that the 125 GeV Higgs boson ϕ is a scalar with a priori unconstrained $\mathcal{CP}$ properties. In general, it can be an admixture of a $\mathcal{CP}$-even (H) and $\mathcal{CP}$-odd (A) state,

$$\phi = H \cos\alpha + A \sin\alpha\,, \tag{2.91}$$

where α is the Higgs mixing angle. Furthermore, it is assumed that the orthogonal physical Higgs state,

$$\phi' = -H \sin\alpha + A \cos\alpha\,, \tag{2.92}$$

is unconstrained by experimental searches.

It is assumed that only the scalar Higgs field H has tree-level couplings to weak gauge bosons. The corresponding couplings are reduced by a factor $(\kappa_V^s \cos\alpha)^2$ compared to the SM, where κ_V^s is a possible coupling modifier. In the 2HDM, the SM Higgs coupling is shared between the $C\mathcal{P}$-even Higgs bosons, i. e.

$$\frac{g^2_{\phi VV} + g^2_{\phi' VV}}{g^2_{H_{\mathrm{SM}}VV}} = \cos^2\alpha + (-\sin\alpha)^2 = 1. \tag{2.93}$$

Thus, κ_V^s can easily be constrained to $0 \leq \kappa_V^s \leq 1$ in any scalar singlet and doublet extension of the SM.

Couplings of the pseudoscalar Higgs field A to massive gauge bosons can be realized only through higher-dimensional interaction operators. In this study, the effective dimension-five operators

$$\mathcal{L}_{\mathrm{dim5}} = \frac{1}{4}\frac{c_G}{(4\pi)^2 v} A G_{\mu\nu}\widetilde{G}^{\mu\nu} + \frac{1}{4}\frac{c_B}{(4\pi)^2 v} A B_{\mu\nu}\widetilde{B}^{\mu\nu} + \frac{1}{4}\frac{c_W}{(4\pi)^2 v} A W_{\mu\nu}\widetilde{W}^{\mu\nu}\,, \tag{2.94}$$

with $\widetilde{G}^{\mu\nu} = \epsilon^{\mu\nu\rho\sigma} G_{\rho\sigma}$ etc. are considered. Effective dimension-five terms for the $C\mathcal{P}$-even Higgs boson H are not taken into account because their effects are typically small compared to the corresponding tree-level couplings. The scale for new physics Λ is assumed to be the electroweak vacuum expectation value which introduces a mass-scale suppression for the operators of $1/\Lambda = \sqrt{2}/v = (174\,\mathrm{GeV})^{-1}$. The additional loop suppression factor $(1/4\pi)^2$ results from the fact that these operators can not be generated at tree level. It is assumed that new physics is perturbative, restricting $|c_i| < 4\pi$.

The following Yukawa Lagrangian for the Higgs interactions with charged leptons (ℓ), up-type (u) and down-type (d) quarks is assumed:

$$\begin{aligned} -\mathcal{L}_{\mathrm{Yuk}} = {} & c_u^s Y_{ij}^{(u)} \bar{u}_i u_j H \quad + c_d^s Y_{ij}^{(d)} \bar{d}_i d_j H \quad + c_\ell^s Y_{ij}^{(\ell)} \bar{\ell}_i \ell_j H \\ & + i c_u^p Y_{ij}^{(u)} \bar{u}_i \gamma_5 u_j A + i c_d^p Y_{ij}^{(d)} \bar{d}_i \gamma_5 d_j A + i c_\ell^p Y_{ij}^{(\ell)} \bar{\ell}_i \gamma_5 \ell_j A + \mathrm{h.\,c.}\,. \end{aligned} \tag{2.95}$$

The coupling factors c_f^s and c_f^p ($f = u, d, \ell$) parametrize the strength of the $C\mathcal{P}$-even and $C\mathcal{P}$-odd Yukawa couplings relative to the corresponding SM couplings $Y_{i,j}^{(f)}$, respectively. The choice of Eq. (2.95) is well motivated since the Higgs phenomenology predominantly depends on the Yukawa couplings of the third generation fermions and, to a lesser extent, on the charm-Yukawa coupling. Moreover, a more general structure with new 3×3 Yukawa matrices generally induces large FCNCs, which contradicts experiments.

Note that this parametrization effectively includes the possibility of mixing between multiple $C\mathcal{P}$-even Higgs fields. The Yukawa interactions normalized to those in the SM follow from Equations 2.91 and 2.95,

$$\frac{g_{\phi ff}}{g_{H_{SM}ff}} = c_f^s \cos\alpha + i c_f^p \gamma_5 \sin\alpha\,. \tag{2.96}$$

These couplings are identical to those of the SM Higgs boson in case of $c_f^s \cos\alpha = 1$ and $c_f^p = 0$, for $f = u, d, \ell$. They become insensitive to the pseudoscalar couplings c_f^p ($f = u, d, \ell$) in the limit $\cos\alpha \to 1$.

Simplified approach: κ-framework for a $C\mathcal{P}$-mixed Higgs boson

So far, the general model setup has been introduced. In the following, the coupling factors $\boldsymbol{c}$ will be replaced by $\boldsymbol{\kappa}$ to account for the fact that only small deviations from the SM are accurately described. It will be assumed that the coupling factors for the second and third-generation fermions of the same type are identical, i. e. $\kappa_c^x = \kappa_t^x$, $\kappa_s^x = \kappa_b^x$ and $\kappa_\mu^x = \kappa_\tau^x$, where $x = s, p$. The Yukawa couplings of the first

generation fermions are not taken into account due to their small values. For a general $C\mathcal{P}$-mixed Higgs boson, the tree-level partial decay widths for the main fermionic decay modes read

$$\frac{\Gamma(\phi \to c\bar{c})}{\Gamma^{SM}(\phi \to c\bar{c})} = \kappa_t^2 = (\kappa_t^s \cos\alpha)^2 + \beta_t^2(\kappa_c^p \sin\alpha)^2 \,, \tag{2.97}$$

$$\frac{\Gamma(\phi \to b\bar{b})}{\Gamma^{SM}(\phi \to b\bar{b})} = \kappa_b^2 = (\kappa_b^s \cos\alpha)^2 + \beta_b^2(\kappa_b^p \sin\alpha)^2 \,, \tag{2.98}$$

$$\frac{\Gamma(\phi \to \tau^+\tau^-)}{\Gamma^{SM}(\phi \to \tau^+\tau^-)} = \kappa_\tau^2 = (\kappa_\tau^s \cos\alpha)^2 + \beta_\tau^2(\kappa_\tau^p \sin^2\alpha)^2 \,, \tag{2.99}$$

with $\beta_f^2 = \tau_f/(\tau_f - 1)$ and $\tau_f = m_\phi^2/(2m_f)^2$, for $f = t, b, \tau$. The prefactors β_f^2 describe the difference between the decay kinematics of a scalar and a pseudoscalar Higgs boson at leading order. In the Born approximation, the partial decay width of a $C\mathcal{P}$-odd Higgs boson A is given by [251]

$$\Gamma(A \to f\bar{f}) = \frac{G_F n_c}{4\sqrt{2}\pi} m_H m_f^2 \beta_f \,, \tag{2.100}$$

which lacks a factor of β_f^2 compared to Equation 2.43. These factors would become relevant near the threshold $m_\phi \approx 2m_f$. However, since the masses of the fermionic final states are much smaller than the Higgs boson mass, these kinematic factors are close to unity. The largest kinematic factor is obtained for the bottom quark ($m_b \approx 4.18\,\text{GeV} \ll m_\phi$) with $\beta_b^2 \approx 1.005$. In general, at next-to-leading order (NLO), there would be different QCD corrections for the decays of a scalar and a pseudoscalar Higgs boson into quarks. However, in the MSSM the relative correction factors $(1 + \Delta_{QCD}^{H\to q\bar{q}})/(1 + \Delta_{QCD}^{A\to q\bar{q}})$ deviate from unity by less than 1 % [252]. Thus, for the purpose of this study, the model description so far is still applicable at NLO in QCD.

The Higgs boson decays into massive gauge bosons read

$$\frac{\Gamma(\phi \to WW^*)}{\Gamma^{SM}(\phi \to WW^*)} = \kappa_W^2 = (\kappa_W^s \cos\alpha)^2 + 0.155 \cdot \left(\frac{c_W}{(4\pi)^2} \sin\alpha\right)^2 \,, \tag{2.101}$$

$$\frac{\Gamma(\phi \to ZZ^*)}{\Gamma^{SM}(\phi \to ZZ^*)} = \kappa_Z^2 = (\kappa_Z^s \cos\alpha)^2 + 0.074 \cdot \left(\frac{s_\theta^2 c_B + c_\theta^2 c_W}{(4\pi)^2} \sin\alpha\right)^2 \,, \tag{2.102}$$

where $s_\theta^2 = \sin^2\theta_W$ and $c_\theta^2 = \cos^2\theta_W$ with θ_W being the Weinberg angle. The loop-induced contributions from the pseudoscalar AVV couplings are parameterized in terms of the Wilson coefficients c_W and c_B. The numerical factors are due to phase-space integrations and taken from Reference [215]. The impact from the higher-dimensional operators is expected to be very small since their "natural" size is of order $O(10^{-6})$ ($\approx 0.1/(4\pi)^4$). The effects of higher-dimensional operators for the $C\mathcal{P}$-even Higgs boson are not explicitly considered, but their effects can be effectively included in κ_W^s and κ_Z^s.

The loop induced Higgs boson decays into gluons and photons are given by

$$\begin{aligned}\frac{\Gamma(\phi \to gg)}{\Gamma^{SM}(\phi \to gg)} = \kappa_g^2 = &\frac{1}{\left|H_{1/2}(\tau_t) + H_{1/2}(\tau_b)\right|^2} \cdot \Big(\cos^2\alpha \left|\kappa_t^s H_{1/2}(\tau_t) + \kappa_b^s H_{1/2}(\tau_b)\right|^2 \\ &+ \sin^2\alpha \left|\kappa_t^p A_{1/2}(\tau_t) + \kappa_b^p A_{1/2}(\tau_b) + \frac{\sqrt{2}c_G}{g_s^2}\right|^2 \Big) \,,\end{aligned} \tag{2.103}$$

$$\frac{\Gamma(\phi \to \gamma\gamma)}{\Gamma^{SM}(\phi \to \gamma\gamma)} = \kappa_\gamma^2 = \frac{1}{\left|\frac{4}{3}H_{1/2}(\tau_t) + \frac{1}{3}H_{1/2}(\tau_b) + H_{1/2}(\tau_\tau) - H_1(\tau_W)\right|^2} \cdot \left(\cos^2\alpha \left| \frac{4}{3}\kappa_t^s H_{1/2}(\tau_t) + \frac{1}{3}\kappa_b^s H_{1/2}(\tau_b) + \kappa_\tau^s H_{1/2}(\tau_\tau) - \kappa_W^s H_1(\tau_W) \right|^2 + \sin^2\alpha \left| \frac{4}{3}\kappa_t^p A_{1/2}(\tau_t) + \frac{1}{3}\kappa_b^p A_{1/2}(\tau_b) + \kappa_\tau^p A_{1/2}(\tau_\tau) + \frac{c_W s_\theta^2 + c_B c_\theta^2}{\sqrt{2}e^2} \right|^2 \right). \tag{2.104}$$

The loop functions $H_{1/2}$ ($C\mathcal{P}$-even scalar attached to a fermion loop), H_1 ($C\mathcal{P}$-even scalar attached to a heavy gauge boson loop) and $A_{1/2}$ ($C\mathcal{P}$-odd scalar attached to a fermion loop) are given by

$$H_{1/2}(\tau) = \frac{(\tau-1)\,f(\tau)+\tau}{\tau^2}, \quad H_1(\tau) = \frac{3(2\tau-1)f(\tau)+3\tau+2\tau^2}{2\tau^2}, \quad A_{1/2}(\tau) = \frac{f(\tau)}{\tau}. \tag{2.105}$$

with

$$f(\tau) = \begin{cases} \arcsin^2(\sqrt{\tau}) & \text{, for } \tau \le 1 \\ -\frac{1}{4}\left(\log\frac{1+\sqrt{1-1/\tau}}{1-\sqrt{1-1/\tau}} - i\pi\right)^2 & \text{, for } \tau > 1 \end{cases}. \tag{2.106}$$

For $Z\gamma$, one arrives at a similar expression. However, at the current stage, there is no available rate measurement for the decay $\phi \to Z\gamma$ and its influence on the total width is very small. Thus, the $C\mathcal{P}$-even contribution is only scaled by $\cos^2\alpha$. However, since the higher-dimensional interaction operators could significantly increase the width, the corresponding $C\mathcal{P}$-odd contribution is taken into account. The modified decay width for the decays into $Z\gamma$ is given by [215]

$$\Gamma(\phi \to Z\gamma) \approx \cos^2\alpha + \sin^2\alpha \frac{s_{2\theta}^2 (c_W - c_B)^2}{8(4\pi)^5 v^2} \frac{(m_\phi^2 - m_Z^2)^3}{m_\phi^3}. \tag{2.107}$$

In addition, Higgs boson decays into states of new physics $\mathrm{BR}(\phi \to \mathrm{NP})$ are explicitly allowed. Such decays modify the total width

$$\Gamma_{\phi,\mathrm{tot}} = \frac{1}{1 - \mathrm{BR}(\phi \to \mathrm{NP})} \sum_{\mathcal{F}} \Gamma(\phi \to \mathcal{F}), \tag{2.108}$$

where $\mathcal{F}$ runs over the allowed SM final states.

At tree level, the production cross-sections can be approximated from the corresponding decay widths:

$$\frac{\sigma(gg \to \phi)}{\sigma(gg \to H_{SM})} \approx \kappa_g^2 = \frac{\Gamma(\phi \to gg)}{\Gamma(H_{SM} \to gg)}, \tag{2.109}$$

$$\frac{\sigma(pp \to \phi W)}{\sigma(pp \to H_{SM} W)} \approx \kappa_W^2 = \frac{\Gamma(\phi \to WW^*)}{\Gamma(H_{SM} \to WW^*)}, \tag{2.110}$$

$$\frac{\sigma(pp \to \phi Z)}{\sigma(pp \to H_{SM} Z)} \approx \kappa_Z^2 = \frac{\Gamma(\phi \to ZZ^*)}{\Gamma(H_{SM} \to ZZ^*)}. \tag{2.111}$$

The latter two are corrected for higher-order effects as described in Section 4.2. These are, in particular, corrections from virtual top-quark loops and box contributions to $gg \to \phi Z$. The VBF cross-section is

given by

$$\frac{\sigma(pp \to \phi qq)}{\sigma(pp \to H_{\mathrm{SM}} qq)} \approx 0.742 \cdot \frac{\Gamma(\phi \to WW^*)}{\Gamma_{\mathrm{SM}}(H_{\mathrm{SM}} \to WW^*)} + 0.258 \cdot \frac{\Gamma(\phi \to ZZ^*)}{\Gamma_{\mathrm{SM}}(H_{\mathrm{SM}} \to ZZ^*)}\,, \tag{2.112}$$

where the prefactors have been evaluated with `HAWK-2.0.1` (using the `NNPDF2.3 NLO` MC PDF set from the `LHAPDF 6.1.6` collection) for a Higgs boson mass of $m_H = 125.09\,\mathrm{GeV}$ and LHC pp collisions at $\sqrt{s} = 8\,\mathrm{TeV}$[1]. In a first step, the Higgs production processes in association with top and bottom quark pairs are approximated by

$$\frac{\sigma(pp \to X\phi)}{\sigma(pp \to XH_{SM})} = \kappa_t^2 \approx (\kappa_t^s \cos\alpha)^2 + (\kappa_t^p \sin\alpha)^2\,, \quad \text{where } X = t\bar{t}, t, tW\,, \tag{2.113}$$

$$\frac{\sigma(pp \to b\bar{b}\phi)}{\sigma(pp \to b\bar{b}H_{SM})} = \kappa_b^2 \approx (\kappa_b^s \cos\alpha)^2 + (\kappa_b^p \sin\alpha)^2\,. \tag{2.114}$$

However, Equation 2.113 is refined to provide a more accurate prediction of the $t\bar{t}\phi$, $t\phi$, and $tW\phi$ cross-section for a $C\mathcal{P}$-mixed coupling (see Section 4.2 for details). The different model parameterizations studied in this thesis are presented in the following.

The first model (**model I**) describes the "minimal" configuration that incorporates possible $C\mathcal{P}$ violation. It is the most restricted one with only two free parameters. The first one, $\cos\alpha$, describes the mixing between a $C\mathcal{P}$-even and a $C\mathcal{P}$-odd state, and the second one, κ_f^p, is a common pseudoscalar coupling factor for fermions (excluding neutrinos). All other parameters are fixed to their SM values, i. e. $\kappa_f^s = \kappa_V^s = 1$ and $\mathrm{BR}(\phi \to \mathrm{NP}) = c_i = 0$, where c_i ($i = G, B, W$) are the Wilson coefficients. The parameterization with a common scale factor for all fermions is only motivated in a few special BSM realizations. In contrast, a split into up-type and down-type Higgs-fermion couplings appears in many BSM models like the 2HDM of Type-II. Moreover, in the MSSM, the degeneracy of down-type quarks and leptons can also be abrogated by radiative Δ_b corrections [253–255].

In **model II**, the custodial global SU(2) symmetry is investigated. To that end, different scale factors for the $C\mathcal{P}$-even Higgs couplings to Z (κ_Z^s) and W (κ_W^s) bosons are employed. The Yukawa couplings are described by generation-independent scale factors κ_i, where $i = t, b, \tau$. For the massless gauge bosons, the scale factors κ_g and κ_γ are treated as free fit parameters. Three different constraints are tested to overcome the degeneracy of the unknown total width of the Higgs boson (see Section 2.4.1). In model II(a), the constraint $\kappa_{W,Z}^s \leq 1$ is used. In model II(b) the constraint is loosened to $\kappa_V^s \cos\alpha \leq 1$ and in II(c) the branching ratio into states of BSM physics is constrained by an invisible Higgs decay search at ATLAS [256], assuming $\mathrm{BR}(\phi \to \mathrm{NP}) = \mathrm{BR}(\phi \to \mathrm{invisible})$.

In **model III**, generation-independent $C\mathcal{P}$-even and $C\mathcal{P}$-odd fermionic coupling factors are used for up-type and down-type quarks, $\kappa_t^{s/p}$ and $\kappa_b^{s/p}$, and leptons $\kappa_\tau^{s/p}$, respectively. In this model, a common coupling modifier for the weak gauge bosons, $\kappa_V^s \equiv \kappa_W^s = \kappa_Z^s$, is employed. The constraint $\kappa_V^s \leq 1$ is employed. The effective Higgs boson couplings to gluons and photons are calculated via Equations 2.103 and 2.104. As in model II, the branching ratio into states of new physics is a free parameter in model III.

Model IV is the most general parameterization. In addition to model III's free parameters, it allows for $C\mathcal{P}$-odd contributions from the higher-dimensional interaction operators. All considered models together with their free fit parameters and additional constraints are summarized in Table 2.8.

[1] Since the ratios are energy dependent, they will be appropriately adjusted based on the cms energy of the pp collisions. For example, for $\sqrt{s} = 13\,\mathrm{TeV}$, the prefactors are 0.733 and 0.267 for $\phi \to WW^*$ and $\phi \to ZZ^*$, respectively.

Table 2.8: Overview of the considered models in the Higgs $C\mathcal{P}$-mixing scenario.

model	free coupling scale factors κ	additional fit parameters	constraint
I	κ_f^p	$\cos\alpha$	$\kappa_V^s = 1$
II(a)	$\kappa_W^s, \kappa_Z^s, \kappa_t, \kappa_b, \kappa_\tau, \kappa_g, \kappa_\gamma$	$\cos\alpha$, BR($\phi \to$ NP)	$\kappa_V^s \leq 1$, for $V = W, Z$
II(b)			$\kappa_V^s \cos\alpha \leq 1$, for $V = W, Z$
II(c)			NP $\equiv$ invisible
III	$\kappa_V^s, \kappa_t^s, \kappa_t^p, \kappa_b^s, \kappa_b^p, \kappa_\tau^s, \kappa_\tau^p$	$\cos\alpha$, BR($\phi \to$ NP)	$\kappa_V^s \leq 1$
IV	$\kappa_V^s, \kappa_t^s, \kappa_t^p, \kappa_b^s, \kappa_b^p, \kappa_\tau^s, \kappa_\tau^p, c_G, c_B, c_W$	$\cos\alpha$, BR($\phi \to$ NP)	$\kappa_V^s \leq 1$

2.4.2.3 The Higgs Characterization Model

The general *Higgs Characterization* (HC) model is a framework for studying the Higgs coupling properties for various spin (J) and parity ($\mathcal{P}$) hypotheses [257]. In this thesis, only the $J = 0$ scenario will be considered. The HC model is similar to the framework presented in the previous section, but it is more general. It assumes that the Higgs boson is a single resonance with a mass of about 125 GeV that does not couple to BSM particles below the cut-off scale Λ. The low-energy effects of new physics above this scale are described by dimension-six operators, which introduce new effective couplings of the Higgs boson to SM particles. In principle, these could include all three-point and four-point couplings. However, only the former are included in the model for practical purposes. The effective Lagrangian of the HC model

$$\mathcal{L}_{\text{HC}} = \mathcal{L}_{\text{SM}-H} + \mathcal{L}_{J=0} \tag{2.115}$$

is formulated in terms of mass eigenstates, i. e. after EWSB where $\text{SU}(2)_L \otimes \text{U}(1)_Y$ is reduced to $\text{U}(1)_Q$. The first term is the SM Lagrangian without the Higgs boson and the second term contains the modified Higgs sector.

Simplified Model Targeting the Top-Yukawa Coupling

The simplified model [258] presented in the following focuses on possible $C\mathcal{P}$-violation in the top-Yukawa coupling, which plays an important role at hadron colliders since it appears in various processes. The model considers only the processes in which the top-Yukawa coupling appears at LO. For example, the dominant LO contribution to the ggF production, illustrated in Figure 2.6(a), is mediated by a top-quark loop. The phenomenologically relevant $H \to \gamma\gamma$ decay mode, shown in Figure 2.13, is also mediated by a top-quark loop beside the dominant (subdominant) contribution of W-boson (bottom-quark) loops. Another production mechanism sensitive to the top-Yukawa coupling is ZH production. However, its dominant contribution, depicted in Figure 2.7(a), does not depend on the top-Yukawa coupling at LO. The subdominant gluon-induced channel comprises two LO contributions. While one of them does not depend on the Htt coupling (see Figure 2.7(b)), the other one does (see Figure 2.7(c)).

Besides, the kinematic properties of the Higgs in $gg \to ZH$ production are sensitive to the $C\mathcal{P}$ nature of the top-Yukawa coupling [259]. The transverse momentum distribution of the Higgs boson can be studied in the STXS framework. By contrast, the p_T-shape of Higgs bosons produced via $gg \to H$ is not sensitive to the $C\mathcal{P}$ nature of the top-Yukawa coupling [260]. However, in Higgs production with two accompanied jets, the correlations in the azimuthal angle between the two jets, $\Delta\phi_{jj}$, offer sensitivity to the $C\mathcal{P}$ nature of the Higgs boson [260]. The p_T distributions of the Higgs boson production processes in association with top quarks, tH, tHW, and $t\bar{t}H$, are also sensitive to the $C\mathcal{P}$ properties of the top-Yukawa

coupling. Exemplary Feynman diagrams for these processes are shown in Figures 2.9 and 2.8, respectively.

The mixing angle α_{tt} between the scalar and the pseudoscalar coupling is absorbed in the coupling modifiers, $c_t := \kappa_{Htt} \cos\alpha_{tt}$ and $\tilde{c}_t := \kappa_{Att} \sin\alpha_{tt}$, respectively, where κ_{Htt} (κ_{Att}) is the Higgs-top coupling in the SM (in a 2HDM with $\tan\beta$=1). The top-Yukawa part of the Lagrangian is given by

$$\mathcal{L}_{\text{yuk}} = -g_{Htt}\bar{\psi}_f \left(c_t + i\tilde{c}_t\gamma_5\right)\psi_f\phi\,. \tag{2.116}$$

The coupling modifier rescaling the SM Higgs interaction strength with weak vector bosons is described by c_V. The model includes a set of operators that directly couple the Higgs boson to gluons and photons,

$$\mathcal{L}_{\text{Hgg,H}\gamma\gamma} = -\frac{1}{4}\frac{1}{v}\left[-\frac{\alpha_s}{3\pi}c_g G^a_{\mu\nu}G^{a,\mu\nu} + \frac{\alpha_s}{2\pi}\tilde{c}_g G^a_{\mu\nu}\widetilde{G}^{a,\mu\nu} - \frac{47\alpha}{18\pi}c_\gamma A_{\mu\nu}A^{\mu\nu} + \frac{4\alpha}{3\pi}\tilde{c}_\gamma A_{\mu\nu}\widetilde{A}^{\mu\nu}\right]. \tag{2.117}$$

The prefactors are taken from Reference [257] and the scale of new physics is set to $\Lambda = v$. These couplings can be generated by heavy BSM particles and the SM limit corresponds to $c_g = \tilde{c}_g = c_\gamma = \tilde{c}_\gamma = 0$.

The LO scale factors for the $gg \to H$ production cross-section and the $H \to \gamma\gamma$ decay rate are

$$\kappa_g^2 = \frac{\sigma(gg\to\phi)}{\sigma^{\text{SM}}(gg\to H)} = \frac{\left|c_t H_{1/2}(\tau_t) + \frac{2}{3}c_g + ...\right|^2 + \left|\tilde{c}_t A_{1/2}(\tau_t) + \tilde{c}_g\right|^2}{\left|H_{1/2}(\tau_t) + ...\right|^2}, \tag{2.118}$$

$$\kappa_\gamma^2 = \frac{\Gamma(\phi\to\gamma\gamma)}{\Gamma^{\text{SM}}(H\to\gamma\gamma)} = \frac{\left|\frac{4}{3}c_t H_{1/2}(\tau_t) - c_V H_1(\tau_W) - \frac{47}{18}c_\gamma + ...\right|^2 + \left|\frac{4}{3}\tilde{c}_t A_{1/2}(\tau_t) + \frac{4}{3}\tilde{c}_\gamma\right|^2}{\left|\frac{4}{3}H_{1/2}(\tau_t) - H_1(\tau_W) + ...\right|^2}, \tag{2.119}$$

where the loop functions are given in Equation 2.105 and $\tau_x = m_\phi^2/(2m_x)^2$ ($x = t, W$). The ellipses (i. e., the "+ ...") denotes the subdominant SM contributions, which are set to their SM values.

The top-quark and the Z-boson associated Higgs production cross-sections are given by Equations 4.6 and 4.3. Since the tH, tHW, and $t\bar{t}H$ production modes are difficult to disentangle experimentally, only the inclusive quantity is measured. The corresponding combined signal strength reads

$$\mu_{t\bar{t}H+tHW+tH} = \frac{\sigma(pp\to t\bar{t}H) + \sigma(pp\to tH) + \sigma(pp\to tHW)}{\sigma^{\text{SM}}(pp\to t\bar{t}H) + \sigma^{\text{SM}}(pp\to tH) + \sigma^{\text{SM}}(pp\to tHW)}. \tag{2.120}$$

In contrast, Higgs decays into a photon and a Z boson are not included in the analysis, since it is not a competitive process given the current experimental precision. In the analysis, it is assumed that $\tilde{c}_g = \tilde{c}_\gamma = 0$. Therefore, the most general parameterization of the adopted effective Lagrangian contains five free parameters: $c_t, \tilde{c}_t, c_V, c_g, c_\gamma$. The following model parameterizations are considered:

- **Model 1:** $c_t, \tilde{c}_t$ free
  In the simplest scenario, only the $C\mathcal{P}$-even and $C\mathcal{P}$-odd components of the top-Yukawa coupling, c_t and $\tilde{c}_t$, respectively, are allowed to float freely. The tree-level Higgs coupling parameter c_V is fixed to its SM value, and the loop-induced couplings are derived assuming $c_g = c_\gamma = 0$.

- **Model 2:** $c_t, \tilde{c}_t, c_V$ free
  The second setup is the same as the first one but treats c_V as an additional free parameter in the fit.

- **Model 3:** $c_t, \tilde{c}_t, c_V, c_\gamma$ free
  The third scenario allows the Higgs coupling to photons, κ_γ, to adopt arbitrary values.

- **Model 4:** $c_t, \tilde{c}_t, c_V, c_\gamma, c_g$ free
  The fourth scenario allows the Higgs couplings to photons and gluons, κ_γ and κ_g, to vary freely.

CHAPTER 3

The Experimental Setup

A large portion of this thesis is based on the experimental data taken at the ATLAS (**A** **T**oroidal **L**HC **A**pparatu**S**) experiment at the Large Hadron Collider (LHC). Section 3.1 provides an overview of the LHC accelerator complex at CERN[1]. This is followed by the description of the ATLAS detector in Section 3.2 and the techniques to reconstruct and identify the different physical objects in Sections 3.3 and 3.4. As a part of this thesis, an improved energy reconstruction of hadronically decaying tau leptons has been developed. The corresponding studies are presented in Sections 3.5.

3.1 The Large Hadron Collider

The LHC [261–263] is a circular particle accelerator and collider situated at the Swiss-French border near Geneva. It has a circumference of 26.7 km and is located 45 − 170 m below ground on a plane inclined at 1.4 % sloping towards the Lake Geneva. The LHC consists of two rings designed to accelerate protons[2] up to cms energies of 14 TeV. While the cms energies have been restricted to $\sqrt{s} = 7 - 8$ TeV during Run-1 (2010–2012) of the LHC program, they have been increased to 13 TeV in Run-2 (2015–2018).

The LHC collider complex is shown in Figure 3.1. Before the protons can be accelerated and brought into collision, they have to be produced. This is done by breaking down hydrogen molecules (H_2) into electrons and protons using an electric field in a Duoplasmatron. The extraction anode accelerates the protons by 90 keV to 1.4 % speed of light. After they have left the Duoplasmatron, they are sent to a radio frequency quadrupole (QRF), which focuses and accelerates the beam up to 750 keV. The protons are then injected into the linear accelerator LINAC 2, a multi-chamber resonant cavity. LINAC 2 increases the proton's total energy to 50 MeV. From here, the protons are sent to the Proton Synchrotron Booster (PSB) [265], a circular accelerator with a central orbit length of 157 m that accelerates the proton beam to 1.4 GeV. The beam is then passed to the Proton Synchrotron (PS) [266], which is four times as big as the PSB. The PS raises the energies of the protons to 25 GeV and splits them into 81 different bunch packets with 25 ns bunch spacing. The bunches are then injected into the Super Proton Synchrotron (SPS) [267], a 7 km circular accelerator, which accelerates the protons up to 450 GeV. Finally, they are filled into the LHC, where they are further accelerated to the targeted collision energy. The bunches circulate clockwise in one of the rings and counterclockwise in the other.

The kinetic energy E_{kin} that a charged particle with charge q attains while traversing an electric field $\boldsymbol{E}$ along the path $\boldsymbol{s}$ is given by

$$E_{\text{kin}} = \int_{\boldsymbol{s}} (\boldsymbol{F} \cdot \mathrm{d}\boldsymbol{s}) = q \int_{\boldsymbol{s}} (\boldsymbol{E} \cdot \mathrm{d}\boldsymbol{s}) \ . \tag{3.1}$$

[1] CERN is the acronym for the French "**C**onseil **E**uropéen pour la **R**echerche **N**ucléaire", or European Council for Nuclear Research.

[2] The LHC has also a program for heavy-ion collisions up to cms energies of $\sqrt{s} = 5.02$ TeV.

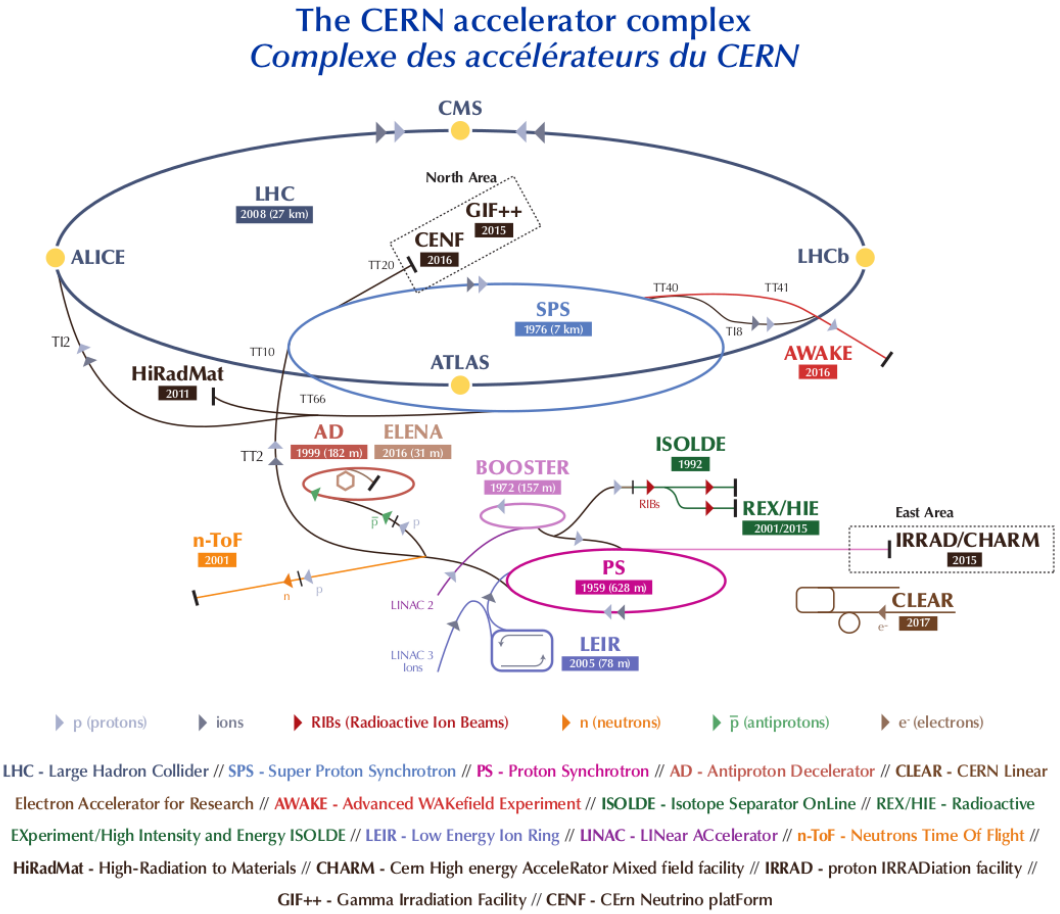

Figure 3.1: The accelerator complex at CERN including the LHC experiments and the injecton chain traversed by the protons. Taken from Reference [264].

While the first few accelerator elements are linear structures, the latter ones are circular. To reach energies in the TeV range using the current linear accelerator technologies requires either extremely strong fields or very long accelerators. This problem is solved by guiding the particles on a ring, consisting of many accelerating, bending, and focusing elements. By repeatedly passing the same elements, the particles can be accelerated much further. However, this cannot be exploited without limitations, as will be explained.

The particles are accelerated by a strong field gradient of $5.5\,\mathrm{MVm}^{-1}$ in cylindrical cavities. For an accelerating effect, they have to be in phase with the standing high-frequency wave within the cavity. Dipole magnets are used to bend the particle's trajectory between the accelerating elements. In total, 1232 dipoles, each with a length of 15 m, are placed along the beam pipe. The coils are made of Niobium-Titanium cable cooled down to 1.9 K using superfluid helium. The dipole magnets can operate at fields up to 8.36 T. 858 quadrupole magnets keep the particles in a tight beam. Using a series of rotated quadrupoles, the beam is effectively squeezed down along the horizontal and vertical directions. Other disturbances in the beam profile like dipole deflections are corrected with higher-order multipole magnets.

Any charged particle that is accelerated radially emits synchrotron radiation. The corresponding energy loss is inversely proportional to the radius of the arc and proportional to the fourth power of E/m, where E is the energy and m the mass of the particle. This means that heavy particles like protons radiate off significantly less energy than light particles like electrons. In fact, the LHC tunnel was built for the Large

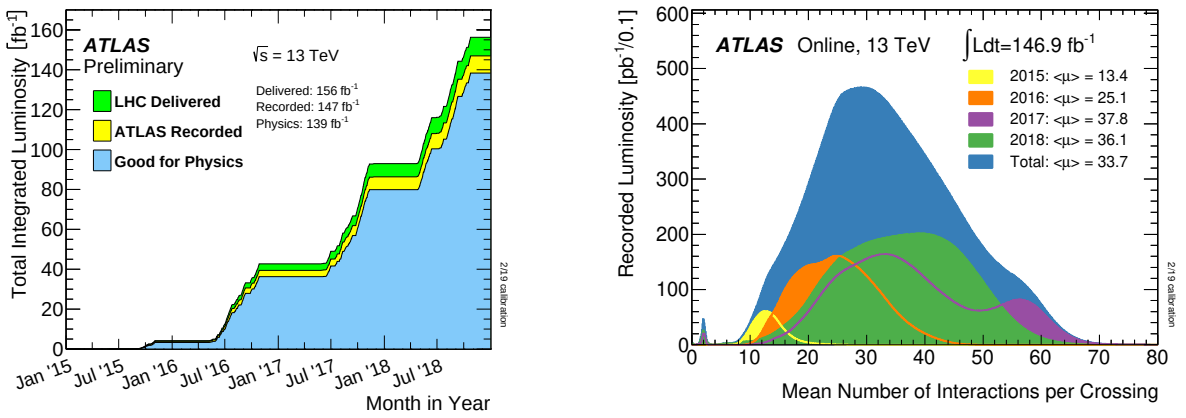

(a) (b)

Figure 3.2: (a) The integrated luminosity versus time delivered to ATLAS (green), recored by ATLAS (yellow), and certified to be good for physics analyses (blue). (b) The mean number of interactions per bunch crossing for the Run-2 *pp* collision data recorded by the ATLAS detector. Taken from Reference [272].

Electron-Positron Collider [268–270] (LEP), which was operating from 1989 to 2000. The energy loss due to synchrotron radiation for a 100 GeV electron at LEP is 3 GeV per cycle, while the corresponding loss for a proton at 7 TeV is only 6 keV. Since the energy loss has to be compensated by the accelerating elements, there is a limit on the effective maximum energy that can be reached at a circular collider.

Besides the colliding particles' energy, one of the most important numbers characterizing a particle collider is the instantaneous luminosity $\mathcal{L}$. For a given process, it describes the proportionality of the production rate $\dot{N}$ to the cross-section σ. The latter depends on the cms energy and the type of particles that are being collided. Another essential measure is the integrated luminosity L, which is related to the total number of collision N via

$$N = \int \dot{N}\,\mathrm{d}t = \int \mathcal{L}\sigma\,\mathrm{d}t = L\sigma\,. \tag{3.2}$$

The instantaneous luminosity is given by the number of bunches n_b, the number of particles per bunch in beam-1 (beam-2) N_{p1} (N_{p2}), the LHC revolution frequency f_r and the widths σ_x and σ_y of the horizontal and vertical beam profiles at the collision point [271],

$$\mathcal{L} = \frac{f_r n_b N_{p1} N_{p2}}{\sigma_x \sigma_y}\,. \tag{3.3}$$

The *inelastic pp* collision cross-section at $\sqrt{s} = 13\,\mathrm{TeV}$ at the LHC is $\sigma(pp) = 79.5 \pm 1.8\,\mathrm{mb}$[1] [273]. In the SM less than 10^{-9} of these collisions are expected to produce a Higgs boson and the predicted cross-section is $\sigma(pp \to H) = 55.7\,\mathrm{pb}$ [74]. The LHC is designed to deliver an instantaneous luminosity of about $\mathcal{L} = 10^{34}\,\mathrm{cm}^{-2}\mathrm{s}^{-1}$, with $N_{p1} = N_{p2} = 1.15 \cdot 10^{11}$ protons per bunch and $n_b = 2808$ bunches per beam. Figure 3.2(a) shows the integrated luminosity that has been delivered to and recorded by ATLAS during Run-2 of the LHC. The largest instantaneous luminosity was obtained in 2018 with $\mathcal{L} = 2.10 \times 10^{34}\,\mathrm{cm}^{-2}\mathrm{s}^{-1}$. In 2017, 2016 and 2015 it has been $\mathcal{L} = 2.09 \times 10^{34}\,\mathrm{cm}^{-2}\mathrm{s}^{-1}$, $\mathcal{L} = 1.38 \times 10^{34}\,\mathrm{cm}^{-2}\mathrm{s}^{-1}$ and $\mathcal{L} = 0.5 \times 10^{34}\,\mathrm{cm}^{-2}\mathrm{s}^{-1}$, respectively. Under the assumption of the peak

[1] $1b = 10^{-24}\mathrm{cm}^2$

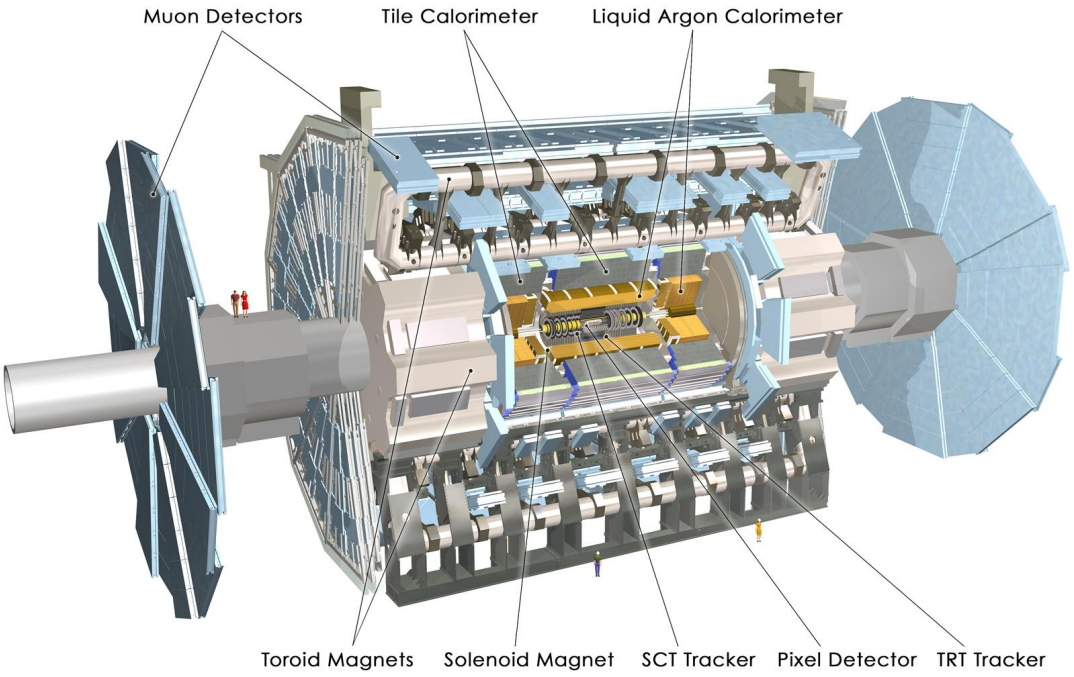

Figure 3.3: Cut-away view of the ATLAS detector showing the main subsytems, including the inner detector (SCT, Pixel and TRT), the electromagnetic (liquid argon) and hadronic calorimeters (tile), and the muon detector [278].

luminosity in 2018 the expected number of generated Higgs bosons per second at the LHC is

$$N_H = 2.1 \cdot 10^{34}\,\mathrm{cm}^{-2}\mathrm{s}^{-1} \cdot 55.7\,\mathrm{pb} \cdot 1\,\mathrm{s} = 1.17\,.$$

The number of interactions per bunch crossing significantly increased over the years. While its mean value has been only 13.4 in 2015, it increased to about 37 in 2017 and 2018 (see Figure 3.2(b)), resulting in significantly more simultaneous interactions (pile-up), which have to be suppressed. The largest numbers were obtained in 2018, with about 70 interactions per bunch crossing.

After acceleration, the beams are brought to collision at four interaction points where the main LHC experiments ATLAS [274], CMS (**C**ompact **M**uon **S**olenoid) [275], ALICE (**A** **L**arge **I**on **C**ollider **E**xperiment) [276] and LHCb (**LHC** **b**eauty) [277] are located. The ATLAS and CMS detectors are designed to search for the Higgs boson and a broad range of new physics phenomena, including dark matter, supersymmetry, and extra dimensions. Moreover, they are also capable of performing high-precision measurements of SM physics. In contrast, the LHCb experiment, which is only sensitive in the very forward region, is designed to measure the parameters of $C\mathcal{P}$ violation in the interactions of B-hadrons. The ALICE detector is optimized to study strongly interacting matter at very high energy densities in heavy-ion collisions.

3.2 The ATLAS Experiment

The ATLAS detector, sketched in Figure 3.3, is a multi-purpose particle detector with a length of 44 m, a diameter of 25 m and a weight of 7 000 t. It has an onion-like structure with different detectors being stacked from the inside to the outside. The high luminosities and cms energies of the LHC require highly granular and radiation hard tracking systems that provide good momentum and origin resolution.

The tracking system measures the momentum and the origin of a charged particle. It is placed closest to the beam pipe and makes up the innermost part of the detector. The energies of photons, electrons, and positrons are measured in the highly-granular *electromagnetic calorimeter* (ECAL). In principle, hadrons can also be measured in an ECAL. However, since hadrons typically penetrate much deeper, very large calorimeters are required. The ECAL is surrounded by a larger, less granular *hadronic calorimeter* (HCAL), specifically designed to measure hadrons. In order to detect as many processes as possible, the calorimeters need to cover a large solid angle. Muons are neither stopped in the ECAL nor the HCAL due to their minimum ionizing character. Thus, a dedicated muon system (MS) is placed at the outermost part of the detector. The readout system needs to be fast due to the 25 ns spacing between the proton bunches.

3.2.1 The Coordinate System at ATLAS

ATLAS uses a right-handed coordinate system with its origin chosen to be the nominal interaction point (IP), located in the center of the detector. The x-axis points to the center of the LHC ring, the y-axis towards the earth's surface and the z-axis along the beam pipe. In the transverse plane cylindrical coordinates (r, ϕ) with $\phi \in [-\pi, \pi]$ are used. Instead of using θ (with $\theta \in [0, \pi]$) like in a spherical coordinate system, the *pseudorapidity*

$$\eta = -\ln \tan\left(\frac{\theta}{2}\right) \tag{3.4}$$

is used as the third coordinate. While $\eta = 0$, i. e. $\theta = 90°$, represents a direction in the transverse plane, $\eta \longrightarrow +\infty$ ($\theta = 0°$) represents a direction that is parallel to the positive z-axis. The advantage of using η over θ is that the pseudorapidity is invariant to Lorentz boosts in the relativistic limit $p \approx E$. In this case, the pseudorapidity equals the rapidity

$$y = \frac{1}{2} \ln\left(\frac{E + p_z}{E - p_z}\right), \tag{3.5}$$

where p_z is the longitudinal momentum along the beam axis. The angular separation ΔR between two particles in this coordinate system is

$$\Delta R = \sqrt{(\Delta\eta)^2 + (\Delta\phi)^2}\,. \tag{3.6}$$

The closest approach of the particle's trajectory to the hard-scatter primary interaction point (primary vertex) is called the *impact parameter*. The impact parameter in the transverse plane is called d_0, while the longitudinal impact parameter is called z_0.

The momenta of the partons in pp collisions are described by PDFs (see Section 2.1.4). Hence, the total momentum of a specific event is unknown. Moreover, fragmentation products of other partons that are not from the hard-scatter process can escape detection along the z-axis. Since the transverse momenta of the partons are negligible, momentum conservation implies that the sum of the transverse momenta $\boldsymbol{p}_{T,i}$, of all collision products i, is zero,

$$\sum_i \boldsymbol{p}_{T,i} = 0\,. \tag{3.7}$$

Using this constraint, the missing transverse energy,

$$E_T^{\text{miss}} \approx p_T^{\text{miss}} = -\left|\sum_i \boldsymbol{p}_{T,i}\right|, \tag{3.8}$$

is defined as a measure for the sum of the momenta carried away by neutrinos in the transverse plane.

3.2.2 The Trigger System

The LHC is operated at a collision rate of 40 MHz creating up to $1.7 \cdot 10^9$ (inelastic) pp collisions per second. This high event rate produces more than 60 TB/s of data at the ATLAS detector. However, it is impossible to record every single collision with the available bandwidth and computing resources. On the other hand, many events will not contain interesting physics and would occupy valuable bandwidth and storage capacities if recorded. To overcome these problems, ATLAS uses a two-level online event selection system – the *Trigger System* – which effectively reduces the 1.7 billion collisions to about 1 000 interesting collisions per second. The first-level (L1) trigger is implemented in hardware, and the high-level trigger (HLT) is based on software [279, 280].

The L1 trigger is constructed with custom-made electronics. It uses a subset of the information from the calorimeter and muon detectors to determine whether an event may contain interesting physics or not. Up to 512 decision items are built based on interesting regions in η and ϕ, which are retrieved from the calorimeter and muon systems. This decision is made in less than 2.5 µs after the collision. Until the decision is made, the event is stored in pipeline storage buffers. The L1 trigger effectively reduces the data stream from 40 MHz to $\approx$ 100 kHz.

The HLT provides about 2 500 independent sequences of offline-like algorithms, which are seeded by the information of the L1 regions of interest. Within 40 ms, fast-tracking algorithms decide whether the event should be further processed or not. Higher precision reconstruction is only performed on events that contain interesting physical signatures. If the HLT accepts an event, it is sent to permanent storage for offline reconstruction. The physics output rate of the HLT is on average 1.2 kHz, which corresponds to a data storage of 1.2 GB/s.

3.2.3 The Inner Detector (ID)

The ATLAS ID is a tracking device that is located directly around the beam pipe and immersed in a 2 T magnetic field, which is parallel to the z-axis and generated by a superconducting solenoid coil. The ID is used to reconstruct the trajectories of charged particles (tracks) traversing the detector volume. These tracks are bend in the magnetic field by the Lorentz force. If the particle's charge is assumed to be known, this allows for precise determination of the particle's momentum by measuring the curvature of the associated track. The polarity of the charge (+ or −) is identified by the deflection direction. The primary vertex and secondary decay vertices are determined by extrapolating the tracks to a common point of origin. The reconstruction of secondary vertices is very important for particles that decay before the ID but live long enough to travel a considerable distance before decaying, like tau leptons or B-hadrons. The ID is shown in Figure 3.4. It comprises three sub-detectors: the Pixel detector, the Semiconductor Tracker (SCT), and the Transition Radiation Tracker (TRT) [281, 282].

The innermost part of the ID is the Pixel Detector. Initially, it was designed as a three-layer system with its layers located at radial distances of 50.5 mm, 88.5 mm and 122.5 mm from the beamline. In the end-cap regions, it is completed by three discs. The Pixel detector has a typical pixel size of 50 µm × 400 µm and covers a pseudorapidity region of $|\eta| < 2.5$ corresponding to $|\theta| > 9.4°$. During the LHC shutdown after Run-1, an additional layer called *insertable B-layer* (IBL) was added to the Pixel detector [283–285]. This layer is located close to the beamline at 33.2 mm distance and features a higher pixel density with a typical pixel size of 50 µm × 250 µm. The IBL covers the pseudorapidity range up to $|\eta| = 2.9$. With this setup, the b-tagging performance and the vertex resolution are significantly improved compared to Run-1. The resolution of the Pixel detector in the transverse plane is 10 µm and in the z direction 115 µm.

The Pixel detector is surrounded by the SCT, a four-layer system consisting of silicon micro-strip sensors in the barrel and nine discs in each of the two end-cap regions. The layers range from 299 mm to 514 mm around the beamline, covering the same pseudorapidity range as the Pixel detector. To obtain

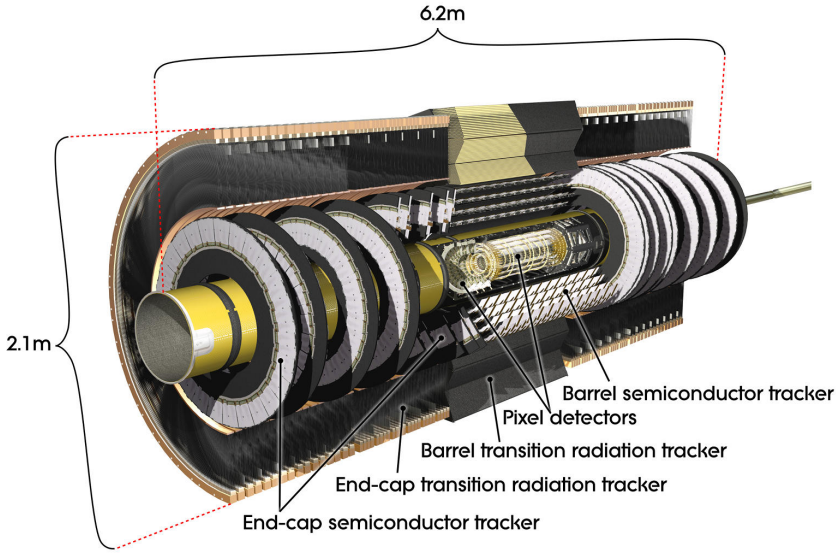

Figure 3.4: Cut-away view of the ATLAS Inner Detector system including the Pixel Detector, the Semiconductor Tracker and the Transition Radiation Tracker. Taken From Reference [274].

information about the z-axis, the strips in each sensor pair are glued back to back with a small stereo angle [286]. The resolution of the SCT is 17 µm in the transverse plane and 580 µm in the z direction.

The outermost tracking component is the TRT, which extends to a radius of 1 082 mm from the IP. In contrast to the other two tracking detectors, it is a gaseous detector composed of straw tubes filled with a gas mixture consisting of 70 % Xe, 27 % CO_2 and 3 % O_2. Materials with different refractive indices are placed between the straw tubes to gain additional information about the particle type. If a charged particle flies by, it emits X-ray photons when crossing the boundaries between the different media. Since heavy particles are less likely to produce transition radiation than light particles, this feature can be used for particle identification. The TRT provides precise track measurements for $|\eta| < 2.0$ [287].

The transverse momentum resolution of the ID is [274]

$$\frac{\sigma(p_T)}{p_T} = 0.05\,\% \cdot p_T \oplus 1\,\%\,, \tag{3.9}$$

where $\sigma(p_T)$ is the uncertainty of the transverse momentum p_T of a charged particle and $\oplus$ means that the different contributions to the overall uncertainty are added in quadrature, i. e. $a \oplus b = \sqrt{a^2 + b^2}$.

3.2.4 The Calorimeter System

The calorimeter system shown in Figure 3.5 measures the total energy of charged and neutral particles. It surrounds the ID and covers a range of $|\eta| < 4.9$ [289, 290]. The particles are absorbed in high-density absorber plates, and the deposited energy is measured in sensing layers between the plates. In the absorbers, the particles get decelerated by interacting with the material, creating a cascade production reaction called *particle shower*. This process is repeated until the particle is stopped.

The inner calorimeter layer, the ECAL, is highly granular and designed to measure electrons, positrons, and photons. It consists of three parts, the central region (barrel) which covers the region $|\eta| < 1.475$ and two end-cap regions covering $1.375 < |\eta| < 3.2$. In general, the electromagnetic showers of these particles are narrow and short compared to hadronic showers. The passive absorber plates are made out

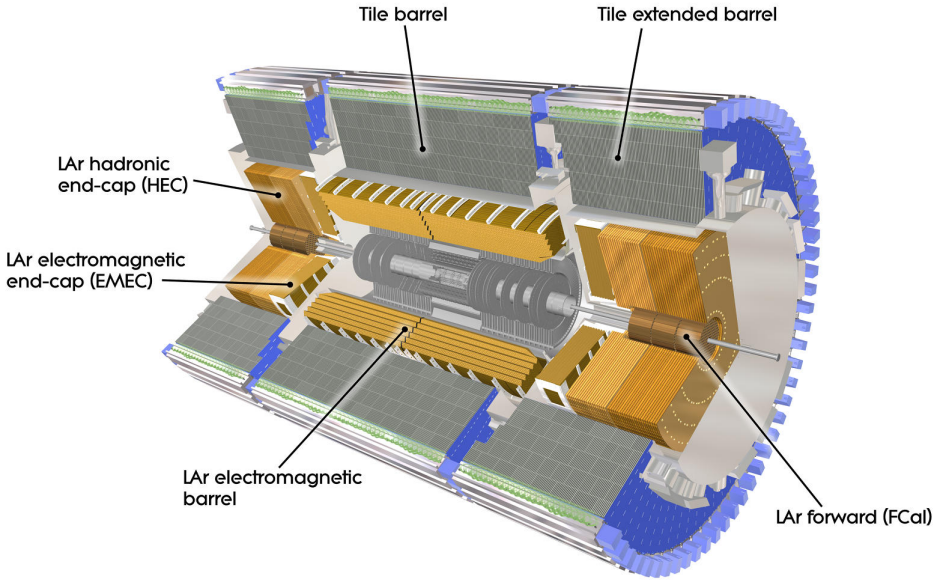

Figure 3.5: Cut-away view of the electromagnetic and hadronic calorimeters of the ATLAS detector [288].

of lead, while the sensing layers are filled with liquid argon (LAr). The latter ones are cooled down to -180° C. The particle shower ionizes argon atoms, which release electrons that drift towards copper electrodes in an electric field. This process produces a measurable signal proportional to the particle's initial energy. To ensure that the whole energy of the particle is absorbed, the ECAL has a thickness of more than 22 times the radiation length X_0 in which the incoming electron energy is decreased to $1/e$ of its initial energy. The innermost layer of the ECAL, the strip layer, has the highest granularity. It plays an important role in resolving the energy deposits of multiple photons with small ΔR separation. This is very important for measuring neutral pions $\left(\pi^0\right)$, which typically decay into two photons with a small opening angle. The energy resolution of the ECAL [274] is

$$\frac{\sigma(E)}{E} = \frac{10\,\%}{\sqrt{E}} \otimes 0.7\,\%\,. \tag{3.10}$$

In addition, a thin presampler layer (PS) is located in front of the ECAL, covering the region $|\eta| < 1.8$. It is used to correct fluctuations in the energy loss upstream of the calorimeter.

The HCAL surrounds the ECAL, and it is designed to measure the energy of charged and neutral hadrons. Since hadronic showers are typically wider and deeper than electromagnetic ones, the HCAL is bigger than the ECAL. In the barrel, a tile calorimeter with steel absorbers and scintillating tiles covering the pseudorapidity range $|\eta| < 1.7$ is used. The end-cap calorimeters cover $1.5 < |\eta| < 3.2$ using interleaving layers of copper absorbers and liquid argon as the active material. The η-coverage is increased by additional forward calorimeters (FCALs) in the region $3.1 < |\eta| < 4.9$. The main motivations for the FCAL are improvements in the E_T^{miss} reconstruction, which are important in many new physics searches and for the identification of forward jets. The term *jet* refers to a collection of hadrons pointing into a similar direction. While the first layer of the FCAL consists of a Cu/LAr absorber matrix designed for electromagnetic calorimetry, the second and third layers use a W/LAr matrix. Hadronic shower remnants that exceed the third layer are absorbed in a passive layer of brass located behind the third layer. The

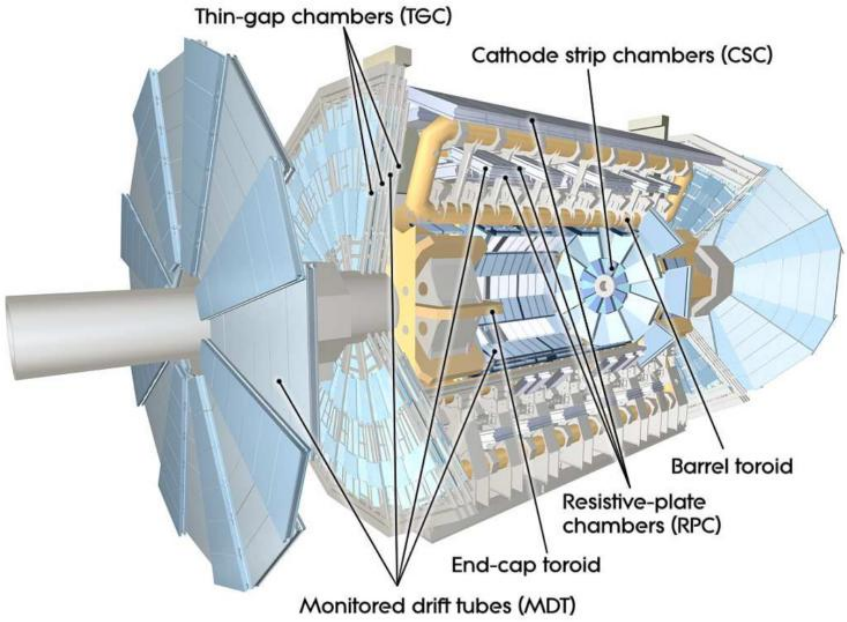

Figure 3.6: Cut-away view of the ATLAS muon system with the trigger (RPC, TGC) and precision tracking (CSC, MDT) chambers. Taken from Reference [274].

energy resolutions of the HCAL [274] in the barrel and end-cap regions are

$$\frac{\sigma(E)}{E} = \frac{50\,\%}{\sqrt{E}} \otimes 3\,\% \qquad \text{and} \qquad \frac{\sigma(E)}{E} = \frac{100\,\%}{\sqrt{E}} \otimes 10\,\%\,. \tag{3.11}$$

It is much less precise than the ECAL for a couple of reasons. On average, it is less granular because a larger detector volume has to be covered. In addition, a significant part of the initial energy is diverted to slowly proceeding nuclear processes with low energies. For example, these are low energetic neutron captures that are not reconstructed. Another reason is related to the fact that the ATLAS calorimeters are non-compensating. This means that the signals of hadrons are smaller than those of electrons, even if both particles deposit the same amount of energy. Since hadronic showers often contain an electromagnetic component like in decay chains involving neutral pions $\left(\pi^0 \to \gamma\gamma\right)$, the energy deposits in the calorimeter cells need to be calibrated appropriately. In ATLAS, the following calibration scheme is applied. First, three-dimensional topological clusters (topo-clusters) are reconstructed at the EM scale, i. e. the scale at which the energy deposits of electromagnetic showers are correctly measured. This is followed by classifying each cluster into mostly hadronic or mostly electromagnetic based on its shape and energy. After that, they are corrected by reweighting their energy to account for non-compensating effects, losses due to noise thresholds, and energy deposits in inactive material. The corresponding local hadronic calibration (LC) weights are determined from Monte Carlo (MC) simulations.

The ATLAS calorimeter is built as a hermetic, confining detector, and in principle, only muons (and neutrinos) should be able to exit the HCAL. However, very high energetic hadrons can punch through into the muon system in some cases. To minimize particle leakage into the muon detector, an additional absorbing layer of lead is placed around the HCAL.

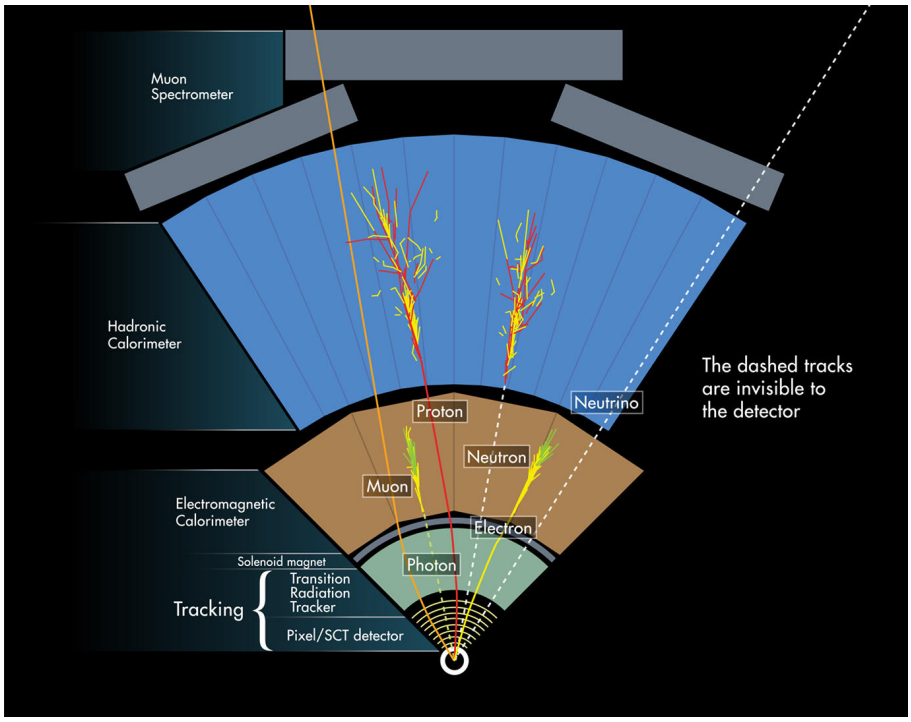

Figure 3.7: The signatures of different particles in the ATLAS detector [292].

3.2.5 The Muon System (MS)

Muons are about 200 times heavier than electrons. Thus, they are less likely to radiate bremsstrahlung and exit the calorimeters with small energy losses. To measure muons, the MS, illustrated in Figure 3.6, is placed outside the HCAL covering a pseudorapidity range of $|\eta| < 2.7$. It consists of high-precision tracking and trigger chambers. The precision tracking is performed in three layers of Monitored Drift Tube (MDT) chambers. The largest backgrounds are observed in the innermost end-cap layers, particularly in the Cathode Strip Chambers (CSCs). These are caused by neutrons and γ-rays emerging from the calorimeter. The muon track is measured in a magnetic field generated by three large superconducting toroidal magnets with field strengths of $0.5 - 1\,\mathrm{T}$ [291]. The transverse momentum resolution of the MS for a muon with $p_T = 100\,\mathrm{GeV}$ ($p_T = 1\,\mathrm{TeV}$) [274] is

$$\frac{\sigma(p_T)}{p_T} = 3\,\%\,(10\,\%)\,. \tag{3.12}$$

Two types of trigger chambers are used. The first ones are Resistive Plate Chambers (RPC) used in the barrel region ($|\eta| < 1.05$) and the second ones are Thin Gap Chambers (TGC) used in the end-cap regions ($1.05 < |\eta| < 2.7$). In contrast, the L1 muon trigger covers a range of $|\eta| < 2.4$.

3.3 Event Reconstruction and Particle Identification

The particles produced in pp collisions at the LHC interact in different ways with the subsystems of the ATLAS detector. Figure 3.7 illustrates how ATLAS detects various particles in different parts of the detector. While charged particles like electrons, muons, and protons leave a track in the ID, neutral particles like photons and neutrons are invisible to the tracking system. However, photons can be observed

in the ECAL due to their electromagnetic shower when interacting with the absorber material. For electrons and positrons, the energy deposits in the calorimeter can be matched to tracks in the ID. The idea of linking energy deposits in the calorimeter to tracks in the ID is very powerful. It leads to the concept of particle flow (PFlow), which is exploited in the reconstruction of different physical objects, as will be explained in Section 3.4. Strongly interacting particles deposit most of their energy in the HCAL. Charged hadrons like protons can be identified using the same strategy, but in this case, the energy deposits in the HCAL are matched to tracks. This allows the identification of neutral hadrons like neutrons because they do not have an associated track. Muons are identified in the MS, and their momentum resolution is improved by matching the MS tracks to tracks in the ID. The only SM particles that cannot be detected with the ATLAS detector are neutrinos. However, their transverse energy can be calculated with Equation 3.8.

The reconstruction and identification of physical objects in ATLAS are outlined in the following.

3.3.1 Electrons and Photons

Electrons are reconstructed from energy deposits in the ECAL and associated tracks in the ID [293–295]. The energy deposits in the calorimeter are reconstructed using a dynamic, topological cell clustering algorithm [296, 297], which considers energy losses due to bremsstrahlung in the ID. This is achieved by matching the electron track to the associated cluster and the satellite photon cluster in case there is a significant mismatch between the reconstructed electron energy in the ECAL and the track momentum.

The starting point for the formation of topo-clusters is *seed cells*. These are calorimeter cells with signals that exceed the expected noise threshold by at least a factor of four. Each seed cell forms a *proto-cluster*. Proceeding from the proto-cluster, the neighboring cells (in all three dimensions) are added to the proto-cluster if their signals exceed the noise threshold by at least a factor of two. Each cell that passes this criterion becomes a seed cell in the next iteration of the algorithm. If all cells with significant signals have been collected, one final set of neighboring cells with positive signals is added to the cluster. This configuration is called a "4-2-0" topo-cluster reconstruction. Particle tracks are reconstructed in the ID with an *inside-out* track finder [298]. Track candidates are formed by combining the hits in the Pixel detector and the SCT. After that, the candidates are ranked based on several track quality requirements to resolve badly reconstructed and overlapping tracks. Before being matched to a track, the topo-cluster has to fulfill additional quality criteria based on the energy profile in η and the hadronic shower leakage. Based on the topo-cluster, a Region of Interest (ROI) for possible track candidates is defined. Standard pattern reconstruction [299] is applied everywhere within the ROI to find track candidates. If the track fit fails, all tracks are fitted again by allowing an energy loss of up to 30 %. Tracks that are loosely matched to the cluster in the ECAL are then refitted using a Gaussian Sum Filter[1] [301] which allows the inclusion of additional calorimeter clusters in the fitting process. This technique significantly improves the track parameter estimation if one or more of these clusters are caused by bremsstrahlung photons emitted by the electron in the ID.

The photon reconstruction runs parallel to the electron reconstruction because both share the same shower development. If no track is matched to the energy cluster, it is considered a photon. It is also defined as a photon cluster if it is matched to two tracks and a conversion vertex ($\gamma \rightarrow e^+e^-$).

Many processes can fake the signatures of prompt electrons, like misidentified jets and electrons from photo conversions and pion decays. Different discriminating variables are used to form a likelihood (LH) discriminant to distinguish prompt electrons from background events. These variables are based on the shower shape in the ECAL, the matching accuracy of clusters to tracks, the signals from the TRT, and whether or not there is a hit in the insertable B-layer. Different LH-identification working points, called

[1] A Gaussian Sum Filter is a non-linear generalization of the Kalman filter [300].

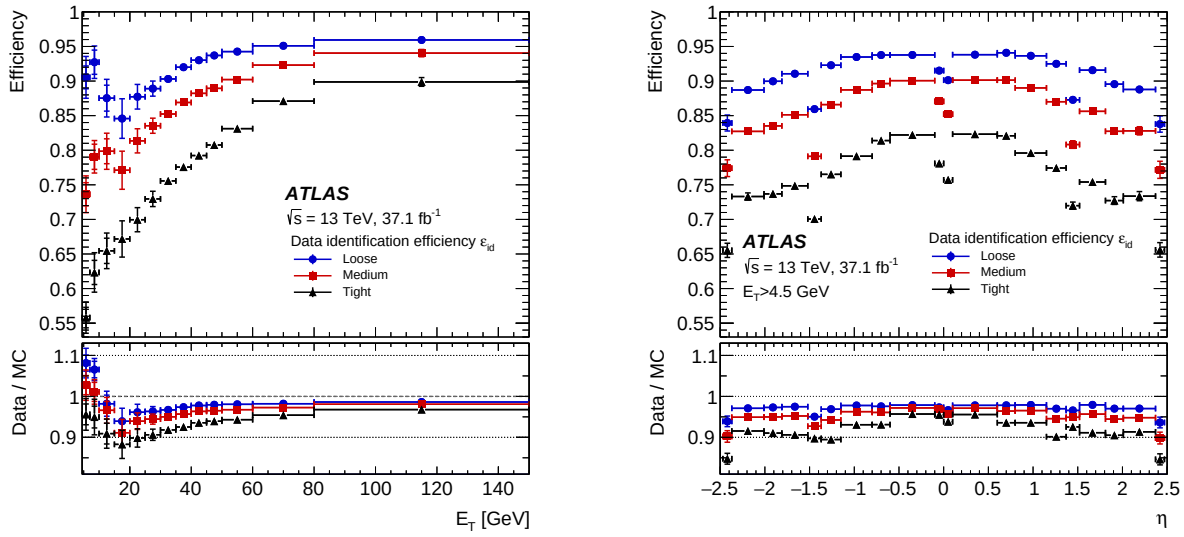

(a) (b)

Figure 3.8: The electron identification efficiencies determined from $Z \to ee$ and $J/\psi \to ee$ events as a function of (a) the transverse energy E_T and (b) the pseudorapidity η for the *Loose*, *Medium* and *Tight* working points. The efficiencies are measured using 37.1 fb^{-1} of data. The bottom panels show the data-to-simulation ratios. Taken from Reference [295].

Loose, *Medium* and *Tight* [294] are defined based on their background rejection. For the $H \to ZZ^* \to 4\ell$ analysis the *Loose* working point is chosen which features an efficiency for identifying prompt electrons with $E_T = 40\,\text{GeV}$ of 93 %. The corresponding efficiencies for the *Medium* and *Tight* working points are 88 % and 80 %, respectively.

The electron identification efficiencies of all three working points are shown in Figure 3.8 for an integrated luminosity of 37.1 fb^{-1}. They are directly measured in data using the *tag-and-probe* method [293–295]. This is done by selecting unbiased electrons from $Z \to ee$ or $J/\psi \to ee$ events. These electrons (probe) have to satisfy either the *Loose*, *Medium* or *Tight* identification criteria, while the second particle (tag) in the decay has to fulfill very strict selection requirements. The identification efficiency is defined as the ratio of the number of identified probe electrons and the total number of probe electrons.

Compared to the *Loose* working point, the identification efficiencies of the *Tight* and *Medium* selections are lower because of the more stringent cuts resulting in an increased background rejection. The identification efficiencies increase with the electron's transverse energy (see Figure 3.8(a)) because there are fewer background events at high energies. The increasing efficiency for energies below 20 GeV in case of the *Loose* and *Medium* working points result from the modeling of the ECAL shower shapes. The η dependence (see Figure 3.8(b)) reflects the calorimeter and ID structure. The drop in efficiency at $\eta = 0, \pm 1.5$ results from non-instrumented regions in the ECAL. The latter corresponds to the transition region between the barrel and the end-cap of the calorimeter.

The electron energy scale is calibrated using $Z \to ee$ events [302]. Differences in the energy scale between data and MC simulation are determined in different η bins (i) and described by a correction factor $(1 + \alpha_i)$ that scales the MC energies. This results in additional η-dependent constant terms c_i in the energy resolution

$$\left(\frac{\sigma(E)}{E}\right)^{\text{data}} = \left(\frac{\sigma(E)}{E}\right)^{\text{MC}} \otimes c_i \,. \tag{3.13}$$

The accuracy varies between 0.03 % and 0.2 % depending on the pseudorapidity of the electron. The additional constant terms are approximately 1 % (1 – 2 %) in the barrel (end-cap) region.

3.3.2 Muons

Muons are identified and reconstructed from tracks in the ID and the MS, supplemented with information from the calorimeters in the central region ($|\eta| < 0.1$) [303, 304]. Depending on the available information of these sub-detector systems, four different types of muon reconstructions are distinguished:

- *Combined muons* are obtained from a combined fit to independently reconstructed ID and MS tracks. MS tracks are extrapolated inward and matched to ID tracks (*outside-in*). During this refitting, hits may be added to or removed from the initial tracks to improve the fit quality. The combined muon reconstruction is the most precise of the different reconstruction types.

- *Segment-tagged muons* are reconstructed from ID tracks that can only be matched to track segments in the MDT or CSC chambers. This is typically the case in MS regions with low acceptance or for low-p_T muons. In this case, the muon's momentum is only measured in the ID.

- *Extrapolated muons* are reconstructed in the MS. Hits from at least two (three) MS layers are required in the central (forward) region. This method is mainly used to reconstruct muons in the forward region ($2.5 < \eta < 2.7$), which is not covered by the ID.

- *Calorimeter-tagged muons* are obtained if an ID track is matched to a calorimeter signature that is compatible with the energy deposit of a minimum ionizing particle. This type of muon reconstruction is the least precise one but becomes relevant for $|\eta| < 0.1$ because the MS is only partially instrumented in this region.

If two or more methods reconstruct a muon candidate, the highest purity method is chosen. The main background for prompt muons originate from charged pion ($\pi^{\pm}$) and kaon ($K^{\pm}$) decays. To suppress these backgrounds, additional quality requirements are applied. Four different identification working points called *Loose*, *Medium*, *Tight* and *High-p_T* are defined. The *Medium* working point provides the default selection for muons in ATLAS. It is optimized to minimize the systematic uncertainties in the muon reconstruction and energy calibration. In this case, only combined and extrapolated muons tracks are used. In contrast, the *Tight* selection only accepts combined muons with high purity. This working point provides excellent background rejection at some efficiency cost. The *Loose* identification criteria trade off background rejection for higher efficiencies. In this case, muon candidates from all four reconstruction methods are accepted. The *High-p_T* working point is optimized for high-mass Z' and W' searches with large transverse momentum tracks ($p_T > 100\,\text{GeV}$). For the $H \to ZZ^* \to 4\ell$ analysis, the *Loose* working point is employed to maximize the reconstruction efficiency.

The muon identification efficiency for $|\eta| < 2.5$ is determined using a tag-and-probe method in $J/\psi \to \mu\mu$ and $Z \to \mu\mu$ events [304]. The identification efficiency in the high-η region ($2.5<|\eta|<2.7$) is measured by comparing the number of muon candidates to the expected number of muons in the SM [303]. Figure 3.9 shows the muon identification efficiency obtained from a subset of the 2017 data set with $15.4\,\text{fb}^{-1}$. The efficiency of the *Medium* selection is about 99 % for muons with $p_T > 10\,\text{GeV}$ and $|\eta| > 0.1$ (see Figure 3.9(a)). For smaller transverse momenta it drops to about 82 % at 5 GeV. While there is almost no η-dependence in the muon identification efficiency for *Loose* muons (see Figure 3.9(b)), it drops quickly from 95 % (98 %) to 70 % (60 %) for the *Medium* (*Tight*) working point near $\eta = 0$. The reason for this difference is that the segment-tagged and calorimeter-tagged muons, which are not considered for the *Medium* and *Tight* selections, recover the efficiency for *Loose* muons in this region.

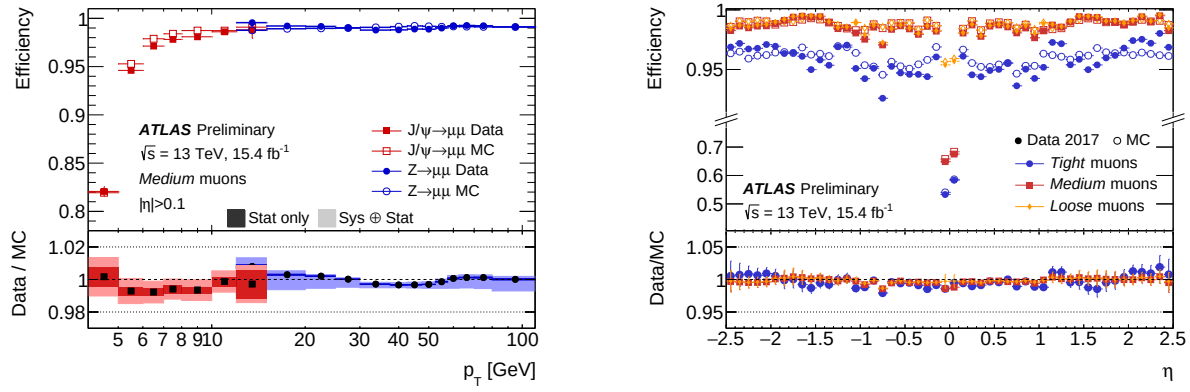

(a) (b)

Figure 3.9: The muon identification efficiency determined from $Z \to \mu\mu$ and $J/\psi \to \mu\mu$ events for (a) the *Medium* identification working point as a function of p_T for $|\eta| > 0.1$ and (b) the *Loose*, *Medium* and *Tight* working points as a function of η for muons with $p_T > 10\,\text{GeV}$. The efficiencies are measured using $15.4\,\text{fb}^{-1}$ of data collected in 2017. The bottom panels show the data-to-simulation ratios. Taken from Reference [305].

The muon momentum scale and resolution are determined from dimuon invariant mass distributions in $Z \to \mu\mu$ and $J/\psi \to \mu\mu$ decays. The transverse momentum resolution $\sigma(p_T)/p_T$ obtained from the former events is 1.7 % (2.3 %) in the central (end-cap) region. The corresponding resolution from the latter events is 2.3 % (2.9 %).

3.3.3 Jets

In particle physics, a jet is a narrow cone of hadrons and other particles produced in the hard scattering process of quarks and gluons. As explained in Section 2.1.2, quarks are never observed as free particles but are always confined within hadrons. However, at the interaction vertex, quarks are produced and not hadrons. If a quark pair $q\bar{q}$ is created with large relative momentum, the process of hadronization will convert the energy stored in the field between the quarks into additional quark-antiquark pairs. This process continues until the energy is below the threshold for pair creation. In this case, the quarks bind together to form hadrons. Since the relative momentum between the colliding quarks is mostly converted into new particles, the remaining relative momentum between the hadrons is typically small compared to the absolute value of the momentum. Thus, the hadrons are collimated in a narrow cone called a jet.

Jets are reconstructed from topo-clusters in the calorimeter supplemented with ID information. In principle, there are two main types of jet finding algorithms. The first type, *cone algorithms*, are solely based on a distance measure in $\eta - \phi$, while the second type, *sequential cluster algorithms*, also take into account the distance in momentum space. Cone algorithms result in jets with rigid circular boundaries and are typically not infrared and collinear (IRC) safe [306]. In contrast, sequential cluster algorithms lead to jets with fluctuating areas in $\eta - \phi$ space. Since they are IRC safe, they are generally preferred.

Clustering algorithms depend on two distance parameters. The first one is a momentum-scaled measure of the $\eta - \phi$ separation $d_{ij} = \min(p_{Ti}^a, p_{Tj}^a) \times {}^{\Delta R_{ij}^2}/_{R^2}$, where ΔR_{ij}^2 is defined in Equation 3.6 and R is the radius parameter which determines the final size of the jet. The second one, $d_{iB} = p_{Ti}^a$, is the distance between the topo-cluster i and the beam axis in momentum space. The exponent a in both expressions defines a particular clustering algorithm. For example, $a = 2$ corresponds to the k_T algorithm [307] and $a = -2$ to the anti-k_T algorithm [308]. Since the latter is widely used for the reconstruction of jets in ATLAS, only the anti-k_T algorithm will be considered in the following.

The distance parameters for the anti-k_T algorithm are

$$d_{ij} = \min\left(\frac{1}{p_{Ti}^2}, \frac{1}{p_{Tj}^2}\right) \times \frac{\Delta R_{ij}^2}{R^2} \qquad \text{and} \qquad d_{iB} = \frac{1}{p_{Ti}^2}\,. \tag{3.14}$$

In ATLAS, the radius parameter $R = 0.4$ is typically used. If the distance d_{ij} is smaller than d_{iB} and d_{jB} the clusters i and j are merged into one cluster and their four-momenta are summed. If $d_{iB} < d_{ij}$ for any j, the cluster i is defined to be a jet and removed from the list of clusters. The distance parameters are then recalculated for the updated list of objects, and the process is repeated until no clusters are left. The negative exponent ($a = -2$) implies that collinear particles with $\Delta R_{ij} \to 0$ are clustered first, while soft particles with $p_{Ti} \to 0$ are clustered last.

The jet energy scale (JES) is calibrated in several stages by correcting the jet's four-momentum. The first step is the *origin correction*, which considers the position of the primary vertex in each event [309]. It recalculates the four-momentum of each jet while keeping its energy constant. This significantly improves the η resolution, especially for jets with large transverse momenta. Origin corrected jets that are reconstructed using only the energy information from the calorimeters are called *EMTopo jets*. The second step is the *pile-up correction*. It removes energy deposits caused by other pp collisions within the same or nearby bunch crossings. The third step is the *absolute JES calibration* which corrects the four-momentum such that their energy and direction agrees with the truth jets derived from dijet MC events. After that, the jet energy is further improved using information from the ID, calorimeters, and MS in the *global sequential calibration*. Finally, a residual *in situ* calibration is performed to correct for differences between data and MC simulation using well-measured photons, Z bosons, and calibrated jets as reference. EMTopo jets calibrated with the full JES are considered to be at the EM+JES scale.

The systematic uncertainty of the EM+JES for central jets with $|\eta| < 1.2$ is below 1 % for 100 GeV $< p_T <$ 2 000 GeV and below 5 % for jets with smaller transverse momenta. The uncertainty of forward jets is up to 2 % worse than the corresponding uncertaintiy for central jets.

The pile-up correction discussed above removes the average energy of pile-up interactions from the reconstructed jet. However, local fluctuations in the pile-up activity can still lead to additional pile-up jets in the event. The jet-vertex tagger (JVT) is used to reject such contributions [310, 311]. It uses a likelihood discriminant that combines two track-based variables, which are sensitive to the jet vertex origin. The JVT method provides signal jet efficiencies of 80 %, 90 %, and 95 % at the cost of pile-up fake rates of 0.4 %, 1.0 %, and 3 %, respectively.

Jets including B-hadrons (b-jets) feature an important property that is used to discriminate between Higgs boson candidates that are created in bbH and ttH production. Compared to light-quark and gluon jets, b-jets are relatively long-lived and can be identified by their decay vertices. Since this is only possible by using additional information from the ID, only jets with $|\eta| < 2.5$ are considered. The output of tracking algorithms that exploit the long lifetime of B-hadrons provide the input for the MV2c10b-tagging algorithm [312, 313]. Four different identification working points for b-jets with efficiencies of 60 %, 70 %, 77 %, and 85 % are defined.

3.3.4 Tau Leptons

The tau lepton, with a mass of $m_\tau = 1\,777$ GeV [54], is the heaviest lepton in the SM. Due to its large mass it has a relatively short lifetime of $\tau_\tau \approx 2.9 \times 10^{-13}$ s, which leads to a proper decay length of 87 µm. This means that it decays inside the beam pipe and can only be identified through its decay products. Besides, each tau lepton decay mode contains at least one neutrino in the final state. Since neutrinos are invisible to the detector, they escape undetected. Thus, their individual momentum is unknown. This makes the tau reconstruction inevitably incomplete and susceptible to backgrounds.

Table 3.1: The main τ^- decay modes and branching fractions [54]. The corresponding decays for the τ^+ are obtained by charge conjugation. The hadronic decay modes are grouped into different categories depending on the number of charged ("prong") and neutral hadrons that are involved in the decay. The five major hadronic decay modes are written in bold letters.

Category	Nomenclature	Decay mode	BR [%]
Hadronic 1-prong	1p	$\tau^- \to h^- \geq 0$ neutrals ν_τ	49.98
	1p0n	$\boldsymbol{\tau^- \to \pi^- \nu_\tau}$	**10.82**
		$\tau^- \to K^- \nu_\tau$	0.70
	1p1n	$\boldsymbol{\tau^- \to \pi^- \pi^0 \nu_\tau}$ (mostly via $\rho(770)^-$)	**25.52**
		$\tau^- \to K^- \pi^0 \nu_\tau$ (via K^{*-})	0.43
	1pXn	$\boldsymbol{\tau^- \to \pi^- 2\pi^0 \nu_\tau}$ (mostly via $a_1(1260)^-$)	**9.26**
		$\tau^- \to K^- 2\pi^0 \nu_\tau$	0.07
		$\tau^- \to \pi^- 3\pi^0 \nu_\tau$	1.04
		$\tau^- \to h^- K^0_S \geq 0$ neutrals ν_τ	0.94
Hadronic 3-prong	3p	$\tau^- \to h^- h^- h^+ \geq 0$ neutrals ν_τ	15.20
	3p0n	$\boldsymbol{\tau^- \to \pi^- \pi^- \pi^+ \nu_\tau}$ (mostly via $a_1(1260)^-$	**9.31**
	3pXn	$\boldsymbol{\tau^- \to \pi^- \pi^- \pi^+ \pi^0 \nu_\tau}$	**4.62**
Hadronic 5-prong	-	$\tau^- \to \geq 5h \geq 0$ neutrals ν_τ	0.1
Leptonic	-	$\tau^- \to e^- \nu_\tau \bar{\nu}_e$	17.82
	-	$\tau^- \to \mu^- \nu_\tau \bar{\nu}_{mu}$	17.39

There are two types of tau lepton decays. The first type is leptonic decays into an electron or a muon. These decay modes cannot be distinguished from promptly produced electrons and muons. Moreover, they contain a second neutrino, making the reconstruction very challenging. The second type is hadronic decays of the tau lepton (τ_{had}) summing up to a branching fraction of 65 %. The main tau lepton decay modes are summarized in Table 3.1, and the five most abundant ones are written in bold letters. The τ_{had} almost exclusively decays into final states with one or three charged hadrons $h^\pm$, called *1-prong* (1p) and *3-prong* (3p), respectively. Besides, they can be accompanied by zero (0n), one (1n), or more than one (Xn) neutral hadrons. In most cases, these hadrons are pions. However, a small fraction of decays also contains charged and neutral kaons. The measurable (or visible) part of the hadronic tau lepton, i. e. the decay products without the neutrino, is called $\tau_{\text{had-vis}}$.

The $\tau_{\text{had-vis}}$ is reconstructed from jets using the anti-k_T algorithm with a radius parameter $R = 0.4$, obtained from energy clusters in the calorimeter at the LC scale [314]. The experimental challenge is to disentangle the jets from the $\tau_{\text{had-vis}}$ decay from those of QCD events. Due to the abundance of QCD jets at the LHC, these events have to be efficiently suppressed. In the following the term *tau* will refer to the $\tau_{\text{had-vis}}$ if not stated otherwise.

Most tau lepton decay modes produce one or three charged tracks in the ID. They are typically collimated in a very narrow cone featuring a characteristic sharing of energy among the decay products. These properties and the impact parameter due to the finite decay length of the tau lepton are effective discriminants for QCD jets. The core region around the initial jet axis is defined by a cone of radius $\Delta R = 0.2$. The transverse momentum of the tau lepton is calculated from EMTopo clusters within the core region using a tau-specific calibration scheme [315]. The LC-calibrated energy of EMTopo clusters is corrected by taking into account contributions from pile-up events. These contributions increase linearly with the number of primary vertices, and they are separately calculated for 1-prong and 3-prong decays.

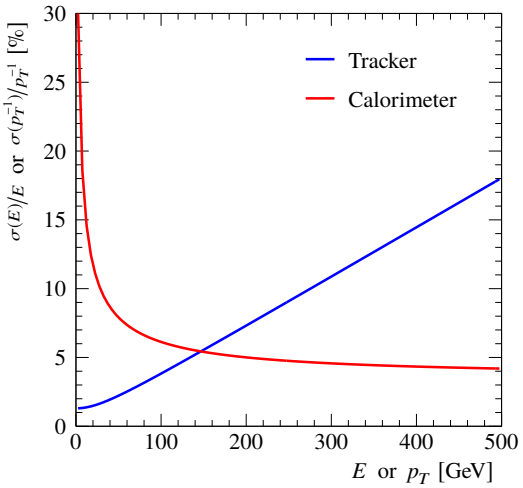

Figure 3.10: The relative energy resolution $\sigma(E)/E$ of the ATLAS calorimeter (red line) and the relative inverse transverse momentum resolution $\sigma(p_T^{-1})/p_T^{-1}$ of the ATLAS tracking detector (blue line). The curves are calculated from Equations 3.15 and 3.16 by adding in quadrature the different contributions.

ID tracks are matched to the tau candidate if they satisfy several quality requirements: Their transverse momenta have to be larger than 1 GeV, they need to have at least two hits in the ID pixel layers, at least seven hits in the pixel and silicon microstrip layers altogether, and their impact parameters have to fulfill $|d_0| < 1\,\text{mm}$ and $z_0 \sin\theta < 1.5\,\text{mm}$.

The tau identification is based on a multi-variant analysis technique, called a *boosted decision tree* (BDT), which combines information from several jet discriminants. These variables are motivated by the specific tau decay kinematics and the properties of QCD jets. In addition, there is also a discriminant to suppress misidentified electrons. Tau candidates are required to satisfy $p_T > 15\,\text{GeV}$ and $|\eta| < 2.5$ and they need to have one or three reconstructed tracks in the ID, where the sum of charges is either plus one or minus one. In the following, the basic tau lepton reconstruction will be called *TauRec*.

To access information about the tau decay mode, the *Tau Particle-Flow Method* [316] is employed. The general PFlow concept and its application in the reconstruction of jets and tau leptons are explained in Section 3.4.

3.4 The Particle-Flow (PFlow) Method

The PFlow method is a technique to combine track and calorimeter information to improve jet reconstruction. In Run-1 of the LHC, jets have been reconstructed solely based on the energy deposits in the calorimeters. The corresponding energy resolution for single charged pions in the central calorimeter region is [317]

$$\frac{\sigma(E)}{E} = \frac{50\,\%}{\sqrt{E}} \oplus 3.4\,\% \otimes \frac{1\,\%}{E}\,, \tag{3.15}$$

while the inverse transverse momentum resolution of the tracker is

$$\frac{\sigma(p_T^{-1})}{p_T^{-1}} = 0.036\,\% \cdot p_T \oplus 1.3\,\%\,. \tag{3.16}$$

Figure 3.10 compares the corresponding resolutions as a function of the energy and the transverse

momentum. For energies below 140 GeV, the tracking system outperforms the calorimeter. Therefore, it seems natural to use the track measurement in the ID to estimate the energy of charged particles with $p_T < 140$ GeV. In this case, only the neutral particles are measured in the calorimeter. However, this is only possible if the algorithm can disentangle the energy clusters from neutral particles from those of charged particles. The PFlow method achieves this by matching the calorimeter clusters to tracks. To avoid double-counting, it is necessary to correctly identify the associated energy deposits in the calorimeter and remove its signals from the reconstructed clusters.

In ATLAS, the PFlow concept is used for the jet [317] and the tau lepton [316] reconstruction. The corresponding methods are briefly introduced in the following subsections.

3.4.1 Particle Flow for Jets

In ATLAS, jets are typically composed of 60 % charged hadrons, 30 % neutral hadrons and 10 % photons. The PFlow-based jet reconstruction combines information from the tracker and the calorimeter to reconstruct the individual jet constituents using the detector component that is best suited for the type and energy of the corresponding particle. For instance, a charged hadron with $E_T < 140$ GeV is most precisely measured in the tracker, while the calorimeter measurement is more precise for high-energetic charged hadrons. In contrast, for neutral hadrons, only the calorimeter measurement is available.

The PFlow jet algorithm consists of several steps to remove overlaps between the momentum measurements in the ID and the energy reconstruction in the calorimeter. It provides a list of tracks and clusters. The latter contains the unmodified EMTopo clusters and new ones resulting from the energy subtraction procedure. The first step of the algorithm tries to match well-measured tracks to a single EMTopo cluster. Next, the expected energy deposit in the calorimeter created by a particle with the measured track momentum is calculated. Since a single particle usually deposits energy in more than one cluster, the algorithm evaluates the probability that the particle's energy is spread over multiple clusters. Based on this probability, it decides whether more clusters are needed to recover the energy of the full particle shower. After that, the expected calorimeter signal generated by the track is subtracted from the set of matched EMTopo clusters. The remaining energy remnants, consistent with the shower fluctuations of a single particle, are removed.

PFlow jets are reconstructed using the anti-k_T algorithm with a radius parameter of $R = 0.4$. The inputs are energy clusters after the energy subtraction procedure and selected tracks with $|z_0 \sin\theta| < 2$ mm that are matched to the primary vertex. This criterion effectively removes tracks from pile-up events. The PFlow jet calibration is similar to the calibration procedure for EMTopo jets with a few modifications, described in Reference [317].

The transverse momentum resolution for PFlow and EMTopo jets after the JES calibration is shown in Figure 3.11. PFlow jets are measured significantly more precisely for $p_T \lessapprox 90$ GeV (Figure 3.11(a)). Note that their energy resolution degrades faster than the resolution profile of the tracker shown in Figure 3.10 because the latter is evaluated for single pions, while a typical jet is a much more complicated object.

3.4.2 Particle Flow for Tau Leptons

In Run-1 of the LHC, hadronically decaying tau leptons have been reconstructed using only the energy information of the calorimeter. Thus, it was impossible to distinguish between the different tau lepton decay modes. The tau PFlow reconstruction, called *CellBased*, provides information about the substructure of the tau decay by identifying the individual charged and neutral particles in the final state. The available tau decay modes motivate the classification into 1p0n, 1p1n, 1pXn, 3p0n, and 3pXn decays. It is optimized to reconstruct tau leptons with $15 < p_T < 100$ GeV. This range is crucial for the measurement of the Higgs boson $\mathcal{CP}$ properties in $H \to \tau\tau$ decays. The charged hadrons $h^{\pm}$ in the decay are measured

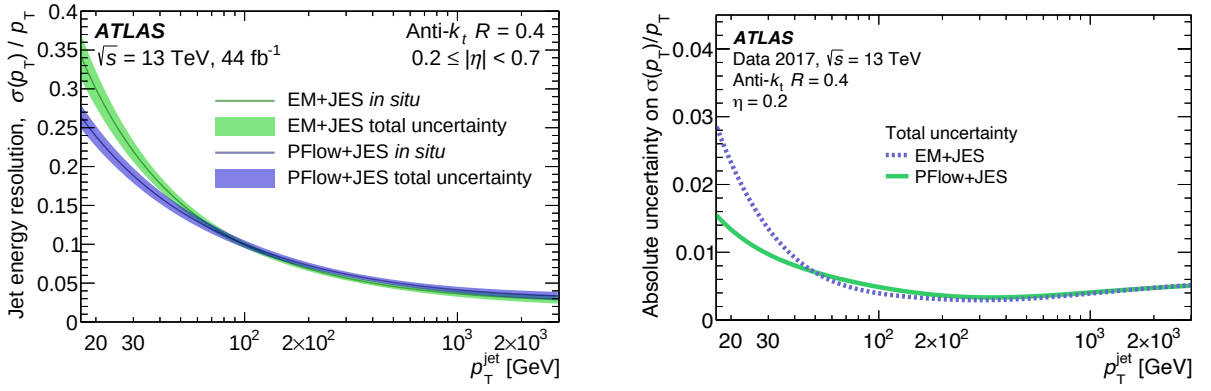

(a) (b)

Figure 3.11: Comparison of the jet energy resolution for fully calibrated jets that are reconstructed either soley based on EM topoclusters (EM+JES) or based on a combination of tracks and EM topocluster (PFlow+JES). (a) The relative jet energy resolution for $0.2 \leq |\eta| < 0.7$ and (b) the corresponding absolute uncertainty for $\eta = 0.2$. Taken from [318].

in the tracker, while the neutral hadrons are measured in the calorimeter after subtracting the charged hadrons' energy deposits. Most neutral pions decay into two highly collimated photons with a typical separation $\Delta R = 0.01 \ldots 0.03$, and they are reconstructed from energy deposits in the ECAL. All deposits in the HCAL are assigned to $h^{\pm}$ and subtracted from the calorimeters.

The energy subtraction procedure in the ECAL is more complicated. For each track with energy $E_{h^{\pm}}^{\text{track}}$ the deposited energy $E_{h^{\pm}}^{\text{EM}}$ is estimated as the difference

$$E_{h^{\pm}}^{\text{EM}} = E_{h^{\pm}}^{\text{track}} - E_{h^{\pm}}^{\text{HAD}}, \tag{3.17}$$

where $E_{h^{\pm}}^{\text{HAD}}$ is the deposited energy in the hadronic calorimeter. $E_{h^{\pm}}^{\text{HAD}}$ is calculated by clustering all energy deposits in the core region assigned to the closest extrapolated track position. The energy $E_{h^{\pm}}^{\text{EM}}$ of each $h^{\pm}$ is then subtracted from the energy of the closest π^0 candidate $\left(\pi^0_{\text{cand}}\right)$ within $\Delta R < 0.04$ of the $h^{\pm}$.

After this subtraction procedure many π^0_{cand} originate from $h^{\pm}$ remnants, pile-up events and other sources. To improve the purity, only neutral pions above a certain p_T threshold are considered. They are identified with a BDT that combines cluster shape variables and the number of photons in the first layer of the calorimeter (EM1), called *shots*, where about 30 % of the photon's energy is stored. The number of shots associated with the cluster is used to reconstruct the tau decay mode. Moreover, the information about the ΔR separation between the neutral pions in 1pXn decays is crucial for the reconstruction of the tau lepton's invariant mass, as shown in Section 3.5.4.

The *PanTau* algorithm further improves the decay mode classification by combining various discriminating variables in a BDT. These are, for example, the angle between the charged and neutral pions in 1p1n decays, the invariant mass of tracks in 3p0n decays, and the number of shots. In order to improve the π^0 reconstruction the following decay modes are tested against each other: 1p0n vs. 1p1n, 1p1n vs. 1pXn, and 3p0n vs. 3pXn.

Figure 3.12(a) shows the decay mode classification efficiency of the CellBased+PanTau (CB+PanTau) algorithm. In total, 74.4 % of the generated tau leptons are correctly reconstructed. The largest fractions of correctly identified decays are found for 1p0n (89.7 %) and 3p0n (92.5 %) decays. The identification of decay modes, including neutral hadrons, is far more complex. Thus, their efficiencies are significantly smaller. The 1pXn and 3pXn decays are most challenging, and many generated events are reconstructed as

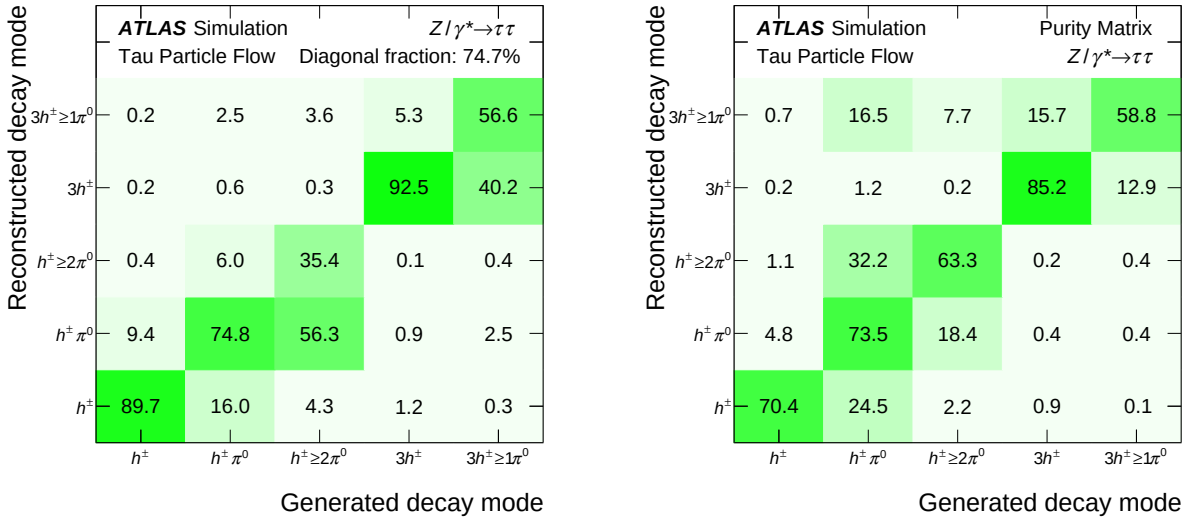

(a) (b)

Figure 3.12: The tau decay mode classification (a) efficiency and (b) purity matrix obtained with the CB+PanTau reconstruction algorithms. The decay modes $h^{\pm}$, $h^{\pm}\pi^0$, $h^{\pm} \geq 2\pi^0$, $3h^{\pm}$ and $3h^{\pm} \geq 1\pi^0$ correspond to 1p0n, 1p1n, 1pXn, 3p0n and 3pXn, respectively. Decays containing neutral kaons are ommited. The columns in the efficiency matrix add up to 100 %. Since neutral kaon decays are omitted the rows in the purity matrix do not quite add up to 100 %. Taken from Reference [316].

1p1n and 3p0n decays, respectively. The purity matrix, provided in Figure 3.12(b), shows the probability of tau candidates in a given reconstructed decay mode that originated from a generated decay mode. The largest purities are achieved for the 1p0n (70.4 %), 1p1n (73.5 %) and 3p0n (85.2 %) decays.

The four-momentum of the tau lepton, reconstructed with the CB+PanTau algorithm, is calculated from the vector sum of the hadrons' four-momenta. This calculation assumes that the reconstructed hadrons are either charged or neutral pions. The neutral pions are ordered according to their BDT identification score. Only the first n neutral pions are included, where n is the number of neutral hadrons in the corresponding PanTau decay mode. Suppose the tau decay is classified as 1p1n, but two neutral pions are reconstructed. In this case, it is most likely that the neutral pions are actually two photons from a single π^0 decay. Thus, their energy is corrected by setting the mass of the particles to zero. If a reconstructed 1pXn decay contains three or more photons in a single π^0_{cand}, only one π^0_{cand} is added to the tau lepton four-momentum and its mass is set to $2m_{\pi^0}$, where $m_{\pi^0} = 134.977\,\text{MeV}$ [54] is the mass of the neutral pion.

3.5 Improved Energy Reconstruction of Hadronic Tau Leptons

In this section, an improved energy reconstruction for tau leptons is presented. The corresponding performance studies are based on simulated $\gamma^* \rightarrow \tau\tau$ events.

The use of substructure-based hadronic tau reconstruction relies on the assumption that energy deposits in the calorimeter are created by charged and neutral pions, $\pi^{\pm}$ and π^0, respectively. However, some hadronic taus also decay into kaons, as shown in Table 3.1. The ATLAS detector cannot distinguish between tracks from charged kaons $K^{\pm}$ and charged pions $\pi^{\pm}$. Thus, the contribution from $K^{\pm}$ will not affect the tau reconstruction. In contrast, neutral kaons K^0 have a very different calorimeter signature than neutral pions. Since the substructure-based reconstruction cannot accurately reconstruct K^0 hadrons, it tries to reconstruct a π^0 instead. This is a problem because neutral kaons typically penetrate into the

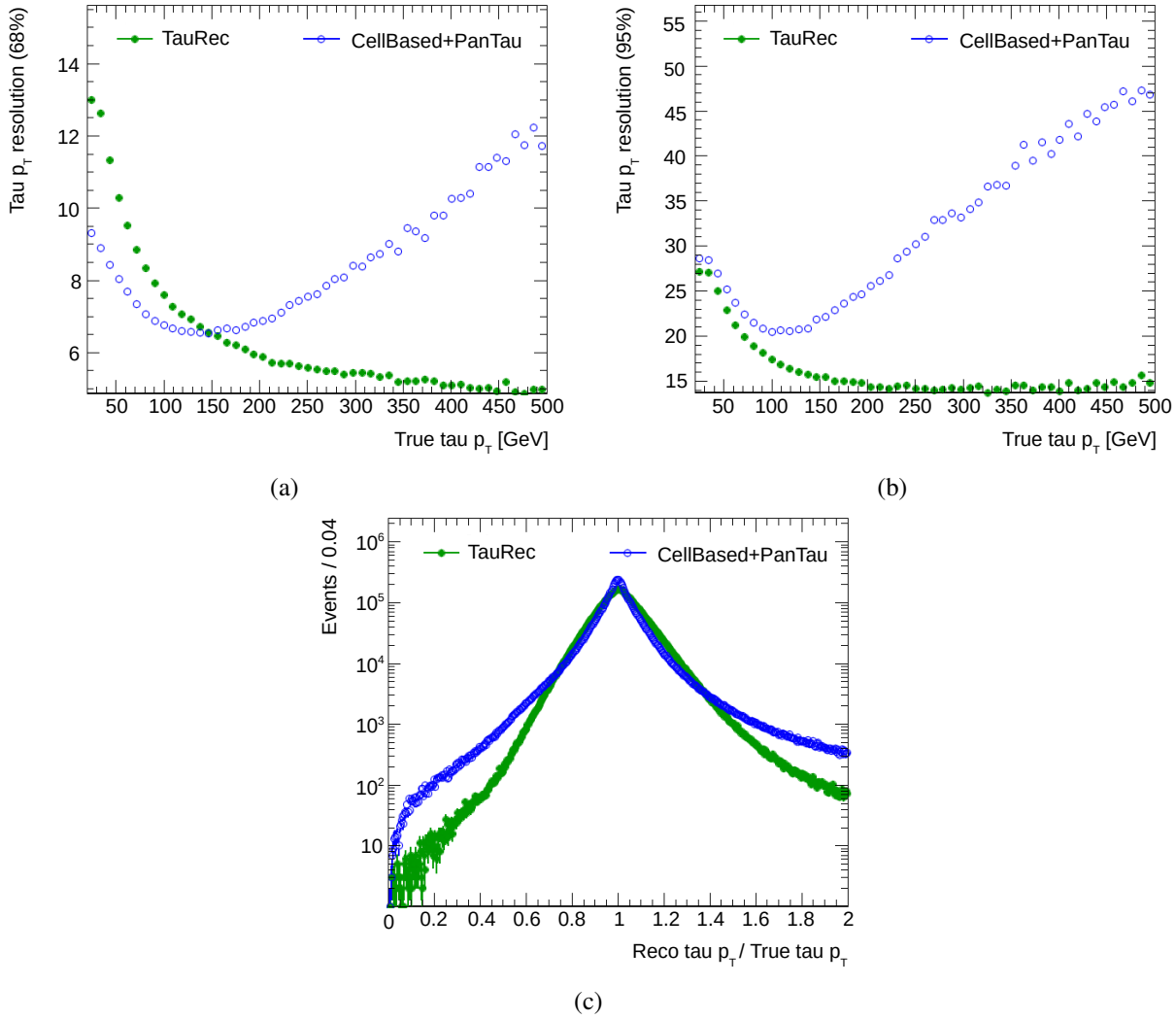

Figure 3.13: The (a) core and (b) tail transverse momentum resolutions of the TauRec and CB+PanTau reconstruction algorithms as a function of the simulated (True) transverse momentum of hadronic tau leptons, and (c) the corresponding responses of the reconstructed (Reco) transverse momentum normalized to the simulated (True) p_T of hadronic tau leptons.

HCAL, while neutral pions deposit all their energy in the ECAL. This means that a substantial amount of the energy of K^0 mesons is not reconstructed correctly, causing long non-Gaussian tails on the left side of the p_T resolution of hadronic taus. However, by combining the information of the Run-1 reconstruction and the CB+PanTau algorithm, it is possible to distinguish between decays with π^0 and K^0 mesons.

Figure 3.13 shows the core and tail resolutions of the TauRec and CB+PanTau algorithms and the corresponding reconstructed (Reco) transverse momentum distributions of hadronic tau leptons normalized to the simulated (True) momentum. As discussed above, the response of the CB+PanTau algorithm, shown in Figure 3.13(c), features highly non-Gaussian tails. These are caused by neutral kaons and mis-reconstructed PanTau decay modes. In particular, they are from false estimations of the number of π^0 candidates. Due to the non-Gaussian response of the substructure-based reconstruction, the core and tail resolutions are defined as the half-width spanned by the 68 % and 95 % quantiles, respectively.

The core p_T resolution of the CB+PanTau algorithm outperforms the Run-1 reconstruction for transverse momenta below 140 GeV. This is expected because the tracking system is significantly more precise in

Table 3.2: The definition of the reconstructed decay modes, η bins and E_T bins used for the energy calibration of tau leptons that are reconstructed with the CB+PanTau and TauRec algorithms. The same binning is also used to calculate the weighted transverse energy in Equation 3.20.

Decay modes:	1p0n, 1p1n, 1pXn, 3p0n, 3pXn
η bins:	$[0.3, 0.8)$, $[0.3, 0.8)$, $[0.8, 1.3)$, $[1.3, 1.6)$, $[1.6, 2.5)$
E_T bins:	Defined such that they contain equal statistics ($N_\tau \approx 5\,000$/bin)

this region than the calorimeter (see Figure 3.10). The higher precision is essential for measuring Higgs boson properties in the $H \rightarrow \tau^+\tau^-$ decay channel. For a hadronic tau lepton with transverse momentum $p_T \approx {}^{m_H}/_2 = 62.5\,\text{GeV}$ the improvement due to the CB+PanTau algorithm is about 20 %. However, for energies above 140 GeV the CB+PanTau resolution deteriorates rapidly. On the other hand, the tail resolution is worse over the whole p_T range (see Figure 3.13(b)) resulting from the large non-Gaussian tails in the substructure-based reconstruction.

The method used to combine the reconstructed energies obtained with the TauRec and CB+PanTau algorithms is presented in the following. It exploits the improved low-p_T performance of CB+PanTau while keeping the superior high-p_T resolution of TauRec. In addition, it also controls the tails and reduces artifacts introduced by the non-Gaussian tails.

The method consists of three steps. First, the reconstruction algorithms are calibrated such that the cores of the difference distributions $\delta E_T = (\text{Reco Tau } E_T - \text{True Tau } E_T)$ are located around zero. This is done in bins of the decay mode m, the pseudorapidity η, and the transverse energy E_T of the reconstructed hadronic tau lepton to account for the different behavior of the algorithms in different regions of the parameter space. For the decay mode binning, the previously introduced modes 1p0n, 1p1n, 1pXn, 3p0n and 3pXn are used. In contrast, the η regions are sliced into $0 \leq |\eta| < 0.3$, $0.3 \leq |\eta| < 0.8$, $0.8 \leq |\eta| < 1.3$, $1.3 \leq |\eta| < 1.6$, and $1.6 \leq |\eta| < 2.5$. The E_T bins are dynamically assigned based on the number of reconstructed events N_τ in a specific E_T region. For the energy calibration $N_\tau = 5\,000$ is chosen. Since the simulated sample contains many low-E_T and only a few high-E_T events, the binning is very fine for small energies ($\approx 1\,\text{GeV}$ for $E_T \approx 20 - 30\,\text{GeV}$) and relatively coarse for large energies ($\gtrapprox 40\,\text{GeV}$ for $E_T > 100\,\text{GeV}$). The bin definitions are summarized in Table 3.2.

After the energy calibration, the weighted average of the reconstructed TauRec and CB+PanTau energies is calculated. This procedure reduces the uncertainty $\sigma(E_T)$ of the energy reconstruction and considers the correlations between both reconstruction algorithms. The weights are calculated from the Gaussian cores of the energy resolutions. Thus, the tails are not properly handled, and an appropriate correction step is employed. The first two steps of the combined TES are explained in Section 3.5.1, and the third step in Section 3.5.2.

3.5.1 Weighted Average of TauRec and CellBased+PanTau

In each bin of the energy calibration procedure, the mean value and the width of the core energy resolution are determined by fitting a Gaussian to the center of the distribution. Depending on the decay mode and η bin, the number of simulated events per E_T slice varies greatly. Most events are generated in 1p1n, and the least events in 3pXn decays. In total, the calibration is performed in more than 300 different bins for each algorithm. Since these are too many to show them all, only one example for each algorithm will be discussed in the following.

Figure 3.14 shows the transverse energy resolution for reconstructed 1p1n decays with $|\eta| \in [0.3, 0.8)$ and the E_T bin that includes ${}^{m_H}/_2$. In addition, it also shows the Gaussian fit to the core region of the distribution. The fit intervals are chosen such that they contain the Gaussian core in each bin. Additional

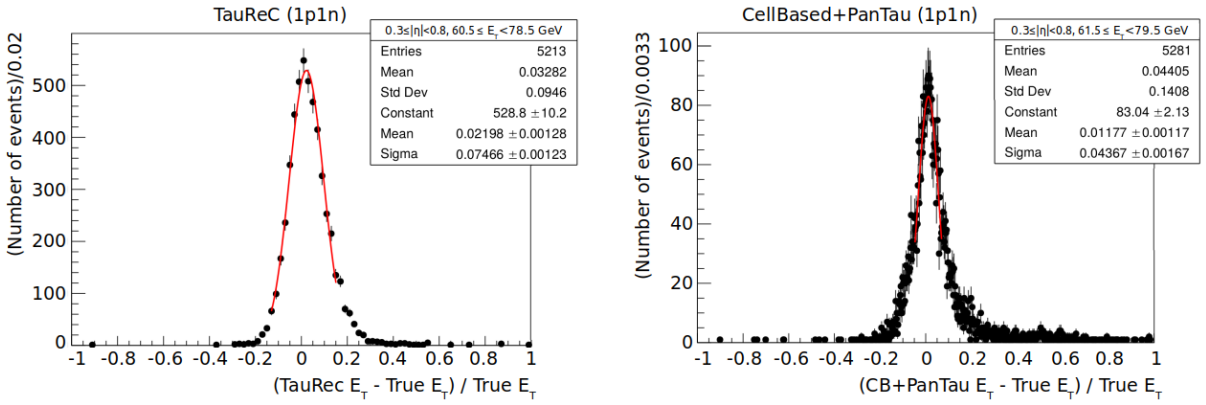

(a) (b)

Figure 3.14: Example fits to the core of the energy resolution of hadronic tau leptons obtained from (a) the TauRec and (b) the CB+PanTau reconstruction algorithm for reconstructed 1p1n decays with $0.3 \leq |\eta| < 0.8$. The E_T bins for the TauRec ($60.5\,\text{GeV} \leq E_T < 78.5\,\text{GeV}$) and CB+PanTau ($61.5\,\text{GeV} \leq E_T < 79.5\,\text{GeV}$) algorithms differ slightly because the bins are defined such that they contain similar statistics. The simulated data points are shown in black, and the Gaussian fit to the core region is shown in red. Additional information about the distributions (three upper entries) and the Gaussian fit parameters (three lower entries) are displayed in the insert.

information like the number of events is displayed in the insert. The TauRec algorithm reconstructs 5 213 events with a transverse energy between 60.5 GeV and 78.5 GeV. These events are displayed as black dots in Figure 3.14(a). The mean value of the distribution is about 0.033, and the standard deviation is 0.095. The corresponding values of the Gaussian fit to the core region are 0.022 and 0.075, respectively. The energy resolution of the CB+PanTau algorithm (Figure 3.14(b)) is significantly narrower than the TauRec distribution in this E_T region due to the good track resolution. Since the non-Gaussian tails are not clearly visible in this representation of the data, the same histograms are displayed in Figure A.1 with a logarithmic scale on the y-axis.

For reconstructed decay modes with no neutral hadron (i. e. 1p0n and 3p0n), the impact of K^0 mesons that are mis-reconstructed as π^0 lead to a prominent shoulder on the left side of the transverse energy resolution. Examples of this behavior are shown in Figure A.2.

The extracted mean energies and widths of the core resolutions for the bins listed in Table 3.2 are summarized in Appendix A.1.1 and A.1.2, respectively. In order to calibrate the reconstructed energies, correction terms $\Delta E_T(E_T, m, \eta)$ are defined at reconstruction level. They are obtained from the linear interpolation between the extracted means of the i-th and the $(i+1)$-th energy bin, Mean(i) and Mean$(i+1)$, respectively, that are just below and above the reconstructed energy E_T,

$$\Delta E_T = \left(\text{Mean}(i) + \frac{\text{Reco } E_T - E_T(i)}{E_T(i+1) - E_T(i)}[\text{Mean}(i+1) - \text{Mean}(i)]\right) \cdot \text{Reco } E_T\,, \tag{3.18}$$

where $E_T(i)$ is the central energy of the i-th bin. The correction terms are then used to calibrate the reconstructed transverse energy of the reconstructed tau lepton,

$$\text{Reco } E_T \rightarrow \text{Reco } E_T - \Delta E_T\,. \tag{3.19}$$

Figure 3.15 shows the mean values of the energy resolution before (red color), and after (blue color) the calibration in 1p1n decays with $|\eta| < 0.3$. Before the calibration, the mean values deviate significantly from zero. but after the calibration, they are consistent with zero. The same is true for the other decay

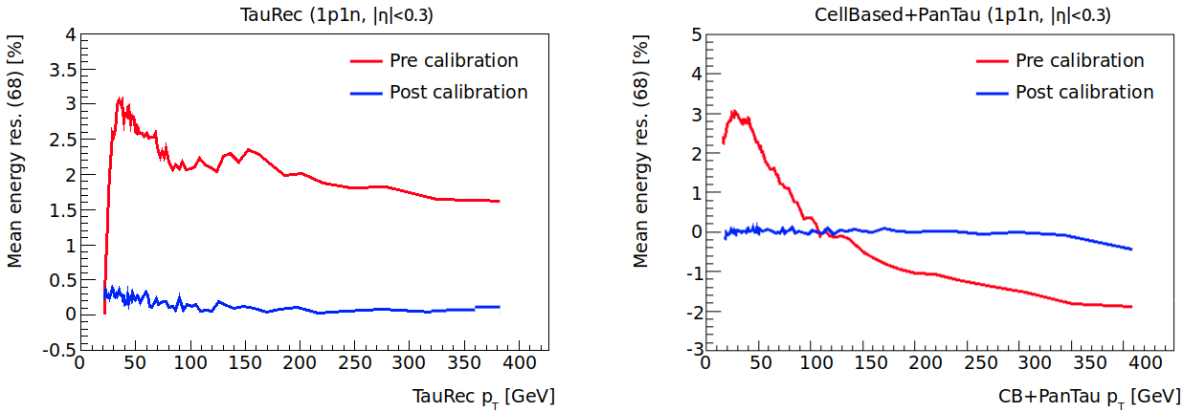

(a) (b)

Figure 3.15: The (a) TauRec and (b) CellBased+PanTau mean values extracted from the Gaussian fits to the core region of the energy resolution, binned in the reconstructed transverse momentum in 1p1n decays with $\eta < 0.3$.

modes and η bins.

In the second step of the improved energy reconstruction, the weighted average $E_{T,\text{Weighted}}$ of the calibrated transverse energies is calculated,

$$E_{T,\text{Weighted}} = w \cdot E_{T,\text{TauRec}} + (1 - w) \cdot E_{T,\text{CB+PanTau}} \,. \tag{3.20}$$

In this equation, the weight $w = w(m, \eta)$ is determined in bins of η and m,

$$w = \frac{\sigma^2_{\text{CB+PanTau}} - \rho \cdot \sigma_{\text{TauRec}} \cdot \sigma_{\text{CB+PanTau}}}{\sigma^2_{\text{CB+PanTau}} + \sigma^2_{\text{TauRec}} - 2 \cdot \rho \cdot \sigma_{\text{TauRec}} \cdot \sigma_{\text{CB+PanTau}}} \,, \tag{3.21}$$

where σ_{TauRec} ($\sigma_{\text{CB+PanTau}}$) is the TauRec (CB+PanTau) core energy resolution and ρ is the correlation coefficient,

$$\rho = \frac{\left\langle E_{T,\text{TauRec}} \cdot E_{T,\text{CB+PanTau}} \right\rangle - \left\langle E_{T,\text{TauRec}} \right\rangle \cdot \left\langle E_{T,\text{CB+PanTau}} \right\rangle}{\sigma_{\text{TauRec}} \cdot \sigma_{\text{CB+PanTau}}} \,. \tag{3.22}$$

The core resolutions are obtained from the interpolated values of the extracted widths from the Gaussian fits, summarized in Appendix A.1.2. The correlation coefficients are obtained from scatter plots of the CB+PanTau resolution vs. the TauRec resolution in bins of η and m.

Figure 3.16 compares the performance of the core weighted energy reconstruction (Weighted) to the pre-calibration and post-calibration resolutions of TauRec and CB+PanTau. In the low-p_T region (Figure 3.16(a)), the calibration and weighting procedure significantly improves the resolution. For tau leptons with $p_T \approx 60\,\text{GeV}$ the resolution is improved by about 30 % compared to the baseline reconstruction (TauRec). For smaller transverse momenta, the improvement is even larger. However, for $p_T > 200\,\text{GeV}$, the weighted average does not provide a good measure for the tau p_T, and the baseline reconstruction is significantly more accurate.

In general, the calculated standard deviations are larger than the corresponding core resolutions. This difference is typically more pronounced for the CB+PanTau reconstruction (see Figure 3.14), which implies that the weight $(1 - w)$ assigned to the CB+PanTau energy is relatively large. In contrast, the weight (w) assigned to TauRec is relatively small. This behavior is intended in the low-p_T region, but it causes problems in regions where the CB+PanTau resolution is worse than the TauRec resolution. This issue could be solved by replacing the core resolutions in Equations 3.21 and 3.22 with the corresponding

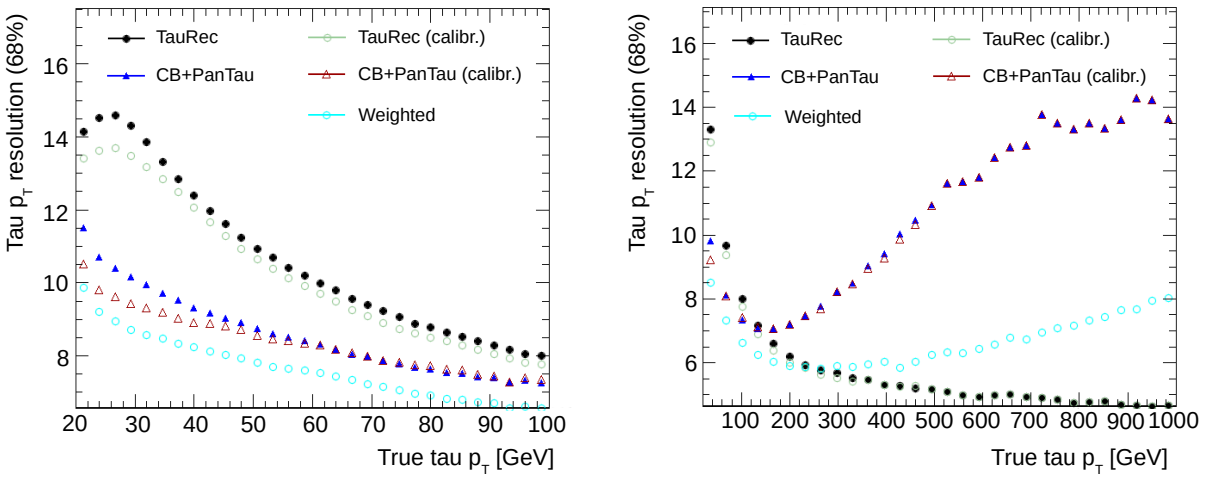

(a) (b)

Figure 3.16: The core p_T resolution of the TauRec, the CB+PanTau and the Weighted energy reconstructions as a function of the simulated (True) p_T of the hadronic tau lepton. The pre-calibration resolutions are represented by filled markers and the post-calibration resolutions by open markers. The low p_T region with 20 GeV $< p_T <$ 100 GeV is shown in (a) and the high-p_T region up to 1 TeV in (b).

standard deviations. However, this would also diminish the core performance at low-p_T. In order to keep the good performance of the 68 % quantiles for low transverse momenta, a different approach to control the tails is used.

3.5.2 Treatment of Non-Gaussian Tails

The tails in CB+PanTau energy are controlled by employing a compatibility condition on the reconstructed tau energies. It is defined such that it captures the outliers in the reconstruction without weakening the low-p_T performance. To achieve this, the following quantities are defined:

$$\Delta E_T^{\text{Reco}} = \left| E_T^{\text{TauRec}} - E_T^{\text{CB+PanTau}} \right| , \tag{3.23}$$

$$\sigma_{\text{Weighted}} = \sqrt{\sigma^2_{\text{CB+PanTau}} + \sigma^2_{\text{TauRec}} - 2 \cdot \rho \cdot \sigma_{\text{TauRec}} \cdot \sigma_{\text{CB+PanTau}}} \, . \tag{3.24}$$

ΔE_T^{Reco} is the absolute value of the difference between the reconstructed energies and σ_{Weighted} is the weighted core resolution. If ΔE_T^{Reco} is large the corresponding event likely contains a K^0 meson. In this case, only the TauRec algorithm should be used for the energy reconstruction. The weighted width σ_{Weighted} serves as a measure for the threshold at which the CB+PanTau energy is rejected. Thus, the compatibility condition is given by

$$\begin{aligned} \Delta E_T^{\text{Reco}} &> N \cdot \sigma_{\text{Weighted}} \quad \Rightarrow \quad \text{use } E_T^{\text{TauRec}} , \\ \Delta E_T^{\text{Reco}} &\leq N \cdot \sigma_{\text{Weighted}} \quad \Rightarrow \quad \text{use } E_T^{\text{Weighted}} , \end{aligned} \tag{3.25}$$

where $N = 5$ is the baseline choice. The energy reconstruction that includes the compatibility condition (Equation 3.25) is called the *Combined* method. The baseline value already provides some suppression of the artifacts discussed above. However, the core and tail resolutions are still worse than the corresponding TauRec resolutions for large p_T. The performance is improved by optimizing the value of N as a

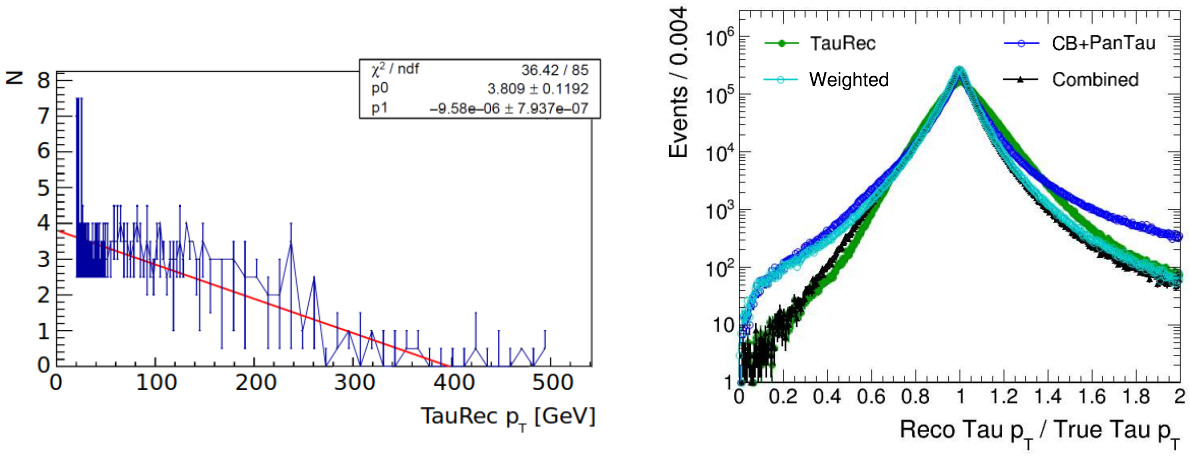

(a) (b)

Figure 3.17: (a) The optimal values for the compatibility condition (N) as a function of the TauRec transverse momentum. The evaluated data points with their uncertainties are shown in blue and the linear fit is shown in red. The best-fit values are shown in the insert. (b) The reconstructed (Reco) transverse momentum responses of the TauRec, CB+PanTau, Weighted and Combined energy reconstruction methods normalized to the simulated (True) p_T of hadronic tau leptons.

function of the TauRec p_T. To that end, the value of N is changed from 0 to 7.5 in steps of 0.5, and the corresponding tail resolutions are evaluated and plotted against the TauRec p_T. The optimal values are then extracted in different p_T bins, and a polynomial is fitted to the data.

Figure 3.17(a) shows the result of this procedure, including a linear fit to the optimal values of N. The corresponding tail resolutions for different compatibility conditions are shown in Figure A.13, and the optimized condition is

$$N(p_T) = -9.6 \cdot 10^{-6} \frac{p_T}{\text{MeV}} + 3.8\,. \tag{3.26}$$

Using this condition, the performance matches the TauRec reconstruction in the high-p_T region. Besides, it also improves the tail resolution in the low- and mid-p_T regions by about $1-3\,\%$. The comparison between the baseline and the optimized compatibility condition is shown in Figure A.14.

In the following, the term Combined will refer to the energy reconstruction method with the optimized compatibility condition where N is given by Equation 3.26. Figure 3.17(b) shows the transverse momentum responses of the TauRec, CB+PanTau, Weighted, and Combined energy reconstruction methods. Compared to TauRec, the Combined energy is significantly narrower in the core region. Moreover, it resolves the issue of the non-gaussian tails from the CB+PanTau and Weighted energies in the high-p_T region (see Figure 3.18).

3.5.3 The MVA Tau Energy Scale

The multivariate analysis (MVA) based energy calibration is a new way of calculating the visible tau four-momentum in ATLAS [315][1]. Since it is not a part of this thesis, it will only be briefly discussed. It uses a BDT regression to combine the calorimeter and substructure-based information. The direction (η

[1] Note that the MVA reconstruction described in this reference uses a different interpolation (called "interp") between the TauRec ("LC") and CB+PanTau ("TPF") reconstructions as input for the BDT regression (see Equations 3 and 4 in Reference [315]). This interpolation differs from the Combined energy described in Section 3.5. The reason for this is that the Combined TES was not ready when the note was written. Once the Combined E_T was available, the "interp" energy was replaced with the Combined energy as input for the MVA method.

and ϕ) is taken from the CB+PanTau reconstruction described in Section 3.4.2. The basic input variables for the MVA method are the transverse momenta obtained from the TauRec, CB+PanTau, and Combined energy reconstruction methods. However, since the BDT regression is less powerful when two variables are highly correlated, the following ratios are used:

$$r_1 = \frac{p_T^{\text{TauRec}}}{p_T^{\text{Combined}}} \qquad \text{and} \qquad r_2 = \frac{p_T^{\text{CB+PanTau}}}{p_T^{\text{Combined}}} \tag{3.27}$$

This approach is very powerful and significantly improves the energy reconstruction for $p_T > 40\,\text{GeV}$.

Initially, the MVA calibration was based on p_T ratios of the true tau and the reconstructed tau obtained from the CB+PanTau algorithm. However, this approach causes severe issues at high p_T due to the inherent problems of the CB+PanTau algorithm discussed above. On the other hand, the usage of the TauRec p_T worsens the resolution at low p_T. To resolve these issues, the input was changed to an interpolated energy between the TauRec and the CB+PanTau reconstruction methods described in Reference [315]. However, this interpolation does not handle the transition region $\approx 100 - 300\,\text{GeV}$ as nicely as anticipated, and it is not corrected for the outliers in the CB+PanTau reconstruction. Both issues are resolved using the Combined TES as input to the MVA method.

In addition to the ratios r_1 and r_2, several other variables are included to improve the energy reconstruction. The number of primary vertices and the average number of interactions per bunch crossing makes the energy reconstruction more robust against pile-up. The inclusion of various cluster variables in the BDT training, like the moments of the individual cluster constituents, significantly improves the low-p_T performance for 1p decays. The performance is further improved by including variables that provide information about the tau decay modes, like the number of reconstructed neutral pions and the relative difference of the total charged and neutral pion energies. These variables improve the performance for 1p (3p) decays with $p_T \lessapprox 140\,\text{GeV}$ ($p_T \lessapprox 250\,\text{GeV}$).

Figure 3.18 shows the transverse momentum resolution of the MVA TES and compares it to the Combined, CB+PanTau, and TauRec energies. The MVA TES provides a significantly better core and tail resolution over the whole p_T range (right panels). While the Combined TES is designed to match the TauRec resolution for high p_T, the additional information used in the BDT regression further improves the high-p_T performance. However, the largest gains are achieved in the low- and mid-p_T ranges. For small transverse momenta, the core and tail resolutions of the MVA TES are approximately $10 - 15\,\%$ better than the corresponding values of the Combined TES (left panels).

The largest improvements of the MVA TES are achieved in 1p1n, 1pXN and 3pXn decays. The improvements for decay modes without neutral pions are much smaller. The resolution graphs for the various decay modes are summarized in Appendix A.3.

3.5.4 Neutral Pion Correction at the MVA TES

The MVA TES provides significant improvements for the energy reconstruction of hadronic tau leptons. Figure 3.19 shows the decay mode-binned responses of the reconstructed transverse momenta of tau leptons obtained from the TauRec, CB+PanTau, and MVA-based reconstruction methods for correctly identified tau decay modes. While the performance of the MVA method is comparable to the CB+PanTau reconstruction for 1p0n and 3p0n decays, it is much better for 1p1n, 1pXn and 3pXn decays. However, in the latter decay modes, the objects obtained from the MVA method are not consistent tau leptons, i. e.

$$p_\tau^{\text{MVA}} \neq \sum_i p_{i,\pi^0} + \sum_i p_{i,\pi^\pm}\,, \tag{3.28}$$

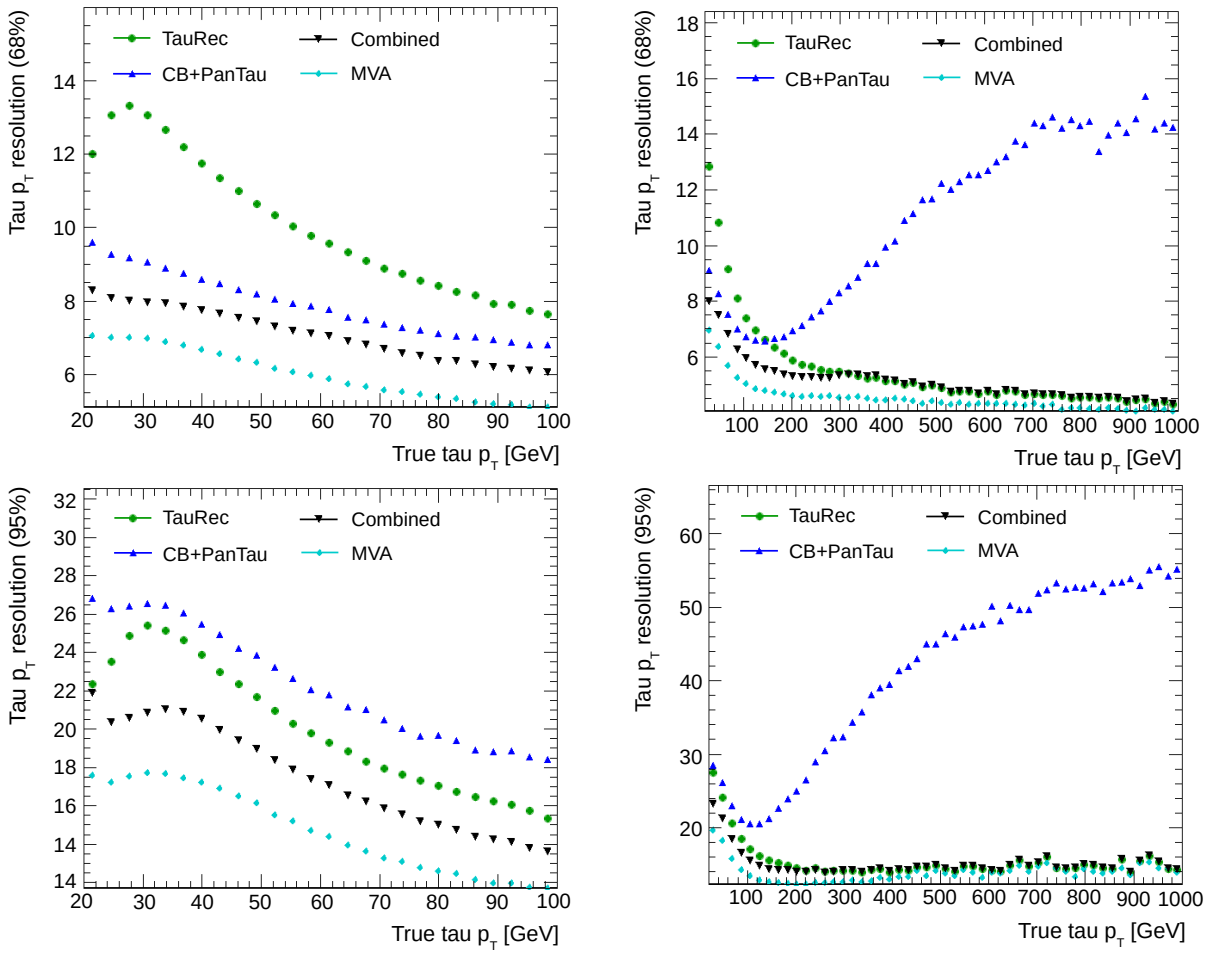

Figure 3.18: The core (upper panels) and tail (lower panels) transverse momentum resolutions of the TauRec, CB+PanTau, Combined and MVA-based energy reconstruction methods as a function of the simulated (True) transverse momentum of the hadronic tau lepton. The low-p_T (high-p_T) range is shown in the left (right) panels.

where p represents the four-momentum. Consistent tau objects are important for all analyses that directly use the neutral pions. In the following, the π^0 momentum correction applied to obtain consistent tau leptons at the MVA TES is presented.

The method assumes that charged pions are correctly reconstructed. The difference between the three-momentum of the CB+PanTau and MVA algorithms is attributed to improvements in the reconstruction of the neutral pions.

3.5.4.1 Correction for 1P1N Decays

Figure 3.20 illustrates the correction of the neutral pion three-momentum for 1p1n decays[1]. The CB+PanTau three-momentum $\boldsymbol{p}_\tau^{\text{CB+PanTau}}$, depicted in Figure 3.20(a), is the sum of the charged and neutral pion three-momenta, $\boldsymbol{p}_{\pi^\pm}$ and $\boldsymbol{p}_{\pi^0}$, respectively. Since the MVA-based reconstruction only changes the absolute value of the momentum, the MVA three-momentum $\boldsymbol{p}_\tau^{\text{MVA}}$ points in the same direction as $\boldsymbol{p}_\tau^{\text{CB+PanTau}}$. The neutral pion momentum correction is a two-step process. First, the 3-vector corrected

[1]The angle between the $\pi^\pm$ and π^0 directions and the length difference between the CB+PanTau and MVA three-momenta are displayed excessively large for illustration purposes.

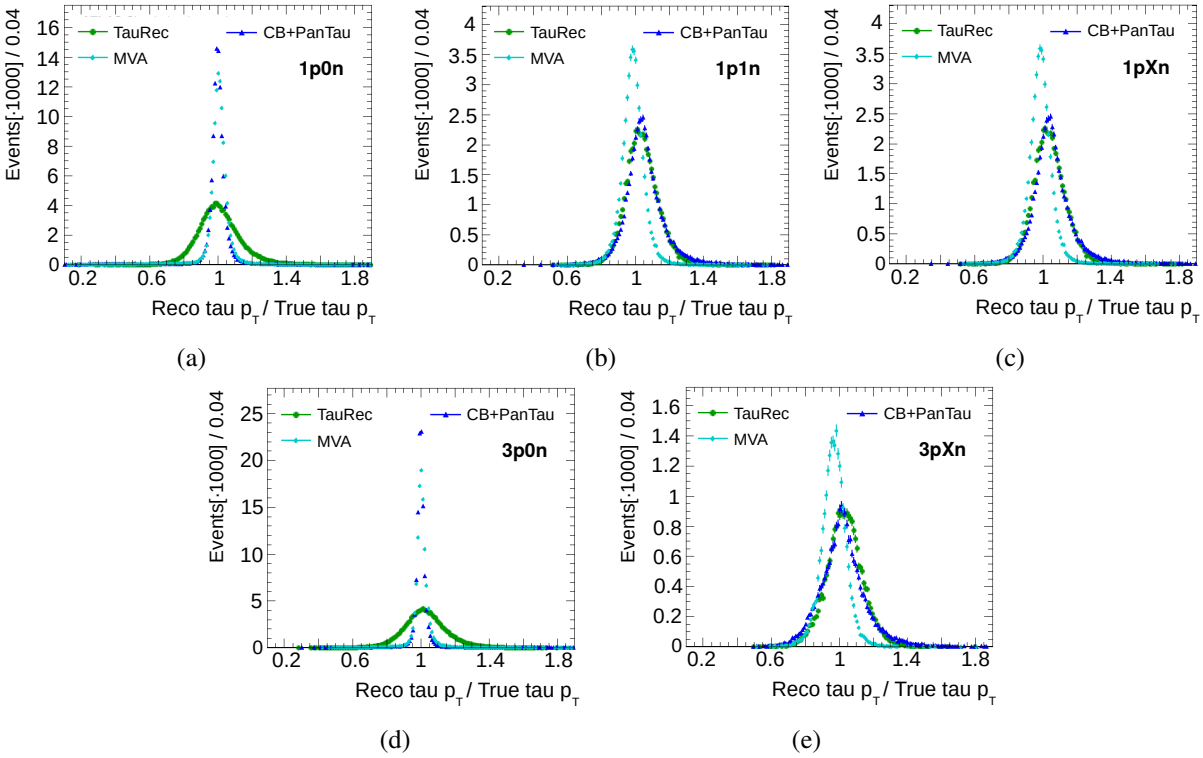

Figure 3.19: The reconstructed (Reco) transverse momentum responses of hadronic tau leptons obtained from the TauRec, CB+PanTau and MVA-based energy reconstruction methods normalized to the corresponding simulated (True) transverse momentum for (a) 1p0n, (b) 1p1n, (c) 1pXn, (d) 3p0n, and (e) 3pXn decays. Only events with correctly classified (i. e. True == Reco) decay modes are considered.

neutral pion momentum is calculated

$$\boldsymbol{p}_{\pi^0}^{\text{3-vec}} = \boldsymbol{p}_{\tau}^{\text{MVA}} - \boldsymbol{p}_{\pi^\pm} \,. \tag{3.29}$$

This correction step (see Figure 3.20(b)) significantly improves the neutral pion's transverse momentum resolution. However, it also introduces an error to the η and ϕ reconstruction because of the angle difference δ between the baseline and the 3-vector corrected neutral pion momentum. The corresponding resolution plots are summarized in Figure A.25. This issue is resolved by only correcting the absolute value of the momentum, while keeping the baseline neutral pion direction (see Figure 3.20(c)). In this case, the corrected neutral pion three-momentum,

$$\boldsymbol{p}_{\pi^0}^{\text{corrected}} = \frac{\left|\boldsymbol{p}_{\pi^0}^{\text{3-vec}}\right|}{\left|\boldsymbol{p}_{\pi^0}\right|} \cdot \boldsymbol{p}_{\pi^0} \,, \tag{3.30}$$

retains the good η and ϕ resolution of the baseline reconstruction while still profiting from the improved transverse momentum resolution of the 3-vector method. The corrected energy of the neutral pion is,

$$E_{\pi^0}^{\text{corrected}} = \sqrt{\left(\boldsymbol{p}_{\pi^0}^{\text{corrected}}\right)^2 + \left(m_{\pi^0}\right)^2} \,, \tag{3.31}$$

where $m_{\pi^0} = 134.977\,\text{MeV}$ [54] is the mass of the neutral pion.

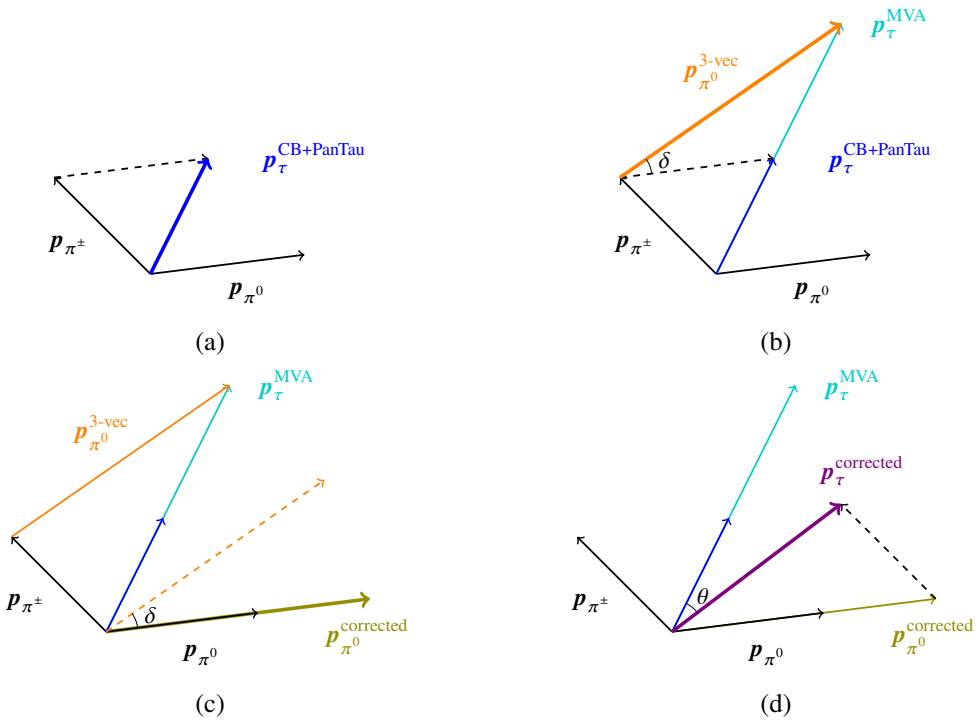

Figure 3.20: Illustration of the different steps of the three-momentum correction of neutral pions in reconstructed 1p1n decays. (a) The tau lepton three-momentum obtained from the CB+PanTau algorithm as a sum of the reconstructed charged and neutral pion momenta, (b) the 3-vector corrected neutral pion momentum calculated as the difference of the MVA-tau and the charged pion momenta, (c) the neutral pion three-momentum correction obtained by scaling the absolute value of the baseline neutral pion momentum (see Equation 3.30), and (d) the corrected three-momentum of the hadronic tau lepton as a sum of the charged and corrected-neutral pion momenta.

To obtain consistent tau objects, the charged and corrected neutral pion four-momenta are added

$$p_\tau^{\text{corrected}} = p_{\pi^0}^{\text{corrected}} + p_{\pi^\pm} \,. \tag{3.32}$$

As illustrated in Figure 3.20(d), this changes the absolute value and the direction of the three-momentum.

Figure 3.21 shows the transverse momentum and the pseudorapidity resolutions of the corrected neutral pions and tau leptons. The relative p_T response (Figure3.21(a)) of the corrected neutral pions is much narrower than the baseline response of the CB+PanTau algorithm, and the corresponding resolution (see Figure 3.21(b)) is significantly improved for $p_{T,\pi^0} \lessapprox 150\,\text{GeV}$. Since the directions of the pions are not changed, the angular resolutions are identical to the baseline resolutions of the CB+PanTau reconstruction (see Figure 3.21(c) for the η resolution).

The neutral pion correction affects the direction and the absolute size of the tau lepton three-momentum. However, it does not deteriorate the p_T resolution shown in Figures 3.21(d) and 3.21(e), and it slighly improves the angular resolution (see Figure 3.21(f)). The precise determination of the energy and momentum is crucial for the calculation of the invariant mass of the $\tau_{\text{had-vis}}$,

$$m_\tau = \sqrt{(E_\tau)^2 - |\boldsymbol{p}_\tau|^2} \,. \tag{3.33}$$

Figure 3.22 shows the $\tau_{\text{had-vis}}$ invariant mass response of the CB+PanTau algorithm and the MVA-based π^0-correction. The former provides a good invariant mass reconstruction if only one neutral particle-flow

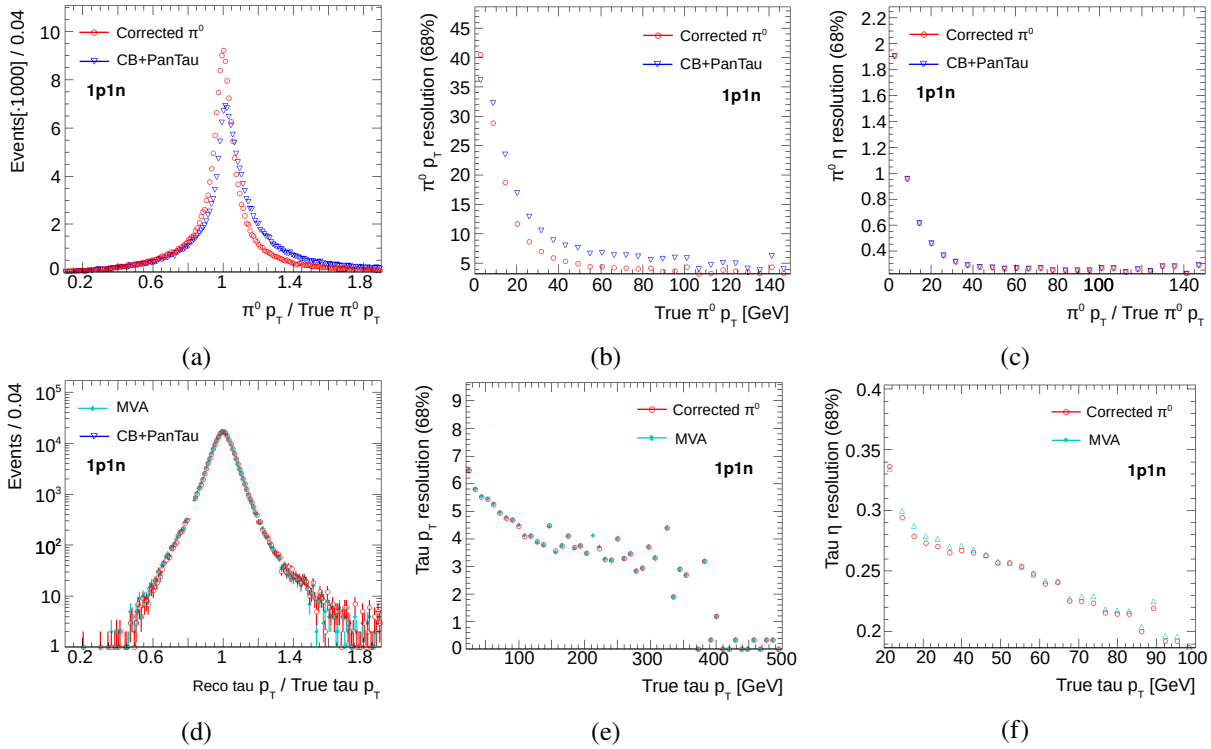

Figure 3.21: The reconstructed (Reco) transverse momentum response for (a) neutral pions and (d) hadronic tau leptons obtained from the baseline and the π^0-corrected reconstruction methods normalized to the corresponding simulated (True) transverse momentum for correctly classified (i. e. True == Reco) 1p1n decays. The corresponding p_T and η resolution are shown in (b,e) and (c,f), respectively.

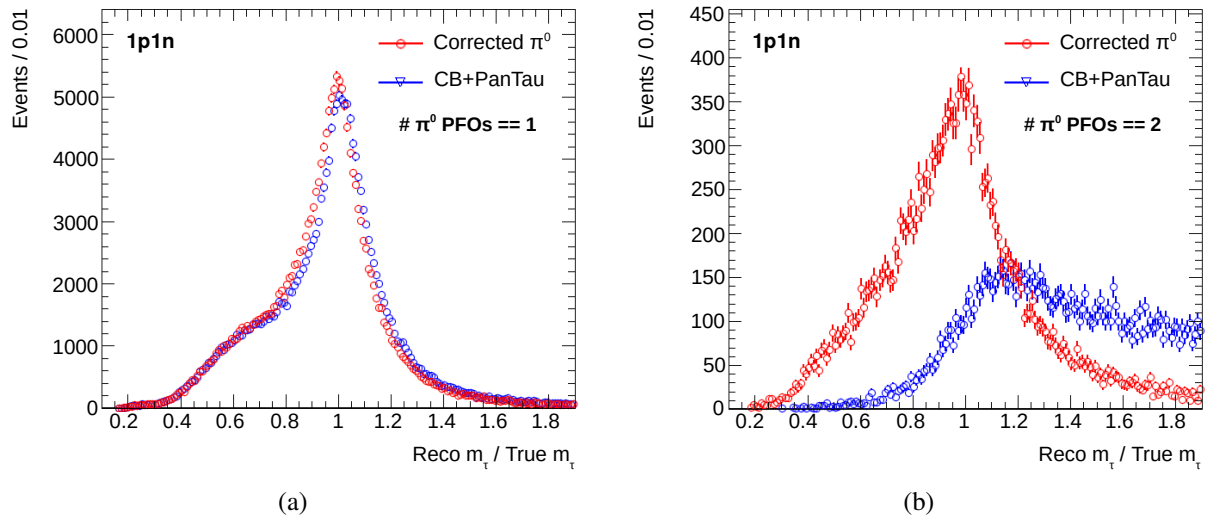

Figure 3.22: The invariant mass response of reconstructed (Reco) $\tau_{\text{had-vis}}$ normalized to the corresponding simulated (True) invariant mass in the case that (a) one and (b) two neutral particle-flow objects (PFOs) are reconstructed. Shown are the baseline (CB+PanTau) and the π^0-corrected invariant mass responses in blue and red, respectively. Only correctly classified 1p1n decays are considered.

object (PFO) is reconstructed (see Figure 3.22(a)), it performs much worse in case of two π^0 PFOs[1] are

[1] If more than one π^0 PFO is reconstructed the decay mode is initially set to Xn. However, the PanTau algorithm re-evaluates

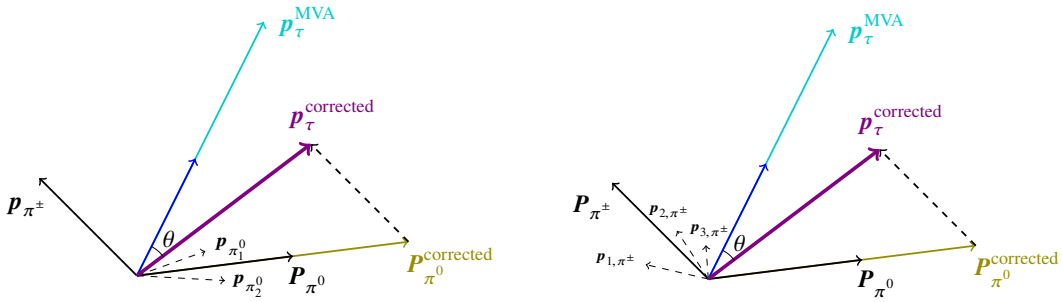

Figure 3.23: Illustration of the three-momentum correction of neutral pions in (a) 1pXn and (b) 3pXn decays.

reconstructed (see Figure 3.22(b)). In this case, the MVA-based neutral pion correction significantly improves the invariant mass reconstruction.

3.5.4.2 Correction for 1PXN and 3PXN Decays

Since it is not possible to individually correct each neutral pion in tau decays with more than one π^0, each neutral pion three-momentum is scaled by the same value. The corresponding factor is determined from the correction of the cumulated neutral pion three-momentum $\boldsymbol{P}_{\pi^0} = \sum_i \boldsymbol{p}_{i,\pi^0}$. Thus, Equation 3.29 is replaced with

$$\boldsymbol{P}_{\pi^0}^{\text{3-vec}} = \boldsymbol{p}_\tau^{\text{MVA}} - \boldsymbol{P}_{\pi^\pm}, \quad \text{where} \quad \boldsymbol{P}_{\pi^\pm} = \begin{cases} \boldsymbol{p}_{\pi^\pm} & \text{, for 1pXn decays} \\ \sum_{i=1}^{3} \boldsymbol{p}_{i,\pi^\pm} & \text{, for 3pXn decays} \end{cases}. \tag{3.34}$$

Equations 3.30 and 3.32 are the same as in 1p1n decays but the pion momenta $\boldsymbol{p}$ are replaced with $\boldsymbol{P}$. These adjustments are illustrated in Figure 3.23 for the main 1pXn (Figure 3.23(a)) and 3pXn (Figure 3.23(b)) decays. While most 1pXn decays contain two neutral pions, most 3pXn decays contain only one π^0. However, both modes also include some decays with three neutral pions.

The neutral pion and tau lepton p_T responses in 1pXn and 3pXn decays are shown in Figures A.26 and A.28, respectively. In both cases, the MVA-based neutral pion correction significantly improves the neutral pion transverse momentum response.

Figure 3.24 shows the tau lepton invariant mass response normalized to the corresponding simulated p_T. Events classified as 1pXn typically contain either one or two π^0 PFOs. The neutral pions are produced with an angular distance ΔR. In case that only one π^0 PFO is reconstructed, this angular separation is neglected, which means that the tau lepton invariant mass (see Figure 3.24(a) is underestimated. Thus, the neutral pion-corrected reconstruction underestimates the tau lepton invariant mass as well. In contrast, the invariant mass reconstruction works well if two neutral PFOs are reconstructed as shown in Figure 3.24(b) because the ΔR distance is measured in this case. Since most 3pXn decays contain only one pion, the invariant mass is well described by the π^0-corrected reconstruction method.

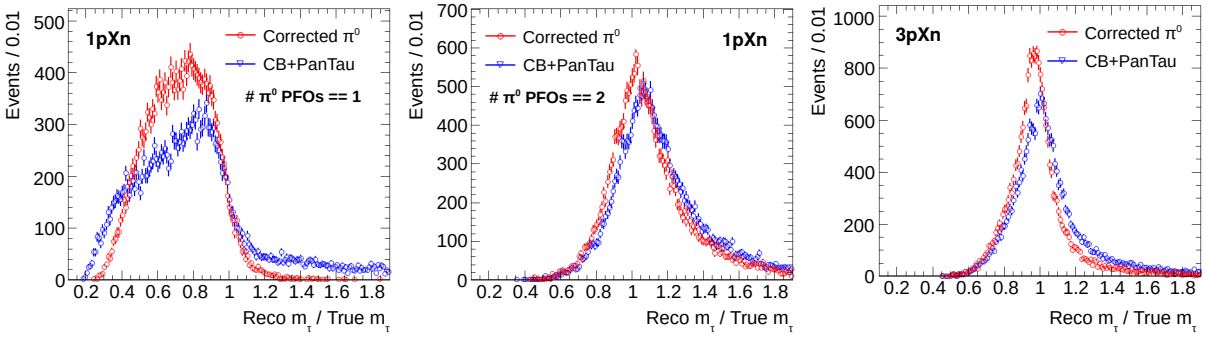

(a) (b) (c)

Figure 3.24: The invariant mass response of the reconstructed (Reco) $\tau_{\text{had-vis}}$ normalized to the corresponding simulated (True) invariant mass in 1pXn decays with (a) one and (b) two reconstructed neutral particle-flow objects (PFOs), and (c) in 3pXn decays. Shown are the CB+PanTau (blue) and the π^0-corrected (red) responses. Only correctly classified decays are considered.

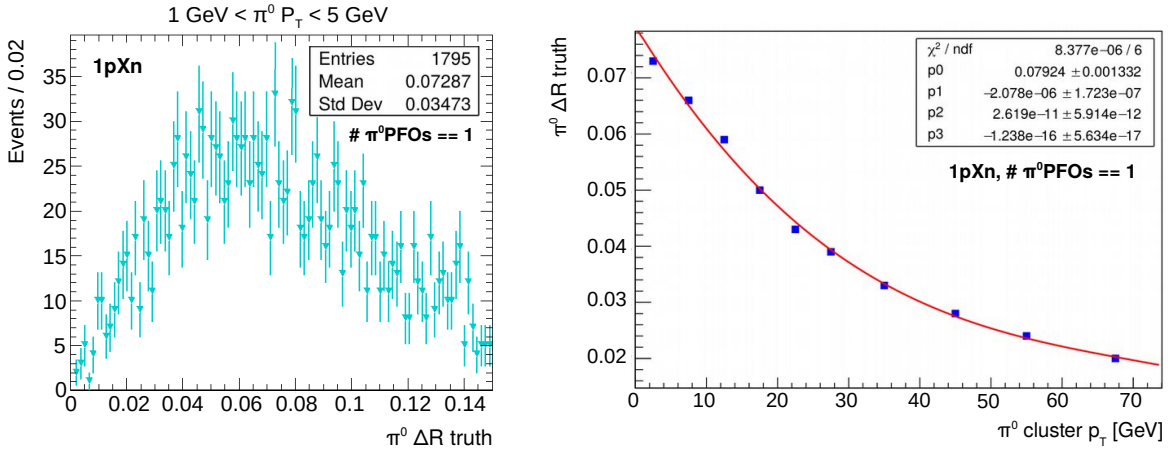

(a) (b)

Figure 3.25: The angular separation ΔR between the simulated (truth) neutral pion three-momenta in 1pXn decays with one reconstructed π^0 PFO. (a) The simulated ΔR distribution for reconstructed transverse momenta between 1 GeV and 5 GeV, and (b) the mean ΔR distance in bins of the reconstructed P_T of the π^0 cluster (blue points) including a third degree polynomial fit to the ΔR values (red line). Additional information is displayed in the inserts.

3.5.4.3 Neutral Pion ΔR Correction for 1PXN Decays

The MVA-based π^0 correction provides consistent tau objects for decay modes that include neutral pions. It also significantly improves the π^0 transverse momentum resolution and the invariant mass reconstruction of the tau lepton. However, in 1pXN decays, the invariant mass is underestimated if only one neutral PFO is reconstructed. In order to compensate the neglected ΔR distance between neutral pions, the average angular separation is estimated from simulated events in bins of the transverse momentum of the reconstructed π^0 PFO. Figure 3.25(a) shows the truth ΔR distribution of simulated 1pXn decays with one reconstructed π^0 PFO for transverse momenta between 1 GeV and 5 GeV. The mean value of the angular distance decreases with increasing neutral pion transverse momentum, as shown in Figure 3.25(b). It is

the decay mode based on various discriminating variables (see Section 3.4.2). Thus, even if two π^0 PFOs are reconstructed, the decay mode can be classified as 1n.

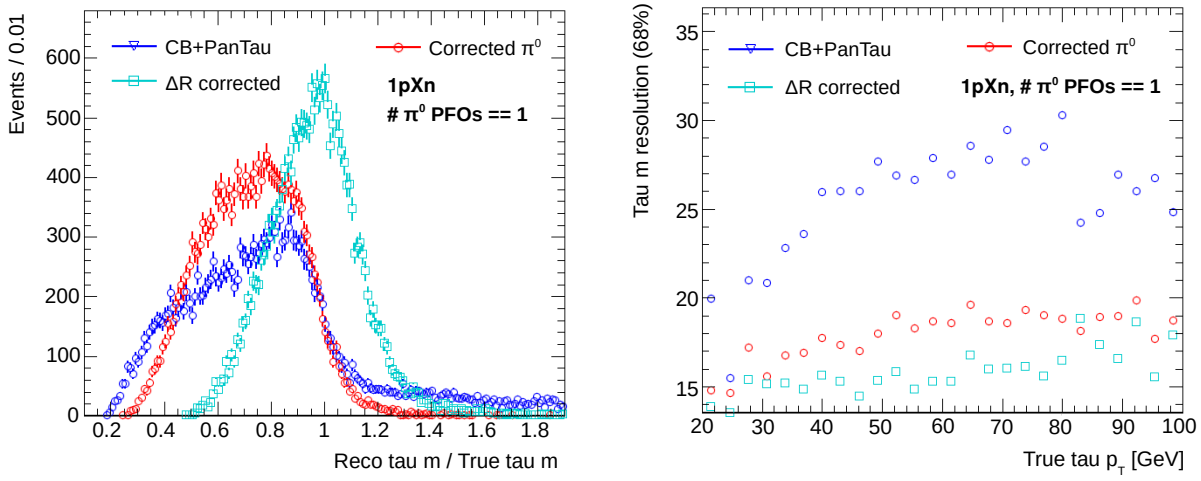

(a) (b)

Figure 3.26: (a) The invariant mass response of reconstructed (Reco) $\tau_{\text{had-vis}}$ normalized to the corresponding simulated (True) mass in 1pXn decays with one reconstructed neutral particle-flow object and (b) the corresponding core resolution for tau leptons with $p_T < 100\,\text{GeV}$. Shown are the results for the CB+PanTau, the π^0-corrected, and the ($\pi^0 + \Delta R$)-corrected reconstruction methods. Only correctly classified decays are considered.

approximated with the third-degree polynomial,

$$\Delta R(P_T) = 0.0792 - 2.078 \cdot 10^{-6} P_T + 2.619 \cdot 10^{-11} P_T^2 - 1.238 \cdot 10^{-16} P_T^3\,, \tag{3.35}$$

shown in red.

Using the estimated ΔR distance, the tau lepton invariant mass is recalculated. Figure 3.26 shows the corresponding invariant mass resolution. The inclusion of a P_T-dependent opening angle between the neutral pions significantly improves the calculation of the invariant mass of the tau lepton. The ΔR-corrected invariant mass distribution is centered around the true mass, and the corresponding width is reduced by about 15 %.

Further improvements in the calculation of the invariant mass of the $\tau_{\text{had-vis}}$ are expected if the angular separation between the pions is measured in the detector. The corresponding angles may be determined from shots in the highly granular EM1 layer of the ECAL. Studies with the generated η and ϕ values of the neutral pions show that one of the major uncertainty in the calculation of the invariant mass of the $\tau_{\text{had-vis}}$ results from the determination of the angular distance between the neutral pions (see Figure A.27).

CHAPTER 4

The HiggsSignals Tool

In this chapter, the public computer code HiggsSignals [319, 320] is presented. As a part of this thesis, the Run-2 Higgs boson signal strength and simplified template cross-section (STXS) measurements published by ATLAS and CMS are implemented in HiggsSignals. Besides, several performance tests using the LHC Run-1 and Run-2 data are performed.

Historically, HiggsSignals evolved as a sister program to HiggsBounds [321–326]. For that reason, both programs are shortly introduced in Section 4.1. Section 4.2 summarizes the recent changes in HiggsBounds-5 [326], which are most relevant for this thesis. After that, the HiggsSignals code [320] and the statistical interpretation in HiggsSignals are presented in Sections 4.3 and 4.4, respectively. Section 4.5 presents various validation and performance studies performed with HiggsSignals.

4.1 Introduction to HiggsBounds and HiggsSignals

HiggsBounds is a tool to test arbitrary Higgs sectors with neutral and/or charged Higgs bosons against the available exclusion bounds from Higgs searches at the LEP, Tevatron, and LHC experiments.

Before the discovery of the Higgs boson in 2012, the non-observation of Higgs signals have been turned into cross-section constraints. However, even after the discovery of the Higgs boson, it is important that the experimental collaborations provide exclusion limits from the non-observation of Higgs bosons in various channels. Such limits are useful to constrain the parameter space of extended Higgs sectors, which correctly describe the observed Higgs signal. Exclusion limits from experimental analyses usually take one of two forms. The first ones are model-independent limits on the cross-sections of individual signal topologies. The second ones are given in the form of combined limits for some of the most popular models, such as the SM. The re-interpretation of the latter in the context of a different model requires detailed knowledge about the individual signal efficiencies (contaminations) of the investigated search channels. In contrast, the limits from the individual topological cross-section constraints can easily be tested against a wide class of models. The implementation and combination of the different exclusion bounds distributed over many different publications is a tedious task. In addition, care must be taken when using multiple analyses to ensure the correct statistical interpretation of the result.

HiggsBounds allows the user to quickly and conveniently perform such a statistical test for a wide variety of models. In addition, the code is frequently updated to ensure that all the latest Higgs searches are implemented in the program. The HiggsBounds code is mostly written in Fortran 90, but it includes a few Fortran 2003 features. It can be operated in a command-line mode or called via Fortran 90 subroutines or from a web interface. A continuously updated technical documentation is available in Reference [327].

Since the discovery of the Higgs boson by ATLAS [4] and CMS [5], it is no longer enough to test for non-exclusion, but the model predictions must be tested against the measured Higgs signals. The phrase Higgs signal refers to any observation of a signal. These can be cross-sections and signal strengths at a

given mass peak or as a function of Higgs mass(es). This complimentary test, e. g. whether a model is compatible with an observed Higgs signal can be performed with HiggsSignals.

HiggsSignals evaluates a χ^2 measure, which quantifies the compatibility of measured Higgs boson signals rates and masses with the predictions of arbitrary models. The default strategy in HiggsSignals to determine the χ^2 value is called the *peak-centered* method. In this method, the predicted (neutral) Higgs signal rates and masses are tested against the published signal rates for a fixed mass hypothesis, i. e. the model is tested at the mass of the observed peak. HiggsSignals is a Fortran 90/2003 code and it relies on the HiggsBounds library. The standard user input is handled via the HiggsBounds framework.

As theoretical input, HiggsBounds and HiggsSignals require the phenomenologically relevant physical quantities of the Higgs sector. These are the number of neutral and charged Higgs bosons, their masses, total widths, decay branching ratios, and production cross-sections. Different input approximations are available. Most relevant for this thesis is the input in terms of effective coupling modifiers $\boldsymbol{\kappa}$, which is based on the narrow width approximation[1]. Internally, these modifiers are used to calculate the corresponding production cross-sections and decay branching ratios. With HiggsBounds-5, the cross-section predictions for various production modes have been updated, and the changes relevant for this thesis are described in the following section.

4.2 HiggsBounds-5: Updated Effective Coupling Approximations

In previous versions of HiggsBounds, the cross-section ratios for associated neutral Higgs boson (ϕ) production with weak gauge bosons ($V = W^{\pm}, Z$) were obtained purely from the effective ϕVV couplings given in Equations 2.110 and 2.111. Similarly, the cross-sections for associated Higgs boson production with a single top quark or a top-quark pair were calculated using the naive effective $t\bar{t}\phi$ coupling approximation given in Equation 2.113. However, this description is only valid for ttH production with a purely scalar coupling. In the case of a general $\mathcal{CP}$-mixed coupling, the LO description is more complex. In its latest update, HiggsBounds-5 introduced valid LO predictions for the top-associated Higg productions $t\bar{t}\phi$, $t\phi$ and $tW\phi$ including the full dependence of the generalized top-Yukawa coupling. In addition, it extended the accuracy of the ϕV production cross-section calculations to NNLO in QCD.

Up to NLO in QCD, the $W\phi$ production process is described by Higgs-strahlung, i. e. it only depends on the ϕWW coupling, $g_{\phi WW}$. The LO Higgs-strahlung process is depicted in Figure 2.7(a). At NNLO in QCD, corrections from virtual top-quark loops arise, which depend on the scalar Higgs coupling to top-quarks, $g_{s,\,\phi t\bar{t}}$. Since the corresponding corrections from bottom quarks are tiny, they are neglected. In contrast, $Z\phi$ production is more complex due to additional box-diagrams. One example of such a diagram is shown in Figure 2.7(c). In this case, all relevant scalar and pseudoscalar Higgs couplings, as well as the corresponding interference terms, have to be considered.

The relevant effective couplings for a spin-0 particle ϕ are

$$\begin{aligned} \kappa_W &:= \left(\frac{g_{\phi WW}}{g^{\mathrm{SM}}_{HWW}}\right), \quad \kappa_Z := \left(\frac{g_{\phi ZZ}}{g^{\mathrm{SM}}_{HZZ}}\right), \\ \kappa_t := \left(\frac{g_{s,\,\phi t\bar{t}}}{g^{\mathrm{SM}}_{Ht\bar{t}}}\right), \quad \kappa_b &:= \left(\frac{g_{s,\,\phi b\bar{b}}}{g^{\mathrm{SM}}_{Hb\bar{b}}}\right), \quad \kappa_{\tilde{t}} := \left(\frac{g_{p,\,\phi t\bar{t}}}{g^{\mathrm{SM}}_{Ht\bar{t}}}\right), \quad \kappa_{\tilde{b}} := \left(\frac{g_{p,\,\phi b\bar{b}}}{g^{\mathrm{SM}}_{Hb\bar{b}}}\right). \end{aligned} \tag{4.1}$$

Note that this notation sligthly differs from the notation introduced in Section 2.4.2.2. The cross-sections

[1] Note that HiggsBounds-5 also provides an input scheme beyond the narrow width approximation, which is explained in detail in Reference [326].

can be expanded in terms of the coupling modifiers,

$$\sigma(W\phi, m_\phi) \approx \kappa_W^2 \bar{\sigma}_{WW}(W\phi, m_\phi) + 2\kappa_W \kappa_t \bar{\sigma}_{Wt}(W\phi, m_\phi)\,, \tag{4.2}$$

$$\sigma(Z\phi, m_\phi) \approx \sum_{a,b\in\{Z,t,b,\tilde{t},\tilde{b}\}} \kappa_a \kappa_b \bar{\sigma}_{ab}(Z\phi, m_\phi)\,. \tag{4.3}$$

The cross-section contributions $\bar{\sigma}$ are calculated with VH@NNLO [328, 329] as a function of the Higgs boson mass m_ϕ. Details about the approximation are given in Reference [326]. It provides a significant improvement over the effective coupling approximation, which can be used for the inclusive $pp \to Z\phi$ cross-section but also for the separate $qq \to \phi Z$ and $gg \to \phi Z$ cross-sections.

The cross-sections for the inclusive top-quark associated productions are calculated for a fixed Higgs boson mass of $m_\phi = 125\,\text{GeV}$ using MADGRAPH5_AMC@NLO 2.7.0 [330, 331] interfaced with PYTHIA 8.244 [332]. The obtained LO cross-sections (in fb) are [258]

$$\sigma(pp \to \phi t\bar{t}) = 371.6\left(\kappa_t^s\right)^2 + 155.8\left(\kappa_t^p\right)^2\,, \tag{4.4}$$

$$\sigma(pp \to t\phi) = 233.7\left(\kappa_W^s\right)^2 + 200.6\left(\kappa_t^s\right)^2 + 60.90\left(\kappa_t^p\right)^2 - 373.2\kappa_W^s\kappa_t^s\,, \tag{4.5}$$

$$\sigma(pp \to t\phi W) = 33.0\left(\kappa_W^s\right)^2 + 45.0\left(\kappa_t^s\right)^2 + 34.0\left(\kappa_t^p\right)^2 - 62.0\kappa_W^s\kappa_t^s\,. \tag{4.6}$$

All studies presented in this thesis that are performed with HiggsSignals and solely based on LHC Run-1 data are performed with HiggsSignals-1 and HiggsBounds-4. Thus, the Equations 2.110, 2.111 and 2.113) are used. In contrast, studies that include LHC Run-2 data are performed with HiggsSignals-2 and HiggsBounds-5. In this case, the improved approximations discussed in this section are employed.

4.3 HiggsSignals-2: Basic Concepts and New Developments

The experimental data used for the statistical evaluation in HiggsSignals is mainly collected at the LHC, but there are also some complementary measurements from the Tevatron collider. However, the HiggsSignals methods can easily be adapted to include data from other upcoming collider experiments.

4.3.1 Higgs Signals in Collider Experiments

In Run-1 of the LHC, the experimental collaborations provided Higgs rate measurements in the form of one-parameter scalings μ of the corresponding SM rate in various signal channels. The best-fit value of a *signal strength modifier* is denoted by $\hat{\mu}$ in the following. Since signal strength modifiers are measured relative to SM predictions, they contain theoretical uncertainties of the SM Higgs boson production cross-sections and decay branching ratios. Before the Higgs boson mass $m_\phi \simeq 125\,\text{GeV}$ had been established, the measured values of $\hat{\mu}$ as well as the corresponding 68 % C. L. regions were provided either as a function of m_ϕ or for a fixed mass hypothesis. For that reason, three different run modes were supported in HiggsSignals-1: The mass-centered method, the peak-centered method, and a combined method. However, since the Higgs boson mass at about 125 GeV has been established, the experimental collaborations no longer provide signal strength measurements for extended Higgs mass intervals. Thus, the mass-centered and the combined methods are no longer relevant and have been removed.

The main Higgs boson production processes at hadron colliders are the partonic subprocesses ggF, VBF, WH, ZH, and ttH. In models with enhanced bottom-Yukawa couplings, bbH can be relevant as well. The corresponding Feynman diagrams for these processes are depicted in Figures 2.6, 2.7, and 2.8. If b quarks are considered as partons (five-flavor scheme) the gluons in the proton can split into a $b\bar{b}$ pairs.

In this case, the $b\bar{b} \to H$ contribution should be matched consistently, and in most cases, added to the ggF subprocess. In HiggsSignals, this combined production is referred to as single Higgs production (singleH).

In HiggsSignals, the predicted Higgs boson signal strength modifier of one specific analysis category (or bin) for some BSM model is calculated via

$$\mu = \frac{\sum_i \epsilon_{\text{Model},i} \left(\sigma_{\text{Model}} \times \text{BR}_{\text{Model}}\right)_i}{\sum_j \epsilon_{\text{SM},j} \left(\sigma_{\text{SM}} \times \text{BR}_{\text{SM}}\right)_j}\,, \tag{4.7}$$

where the sums run over all channels consisting of one Higgs boson production and one decay mode, which contribute to the experimental analysis category. The numerator contains the model prediction for the production cross-section (σ_{Model}), the decay branching ratio (BR_{Model}) and the signal efficiency ($\epsilon_{\text{Model,i}}$) of each channel i. The denominator contains the corresponding SM predictions. In general, the signal efficiencies in the model can be different than those in the SM, if the Higgs boson candidate has different kinematic properties. Per default, HiggsSignals assumes $\epsilon_{\text{Model},i} = \epsilon_{\text{SM},i}$.

On the experimental side, the measurement of the signal strength (assuming $m_\phi = 125\,\text{GeV}$) in a specific analysis category is performed by assuming the properties of the SM Higgs boson, i. e. $\epsilon_i = \epsilon_{\text{SM},i}$. This means that the contribution of each channel is scaled by a universal factor $\widetilde{\mu}$,

$$(\sigma \times \text{BR})_i = \widetilde{\mu} \left(\sigma_{\text{SM}} \times \text{BR}_{\text{SM}}\right)_i\,. \tag{4.8}$$

The scale factor that best fits the observation, $\hat{\mu} = \widetilde{\mu}|_{\text{best-fit}}$, is the central value of the measurement. The lower and upper 68 % uncertainties are called $\Delta\hat{\mu}_{\text{low}}$ and $\Delta\hat{\mu}_{\text{up}}$, respectively.

After Run-1 of the LHC program, ATLAS and CMS released combined measurements of the Higgs signal rates [333] and mass [334]. These combinations provide the signal rates as unfolded inclusive measurements in 20 pure channels, supplemented with a 20×20 correlation matrix. The Higgs boson mass is measured to be $125.09 \pm 0.21 \pm 0.11$ GeV. The combined signal strength results give rise to a separate χ^2 contribution in HiggsSignals-2.

In Run 2 of the LHC, a different scheme for presenting the results of Higgs signal rate measurements, called *simplified template cross-sections*, emerged. This input is handled by a new Fortran module introduced in HiggsSignals-2. It is more versatile and provides additional features. For example, the corresponding input scheme is able to handle both the signal strength and STXS input formats. The STXS observables give rise to a third χ^2 contribution in HiggsSignals-2.

If there is no statistical overlap in the corresponding measurements, the different contributions can be added. Examples for this are presented in Chapter 7. In the following, the χ^2 calculations for the different contributions are shortly explained. Details are found in Reference [320].

4.3.2 The Peak-Centered χ^2 Method

The aim of the peak-centered χ^2 method is to perform a χ^2 test for the hypothesis that the model generates a local excess in the observed data at the specified mass. The experimental inputs are the signal strength measurements performed at the mass $\hat{m}$ and the Higgs boson mass measurements in $H \to \gamma\gamma$ and $H \to ZZ^* \to 4\ell$ final states.

The total χ^2 of the peak-centered method is given by

$$\chi^2_{\text{peak}} = \chi^2_{\text{peak},\mu} + \chi^2_{\text{peak},m}\,, \tag{4.9}$$

where $\chi^2_{\text{peak},\mu}$ describes the contribution from signal strength observables and $\chi^2_{\text{peak},m}$ the contribution

from mass observables. For N peak observables, the signal strength part is given by

$$\chi^2_{\text{peak},\mu} = (\hat{\boldsymbol{\mu}} - \boldsymbol{\mu})^T \, \boldsymbol{C}_{\boldsymbol{\mu}}^{-1} \, (\hat{\boldsymbol{\mu}} - \boldsymbol{\mu}) \,, \tag{4.10}$$

where $\hat{\boldsymbol{\mu}}$ and $\boldsymbol{\mu}$ are N-dimensional vectors containing the measured and predicted signals strengths, respectively. The signal rate uncertainties and the correlations of the major uncertainties are incorporated in the covariance matrix $\boldsymbol{C}_{\boldsymbol{\mu}}$. The latter contains the correlations of experimental and theoretical uncertainties (if available). For the calculation of $\chi^2_{\text{peak},m}$, three different choices to model the probability density function (pdf) of the Higgs boson mass are available. First, a uniform distribution, second, a Gaussian distribution, and third, a uniform distribution with Gaussian tails. For the Gaussian pdf, the theoretical mass uncertainty is treated as fully correlated between the sensitive peak observables.

In the default case of a Gaussian pdf, the total χ^2 contribution from the Higgs mass reads

$$\chi^2_{\text{peak},m} = (\hat{\boldsymbol{m}} - \boldsymbol{m}_i)^T \boldsymbol{C_m}^{-1} (\hat{\boldsymbol{m}} - \boldsymbol{m}_i) \,. \tag{4.11}$$

In this equation, the vectors $\hat{\boldsymbol{m}}$ and $\boldsymbol{m}$ contain the measured and predicted Higgs mass for the mass-sensitive peak observables, respectively. The covariance matrix, $\boldsymbol{C_m}$, contains the squared experimental and theoretical mass uncertainties.

4.3.3 The χ^2 Contribution from the LHC Run-1 Combination

The ATLAS and CMS collaborations also published a combined analysis [333] of the Run-1 dataset. The results are presented as signal rate measurements of the dominant production modes

$$pp \to H \,, \text{VBF}, \; WH \,, ZH \,, ttH \,,$$

and the five dominant decay modes

$$H \to \gamma\gamma \,, H \to ZZ^* \,, H \to WW^* \,, H \to \tau^+\tau^- \,, H \to b\bar{b} \,.$$

In the $H \to ZZ^*$ decay mode, only the $pp \to H$ and the VBF production processes are measured with meaningful precision. Thus, the other production modes are omitted. In contrast, in the case of the $H \to bb$ decay mode, the $pp \to H$ and the VBF production processes are not measured at all. Therefore, they are fixed to the corresponding SM predictions. In total, 20 different channels are measured. The analysis is performed for a Higgs boson mass of 125.09 GeV [334] and the correlations between the theoretical and experimental systematic uncertainties are provided in the form of a 20×20 correlation matrix.

The 20 signal rate measurements and the corresponding correlations are implemented in `HiggsSignals` and can be used with a dedicated run routine (see online documentation [335]). Besides, a χ^2 contribution from the Higgs mass measurement, taken to be 125.09 ± 0.24 GeV in `HiggsSignals`, arises if a Higgs boson is assigned to the theses measurements. If there is no statistical overlap, the resulting χ^2 contributions from the LHC Run-1 signal rate and mass measurements can be added to the χ^2 values obtained in other `HiggsSignals` runs.

4.3.4 The χ^2 Contribution from STXS Measurements

In Run 2 of the LHC program, the experimental collaborations started to present Higgs rate measurements in the form of cross-sections of mutually exclusive phase space regions defined per production process. These STXS measurements aim to maximize the measurement's sensitivity while minimizing its theory

dependence. In comparison, the signal rate measurements $\mu = {}^{\sigma}/_{\sigma_{\mathrm{SM}}}$ presented in Run 1 are more theory dependent because they also contain information about the SM theory prediction σ_{SM}. Moreover, the STXS phase-space regions, called *bins*, are defined such that they isolate possible BSM contributions.

With increasing amounts of data, measurements of differential distributions of the various Higgs processes are possible. To account for that, different Stages of STXS bins can be used. In the current version of the framework, the "Stage 0", "Stage 1", and "Stage 2" bins are defined[1], which allows a transition from more inclusive to more differential measurements [336]. This transition can be performed independently in each production mode. In addition, different decay modes can be combined in the determination of the STXS bins to maximize the sensitivity of the current data. The STXS framework is not completely theory-independent. For instance, the unfolding procedure from the measurements in the reconstructed event categories to the measurements in the particle-level STXS bins still requires an assumption about the kinematic properties of the Higgs boson. The kinematic template for this unfolding step is based on the SM Higgs boson.

The STXS measurements comprise a different type of input observable in HiggsSignals, resulting in an additional χ^2 contribution that is evaluated in a new module. Not all STXS bins represent "pure" signal channels with respect to the underlying process and the Higgs coupling dependence. In particular, the Stage 0 production bins VH and VBF. The former contains the Higgs-strahlung processes $pp \to WH$ and $pp \to ZH$ (with a leptonically decaying vector boson). The latter contains $pp \to q\bar{q}H$ and Higgs-strahlung processes with a hadronically decaying vector boson as they lead to the same final state particles. In general, HiggsSignals treats the STXS observables as multi-channel measurements. If no further information is given, it assumes that the combined processes have the signal efficiencies of the SM Higgs boson.

In order to test arbitrary BSM models with differential distributions of Higgs processes that differ from the SM prediction, it is possible to specify independent predictions individually for every STXS observable. This is done with a new routine in HiggsSignals-2 which applies *rate modification factors* for each STXS bin. Internally, these modifiers are used to calculate the model-predicted STXS-bin rate, which is then used for the χ^2 evaluation.

4.4 Statistical Interpretation in HiggsSignals

HiggsSignals is a tool for the statistical discrimination between different models using Higgs boson rate and mass observables. Three different types of applications which can be performed with HiggsSignals are distinguished:

- *Parameter fitting*:
  The question of parameter fitting is: Which parameter regions of a given model with the parameters $\boldsymbol{p}$ are preferred (or excluded) at a specific confidence level (C. L.). Questions of this type are answered by calculating the two-sided confidence interval (C. I.) for each model parameter.

  If the relation between the model parameters and the observables is approximately linear and the uncertainties are approximately Gaussian, the so-called *Gaussian limit* approximation can be used. In this case, for one-dimensional parameter spaces, the two-sided C. I. for the parameter p corresponding to a specific significance level α[2] of the statistical test is determined by symmetrically integrating over the tails of the one-dimensional Gaussian pdf, $f(p)$. The lower and upper integration

[1] It is also possible to define intermediate stages. An example for this is the ATLAS $H \to ZZ^* \to 4\ell$ coupling analysis presented in Section 5. In this analysis, a Reduced Stage 1.1 binning is introduced (see Figure 5.5).

[2] α is the probability of rejecting the null hypothesis when it is actually true (type I error). In constrast, β is the probability for failing to reject the null hypothesis when it is actually false (tyoe II error).

boundaries, p_β^{low} and p_β^{up}, respectively, represent the points where the integrated probability matches the α level. The C. L. $\beta = 1 - \alpha$, represents the corresponding probability of the central region,

$$\beta = \int_{p_\beta^{\text{low}}}^{p_\beta^{\text{up}}} f(p)\mathrm{d}p\,. \tag{4.12}$$

For example, the 1σ (2σ) C. L. corresponding to $\beta = 0.6827$ ($\beta = 0.9545$), is given by the ensemble of parameter points with $\Delta\chi^2(\boldsymbol{p}) \leq 1$ (4) above the best-fit point at $\Delta\chi^2(\boldsymbol{p}) = 0$. For two-dimensional parameter spaces, the integration has to be performed over both parameters. In this case, the corresponding 1σ (2σ) C. L. is given by $\Delta\chi^2(\boldsymbol{p}) \leq 2.30$ (6.18). For these values, it does not matter how many additional parameters are free in the fit as long as all parameters apart from those for which the C. I. is determined are profiled (marginalized) in the frequentist (bayesian) interpretation. Information about the relation between many different parameters, are difficult to visualize. Therefore, they are usually provided in the form of a covariance matrix based on linear correlation factors and on the 1σ one-dimensional uncertainties.

Caution is required if the Gaussian limit approximation is not valid, i. e. where the χ^2 profile around the minimum is not parabolical. In this case, the $\Delta\chi^2$ ranges given above do not correspond to the quoted frequentist coverage of e. g. 68.27 %. In addition, the interdependence of the parameters might not properly be described by linear correlations anymore. In this case, it is recommended to employ different methods like Toy-Monte-Carlo-based techniques (see Reference [337]).

- *Limit setting*:
  In limit setting, one is only interested in the lower or upper boundaries of the parameters $\boldsymbol{p}$. In this case, the calculation of one-sided confidence-level intervals can be appropriate. The main difference to parameter fitting is that the integration only covers one of the tails of the Gaussian pdf. For instance, the lower limit p_β^{low} on the parameter p for a one-dimensional parameter space is determined from

$$\beta = \int_{p_\beta^{\text{low}}}^{\infty} f(p)\mathrm{d}p\,, \tag{4.13}$$

  where β is again the C. L. of the statistical test. A detailed discussion about limit setting with HiggsSignals is given in Reference [320].

- *Goodness-of-fit* test:
  A goodness-of-fit test provides information about how well a model fits a set of observations. It is evaluated for a single parameter point. For example, this could be the best-fit point obtained from a preceding parameter fitting routine. However, for the correct interpretation of a goodness-of-fit test, one needs to be aware of certain caveats. First, in many fits of BSM models, two different parameter regimes are within the allowed C. I.: The first ones are decoupled regimes where the observables are effectively independent of the parameters. The second ones are strongly coupled regimes. In such cases, the analytic χ^2 probability determined in the Gaussian approximation is invalid because it assumes that the observables depend linearly on the parameters. The second caveat is that the goodness-of-fit test differs from the confidence level calculation. While the C. I. cannot increase if the data is presented in an increased number of subchannels, the goodness-of-fit test increases if the separate measurements are statistically consistent with each other. The consequences of this effect will be clearly visible in the validation of the LHC Run 1 combination presented in Section 4.5.

The first two applications are *hypothesis tests* that are based on a likelihood ratio (LR). The LR test is the most powerful test among all possible statistical tests (Neyman-Pearson lemma [338]). The LR quantifies the (dis)agreement of two competing statistical models based on the ratio of their likelihoods. In analyses of the LHC experiments, it is typically constructed such that one model is determined by maximizing the likelihood over the entire phase space (null hypothesis) and the other model represents an alternative parameter point under study. The alternative hypothesis is rejected if its likelihood is significantly lower than the likelihood of the null hypothesis.

The full likelihood, $\mathcal{L}(\boldsymbol{p}|\boldsymbol{x})$, of the model parameters, $\boldsymbol{p}$, given the observed data, $\boldsymbol{x}$, is not provided by the LHC experiments. Therefore, it needs to be approximated based on the publicly available information about the measurements. The χ^2 evaluation in HiggsSignals approximates the full log-likelihood, $\chi^2(\boldsymbol{p}|\boldsymbol{x}) \approx -2\ln\mathcal{L}(\boldsymbol{p}|\boldsymbol{x})$. Thus, the negative log-likelihood ratio can be constructed as

$$q(\boldsymbol{p}) = -2\ln\frac{\mathcal{L}(\boldsymbol{p}|\boldsymbol{x})}{\mathcal{L}(\hat{\boldsymbol{p}}|\boldsymbol{x})} = -2\left(\ln\mathcal{L}(\boldsymbol{p}|\boldsymbol{x}) - \ln\mathcal{L}(\hat{\boldsymbol{p}}|\boldsymbol{x})\right) \approx \chi^2(\boldsymbol{p}|\boldsymbol{x}) - \chi^2(\hat{\boldsymbol{p}}|\boldsymbol{x}) \equiv \Delta\chi^2 \,. \tag{4.14}$$

In this notation, $\hat{\boldsymbol{p}}$ denotes the parameter point at which the χ^2 is minimized, i. e. the best-fit point, and $q(\boldsymbol{p})$ is the test statistics. In the presence of additional nuisance parameters $\boldsymbol{\theta}$, which account for all possible systematic or parametric uncertainties, the test statistics generalizes to

$$q(\boldsymbol{p}) = -2\ln\frac{\mathcal{L}(\boldsymbol{p},\hat{\hat{\boldsymbol{\theta}}}|\boldsymbol{x})}{\mathcal{L}(\hat{\boldsymbol{p}},\hat{\boldsymbol{\theta}}|\boldsymbol{x})} \,. \tag{4.15}$$

In the numerator, the nuisance parameters are optimized for each tested parameter point, $\boldsymbol{p}$, in the nuisance parameter space, with the optimum denoted by $\hat{\hat{\boldsymbol{\theta}}}$, while in the denominator $\boldsymbol{p}$ and $\boldsymbol{\theta}$ are optimized simultaneously to find the global likelihood maximum at the point $\hat{\boldsymbol{p}}$ and $\hat{\boldsymbol{\theta}}$.

4.5 Performance Tests

In this section, different performance tests of HiggsSignals for selected experimental analyses are presented. The results obtained with HiggsSignals are compared to the official results for various benchmark models that parametrize Higgs boson couplings or certain Higgs production rates. In Section 4.5.1, the performance of HiggsSignals for the ATLAS and CMS Run-1 combination [333] of Higgs boson measurements are tested using two different input formats. The first one comprises the measurements of the official Run-1 combination, and the second one the measurements from the individual Run-1 analyses. This is followed by the discussion of exemplary studies using different Run-2 analyses, either using signal strength or STXS measurements as input. Finally, a set of recommendations for the presentation of future Higgs signal rate measurements is given.

4.5.1 Reproduction of the ATLAS and CMS Run-1 Combination

The ATLAS and CMS collaborations published results for the Higgs boson production rates in the main search channels from a combined analysis of the LHC pp collision data at $\sqrt{s} = 7$ and 8 TeV [333]. Besides, they also studied the properties of the Higgs boson using several benchmark parameterizations based on Higgs coupling scale factors $\boldsymbol{\kappa}$. A short introduction to the κ-framework is given in Section 2.4.1. In order to test the performance of HiggsSignals, the same benchmark scenarios are investigated with HiggsSignals using two different experimental inputs:

1. The combined ATLAS and CMS results for production cross-section, σ_i, times decay branching

ratio, $\mathrm{BR}(H \to f)$, of the various measurement channels $\sigma(i \to H \to f)$ together with the provided correlation matrix from Reference [333]. This input is described in Section 4.3.3.

2. The latest signal strength measurements published in individual Run-1 analyses by ATLAS [339–344] and CMS [345–353].

The results obtained with `HiggsSignals` are then compared to each other and the official experimental fit results for each benchmark parameterization.

4.5.1.1 Parameterization through Coupling Scale Factors

In the κ framework, BSM effects are parameterized through seven independent Higgs coupling modifiers. These are the generation-independent scale factors for up-type quarks, down-type quarks and leptons, κ_t, κ_b and κ_τ, as well as the scale factors for the heavy gauge bosons, κ_Z and κ_W, and the loop-induced gluon and photon scale factors, κ_g and κ_γ, respectively. In a second fit, the branching fraction into states of new physics

$$\mathrm{BR}(H \to \mathrm{NP}) = \frac{\Gamma_H^{\mathrm{NP}}}{\Gamma_H} = 1 - \frac{\kappa_H^2 \Gamma_H^{\mathrm{SM}}}{\Gamma_H}\,, \tag{4.16}$$

is introduced as an additional free parameter. In this equation, the scale factor

$$\kappa_H^2 = \sum_j \mathrm{BR}_{\mathrm{SM}}^j \kappa_j^2 \tag{4.17}$$

is used to characterize modifications to the total Higgs boson width that includes only SM decays. In both fit setupes, it is assumed that the coupling scale factor κ_t is positive, without loss of generality. To overcome the degeneracy induced by the unknown total width of the Higgs boson (for details see Section 2.4.1), it is assumed that $\mathrm{BR}(H \to \mathrm{NP}) = 0$ ($\kappa_{W,Z} \leq 1$) in the first (second) fit setup.

Figure 4.1 shows the fit results for both scenarios. The `HiggsSignals-2` results with the combination (individual signal strength) input are shown in blue (red). `HiggsSignals` produces similar results with the different input formats, and both results are consistent with the official results shown in black. Differences in the sign of the best-fit point in the `HiggsSignals` results are typically due to χ^2 distributions that are insensitive (e. g. κ_W in the former fit setup) or almost insensitive to the sign of the parameter. For $\mathrm{BR}(H \to \mathrm{NP}) = 0$ (see Figure 4.1(a)) in the case of the individual signal strength input, the goodness-of-fit quality of $\chi^2_{\mathrm{min}}/\mathrm{ndf} = 52.6/69$ leads to a p-value compatibility between the data and the SM prediction of 92.87 %. In the case of the ATLAS and CMS combination, the goodness-of-fit is $\chi^2_{\mathrm{min}}/\mathrm{ndf} = 14.95/13$ resulting in a p-value estimate of 31.0 %. The reason for this large discrepancy is the sensitivity of the goodness-of-fit to the structure of the experimental data. When many separate measurements are included, the p-value mostly measures the agreement between the separate measurements instead of quantifying the agreement of the model with the data [337]. In general, this effect is not a big concern as long as the quoted p-value is large, but it has to be taken into account if it approaches the significance level α of the statistical test. For this reason, the goodness-of-fit will not be quoted for the remainder of this section.

For the assumption $|\kappa_{W,Z}| \leq 1$ (see Figure 4.1(b)), the largest differences between `HiggsSignals-2` and the official results appear in the contributions of BSM decays. The `HiggsSignals` analysis returns $\mathrm{BR}(H \to \mathrm{NP}) < 0.37$ (< 0.28) as the 68 C L region using the combined (individual) input format. Both are notably larger than the official results $\mathrm{BR}(H \to \mathrm{NP}) < 0.16$. This discrepancy can be caused by the assumption of Gaussian uncertainties, which may not be fully applicable in all parts of the parameter space.

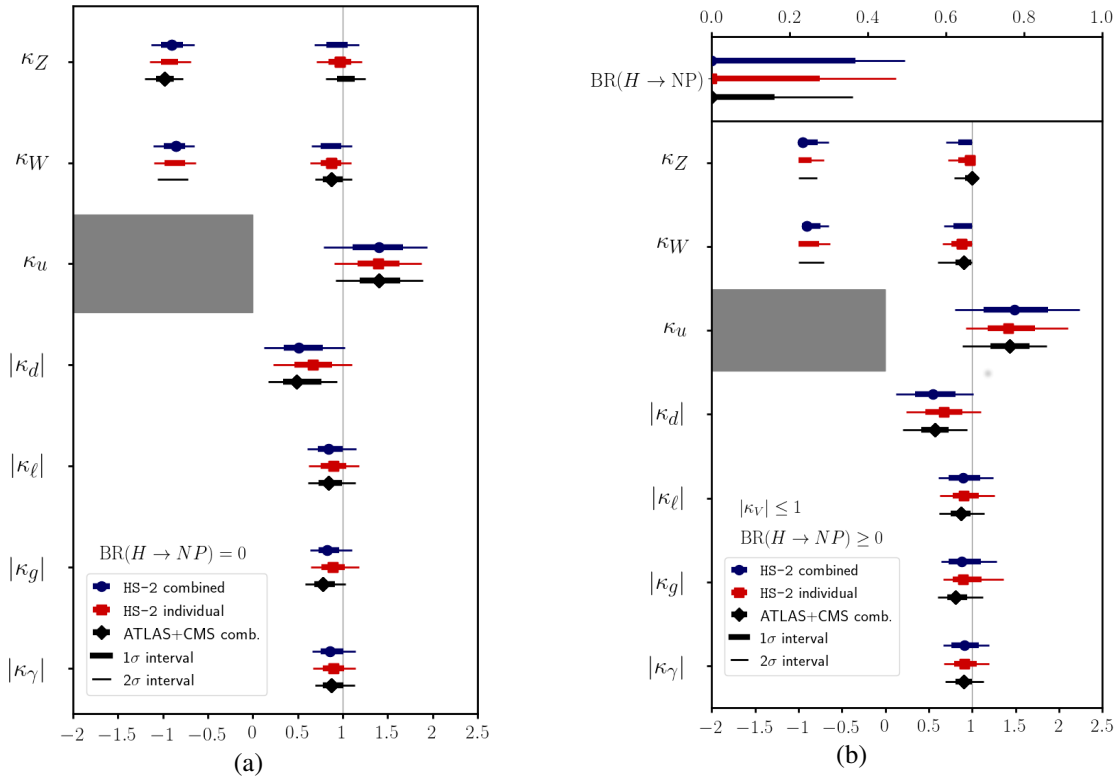

Figure 4.1: Official and reproduced ATLAS and CMS combined Run-1 results in the Higgs coupling scale factor parameterization, assuming (a) no new Higgs boson decay modes and (b) $\kappa_{W,Z} \leq 1$. The HiggsSignals-2 results are obtained using as input either the combined measurements (blue) or measurements from individual analyses (red). The official results are included in black. The gray areas indicate that $\kappa_u > 0$ is assumed without loss of generality. Only absolute values are shown for sign-insensitive parameters. The error bars indicate the 1σ (thick lines) and 2σ (thin lines) intervals.

4.5.1.2 Parameterization using Ratios of Coupling Scale Factors

The second benchmark parameterization is in terms of ratios of κ scale factors. The $gg \to H \to ZZ$ channel serves as reference channel for the normalization because its overall uncertainties and background contamination are very small. It is parameterized as a function of $\kappa_{gZ} = \kappa_g \cdot \kappa_Z/\kappa_H$, with κ_H being defined in Equation 4.16. The ratios $\lambda_{Zg} = \kappa_Z/\kappa_g$ and $\lambda_{tg} = \kappa_t/\kappa_g$ are probed by measurements of VBF and ZH, and $t\bar{t}H$ production, respectively. Similarly, the decay modes $H \to WW$, $H \to \tau\tau$, $H \to bb$, and $H \to \gamma\gamma$ probe the four ratios $\lambda_{WZ} = \kappa_W/\kappa_Z$, $\lambda_{\gamma Z} = \kappa_\gamma/\kappa_Z$, $\lambda_{\tau Z} = \kappa_\tau/\kappa_Z$ and $\lambda_{bZ} = \kappa_b/\kappa_Z$. Without loss of generality, κ_Z and κ_g are assumed to have the same sign, constraining λ_{Zg} and κ_{gZ} to be positive.

Figure 4.2 compares the official and the HiggsSignals-2 fit results for κ_{gZ} and the various λ parameters. The general agreement between the HiggsSignals-2 and the official results is very good. However, HiggsSignals tends to produce slightly larger 68 % and 95 % C. L. intervals. There are two main reasons for these differences. Firstly, the Gaussian approximation may not be valid for the experimental uncertainties in all regions of parameter space. Secondly, the parameterization in terms of ratios should lead to partial cancellation of common theoretical uncertainties, which are not expected to be entirely captured in the HiggsSignals approach. While the HiggsSignals result with the individual signal strength input reproduces the positive sign of the best-fit value for λ_{tg}, the fit with the combined input tends to prefer negative values. However, the $\Delta\chi^2$ between the negative and the positive best-fit value is very small, and thus there is no clear preference for one particular sign.

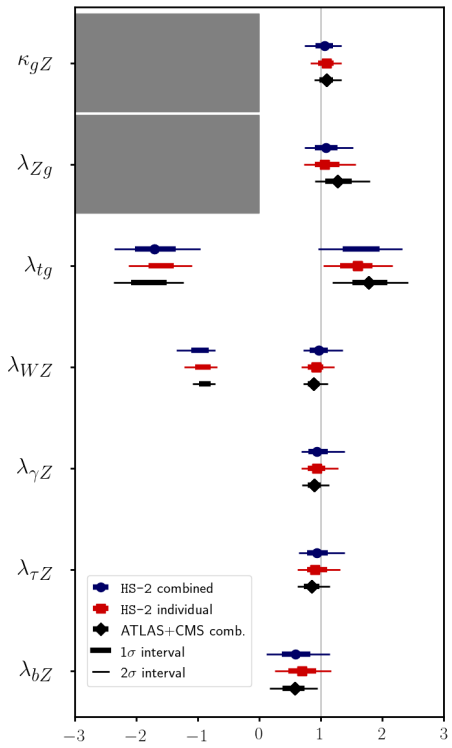

Figure 4.2: Official and reproduced ATLAS and CMS combined Run-1 results for ratios of Higgs coupling scale factors. The `HiggsSignals` results using the combined ATLAS and CMS data (the individual signal strength measurements) as input are shown in blue (red). The official results are shown in black. The error bars indicate the 1σ (thick lines) and 2σ (thin lines) intervals. The gray areas indicate the parameters that are assumed to be positive.

4.5.1.3 Parameterization using Ratios of Cross-Sections and Branching Fractions

Using the narrow-width approximation, the signal strength μ_i^f can be decomposed into the signal strength for the production, $\mu_i = \sigma_i/\sigma_i^{\mathrm{SM}}$, and the signal strength for the decay, $\mu^f = \mathrm{BR}^f/\mathrm{BR}^f_{\mathrm{SM}}$, where $\mathrm{BR}^f \equiv \mathrm{BR}(H \to f)$.

Choosing the $gg \to H \to ZZ*$ channel as a reference, the product of the production cross-section σ_i and the branching fraction BR^f can be expressed as

$$\sigma_i \cdot \mathrm{BR}^f = \sigma(gg \to H \to ZZ) \cdot \left(\frac{\sigma_i}{\sigma_{\mathrm{ggF}}}\right) \cdot \left(\frac{\mathrm{BR}^f}{\mathrm{BR}^{ZZ}}\right) . \tag{4.18}$$

In accordance with the ATLAS and CMS analysis [333], it is assumed that the ggF and the bbH production signal strengths are equal, $\mu_{\mathrm{ggF}} = \mu_{bbH}$, the $H \to Z\gamma$ and $H \to \gamma\gamma$ decay signal strengths are equal, $\mu^{Z\gamma} = \mu^{\gamma\gamma}$, and the $H \to gg$, $H \to cc$, and $H \to bb$ decay signal strengths are equal, $\mu^{gg} = \mu^{cc} = \mu^{bb}$.

Figure 4.3 shows the `HiggsSignals` fit results to the combined ATLAS and CMS input and the fit to individual signal strength measurements in blue and red, respectively. The fit result from the official ATLAS and CMS combination is shown in black. While the `HiggsSignals` result with the combined input agrees with the official result, notable discrepancies for various parameters are observed when using individual measurements, most strikingly for $\sigma_{ZH}/\sigma_{\mathrm{ggF}}$ and $\mathrm{BR}^{bb}/\mathrm{BR}^{ZZ}$ which are strongly anti-correlated. Furthermore, the central values of $\sigma_{ttH}/\sigma_{\mathrm{ggF}}$ and $\sigma_{\mathrm{VBF}}/\sigma_{\mathrm{ggF}}$ are shifted towards the SM

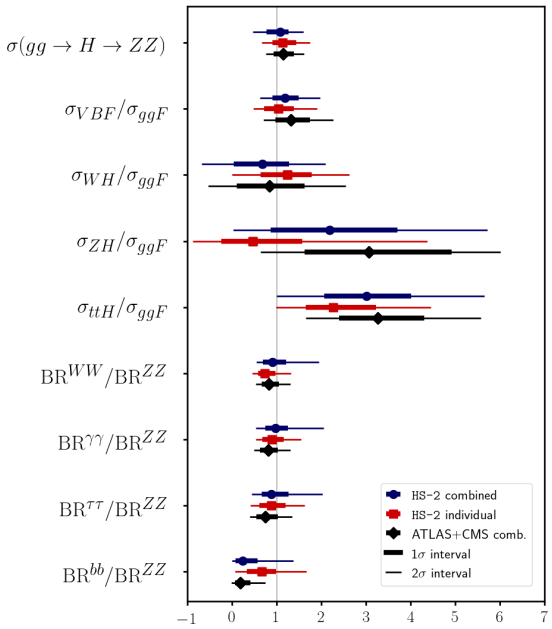

Figure 4.3: HiggsSignals-2 and official fit results for the $\sigma(gg \to H \to ZZ)$ cross-section and ratios of cross-sections and branching fractions. The HiggsSignals-2 result using the combined ATLAS and CMS data (the individual signal strength measurements) as experimental input are shown in blue (red). The official result from ATLAS and CMS are shown in black. The error bars indicate the 1σ (thick lines) and 2σ (thin lines) intervals. The results are normalized to the respective SM predictions.

prediction. The reason for this might be the fact that some analyses — in particular in CMS — have been improved for the combined result, but no updated individual measurements have been released. Figure 4.4 shows a comparison between the official ATLAS-only [354] (4.4(a)) and CMS-only [355] (4.4(b)) fit results and the corresponding HiggsSignals-2 results when using the individual signal strengths from ATLAS and CMS. HiggsSignals-2 reproduces the official ATLAS-only fit result very well. However, for the CMS-only fit similar discrepancies as for Figure 4.3 are observed, namely smaller values for $\sigma_{\mathrm{VBF}}/\sigma_{\mathrm{ggF}}$, $\sigma_{ZH}/\sigma_{\mathrm{ggF}}$, and $\sigma_{ttH}/\sigma_{\mathrm{ggF}}$ as well as a larger value for $\mathrm{BR}^{bb}/\mathrm{BR}^{ZZ}$.

In summary, the performed comparisons in all three model parametrizations have demonstrated excellent agreement between the HiggsSignals implementation of the LHC Run-1 measurements both using the individual and the combined experimental input and the official ATLAS/CMS fit results. The agreement between the two possible HiggsSignals implementations is, on the one hand, a successful closure test of the HiggsSignals peak-centered χ^2 method, and on the other hand, motivates the choice of using the LHC Run-1 combined experimental measurements as default input for the LHC Run-1 legacy χ^2 evaluation in HiggsSignals-2. Computationally, this implementation is much faster.

4.5.2 Examples for Run 2 Analyses in HiggsSignals-2

During Run 1 of the LHC, Higgs rate measurements were mainly represented in terms of signal strengths, $\mu = \sigma/\sigma_{\mathrm{SM}}$, and coupling modifiers, κ_i. For LHC Run 2, the experimental collaborations increasingly presented their results in the STXS framework (see Section 4.3.4). In some analyses, both STXS measurements and conventional signal strengths measurements in various event categories were presented, along with the correlation matrices, which are necessary to allow a comparison of the performance of the two experimental input formats.

In this section, the performance of HiggsSignals-2 with the provided experimental input for a

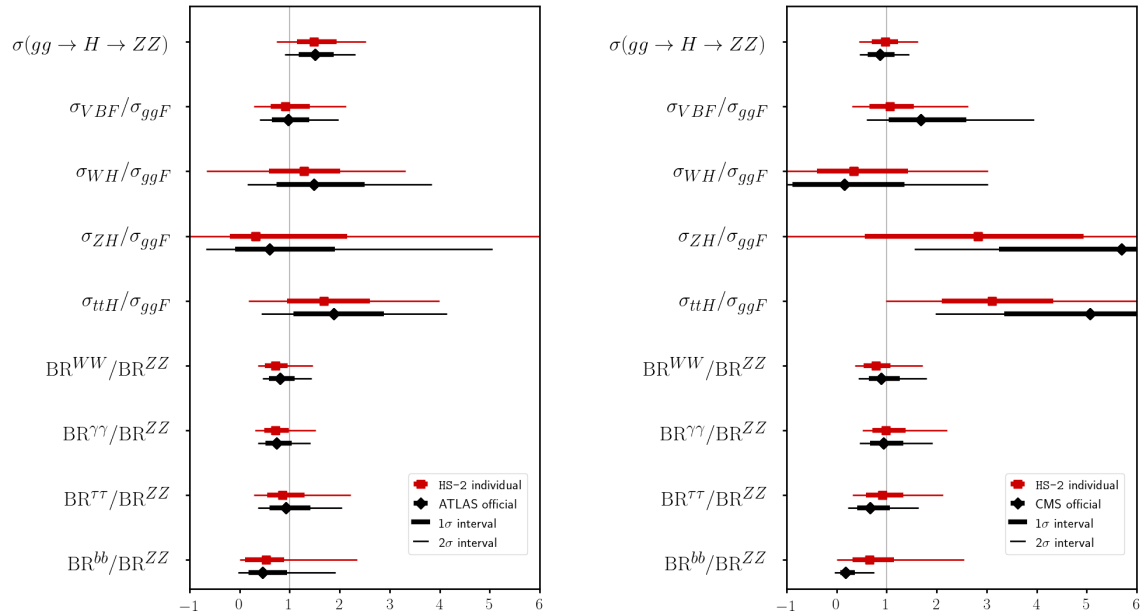

Figure 4.4: `HiggsSignals-2` and official (a) ATLAS-only and (b) CMS-only fit results for the $\sigma(gg \to H \to ZZ)$ cross-section and ratios of cross-sections and branching fractions. The `HiggsSignals-2` (the official) results are shown in red (black). The error bars indicate the 1σ (thick lines) and 2σ (thin lines) intervals. The results are normalized to the respective SM predictions.

selection of LHC Run-2 analyses is presented. These examples are primarily chosen to illustrate the level of agreement of the reconstructed `HiggsSignals` result with official results from ATLAS and CMS, and to highlight difficulties in the usage of the experimental results, which are often related to incomplete information in the public documentation of the experimental analysis. With the increasing amount of data during Run 2, the statistical uncertainty can be assumed to be Gaussian to very good approximation in most Higgs boson search channels. However, a decreasing statistical uncertainty also entails the fact that systematic uncertainties and their correlations among different measurements become more relevant. Therefore, it has become common practice for ATLAS and CMS to provide a correlation matrix of the experimental (statistical and systematic) uncertainties for the Run-2 measurements.

In the following, the performance of the two input types (signal strength modifiers and STXS measurements) for a few selected Run-2 examples are presented, illustrating what experimental information is needed to enable a successful application of the results to BSM models. Unless otherwise noted, a Higgs boson mass of $m_H = 125.09\,\mathrm{GeV}$ is assumed. The chosen examples do not necessarily represent the latest measurements implemented in `HiggsSignals-2`. The complete list of the ATLAS and CMS Run-2 Higgs signal rate measurements are summarized in Tables B.1, B.2, and B.3, respectively.

4.5.2.1 Input given in Terms of Signal Strength Modifiers

The first example analyses discussed are two CMS measurements in the $H \to W^+W^-$ decay channel. The first one is based on 2015 ($2.3\,\mathrm{fb}^{-1}$) and early 2016 ($12.9\,\mathrm{fb}^{-1}$) data [356]. The results of these early analyses are given in terms of sub-channel signal strength modifiers, where the different channels are tailored towards different Higgs productions modes (ggF, VBF, ZH and WH). However, in the former analysis, no signal efficiencies that would allow a better estimate of the signal composition in the different channels are provided.

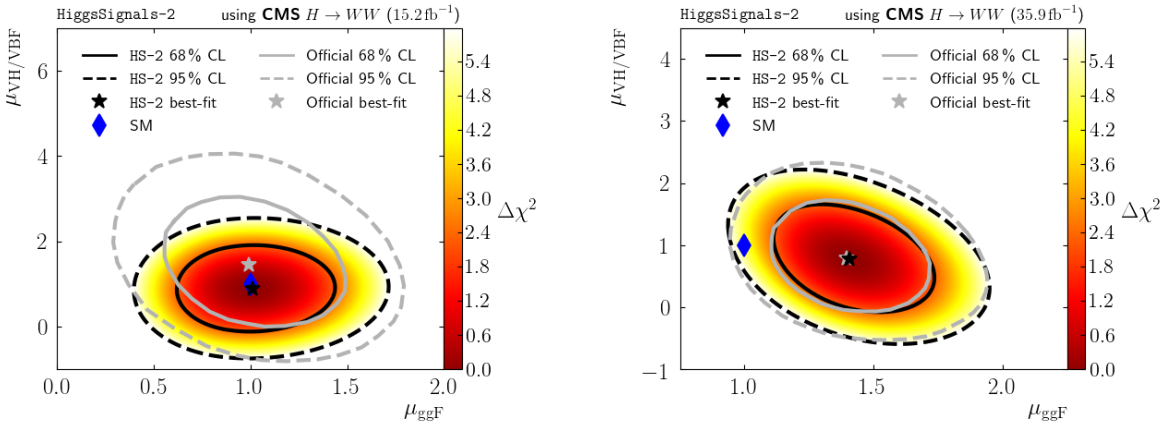

(a) CMS $H \to W^+W^-$ analysis using 15.2 fb^{-1} [356]. (b) CMS $H \to W^+W^-$ analysis using 35.9 fb^{-1} [357].

Figure 4.5: Comparison of the reconstructed fit results for the scale factors for fermionic (μ_{ggF}) and bosonic ($\mu_{VH/VBF}$) production modes with the official results presented by CMS. The stars indicate the best fit points, and the solid (dashed) contours correspond to the 68 % (95 %) C. L. regions. The HiggsSignals results are shown in dark and the official results in light shades. The diamonds indicate the SM prediction.

Figure 4.5(a) illustrates the performance achieved by HiggsSignals with the limited information available for this analysis. The comparison is performed in the signal strength scale factor parametrization, with μ_{ggF} and $\mu_{VH/VBF}$ rescaling the SM cross-section prediction for the fermionic and bosonic production modes, respectively. The Higgs boson decay rates are fixed to their SM prediction. The colormap represents the $\Delta\chi^2$ profiles reconstructed by HiggsSignals and the 68 % (95 %) C. L. regions are highlighted as black solid (dashed) lines. The corresponding official contours published by CMS are overlaid as gray solid (dashed) lines. The fits show reasonable agreement between the reconstructed and official intervals and the corresponding best-fit points for μ_{ggF}. However, the size of the allowed $\mu_{VH/VBF}$ intervals and the observed anti-correlation between μ_{ggF} and $\mu_{VH/VBF}$ is not reproduced. The reason for this discrepancy is the lack of public information on signal efficiencies for the sub-channel rate measurements. The anti-correlation observed by CMS indicates that these sub-channels are composed of signal contributions from fermionic and bosonic production modes.

Information on sub-channel signal efficiencies was made available in the CMS $H \to W^+W^-$ analysis at 35.9 fb^{-1} [357]. Figure 4.5(b) shows the HiggsSignals performance using the sub-channel signal strength results and the corresponding efficiencies. Excellent agreement between the reconstructed $\Delta\chi^2$ and the official likelihood results is observed. This demonstrates the importance of publicly available detailed sub-channel information on signal strengths and signal efficiencies. The analysis performed by CMS with 35.9 fb^{-1} also includes first results for $H \to W^+W^-$ in the stage-0 STXS framework. However, no information on the correlations between the STXS bins is provided for this analysis, which severely limits the usefulness of the STXS results. The performance achieved using this partial STXS input (not shown) is significantly worse than for the signal strength results.

A further update in the $H \to W^+W^-$ channel to 137 fb^{-1} [358] has since been released by CMS and is implemented in the current HiggsSignals datasets. The results of this analysis are given in terms of n-jet differential cross-sections in the STXS framework. Per-bin signal efficiencies and inter-bin correlations are available as well. This analysis provides the most complete input to date, and it is expected that its implementation in HiggsSignals is the best performing one. However, the analysis does not include any interpretations that could be used for a performance comparison with HiggsSignals.

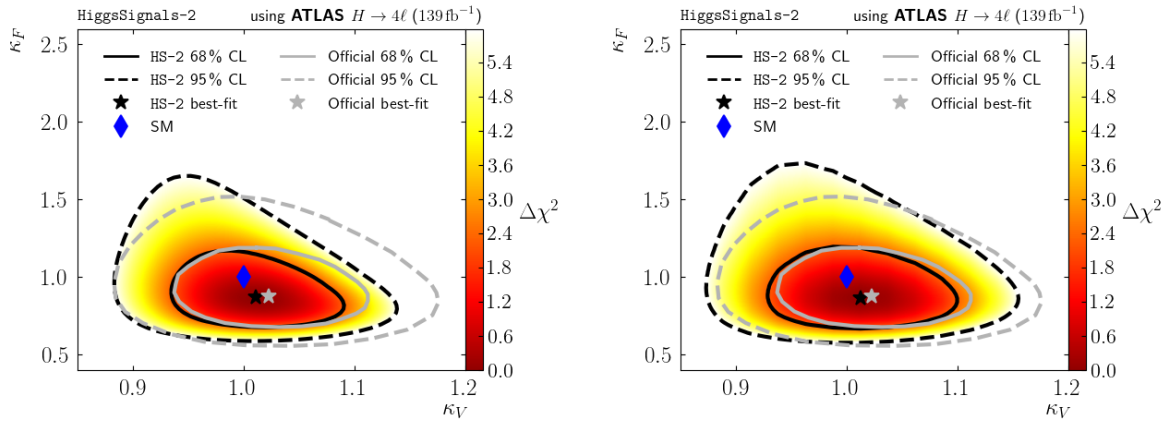

(a) Without theoretical rate uncertainty correlations in the $gg \to H$ process.

(b) With theoretical rate uncertainty correlations in the $gg \to H$ process.

Figure 4.6: Performance tests in the (κ_V, κ_F) parameter plane using the STXS measurements of the ATLAS $H \to ZZ^* \to 4\ell$ analysis with 139 fb^{-1} [359] as `HiggsSignals` input. Correlations of experimental uncertainties are included in both figures, while the correlations of theoretical uncertainties on the STXS bin predictions are (a) neglected and (b) included (see text for details). The stars indicate the best-fit points, and the solid (dashed) contours correspond to the 68 % (95 %) C. L. regions. The `HiggsSignals` results are shown in dark and the official results in light shades. The diamonds indicate the SM prediction.

4.5.2.2 Input given in Terms of Simplified Template Cross-Sections

In this section, some example applications for which the input to `HiggsSignals-2` is given in the STXS framework are discussed.

The first example is the `HiggsSignals` performance study for the ATLAS measurements in the $H \to ZZ^* \to 4\ell$ channel with 139 fb^{-1}[1] of data [359] as STXS observables. The experimental results are presented in 12 Reduced Stage-1.1 STXS bins along with the correlation matrix for the experimental uncertainties (Figure 10 of Ref. [359]). The `HiggsSignals` $\Delta\chi^2$ distribution in the (κ_V, κ_F) parameter plane based on this input, neglecting correlations of theoretical uncertainties on the STXS bin predictions, is shown in Figure 4.6(a) in comparison to the official ATLAS result (shown as gray contours). The agreement at lower values of κ_V and κ_F with the ATLAS results is very good. However, at larger values, a small mismatch between the reproduced and official confidence region contours is observed. In these regions, the agreement can be improved if correlations of theoretical uncertainties on the gluon fusion STXS bin predictions are included in the χ^2 calculation, as shown in Figure 4.6(b). These correlations have been evaluated by the ggF-subgroup of the LHC HXSWG and are taken from Reference [360] ("2017 scheme"). The evaluation of similar correlations for the STXS bins of other production modes is still in progress. As can be seen, these correlations lead to a flattening of the likelihood at large coupling scale factors, i. e. in the regions where the corresponding cross-sections (and thus their uncertainties) are larger than the SM prediction.

The second analysis is the CMS measurement in the $H \to \tau\tau$ decay channel at 77 fb^{-1} [361]. CMS provides cross-section measurements for nine different kinematic regions together with the expected acceptances, the SM predictions and the correlations between the bins. Figure 4.7 shows the comparison between the official and the reproduced $\Delta\chi^2$ contours in the $(\mu_{\text{ggF},b\bar{b}H}, \mu_{VH,\text{VBF}})$ (Figure 4.7(a)) and (κ_V, κ_F) (Figure 4.7(b)) parameter planes. Reasonable agreement is observed in the former, but a substantial disagreement is found in the latter. This discrepancy is explained by the fact that CMS included

[1] This analysis is discussed in Chapter 5 and used for the interpretation studies presented in Chapter 6 and Section 7.3.

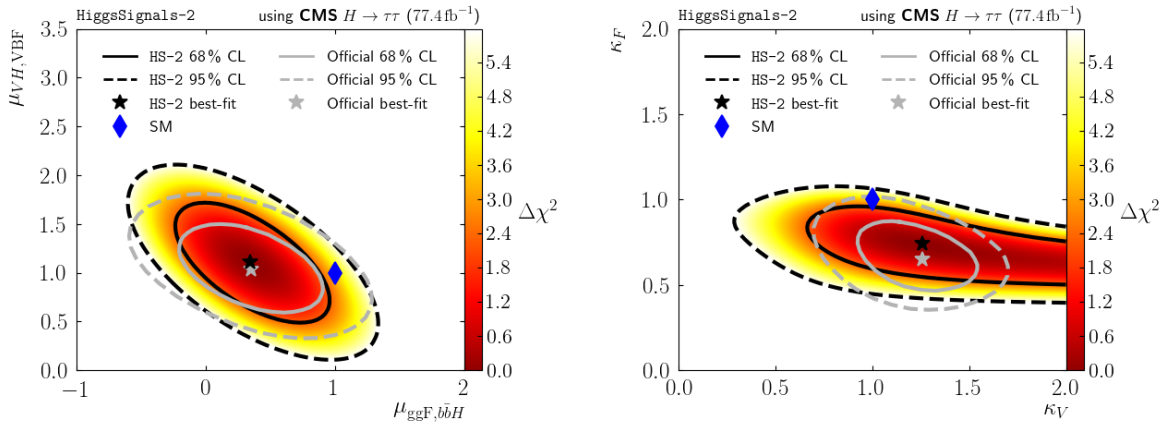

(a) (b)

Figure 4.7: Performance test in the (a) ($\mu_{\mathrm{ggF},b\bar{b}H}$,$\mu_{VH,\mathrm{VBF}}$) and (b) (κ_V ,κ_F) parameter plane using the STXS measurements of the CMS $H \to \tau\tau$ analysis with 77 fb^{-1} [361] as HiggsSignals input. The stars indicate the best-fit points, and the solid (dashed) contours correspond to the 68 % (95 %) C. L. regions. The HiggsSignals results are shown in dark and the official results in light shades. The diamonds indicate the SM prediction.

the contribution from $H \to WW$ to the $e\mu$ final state to remove an unconstrained direction along κ_V. As the $H \to WW$ contribution is not accounted for in the presented STXS measurements, it is not possible to properly implement it in HiggsSignals. Thus, HiggsSignals finds this open direction. However, in a global picture where $H \to \tau\tau$ and $H \to WW$ are simultaneously taken into account in HiggsSignals, the flat direction is lifted. This is already the case when adding only the measurements in the $e\mu$ final state, e. g. from a dedicated $H \to WW$ analysis.

The last example in this context is the ATLAS combination of Higgs analyses in the $\gamma\gamma$, ZZ^*, WW^*, $\tau^+\tau^-$, $b\bar{b}$ and $\mu^+\mu^-$ final states based on up to 79.8 fb^{-1} of Run-2 data [362]. Within the STXS framework — under the assumption of a single particle being responsible for the observed signals — the various measurements are combined to determine the cross-sections in various STXS bins. These bins represent a production process in a specific kinematic regime, e. g. gluon fusion in association with one additional jet and a Higgs boson transverse momentum of 60 GeV $\leq p_T^H \leq$ 120 GeV, times the branching fraction of the Higgs boson to Z bosons, BR($H \to ZZ^*$). In addition, ratios of branching ratios are determined for the various final states, with BR($H \to ZZ^*$) taken in the denominator. Here the measurements (given in Fig. 9 of Ref. [362]) and the corresponding correlation matrix are used as experimental input for HiggsSignals.

The performance of HiggsSignals using the ATLAS Higgs combination data is shown in Figure 4.8 in the (κ_V ,κ_F) (*left panels*) and (κ_g ,κ_γ) (*right panels*) parameter planes. For illustration, the top panels show the resulting likelihood profile if correlations between both experimental and theoretical uncertainties are neglected. A clear mismatch in size, shape, and location of the allowed regions with respect to the official ATLAS result (shown as gray contours) is observed in this case. Once the correlations of experimental uncertainties are included, the agreement of the reproduced and official confidence regions strongly improves, as shown in the middle panels of Figure 4.8. Finally, the bottom panels show the result when correlations of theoretical uncertainties in the $gg \to H$ STXS bins are also included (see above for details). From the comparison of the middle and bottom panels in Figure 4.8, one finds that these correlations have a small impact, giving rise to a slight improvement of the agreement between the HiggsSignals result and the official result.

Note that combination results with a separate determination of production and (ratios of) decay rates rely on the assumption that only one Higgs boson is responsible for the signal. Thus, these combined

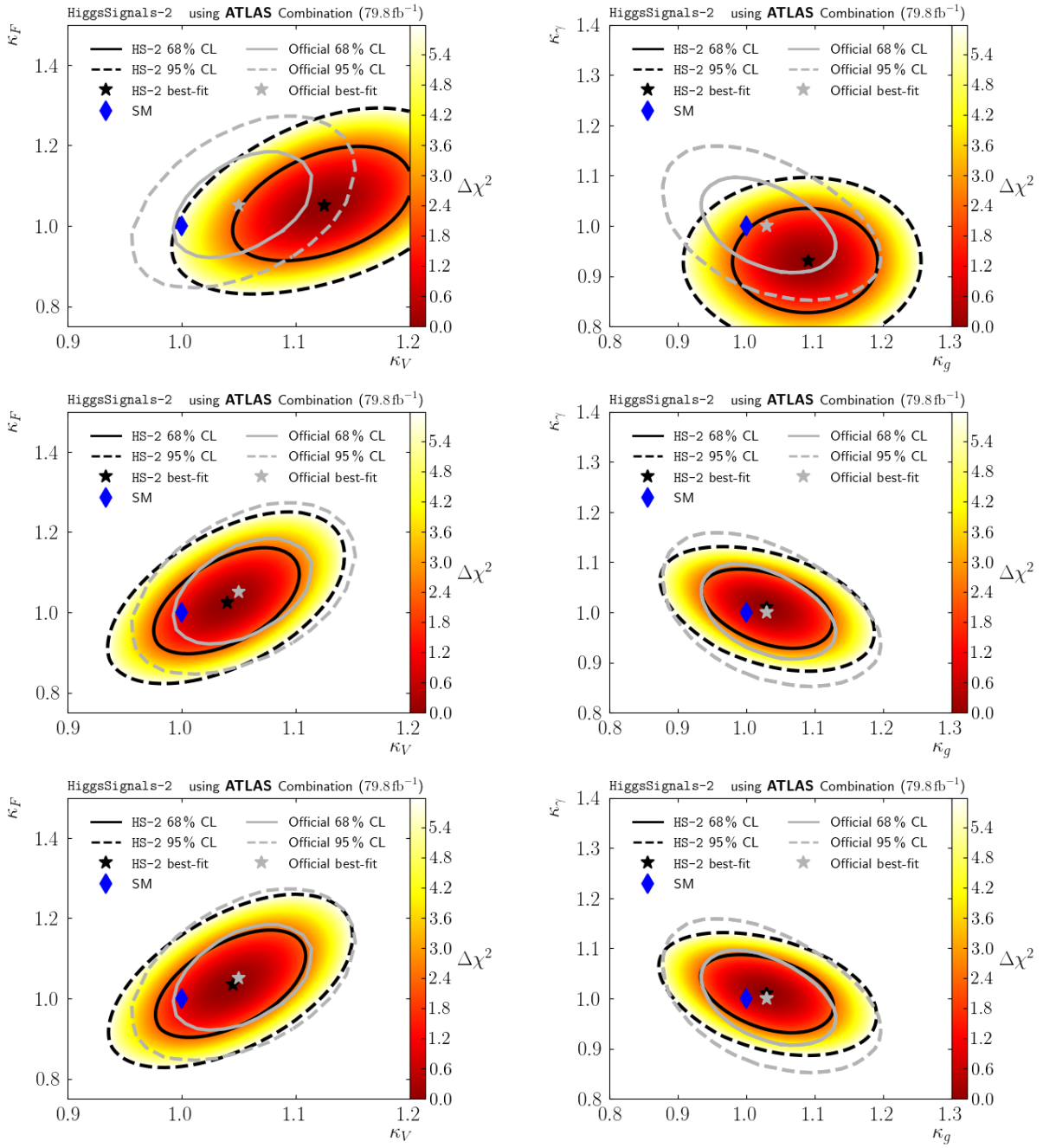

Figure 4.8: Performance test in the (κ_F, κ_V) (*left panels*) and $(\kappa_g, \kappa_\gamma)$ (*right panels*) parameter plane using the STXS measurements of the ATLAS Run-2 Higgs combination with 80 fb^{-1} as `HiggsSignals` input. Correlations of experimental uncertainties are either neglected (*top panels*) or included (*middle* and *bottom panels*). Theoretical rate uncertainties for the $gg \to H$ process are treated either uncorrelated (*top* and *middle panels*) or correlated (*bottom panels*). The stars indicate the best-fit points and the solid (dashed) contours correspond to the 68 % (95 %) C. L. regions. The `HiggsSignals` results are shown in dark and the official results in light shades. The diamonds indicate the SM prediction.

experimental results cannot be simply treated as peak or STXS observables in HiggsSignals, where per default, any superposition of Higgs bosons in the model is considered as a possible explanation of the signal. Therefore, in the officially provided observable sets, the use of individual (uncombined) measurements as experimental input is preferred. If only one Higgs boson is present in the model (or the other Higgs bosons have masses far away from 125 GeV, the combined measurements can still be safely used as experimental input.

4.6 Summary

In this chapter, the latest updates of the public computer programs HiggsBounds and HiggsSignals, which are most relevant for this thesis, and several performance tests of the statistical approach of HiggsSignals are presented.

The experimental results used by HiggsSignals-2 are either signal strength modifiers, $\hat{\mu}$, as a function of the Higgs mass in the various search channels or cross-sections, $\hat{\sigma}$, in the STXS framework. In both cases, the results have to be supplemented by their experimental uncertainties, $\Delta\hat{\mu}$ and $\Delta\hat{\sigma}$, respectively. It is shown that the achievable agreement with the official results published by ATLAS and CMS strongly depends on the information made available by the experiments. As a first step, the ATLAS and CMS combination of the full Run-1 data within the κ framework for different assumptions regarding the Higgs boson's total width are in good agreement with corresponding HiggsSignals results. When validating Run-2 results against κ fits performed by ATLAS or CMS the best agreement is found if the sub-channel signal strength modifiers are given together with the corresponding signal efficiencies. If signal strengths are given in terms of the targeted production processes, the best-fit point is typically well reconstructed by HiggsSignals-2 while the correlations are not correctly reproduced. However, further improvements from additional information about correlations of experimental uncertainties are expected. In the case of the stage-1 framework of STXS measurements, the information about experimental correlations is crucial in order to reconstruct official results. If STXS measurements are not given in terms of pure signal channels, additional information about the production processes could further improve the reconstruction, for example, the WH and ZH composition in the leptonic VH bins.

As the STXS observables are defined for specific particle level topologies of the Higgs boson production process, they can incorporate several production processes that depend on different Higgs couplings. For instance, $gg \to H$(+jets) STXS observables target the gluon fusion production mode including gg-induced EW corrections. These are composed of virtual electroweak (EW) corrections to the $gg \to H$ form factor as well as real EW corrections, corresponding to $gg \to (Z \to q\bar{q})H$. However, in HiggsBounds gluon fusion and $gg \to ZH$ are treated as separate processes, as their dependences on the Higgs coupling properties are different. Another example is the STXS observables of the class "EW qqH", which include the VBF and $qq \to (V \to qq)H$ (with $V = W, Z$) processes, with all three treated as separate processes in HiggsBounds. While higher STXS stages aim at separating these subprocesses, the earlier stages must be regarded as inclusive in these processes[1]. For such STXS measurements, it would be beneficial to publicly release the signal composition for the involved processes, analogous to the case of μ measurements.

For completeness, measurements should always be accompanied with a reference value for the signal rate expected for a SM Higgs boson. In case the measurement is quoted as a normalized signal strength, this allows the recalculation of the observed signal rate. Furthermore, BSM model predicted signal strengths can in many cases be approximated by a simple rescaling of the SM value.

[1] The general claim for early STXS stage measurements is that, at the present level of precision, these processes cannot be resolved. However, this claim relies on the assumption of SM signal strengths for all involved processes and may not be true if a BSM model predicts a strong enhancement in one or more of these processes.

CHAPTER 5

Higgs Boson Cross-Section Measurement in the $H \to ZZ^* \to 4\ell$ Decay Channel at ATLAS

In this chapter, the Higgs boson production cross-section measurement in the $H \to ZZ^* \to 4\ell$ decay channel at ATLAS with an integrated luminosity of $139\,\text{fb}^{-1}$ of pp collisions at a cms energy of $\sqrt{s} = 13\,\text{TeV}$ is outlined.

This chapter is organized as follows. The relevant signal and background processes in the $H \to 4\ell$ analysis are described in Section 5.1, followed by a summary of the data and Monte Carlo samples in Section 5.2. Section 5.3 summarizes the inclusive event selection criteria for Higgs boson candidates. The reconstructed event categories and the particle-level production bins are described in Section 5.4. Section 5.5 summarizes several performance studies of PFlow jets in the $H \to ZZ^* \to 4\ell$ analysis. This is followed by the discussion of the systematic uncertainties and the statistical analysis model in Sections 5.6 and 5.7, respectively. The cross-section measurement is presented in Section 5.8.

5.1 Signal and Background Processes

The $H \to ZZ^* \to 4\ell$ signal is characterized by final states with two pairs of oppositely charged light leptons originating from the same primary vertex and mediated by an intermediate state of two Z bosons. One of them is produced off-shell (Z^*) since the mass of the Higgs boson $m_H = 125.10 \pm 0.14\,\text{GeV}$ is below the threshold for the decay into two real Z bosons ($m_H < 2m_Z$, where $m_Z = 91.1876 \pm 0.0021\,\text{GeV}$ [54] is the Z boson mass).

5.1.1 The $H \to ZZ^* \to 4\ell$ Signal

In the SM, about 3 % of the generated Higgs bosons decay to a pair of Z bosons. Due to its large mass, the Z boson has access to hadronic and leptonic decay modes [363]. The $H \to ZZ^* \to 4\ell$ analysis targets a subgroup of the latter processes because of its clean signatures and outstanding signal-to-background ratio. However, in the SM, most Z bosons decay hadronically. Since it is rather difficult to distinguish these processes from QCD multijets, they make up a large proportion of the background. The leptonic decays contribute only to 30.1 % to all Z boson decays. Moreover, about two-thirds of them are decays into neutrinos, which are not directly measured and can only be partially reconstructed from missing transverse energy in the detector. The remaining branching fraction is shared between $\tau^+\tau^-$, $\mu^+\mu^-$ and e^+e^- with approximately equal probabilities. However, only the light-charged leptons provide clear signatures in the detector. In this context, the term "light leptons" refers to electrons and muons ($\ell = e, \mu$). On the other hand, tau leptons are not targeted due to their large mass ($m_\tau = 1.777\,\text{GeV}$). The associated implications are explained in Section 3.3.4. Although the muon is an unstable particle, its typical decay length exceeds

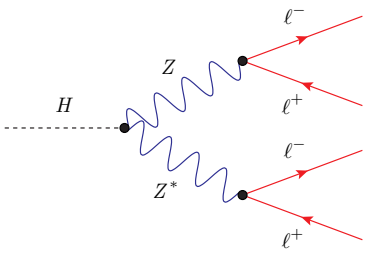

Figure 5.1: The tree-level Feynman diagram of the Higgs boson decay into four light leptons ($\ell = e, \mu$).

the size of modern detector systems by several orders of magnitude. For example, a 40 GeV muon decays on average after 250 km. In comparison, the diameter of the largest volume detector ever constructed for a particle collider, the ATLAS detector introduced in Section 3.2, is about 25 m. Thus, the muon can be considered a stable particle for most practical purposes.

The $H \to ZZ^* \to 4\ell$ decay channel is an experimentally very promising decay mode of the Higgs boson with a branching ratio of $1.251 \cdot 10^{-2}$ % [364]. In this mode, both the on-shell and off-shell Z bosons decay into a pair of oppositely charged electrons or muons, as illustrated in Figure 5.1.

The decay lengths of the Z and the Higgs bosons are very short due to their large mass. As a result, the four final state leptons can effectively be considered originating from the same primary vertex. The measurement of the $H \to 4\ell$ process requires a high electron and muon reconstruction efficiency, both provided by the ATLAS detector. This allows for an accurate reconstruction of the Higgs and Z boson four-momentum. Besides, the energy deposits of light leptons originating from the Z boson decays are typically concentrated in a small region, which allows for good discrimination against the reducible background processes. The excellent energy resolution allows for a precise determination of the four-lepton invariant mass, and the currently achieved mass resolution is about 1 – 2 %.

5.1.2 Background Contributions

For any particle physics analysis, there are, in general, two kinds of background. The first one is particles that generate detector signatures that look similar to the final state of interest. These particles are called fakes, and appropriate selection criteria can reduce them. The corresponding background is called the *reducible background*. The second kind of background comprises final state particles that are identical to the final state of the signal process. In this case, the background is called *irreducible*. For the $H \to ZZ^* \to 4\ell$ decay channel, the reducible background consists of four non-prompt or fake leptons in the final state and the irreducible background of four prompt leptons.

5.1.2.1 Irreducible Background

The largest background is from non-resonant ZZ^* production, resulting in four leptons in the final state. The dominant contribution is from quark-antiquark annihilation, and the corresponding processes ($q\bar{q} \to Z/\gamma^* \to 4\ell$) are depicted in Figure 5.2(a) and 5.2(b). A much smaller contribution to the ZZ^* background is from gluon-gluon fusion ($gg \to ZZ^*$). However, since gluons do not couple directly to heavy gauge bosons, these processes are only possible via box diagrams that include (heavy) quarks. Figure 5.2(c) shows the corresponding Feynman diagram for the gluon-induced production process. The smallest relevant contributions to the final state with four prompt leptons are from vector-boson scattering (VVV) where at least one of the vector bosons is a Z boson and $t\bar{t}Z$ production. The corresponding Feynman diagrams are shown in Figure 5.3.

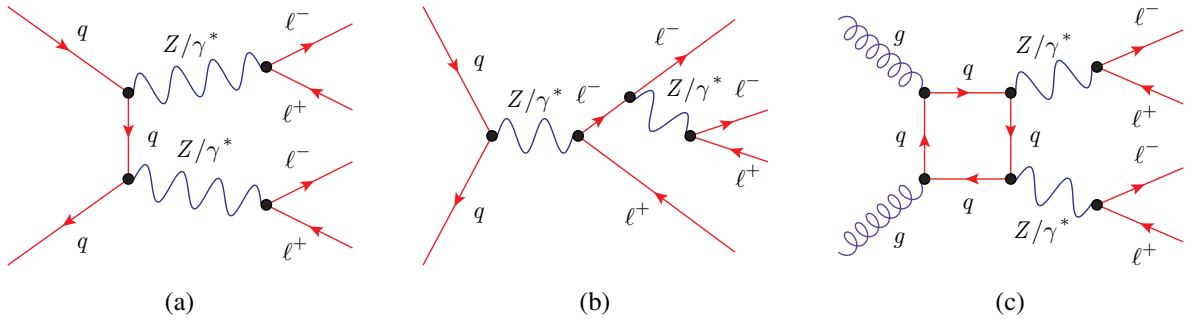

Figure 5.2: Feynman diagrams for non-resonant ZZ^* production with subsequent decays into four leptons for (a) and (b) quark-antiquark annihilation, and (c) gluon-gluon fusion.

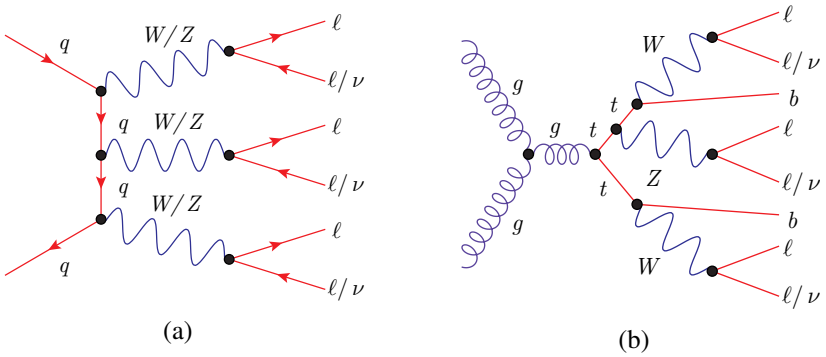

Figure 5.3: Feynman diagrams for the minor processes (a) VVV and (b) $t\bar{t}Z$ contributing to the irreducible background.

All of the above-mentioned processes contribute to the irreducible background in the $H \rightarrow ZZ^* \rightarrow 4\ell$ decay channel. However, by exploiting the kinematic properties of the four final state leptons, it is possible to reduce some of these background processes to a certain extent. The size of the individual background contributions is estimated from Monte Carlo simulations summarized in Section 5.2.2.2.

5.1.2.2 Reducible Background

The dominant contribution to the reducible background originates from Z + jets events. Additional but smaller contributions are from $t\bar{t}$ and WZ production, shown in Figure 5.4. The reducible background is significantly smaller than the non-resonant ZZ^* background. It is characterized by the fact that at least one of the final state particles is misidentified as a prompt lepton. These are typically jets, photons, or leptons from hadronic decays, which can be distinguished from the signal using lepton isolation criteria.

The reducible background contributions are estimated from data using different approaches depending on the flavor of the lepton pair that is farthest from the Z boson mass. The different final states that are considered are $\ell\ell + \mu\mu$ and $\ell\ell + ee$, where $\ell\ell$ is the lepton pair closest to the Z boson mass. It is assigned to a Z boson decay and called the *leading lepton pair*. The $\ell\ell + \mu\mu$ final states mainly result from heavy hadrons carrying charm or bottom quarks (also called heavy-flavor hadrons) that decay semi-leptonically. The normalization of the Z + jets and $t\bar{t}$ backgrounds are derived from fits to the invariant mass of the prompt lepton pair in dedicated, independent control regions. The invariant mass distribution is individually parameterized for each region using simulated samples. The contribution from WZ production is negligible in this case. The fake electron candidates in the $\ell\ell + ee$ final states are mainly misidentified light-flavor jets, electrons from photon conversion, or electrons from semileptonic decays

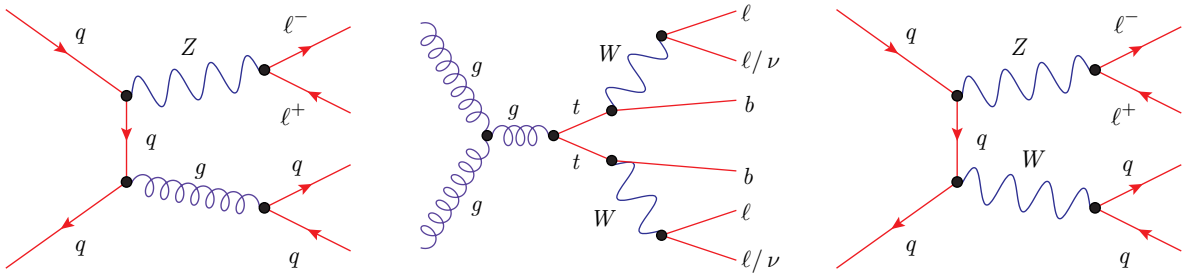

Figure 5.4: Feynman diagrams for the main processes (a) Z + jets, (b) $t\bar{t}$, and (c) WZ contributing to the reducible background.

of heavy-flavor hadrons. Z + jets, $t\bar{t}$ and WZ production contribute to the reducible background in the $\ell\ell + ee$ final state. The size of the background contribution from heavy-flavor decays is determined from simulation. In contrast, the light-flavor and photon conversion background components are estimated from dedicated control data depleted in signal. This is achieved by separating the two background components using the sPlot method [365] followed by a template fit to the number of hits from the electron candidate in the innermost layer of the inner tracking detector in the $\ell\ell + ee$ control region. In the final step, the background contributions are extrapolated to the signal region using transfer factors. These are obtained from simulated events with an on-shell Z boson decay candidate accompanied by an appropriate electron candidate.

5.2 Event Samples

The measurements in the $H \to ZZ^* \to 4\ell$ decay channel that are presented in this chapter are based on pp collision data at a cms energy of $\sqrt{s} = 13$ TeV with a 25 ns bunch spacing configuration[1] recorded by the ATLAS detector during the Run-2 data taking period of the LHC. The corresponding data set is described in Section 5.2.1. To optimize the analysis and to confront the measurement with the SM predictions, simulated Monte Carlo samples are used. These are introduced in Section 5.2.2.

5.2.1 The ATLAS Run-2 Data Set

Between 2015 and 2018 the LHC delivered an integrated luminosity of $L = 156.1\,\text{fb}^{-1}$ of pp collisions at $\sqrt{s} = 13$ TeV. The ATLAS detector recorded 93.2 % of these collisions which amounts to $146.9\,\text{fb}^{-1}$. In 2015, $3.86\,\text{fb}^{-1}$ of luminosity with a peak instantaneous luminosity of $5.0 \times 10^{33}\,\text{cm}^{-2}\text{s}^{-1}$, an average pile-up of $\langle\mu\rangle = 13.4$ and a peak pile-up of 40.5 was recorded. In 2016, the recorded integrated luminosity was $35.6\,\text{fb}^{-1}$, with a peak instantaneous luminosity of $13.7 \times 10^{33}\,\text{cm}^{-2}\text{s}^{-1}$, an average pile-up of $\langle\mu\rangle = 25.1$ and a peak pile-up of 51.1. In 2017, the recorded integrated luminosity was $46.9\,\text{fb}^{-1}$, with a peak instantaneous luminosity of $20.9 \times 10^{33}\,\text{cm}^{-2}\text{s}^{-1}$, an average pile-up of $\langle\mu\rangle = 37.8$ and a peak pile-up of 80. In 2018, the recorded integrated luminosity was $62.2\,\text{fb}^{-1}$, with a peak instantaneous luminosity of $21.4 \times 10^{33}\,\text{cm}^{-2}\text{s}^{-1}$, an average pile-up of $\langle\mu\rangle = 36.1$, and a peak pile-up of 90. The data taking efficiency improved over the years from 92.0 % in 2015 to 95.7 % in 2018. The pile-up distributions for the recorded datasets are shown in Fig. 3.2(b).

However, not all recorded events fulfill the quality requirements imposed by the experiment. Events recorded during periods when relevant detector components were not operating properly are rejected.

[1] This excludes the $0.13\,\text{fb}^{-1}$ of data collected in 2015 using the 50 ns bunch spacing configuration.

Table 5.1: The integrated luminosity of pp collision data at $\sqrt{s}$ = 13 TeV for each year of the Run-2 data taking period as delivered by the LHC, recorded by the ATLAS detector, and analyzed by the experiment. The average number of interactions per bunch crossing (pile-up) is shown as well.

Integrated	Data taking period			
luminosity [fb^{-1}]	2015	2016	2017	2018
Delivered	4.2	38.5	50.2	63.3
Recorded	3.9	35.6	46.9	60.0
Analyzed	3.2	32.9	43.7	59.2
Average pile-up $< \mu >$	13.4	25.1	37.8	36.1

Thus, the data that is actually analyzed is smaller than the recorded one. The integrated luminosity of the analyzed data is 139.0 fb^{-1}. The detailed breakdown of the delivered, recorded, and analyzed luminosities for the different data-taking periods of Run 2 of the LHC program is summarized in Table 5.1.

5.2.2 Monte Carlo Event Simulation

In particle physics, high-energy hadron collisions are typically modeled by first simulating the hard scattering of partons (quarks or gluons) with a Monte Carlo event generator. To simulate the hadronization of the final state as well as initial and final state radiation, appropriately tuned parton-shower programs are used in conjunction with the event generator. In the second step, the generated events are fed through a detector simulation framework to simulate the response of the various detector components and triggers. In ATLAS, this task is performed with the GEANT4 simulation toolkit [366, 367]. A real-world hadron collider undergoes multiple proton-proton interactions per bunch crossing. Minimum bias events of the simulated signal events are superimposed, and the resulting pile-up distribution is reweighted to match the observed distribution in data. The event generators used to simulate the relevant SM processes in the $H \to ZZ^* \to 4\ell$ analysis are discussed in the following.

5.2.2.1 The Higgs Boson Signal Model

The Higgs boson production modes gluon-gluon fusion (ggF), vector-boson fusion (VBF), associated production with a vector boson (VH) and with a top quark pair (ttH) are simulated with the Powheg-Box v2 Monte Carlo event generator [368–370]. The parton distribution functions (PDF) for all production modes, except ggF, are modeled with the PDF4LHC next-to-leading-order (NLO) PDF set. In the case of ggF, the more precise PDF4LHC next-to-next-to-leading-order (NNLO) set is used [371].

For the simulation of the Higgs boson production via ggF with additional jets in the final state, the Powheg method for merging the NLO Higgs boson cross-section with the parton shower and the multi-scale improved NLO (MiNLO) method [372–375] is used to achieve NLO accuracy for the inclusive cross-section. To achieve NNLO accuracy in the strong coupling constant (α_s) a reweighting procedure (NNLOPS) [376, 377] is applied using the HNNLO program [378, 379].

For the VBF, $q\bar{q} \to VH$ and $t\bar{t}H$ production processes the matrix elements are calculated up to NLO in QCD. In the case of VH production, the MiNLO method is applied to merge events with zero and one jets [372, 374, 380–383]. For the $gg \to ZH$ production process, the matrix elements are calculated at LO in QCD with the PDF4LHC set.

The Higgs boson associated production with a bottom quark pair (bbH) is simulated with the Madgraph5_aMC@NLO v2.3.3 program [330, 331] using the CT10 NLO PDF set [384]. The Higgs

Table 5.2: The predicted SM Higgs boson production cross-sections and systematic uncertainties of ggF, VBF, WH, ZH, ttH, bbH and tH production in pp collisions for a Higgs mass of 125 GeV at $\sqrt{s} = 13$ TeV [73, 229, 328, 329, 387–426]. The theoretical systematic uncertainties are calculated by adding in quadrature the uncertainties due to the QCD scale and PDF+α_s.

Production process	cross-section σ [pb]	accuracy in QCD
ggF ($gg \to H$)	48.6 ± 2.4	NNLO in y^H [427], p_T^H consistent with HqT (NNLO+NNLL) [378, 379]
VBF ($qq \to H$)	3.78 ± 0.08	NLO
WH ($qq \to WH$)	1.373 ± 0.028	NLO
ZH ($gg/qq \to ZH$)	0.88 ± 0.04	NLO
ttH ($gg/qq \to t\bar{t}H$)	0.51 ± 0.05	NLO
bbH ($gg/qq \to b\bar{b}H$)	0.49 ± 0.12	NLO
tH ($gg/qq \to tH$)	0.09 ± 0.01	NLO
Decay process	branching ratio BR $\left[\cdot 10^{-4}\right]$	
$H \to ZZ^*$	262 ± 6	NLO
$H \to ZZ^* \to 4\ell$	1.240 ± 0.027	NLO

production in association with a single top quark (tH) is taken into account. These processes are called $tH + X$ to account for the fact that they are accompanied by either a b-jet ($X = jb$) or a W boson ($X = W$). Both are simulated with MadGraph5_aMC@NLO v2.6.0 using the NNPDF3.0nlo PDF set [73].

The Higgs boson decays into four lepton final states are simulated with the PYTHIA8 [332] generator for all production mechanisms. PYTHIA8 is also used to generate the model for the parton shower, the hadronization, and the underlying event. For the ttH, bbH, and tH production processes, the AZNLO [385] tuned parameter set is used. In contrast, the A14 [386] set is used for the ggF, VBF, and VH production processes.

For the simulation of the Higgs boson signal samples, a Higgs boson mass of $m_H = 125$ GeV is assumed. The production cross-sections, the decay branching ratios, and the corresponding uncertainties are taken from References [73, 229, 336, 387–392]. The Higgs boson's branching ratio to the four-lepton final states is calculated with PROPHECY4F [393, 394], which incorporates NLO EW corrections and interference effects between identical final-state fermions. Table 5.2 summarizes the SM predictions for the Higgs boson production cross-sections and the branching ratio of the $H \to ZZ^* \to 4\ell$ decay.

5.2.2.2 The Background Model

This section describes the programs and methods used to simulate the relevant processes contributing to the $H \to ZZ^* \to 4\ell$ background. The corresponding Feynman diagrams are given in Section 5.1.2. For the simulation of the different contributions to the ZZ^* continuum background SHERPA 2.2.2 [428–431] is used. In all cases, the NNPDF3.0nnlo PDF set [73] is used in conjunction with a dedicated set of tuned parton-shower parameters. The matrix elements for the $q\bar{q} \to ZZ^{(*)}$ ($gg \to ZZ^{(*)}$ and VVV) processes are accurate to NLO (LO) in α_s for zero- and one-jet final states. Final states with two or three jets are modeled in LO QCD. The contribution from quark-antiquark annihilation is further refined by NLO EW corrections that are applied as a function of the invariant mass m_{ZZ^*} of the ZZ^* system [432, 433]. For the calculation of higher-order QCD corrections to the $gg \to ZZ^{(*)}$ process, the interference with the $gg \to H^* \to ZZ$ processes [434, 435] are taken into account, and the heavy top-quark approximation [436] is used, i. e.

the masses of light quarks in the loops are set to zero [437–439]. To account for higher-order effects, the LO cross-section is scaled by $k = 1.7 \pm 1.0$. The jet merging is performed using the SHERPA parton shower [440] applying the ME+PS@NLO [441] prescription for quark-antiquark and gluon-induced productions. In case of vector-boson scattering, ME+PS@LO is used.

The background contribution from events containing Z bosons and jets (Z + jets) is simulated with SHERPA v2.2.1 at NLO (LO) for up to two (three and four) partons using COMIX [429] and OPENLOOPS [430]. The merging is performed with the SHERPA parton shower using the ME+PS@NLO prescription. For the simulation, the NNPDF3.0nnlo PDF set is used alongside a dedicated set of tuned parton-shower parameters.

The WZ background [442] is modeled using POWHEG-BOX v2 with the CT10 NLO PDF set and interfaced to PYTHIA 8 for the parton shower and hadronization using the AZNLO parameter set. For the simulation of B-hadron decays, EVTGEN v1.2.0 is used.

The modelling of the $t\bar{t}$ background is performed with POWHEG-BOX v2 using the the NNPDF3.0nlo PDF set interfaced to PYTHIA 8 using the A14 set of tuned parameters. Decays of heavy-flavor hadrons are simulated with EVTGEN v1.2.0.

For the simulation of $t\bar{t}Z$ and tXX events MADGRAPH5_AMC@NLO is used with the NNPDF3.0nlo PDF set and interfaced to PYTHIA 8 using the A14 set of tuned parameters. The latter processes refer to tWZ, $ttWW$, $ttWZ$, $tt\gamma$, $ttZZ$, ttt, $tttt$ and tZ backgrounds.

5.3 Event Selection

The selection and categorization of Higgs boson candidates rely on the correct reconstruction and identification of the final state leptons and jets. This section summarizes the event selection criteria in the $H \to ZZ^* \to 4\ell$ decay channel starting from the data taking quality requirements to the trigger selection, the particle reconstruction, and finally to the Higgs boson candidate selection criteria. A summary of the event selection criteria is given in Table C.1.

Data Quality Requirements

As explained in Section 5.2.1, not all recorded data meets the quality requirements of the ATLAS experiment. For example, events are rejected if a relevant detector component was not properly operating during the time of recording. The minimum requirement for events to be recorded is that the inner detector system finds at least one collision vertex with two or more associated tracks. The transverse momentum p_T of each track is required to be larger than 500 MeV. If more than one collision vertex is found, the primary vertex is defined as the vertex with the largest sum of squared track transverse momenta, $\sum p_T^2$.

$H \to ZZ^* \to 4\ell$ Trigger Selection

In the $H \to ZZ^* \to 4\ell$ analysis, events are selected by a combination of single-lepton, dilepton, and trilepton triggers with different p_T-tresholds. During the Run-2 data-taking period, the thresholds of the single-electron and single-muon triggers have been slightly increased due to an increased peak luminosity. The former was raised from 24 to 26 GeV and the latter from 20 to 26 GeV. The trigger efficiency for the Higgs boson candidates passing the final selection is about 98 %.

Final State Particle Selection

Electrons and muons selected by the lowest threshold single-lepton triggers must satisfy a strict identification and isolation requirement. Both the high-threshold and the lepton triggers have looser

selection criteria. Electrons are required to have a transverse energy of $E_T > 7\,\text{GeV}$, a pseudorapidity of $|\eta| < 2.47$ and a longitudinal impact parameter of $|z_0 \cdot \sin\theta| < 0.5\,\text{mm}$. Their energy is calibrated as described in Reference [443]. Muons are selected if they have a transverse momentum of at least 5 GeV and an inner detector coverage of $|\eta| < 2.47$. In addition, their impact parameters are required to be $|z_0 \cdot \sin\theta| < 0.5\,\text{mm}$ and $|d_0| < 1\,\text{mm}$. This assures that the backgrounds from hadronized bottom quarks and cosmic muons are sufficiently suppressed. If muons are tagged by the calorimeter system, their p_T threshold is raised to 15 GeV to compensate for the lower purity. The muon momentum is calibrated according to Reference [304].

In contrast to previous analyses in this decay channel, jets are reconstructed using the PFlow algorithm [317] from noise-suppressed EMTopo clusters in the calorimeter [297] using the anti-k_T algorithm [308, 444] with a radius parameter $R = 0.4$. In earlier analyses, jets were directly reconstructed from EMTopo clusters [445, 446]. In this case, jets from other pp collisions with $|\eta| < 2.5$ were suppressed by applying a cut on the jet-vertex-tagger (JVT) multivariate discriminant [310, 311]. Jets with $p_T < 60\,\text{GeV}$, $\eta < 2.4$ and JVT < 0.59 have been rejected resulting in a selection efficiency of 92 %. However, for PFlow jets, no appropriate JVT cut has been available when the analysis was finalized. To circumvent this problem, an additional cut on forward jets has been developed, as explained in Section 5.5.

The PFlow algorithm subtracts and replaces the energy of charged particles measured in the calorimeter with the corresponding track measurement. For jets with $30 \lessapprox p_T \lessapprox 100\,\text{GeV}$, the transverse momentum resolution for PFlow jets is about 10 % better than the resolution of EMTopo jets. All jets are required to have $p_T > 30\,\text{GeV}$ and $|\eta| < 4.5$. For b-tagged jets, the MV2c10b-tagging algorithm is used [312, 447], and a pseudo-continuous b-tagging weight [448] is assigned to each jet. This weight combines the 60 %, 70 %, 77 %, and 85 % efficiency working points.

If lepton (electron or muon) or jet candidates overlap and share the same detector information, the ambiguities are resolved with an appropriate overlap removal. Reconstructed jets that are geometrically overlapping in a ΔR-cone of size 0.1 (0.2) with a muon (an electron) are removed. If a reconstructed electron and a muon share the same ID track information, the electron is usually rejected. However, if the muon is obtained from the calorimeter-tagged reconstruction, the muon is removed, and the electron is kept in the event. In case that two electrons are overlapping, the electron with lower E_T is removed.

Lepton Quadruplet Selection

Higgs boson candidates are based on lepton quadruplets with two same-flavor and opposite-charge lepton pairs in the final state. All leptons in the quadruplet are required to originate from a common vertex, and the three leptons with the highest transverse momentum are required to have $p_T > 20\,\text{GeV}$, $p_T > 15\,\text{GeV}$ and $p_T > 10\,\text{GeV}$, respectively. Background contributions from non-prompt muons are reduced by only allowing one calorimeter-tagged or stand-alone muon per quadruplet. Each quadruplet contains a leading and a subleading lepton pair. The leading lepton pair is the one with the invariant mass m_{12} that is closest to the Z boson mass, while the subleading lepton pair corresponds to the off-shell Z boson with invariant mass m_{34}. Quadruplets are classified based on their lepton flavor into 4μ, $2e2\mu$, $2\mu2e$ and $4e$. In this notation, the first two leptons correspond to the leading and the latter two leptons to the subleading leptons pair.

All lepton quadruplets are required to pass the following selection cuts. The leading pair is required to satisfy $50\,\text{GeV} < m_{12} < 106\,\text{GeV}$. The subleading pair is required to have $m_{\text{min}} < m_{34} < 115\,\text{GeV}$. To suppress the contributions from processes with leptonically decaying mesons or virtual photons, the threshold m_{min} is linearly increased from 12 GeV for $m_{4\ell} < 140\,\text{GeV}$ to 50 GeV for $140\,\text{GeV} \leq m_{4\ell} < 190\,\text{GeV}$. For even higher $m_{4\ell}$ the treshold stays at 50 GeV. Leptons from J/ψ decays are reduced by requiring that for the $4e$ and 4μ final states the opposite-charge dilepton mass is $m_{\ell\ell} > 5\,\text{GeV}$. Lepton quadruplets with an angular separation $\Delta(\ell, \ell') < 0.1$ between the leptons $\ell, \ell' = 1, 2, 3, 4$ are rejected.

While leptons from Higgs boson decays are effectively originating from the primary vertex (due to the short lifetime of the Higgs boson), leptons from heavy-flavor hadron decays typically originate from the secondary vertex. Using this distinctive feature, the heavy-flavor background is suppressed by requiring that the transverse impact parameter significance satisfies $|d_0/\sigma(d_0)| < 3$ (5) for muons (electrons). Non-prompt leptons from Z + jets and $t\bar{t}$ processes are further suppressed with track-based and calorimeter-based isolation criteria [296, 304]. The track isolation is defined as the sum of the transverse momenta p_T^i of all tracks i, that originate from the primary vertex or that have $|z_0 \cdot \sin\theta| < 3$ mm and lie within a ΔR-cone of 0.3 around the lepton, divided by the p_T of the lepton (p_T^L), $I_{\text{track}} = 1/p_T^L \sum_i p_T^i$, . For leptons with $p_T > 33$ GeV the cone size is linearly reduced with p_T until $\Delta R = 0.2$ at 50 GeV. The calorimeter isolation I_{calo} is based on the positive-energy topological clusters that are not associated with leptonic tracks in a ΔR-cone of 0.2 around electrons and muons. Leptons are required to have a combined track and calorimeter isolation of $I_{\text{track}} + 0.4 \cdot I_{\text{calo}} < 0.16$. Compared to previous analyses, the signal efficiency is increased by about 5 % to a total efficiency of more than 80 % while keeping the same background rejection.

Higgs Boson Candidate Selection

If an event contains more than one lepton quadruplet with the same final state particles, all satisfying the selection criteria discussed above, the Higgs boson candidate is chosen to be the priority quadruplet. It is defined as the quadruplet with m_{12} closest to the Z boson mass. In case that different final state quadruplets are selected, the Higgs boson candidate is chosen from the final state with the highest selection efficiency. They are ordered as follows 4μ, $2e2\mu$, $2\mu2e$, $4e$.

Higgs bosons produced via VH and ttH production are special because they may contain additional leptons in the final state that do not belong to the lepton quadruplet. In this case, the quadruplet selection is improved by a matrix-element based pairing method for all events with at least one additional final state lepton with $p_T > 12$ GeV[1]. For each possible combination of four final state leptons, the matrix element of the Higgs boson decay is computed at LO with MADGRAPH5_AMC@NLO and the quadruplet with the largest matrix element is chosen to be the Higgs boson candidate.

The four-lepton invariant mass ($m_{4\ell}$) reconstruction is optimized by taking into account energy losses due to final-state radiation (FSR) in Z boson decays. Collinear FSR candidates with $\Delta R < 0.15$ around the nearest lepton in the quadruplet are only considered if the leading lepton pairs consist of muons, while non-collinear candidates are considered for the leading and subleading lepton pairs regardless of the lepton type. The Higgs boson signal region is defined for a mass window of 115 GeV $< m_{4\ell} <$ 130 GeV. The sideband region 130 GeV $< m_{4\ell} <$ 160 GeV is used to estimate the leading order backgrounds discussed in Section 5.1.2.

5.4 Event Categorization

The selected Higgs boson candidates in the signal region are classified into reconstructed event categories shown in the middle-right panel in Figure 5.5. These categories are optimized to accumulate Higgs bosons generated in a specific production mode. The relevant schemes for the binning of the Higgs boson production modes in this thesis are the Stage 0 (left panel) and the Reduced Stage 1.1 (middle-left panel) simplified template cross-sections (STXS). While the former only distinguishes between the main Higgs boson production modes ggF, VBF, VH and ttH, the latter introduces a finer binning based on different kinematic properties and the number of jets in the final state. The categorization of the reconstructed physical objects (middle-right panel) is based on the binning of template cross-sections.

[1] The additional lepton has to fulfill the previously mentioned lepton selection criteria.

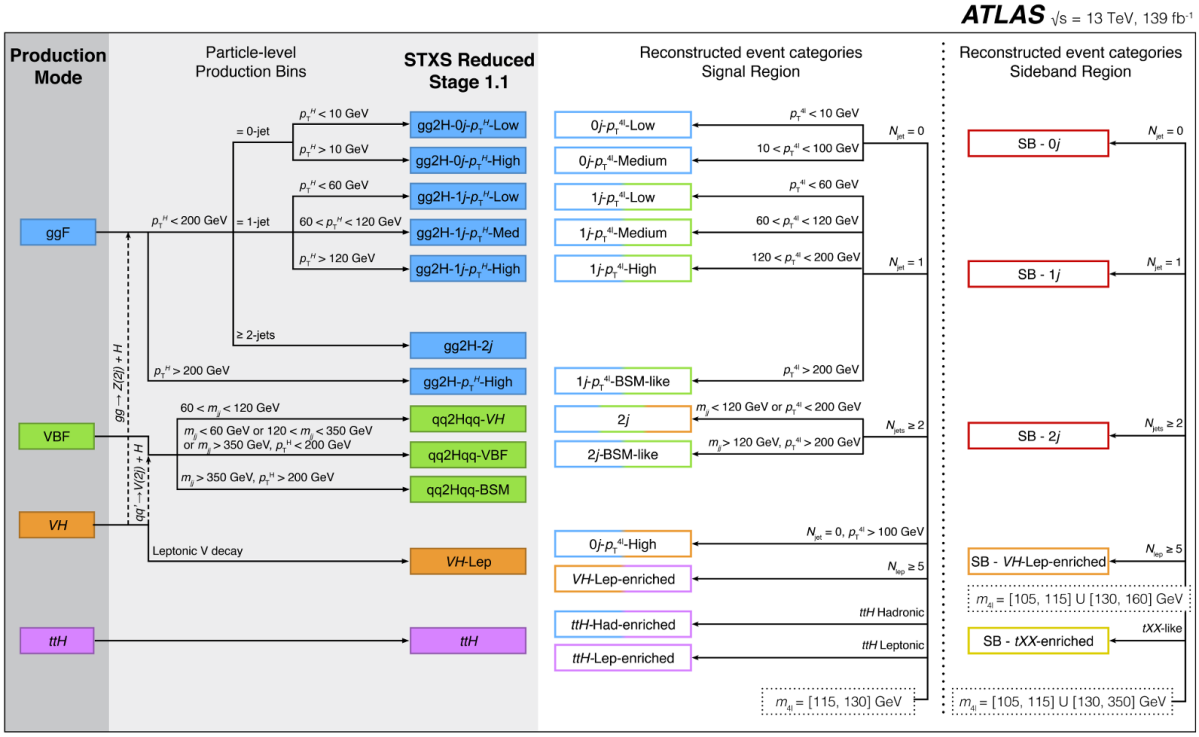

Figure 5.5: The exclusive production bins at particle level for the Stage 0 (left panel) and the Reduced Stage 1.1 (middle-left panels) simplified template cross-section scheme. The reconstructed event categories for the signal and sidebands regions are displayed in the middle-right and the right panel, respectively. Taken from Reference [359].

However, since the distinction between different production processes is not perfect, there is a large overlap between different signal and background processes in each reconstructed event category. The different reconstructed event categories are discussed in the following.

Events that are classified as enriched in ttH are classified first. The top quark predominantly decays into a W boson and a bottom quark. Thus, at least one b-tagged jet is required in the final state. If the W boson decays fully hadronically, the event will be collected in the *ttH-Had-enriched* category. However, if at least one W boson decays leptonically, the event will be added to the *ttH-Lep-enriched* category. The VH-Lep-enriched category is defined by events that feature one additional lepton in the final state. The hadronic VH categories accumulate events that are characteristic of VBF and VH-Had associated production. Events with two or more reconstructed jets are divided based on the dijet invariant mass m_{jj}. If $m_{jj} > 120\,\text{GeV}$ and $p_T^{4\ell} > 200\,\text{GeV}$ they will be classified as BSM-like ($2j$-*BSM-like*). Otherwise, they are collected in the $2j$ bin. On the other hand, if events do not contain any jets or just one jet, they are expected to be mostly ggF. In both cases, the events are divided based on the four-lepton invariant mass. The 1-jet events are collected in $1j$-$p_T^{4\ell}$-*Low* if $p_T^{4\ell} > 60\,\text{GeV}$, $1j$-$p_T^{4\ell}$-*Medium* if $60 < p_T^{4\ell} < 120\,\text{GeV}$, $1j$-$p_T^{4\ell}$-*High* if $120 < p_T^{4\ell} < 200\,\text{GeV}$, and $1j$-$p_T^{4\ell}$-*BSM* if $p_T^{4\ell} > 200\,\text{GeV}$. The 0-jet events are collected in $0j$-$p_T^{4\ell}$-*Low* if $p_T^{4\ell} < 10\,\text{GeV}$, and $0j$-$p_T^{4\ell}$-*Medium* if $p_T^{4\ell} > 60\,\text{GeV}$.

The side-band categories comprise the mass windows of $105\,\text{GeV} < m_{4\ell} < 115\,\text{GeV}$ and $130\,\text{GeV} < m_{4\ell} < 350\,\text{GeV}$ and they are used to estimate the background contributions. Events in the former mass window are split according to the number of jets into SB-$0j$, SB-$1j$, and SB-$2j$. Sideband events with two or more final state jets, including at least one tagged as a b-jet with 60 % and $E_T^{\text{miss}} > 100\,\text{GeV}$ are assigned to the SB-tXX-enriched category. For the remaining events, the upper limit of the upper mass window is reduced to 160 GeV. If a remaining sideband event contains an additional lepton, it is collected

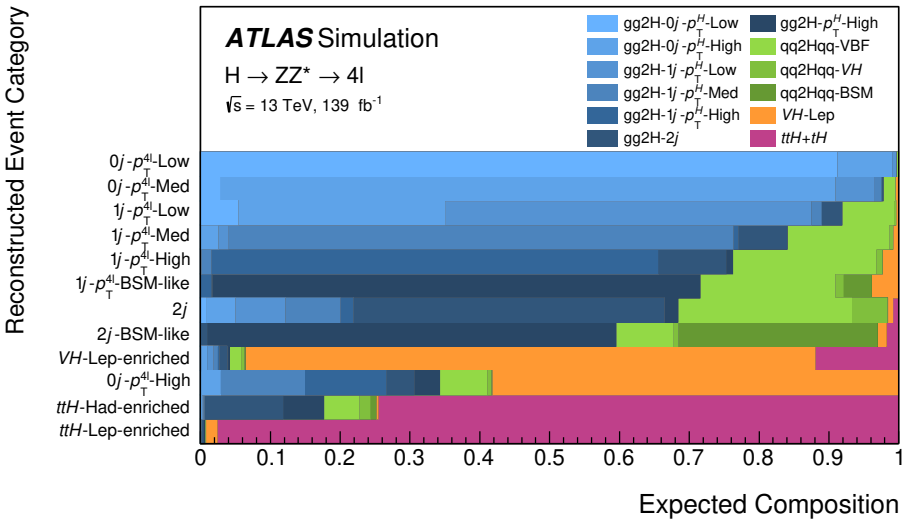

Figure 5.6: The SM expected signal composition of each reconstructed event category given in terms of the Reduced Stage-1.1 particle level production bins. The contributions from $b\bar{b}H$ production is included in the ggF production bins. Taken from Reference [359].

in the SB-VH-Lep-enriched category.

The expected SM signal composition is shown in Figure 5.6 for each reconstructed event category. While some categories are very pure in their production process, like 0j-p_T^H-Low or ttH-Lep-enriched, others are highly contaminated.

To improve the discrimination between different Higgs boson production modes and background processes, neural network (NN) discriminants are employed. They are trained on simulated SM Higgs boson signal and background samples in each reconstructed event category using several discriminating input variables. Details about the training can be found in Reference [359]. The NN discriminants improve the measurement sensitivity by up to 20 % compared to previous approaches that have been based on boosted decision trees.

5.5 Performance Studies for PFlow Jets

This section summarizes the comparison studies between the PFlow and the EMTopo jet collections in the $H \to ZZ^* \to 4\ell$ decay channel at ATLAS. The comparisons are performed for a variety of differential variables using response matrix unfolding and the extended 105 – 160 GeV mass window with floating ZZ normalization.

Figure 5.7(a) shows the ratio of response matrices for the number of correctly reconstructed jets (N_{jets}) derived from simulated datasets with EMTopo jets divided by the corresponding response matrices derived with PFlow jets. While the number of correctly reconstructed events without final state jets is slightly larger for the EMTopo jet collection, the PFlow algorithm performs better for events that contain jets in the final state, i. e. if $N_{\text{jets}} \geq 1$. The Asimov data and the corresponding fit result for the PFlow jet collection, binned in different N_{jets} categories, is shown in Figure 5.7(b). Since the fit results for the EMTopo jet collection (not shown) cannot be distinguished from the PFlow result by eye, the simulated (injected) cross-sections, σ_{inj}, as well as the fit results for both jet collections (excluding reducible background), are compared in Table 5.3. The fit results are very similar and the best-fit values reproduce the injected cross-section in both cases. However, the statistical error is slightly worse in the $N_{\text{jets}} \geq 3$ bin, with the

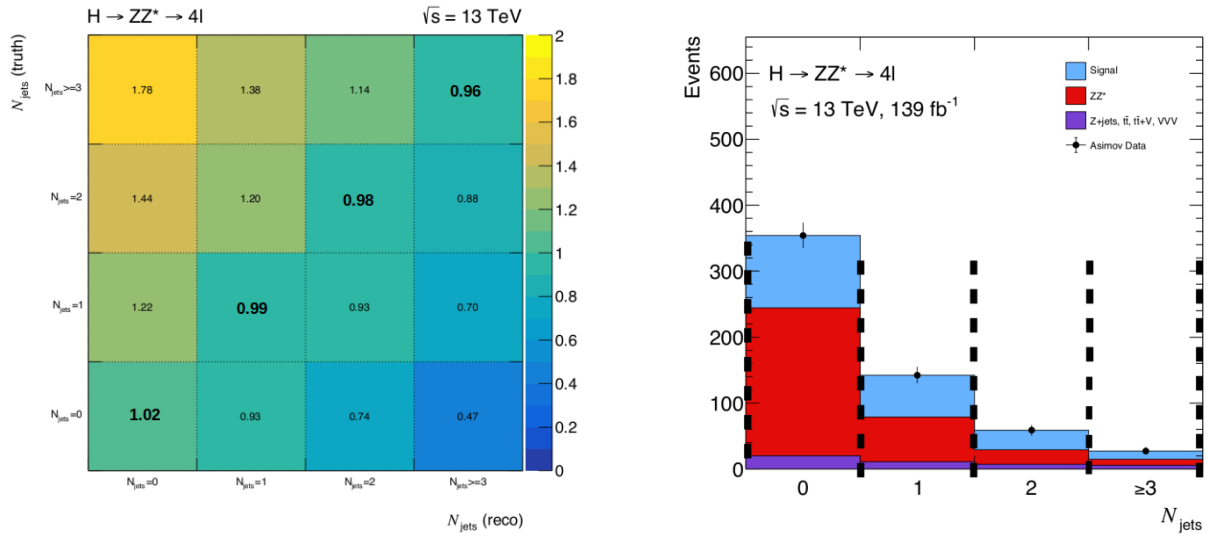

(a) (b)

Figure 5.7: (a) The N_{jets} ratio of response matrices for EMTopo jets derived using simulated datasets divided by the corresponding matrices for PFlow jets and (b) the Asimov results for the N_{jets} distribution for the PFlow dataset. The corresponding result for the EMTopo dataset is very similar (see text), and thus not shown.

Table 5.3: Comparison of Asimov results for N_{jets} using response matrix unfolding for MC datasets using EMTopo and PFlow jets. Only statistical errors are considered.

POI	σ_{inj}	EMTopo		PFlow	
		σ_{fit} [fb]	rel. error	σ_{fit} [fb]	rel. error
$\sigma(N_{\text{jets}} = 0)$	1.86	$1.86^{+0.269}_{-0.256}$	$^{+14.5\%}_{-13.8\%}$	$1.86^{+0.269}_{-0.255}$	$^{+14.5\%}_{-13.8\%}$
$\sigma(N_{\text{jets}} = 1)$	0.951	$0.951^{+0.226}_{-0.212}$	$^{+23.7\%}_{-22.3\%}$	$0.951^{+0.225}_{-0.211}$	$^{+23.6\%}_{-22.2\%}$
$\sigma(N_{\text{jets}} = 2)$	0.431	$0.431^{+0.160}_{-0.145}$	$^{+37.1\%}_{-56.1\%}$	$0.431^{+0.159}_{-0.145}$	$^{+36.9\%}_{-33.6\%}$
$\sigma(N_{\text{jets}} \geq 3)$	0.173	$0.173^{+0.097}_{-0.083}$	$^{+56.1\%}_{-47.8\%}$	$0.173^{+0.098}_{-0.085}$	$^{+56.8\%}_{-49.0\%}$

Table 5.4: Proportion of hard scatter (HS), pile-up (PU), and out-of-time (NA) jets.

	All Jets		Forward jets ($p_T < 60$ GeV)		All forward jets	
Mode	ggH	VBF	ggH	VBF	ggH	VBF
% HS	85.97	93.81	56.91	53.35	64.48	89.98
% PU	11.24	4.97	37.93	41.04	31.27	31.27
% NA	2.79	1.22	5.15	5.60	4.25	1.47

move to PFlow. This is related to the lack of the forward JVT cut, which at the time was not available for PFlow jets.

The same comparison is also performed for the number of b-jets, the jet transverse momentum, and various dijet variables, yielding similar results. The corresponding plots are shown in Figures C.1 and C.2, while the injected and fitted binned cross-sections are summarized in Table C.2. The largest differences between the jet collections are observed for the number of reconstructed jets and the jet transverse momentum. In general, the diagonal efficiency of response matrices for PFlow jets is slightly better than for EMTopo jets. The PFlow-based reconstruction excels in particular in the central detector region, where $|\eta| < 2.5$. The corresponding improvements are about $2-3\,\%$ as shown in Figure C.3 for the $ggH + bbH$, VBF, and VH production modes.

In contrast to the jet variables, the performance for the Higgs boson-related variables are almost identical between the two jet collections (see Figure C.5). This is expected since they are not derived using jets. The small differences seen are attributed to changes in the overlap removal between leptons and jets.

For the differential cross-section measurements, the jet variables suffer from large bin migrations. For instance, the off-diagonal elements of the N_{jets} migration matrix are as high as 20%. Jet multiplicity is difficult to model due to the presence of pileup jets. In high pileup environments, a buildup of jets at high pseudorapidity is seen, and the jet multiplicity increases. A JVT was introduced in earlier analyses with EMTopo jets, which mitigated these effects to some extend. However, by introducing further cuts in the forward region, it may be possible to see further improvements. Two additional cuts beyond JVT are investigated:

1. Forward transverse momentum cut (fpT): An additional cut on the p_T of forward region jets, where for all jets at $|\eta| > 2.5$, the p_T cut is increased to $p_{Tj} > 60$ GeV.

2. Removal of entire forward region (fη): all jets with $|\eta_j| > 2.5$ are not considered.

The standard jet selection, including the JVT cut, is considered the nominal case for this study. Figure C.7 shows the p_T distribution of truth-matched jets which pass or fail the JVT cut. Even with the JVT cut applied, some pileup jets remain.

The $|\eta_j|$ and N_{jets} distributions for ggH and VBF MC samples for the three scenarios are shown in Figure C.8. The impact at high η for each of the cuts can be clearly seen. The $|\eta_j| < 2.5$ cut results in the lowest jet multiplicity for the N_{jets} distribution. The proportion of hard scatter vs. pileup jets for the various cuts is summarized in Table 5.4. Forward jets with $p_T < 60$ GeV have the highest proportion of pileup jets, suggesting that an additional p_T cut on forwarding jets could be beneficial.

To test the three scenarios (nominal, fpT, and fη), unfolding of the ggH sample is performed using both the response matrix calculated using the corresponding ggH sample itself and using the VBF response matrix. If model dependence has been minimized, both response matrices (which should reflect the detector itself) should give similar results. Figure 5.8 shows the differences between the ggH sample unfolded with the ggH response matrix and the ggH sample unfolded with the VBF response matrix.

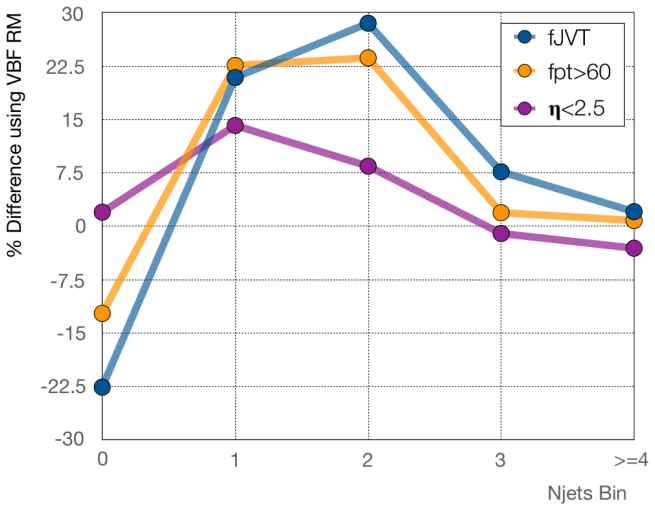

Figure 5.8: Differences in the unfolding of the ggH sample using the response matrix derived from the ggH sample itself versus the response matrix unfolded from the VBF sample.

As can be seen, an additional forward p_T cut on the jets does not show significant improvement, while removing all forward jets minimizes the differences to under 15 %. However, when comparing the response matrices themselves, the fpT cut does improve bin migrations.

Since removing all forward jets would result in the loss of the VBF signal, the fpT cut is chosen. Figure C.9 summarizes the migration matrices of the various jet variables in the restricted jet phase space (i. e. with the fpT cut applied) compared to the nominal jet selection.

The impact on the expected statistic-only uncertainty on the Stage 0 and Reduced Stage 1.1 parameters of interest (POI) when changing the EMTopo to the PFlow jet collections is very small, as shown in Figure C.6. The largest differences are found in the VH-Had and sideband bins with relative differences of about 2 – 5 %. In most other bins, the differences are below 1 %.

5.6 Systematic Uncertainties

Systematic uncertainties result from limited knowledge about the theoretical modeling of the physical processes and the experimental setup. The former group includes uncertainties from the choice of the renormalization and factorization scales (QCD scale), the PDF, the parton showering, and the migration between different particle-level bins. The latter group consists of uncertainties from the particle reconstruction, identification and isolation, the energy scale and resolution, the total integrated luminosity, and the methods to derive data-driven background estimates. The individual uncertainties are summarized in Table 5.5 and shortly explained in the following sections.

5.6.1 Experimental Uncertainties

The uncertainty in the integrated luminosity affects the normalization of simulated signal and background events resulting in uncertainties of the measured cross-sections. For the combined 2015-2018 data, the corresponding cross-section uncertainty is 1.7 % [271]. The uncertainty of the pile-up modeling ranges from 1 % to 2 % [449]. The muons (electron) reconstruction and identification uncertainties are 1 % (1 % - 2 %) and the uncertainties on the lepton momentum scale and resolution are below 1 %.

Table 5.5: The impact of the dominant (left) experimental and (right) theoretical systematic uncertainties on the cross-section measurement in the (upper half) Stage 0 and (lower half) Reduced Stage 1.1 particle level production bins. The uncertainties from similar sources are grouped together and they are rounded to the nearest 0.5 % (except for the luminosity uncertainty).

	Experimental uncertainties [%]				Theory uncertainties [%]				
Measurement	lumi.	e, μ,	jets,	reducible	background		signal		
		pile-up	flav. tag	background	ZZ^*	tXX	PDF	QCD	Shower
Stage 0 production cross-sections									
ggF	1.7	2.5	1	≤ 0.5	1.5	≤ 0.5	0.5	1	2
VBF	1.7	2	4	≤ 0.5	1.5	≤ 0.5	1	5	7
VH	1.9	2	4	1	6	≤ 0.5	2	13.5	7.5
ttH	1.7	2	6	≤ 0.5	1	0.5	0.5	12.5	4
Reduced Stage 1.1 production cross-sections									
gg2H-0j-p_T^H-Low	1.7	3	1.5	0.5	6.5	≤ 0.5	≤ 0.5	1	1.5
gg2H-0j-p_T^H-High	1.7	3	5	≤ 0.5	3	≤ 0.5	≤ 0.5	0.5	5.5
gg2H-1j-p_T^H-Low	1.7	2.5	12	0.5	7	≤ 0.5	≤ 0.5	1	6
gg2H-1j-p_T^H-Med	1.7	3	7.5	≤ 0.5	1	≤ 0.5	≤ 0.5	1.5	5.5
gg2H-1j-p_T^H-High	1.7	3	11	0.5	2	≤ 0.5	≤ 0.5	2	7.5
gg2H-2j	1.7	2.5	16.5	1	12.5	0.5	≤ 0.5	2.5	10.5
gg2H-p_T^H-High	1.7	1.5	3	0.5	3.5	≤ 0.5	≤ 0.5	2	3.5
qq2Hqq-VH	1.8	4	17	1	4	1	0.5	5.5	8
qq2Hqq-VBF	1.7	2	3.5	≤ 0.5	5	≤ 0.5	≤ 0.5	6	10.5
qq2Hqq-BSM	1.7	2	4	≤ 0.5	2.5	≤ 0.5	≤ 0.5	3	8
VH-Lep	1.8	2.5	2	1	2	0.5	≤ 0.5	1.5	3
ttH	1.7	2.5	5	0.5	1	0.5	≤ 0.5	11	3

The uncertainties in the jet energy scale and resolution are relevant for the predicted event yields in the VH, VBF, and ttH production modes (about 3 % - 5 %), and the Reduced Stage-1.1 cross-section measurements (about 5 % - 20 %). The expected impact of the uncertainty in the calibration of the b-tagging algorithm is about 1 %.

The data-driven measurements of the reducible background are affected by the following uncertainties. The first one is the uncertainty from the extrapolation of the statistical fit in the control region to the inclusive background estimate. The second one is the systematic uncertainty from the transfer factor extrapolation from the control to the signal region. Both are about 3 %. The third and largest one is uncorrelated uncertainties from the fraction of the reducible background in the various event categories. They vary between 8 % and 70 %.

5.6.2 Theoretical Uncertainties

The impact of the theoretical uncertainties depends on the kind of measurement that is performed. For example, signal strength measurements ($\mu = \sigma/\sigma_{\mathrm{SM}}$) are more theory dependent than direct cross-section measurements (σ). In case of the former, the uncertainties affect both the acceptance and the SM prediction for the cross-section (σ_{SM}), while in the case of the latter, only the effects on the acceptance are relevant.

One of the largest theoretical uncertainty results from missing higher-order QCD terms in the

prediction of the ggF process in the different N_{jets} categories. The ggF production processes provide large contributions to the reconstructed event categories that contain at least one reconstructed jet (see Figure 5.6). The uncertainty from the choice of the factorization and renormalization scales, μ_F and μ_R, and the migrations between different jet multiplicities are taken into account [450–452]. QCD scale variations on p_T^H and higher-order corrections originating from the assumption of infinite top quark mass in the loops are considered. The former is derived from a ggF Powheg sample generated with NNLOPS, and the latter is taken into account by comparing the predictions with finite-mass calculations. Additional uncertainty is assigned to the acceptance of the ggF process in the VBF and VH-Had-enriched categories, accounting for missing higher-order predictions in QCD.

For the VBF, VH and ttH production modes, the uncertainties from missing higher-order predictions in QCD are evaluated by varying μ_F and μ_R by a factor of two compared to the nominal choice. The configuration with the largest impact is chosen to define the corresponding uncertainty. The QCD scale uncertainty in VBF is about 5 %, in VH it is 13.5 % and in ttH 12.5 %.

The calculated properties of pp collisions like kinematic distributions and production cross-sections depend on the choice of the PDF set. The impact of the PDF uncertainty is estimated by eigenvector variations of the PDF4LHC_NLO_30 PDF set following the recommendations given in Reference [371]. The PDF4LHC_NLO_30 PDF set contains 30 eigenvector variations, and the corresponding uncertainties of each variation are propagated as a separate source of uncertainty in the model. Since this procedure is used for all Higgs boson production processes, the correlations between the various production modes can be taken into account. The PDF uncertainty in the Stage 0 production bins ggF and ttH are 0.5 %, in VBF 1 % and in VH 2 %.

The impact of parton shower uncertainties is estimated with AZNLO eigenvector variations using the automated shower variations in PYTHIA 8 and HERWIG 7 [453] for all signal processes. Correlations between the AZNLO tune variations for the different production bins are considered. The parton shower uncertainties in the ggF, VBF, VH and ttH productions modes are 2 %, 7 %, 7.5 % and 4 %, respectively.

5.7 Statistical Treatment

The product $\sigma \cdot \text{BR}(H \to ZZ^* \to 4\ell)$ is measured for the Stage 0 and the Reduced Stage 1.1 schemes of the STXS framework. This is done by performing a binned maximum-likelihood fit to the discriminating observables using the likelihood function $\mathcal{L}(\boldsymbol{\sigma}, \boldsymbol{\theta})$. This function depends on the various particle-level production cross-sections $\boldsymbol{\sigma} = \{\sigma_1, \sigma_2, ..., \sigma_N\}$, which are treated as independent variables and the set of nuisance parameters $\boldsymbol{\theta}$ that accounts for the systematic uncertainties. $\mathcal{L}(\boldsymbol{\sigma}, \boldsymbol{\theta})$ is formed from Poisson distributions $P(N_{i,j}|S_{i,j}(\boldsymbol{\sigma}, \boldsymbol{\theta}) + B_{i,j}(\boldsymbol{\sigma}, \boldsymbol{\theta}))$ of the number of observed events $N_{i,j}$ in each bin i of the discriminant observable in a specific reconstructed signal or sideband event category j given the expectations for each signal $S_{i,j}(\boldsymbol{\sigma}, \boldsymbol{\theta}) = L \cdot \boldsymbol{\sigma} \cdot \text{BR} \cdot \mathcal{A}_{i,j}(\boldsymbol{\theta})$ and background process $B_{i,j}(\boldsymbol{\theta})$. The signal acceptance $\mathcal{A}_{i,j}^p = a^p \cdot \epsilon_{i,j}^p$ is defined as the product of the acceptance a^p in the fiducial region of the particle-level production bin p and the reconstruction efficiency $\epsilon_{i,j}^p$ of the particle-level events.

The likelihood function is given by

$$\mathcal{L}(\boldsymbol{\sigma}, \boldsymbol{\theta}) = \prod_j^{N_{\text{categories}}} \prod_i^{N_{\text{bins}}} P\left(N_{i,j}|L \cdot \boldsymbol{\sigma} \cdot \text{BR} \cdot \mathcal{A}_{i,j}(\boldsymbol{\theta}) + B_{i,j}(\boldsymbol{\theta})\right) \times \prod_m^{N_{\text{nuisance}}} C_m(\boldsymbol{\theta}), \tag{5.1}$$

where $C_m(\theta)$ represents the constraints on the nuisance parameters corresponding to the systematic

uncertainties. The test statistic q used for the measurement is the profile likelihood ratio [454],

$$q(\boldsymbol{\sigma}) = -2\ln\frac{\mathcal{L}(\boldsymbol{\sigma}, \hat{\hat{\boldsymbol{\theta}}}(\boldsymbol{\sigma}))}{\mathcal{L}(\hat{\boldsymbol{\sigma}}, \hat{\boldsymbol{\theta}}(\boldsymbol{\sigma}))} = -2\ln(\lambda)\,. \tag{5.2}$$

$\mathcal{L}(\boldsymbol{\sigma}, \hat{\hat{\boldsymbol{\theta}}}(\boldsymbol{\sigma}))$ is the estimator of a conditional fit in which the parameters of interest (POI) $\boldsymbol{\sigma}$ are fixed to a given value, while the remaining parameters are free in the fit. The double-hat symbol above the nuisance parameters indicate that the corresponding values $\hat{\hat{\boldsymbol{\theta}}}$ maximize the likelihood if the POIs are held constant in the fit. On the other hand, $\mathcal{L}(\hat{\boldsymbol{\sigma}}, \hat{\boldsymbol{\theta}}(\boldsymbol{\sigma}))$ is the estimator of an unconditional fit in which all parameters ($\boldsymbol{\sigma}$ and $\boldsymbol{\theta}$) are free-floating. The hat symbol above the parameters indicates that these are unconditional maximum likelihood estimators.

Large values of q indicate that the tested hypothesis is disfavoured compared to the best-fit hypothesis. In an alternative fit, the POIs are replaced by $\mu \cdot \sigma_{\mathrm{SM}}(\boldsymbol{\theta})$ which allows for an interpretation in terms of the signal strength μ which scales the cross-section prediction $\sigma_{\mathrm{SM}}(\boldsymbol{\theta})$ in the SM.

5.8 Results

The inclusive $H \to ZZ^*$ production cross-section for $|y_H| < 2.5$ is measured under the assumption that the relative signal fractions in the various production bins are given by the SM prediction. It is measured to be

$$\sigma \cdot B \equiv \sigma \cdot \mathrm{BR}(H \to ZZ^*) = 1.34 \pm 0.11(\mathrm{stat.}) \pm 0.04(\mathrm{exp.}) \pm 0.04(\mathrm{th.})\,\mathrm{pb} = 1.34 \pm 0.12\,\mathrm{pb}.$$

The statistical (stat.) uncertainty is the dominant contribution to the overall uncertainty. The experimental (exp.) and theoretical (th.) systematic uncertainties are much smaller.

The measurement is in good agreement with the SM prediction: $(\sigma \cdot B)_{\mathrm{SM}} = 1.33 \pm 0.08\,\mathrm{pb}$. The interpretation of the data in terms of the global signal strength μ yields:

$$\mu = 1.01 \pm 0.08(\mathrm{stat.}) \pm 0.04(\mathrm{exp.}) \pm 0.05(\mathrm{th.}) = 1.01 \pm 0.11\,.$$

The p-values of the best-fit points for both compatibility tests are 98.6 %. The likelihood scans are shown in Figure C.10.

The expected SM cross-sections, the observed values of $\sigma \cdot B$, and their ratio for the inclusive production and in each Stage 0 production bin are shown in Figure 5.9(a). The correlations between the production mode bins and the ZZ and tXX normalization factors are summarized in Figure 5.9(b). Since the measurements agree well with the SM prediction, the p-value of the compatibility test is very high with 91 %.

The results for the Reduced Stage 1.1 measurements are shown in Figure 5.9(c), and the corresponding correlations are summarized in Figure 5.9(d). The p-value of the best-fit point is 77 % in this case.

The dominant contribution to the systematic uncertainty in the ggF Stage 0 bin originates from the experimental uncertainty in the lepton efficiency and the integrated luminosity measurements and from theoretical uncertainties related to the parton shower modeling, which affects the acceptance. For the VBF production bin, the dominant systematic uncertainties are related to the jet energy scale and resolution and parton showering modeling. The VBF, VH, and ttH productions bins are also affected by the theoretical uncertainties related to the modeling of the ggF process. The dominant uncertainty contributions in the Reduced Stage-1.1 bins are from the jet energy scale and resolution and parton shower uncertainties.

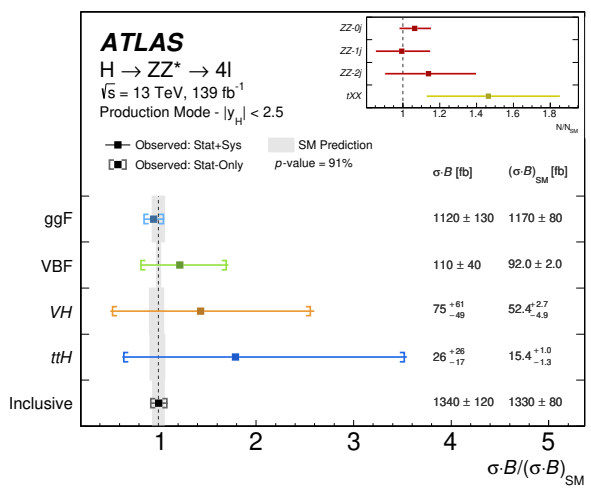

(a)

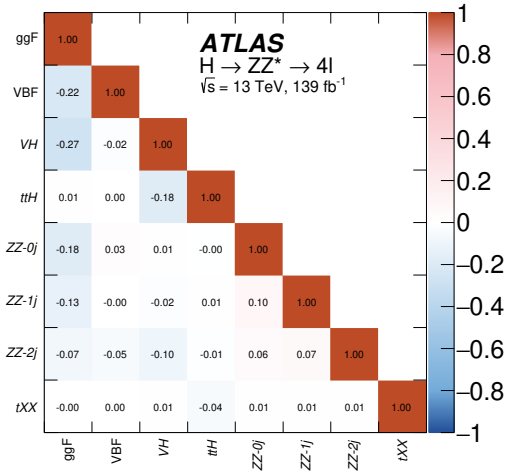

(b)

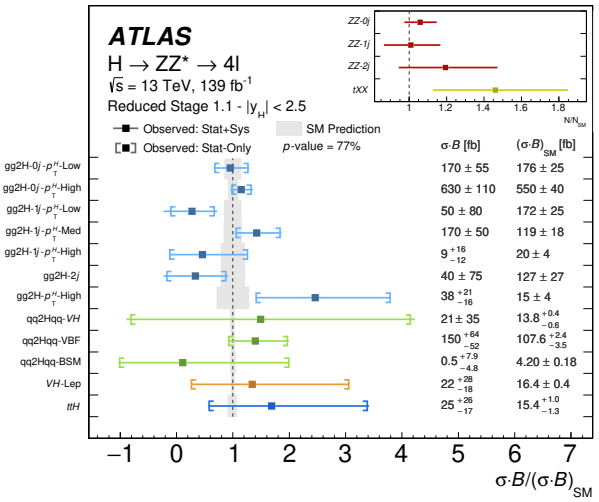

(c)

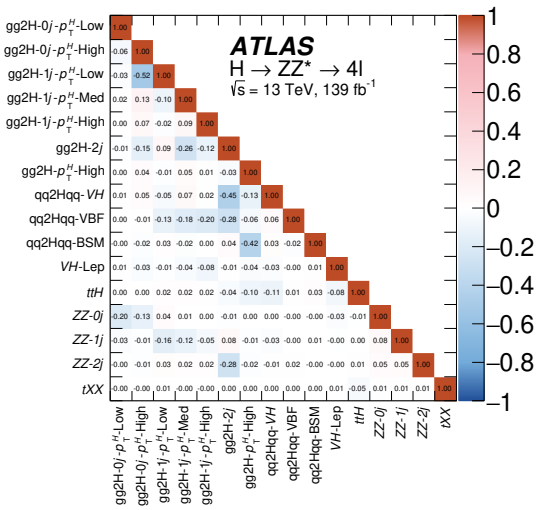

(d)

Figure 5.9: The observed and SM expected values of the cross-sections, $\sigma \cdot \mathrm{BR}$, normalized to the SM prediction, $(\sigma \cdot \mathrm{BR})_{\mathrm{SM}}$, in the $H \to ZZ^* \to 4\ell$ decay channel for (a) the inclusive production and the Stage 0 particle-level bins, and (c) the Reduced Stage 1.1 production modes for an integrated luminosity of 139 fb^{-1} at $\sqrt{s} = 13$ TeV. The fitted normalization factors for the ZZ and ttX backgrounds are shown in the insert. Different colors indicate the different production modes (and background sources). The gray vertical band represents the theory uncertainty in the signal prediction. The correlation matrices for the (c) Stage 0 and (d) Reduced Stage 1.1 STXS schemes include the correlations between the measured cross-sections and the background normalization factors.

CHAPTER 6

EFT Interpretation in the $H \to ZZ^* \to 4\ell$ Decay Channel at ATLAS

In this chapter, the effective field theory (EFT) interpretation in the $H \to ZZ^* \to 4\ell$ decay channel at ATLAS is presented. It is performed in the $U(3)^5$ limit of the SMEFT (see Section 2.4.2.1) and takes into account the dimension-six operators that are sensitive to Higgs boson production and decay vertices in the $H \to 4\ell$ decay channel. The relevant $C\mathcal{P}$-even and $C\mathcal{P}$-odd operators describing the new physics contributions to the Higgs boson couplings to Z bosons, W bosons, gluons, and top quarks are

$$\begin{aligned} &O_{HW},\ O_{HB},\ O_{HWB},\ O_{HG},\ O_{uH} && (C\mathcal{P}\text{-even}),\\ &O_{H\widetilde{W}},\ O_{H\widetilde{B}},\ O_{H\widetilde{W}B},\ O_{H\widetilde{G}},\ O_{\widetilde{u}H} && (C\mathcal{P}\text{-odd}). \end{aligned}$$

The strength of each dimension-six operator O_i is characterized by the respective BSM coupling parameter $c_i = {}^{C_i}/_{\Lambda^2}$, where C_i is the operator's Wilson coefficient and Λ is the energy scale of new physics. The coupling modifiers for the above given operators are the following:

$$\begin{aligned} &c_{HW},\ c_{HB},\ c_{HWB},\ c_{HG},\ c_{uH} && (C\mathcal{P}\text{-even})\\ &c_{H\widetilde{W}},\ c_{H\widetilde{B}},\ c_{H\widetilde{W}B},\ c_{H\widetilde{G}},\ c_{\widetilde{u}H} && (C\mathcal{P}\text{-odd}) \end{aligned}$$

The EFT interpretation is based on the Reduced Stage 1.1 Higgs boson cross-section measurement (see Section 5) obtained with the full Run-2 data set with an integrated luminosity of 139 fb^{-1}. The cross-section in each STXS production bin is parameterized as a function of the BSM coupling parameters. This is achieved by individually parameterizing the production and decay processes of the Higgs boson as described in Section 6.1 and Section 6.2, respectively. Some of the observables that are used to select the Higgs boson candidates depend on the BSM coupling parameters. Therefore, an appropriate correction of the signal acceptance is performed. This acceptance correction is presented in Section 6.3. In Section 6.4, the intermediate parameterizations are combined, and various validation studies of the full EFT signal model are presented in Section 6.5. It is assumed that the reconstruction efficiencies ϵ_j for the reconstructed event categories j are independent of the BSM contributions. This assumption does not hold generally, but it is valid for the $H \to ZZ^* \to 4\ell$ decay channel as demonstrated in Section 6.5.3. Hence, it is justified to perform the EFT interpretation at particle level instead of reconstruction level, which avoids the need for fully simulating the detector response for the BSM signal samples. The systematic uncertainties and the statistical model are discussed in Sections 6.6 and 6.7, respectively. Section 6.8 presents the measurement of the BSM coupling modifiers in the $H \to ZZ^* \to 4\ell$ decay channel.

The cross-section is proportional to the square of the matrix element of the underlying process. It contains linear (effective dimension six) terms describing the SM-BSM interference and quadratic (effective dimension eight) terms accounting for the pure BSM contributions. The former are suppressed

by $1/\Lambda^2$ and the latter by $1/\Lambda^4$. Thus, the pure BSM terms are expected to be much smaller than the linear terms. If the BSM coupling parameters are small enough, a linear approximation typically holds for the $C\mathcal{P}$-even operators. However, in the $H \to ZZ^* \to 4\ell$ decay channel, there is not enough sensitivity in the VBF+VH-Had, VH-Lep, and $ttH + tH$ production modes for the linear approximation to be valid. The comparison between the expected limits using linear terms only and linear + quadratic terms reveal differences in sensitivity of up to a factor of 10. Thus, the quadratic terms are also taken into account. In contrast to the $C\mathcal{P}$-even operators, there are no linear terms for the $C\mathcal{P}$-odd ones as will be explained. Therefore, their contributions are solely described by the quadratic terms. The leading order terms of dimension eight operators are suppressed by $1/\Lambda^4$ and expected to be of similar size as the quadratic dimension-six terms. However, the SMEFT simulation package does not currently support operators above mass dimension six. Thus, they are not included in the presented interpretation.

At the current stage, the analysis is only expected to be sensitive to the BSM coupling parameters given above. Thus, no other BSM operators are probed. Also, for some of the other BSM parameters, constraints have already been set using the LEP and LHC data [455], and therefore, they are not taken into account. The parameterization of the signal model is divided into two main categories. The first set is restricted to operators with $C\mathcal{P}$-even symmetry and the second set to operators with $C\mathcal{P}$-odd symmetry. This split is motivated by the fact that leading order effects of interfering a $C\mathcal{P}$-even with a $C\mathcal{P}$-odd amplitude is expected to vanish[1] [456]. However, this is not a general statement and it only applies if the integration is performed over all phase space. The interference effect becomes apparent by applying more stringent cuts or by looking at specific kinematic distributions. This also serves as a motivation to probe the Higgs $C\mathcal{P}$ invariance using appropriately constructed $C\mathcal{P}$-odd observables [457, 458]. A third set of samples is generated to ensure that the interference effects between the scalar and pseudoscalar operators vanish for the studied phase space. These samples include both the $C\mathcal{P}$-even and $C\mathcal{P}$-odd operators.

The Higgs boson acceptance is modeled as a three-dimensional Lorentzian with 13 free parameters including the relevant BSM couplings that contribute to the $H \to ZZ^*$ decay vertex. Compared to a one-dimensional approach, this can lead to differences of up to 10 % for some of the BSM parameters. The acceptance is individually parameterized for $C\mathcal{P}$-even and $C\mathcal{P}$-odd operators. The size of the interference effects between the scalar and pseudoscalar operators in the signal acceptance is studied in Section 6.3.2.

This thesis focuses on the derivation, implementation, and evaluation of the parameterization for the $C\mathcal{P}$-odd BSM coupling parameters. The corresponding parameterization for the $C\mathcal{P}$-even operators has been developed by Verena Maria Walbrecht and can be found in [459]. However, a subset of the $C\mathcal{P}$-even samples has been reproduced to guarantee consistency between both parameterizations and for the evaluation of the interference effects between the scalar and pseudoscalar amplitudes (see Section 6.3.2) and the production-mode dependency of signal acceptance (see Section 6.5.1).

For the EFT interpretation, the Reduced-Stage-1.1 scheme of the STXS framework is used (middle-left panel in Figure 5.5). In this scheme, the VBF and VH-Had particle-level production bins are merged into the qq2Hqq bin due to large interference effects, which appear by turning on the BSM couplings.

6.1 Parameterization of the Higgs Boson Production Cross-Section

In this Section, the parameterization of the Higgs boson production cross-section in terms of the BSM coupling parameters c_i is discussed. To that end, the SMEFT Lagrangian is decomposed into its SM

[1] In contrast a squared dimension-six operator ($1/\Lambda^4$ dependence) produces a $C\mathcal{P}$-even effect regardless of the nature of the operator. Thus, its interference with a scalar amplitude would lead to non-vanishing contributions to the inclusive rate.

contribution, $\mathcal{L}_{\text{SM}}$, and the contributions from the dimension-six operators, $O_i^{(6)}$,

$$\mathcal{L}_{\text{SMEFT}} = \mathcal{L}_{\text{SM}} + \sum_i c_i O_i^{(6)} \,. \tag{6.1}$$

From Equation 6.1 follows directly that the matrix element for some process can be expressed as the sum of a SM and a BSM component

$$\mathcal{M} = \mathcal{M}_{\text{SM}} + \mathcal{M}_{\text{BSM}} = \mathcal{M}_{\text{SM}} + \sum_i c_i \mathcal{M}_i \,. \tag{6.2}$$

The sum runs over all matrix elements $\mathcal{M}_i$ generated by the operators $O_i^{(6)}$. In general, the cross-section is proportional to the square of the matrix element of the underlying process,

$$\begin{aligned} \sigma \propto |\mathcal{M}|^2 &= \left|\mathcal{M}_{\text{SM}}\right|^2 + \sum_i \left(c_i \mathcal{M}_{\text{SM}}^* \mathcal{M} + c_i^* \mathcal{M}_{\text{SM}} \mathcal{M}_i^*\right) + \sum_{i,j} \left(c_i^* c_j \mathcal{M}_i^* \mathcal{M}_j + c_i c_j^* \mathcal{M}_i \mathcal{M}_j^*\right) \\ &= \left|\mathcal{M}_{\text{SM}}\right|^2 + \sum_i c_i \cdot 2\,\text{Re}\left(\mathcal{M}_{\text{SM}}^* \mathcal{M}_i\right) + \sum_{i,j\geq i} c_i c_j \cdot 2\,\text{Re}\left(\mathcal{M}_i^* \mathcal{M}_j\right) \,. \end{aligned} \tag{6.3}$$

The second equal sign exploits the fact that the Wilson coefficients are real numbers. The first part of this expression is governed by SM physics. The second part describes SM-BSM interference terms, which are linear in the BSM coupling parameters $c_i = C_i/\Lambda^2$. Thus, they are suppressed by $1/\Lambda^2$. The integration over these terms is expected to vanish for the $\mathcal{CP}$-odd operators at mass dimension six [456]. The last part accounts for the pure BSM terms. These are quadratic in the Wilson coefficients and therefore suppressed by $1/\Lambda^4$. Thus, the cross-section can be separated into a SM, an interference, and a pure BSM component,

$$\sigma = \sigma_{\text{SM}} + \sigma_{\text{INT}} + \sigma_{\text{BSM}} \,. \tag{6.4}$$

The dependence of the Higgs production cross-section $\sigma^p(\boldsymbol{c})$ in a given particle-level production bin p on the BSM coupling parameters can be formulated as

$$\frac{\sigma^p(\boldsymbol{c})}{\sigma^p_{\text{SM}}} = 1 + \sum_i A_i^p c_i + \sum_{i,j\geq i} B_{ij}^p c_i c_j \,, \tag{6.5}$$

where $A_i^p = 2\,\text{Re}\left(\mathcal{M}_{\text{SM}}^{p*} \mathcal{M}_i^p\right)/|\mathcal{M}_{\text{SM}}^p|^2$ and $B_{ij}^p = 2\,\text{Re}\left(\mathcal{M}_i^{p*} \mathcal{M}_j^p\right)/|\mathcal{M}_{\text{SM}}^p|^2$ are the prefactors of the linear and quadratic terms, respectively. They are determined from Monte Carlo simulation using the MadGraph5_aMC@NLO [330, 331] event generator and the `SMEFTsim_A_U35_MwScheme_UFO_v2.1 UFO` model [460, 461]. It provides a complete implementation of the lepton and baryon number conserving dimension-six operators in the Warsaw basis [462]. The Universal FeynRules Output (`UFO`) model is designed for `LO` computations of the SMEFT-SM interference and extended to derive effective Higgs couplings to gluons and photons. However, the above given parameterization can be used as a general correction to the SM prediction calculated at `NLO` and `NNLO` because it can be assumed that the higher-order corrections are the same for the SM and the BSM `LO` predictions [376],

$$\frac{\sigma^p(\boldsymbol{c})}{\sigma^p_{\text{SM}}} = \frac{\sigma^{p,\texttt{NLO}}(\boldsymbol{c})}{\sigma^{p,\texttt{NLO}}_{\text{SM}}} = \frac{\sigma^{p,\texttt{NNLO}}(\boldsymbol{c})}{\sigma^{p,\texttt{NNLO}}_{\text{SM}}} = 1 + \sum_i A_i^p c_i + \sum_{i,j\geq i} B_{ij}^p c_i c_j. \tag{6.6}$$

The prefactors A_i^p and B_{ij}^p are derived from simulated samples generated with MadGraph5_aMC@NLO, showered by Pythia8 [332] and analyzed on particle level to get the fraction of the cross-section in each

Table 6.1: MADGRAPH5_aMC@NLO syntax and BSM dependence for the pure SM, the SM-BSM interference, and the pure BSM part of the production cross-section.

Term	cross-section	syntax	BSM dependence	suppressed by
Pure SM	σ_{SM}	`NP^2==0`	-	1
SM-BSM interference	σ_{INT}	`NP^2==1`	linear	$1/\Lambda^2$
Pure BSM	σ_{BSM}	`NP^2==2`	quadratic	$1/\Lambda^4$

Table 6.2: Required Monte Carlo samples and MADGRAPH5_aMC@NLO syntax for a cross-section parameterization with two arbitrary BSM coupling parameters c_i and c_j.

Sample name	syntax	cross-section
SM	`NP^2==0`	$\sigma^p_{\text{SM}} = \sigma^p_{\text{SM}}(c_i = 0, c_j = 0)$
INT_ci	`NP^2==1`	$\sigma^p_{A,i} = \sigma^p_{\text{INT}}(c_i = 1, c_j = 0)$
BSM_ci	`NP^2==2`	$\sigma^p_{B,ii} = \sigma^p_{\text{BSM}}(c_i = 1, c_j = 0)$
INT_cj	`NP^2==1`	$\sigma^p_{A,j} = \sigma^p_{\text{INT}}(c_i = 0, c_j = 1)$
BSM_cj	`NP^2==2`	$\sigma^p_{B,jj} = \sigma^p_{\text{BSM}}(c_i = 0, c_j = 1)$
BSM_cicj	`NP^2==2`	$\sigma^p_{B,ij} = \sigma^p_{\text{BSM}}(c_i = 1, c_j = 1)$

STXS bin. The MADGRAPH5_aMC@NLO syntax and their BSM dependence is summarized in Table 6.1.

The prefactors are derived as follows. The parameterization of the cross-section is a quadratic function in the BSM coupling parameters. Therefore, the maximum number of BSM coupling parameters in each term of the expansion is two. Thus, it is possible to calculate the prefactors by taking into account only two of the relevant Wilson coefficients at a time while setting all others to zero. This approach is then repeated for all possible pairs of BSM parameters. For example, consider the pair of Wilson coefficients c_i and c_j. In this case, the EFT parameterization for a given production bin p reads

$$\frac{\sigma^p(c_i, c_j)}{\sigma^p_{\text{SM}}} = 1 + A^p_i c_i + A^p_j c_j + B^p_{ii} c_i^2 + B^p_{jj} c_j^2 + B^p_{ij} c_i c_j \,. \tag{6.7}$$

In order to calculate the five coefficients in Equation 6.7, six Monte Carlo samples are required targeting the different contributions to the production cross-section. The first one is a SM sample generated by setting all Wilson coefficients to zero. The second and third samples called INT_ci and INT_cj, include only the SM-BSM interference terms. The corresponding MADGRAPH5_aMC@NLO syntax is `NP^2==1` and the BSM coupling parameter of interest is set to 1, while all others are set to zero. The fourth and fifth sample, called BSM_ci and BSM_cj, are generated with a similar setup but they only include the pure BSM terms proportional to $|\mathcal{M}_i|^2$ and $|\mathcal{M}_j|^2$, respectively. The corresponding MADGRAPH5_aMC@NLO syntax is `NP^2==2`. For the last sample, BSM_cicj both BSM parameters are set to one.

The cross-section σ_x for the different contribution x = SM, INT, BSM, and the corresponding configurations are summarized in Table 6.2. To obtain the production cross-section $\sigma^p_x = f_p \sigma_x$ in a given particle-level production bin p, the fraction f_p of events that fall into the respective bin is determined using an event categorization algorithm. This is achieved by, first, adding up the weights w^p_i of the generated events i that belong to p and second, by dividing this sum by the sum of the weights for all events.

The prefactors of the linear and pure quadratic terms are determined from the production bin-corrected cross-section σ^p_{INT} and σ^p_{BSM} of the SM-BSM interference and the pure BSM samples, respectively,

$$A^p_i = \frac{\sigma^p_{A,i}}{\sigma^p_{\text{SM}}}, \quad A^p_j = \frac{\sigma^p_{A,j}}{\sigma^p_{\text{SM}}}, \quad B^p_{ii} = \frac{\sigma^p_{B,ii}}{\sigma^p_{\text{SM}}} \quad \text{and} \quad B^p_{jj} = \frac{\sigma^p_{B,jj}}{\sigma^p_{\text{SM}}}. \tag{6.8}$$

The production cross-section of the BSM_cicj sample $\sigma^p_{B,ij}$ includes not just the isolated mixed BSM contribution but also the pure terms $\sigma^p_{B,ii}$ and $\sigma^p_{B,jj}$. Thus, the prefactor for the quadratic term B_{ij} is derived by subtracting the additional contributions from $\sigma^p_{B,ij}$,

$$B_{ij} = \frac{\sigma_{B,ij} - \sigma_{B,ii} - \sigma_{B,jj}}{\sigma_{\text{SM}}}. \tag{6.9}$$

For the Higgs production cross-section parameterization, 113 different Monte Carlo samples are generated with 100 000 events each. They are produced in bunches of 10 000 events to speed up the sample generation. Seven samples are generated to cover the main SM production processes. In addition, 37 BSM samples with $C\mathcal{P}$-even operators, and the same amount of samples with $C\mathcal{P}$-odd operators are generated. To validate that the interference between the scalar and pseudoscalar operators vanishes, 32 samples with mixed $C\mathcal{P}$-even and $C\mathcal{P}$-odd operators are produced. The number of simulated samples in the different particle-level production bins and the respective MADGRAPH5_AMC@NLO configuration is summarized in Table 6.3. The detailed configuration of each generated BSM signal sample is given in Appendix D.1 (Table D.1-D.4). The ggF and bbH production processes are considered as a part of the same production bin, called gg2H. The associated processes only depend on one scalar and one pseudoscalar BSM parameter, c_{HG} and $c_{H\widetilde{G}}$, respectively. Thus, only six Monte Carlo samples are required to parameterize the gg2H cross-section. The same is true for WH-Lep production which is only affected by c_{HW} and $c_{H\widetilde{W}}$. In contrast to that the ZH-Lep production mode depends on three $C\mathcal{P}$-even (c_{HW}, c_{HB}, and c_{HWB}) and three $C\mathcal{P}$-odd ($c_{H\widetilde{W}}$, $c_{H\widetilde{B}}$, and $c_{H\widetilde{W}B}$) BSM coupling parameters. The corresponding number of samples for the parameterization is 28. WH-Lep and ZH-Lep events are summarized in a single bin called VH-Lep. Processes corresponding to the qq2Hqq production bin depend on the same operators as the ZH-Lep process. Therefore, the same number of samples is required. The ttH, $tHjb$ and tHW production processes are affected by c_{uH}, $c_{\widetilde{u}H}$, c_{HG} and $c_{H\widetilde{G}}$ resulting in a total of 17 samples each. They are merged in the so-called ttH+tH bin. The parameterization of the $gg \to Z(\to \ell\ell)H$ cross-section is assumed to be identical to the $qq \to Z(\to \ell\ell)H$ cross-section. Thus, no additional BSM Monte Carlo samples are produced, and the background modifications are neglected.

For the sample generation, the Higgs mass is set to 125 GeV and the lepton masses as well as the masses of the light quarks (up, down, strange, and charm) are set to zero without loss of generality. Events with transverse momenta of the leading jet below 10 GeV or di-jet invariant mass below 3 GeV are rejected at generator level. The events passing the generator level cuts are showered with PYTHIA8 using `CKKW-L` matching [332] to match the computation of the matrix elements to the parton showering for different jet multiplicities. The Durham algorithm [463] is used for k_T clustering with a longitudinally invariant k_T separation of `Dparameter=0.4`. The number of additional jets in the matrix element is restricted to 2. For all processes, except tHW production, the 4-flavor merging scheme (4FS) is applied. This means that only u-, d-, s- and c-quarks are considered. For tHW production, b-quarks are considered as well, i. e. the five flavor scheme (5FS) is used in this case [330].

The cross-sections obtained from the `UFO` model of the SMEFT are calculated at LO. However, since the cross-section analysis uses the best prediction of the cross-section in each of the STXS bins, the LO cross-section is scaled to that value. It is assumed that the impact of higher-order corrections is independent of the BSM coupling parameters. The inclusive cross-sections for the generated SM and BSM

Table 6.3: MADGRAPH5_AMC@NLO syntax and the number of samples required to parameterize the cross-sections for the relevant Higgs boson production modes. 5FS denotes the five flavor scheme.

Production mode	Madgraph syntax	number of SM samples	number of BSM samples		
			pure $C\mathcal{P}$-even	pure $C\mathcal{P}$-odd	mixed

ggF+bbH	`define jb = j b b~`
	`generate p p > h QED=1`
	`add process p p > h jb QED=1`
	`add process p p > h jb jb QED=1`
		1	2	2	1

VBF+VH-Had	`generate p p > h j j QCD=0`	1	9	9	9
ZH-Lep	`generate p p > h l+ l-` `add process p p > h vl vl~`	1	9	9	9
WH-Lep	`generate p p > h l+ vl` `add process p p > h l- vl~`	1	2	2	1
ttH	`generate p p > h t t ~`	1	5	5	4
$tHjb$	`generate p p > h t b~` `add process p p > h t~ b j`	1	5	5	4

tHW (5FS)	`define p = p b b~`
	`generate p p > h t w-`
	`add process p p > h t~ w+`
		1	5	5	4

samples are given in Table 6.4. The table is divided into seven main segments accounting for the different particle-level production modes ggF+bbH, VBF+VH-Had, ZH-Lep, WH-Lep, ttH, $tHjb$ and tHW. Within each segment, the $C\mathcal{P}$-even, the $C\mathcal{P}$-odd and the mixed terms are grouped to improve readability, and the corresponding cross-sections are given separately for each, the SM, the SM-BSM interference, and the pure BSM terms. In the case of linear $C\mathcal{P}$-odd terms, only upper limits on the cross-sections are stated because they are all consistent with zero. They are given by the statistical uncertainties of the MC generation, and they are below 1 % (in some cases even below 1 ‰) of the corresponding $C\mathcal{P}$-even cross-section. The relative statistical errors on the cross-sections is largest for the c_{HB} interference term in VBF+VH-Had production with $\delta\sigma = 1.8$ %. For all other terms, the relative error is below 1 %, which fits the expectation for interfering the SM with a pseudoscalar amplitude. The quadratic $C\mathcal{P}$-odd terms tend to be slightly smaller than the corresponding $C\mathcal{P}$-even ones. The mixed BSM terms with $C\mathcal{P}$-even and $C\mathcal{P}$-odd operators are also given in the table. However, no significant contributions from the interference terms are observed. For comparison, the expected cross-section given by the sum of the corresponding scalar and pseudoscalar pure BSM terms is given in gray together with relative deviations, which are below 1 % in all cases. Thus, within the statistical uncertainty, they are consistent with zero.

6.1.1 Parameterization in gg2H Production

To obtain the cross-section parameterization in the particle-level production bins, the fraction of events falling into each bin is determined at particle level. The bins are defined by event kinematics and the number of jets. For the gg2H production bin, the relevant variables are the transverse momenta of the Higgs boson and the final state jets, p_T^H and p_T^j, respectively, the pseudorapidity of the Higgs boson η^H and the number of final state jets N_j with $p_T^j \geq 30\,\text{GeV}$. To illustrate the effect of the dimension-six operators O_{HG} and $O_{H\tilde{G}}$ on these variables, the corresponding distributions for each, the SM, the SM-BSM interference, and the pure BSM terms are compared in Figure 6.1. The corresponding BSM

Table 6.4: Inclusive cross-section (σ) terms for all production modes. INT denotes the SM-BSM interference (MADGRAPH5_AMC@NLO syntax `NP^2==1`), and BSM the pure BSM terms (MADGRAPH5_AMC@NLO syntax `NP^2==2`). Cross-section terms with two BSM coupling parameters set to 1 correspond to pure BSM terms, and the abbreviation 'BSM' is dropped to improve readability.

ggF+bbH										
$\mathcal{CP}$-even	SM	$c_{HG}=1$, INT	$c_{HG}=1$, BSM							
σ [pb]	27.6	827	7060							
$\mathcal{CP}$-odd		$c_{H\widetilde{G}}=1$, INT	$c_{H\widetilde{G}}=1$, BSM							
σ [pb]		$< 10^{-3}$	7050							
Mixed terms		$c_{H\widetilde{G}}=c_{H\widetilde{G}}=1$								
σ [pb]		14064								
expected		14110 (+0.33 %)								
VBF+VH-Had										
$\mathcal{CP}$-even	SM	$c_{HW}=1$, INT	$c_{HW}=1$, BSM	$c_{HB}=1$, INT	$c_{HB}=1$, BSM	$c_{HWB}=1$, INT	$c_{HWB}=1$, BSM	$c_{HW}=c_{HB}=1$	$c_{HW}=c_{HWB}=1$	$c_{HB}=c_{HWB}=1$
σ [fb]	4150.3	541.3	533.3	14.9	113.3	181.1	82.6	704.9	567.1	107.4
$\mathcal{CP}$-odd		$c_{H\widetilde{W}}=1$, INT	$c_{H\widetilde{W}}=1$, BSM	$c_{H\widetilde{B}}=1$, INT	$c_{H\widetilde{B}}=1$, BSM	$c_{H\widetilde{W}B}=1$, INT	$c_{H\widetilde{W}B}=1$, BSM	$c_{H\widetilde{W}}=c_{H\widetilde{B}}=1$	$c_{H\widetilde{W}}=c_{H\widetilde{W}B}=1$	$c_{H\widetilde{B}}=c_{H\widetilde{W}B}=1$
σ [fb]		< 0.1	389.7	< 0.1	106.8	< 0.1	67.3	553.0	382.1	75.6
Mixed terms		$c_{HW}=c_{H\widetilde{W}}=1$	$c_{HW}=c_{H\widetilde{B}}=1$	$c_{HW}=c_{H\widetilde{W}B}=1$	$c_{HB}=c_{H\widetilde{W}}=1$	$c_{HB}=c_{H\widetilde{B}}=1$	$c_{HB}=c_{H\widetilde{W}B}=1$	$c_{HWB}=c_{H\widetilde{W}}=1$	$c_{HWB}=c_{H\widetilde{B}}=1$	$c_{HWB}=c_{H\widetilde{W}B}=1$
σ [fb]		922.0	640.5	601.1	503.5	220.2	180.5	471.7	189.8	149.9
expected		923.0 (+0.11 %)	640.1 (−0.06 %)	600.6 (−0.08 %)	503.0 (−0.10 %)	220.1 (−0.05 %)	180.6 (+0.06 %)	472.3 (+0.13 %)	189.4 (−0.21 %)	149.9 (+0.0 %)
ZH-Lep										
$\mathcal{CP}$-even	SM	$c_{HW}=1$, INT	$c_{HW}=1$, BSM	$c_{HB}=1$, INT	$c_{HB}=1$, BSM	$c_{HWB}=1$, INT	$c_{HWB}=1$, BSM	$c_{HW}=c_{HB}=1$	$c_{HW}=c_{HWB}=1$	$c_{HB}=c_{HWB}=1$
σ [fb]	150.5	109.4	39.9	13.3	4.7	49.0	9.9	44.6	72.2	23.1
$\mathcal{CP}$-odd		$c_{H\widetilde{W}}=1$, INT	$c_{H\widetilde{W}}=1$, BSM	$c_{H\widetilde{B}}=1$, INT	$c_{H\widetilde{B}}=1$, BSM	$c_{H\widetilde{W}B}=1$, INT	$c_{H\widetilde{W}B}=1$, BSM	$c_{H\widetilde{W}}=c_{H\widetilde{B}}=1$	$c_{H\widetilde{W}}=c_{H\widetilde{W}B}=1$	$c_{H\widetilde{B}}=c_{H\widetilde{W}B}=1$
σ [fb]		< 0.1	24.7	< 0.01	5.0	< 0.1	5.7	29.4	38.4	13.9
Mixed terms		$c_{HW}=c_{H\widetilde{W}}=1$	$c_{HW}=c_{H\widetilde{B}}=1$	$c_{HW}=c_{H\widetilde{W}B}=1$	$c_{HB}=c_{H\widetilde{W}}=1$	$c_{HB}=c_{H\widetilde{B}}=1$	$c_{HB}=c_{H\widetilde{W}B}=1$	$c_{HWB}=c_{H\widetilde{W}}=1$	$c_{HWB}=c_{H\widetilde{B}}=1$	$c_{HWB}=c_{H\widetilde{W}B}=1$
σ [fb]		64.5	44.8	45.6	29.3	9.7	10.4	34.7	15.1	15.7
expected		64.6 (+0.02 %)	44.9 (+0.22 %)	45.6 (+0.0 %)	29.4 (+0.3 %)	9.7 (0.0 %)	10.4 (+0.0 %)	34.6 (−0.29 %)	14.9 (−0.7 %)	15.6 (−0.6 %)
WH-Lep										
$\mathcal{CP}$-even	SM	$c_{HW}=1$, INT	$c_{HW}=1$, BSM							
σ [fb]	238.2	210.2	82.9							
$\mathcal{CP}$-odd		$c_{H\widetilde{W}}=1$, INT	$c_{H\widetilde{W}}=1$, BSM							
σ [fb]		< 0.2	52.7							
Mixed terms		$c_{HW}=c_{H\widetilde{W}}=1$, BSM								
σ [fb]		135.7								
expected		135.6 (−0.07 %)								
ttH										
$\mathcal{CP}$-even	SM	$c_{uH}=1$, INT	$c_{uH}=1$, BSM	$c_{HG}=1$, INT	$c_{HG}=1$, BSM	$c_{HG}=c_{uH}=1$				
σ [fb]	412.8	−48.9	1.45	228.9	280.4	277.8				
$\mathcal{CP}$-odd		$c_{\widetilde{u}H}=1$, INT	$c_{\widetilde{u}H}=1$, BSM	$c_{H\widetilde{G}}=1$, INT	$c_{H\widetilde{G}}=1$, BSM	$c_{H\widetilde{G}}=c_{\widetilde{u}H}=1$				
σ [fb]		$< 10^{-3}$	0.63	< 0.05	285.0	306.4				
Mixed terms		$c_{uH}=c_{\widetilde{u}H}=1$	$c_{uH}=c_{H\widetilde{G}}=1$	$c_{HG}=c_{\widetilde{u}H}=1$	$c_{HG}=c_{H\widetilde{G}}=1$					
σ [fb]		2.08	286.8	282.6	567.4					
expected		2.08 (+0.0 %)	286.5 (−0.5 %)	281.0 (−0.6 %)	565.4 (−0.4 %)					
$tHjb$										
$\mathcal{CP}$-even	SM	$c_{uH}=1$, INT	$c_{uH}=1$, BSM	$c_{HG}=1$, INT	$c_{HG}=1$, BSM	$c_{HG}=c_{uH}=1$				
σ [fb]	64.7	-1.99	2.72	0.45	2.68	2.73				
$\mathcal{CP}$-odd		$c_{\widetilde{u}H}=1$, INT	$c_{\widetilde{u}H}=1$, BSM	$c_{H\widetilde{G}}=1$, INT	$c_{H\widetilde{G}}=1$, BSM	$c_{H\widetilde{G}}=c_{\widetilde{u}H}=1$				
σ [fb]		<0.01	0.24	<0.01	2.68	2.92				
Mixed terms		$c_{uH}=c_{\widetilde{u}H}=1$	$c_{uH}=c_{H\widetilde{G}}=1$	$c_{HG}=c_{\widetilde{u}H}=1$	$c_{HG}=c_{H\widetilde{G}}=1$					
σ [fb]		2.96	5.43	2.95	5.36					
expected		2.96 (+0.0 %)	5.40 (−0.55 %)	2.92 (−1.0 %)	5.36 (+0.0 %)					
tHW										
$\mathcal{CP}$-even	SM	$c_{uH}=1$, INT	$c_{uH}=1$, BSM	$c_{HG}=1$, INT	$c_{HG}=1$, BSM	$c_{HG}=c_{uH}=1$				
σ [fb]	17.7	-1.83	0.18	8.64	6.92	5.81				
$\mathcal{CP}$-odd		$c_{\widetilde{u}H}=1$, INT	$c_{\widetilde{u}H}=1$, BSM	$c_{H\widetilde{G}}=1$, INT	$c_{H\widetilde{G}}=1$, BSM	$c_{H\widetilde{G}}=c_{\widetilde{u}H}=1$				
σ [fb]		<0.001	0.14	<0.005	6.93	7.46				
Mixed terms		$c_{uH}=c_{\widetilde{u}H}=1$	$c_{uH}=c_{H\widetilde{G}}=1$	$c_{HG}=c_{\widetilde{u}H}=1$	$c_{HG}=c_{H\widetilde{G}}=1$					
σ [fb]		0.32	7.13	7.09	13.86					
expected		0.32 (+0.0 %)	7.11 (−0.28 %)	7.06 (.0.4 %)	13.85 (−0.07 %)					

coupling parameters are set to one in this case, and operators currently not investigated are set to zero. Higgs bosons generated by the pure BSM terms tend to have slightly smaller transverse momenta (see Figure 6.1(a)) and are produced less centrally in the detector (see Figure 6.1(b)) compared to their SM counterparts. The jet transverse momentum (see Figure 6.1(c)) and the number of jets (see Figure 6.1(d)) in the final state with $p_T^j \geq 30\,\text{GeV}$ tend to be larger for the SM. Differences between the quadratic $\mathcal{CP}$-even and $\mathcal{CP}$-odd terms are small, and no interference effects are observed in the distributions.

The fraction of the ggF+bbH cross-section in each gg2H particle-level production bin is summarized in

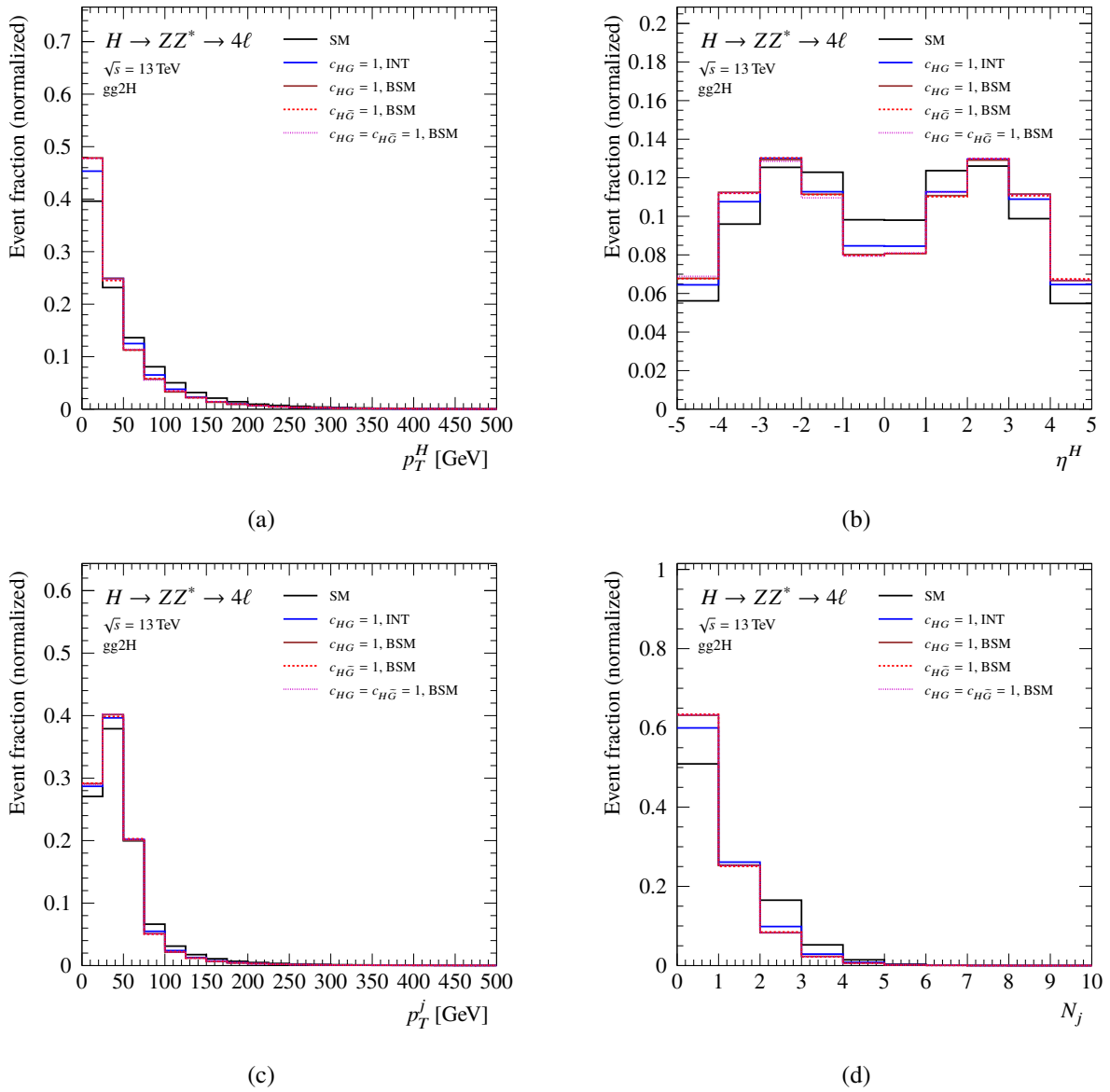

Figure 6.1: The simulated distributions of the Higgs boson (a) transverse momentum (p_T^H) and (b) pseudorapidity (η^H) as well as (c) the jet transverse momentum (p_T^j) and (d) the number of jets (N_j) with $p_T^j > 30\,\text{GeV}$ in the gg2H production bin. Shown are the SM, the c_{HG} interference and the pure BSM terms for c_{HG} and $c_{H\tilde{G}}$. All distributions are normalized to unit area.

Table 6.5. For the pure BSM terms, it is largest in the low transverse momentum (p_T^H-Low) and zero-jet ($0j$) categories. The relative differences between the $C\mathcal{P}$-even, the $C\mathcal{P}$-odd, and the mixed BSM terms are within the statistical uncertainty of the simulation. It is estimated by classifying the generated bunches with 10 000 events each, separately, and calculating the variance of the event fraction f in each bin. The largest absolute uncertainty is $\Delta f = 0.25\,\%$ for the gg2H-$0j$-p_T^H-High bin, which corresponds to a relative uncertainty estimate of $\delta f = {}^{\Delta f}/_{f} = 0.6\,\%$. In contrast, the largest relative uncertainty is found for the gg2H-$1j$-p_T^H-High bin in the SM case with 2.6 %.

The prefactors for the cross-section parameterization are determined by, first, calculating the simulated cross-section terms in each particle-level production bin σ_X^p using the inclusive gg2H production cross-

Table 6.5: Percentage of ggF+bbH events in the gg2H particle-level production bins of the Reduced-Stage-1.1 scheme. INT denotes the SM-BSM interference terms (MADGRAPH5_aMC@NLO syntax `NP^2==1`), and BSM denotes pure BSM terms (MADGRAPH5_aMC@NLO syntax `NP^2==2`).

STXS bin	SM	$c_{HG} = 1$ INT	$c_{HG} = 1$ BSM	$c_{H\widetilde{G}} = 1$ BSM	$c_{HG} = c_{H\widetilde{G}} = 1$ BSM
gg2H-0j-p_T^H-Low	11.9 %	14.2 %	15.1 %	14.9 %	15.1 %
gg2H-0j-p_T^H-High	32.6 %	38.6 %	40.6 %	40.8 %	40.6 %
gg2H-1j-p_T^H-Low	10.8 %	11.5 %	11.4 %	11.5 %	11.4 %
gg2H-1j-p_T^H-Medium	9.3 %	9.2 %	8.5 %	8.7 %	8.5 %
gg2H-1j-p_T^H-High	2.3 %	2.2 %	2.1 %	2.1 %	2.1 %
gg2H-2j	19.2 %	11.4 %	9.0 %	8.5 %	8.8 %
gg2H-p_T^H-High	4.2 %	2.5 %	2.6 %	2.8 %	2.7 %

sections given in Table 6.4 and the event fractions given in Table 6.5. Second, by applying the Equations 6.8 and 6.9 for all terms. The resulting formulas are summarized in Table 6.9. They do not contain linear terms for $c_{H\widetilde{G}}$ since the corresponding prefactors are consistent with zero. The same is true for the interference between O_{HG} and $O_{H\widetilde{G}}$. The relative difference between the scalar and pseudoscalar quadratic prefactors is between 0.3 % and 6 %. The zero-jet categories are most affected by BSM contributions, while the gg2H-2j bin is the least dependent category due to the relatively small quadratic contributions. However, this statement is not true for small values of c_{HG} because of the additional linear term. Figure 6.2 shows the one-dimensional dependence of the cross-section ratio $\sigma^p/\sigma^p_{\text{SM}}$ for the gg2H particle-level production bins p on both BSM parameters separately, while the other is set to zero. The gg2H-0j-p_T^H-High bin is the most sensitive production bin in the cross-section analysis. Its expected sensitivity, 1.00 ± 0.16 (not including systematic errors), is shown as a gray band in both figures. Therefore, the relevant scope of c_{HG} is expected to be $-0.005 < c_{HG} < 0.005$ (see Figure 6.2(a)). In this range, all gg2H particle-level production bins are very linear, and the quadratic terms play a minor role. The gg2H-p_T^H-High bin is even slightly less dependent on c_{HG} than gg2H-2j. The situation differs for $c_{H\widetilde{G}}$ (see Figure 6.2(b)). In this case, the curves are purely quadratic, and the overall sensitivity on $c_{H\widetilde{G}}$ is much weaker. It is expected to be $-0.022 < c_{H\widetilde{G}} < 0.022$.

6.1.2 Parameterization in qq2Hqq Production

For the classification in the qq2Hqq production category, the number of jets is dropped from the above list of variables, but the invariant mass of the two leading jets m_{jj} is added to identify VH-like and BSM-like events. Figure 6.3 shows the relevant kinematic distributions for the dimension-six operators O_{HW} and $O_{H\widetilde{W}}$. The transverse momentum of the Higgs boson is largest for the pure BSM terms (see Figure 6.3(a)). Since the production cross-section is slightly larger in the case of c_{HW} compared to $c_{H\widetilde{W}}$, the mixed BSM distributions are slightly closer to the scalar ones. The Higgs boson transverse momentum is the smallest in the SM case. The hierarchy is similar for the jet transverse momentum (Figure 6.3(c)), but in this case, the SM-BSM interference term for c_{HW} is the smallest. While most SM Higgs bosons are generated within $1 < |\eta| < 2$, the pure BSM terms generate Higgs bosons with smaller pseudorapidities ($|\eta| < 1$). They are most central for the $\mathcal{CP}$-odd BSM terms (Figure 6.3(b)). The dijet invariant mass spectra (Figure 6.3(d)) of the interference and the pure BSM terms are very similar. Compared to the SM, the fraction of the events is increased by about ≈ 60 % in the $50 < m_{jj} < 100$ GeV region. The respective distributions for the operators $O_{HB}/O_{H\widetilde{B}}$ and $O_{HWB}/O_{H\widetilde{W}B}$ are presented in Appendix D.2.2.

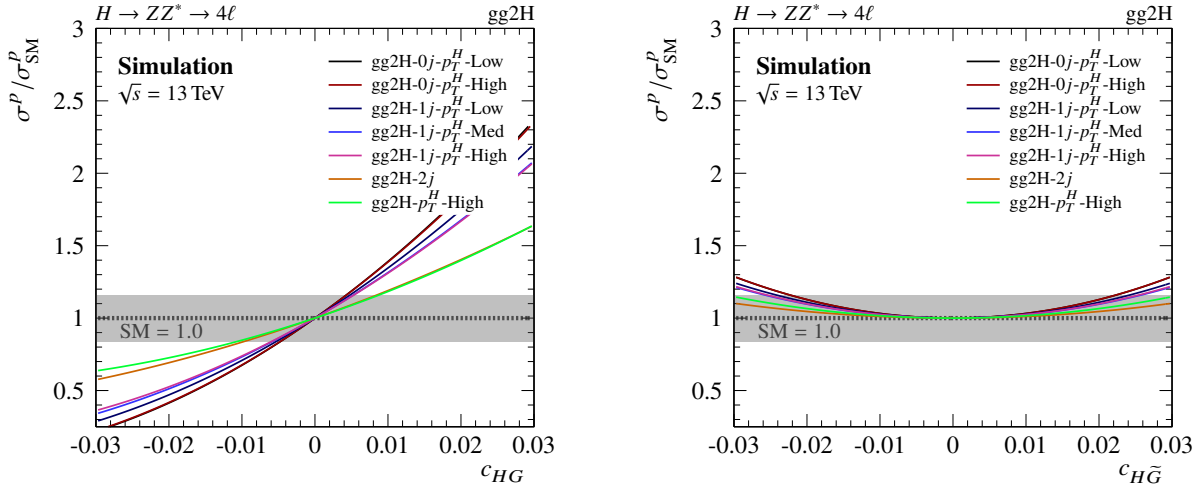

(a) (b)

Figure 6.2: The one-dimensional dependence of the cross-section ratio, $\sigma/\sigma_{\mathrm{SM}}$, in the Reduced Stage 1.1 gg2H particle-level production bins on the BSM parameters (a) c_{HG} and (b) $c_{H\tilde{G}}$.

Table 6.6: Percentage of VBF+VH-Had events in the qq2Hqq particle-level production bins of the Reduced-Stage-1.1 scheme. INT denotes SM-BSM interference terms,and BSM denotes pure BSM terms. For terms with two BSM coupling parameters set to 1, the abbreviation 'BSM' is dropped to improve readability.

STXS bin	SM	$c_{HW}=1$ INT	$c_{HW}=1$ BSM	$c_{HB}=1$ INT	$c_{HB}=1$ BSM	$c_{HWB}=1$ INT	$c_{HWB}=1$ BSM	$c_{HW}=1$, $c_{HB}=1$	$c_{HW}=1$, $c_{HWB}=1$	$c_{HB}=1$, $c_{HWB}=1$
qq2Hqq-VBF	77.8 %	35.0 %	55.7 %	33.6 %	76.9 %	66.1 %	69.8 %	61.4 %	53.5 %	62.9 %
qq2Hqq-VH-Like	10.0 %	45.2 %	20.1 %	56.0 %	5.3 %	20.5 %	11.2 %	16.3 %	23.2 %	16.5 %
qq2Hqq-BSM	3.9 %	5.7 %	15.4 %	< 1 %	8.2 %	3.6 %	9.8 %	13.2 %	14.4 %	11.5 %

STXS bin	$c_{H\widetilde{W}}=1$ BSM	$c_{H\widetilde{B}}=1$ BSM	$c_{H\widetilde{W}B}=1$ BSM	$c_{H\widetilde{W}}=1$, $c_{H\widetilde{B}}=1$	$c_{H\widetilde{W}}=1$, $c_{H\widetilde{W}B}=1$	$c_{H\widetilde{B}}=1$, $c_{H\widetilde{W}B}=1$
qq2Hqq-VBF	51.3 %	76.8 %	71.4 %	59.6 %	48.7 %	62.3 %
qq2Hqq-VH-Like	19.9 %	4.8 %	7.5 %	15.1 %	22.6 %	13.3 %
qq2Hqq-BSM	21.1 %	8.8 %	12.4 %	16.8 %	20.9 %	16.3 %

STXS bin	$c_{HW}=1$, $c_{H\widetilde{W}}=1$	$c_{HW}=1$, $c_{H\widetilde{B}}=1$	$c_{HW}=1$, $c_{H\widetilde{W}B}=1$	$c_{HB}=1$, $c_{H\widetilde{W}}=1$	$c_{HB}=1$, $c_{H\widetilde{B}}=1$	$c_{HB}=1$, $c_{H\widetilde{W}B}=1$	$c_{HWB}=1$, $c_{H\widetilde{W}}=1$	$c_{HWB}=1$, $c_{H\widetilde{B}}=1$	$c_{HWB}=1$, $c_{H\widetilde{W}B}=1$
qq2Hqq-VBF	53.8 %	59.5 %	57.3 %	57.1 %	76.9 %	74.7 %	54.6 %	73.6 %	70.4 %
qq2Hqq-VH-Like	20.0 %	17.6 %	18.7 %	16.4 %	5.0 %	6.1 %	18.1 %	7.7 %	9.5 %
qq2Hqq-BSM	17.9 %	14.1 %	15.3 %	18.4 %	8.5 %	9.9 %	19.1 %	9.4 %	11.1 %

The fraction of the qq2Hqq production cross-section in each particle-level production bin is summarized in Table 6.6. Applying the uncertainty estimation scheme from above, the largest uncertainty is found for the linear c_{HB} term in the qq2Hqq-VBF bin with $\Delta f = 0.9\,\%$. This is also the term with the largest cross-section uncertainty. However, the impact of this uncertainty on the cross-section parameterization is negligible due to the smallness of the prefactor when compared to the quadratic term. The formulas for the cross-section parameterization in qq2Hqq production are summarized in Table 6.9. The prefactors of interference terms between $\mathcal{CP}$-even and $\mathcal{CP}$-odd amplitudes are again consistent with zero.

The one-dimensional projections of the cross-section ratio in each particle-level bin are shown in Figure 6.4. The cross-section ratio is most dependent on c_{HW} and $c_{H\widetilde{W}}$, while the other BSM parameters have smaller impact. In contrast to the gg2H production mode, the quadratic terms are most dominant in

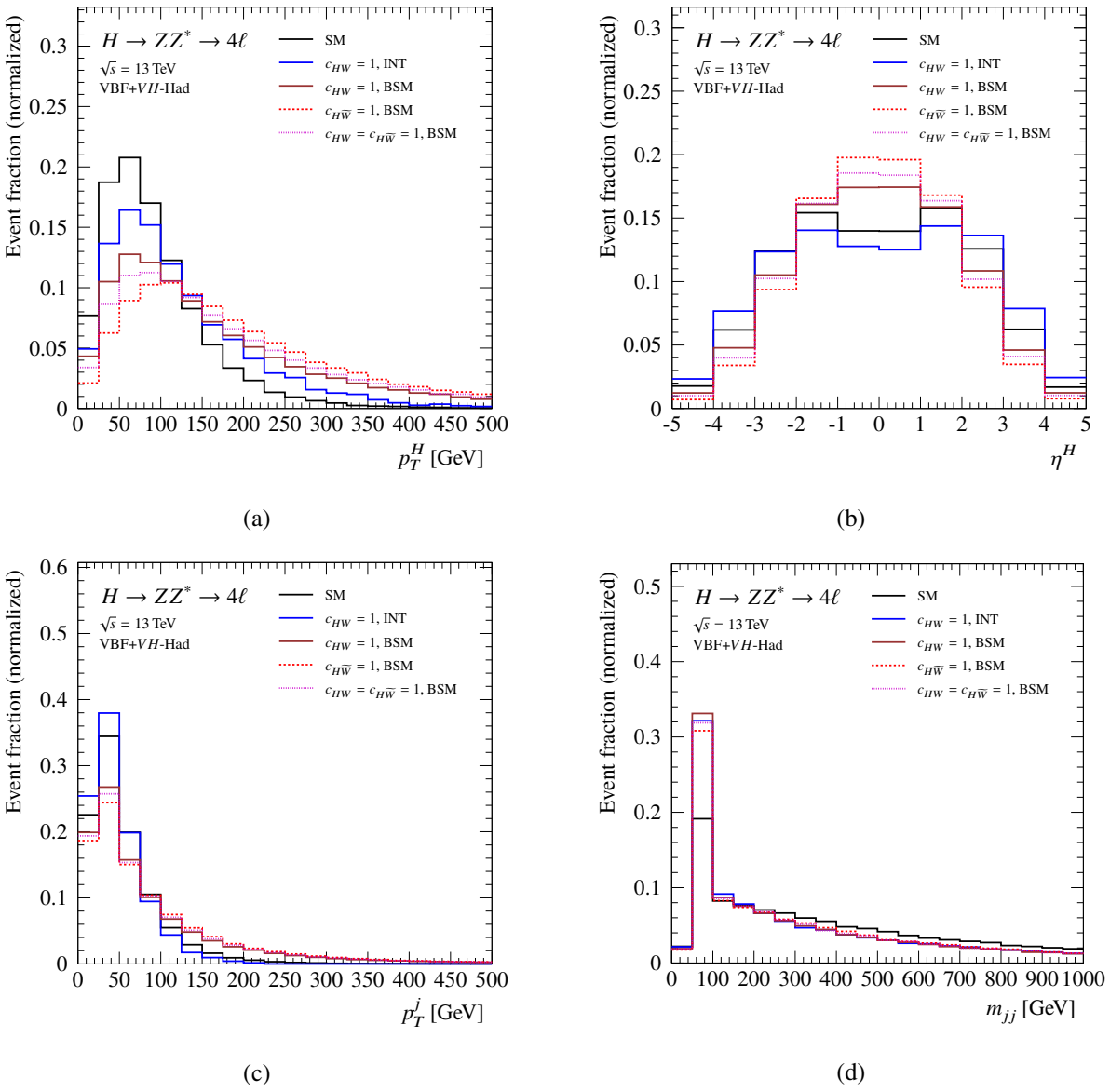

Figure 6.3: The simulated distributions of the Higgs boson (a) transverse momentum (p_T^H) and (b) pseudorapidity (η^H) as well as (c) the jet transverse momentum (p_T^j) and (d) the dijet invariant mass (m_{jj}) in the VBF+VH-Had production mode. Shown are the SM, the c_{HW} interference and the pure BSM terms for c_{HW} and $c_{H\widetilde{W}}$. All distributions are normalized to unit area.

the expected sensitivity range highlighted by the gray band. The linear terms only lead to small shifts of the parabola for the $C\mathcal{P}$-even parameters. Although the qq2Hqq-BSM bin has the largest dependence on the Wilson coefficients, its statistical uncertainty in the SM analysis ($1.0^{+2.0}_{-1.1}$) is lower than that of the qq2Hqq-VBF bin, which is $1.0^{+0.6}_{-0.5}$. The BSM coupling parameters shown in Figure 6.4 also play a major role in the Higgs boson decay into four-leptons. Thus, the sensitivity can be improved by taking the parameterization of the $H \to 4\ell$ branching ratio into account. This is shown in detail in Section 6.2.

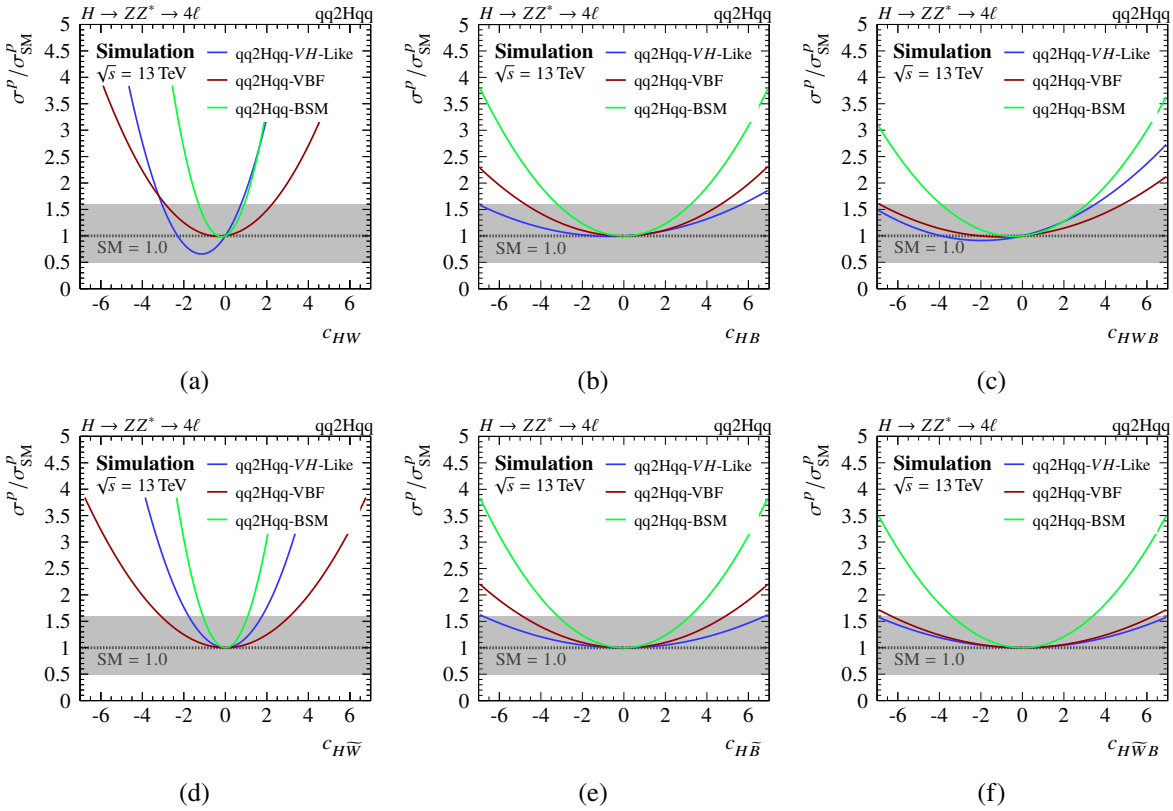

Figure 6.4: The one-dimensional dependence of the cross-section ratio, $\sigma/\sigma_{\text{SM}}$, in the Reduced Stage 1.1 qq2Hqq particle-level production bins on the BSM parameters (a) c_{HW}, (b) c_{HB}, (c) c_{HWB}, (d) $c_{H\widetilde{W}}$, (e) $c_{H\widetilde{B}}$, and (f) $c_{H\widetilde{W}B}$.

6.1.3 Parameterization in VH-Lep Production

The definition of the remaining particle-level production bins is based on the jet transverse momenta and the pseudorapidity of the Higgs boson. The corresponding distributions for the operators O_{HW} and $O_{H\widetilde{W}}$ in ZH-Lep and WH-Lep production are compared in Figure 6.5 and 6.6, respectively. In both cases, the kinematic distributions are similar for the SM and the SM-BSM interference terms, which are widest in the pseudorapidity. In contrast, the pure BSM terms are most central (Figure 6.5(b) and 6.6(b)). On the other hand, the transverse momenta of jets tend to be slightly smaller for the SM and the interference term (Figure 6.5(a) and 6.6(a)). Similar distributions for c_{HB}, $c_{H\tilde{B}}$, c_{HWB} and $c_{H\tilde{W}B}$ for the ZH-Lep production bin are shown in Appendix D.2.3.

The fractions of the ZH-Lep and WH-Lep production cross-sections in the particle-level production bin VH-Lep are summarized in Table 6.7. The estimated absolute uncertainties are below $\Delta f = 0.8\,\%$. In contrast to the gg2H and qq2Hqq bins parameterized above, two production processes contribute to the VH-Lep bin. Moreover, different sets of operators are associated with them. In case of ZH-Lep the operators are O_{HW}, O_{HB}, O_{HWB}, $O_{H\widetilde{W}}$, $O_{H\widetilde{B}}$ and $O_{H\widetilde{W}B}$, while only O_{HW} and $O_{H\widetilde{W}}$ are contributing to WH-Lep production. To account for that, the relevant ZH-Lep and WH-Lep cross-section terms are added before the parameterization is derived. Applying the nomenclature introduced in Table 6.2 and the

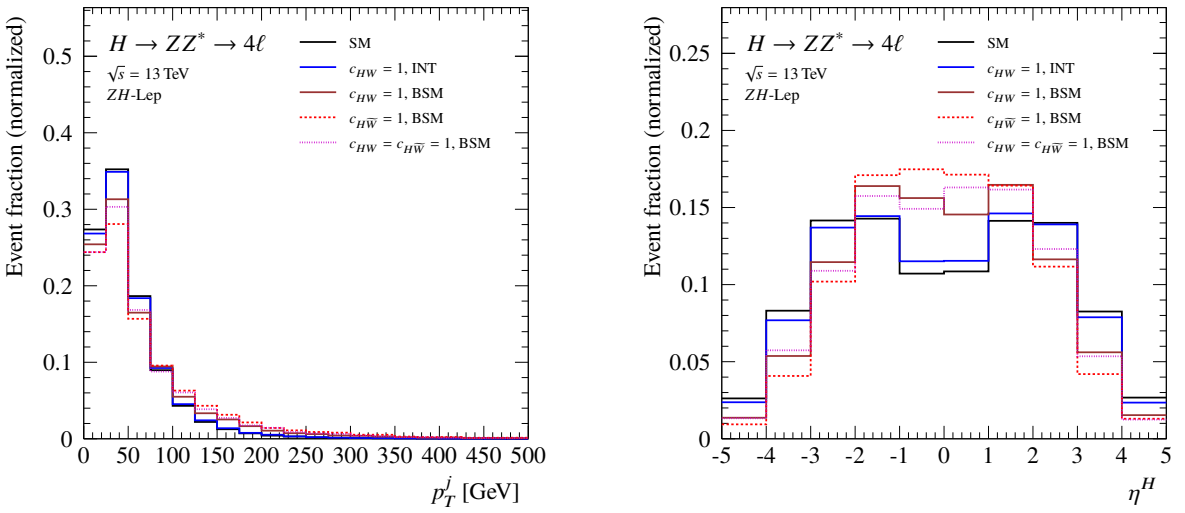

(a) (b)

Figure 6.5: The simulated distributions of (a) the jet transverse momentum (p_T^j) and (b) the pseudorapidity of the Higgs boson (η^H) in the ZH-Lep production mode normalized to unit area. Shown are the SM, the c_{HW} interference and the pure BSM terms for c_{HW} and $c_{H\widetilde{W}}$.

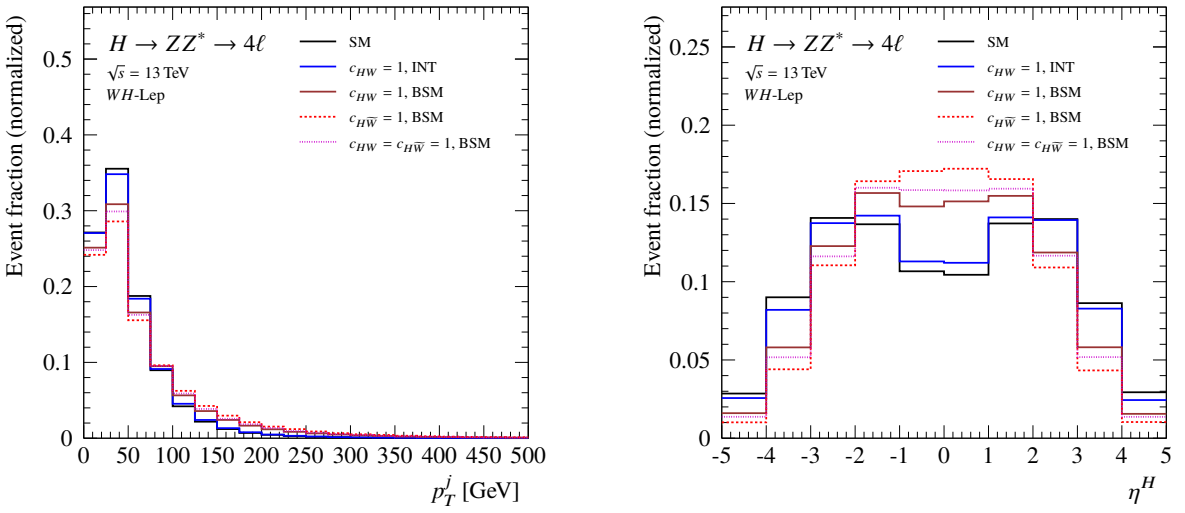

(a) (b)

Figure 6.6: The simulated distributions of (a) the jet transverse momentum (p_T^j) and (b) the pseudorapidity of the Higgs boson (η^H) in the WH-Lep production mode normalized to unit area. Shown are the SM, the c_{HW} interference and the pure BSM terms for c_{HW} and $c_{H\widetilde{W}}$.

abbreviations $i = c_{HW}$, $j = c_{H\widetilde{W}}$ and $p = VH$-Lep the relevant terms read

$$\begin{aligned}
\sigma^p_{\text{SM}} &= \sigma^p_{\text{SM}}(ZH\text{-Lep}) + \sigma^p_{\text{SM}}(WH\text{-Lep}),\\
\sigma^p_{A,i} &= \sigma^p_{A,i}(ZH\text{-Lep}) + \sigma^p_{A,i}(WH\text{-Lep}),\\
\sigma^p_{B,ii} &= \sigma^p_{B,ii}(ZH\text{-Lep}) + \sigma^p_{B,ii}(WH\text{-Lep}),\\
\sigma^p_{B,jj} &= \sigma^p_{B,jj}(ZH\text{-Lep}) + \sigma^p_{B,jj}(WH\text{-Lep}),\\
\sigma^p_{B,ij} &= \sigma^p_{B,ij}(ZH\text{-Lep}) + \sigma^p_{B,ij}(WH\text{-Lep}).
\end{aligned}$$

Table 6.7: Percentage of ZH-Lep and WH-Lep events in the VH-Lep particle-level production bin of the Reduced-Stage-1.1 scheme. INT denotes the SM-BSM interference terms (MADGRAPH5_aMC@NLO syntax `NP^2==1`), and BSM denotes pure BSM terms (MADGRAPH5_aMC@NLO syntax `NP^2==2`). For terms with two BSM coupling parameters set to 1, the abbreviation 'BSM' is dropped to improve readability.

***ZH*-Lep**										
STXS bin	SM	$c_{HW}=1$ INT	$c_{HW}=1$ BSM	$c_{HB}=1$ INT	$c_{HB}=1$ BSM	$c_{HWB}=1$ INT	$c_{HWB}=1$ BSM	$c_{HW}=1$, $c_{HB}=1$	$c_{HW}=1$, $c_{HWB}=1$	$c_{HB}=1$, $c_{HWB}=1$
VH-Lep	87.6 %	88.0 %	90.4 %	88.5 %	91.7 %	88.3 %	90.7 %	90.5 %	89.8 %	89.3 %
STXS bin			$c_{H\widetilde{W}}=1$ BSM		$c_{H\widetilde{B}}=1$ BSM		$c_{H\widetilde{W}B}=1$ BSM	$c_{H\widetilde{W}}=1$, $c_{H\widetilde{B}}=1$	$c_{H\widetilde{W}}=1$, $c_{H\widetilde{W}B}=1$	$c_{H\widetilde{B}}=1$, $c_{H\widetilde{W}B}=1$
VH-Lep			91.6 %		95.1 %		94.3 %	92.2 %	90.9 %	93.1 %
STXS bin		$c_{HW}=1$, $c_{H\widetilde{W}}=1$	$c_{HW}=1$, $c_{H\widetilde{B}}=1$	$c_{HW}=1$, $c_{H\widetilde{W}B}=1$	$c_{HB}=1$, $c_{H\widetilde{W}}=1$	$c_{HB}=1$, $c_{H\widetilde{B}}=1$	$c_{HB}=1$, $c_{H\widetilde{W}B}=1$	$c_{HWB}=1$, $c_{H\widetilde{W}}=1$	$c_{HWB}=1$, $c_{H\widetilde{B}}=1$	$c_{HWB}=1$, $c_{H\widetilde{W}B}=1$
VH-Lep		90.9 %	90.7 %	90.9 %	91.6 %	93.7 %	93.2 %	91.5 %	92.7 %	92.3 %
***WH*-Lep**										
STXS bin	SM	$c_{HW}=1$ INT	$c_{HW}=1$ BSM	$c_{H\widetilde{W}}=1$ BSM	$c_{HW}=1$, $c_{H\widetilde{W}}=1$					
VH-Lep	86.6 %	87.4 %	89.2 %	90.4 %	89.8 %					

Using these formulas, the parameterization of the VH-Lep particle-level cross-section is derived as usual via Equation 6.8 and 6.9. The result is given in Table 6.9.

Figure 6.7 shows the one-dimensional projections of the cross-section ratio in the VH-Lep bin. Similar to the qq2Hqq bins the cross-section ratio depends the most on c_{HW} and $c_{H\widetilde{W}}$ in the expected sensitivity range. The statistical uncertainty in the SM analysis is $1.0^{1.4}_{-0.8}$. Thus, the expected sensitivities in this production bin are $-3.7 < c_{HW} < 1.1$ and $-2.5 < c_{H\widetilde{W}} < 2.5$.

6.1.4 Parameterization in ttH Production

The ttH+tH bin accounts for the Higgs production processes ttH, $tHjb$ and tHW. The particle-level production bin targeting these processes is called ttH, and it is based on the jet transverse momentum and the pseudorapidity of the Higgs boson. Figure 6.8 shows the kinematic distributions for the operators O_{uH} and $O_{\widetilde{u}H}$ in the ttH production mode. The $C\mathcal{P}$-even terms, including the SM, the interference, and the pure BSM term, follow almost identical shapes, while the $C\mathcal{P}$-odd pure BSM term is most central in η^H (Figure 6.8(b)). However, the jet transverse momentum is typically similar in all cases (Figure 6.8(a)). Figure 6.9 shows the same distributions for the operators O_{HG} and $O_{H\widetilde{G}}$. The corresponding distributions for the $tHjb$ and tHW production processes are shown in Appendix D.2.4.

The fraction of the cross-section in each STXS bin is summarized in Table 6.8. The estimated absolute uncertainties are $\Delta f = 0.1 - 0.5\,\%$. Different Higgs boson production modes contribute to the same particle-level production bin similar to the qq2Hqq bin discussed above. However, in this case, the same operators are relevant for the different production processes. Therefore, the corresponding cross-section terms are added for each production mode. In the case of $tHjb$ values above 100 % event fraction are found for the linear $C\mathcal{P}$-terms, which is, at first glance, a nonsensical statement. However, some of the events that do not contribute to the particle-level production bin ttH are assigned negative weights. Thus, the sum of weights in the ttH bin is larger than the sum of all event weights. The parameterization for the ttH production cross-section is given in Table 6.9 together with the parameterizations of the other particle-level production bins.

Figure 6.10 shows the one-dimensional dependence of the cross-section ratio, $\sigma^p/\sigma^p_{\text{SM}}$, for the ttH particle-level production bin on the BSM coupling parameters c_{uH} and $c_{\widetilde{u}H}$. The expected sensitivity

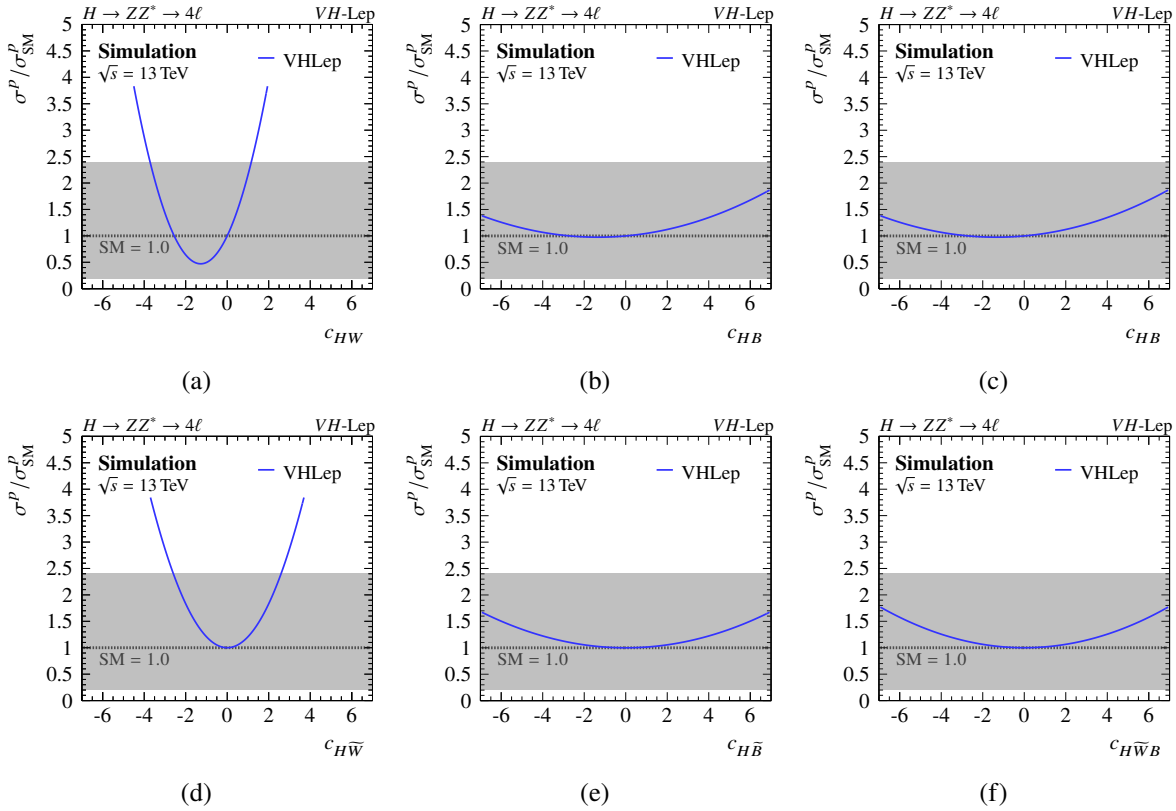

Figure 6.7: The one-dimensional dependence of the cross-section ratio, $\sigma/\sigma_{\mathrm{SM}}$, in the VH-Lep particle-level production bin of the Reduced Stage 1.1 scheme on the BSM coupling parameters (a) c_{HW}, (b) c_{HB}, (c) c_{HWB}, (d) $c_{H\widetilde{W}}$, (e) $c_{H\widetilde{B}}$, and (f) $c_{H\widetilde{W}B}$ assuming that all others are set to zero.

in this bin ($1.0^{+1.3}_{-0.8}$) is shown as a gray band in both figures. Therefore, the expected range of c_{uH} is approximately $-9 < c_{uH} < 20$ (see Figure 6.10(a)). The corresponding range for $c_{\widetilde{u}H}$ is expected to be $-26 < c_{\widetilde{u}H} < 26$.

6.2 Parameterization of the Higgs Boson Decay

The Higgs boson decay widths are also affected by the dimension-six operators of the SMEFT and they need to be parameterized as a function of the BSM couplings parameters. Both the partial decay width into four lepton final states, $\Gamma^{4\ell}$, and the total Higgs boson width, $\Gamma^{\mathrm{tot}} = \sum_f \Gamma^f$ where f are all available final states, are individually parameterized. Using the same approach as is in Section 6.1, the decay widths can be separated into a SM, an interference, and a pure BSM part,

$$\Gamma^{4\ell}(\boldsymbol{c}) = \Gamma^{4\ell}_{\mathrm{SM}} + \Gamma^{4\ell}_{\mathrm{INT}} + \Gamma^{4\ell}_{\mathrm{BSM}} = \Gamma^{4\ell}_{\mathrm{SM}} \left(1 + \sum_i A^{4\ell}_i c_i + \sum_{i,j\geq i} B^{4\ell}_{ij} c_i c_j\right) , \tag{6.10}$$

and

$$\Gamma^{\mathrm{tot}}(\boldsymbol{c}) = \Gamma^{\mathrm{tot}}_{\mathrm{SM}} + \Gamma^{\mathrm{tot}}_{\mathrm{INT}} + \Gamma^{\mathrm{tot}}_{\mathrm{BSM}} = \Gamma^{\mathrm{tot}}_{\mathrm{SM}} \left(1 + \sum_f \left[\sum_i A^f_i c_i + \sum_{i,j\geq i} B^f_{ij} c_i c_j\right]\right) . \tag{6.11}$$

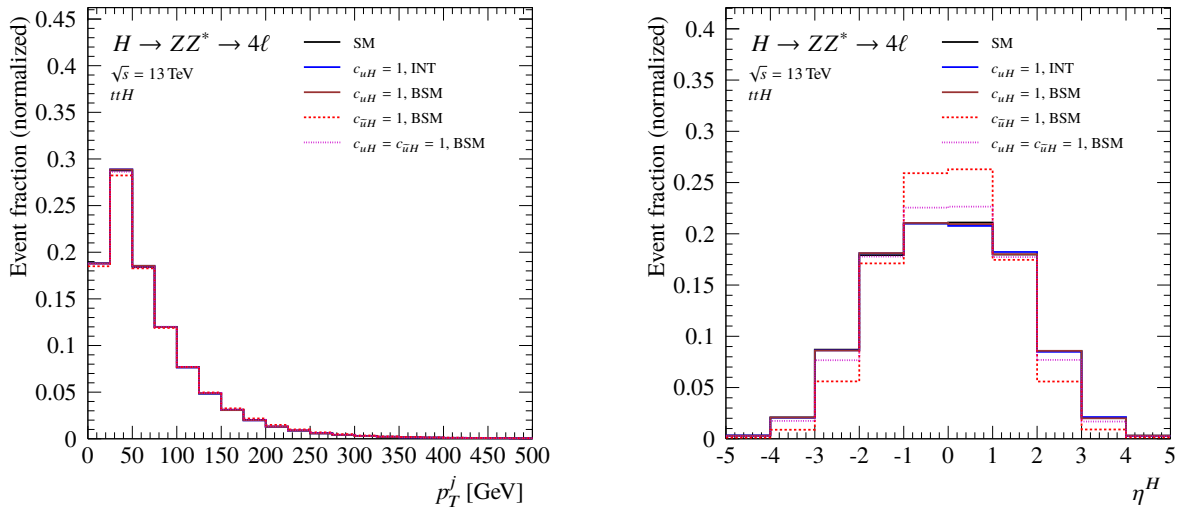

(a) (b)

Figure 6.8: The simulated distributions of (a) the jet transverse momentum p_T^j and (b) the pseudorapidity of the Higgs boson η^H in the ttH production mode. Shown are the SM, the c_{uH} interference and the pure BSM terms for c_{uH} and $c_{\tilde{u}H}$. All distributions are normalized to unit area.

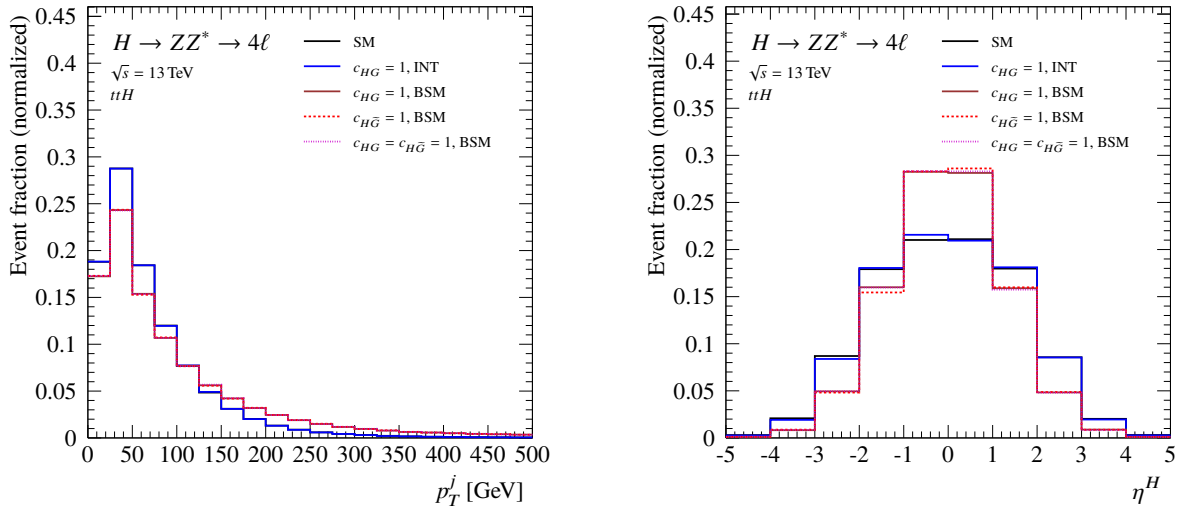

(a) (b)

Figure 6.9: The simulated distributions of (a) the jet transverse momentum p_T^j and (b) the pseudorapidity of the Higgs boson η^H in the ttH production mode. Shown are the SM, the c_{HG} interference and the pure BSM terms for c_{HG} and $c_{H\tilde{G}}$. All distributions are normalized to unit area.

$A_i^{4\ell}$ and $B_{ij}^{4\ell}$ are the prefactors of the linear and quadratic EFT terms in the Higgs boson decay to four leptons, and A_i^f and B_{ij}^f are the corresponding prefactors in the decay into the final state f. The

Table 6.8: Percentage of ttH, $tHjb$ and tHW events in the ttH particle-level production bin of the Reduced-Stage-1.1 scheme. INT denotes the SM-BSM interference terms (MADGRAPH5_aMC@NLO syntax `NP^2==1`), and BSM denotes pure BSM terms (MADGRAPH5_aMC@NLO syntax `NP^2==2`).

			ttH			
STXS bin ttH	SM 98.3 %	$c_{uH}=1$, INT 98.4 %	$c_{uH}=1$, BSM 98.4 %	$c_{HG}=1$, INT 97.8 %	$c_{HG}=1$, BSM 98.1 %	$c_{uH}=c_{HG}=1$, BSM 98.2 %
STXS bin ttH			$c_{\bar{u}H}=1$, BSM 99.1 %		$c_{H\tilde{G}}=1$, BSM 98.2 %	$c_{\bar{u}H}=c_{H\tilde{G}}=1$, BSM 98.2 %
STXS bin ttH		$c_{uH}=c_{\bar{u}H}=1$, BSM 98.6 %	$c_{uH}=c_{H\tilde{G}}=1$, BSM 98.2 %	$c_{HG}=c_{\bar{u}H}=1$, BSM 98.1 %	$c_{HG}=c_{H\tilde{G}}=1$, BSM 98.2 %	
			tHjb			
STXS bin ttH	SM 90.6 %	$c_{uH}=1$, INT 103.8 %	$c_{uH}=1$, BSM 97.9 %	$c_{HG}=1$, INT 102.7 %	$c_{HG}=1$, BSM 95.7 %	$c_{uH}=c_{HG}=1$, BSM 95.9 %
STXS bin ttH			$c_{\bar{u}H}=1$, BSM 98.3 %		$c_{H\tilde{G}}=1$, BSM 95.8 %	$c_{\bar{u}H}=c_{H\tilde{G}}=1$, BSM 96.1 %
STXS bin ttH		$c_{uH}=c_{\bar{u}H}=1$, BSM 98.4 %	$c_{uH}=c_{H\tilde{G}}=1$, BSM 95.9 %	$c_{HG}=c_{\bar{u}H}=1$, BSM 96.0 %	$c_{HG}=c_{H\tilde{G}}=1$, BSM 96.1 %	
			tHW			
STXS bin ttH	SM 99.3 %	$c_{uH}=1$, INT 99.3 %	$c_{uH}=1$, BSM 99.1 %	$c_{HG}=1$, INT 98.7 %	$c_{HG}=1$, BSM 97.9 %	$c_{uH}=c_{HG}=1$, BSM 98.0 %
STXS bin ttH			$c_{\bar{u}H}=1$, BSM 99.1 %		$c_{H\tilde{G}}=1$, BSM 97.9 %	$c_{\bar{u}H}=c_{H\tilde{G}}=1$, BSM 98.0 %
STXS bin ttH		$c_{uH}=c_{\bar{u}H}=1$, BSM 98.5 %	$c_{uH}=c_{H\tilde{G}}=1$, BSM 97.5 %	$c_{HG}=c_{\bar{u}H}=1$, BSM 97.4 %	$c_{HG}=c_{H\tilde{G}}=1$, BSM 97.4 %	

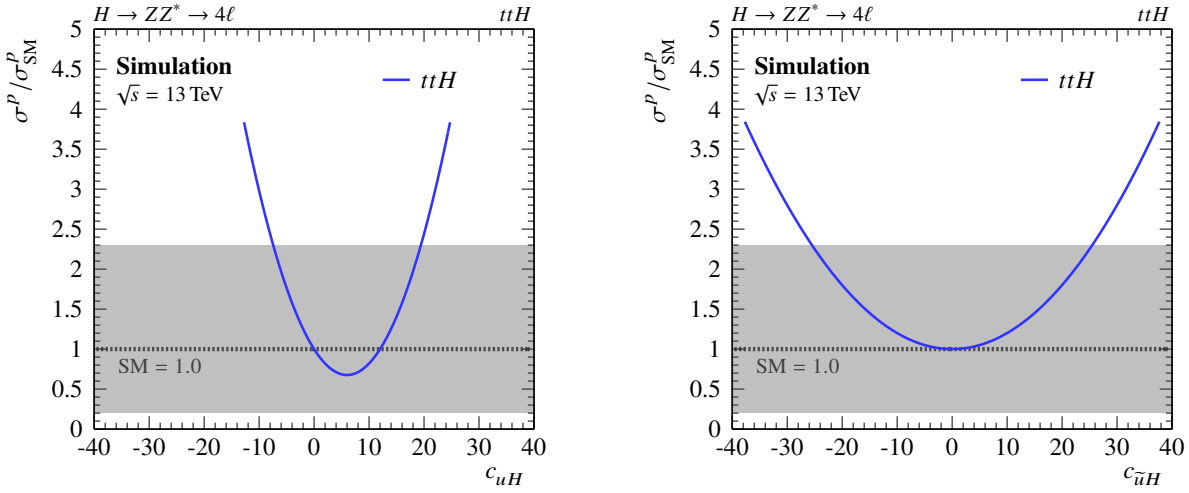

(a) (b)

Figure 6.10: The one-dimensional dependence of the cross-section ratio, $\sigma/\sigma_{\mathrm{SM}}$, in the ttH particle-level production bin in the Reduced Stage 1.1 scheme on the BSM coupling parameters (a) c_{uH} and (b) $c_{\bar{u}H}$ assuming that all others are set to zero.

$H \to ZZ^* \to 4\ell$ decay branching ratio is given by

$$\mathrm{BR}^{4\ell}(\boldsymbol{c}) = \frac{\Gamma^{4\ell}(\boldsymbol{c})}{\Gamma^{\mathrm{tot}}(\boldsymbol{c})} = \frac{\Gamma^{4\ell}_{\mathrm{SM}}}{\Gamma^{\mathrm{tot}}_{\mathrm{SM}}} \cdot \frac{1 + \sum_i A^{4\ell}_i c_i + \sum_{i,j\geq i} B^{4\ell}_{ij} c_i c_j}{1 + \sum_f \left(\sum_i A^f_i c_i + \sum_{i,j\geq i} B^f_{ij} c_i c_j \right)} . \tag{6.12}$$

Table 6.9: EFT parameterization of the production cross-section ratio, $\sigma/\sigma_{\text{SM}}$, for each particle-level bin of the Reduced Stage 1.1 scheme depending on the $C\mathcal{P}$-even and $C\mathcal{P}$-odd BSM coupling parameters.

STXS bin	EFT parameterization for $\sigma/\sigma_{\text{SM}}$
gg2H-0j-p_T^H-Low	$1 + 35.8c_{HG} + 325c_{HG}^2 + 319c_{H\widetilde{G}}^2$
gg2H-0j-p_T^H-High	$1 + 35.5c_{HG} + 319c_{HG}^2 + 320c_{H\widetilde{G}}^2$
gg2H-1j-p_T^H-Low	$1 + 31.9c_{HG} + 270c_{HG}^2 + 272c_{H\widetilde{G}}^2$
gg2H-1j-p_T^H-Medium	$1 + 29.1c_{HG} + 234c_{HG}^2 + 240c_{H\widetilde{G}}^2$
gg2H-1j-p_T^H-High	$1 + 28.6c_{HG} + 244c_{HG}^2 + 246c_{H\widetilde{G}}^2$
gg2H-2j	$1 + 17.8c_{HG} + 120c_{HG}^2 + 114c_{H\widetilde{G}}^2$
gg2H-p_T^H-High	$1 + 16.8c_{HG} + 155c_{HG}^2 + 164c_{H\widetilde{G}}^2$
qq2Hqq-VBF	$1 + 0.059c_{HW} + 0.092c_{HW}^2 + 0.002c_{HB} + 0.027c_{HB}^2 + 0.037c_{HWB} + 0.018c_{HWB}^2 + 0.015c_{HW}c_{HB} - 0.016c_{HW}c_{HWB} - 0.024c_{HB}c_{HWB}$ $+ 0.062c_{H\widetilde{W}}^2 + 0.025c_{H\widetilde{B}}^2 + 0.015c_{H\widetilde{W}B}^2 + 0.015c_{H\widetilde{W}}c_{H\widetilde{B}} - 0.017c_{H\widetilde{W}}c_{H\widetilde{W}B} - 0.026c_{H\widetilde{B}}c_{H\widetilde{W}B}$
qq2Hqq-VH-Like	$1 + 0.598c_{HW} + 0.260c_{HW}^2 + 0.020c_{HB} + 0.015c_{HB}^2 + 0.090c_{HWB} + 0.023c_{HWB}^2 + 0.005c_{HW}c_{HB} + 0.036c_{HW}c_{HWB} + 0.005c_{HB}c_{HWB}$ $+ 0.191c_{H\widetilde{W}}^2 + 0.013c_{H\widetilde{B}}^2 + 0.012c_{H\widetilde{W}B}^2 + 0.002c_{H\widetilde{W}}c_{H\widetilde{B}} + 0.010c_{H\widetilde{W}}c_{H\widetilde{W}B}$
qq2Hqq-BSM	$1 + 0.191c_{HW} + 0.510c_{HW}^2 - 0.001c_{HB} + 0.058c_{HB}^2 + 0.040c_{HWB} + 0.049c_{HWB}^2 + 0.011c_{HW}c_{HB} - 0.057c_{HW}c_{HWB} - 0.029c_{HB}c_{HWB}$ $+ 0.514c_{H\widetilde{W}}^2 + 0.059c_{H\widetilde{B}}^2 + 0.052c_{H\widetilde{W}B}^2 + 0.011c_{H\widetilde{W}}c_{H\widetilde{B}} - 0.067c_{H\widetilde{W}}c_{H\widetilde{W}B} - 0.033c_{H\widetilde{B}}c_{H\widetilde{W}B}$
VH-Lep	$1 + 0.828c_{HW} + 0.324c_{HW}^2 + 0.035c_{HB} + 0.013c_{HB}^2 + 0.128c_{HWB} + 0.027c_{HWB}^2 - 0.219c_{HW}c_{HB} - 0.160c_{HW}c_{HWB} + 0.021c_{HB}c_{HWB}$ $+ 0.208c_{H\widetilde{W}}^2 + 0.014c_{H\widetilde{B}}^2 + 0.016c_{H\widetilde{W}B}^2 - 0.142c_{H\widetilde{W}}c_{H\widetilde{B}} - 0.121c_{H\widetilde{W}}c_{H\widetilde{W}B} + 0.008c_{H\widetilde{B}}c_{H\widetilde{W}B}$
ttH	$1 - 0.108c_{uH} + 0.009c_{uH}^2 + 0.483c_{HG} + 0.590c_{HG}^2 - 0.016c_{uH}c_{HG}$ $+ 0.002c_{\widetilde{u}H}^2 + 0.599c_{H\widetilde{G}}^2 + 0.043c_{\widetilde{u}H}c_{H\widetilde{G}}$

Table 6.10: MADGRAPH5_aMC@NLO syntax and BSM dependence for the SM, the SM-BSM interference, and the pure BSM part of the Higgs boson partial decay widths.

Term	partial decay width	syntax	BSM dependence	suppressed by
Pure SM	$\Gamma_{\text{SM}}^{4\ell/\text{tot}}$	`NP^2==0`	-	1
SM-BSM interference	$\Gamma_{\text{INT}}^{4\ell/\text{tot}}$	`NP^2==1`	linear	$1/\Lambda^2$
Pure BSM	$\Gamma_{\text{BSM}}^{4\ell/\text{tot}}$	`NP^2==2`	quadratic	$1/\Lambda^4$

By changing the summation order, the prefactors in the denominator can be expressed as $A_i^{\text{tot}} = \sum_f A_i^f$ and $B_{ij}^{\text{tot}} = \sum_f B_{ij}^f$. The decay width of the Higgs boson is computed at `LO` using MADGRAPH5_aMC@NLO. Assuming that higher-order corrections of the SM and BSM processes are identical, the branching ratio can be expressed as a relative correction to the SM prediction at `NLO`,

$$\frac{\text{BR}^{4\ell,\texttt{NLO}}(\boldsymbol{c})}{\text{BR}_{\text{SM}}^{4\ell,\texttt{NLO}}} = \frac{\text{BR}^{4\ell}(\boldsymbol{c})}{\text{BR}_{\text{SM}}^{4\ell}} = \frac{\Gamma^{4\ell}(\boldsymbol{c})/\Gamma_{\text{SM}}^{4\ell}}{\Gamma^{\text{tot}}(\boldsymbol{c})/\Gamma_{\text{SM}}^{\text{tot}}} = \frac{1 + \sum_i A_i^{4\ell} c_i + \sum_{i,j\geq i} B_{ij}^{4\ell} c_i c_j}{1 + \sum_i A_i^{\text{tot}} c_i + \sum_{i,j\geq i} B_{ij}^{\text{tot}} c_i c_j}\,. \tag{6.13}$$

The MADGRAPH5_aMC@NLO input syntax and the BSM dependence are summarized in Table 6.10.

To parameterize the scale factor for the $H \to ZZ^* \to 4\ell$ branching ratio, 61 samples with 100 000 events, each, are generated. The Higgs boson's total width is calculated by considering the dominant decay modes of the Higgs boson given in Table 6.11. It depends on the BSM coupling parameters c_{HW}, c_{HB}, c_{HWB}, c_{HG}, $c_{H\widetilde{W}}$, $c_{H\widetilde{B}}$, $c_{H\widetilde{W}B}$, and $c_{H\widetilde{G}}$. However, c_{HG} and $c_{H\widetilde{G}}$ do not contribute to the HVV interaction vertex. Thus they do not appear together with the other Wilson coefficients. Thus, 33 samples are required to determine the total width of the Higgs boson. Since the $H \to 4\ell$ decay channel does not depend on c_{HG} and $c_{H\widetilde{G}}$, only 28 samples are required in this case. Theoretically, the total number of samples can be reduced since the $C\mathcal{P}$-odd interference terms are expected to vanish. However, these terms are generated to guarantee that the widths are consistent with zero. For the sample generation,

Table 6.11: MADGRAPH5_aMC@NLO syntax and the number of samples required to parameterize the total width of the Higgs boson and the partial decay width for the decay into the four-lepton final states.

Decay mode	Madgraph syntax	number of SM samples	number of BSM samples		
			pure $C\mathcal{P}$-even	pure $C\mathcal{P}$-odd	mixed
$H \to \gamma\gamma$	`generate h > a a`				
$H \to Z\gamma$	`add process h > z a`				
$H \to bb$	`add process h > b b~`				
$H \to gg$	`add process h > g g`				
$H \to W\ell\nu$	`add process h > w+ l- vl~` `add process h > w- l+ vl`				
$H \to Wjj$	`add process h > w+ j j` `add process h > w- j j`				
$H \to Z\ell\ell$	`add process h > z l+ l-`				
$H \to Zjj$	`add process h > z j j`				
$H \to Z\nu\nu$	`add process h > z vl vl~`	1	11	11	10
$H \to 4\ell$	`add process h > l+ l- l+ l-`	1	9	9	9

the massless version of the SMEFT model is used. The Higgs boson decay width is set to its SM value at LO, $\Gamma_{\text{SM}}^{\text{tot,LO}} = 4.995\,\text{MeV}$ and its mass is set to 125 GeV. Two generator-level cuts are applied in the sample generation. The first one is a cut on the tails of the Breit-Wigner distribution of the resonance. It requires the Higgs boson to be on-shell if its invariant mass is within $m_H \pm 15 \cdot \Gamma^{\text{tot}}$. The second one rejects leptons if their angular separation $\Delta R(\ell_i, \ell_j)$ is below 0.05. The MADGRAPH5_aMC@NLO syntax for these cuts is

$$\text{bwcutoff} = 15 \quad \text{and} \quad \text{drll} = 0.05,$$

respectively.

The calculated $H \to 4\ell$ and total decay widths for the SM, the SM-BSM interference, and the pure BSM terms are shown in Table 6.12. All SM-BSM interference terms containing $C\mathcal{P}$-odd operators are consistent with zero and only upper limits given by the statistical uncertainty are stated. In the case of mixed BSM terms with $C\mathcal{P}$-even and $C\mathcal{P}$-odd amplitudes, no contributions from the interference are observed. For the $H \to 4\ell$ decay mode, the differences between the $C\mathcal{P}$-even and $C\mathcal{P}$-odd quadratic terms are small but significantly larger than the statistical uncertainty given by MADGRAPH5_aMC@NLO. The resulting EFT parameterizations for the scale factors of the partial and total decay widths, $\Gamma^{4\ell}(\boldsymbol{c})/\Gamma^{4\ell}_{\text{SM}}$ and $\Gamma^{\text{tot}}(\boldsymbol{c})/\Gamma^{\text{tot}}_{\text{SM}}$, respectively, are given in Table 6.13.

Figure 6.11 shows the one-dimensional projections of $\text{BR}(c))/\text{BR}_{\text{SM}}$ onto the relevant CP-even and CP-odd BSM coupling parameters. The branching ratio raises with the Wilson coefficients that contribute to the HZZ vertex, and is most affected by c_{HW} and $c_{H\widetilde{W}}$ (see Figure 6.11(a)). This leads to an increase in sensitivity for the corresponding BSM parameters when the production and decay parameterizations are combined compared to the production-only parameterization (see Section 6.3.1). For absolute values of $|c_{HB}| \approx |c_{H\widetilde{B}}| \approx 1$, the branching ratio quickly doubles compared to the SM prediction, but the further increase has little impact (see Figure 6.11(b)). A similar behavior is observed for c_{HWB} and $c_{H\widetilde{W}B}$ (see Figure 6.11(c)). The $H \to 4\ell$ branching ratio drops quickly if c_{HG} or $c_{H\widetilde{G}}$ are increased as shown in Figure 6.11(d)). However, for the $C\mathcal{P}$-even coupling parameter, there is even a small window between -0.1 and 0.0 where the branching ratio is slightly increased. This is caused by the positive linear term, which reduces the total decay width Γ^{tot} for small negative values of c_{HG}. The overall impact of c_{HG} and $c_{H\widetilde{G}}$ on the decay branching ratio is expected to be very small. Within the expected sensitivity of c_{HG}

Table 6.12: The Higgs boson partial decay width into four-lepton final states and the total Higgs boson decay width in the SM and for different EFT terms. INT denotes the SM-BSM interference terms (MADGRAPH5_aMC@NLO syntax `NP^2==1`), and BSM denotes pure BSM terms (MADGRAPH5_aMC@NLO syntax `NP^2==2`). For terms with two BSM coupling parameters set to 1, the abbreviation 'BSM' is dropped to improve readability.

					$H \to 4\ell$					
$C\mathcal{P}$-even	SM	$c_{HW} = 1$ INT	$c_{HW} = 1$ BSM	$c_{HB} = 1$ INT	$c_{HB} = 1$ BSM	$c_{HWB} = 1$ INT	$c_{HWB} = 1$ BSM	$c_{HW} = 1$, $c_{HB} = 1$	$c_{HW} = 1$, $c_{HWB} = 1$	$c_{HB} = 1$, $c_{HWB} = 1$
Width [MeV]	$5.02 \cdot 10^{-4}$	$-1.00 \cdot 10^{-4}$	$3.78 \cdot 10^{-4}$	$-5.63 \cdot 10^{-5}$	$1.34 \cdot 10^{-3}$	$9.06 \cdot 10^{-5}$	$3.82 \cdot 10^{-4}$	$1.70 \cdot 10^{-3}$	$1.13 \cdot 10^{-4}$	$1.02 \cdot 10^{-3}$
$C\mathcal{P}$-odd		$c_{H\widetilde{W}} = 1$ INT	$c_{H\widetilde{W}} = 1$ BSM	$c_{H\widetilde{B}} = 1$ INT	$c_{H\widetilde{B}} = 1$ BSM	$c_{H\widetilde{W}B} = 1$ INT	$c_{H\widetilde{W}B} = 1$ BSM	$c_{H\widetilde{W}} = 1$, $c_{H\widetilde{B}} = 1$	$c_{H\widetilde{W}} = 1$, $c_{H\widetilde{W}B} = 1$	$c_{H\widetilde{B}} = 1$, $c_{H\widetilde{W}B} = 1$
Width [MeV]		$< 10^{-6}$	$3.52 \cdot 10^{-4}$	$< 10^{-6}$	$1.30 \cdot 10^{-3}$	$< 10^{-6}$	$4.07 \cdot 10^{-4}$	$1.68 \cdot 10^{-3}$	$9.43 \cdot 10^{-5}$	$9.85 \cdot 10^{-4}$
Mixed terms		$c_{HW} = 1$, $c_{H\widetilde{W}} = 1$	$c_{HW} = 1$, $c_{H\widetilde{B}} = 1$	$c_{HW} = 1$, $c_{H\widetilde{W}B} = 1$	$c_{HB} = 1$, $c_{H\widetilde{W}} = 1$	$c_{HB} = 1$, $c_{H\widetilde{B}} = 1$	$c_{HB} = 1$, $c_{H\widetilde{W}B} = 1$	$c_{HWB} = 1$, $c_{H\widetilde{W}} = 1$	$c_{HWB} = 1$, $c_{H\widetilde{B}} = 1$	$c_{HWB} = 1$, $c_{H\widetilde{W}B} = 1$
Width [MeV]		$7.30 \cdot 10^{-4}$	$1.67 \cdot 10^{-3}$	$7.85 \cdot 10^{-4}$	$1.69 \cdot 10^{-3}$	$2.63 \cdot 10^{-3}$	$1.74 \cdot 10^{-3}$	$7.35 \cdot 10^{-4}$	$1.68 \cdot 10^{-3}$	$7.89 \cdot 10^{-4}$
					$\sum_f H \to f$					
$C\mathcal{P}$-even	SM	$c_{HW} = 1$ INT	$c_{HW} = 1$ BSM	$c_{HB} = 1$ INT	$c_{HB} = 1$ BSM	$c_{HWB} = 1$ INT	$c_{HWB} = 1$ BSM	$c_{HW} = 1$, $c_{HB} = 1$	$c_{HW} = 1$, $c_{HWB} = 1$	$c_{HB} = 1$, $c_{HWB} = 1$
Width [MeV]	4.99	-0.269	0.808	-0.377	6.03	0.309	1.782	9.42	0.392	2.169
		$c_{HG} = 1$ INT	$c_{HG} = 1$ BSM							
		7.58	74.4							
$C\mathcal{P}$-odd		$c_{H\widetilde{W}} = 1$ INT	$c_{H\widetilde{W}} = 1$ BSM	$c_{H\widetilde{B}} = 1$ INT	$c_{H\widetilde{B}} = 1$ BSM	$c_{H\widetilde{W}B} = 1$ INT	$c_{H\widetilde{W}B} = 1$ BSM	$c_{H\widetilde{W}} = 1$, $c_{H\widetilde{B}} = 1$	$c_{H\widetilde{W}} = 1$, $c_{H\widetilde{W}B} = 1$	$c_{H\widetilde{B}} = 1$, $c_{H\widetilde{W}B} = 1$
Width [MeV]		$< 10^{-6}$	0.807	$< 10^{-6}$	6.03	$< 10^{-7}$	1.782	9.42	0.390	2.168
		$c_{H\widetilde{G}} = 1$ INT	$c_{H\widetilde{G}} = 1$ BSM							
		$< 10^{-5}$	74.4							
Mixed terms		$c_{HW} = 1$, $c_{H\widetilde{W}} = 1$	$c_{HW} = 1$, $c_{H\widetilde{B}} = 1$	$c_{HW} = 1$, $c_{H\widetilde{W}B} = 1$	$c_{HB} = 1$, $c_{H\widetilde{W}} = 1$	$c_{HB} = 1$, $c_{H\widetilde{B}} = 1$	$c_{HB} = 1$, $c_{H\widetilde{W}B} = 1$	$c_{HWB} = 1$, $c_{H\widetilde{W}} = 1$	$c_{HWB} = 1$, $c_{H\widetilde{B}} = 1$	$c_{HWB} = 1$, $c_{H\widetilde{W}B} = 1$
Width [MeV]		1.62	6.84	2.591	6.84	12.06	7.81	2.589	7.81	3.56
		$c_{HG} = c_{H\widetilde{G}} = 1$ 149.2								

Table 6.13: EFT parameterization of the scale factors for the Higgs boson decay width into four-lepton final states and total Higgs decay width in terms of the BSM parameters c_{HW}, c_{HB}, c_{HWB}, c_{HG}, $c_{H\widetilde{W}}$, $c_{H\widetilde{B}}$, $c_{H\widetilde{W}B}$, and $c_{H\widetilde{G}}$.

Decay process	EFT parameterization of $\Gamma/\Gamma_{\text{SM}}$
$\frac{\Gamma^{4\ell}(\mathbf{c})}{\Gamma^{4\ell}_{\text{SM}}}$	$1 - 0.199c_{HW} + 0.753c_{HW}^2 - 0.112c_{HB} + 2.67c_{HB}^2 + 0.181c_{HWB} + 0.760c_{HWB}^2 - 0.042c_{HW}c_{HB} - 1.29c_{HW}c_{HWB} - 1.40c_{HB}c_{HWB}$ $+ 0.702c_{H\widetilde{W}}^2 + 2.59c_{H\widetilde{B}}^2 + 0.811c_{H\widetilde{W}B}^2 + 0.050c_{H\widetilde{W}}c_{H\widetilde{B}} - 1.33c_{H\widetilde{W}}c_{H\widetilde{W}B} - 1.43c_{H\widetilde{B}}c_{H\widetilde{W}B}$
$\frac{\Gamma^{\text{tot}}(\mathbf{c})}{\Gamma^{\text{tot}}_{\text{SM}}}$	$1 - 0.054c_{HW} + 0.162c_{HW}^2 - 0.075c_{HB} + 1.21c_{HB}^2 + 0.062c_{HWB} + 0.36c_{HWB}^2 + 1.52c_{HG} + 14.9c_{HG}^2 + 0.52c_{HW}c_{HB} - 0.44c_{HW}c_{HWB} - 1.13c_{HB}c_{HWB}$ $+ 0.161c_{H\widetilde{W}}^2 + 1.21c_{H\widetilde{B}}^2 + 0.36c_{H\widetilde{W}B}^2 + 14.9c_{HG}^2 + 0.52c_{H\widetilde{W}}c_{H\widetilde{B}} - 0.44c_{H\widetilde{W}}c_{H\widetilde{W}B} - 1.13c_{H\widetilde{B}}c_{H\widetilde{W}B}$

and $c_{H\widetilde{G}}$ (given in Section 6.1.1) it deviates by less than 1 % from the SM prediction.

6.3 Parameterization of the Acceptance

The previous sections showed that the introduction of higher-dimensional interaction operators leads to modifications of the production cross-section and decay width of processes that are sensitive to the respective operator. The overall magnitude of the effect is parameterized as a function of the corresponding Wilson coefficients as demonstrated in Equation 6.6 and 6.13, respectively. The latter is given as a scale factor for the branching ratio of the Higgs boson decay into four-lepton final states. The combined effect of production cross-section times decay branching ratio is found by multiplying both equations. At first

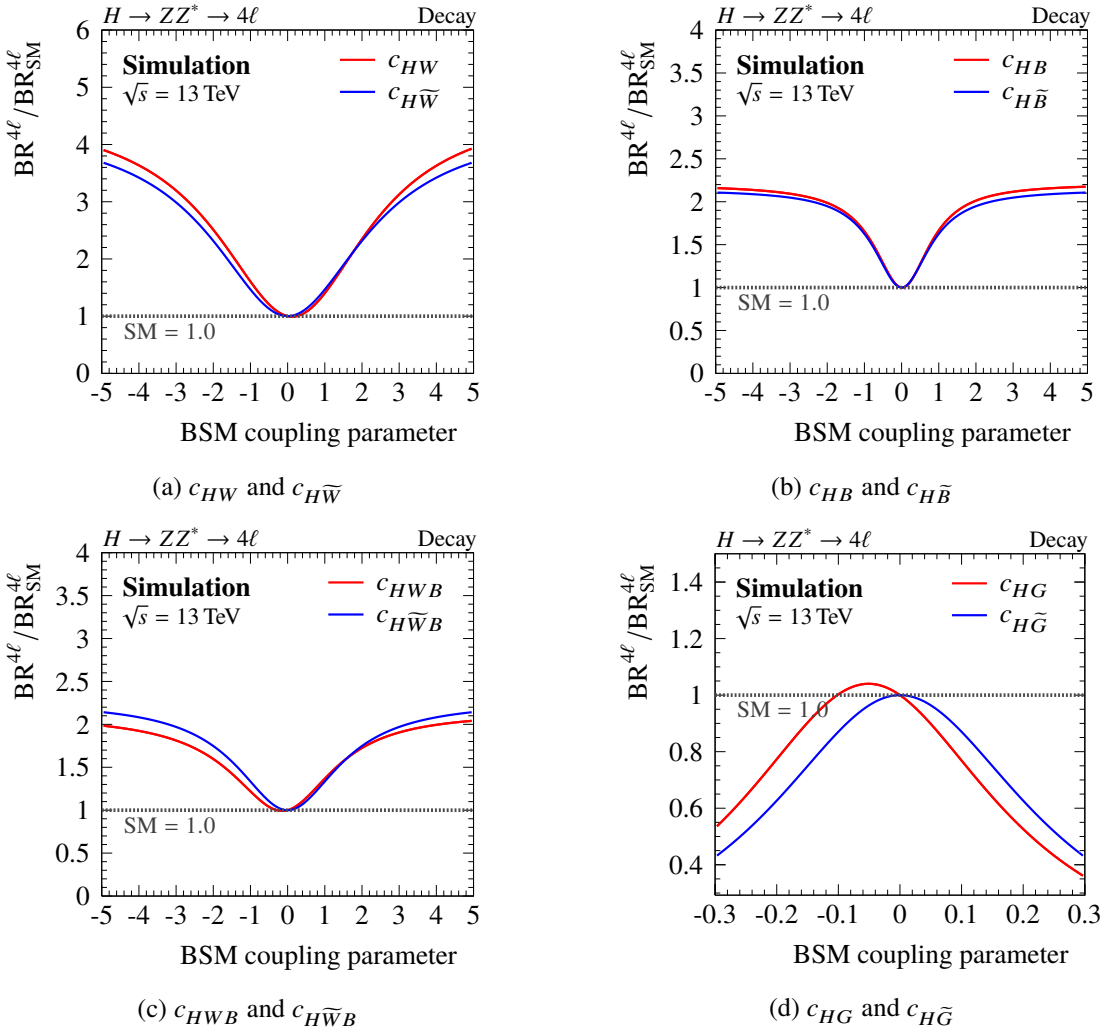

(a) c_{HW} and $c_{H\widetilde{W}}$ (b) c_{HB} and $c_{H\widetilde{B}}$

(c) c_{HWB} and $c_{H\widetilde{W}B}$ (d) c_{HG} and $c_{H\widetilde{G}}$

Figure 6.11: The one-dimensional dependence of the branching ratio modifier $\mathrm{BR}^{4\ell}/\mathrm{BR}^{4\ell}_{\mathrm{SM}}$ on the relevant BSM coupling modifiers, assuming that all others are set to zero.

glance, this prescription seems to provide a complete description of the EFT signal processes. However, new physics operators can also modify the shape of kinematic variables. For instance, in Section 6.1, it is shown that the pure BSM terms tend to generate the Higgs boson more centrally in the detector and with smaller transverse momentum compared to the SM prediction. The magnitude of the effect depends on the sensitivity of the kinematic variables on the BSM coupling parameters. In the $H \to ZZ^* \to 4\ell$ cross-section analysis, some observables that are used to select the Higgs boson candidates strongly depend on some of the EFT parameters. This typically results in fewer events that are accepted by the analysis compared to the SM. Section 6.3.1 discusses the acceptance parameterization for the $C\mathcal{P}$-odd BSM operators. The corresponding $C\mathcal{P}$-even parameterization is found in the References [359, 459]. However, the main results are summarized in Appendix D.5.

Higher-dimensional interaction operators do not just affect the kinematic variables that influence the Higgs boson selection in the $H \to 4\ell$ decay; they also affect variables that define the Higgs boson production bins to some extent. This could lead to varying event fractions in the different particle-level production bins if the Wilson coefficients are increased. However, for the gg2H bins, this effect is expected to be very small since the bin-defining variables are rather stable with respect to BSM contributions

(see Figure 6.1). Moreover, in the expected sensitivity range $|c_{H\widetilde{G}}| < 0.022$ ($|c_{HG}| < 0.005$), the BSM contribution to the gg2H production cross-section is smaller than 12 % (16 %).

For the production and decay parameterizations, it was shown that the $C\mathcal{P}$-even/$C\mathcal{P}$-odd interference terms vanish for dimension-six operators. However, due to the more stringent cuts of the Higgs boson candidate selection, the corresponding terms in the signal acceptance are separately studied in Section 6.3.2.

6.3.1 Signal Acceptance in the $H \to 4\ell$ Channel

Two variables that are used to select Higgs boson candidates in the $H \to 4\ell$ channel are the invariant mass of the on-shell (m_{12}) and off-shell (m_{34}) Z bosons. Both distributions are shown in Figure 6.12 for the SM and for different values of the BSM coupling parameters $c_{H\widetilde{W}}$ and $c_{H\widetilde{B}}$. The invariant mass distribution of the leading lepton pair is almost stable with respect to $c_{H\widetilde{W}}$ (see Figure 6.12(a)). However, this is not true for the parameters $c_{H\widetilde{B}}$ (see Figure 6.12(b)) and $c_{H\widetilde{W}B}$ (see Figure D.1(c)). In these cases, many events are generated outside of the acceptance region (50 GeV $< m_{12} <$ 106 GeV). The invariant mass of the subleading lepton pair is required to be at least 12 GeV if the four-lepton invariant mass $m_{4\ell}$ is smaller than 140 GeV. For larger $m_{4\ell}$, the requirement on m_{34} is raised to 50 GeV. The spectrum changes drastically within this interesting mass window if BSM contributions are turned on. In the SM, most events are generated between 20 GeV and 30 GeV. In contrast, in scenarios with sizable BSM contributions, most of the events are generated for invariant masses below 10 GeV. This is shown in Figures 6.12(c) and6.12(d), and it implies that the larger the absolute value of a single BSM coupling parameter, the fewer Higgs boson candidates are accepted, i. e. the less sensitive the measurement.

For a single $C\mathcal{P}$-odd BSM coupling parameter, these distributions are symmetric with respect to the sign of the corresponding Wilson coefficient since there are no linear EFT terms in this case. This is different for $C\mathcal{P}$-even operators, and in particular for small coupling parameters as demonstrated in Figures D.1 and D.2. In this case, the SM-BSM interference terms break the symmetry with respect to the sign of the Wilson coefficient. Therefore, separate acceptance models for the $C\mathcal{P}$-even and $C\mathcal{P}$-odd parameterizations are considered. The invariant mass distributions corresponding to the $C\mathcal{P}$-even case are discussed in detail in Reference [459], but they are also added to Appendix D.2.1 for a direct comparison.

Figure 6.13 shows the invariant mass distributions in case that more than one Wilson coefficient is simultaneously unequal to zero and compares them to the SM prediction. Due to the negative interferences (see Table 6.13) between $c_{H\widetilde{W}}$ and $c_{H\widetilde{W}B}$ (and $c_{H\widetilde{B}}$ and $c_{H\widetilde{W}B}$) some parameter combinations result in larger event fractions that are accepted compared to the case in which only one parameter is turned on. For example, the parameter combination $c_{H\widetilde{W}} = c_{H\widetilde{B}} = c_{H\widetilde{W}B} = 0.3$ results in more events that pass the selection criteria for m_{34} than the parameter combination $c_{H\widetilde{W}} = c_{H\widetilde{B}} = 0.3$ with $c_{H\widetilde{W}B} = 0$. This is shown in Figure 6.13(c) with the solid-magenta and the solid-red line, respectively. The relative sign between two parameters also impacts the shape of the invariant mass distributions. The red-solid and red-dashed lines illustrate this behaviour for the parameter combinations ($c_{H\widetilde{W}} = 0.3, c_{H\widetilde{B}} = 0.3$) and ($c_{H\widetilde{W}} = 0.3, c_{H\widetilde{B}} = -0.3$). This effect results from the mixed BSM terms that are proportional to $c_i c_j$, where $i \neq j$. However, if all $C\mathcal{P}$-odd BSM parameters are multiplied by -1 at the same time, the distributions will be equal to the original ones, as demonstrated with the red-dashed and red-dotted lines. The minor differences are due to statistical fluctuations. These statements hold in general for pseudoscalar BSM coupling parameters of any size, as demonstrated in Figures 6.13(b) and 6.13(d) for ten times larger BSM couplings. However, this will be different for $C\mathcal{P}$-even operators if the linear terms dominate over the quadratic BSM contributions.

The lesson learned from this discussion is that the signal acceptance $\mathcal{A}(\boldsymbol{c})$ is a complex function of the

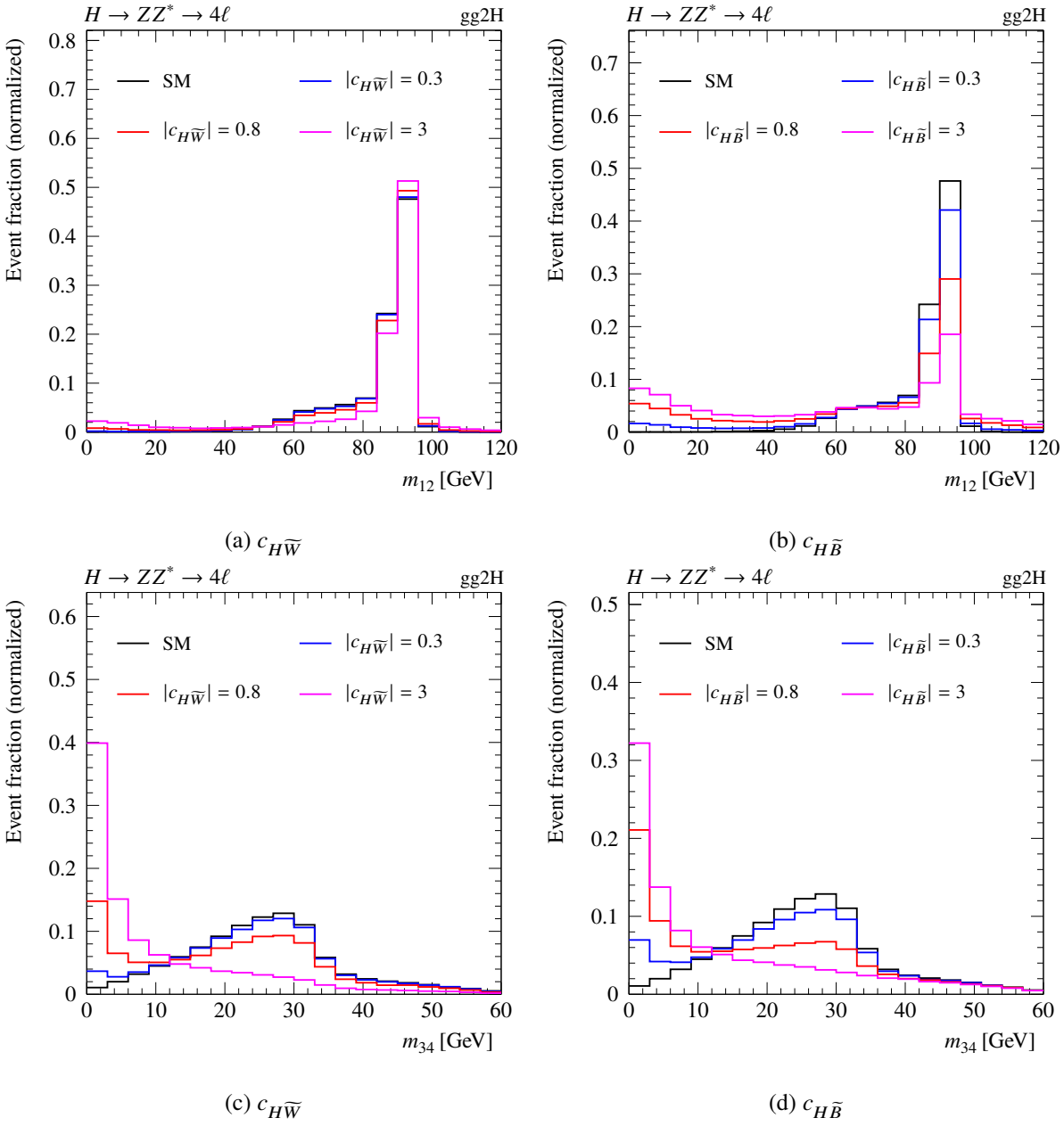

(a) $c_{H\widetilde{W}}$ (b) $c_{H\widetilde{B}}$

(c) $c_{H\widetilde{W}}$ (d) $c_{H\widetilde{B}}$

Figure 6.12: The SM expected invariant mass spectrum m_{12} of the on-shell produced Z boson (top panels), and m_{34} of the off-shell produced Z boson (bottom panels), together with the corresponding spectrum for different absolute values of the $C\mathcal{P}$-odd BSM coupling parameters $c_{H\widetilde{W}}$ and $c_{H\widetilde{B}}$. All other Wilson coefficients are set to zero.

BSM coupling parameters, which is not expected to factorize into individual acceptance factors $\mathcal{A}_i(c_i)$,

$$f(\boldsymbol{c}) = \frac{\mathcal{A}(\boldsymbol{c})}{\mathcal{A}_{SM}} \neq \frac{\prod_i \mathcal{A}_i(c_i)}{\mathcal{A}_{SM}} \,. \tag{6.14}$$

In this equation $f(\boldsymbol{c})$ refers to the correction factor that scales the SM acceptance $\mathcal{A}_{SM}$. However, such a one-dimensional approximation would significantly reduces the number of MC samples that have to be generated. To determine the 1D-acceptance correction factors for the $C\mathcal{P}$-odd parameters, $3 \times n + 1$ MC

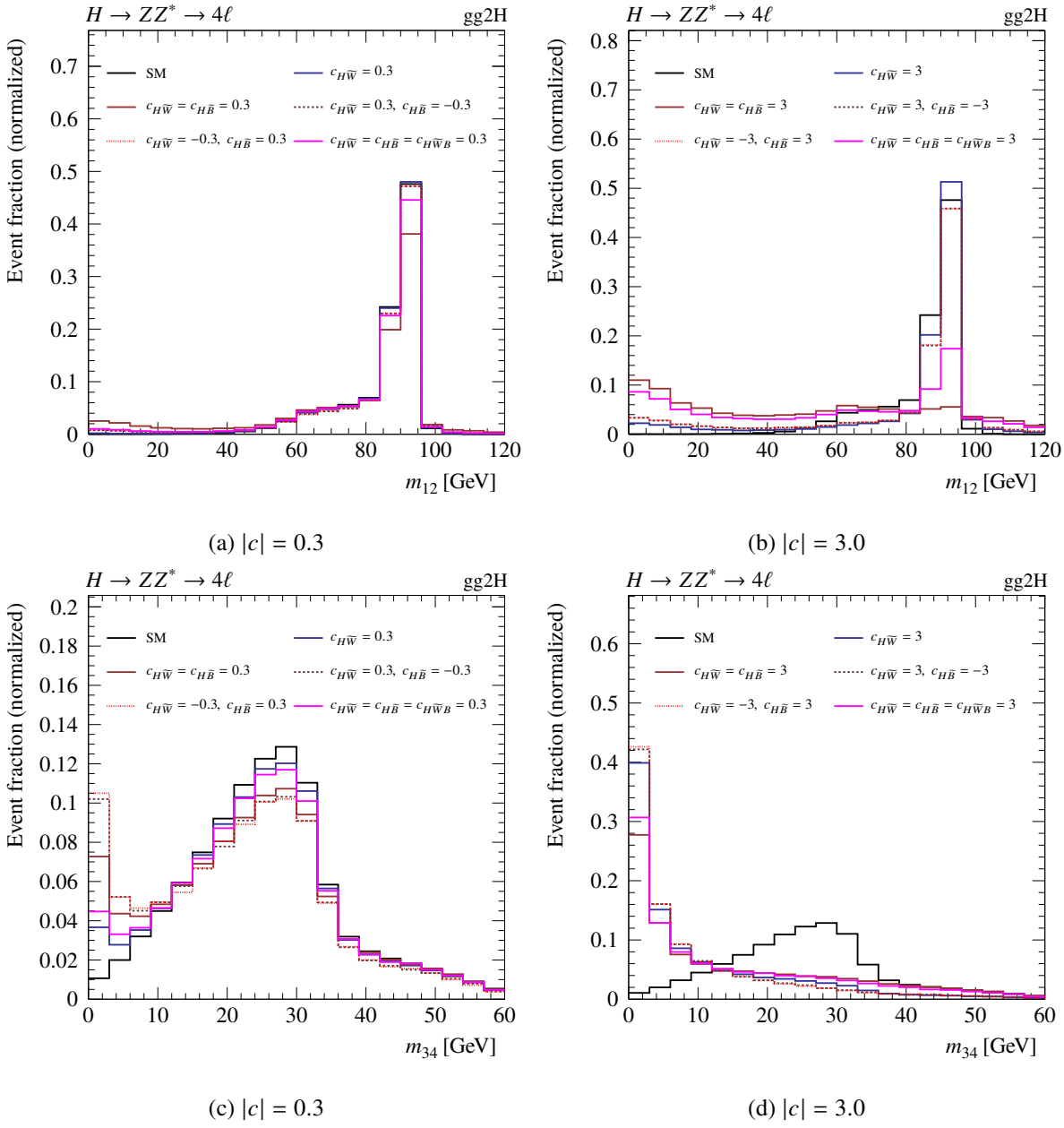

(a) $|c| = 0.3$ (b) $|c| = 3.0$

(c) $|c| = 0.3$ (d) $|c| = 3.0$

Figure 6.13: The SM expected invariant mass spectrum m_{12} of the on-shell produced Z boson (top panels), and m_{34} of the off-shell produced Z boson (bottom panels), together with different BSM scenarios featuring the same absolute values of the $C\mathcal{P}$-odd BSM coupling parameters. All other Wilson coefficients are set to zero.

samples are required with n being the number of generated BSM points on a one-dimensional grid. The additional sample is for the SM prediction. The chosen 1D grid consists of twelve BSM points,

$$c_i = \pm 10, \pm 3, \pm 2, \pm 0.8, \pm 0.5, \pm 0.3, \tag{6.15}$$

where $c_i = c_{H\widetilde{W}}, c_{H\widetilde{B}}, c_{H\widetilde{W}B}$. Including the SM point, a total of $3 \times 12 + 1 = 37$ samples are required. Using the same parameter spacing in a more realistic model with three BSM parameters requires already $12^3 + 1 = 1\,729$ samples. To reduce this number, only a subset of the grid points is chosen. The decision

is based on the criterion that the final fit results provide a reasonable description of the signal acceptance, with an emphasis on the center of the parameter region close to the SM prediction. Consequently, the point density in this region is kept high while the density in the outer region is reduced. The resource requirement for anything beyond three dimensions, i. e. including both, the $C\mathcal{P}$-even and $C\mathcal{P}$-odd operators simultaneously is huge, and as such, no effort was put into such an attempt. However, specific combinations of scalar and pseudoscalar operators are discussed in Section 6.3.2 to estimate the magnitude of corresponding interference terms. It turns out that the well-motivated approach of splitting up the $C\mathcal{P}$-even and $C\mathcal{P}$-odd acceptance factors is justified.

The acceptance scale factor is described by a three-dimensional Lorentzian function,

$$f(\boldsymbol{c}) = \widetilde{\alpha}_0 + \frac{(\widetilde{\alpha}_1)^2}{\widetilde{\alpha}_2 + \sum\limits_i \delta_i \cdot (c_i + \beta_i)^2 + \sum\limits_{i,j \geq j} \delta_{(i,j)} \cdot c_i c_j + \sum\limits_{i<j<k} \delta_{(i,j,k)} \cdot c_i c_j c_k}\,, \tag{6.16}$$

where $\widetilde{\alpha}_0$, $\widetilde{\alpha}_1$, $\widetilde{\alpha}_2$, δ_i, $\delta_{(i,j)}$ and $\delta_{(i,j,k)}$ are the free parameters, and i, j and k run over $H\widetilde{W}$, $H\widetilde{B}$ and $H\widetilde{W}B$. In order to determine the free parameters in Equation 6.16, 117 Monte Carlo samples with different BSM coupling parameters are generated. These samples include the SM, INT, and pure BSM terms, and target Higgs bosons produced via gg2H and decaying into four lepton final states. The signal acceptances are determined by feeding each sample through the event selection of the inclusive analysis and by calculating the ratio of events that pass the $H \longrightarrow 4\ell$ selection, N_{pass}, and the total number of generated events, N_{tot},

$$\mathcal{A}(\boldsymbol{c}) = \frac{N_{\text{pass}}(\boldsymbol{c})}{N_{\text{tot}}(\boldsymbol{c})}\,. \tag{6.17}$$

The generated samples and the corresponding acceptance scale factors are summarized in Table D.5. They are used as input for the fit to determine the values of the acceptance parameters listed above. A high weight is assigned to the SM point to ensure, that the fit returns the SM point for vanishing BSM coupling parameters. The result of this fit is summarized in Table 6.14 and the projections onto the $c_{H\widetilde{W}}$-$c_{H\widetilde{B}}$, $c_{H\widetilde{W}}$-$c_{H\widetilde{W}B}$ and $c_{H\widetilde{B}}$-$c_{H\widetilde{W}B}$ planes are visualized in Figure 6.14. The general agreement between the fit and simulated data is very good. Compared to the SM, the acceptance is strongly reduced in all scenarios with sizable BSM contributions. For the parameter point $(c_{H\widetilde{W}}, c_{H\widetilde{B}}, c_{H\widetilde{W}B}) = (0.8, 0, 0)$, it drops to 73.0 %, while for $(3, 0, 0)$ it is already down to 23.6 %. The acceptance typically decreases even faster if two BSM operators contribute at the same time. For instance, the acceptance is at 40.9 % and 15.2 % for $(0.8, 0.8, 0)$ and $(3, 3, 0)$, respectively. However, along the diagonal in the $c_{H\widetilde{W}}$-$c_{H\widetilde{W}B}$ plane it decreases significantly slower. In the case of $c_{H\widetilde{W}} = c_{H\widetilde{W}B} = 0.8$ ($c_{H\widetilde{W}} = c_{H\widetilde{W}B} = 3$) 91.0 % (45.8 %) are accepted. Note that the same is not true along the anti-diagonal direction.

The one-dimensional projections of the 3D-acceptance onto the $C\mathcal{P}$-even and $C\mathcal{P}$-odd BSM coupling parameters are compared in Figure 6.15. The functional dependence is very similar for scalar and pseudoscalar operators, and each projection agrees well with a one-dimensional Lorentzian function. The BSM acceptance for $C\mathcal{P}$-odd operators is always smaller than the SM acceptance. The same is not necessarily the case for $C\mathcal{P}$-even operators. In regions where the SM-BSM interference term dominates, the acceptance can be slightly larger than the SM expectation in this case.

6.3.2 Interference between $C\mathcal{P}$-Even and $C\mathcal{P}$-Odd Operators

The signal acceptance is individually parameterized for the scalar and pseudoscalar dimension-six operators using the gg2H production mode. To validate this approach, different BSM samples with mixed $C\mathcal{P}$-even and $C\mathcal{P}$-odd operators (100 000 events each) are generated.

Table 6.14: Fit parameters for the three-dimensional parameterization of the signal acceptance for the $\mathcal{CP}$-odd BSM coupling modifiers $c_{H\widetilde{W}}$, $c_{H\widetilde{B}}$ and $c_{H\widetilde{W}B}$.

Parameter	fit result	parameter	fit result
$\widetilde{\alpha}_0$	0.118 ± 0.001	$\delta_{H\widetilde{W}}$	0.572 ± 0.003
$\widetilde{\alpha}_1$	0.853 ± 0.001	$\delta_{H\widetilde{B}}$	2.022 ± 0.004
$\widetilde{\alpha}_2$	0.826 ± 0.002	$\delta_{H\widetilde{W}B}$	0.644 ± 0.001
$\beta_{H\widetilde{W}}$	-0.001 ± 0.001	$\delta_{(H\widetilde{W},H\widetilde{B})}$	-0.003 ± 0.008
$\beta_{H\widetilde{B}}$	-0.001 ± 0.001	$\delta_{(H\widetilde{W},H\widetilde{W}B)}$	-1.070 ± 0.004
$\beta_{H\widetilde{W}B}$	0.001 ± 0.001	$\delta_{(H\widetilde{B},H\widetilde{W}B)}$	-1.085 ± 0.006
		$\delta_{(H\widetilde{W},H\widetilde{B},H\widetilde{W}B)}$	-0.010 ± 0.008

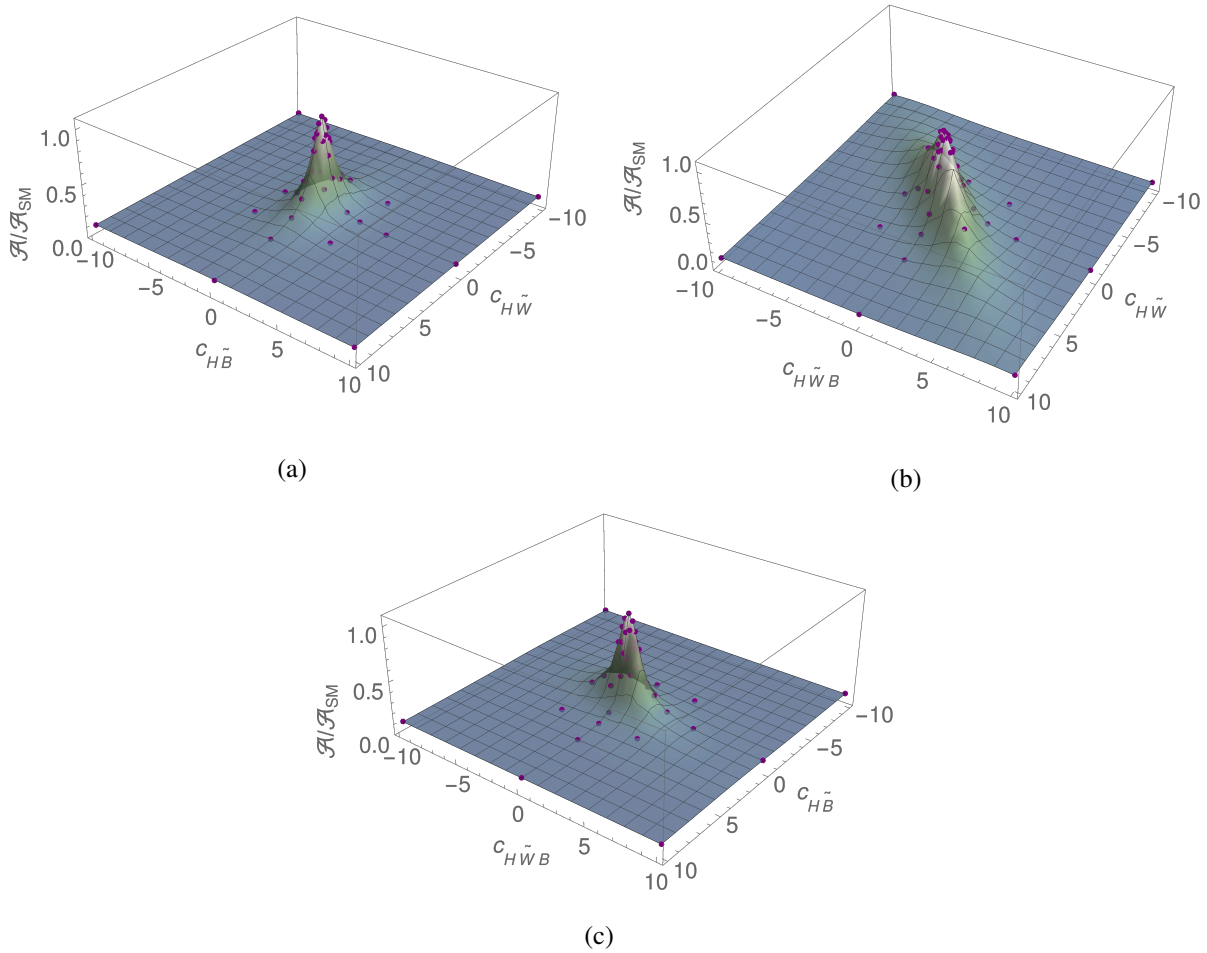

(a) (b)

(c)

Figure 6.14: Two-dimensional projections of the fit result for the BSM parameterization of the acceptance correction factor $\mathcal{A}/\mathcal{A}_{SM}$ onto the (a) $c_{H\widetilde{W}}$-$c_{H\widetilde{B}}$, (b) $c_{H\widetilde{W}}$-$c_{H\widetilde{W}B}$ and (c) $c_{H\widetilde{B}}$-$c_{H\widetilde{W}B}$ planes. The dots represent simulated data.

The acceptance for two operators can be modeled with a two-dimensional Lorentzian function,

$$\mathcal{A}(c_1, c_2) = \alpha_0 + \frac{(\alpha_1)^2}{\alpha_2 + K_1(c_1) + K_2(c_2) + K_{\text{int}}(c_1 c_2)}\,, \tag{6.18}$$

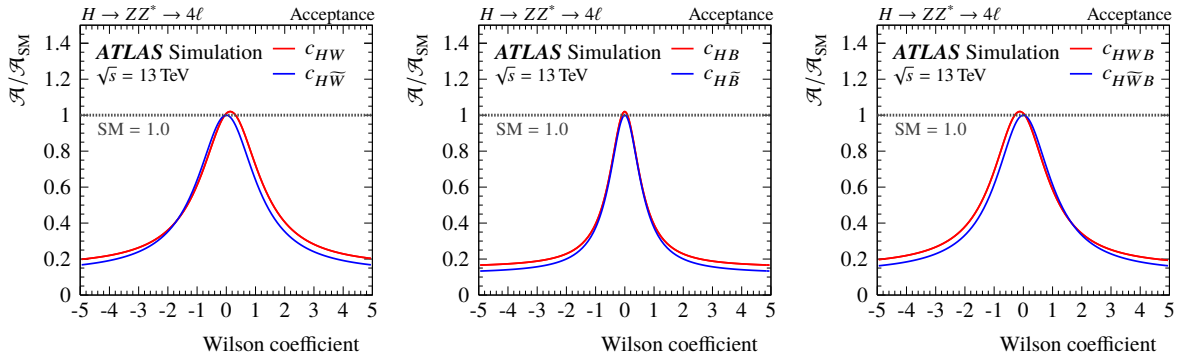

(a) c_{HW} and $c_{H\widetilde{W}}$ (b) c_{HB} and $c_{H\widetilde{B}}$ (c) c_{HWB} and $c_{H\widetilde{W}B}$

Figure 6.15: One-dimensional projections of the 3D parameterizations of the acceptance scale factor $f = \mathcal{A}/\mathcal{A}_{SM}$ for $C\mathcal{P}$-even and $C\mathcal{P}$-odd operators.

Table 6.15: Fit parameters of the two-dimensional parameterization of the acceptance for one $C\mathcal{P}$-even and one $C\mathcal{P}$-odd BSM coupling modifier in the gg2H production mode.

$c_{HW} - c_{H\widetilde{W}}$			
Parameter	fit result	parameter	fit result
α_0	0.168 ± 0.009	$K_{\text{even}}/(c_{HW}^2)$	0.813 ± 0.046
α_1	1.024 ± 0.018	$K_{\text{odd}}/(c_{H\widetilde{W}}^2)$	0.935 ± 0.053
α_2	1.252 ± 0.035	$K_{\text{int}}/(c_{HW}c_{H\widetilde{W}})$	0.024 ± 0.060
$c_{HB} - c_{H\widetilde{B}}$			
Parameter	fit result	parameter	fit result
α_0	0.136 ± 0.004	$K_{\text{even}}/(c_{HW}^2)$	2.331 ± 0.079
α_1	0.909 ± 0.019	$K_{\text{odd}}/(c_{H\widetilde{W}}^2)$	2.281 ± 0.080
α_2	0.956 ± 0.037	$K_{\text{int}}/(c_{HW}c_{H\widetilde{W}})$	0.015 ± 0.091
$c_{HWB} - c_{H\widetilde{W}B}$			
Parameter	fit result	parameter	fit result
α_0	0.129 ± 0.004	$K_{\text{even}}/(c_{HW}^2)$	0.500 ± 0.017
α_1	0.828 ± 0.008	$K_{\text{odd}}/(c_{H\widetilde{W}}^2)$	0.575 ± 0.016
α_2	0.776 ± 0.010	$K_{\text{int}}/(c_{HW}c_{H\widetilde{W}})$	-0.024 ± 0.020

where $K_i(c_i) = \delta_i \cdot (c_i + \beta_i)^2$, for $i = 1, 2$, is a measure for the BSM effect of the single parameter c_i, and $K_{\text{int}}(c_1 c_2) = \delta_{1,2} c_1 c_2$ is a measure for the BSM interference effect. The samples are generated for the parameter combinations c_{HW} and $c_{H\widetilde{W}}$, c_{HB} and $c_{H\widetilde{B}}$, and c_{HWB} and $c_{H\widetilde{W}B}$. The corresponding acceptances for different absolute values of the BSM parameters are summarized in Table D.6 and the fit results are shown in Table 6.15.

For all three parameter combinations, the contributions from the interference terms $K_{\text{int}}(c_i c_j)/(c_i c_j)$ are consistent with zero. Thus, the approach for splitting up the parameterizations into two sets according to the $C\mathcal{P}$ nature of BSM operators is justified in the $H \to 4\ell$ decay channel. Corresponding tests with the

other production modes qq2Hqq, WH-Lep, and ZH-Lep show similar results.

6.4 The Complete EFT Signal Model

The EFT signal model describes the expected event rate in each particle-level production bin p of the Reduced-Stage-1.1 STXS scheme. It is parameterized as a function of BSM coupling parameters $\boldsymbol{c}$ and consists of three parts, production cross-section $\sigma^p(\boldsymbol{c})$, decay branching ratio $\mathrm{BR}^{4\ell}(\boldsymbol{c})$ and signal acceptance $\mathcal{A}^p(\boldsymbol{c})$. The description for the individual parts is derived in the previous sections and given by Equations 6.6, 6.13, and 6.16. In this section, the signal model for the $C\mathcal{P}$-odd operators is discussed. As such, all $C\mathcal{P}$-even BSM coupling parameters are set to zero. The final signal parameterization is given by

$$\begin{aligned}\left(\sigma^p \cdot \mathrm{BR}^{4\ell} \cdot \mathcal{A}^p\right)(\boldsymbol{c}) = \left(\sigma^{p,\,(\mathrm{N})\mathrm{NLO}} \cdot \mathrm{BR}^{4\ell,\mathrm{NLO}} \cdot \mathcal{A}^p\right)_{SM} \\ \cdot \left(1 + \sum_{i,j\geq i} B^p_{ij} c_i c_j\right) \cdot \frac{1 + \sum\limits_{i,j\geq i} B^{4\ell}_{ij} c_i c_j}{1 + \sum\limits_{i,j\geq i} B^{\mathrm{tot}}_{ij} c_i c_j} \\ \cdot \left(\widetilde{\alpha}_0 + \frac{(\widetilde{\alpha}_1)^2}{\widetilde{\alpha}_2 + \sum\limits_i \delta_i \cdot (c_i + \beta_i)^2 + \sum\limits_{i,j\geq i} \delta_{(i,j)} \cdot c_i c_j + \sum\limits_{\substack{\delta_{(i,j,k)} \\ i>j>k}} \cdot c_i c_j c_k}\right),\end{aligned} \tag{6.19}$$

where $\boldsymbol{B}^p$, $\boldsymbol{B}^{4\ell}$ and $\boldsymbol{B}^{\mathrm{tot}}$ are the prefactors of the quadratic terms in the expansion of production cross-section, $H \to 4\ell$ decay width and total Higgs boson decay width, respectively. $\widetilde{\alpha}_0$, $\widetilde{\alpha}_1$, $\widetilde{\alpha}_2$, δ_i, $\delta_{(i,j)}$ and $\delta_{(i,j,k)}$ are the fit parameters of the three-dimensional Lorenztian function given in Table 6.14. Note that Equation 6.19 does not contain linear terms since the corresponding SM-BSM interferences vanish for pseudoscalar operators (see Table 6.4 and 6.12). This is not case for the signal model in the $C\mathcal{P}$-even scenario which is given in Appendix D.5.

To illustrate the functional dependence of the full signal model on the $C\mathcal{P}$-odd BSM coupling parameters, one- and two-dimensional projections of the expected event yield are presented in the following. Due to the large number of particle-level production bins, the focus is on categories with the largest sensitivity in each production mode. The projections of the remaining bins are summarized in Appendix D.4. Differences to the $C\mathcal{P}$-even signal model are discussed in the text, and only selected examples are explicitly shown. However, for a complete comparison, the corresponding one- and two-dimensional projections are summarized in Appendix D.5.2.

gg2H production:

The gg2H production mode provides the largest sensitivity in the $H \to 4\ell$ cross-section analysis. The bins with the largest and smallest sensitivity in this production mode are gg2H-0j-p_T^H-High ($\mu = 1.0 \pm 0.16$) and gg2H-p_T^H-High ($\mu = 1.0^{+1.0}_{-0.7}$), respectively. Figure 6.16 shows the one-dimensional dependence of the expected event yield in these bins on the BSM coupling parameters c_{HG} and $c_{H\widetilde{G}}$ given that all other Wilson coefficients are set to zero. The corresponding expected sensitivities in the cross-section analysis are indicated by gray bands around the SM value. Note that neither c_{HG} nor $c_{H\widetilde{G}}$ do affect the Higgs boson candidate selection. As such, the $\sigma \cdot \mathrm{BR}$ parameterization represents the full signal model in this case. For comparison, the prediction without the branching ratio correction is shown as well. The differences to the full signal model are minimal because both parameters only affect the effective

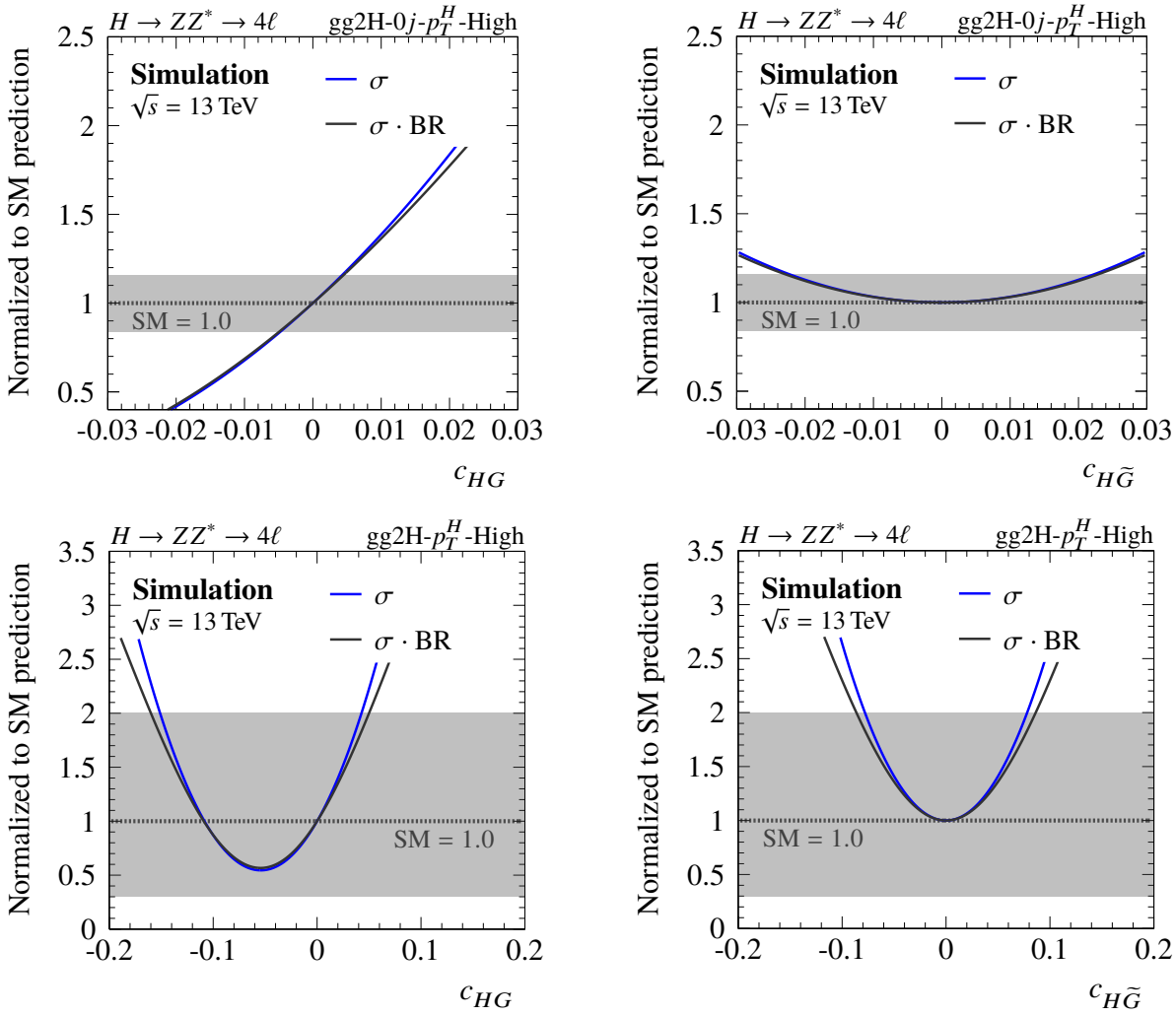

Figure 6.16: The one-dimensional projections of the expected event yield relative to the SM prediction onto the BSM coupling parameter (left panels) c_{HG} and (right panels) $c_{H\widetilde{G}}$ in the (top panels) gg2H-0j-p_T^H-High and (bottom panels) gg2H-p_T^H-High production bins of the Reduced-Stage-1.1 scheme. The gray bands indicate the expected 68 % C. L. interval from the cross-section analysis.

Higgs boson coupling to gluons, which contribute little to the total Higgs boson decay width in the expected sensitivity range. Therefore, the full signal only deviates slightly from the parabolic shape of the production cross-section parameterization. In the case of c_{HG}, a linear EFT approximation is justified for the particle production bins with the largest sensitivities, like gg2H-0j-p_T^H-High (see the top-left panel in Figure 6.16). However, it is not valid for bins with lower sensitivities since the pure BSM terms also contribute in this case (see bottom-left panel). In the case of the pseudoscalar operators, only the quadratic terms contribute, which results in significantly weaker sensitivity (see the top-right panel in Figure 6.16). The one-dimensional projections for the other gg2H production bins are summarized in Figure D.13 and Figure D.19 for the $C\mathcal{P}$-odd and $C\mathcal{P}$-even EFT parameterizations, respectively.

The BSM coupling parameters $c_{H\widetilde{W}}$, $c_{H\widetilde{B}}$ and $c_{H\widetilde{W}B}$ (as well as their $C\mathcal{P}$-even counterparts) contribute mainly to the qq2Hqq and VH-Lep production processes. However, they can also be probed in gg2H production due to their sensitivity to the $H \to ZZ^* \to 4\ell$ decay and the Higgs boson candidate selection. Figure 6.17 shows the expected dependence of the event yield relative to the SM prediction and compares

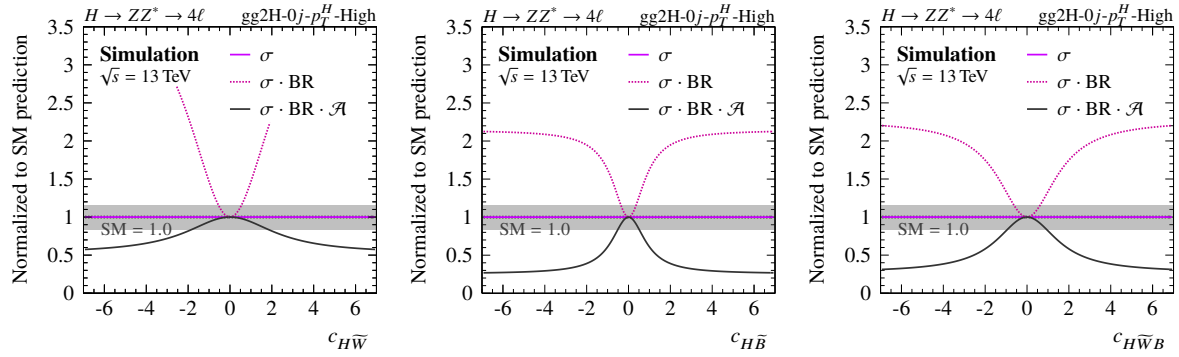

(a) $c_{H\widetilde{W}}$ (b) $c_{H\widetilde{B}}$ (c) $c_{H\widetilde{W}B}$

Figure 6.17: The one-dimensional projections of the expected event yield relative to the SM prediction onto the BSM coupling parameters (a) $c_{H\widetilde{W}}$, (b) $c_{H\widetilde{B}}$, and (c) $c_{H\widetilde{W}B}$ in the gg2H-0j-p_T^H-High production bin of the Reduced-Stage-1.1 scheme. The gray band indicates the expected 68 % C. L. interval from the cross-section analysis.

them to the prediction without the acceptance modification ($\sigma \cdot$ BR). The production-only dependence (σ), which is trivial in this case, is shown for completeness. Disregarding the acceptance results in relative event rates that positively correlate with the absolute magnitude of the pseudoscalar BSM coupling parameters. In contrast, when taking the signal acceptance into account, the correlation is negative. Note that similar statements hold for the $\mathcal{CP}$-even parameterization. The corresponding one-dimensional projections are summarized in Appendix D.5. Coming back to Figure 6.17, at first glance, it seems straightforward to constrain the $\mathcal{CP}$-odd Wilson coefficients with a global fit since the event rate is constrained from below and the BSM scenarios discussed in Figure 6.17 reduces the expected event yield. However, this argument misses two points. First, the mixed terms $c_i c_j$, with $i \neq j$, can be negative and sizable for some parameter combinations. Second, $c_{H\widetilde{G}}$ and $c_{\widetilde{u}H}$ naturally increase the expected event yield which counteracts the effect of the other BSM coupling parameters. Both effects drastically increase the allowed parameter space for the BSM coupling parameters.

To visualize the effect of the mixed BSM terms, two-dimensional projections of the expected event yield are generated. Figure 6.18 shows these projections for the gg2H-0j-p_T^H-High production bin. The solid (dashed) contours indicate the lower (upper) limit of the expected 68 % C. L. region of the cross-section analysis. The region within these contours corresponds to the gray band in Figure 6.17. This is most easily seen by comparing the intercepts of two-dimensional contours with the position at which the corresponding one-dimensional projection hits the border of the gray band. For example, in Figure 6.17(a) the dashed line hits the gray band's upper limit at $c_{H\widetilde{W}} \approx \pm 0.6$. The same values for $c_{H\widetilde{W}}$ are found when looking at values of the ellipse where $c_{H\widetilde{B}}$ ($c_{H\widetilde{W}B}$) is zero in Figure 6.18(a) (6.18(b)). In many cases, only one contour is shown since the sensitivity of the other limit is not met by any point in the two-dimensional plane. The top row in Figure 6.18 shows the two-dimensional projections onto the $c_{H\widetilde{W}}$-$c_{H\widetilde{B}}$, $c_{H\widetilde{W}}$-$c_{H\widetilde{W}B}$ and $c_{H\widetilde{B}}$-$c_{H\widetilde{W}B}$ planes for the parameterization ignoring acceptance effects. In this case, the BSM couplings parameters are restricted to small values within the dashed contours. This is not the case for the full signal model shown in the bottom row of Figure 6.18. In this case, the allowed parameter space opens up along some direction where both parameters are unequal to zero. By simply looking at the two-dimensional profiles, a successful fit with more than one free BSM coupling parameter seems discouraging since the contours are not closed in the regime where the EFT is perturbative, i. e. $|c_i| < 4\pi$. In addition, the parameter space is even less constrained if more than two Wilson coefficients are allowed to float free at the same time. To constrain the BSM coupling parameters in a global fit,

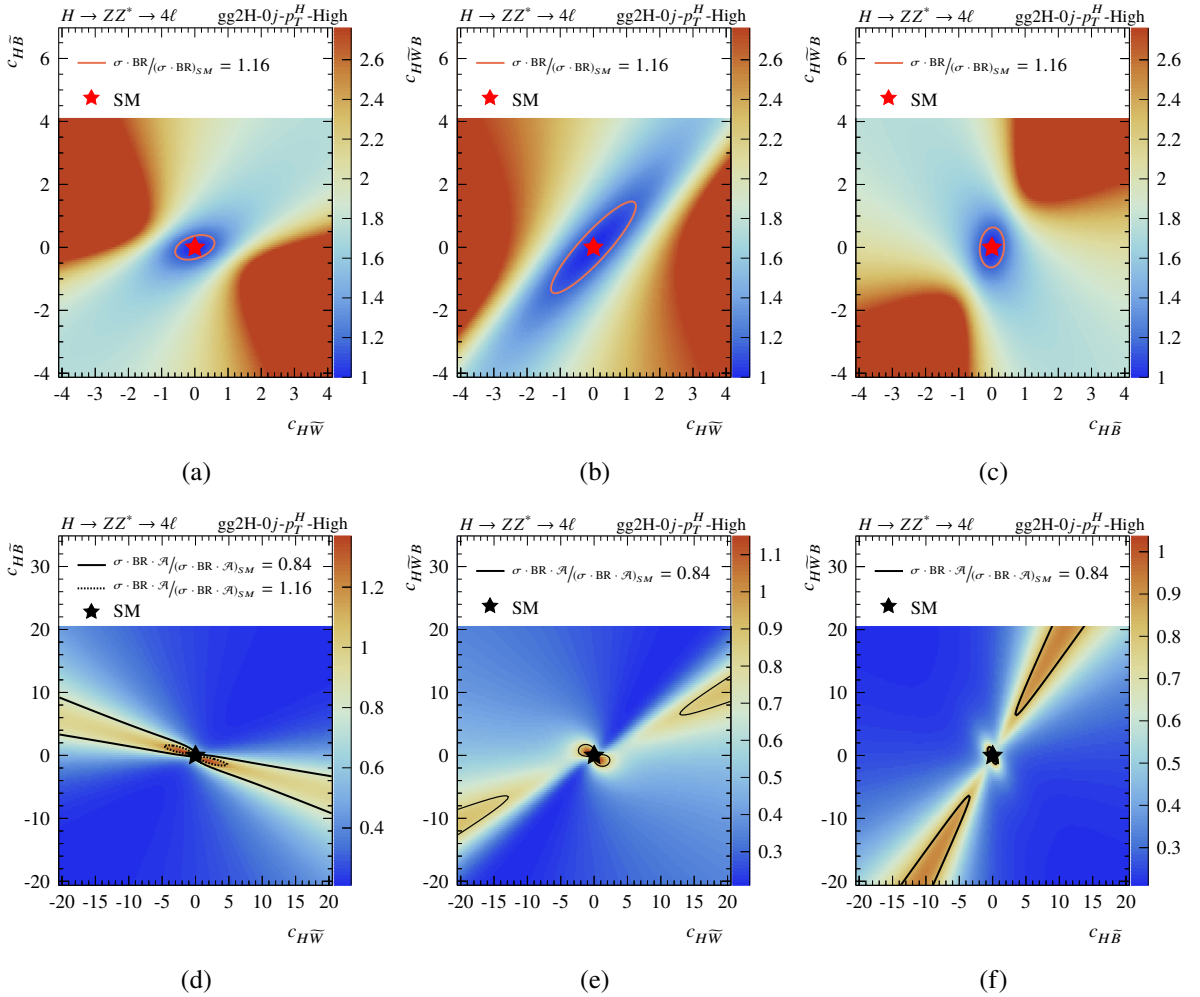

Figure 6.18: The two-dimensional projections of the expected event yield relative to the SM prediction onto the parameter planes $c_{H\widetilde{W}}$-$c_{H\widetilde{B}}$, $c_{H\widetilde{W}}$-$c_{H\widetilde{W}B}$, and $c_{H\widetilde{B}}$-$c_{H\widetilde{W}B}$ for the full signal model (bottom row) and the prediction without acceptance parameterization (top row) in the gg2H-0j-p_T^H-High production bin of the Reduced Stage 1.1 scheme. The solid (dashed) contours indicate the lower (upper) limit of the expected 68 % C. L. interval from the cross-section analysis.

the other particle-level production bins have to provide enough sensitivity in the regions where the contours in the gg2H-0j-p_T^H-High bin are unconstrained. Since the other bins of the gg2H production mode lack sensitivity in the same region of the parameter space, they only slightly improve the overall sensitivity and are not discussed here in detail. However, they are added to Appendix D.4 (D.5.2) for the CP-odd (CP-even) EFT parameterization. Thus, the gg2H bins alone are not expected to provide enough sensitivity to constrain the Wilson coefficients in a global fit.

qq2Hqq and VH-Lep production:

The qq2Hqq production mode comprises events from vector-boson fusion (VBF) and associated production with a hadronically decaying weak gauge boson (VH-Had). Events from associated production with leptonically decaying vector bosons are categorized in the VH-Lep bin. The largest sensitivity in the cross-section analysis is obtained in the qq2Hqq-VBF production bin ($\mu = 1.0^{+0.6}_{-0.5}$). Figure 6.19 shows

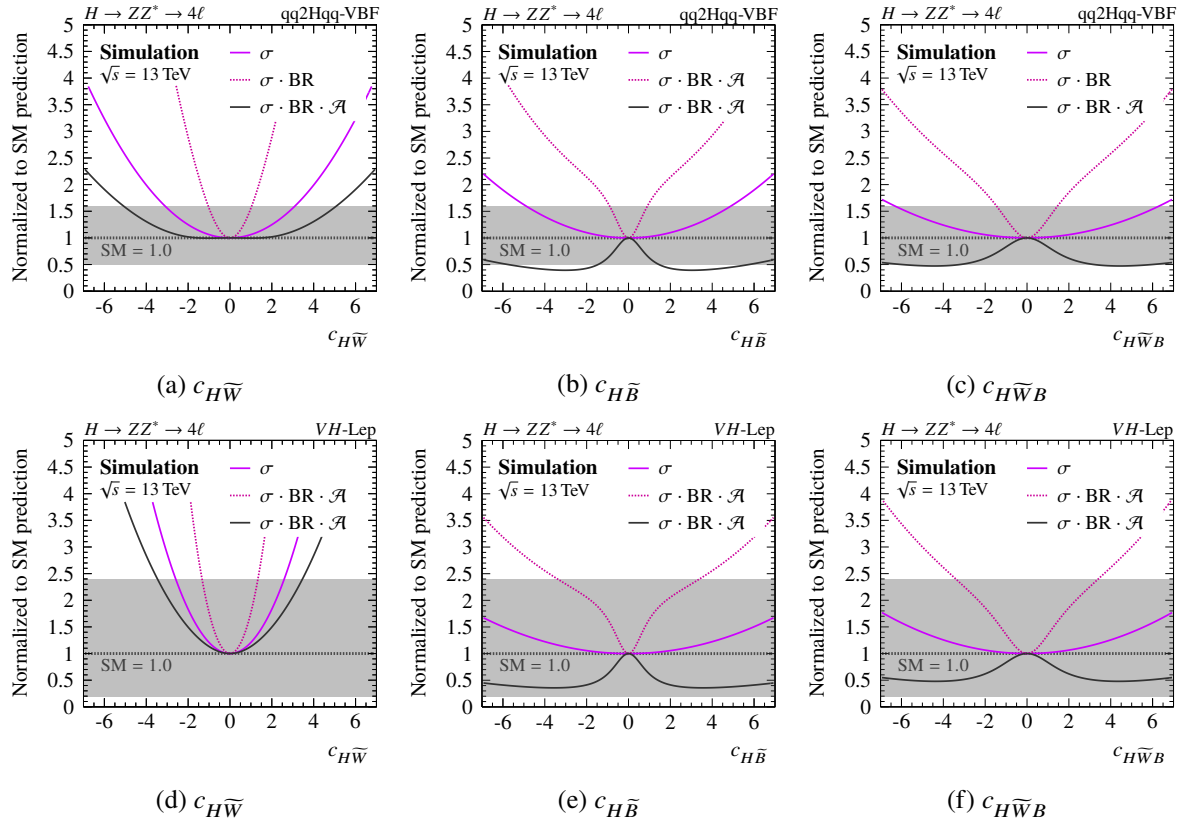

(a) $c_{H\widetilde{W}}$ (b) $c_{H\widetilde{B}}$ (c) $c_{H\widetilde{W}B}$

(d) $c_{H\widetilde{W}}$ (e) $c_{H\widetilde{B}}$ (f) $c_{H\widetilde{W}B}$

Figure 6.19: The one-dimensional projections of the expected event yield relative to the SM prediction onto the BSM coupling parameters $c_{H\widetilde{W}}$, $c_{H\widetilde{B}}$, and $c_{H\widetilde{W}B}$ in the qq2Hqq-VBF (top row) and VH-Lep (bottom row) particle-level production bins of the Reduced-Stage-1.1 scheme. The gray bands indicate the expected 68 % C. L. interval from the cross-section analysis.

the one-dimensional projections of the expected event yield relative to the SM prediction for the relevant $C\mathcal{P}$-odd BSM parameters in the qq2Hqq-VBF (top row) and VH-Lep (bottom row) bins. Compared are the full signal model ($\sigma \cdot \text{BR} \cdot \mathcal{A}$), the parameterization without acceptance correction ($\sigma \cdot \text{BR}$) and the production-only models (σ). While for the latter two parameterizations, any deviation from the SM results in event yields that exceed the SM prediction, the full signal model predicts typically fewer signal events. However, for the parameter $c_{H\widetilde{W}}$, the predicted event yield is still larger than the SM prediction. Similar statements also hold for the $C\mathcal{P}$-even parameterizations summarized in Appendix D.5.2. In the qq2Hqq-VBF bin, for small absolute values of $c_{H\widetilde{W}}$, the expected event yield is approximately equal to the SM prediction. In contrast, the effective impact of $c_{H\widetilde{B}}$ or $c_{H\widetilde{W}B}$ on the number of signal events is quite different. The event rate drops quickly to about 50 % of the SM prediction. However, it raises again for larger BSM couplings. For $c_{H\widetilde{B}}$ ($c_{H\widetilde{W}B}$) the SM rate is reached at about ±11 (±13) which is roughly in the region where the EFT is no longer pertubative ($4\pi \approx 12.6$). The functional dependence of the expected event yield in the other qq2Hqq bins is similar and summarized in Figure D.17.

Figure 6.20 shows the two-dimensional projections of expected event yield in the qq2Hqq-VBF and VH-Lep particle-level production bins relative to the SM prediction in the $c_{H\widetilde{W}}$-$c_{H\widetilde{B}}$, $c_{H\widetilde{W}}$-$c_{H\widetilde{W}B}$ and $c_{H\widetilde{B}}$-$c_{H\widetilde{W}B}$ parameter planes. In contrast to the gg2H bins, closed contours are found for the qq2Hqq-VBF bin (upper row). In this case, both the upper and lower boundaries of the expected 68 % C. L. interval of the cross-section analysis are met. They are indicated by dashed and solid contours, respectively. Absolut values of $c_{H\widetilde{B}}$ and $c_{H\widetilde{W}B}$ larger than 4π are not disfavoured by the expected sensitivity in the qq2Hqq

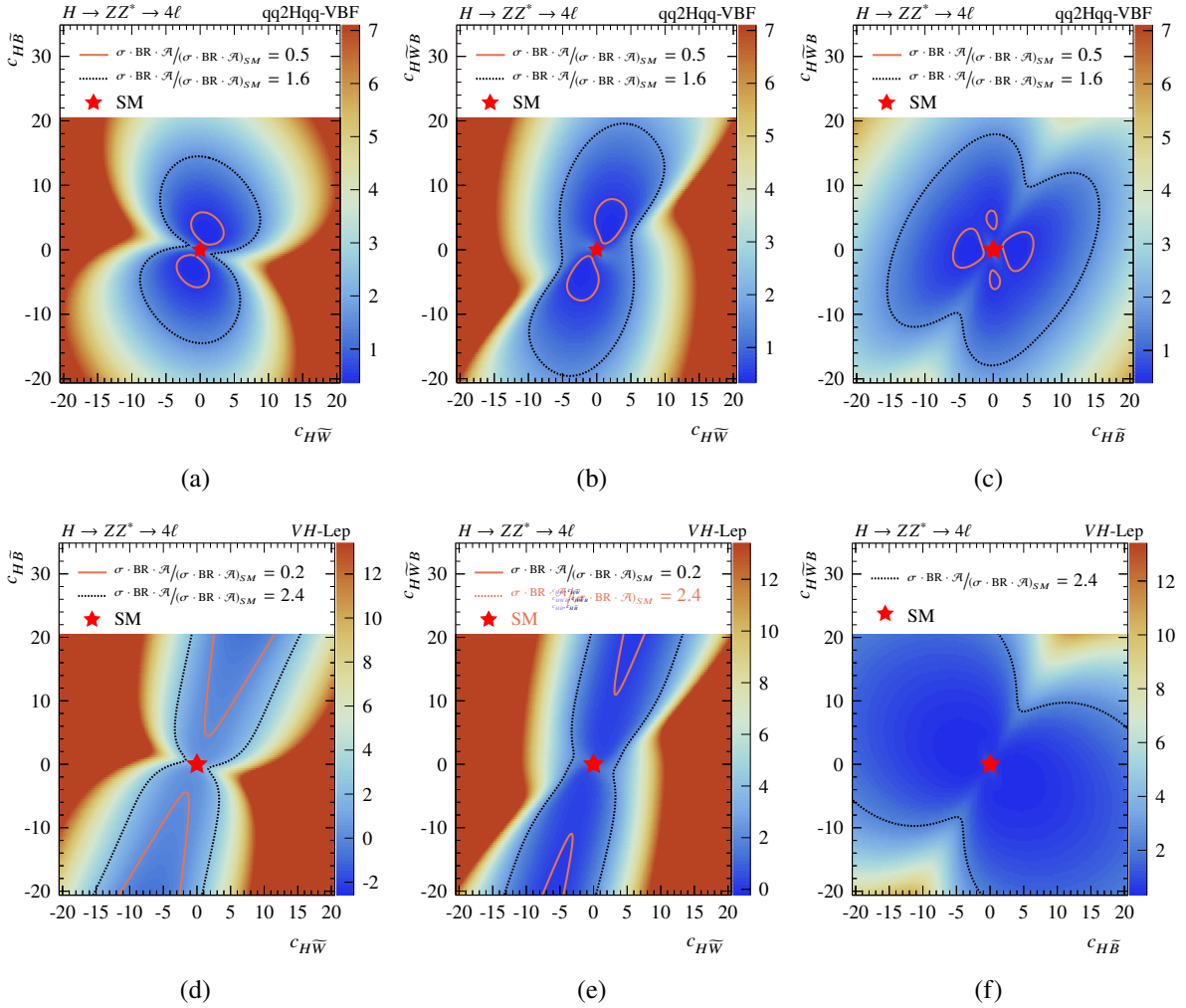

Figure 6.20: The two-dimensional projections of the expected event yield relative to the SM prediction onto the parameter planes $c_{H\widetilde{W}}$-$c_{H\widetilde{B}}$, $c_{H\widetilde{W}}$-$c_{H\widetilde{W}B}$, and $c_{H\widetilde{B}}$-$c_{H\widetilde{W}B}$ for the full signal model in the qq2Hqq-VBF (top row) and VH-Lep (bottom row) particle-level production bins of the Reduced-Stage-1.1 scheme. The solid (dashed) contours indicate the lower (upper) limit of the expected 68 % C. L. interval from the cross-section analysis.

categories. The VH-Lep bin provides typically less sensitivity than the qq2Hqq bins. In this case, none of the two-dimensional contours is closed in the displayed parameter region (lower row). The important feature is that the two-dimensional projections of the VBF and VH categories are constrained along the directions in which the gg2H bins are not constrained, and vice versa. This statement is true for all 2D planes shown in Figure 6.20 and 6.18 and also holds for the corresponding $C\mathcal{P}$-even Wilson coefficients summarized in Appendix D.5.2. Thus, the different particle-level production bins compensate each other's weaknesses, suggesting that a two-dimensional fit with the discussed BSM parameters is possible.

ttH production:

The ttH particle-level production bin contains events from ttH, $tHjb$, and tHW production. These processes are affected by the BSM coupling parameters $c_{H\widetilde{G}}$ and $c_{\widetilde{u}H}$ as well as their $C\mathcal{P}$-even counterparts. Neither of them is considered in the Higgs boson candidate selection since they do not contribute to the

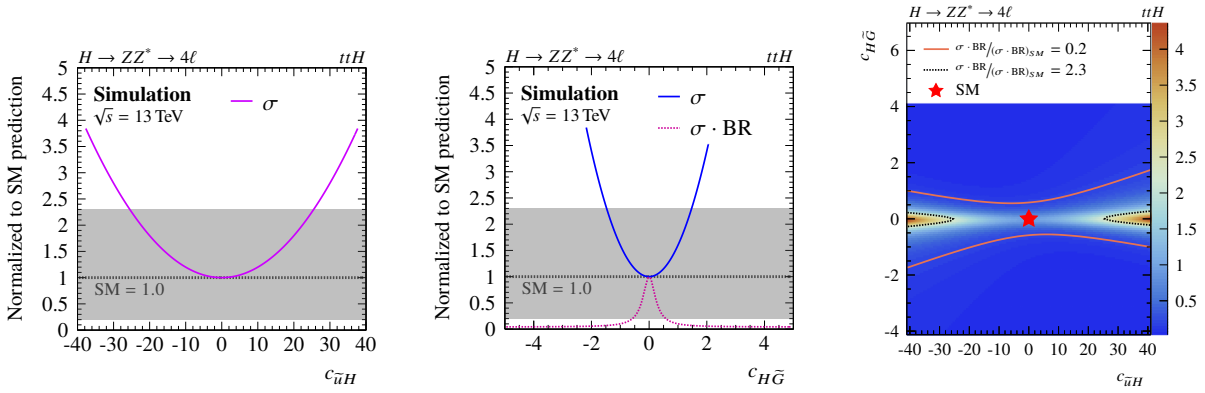

(a) (b) (c)

Figure 6.21: The one-dimensional projections of the expected event yield relative to the SM prediction onto the BSM coupling parameters (a) $c_{H\widetilde{G}}$ and (b) $c_{\widetilde{u}H}$ in the ttH particle-level production bins of the Reduced-Stage-1.1 scheme. The gray bands indicate the expected 68 % C. L. interval from the cross-section analysis. (c) The corresponding two-dimensional projection in $c_{H\widetilde{G}} - c_{\widetilde{u}H}$ plane. The dashed contour indicates the upper limit of the expected 68 % C. L. interval from the cross-section analysis. The corresponding lower limit is not met by any point in the two-dimensional plane.

$H \to 4\ell$ decay process. In addition, the impact of $c_{\widetilde{u}H}$ (as well as c_{uH}) on the total width of the Higgs boson is insignificant. Thus, they are not considered in the parameterization of the branching ratio to four-lepton final states as explained in Section 6.2. Figure 6.21 shows the one- and two-dimensional projections of the signal model in the ttH bin. The expected 68 % C. L. limits in this bin are very weak. For $c_{\widetilde{u}H}$ they are expected to be at $\mu = \pm 26$ (see Figure 6.21(a)) and for $c_{H\widetilde{G}}$ at $\mu = \pm 0.5$ (see Figure 6.21(b)). The latter one is more than one order of magnitude larger than the corresponding limit provided by the gg2H production bins. Therefore, the impact of the ttH bin on $c_{H\widetilde{G}}$ is very weak. In the two-dimensional projection, shown in Figure 6.21(c), even larger absolutes values of $c_{\widetilde{u}H}$ are allowed if $c_{H\widetilde{G}} \neq 0$. The corresponding $\mathcal{CP}$-even projections are summarized in Figure D.28.

6.5 Validation of the EFT Signal Model

The acceptance model is derived based on the BSM coupling parameters that are directly involved in the HZZ interaction vertex, and it is assumed to be independent of the particle level production bins. These assumptions are investigated in Section 6.5.1. The cross-section parameterization is tested against dedicated BSM Monte Carlo samples for different values of the Wilson coefficients in each particle-level production bin. These studies are discussed in Section 6.5.2. In addition, the parameterization of the full signal model is also validated with dedicated BSM signal samples at reconstruction level. Since the corresponding studies have not been performed as a part of this thesis, only the main conclusion are summarized in Section 6.5.3. More details can be found in Reference [459].

6.5.1 Validation of the Acceptance Model

The acceptance correction of the signal model is based on a common description for the different particle-level production bins using the dominant gg2H production mode. This approach is motivated since the Higgs boson selection is based on the Higgs boson decay and not the Higgs boson production processes. This section quantifies the production mode dependence of the signal acceptance.

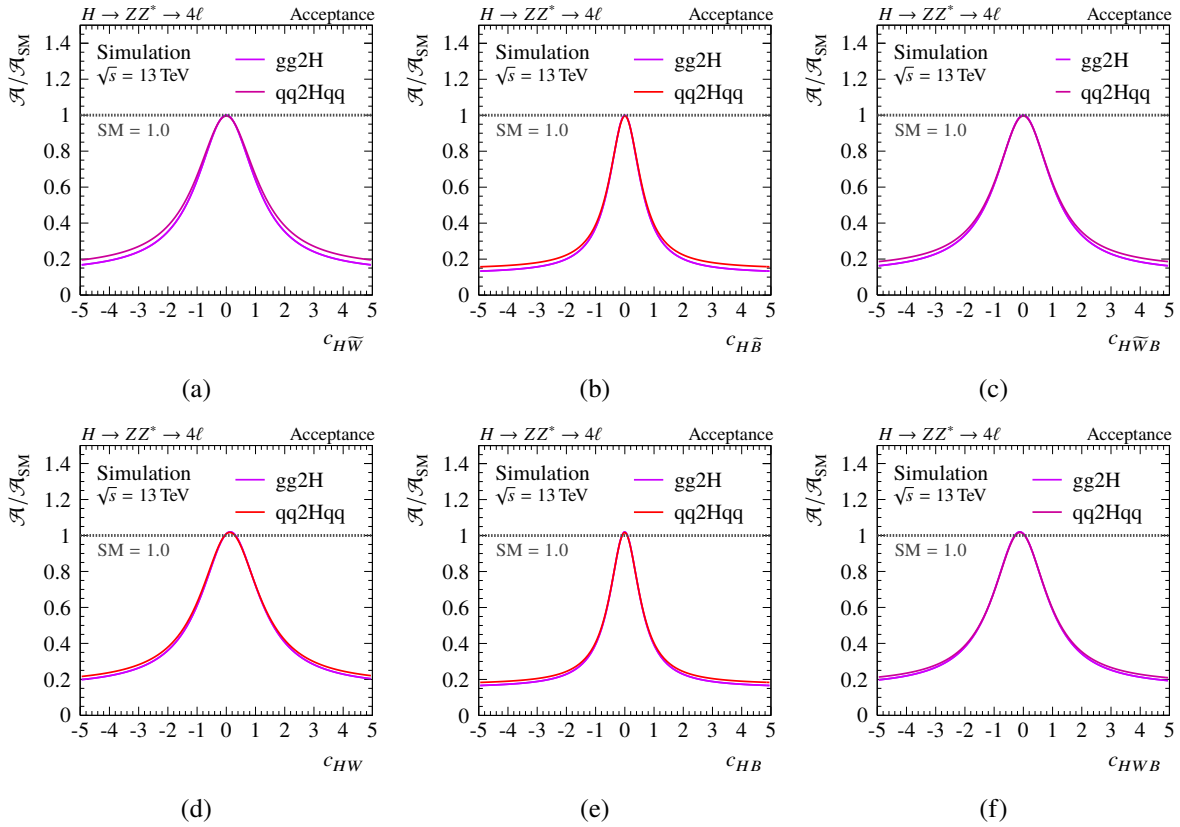

Figure 6.22: Comparison of the one-dimensional projections of the acceptance modifier for the $C\mathcal{P}$-odd (upper row) and $C\mathcal{P}$-even (lower row) operators obtained from the parameterization using the gg2H and qq2Hqq productions.

The qq2Hqq bin is the second-most prominent production bin. Thus, it is of particular interest when it comes to the discussion of the production-mode dependence of the signal acceptance. The fit results for the three-dimensional acceptance model in the $C\mathcal{P}$-odd ($C\mathcal{P}$-even) scenario based on the gg2H production mode are summarized in Table 6.14 (D.10). For the qq2Hqq production, the same machinery is applied, and Figure 6.22 compares the one-dimensional projections of the acceptance models obtained using the gg2H and qq2Hqq production modes. The differences between both production processes are minor and only noticeable for large absolute values of the BSM coupling parameters. Overall, the differences are below the statistical sensitivity of the measurement, and thus, a common description is justified.

Tables 6.16 and 6.17 show the acceptance modifier for specifically chosen values of the $C\mathcal{P}$-even and $C\mathcal{P}$-odd BSM coupling parameters, respectively. Compared to the main production modes, the acceptance of the associated productions with a leptonically decaying weak gauge boson is smaller. In particular, for the BSM coupling parameters c_{HB}, $c_{H\widetilde{B}}$, c_{HWB}, and $c_{H\widetilde{W}B}$ in ZH-Lep production. However, the sensitivity in this bin is significantly smaller than the sensitivity in the gg2H bins (compare Figures 6.17 and 6.19). Therefore, the expected impact on the final result is tiny. While a minor dependence of the signal acceptance on c_{HG} and $c_{H\widetilde{G}}$ is observed, its effect is negligible in the relevant parameter range. As expected, neither c_{uH} nor $c_{\widetilde{u}H}$ do not affect the acceptance, even for large values of the BSM couplings.

6.5.2 Validation of the Production Cross-Section Parameterization

The cross-section parameterization is validated with dedicated BSM Monte Carlo samples that include both the SM and the BSM contributions, i. e. all three terms in Table 6.1. The samples are generated

Table 6.16: Comparison of the acceptance modifier, f, for specifically chosen $C\mathcal{P}$-even BSM points in the gg2H, qq2Hqq, ZH-Lep, WH-Lep, and ttH production modes. Only one parameter is non-zero at a time.

c_{HW}	acceptance modifier f				c_{HG}	f	c_{uH}	f
	gg2H	qq2Hqq	ZH-Lep	WH-Lep		gg2H		ttH
0.4	0.98	0.97	0.85	0.94	0.005	0.99	1	1.00
0.5	0.94	0.92	0.79	0.77	0.01	0.99	8	1.00
1.0	0.70	0.71	0.48	0.41	0.1	0.98	15	1.00
3.0	0.29	0.31	0.27	0.21	1.0	0.96	40	1.00

c_{HB}	acceptance modifier f			c_{HWB}	acceptance modifier f		
	gg2H	qq2Hqq	ZH-Lep		gg2H	qq2Hqq	ZH-Lep
0.4	0.76	0.77	0.36	0.4	0.86	0.86	0.47
0.5	0.67	0.68	0.26	0.5	0.82	0.82	0.45
1.0	0.37	0.38	0.20	1.0	0.59	0.60	0.24
3.0	0.17	0.18	0.10	3.0	0.24	0.25	0.19

Table 6.17: Comparison of the acceptance modifier, f, for specifically chosen $C\mathcal{P}$-odd BSM points in the gg2H, qq2Hqq, ZH-Lep, WH-Lep, and ttH production modes. Only one parameter is non-zero at a time.

$c_{H\widetilde{W}}$	acceptance modifier f				$c_{H\widetilde{G}}$	f	$c_{\widetilde{u}H}$	f
	gg2H	qq2Hqq	ZH-Lep	WH-Lep		gg2H		ttH
0.4	0.90	0.91	0.74	0.76	0.005	1.00	1	1.00
0.5	0.87	0.88	0.64	0.67	0.01	1.00	8	1.00
1.0	0.65	0.66	0.46	0.33	0.1	0.98	15	1.00
3.0	0.24	0.26	0.22	0.18	1.0	0.97	40	1.00

$c_{H\widetilde{B}}$	acceptance modifier f			$c_{H\widetilde{W}B}$	acceptance modifier f		
	gg2H	qq2Hqq	ZH-Lep		gg2H	qq2Hqq	ZH-Lep
0.4	0.75	0.76	0.28	0.4	0.91	0.91	0.60
0.5	0.67	0.68	0.25	0.5	0.86	0.86	0.51
1.0	0.38	0.40	0.24	1.0	0.62	0.63	0.21
3.0	0.16	0.17	0.18	3.0	0.22	0.24	0.22

for different values of the relevant Wilson coefficients. The resulting cross-section in each particle-level production bin is compared to the expected value from the EFT parameterization. Figure 6.23 shows the validation results for different values of the $C\mathcal{P}$-odd BSM coupling parameters. Their values are chosen such that the expected sensitivity range at 68 % C. L. is covered. All generated production cross-sections agree with the EFT parameterization predictions within the statistical errors. The validation results not shown in this section are summarized in Section D.2.5.

6.5.3 BSM Dependence of the Reconstruction Efficiency

The EFT parameterization is developed at particle level. However, the cross-section measurement in the $H \to 4\ell$ decay channel is performed simultaneously in various event categories targeting different Higgs boson production processes. The validity of the particle-level description is probed with fully

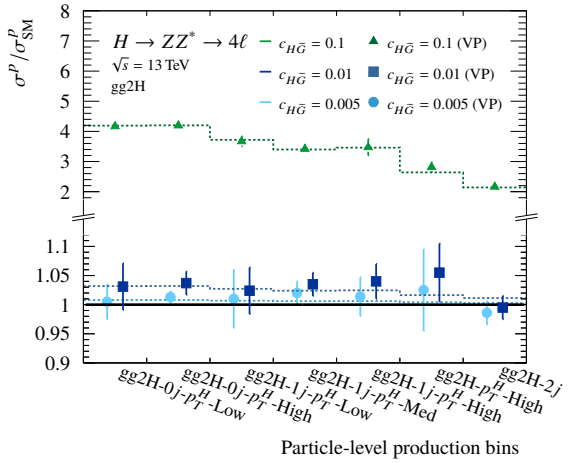

(a)

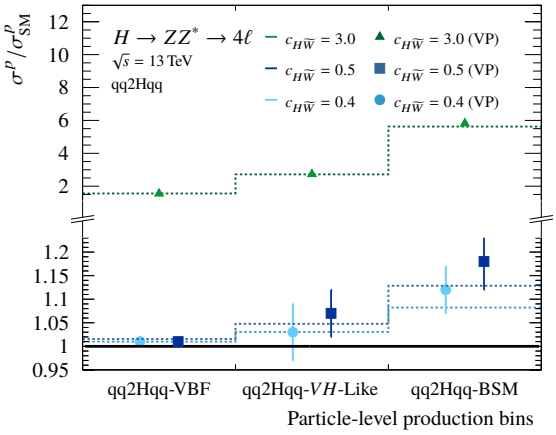

(b)

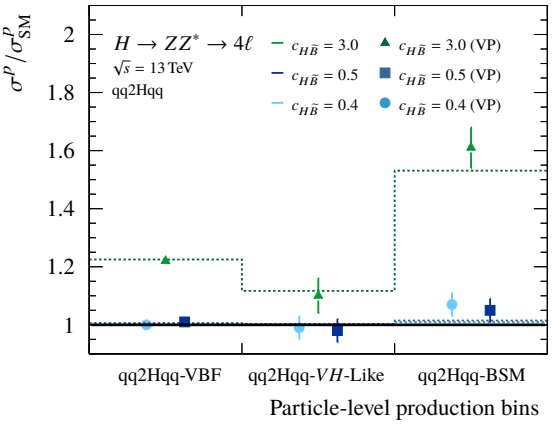

(c)

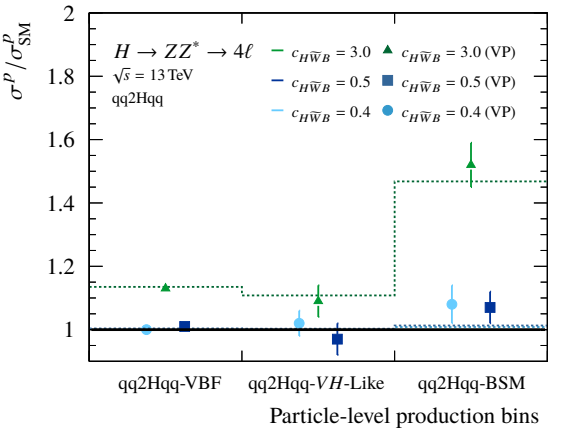

(d)

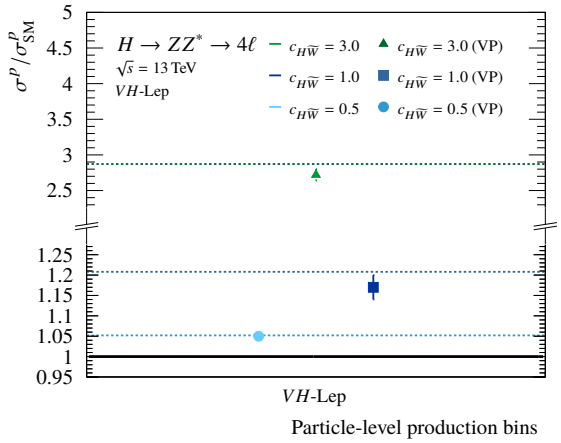

(e)

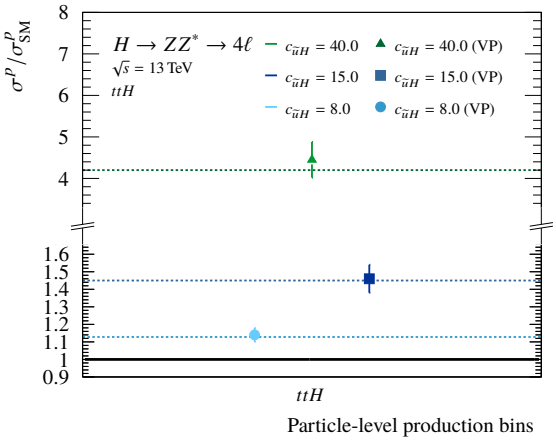

(f)

Figure 6.23: Comparison of the relative cross-sections, $\sigma/\sigma_{\text{SM}}$, for each particle-level production bin of the Reduced Stage 1.1 scheme for different values of the $C\mathcal{P}$-odd BSM coupling parameters. Compared are the predicted cross-sections from the EFT parameterization (dotted line) and the cross-section from generated validation Monte Carlo samples (validation points (VP)) for (a) gg2H, (b)-(d) qq2Hqq, (e) VH-Lep, and (f) ttH production.

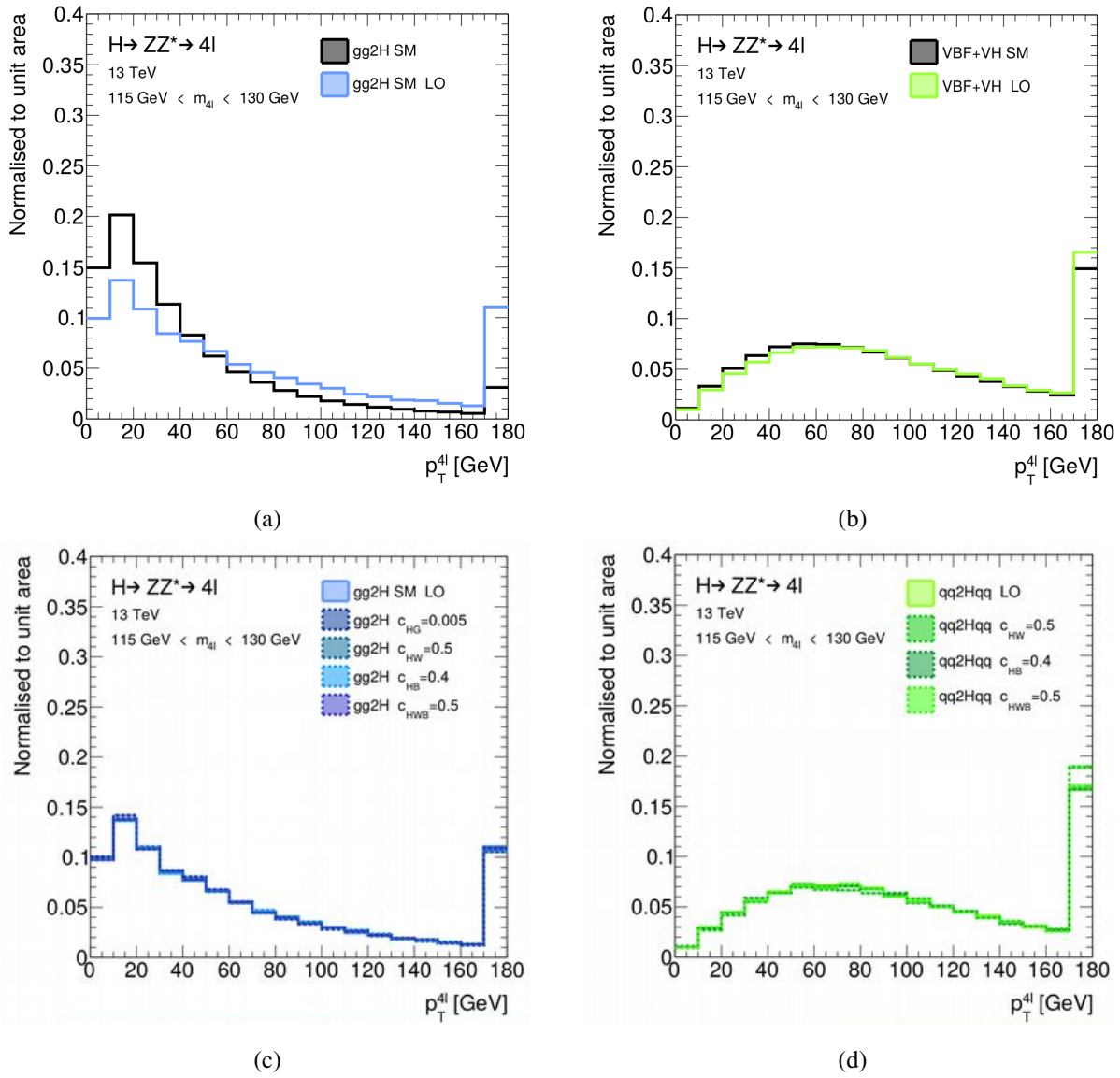

Figure 6.24: Comparison between the expected distributions of $p_T^{4\ell}$ for the SM SMEFT LO predictions and (upper panels) the SM (N)NLO predictions and (lower panels) different values of the BSM coupling parameters in (left panels) gg2H and (right panels) qq2Hqq production. Taken from Reference [459].

reconstructed BSM signal samples. Since these studies have not been performed as a part of this thesis, only the main conclusions are summarized. More information can be found in Reference [459].

Figure 6.25 compares the $p_T^{4\ell}$ distribution obtained with the SM SMEFT LO samples, the SM NNLO prediction, and various SMEFT BSM samples with different values of the BSM coupling parameters for the gg2H and the VBF+VH-Had Higgs boson production processes. In case of the former, the SMEFT LO sample differs slightly from the NNLO prediction (see Figure 6.24(a)). However, it matches the LO expectation. The distributions of other kinematic variables agree well with the NLO prediction [459]. In case of VBF+VH-Had production, the SMEFT LO $p_T^{4\ell}$ distribution resembles the higher-order prediction (see Figure 6.24(b)). The same is true for other production modes and kinematic distributions. The differences between the $p_T^{4\ell}$ distributions of the reconstructed SM and BSM signal samples are minor.

In the previous sections, it was assumed that the event reconstruction efficiency ϵ, i. e. the ratio

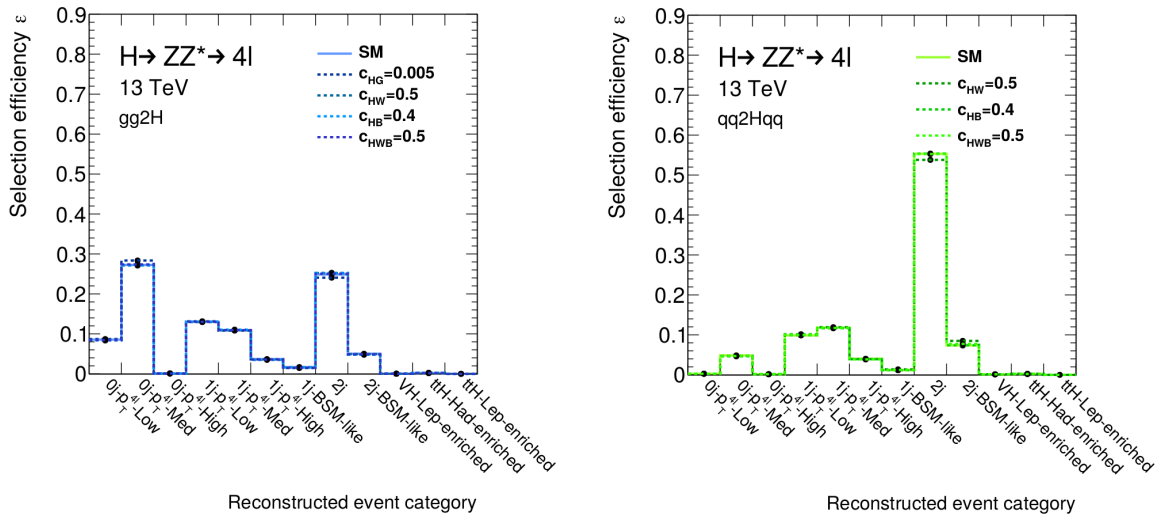

(a) (b)

Figure 6.25: Comparison between the event reconstruction efficiency for the SM and different values of the BSM coupling parameters for the (a) gg2H and (b) qq2Hqq production. Taken from Reference [459].

of the total number of events and the number of events after the inclusive four-lepton signal selection is independent of the BSM coupling parameters. Figure 6.25 shows the reconstruction efficiencies in each reconstructed event category for the gg2H and qq2Hqq production modes. Within the statistical uncertainty, no significant deviations between the SM and BSM samples are observed. The same is true for other production modes [459]. Thus, no parameterization of the reconstruction efficiency is required.

6.6 Systematic Uncertainties

The impact of systematic theoretical uncertainties is estimated using MADGRAPH5_aMC@NLO. For the QCD scale uncertainties, the nominal choice for the renormalization and factorization scales, $\mu_{0,R}$ and $\mu_{0,F}$, respectively, are either multiplied or divided by a factor two. The possible variation pairs are then compared to the nominal choice. The impact of the PDF uncertainties is evaluated using internal variations of the NNPDF23loPDF set.

Figure 6.26 shows the evaluated uncertainties on the event yield for selected gg2H particle-level production bins. The evaluated QCD scale (PDF) uncertainties the gg2H-0j-p_T^H-High and gg2H-1j-p_T^H-High bin are displayed in the top (bottom) panels. While the absolute size of both, the QCD scale and PDF uncertainties is relatively large, they are almost independent of the BSM contributions. This statement also holds for the other particle-level production bins summarized in Appendix D.6.

The large systematic theoretical uncertainties result from the LO accuracy of the MC sample generation. Instead of using these uncertainties, the corresponding values from the SM best prediction are used. This is possible because the BSM parameterization is described as a relative correction to the best SM prediction, and the BSM dependence of the QCD scale and PDF uncertainties is negligible.

The experimental systematic uncertainties are assumed to be independent of the Wilson coefficients, and their values are taken from the corresponding production cross-section measurement (see Section 5.6.1).

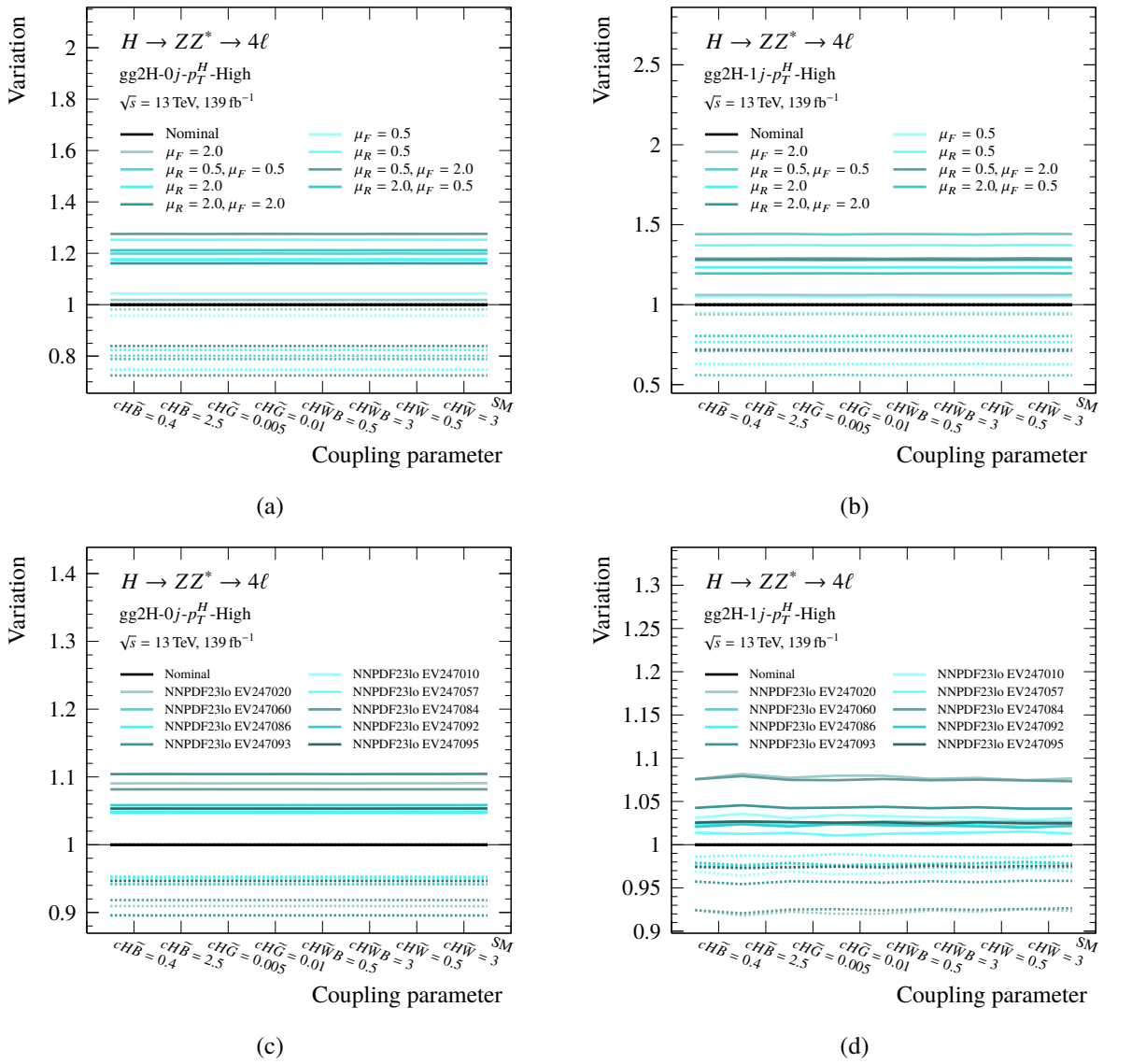

Figure 6.26: QCD scale (top panels) and PDF (bottom panels) uncertainties in the gg2H production bins for different values of $C\mathcal{P}$-odd BSM coupling parameters.

6.7 Statistical Treatment

The full signal model of the SMEFT in the $H \to ZZ^* \to 4\ell$ decay channel is given in Equation 6.19 (D.2) for the $C\mathcal{P}$-odd ($C\mathcal{P}$-even) BSM parameterization. For the statistical interpretation, the expected event rates in the various particle-level production bins p are expressed in terms of signal strength modifiers,

$$\mu^p(\boldsymbol{c}) = \frac{\sigma^p(\boldsymbol{c}) \cdot \mathrm{BR}^{4\ell}(\boldsymbol{c}) \cdot \mathcal{A}(\boldsymbol{c})}{\sigma^p_{\mathrm{SM}} \cdot \mathrm{BR}^{4\ell}_{\mathrm{SM}} \cdot \mathcal{A}_{\mathrm{SM}}}\,, \tag{6.20}$$

which scale the corresponding SM prediction as a function of the BSM coupling modifiers. The signal strengths $\mu^p(\boldsymbol{c})$ are incorporated into the statistical analysis model by replacing the SM-expected signals, $S_{i,j}(\boldsymbol{\sigma}, \boldsymbol{\theta})$ (see Section 5.7), with $\mu^p(\boldsymbol{c}) \cdot S_{i,j}(\boldsymbol{\sigma}, \boldsymbol{\theta})$. As mentioned earlier BSM effects in the reconstruction

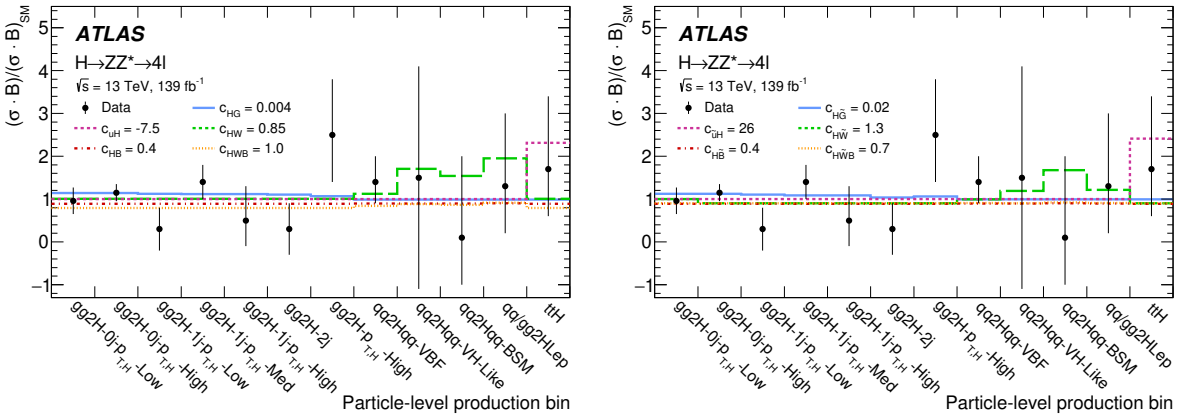

Figure 6.27: The measured signal yield ratio in each particle-level production bin of the Reduced Stage 1.1 scheme together with the prediction for a chosen set of (a) $C\mathcal{P}$-even and (b) $C\mathcal{P}$-odd BSM parameter values. The values are chosen such that they correspond to the expected 68 % C. L. interval of the cross-section measurement.

efficiency $\epsilon^{p}_{i,j}$ are expected to be negligible and thus not taken into account. The likelihood function in the EFT interpretation is given by

$$\mathcal{L}(\boldsymbol{\sigma},\boldsymbol{\theta}) = \prod_{j}^{N_{\text{categories}}} \prod_{i}^{N_{\text{bins}}} P\left(N_{i,j}|\mu^{p}(\boldsymbol{c})\cdot L\cdot\boldsymbol{\sigma}\cdot \text{BR}\cdot\mathcal{A}_{i,j}(\boldsymbol{\theta}) + B_{i,j}(\boldsymbol{\theta})\right) \times \prod_{m}^{N_{\text{nuisance}}} C_{m}(\boldsymbol{\theta})\,. \tag{6.21}$$

Note that BSM contributions to the background predictions $B_{i,j}(\boldsymbol{\theta})$ are neglected. Constraints on the BSM coupling parameters are obtained using the profile likelihood ratio (Equation 5.2) discussed in Section 5.7.

6.8 Results

The measured signal yield normalized to its SM prediction is shown in Figure 6.27 for each particle-level production bin of the Reduced Stage 1.1 scheme, together with the expected yield in chosen BSM scenarios. No significant deviations from the SM prediction are observed. The EFT parameters are chosen to be compatible with the error on the cross-section measurement at 68 % C. L. interval. The chosen parameters affect the signal yield in the gg2H bins by up to 20 % with c_{HW}, c_{uH}, and $c_{\widetilde{u}H}$ having the smallest impact. Observable BSM effects in the qq2Hqq production bins are mostly due to the parameters c_{HW} and $c_{H\widetilde{W}}$. This can be explained by their significantly larger contribution to the production vertex compared to the other EFT parameters, presented in Figure 6.4. The same is true for the Higgs boson decay. However, in this case, the effects are compensated by taking the BSM dependence of the signal acceptance into account. The ttH production bin depends almost exclusively on c_{uH} and $c_{\widetilde{u}H}$ because possible contributions from c_{HG} and $c_{H\widetilde{G}}$ are very much constrained by the gg2H bins. The Wilson coefficients c_{HB}, $c_{H\widetilde{B}}$, c_{HWB}, and $c_{H\widetilde{W}B}$ are most sensitive to the decay vertex and predominantly measured in gg2H production.

Due to the limited sensitivity, a simultaneous maximum likelihood fit with all BSM parameters is not possible at the current stage. Thus, at most, two Wilson coefficients are fitted simultaneously. Figure 6.28 shows the one-dimensional fit results with only one BSM coupling parameter fitted at a time while all others are set zero. The corresponding $-2\ln(\lambda)$ profiles of the $C\mathcal{P}$-even and $C\mathcal{P}$-odd BSM coupling parameters are shown in Figures 6.29 and 6.30. The best-fit values with their corresponding p-value as well as the observed and expected 68 % and 95 % C. L. intervals are summarized in Table 6.18. The measurements are dominated by statistical uncertainty. In case of the $C\mathcal{P}$-odd BSM coupling parameters,

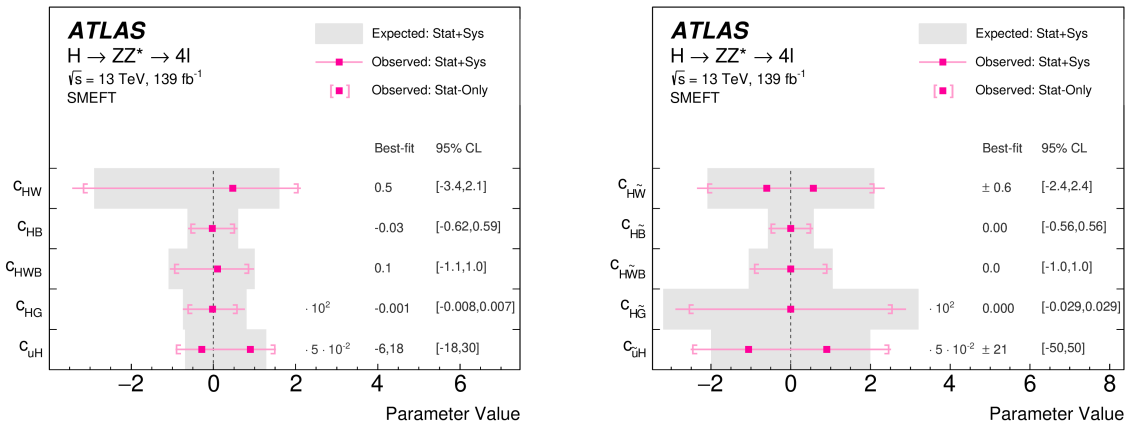

Figure 6.28: The observed best-fit values for the BSM coupling parameters in the SMEFT together with the 95 % C. L. regions (horizontal bands) for (a) $C\mathcal{P}$-even and (b) $C\mathcal{P}$-odd operators obtained for an integrated luminosity of 139 fb^{-1} at $\sqrt{s}$ = 13 TeV. Only one parameter is fitted at a time while all others are set to zero. The values for c_{HG} and $c_{H\widetilde{G}}$ (c_{uH} and $c_{\widetilde{u}H}$) are multiplied by 100 (0.05) to improve the readability of the graphic. The dashed vertical line represents the SM expectation.

Table 6.18: The observed best-fit values of the SMEFT coupling parameters together with their p-values and the observed and expected confidence intervals at 68 % and 95 % C. L. for an integrated luminosity of 139 fb^1 at $\sqrt{s}$ = 13 TeV. The limits are computed using the confidence-level interval method. Only one Wilson coefficient is fitted at a time while all others are set to zero.

Wilson	Best-fit		observed		SM expected	
Coeffcient	value	p-value	68 % C. L.	95 % C. L.	68 % C. L.	95 % C. L.
c_{HW}	0.5	0.66	$[-1.5, 1.3]$	$[-3.4, 2.1]$	$[-1.6, 0.9]$	$[-2.9, 1.6]$
c_{HB}	−0.03	0.98	$[-0.42, 0.37]$	$[-0.62, 0.59]$	$[-0.43, 0.38]$	$[-0.62, 0.60]$
c_{HWB}	0.10	0.93	$[-0.71, 0.63]$	$[-1.06, 0.99]$	$[-0.75, 0.63]$	$[-1.09, 0.99]$
c_{HG}	−0.0002	0.79	$[-0.0048, 0.0029]$	$[-0.0083, 0.0068]$	$[-0.0038, 0.0040]$	$[-0.0073, 0.0080]$
c_{uH}	−6	0.50	$[-12, 6]$	$[-18, 30]$	$[-8, 20]$	$[-14, 26]$
$c_{H\widetilde{W}}$	0.6	0.84	$[-1.5, 1.5]$	$[-2.4, 2.4]$	$[-1.3, 1.3]$	$[-2.1, 2.1]$
$c_{H\widetilde{B}}$	0.00	1.00	$[-0.37, 0.37]$	$[-0.56, 0.56]$	$[-0.39, 0.39]$	$[-0.57, 0.57]$
$c_{H\widetilde{W}B}$	0.0	1.00	$[-0.69, 0.69]$	$[-1.03, 1.03]$	$[-0.71, 0.71]$	$[-1.05, 1.05]$
$c_{H\widetilde{G}}$	−0.000	1.00	$[-0.019, 0.019]$	$[-0.029, 0.029]$	$[-0.022, 0.022]$	$[-0.031, 0.031]$
$c_{\widetilde{u}H}$	−21	0.48	$[-37, 37]$	$[-50, 50]$	$[-26, 26]$	$[-40, 40]$

the profiles are symmetrical with respect to the BSM parameter featuring two degenerate minima. This is explained by their pure quadratic BSM dependence for pseudoscalar operators at mass dimension six. The only $C\mathcal{P}$-even parameter which also shows two distinct minima is c_{uH}. However, the two minima are not symmetrical around zero in this case because the EFT parameterization of the ttH production crosses the expected SM value at two different values of c_{uH} (see Figure 6.10(a)).

The strongest constraint is obtained for the parameter c_{HG} describing the BSM contribution to the $C\mathcal{P}$-even Higgs boson interactions with gluons. The 95 % C. L. interval is found to be $[-0.008, 0.007]$ in this case. This stringent constraint results from the fact that the linear terms in the EFT parameterization dominate over the quadratic terms (see Figure 6.2(a)) within the measurement's sensitivity range. Although the gg2H-p_T^H-High bin is designed to target effects from BSM physics, c_{HG} is actually more sensitive to

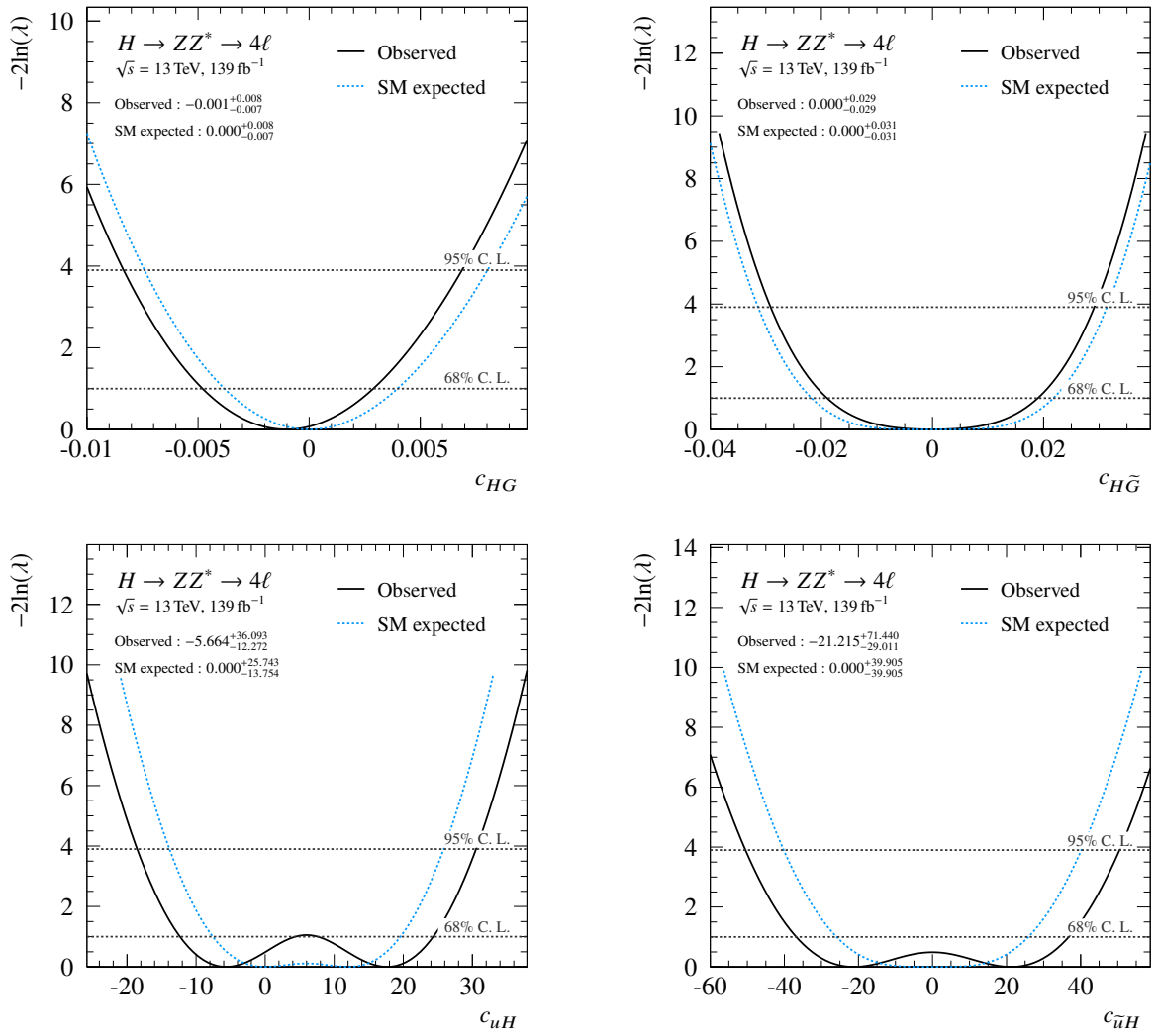

Figure 6.29: The one-dimensional fit results for the observed (black solid) and SM expected (blue dashed) statistical scans of the BSM coupling parameters c_{HG} and c_{uH} (*left panels*), and $c_{H\widetilde{G}}$ and $c_{\widetilde{u}H}$ (*right panels*) for an integrated luminosity of 139 fb[1] at $\sqrt{s}$ = 13 TeV. The 68 % and 95 % C. L. regions for the scanned parameter are indicated by dashed horizontal lines. Note that except for the fitted parameter, all other Wilson coefficients are set to zero.

the gg2H-0j-p_T^H-Low and gg2H-0j-p_T^H-High particle-level production bins. The reason for this is the small absolute number of events in the dedicated BSM bin compared to the zero-jet bins. The constraint on $c_{H\widetilde{G}}$ is about three times weaker with $[-0.029, 0.029]$ since the linear terms do not contribute to the total cross-section in this case.

The next-strongest constraints are obtained for the BSM coupling parameters related to the operators that directly contribute to the HZZ interaction vertex. These are $c_{H\widetilde{B}}$, c_{HB}, c_{HWB}, $c_{H\widetilde{W}B}$, $c_{H\widetilde{W}}$ and c_{HW} in that order. Since the first four of these BSM couplings parameters are mainly measured in the gg2H production bins, the corresponding constraints are more stringent than the constraints on c_{HW} and $c_{H\widetilde{W}}$. The latter constraints are mostly obtained from the qq2Hqq-VBF and qq2Hqq-BSM bins. Since both the scalar and pseudoscalar parameterizations are dominated by the quadratic terms, the constraints on the $C\mathcal{P}$-even and $C\mathcal{P}$-odd parameters are comparable in size. Even smaller constraints are set on c_{uH} and $c_{\widetilde{u}H}$ which describe the scalar and pseudoscalar BSM contributions to the top-Yukawa coupling. The

Table 6.19: The observed best-fit points and their p-values obtained from the two-dimensional likelihood scans for an integrated luminosity of 139 fb^{1} at $\sqrt{s}$ = 13 TeV. The limits are computed using the confidence-level interval method. Only two BSM coupling parameters are fitted at a time while all others are set to zero.

Parameter	best-fit point		best-fit	parameter	best-fit point		best-fit
combination	1. parameter	2. parameter	p-value	combination	1. parameter	2. parameter	p-value
c_{HW}, c_{HB}	0.57	0.05	0.88	$c_{H\widetilde{W}}, c_{H\widetilde{B}}$	±1.12	∓0.21	0.91
c_{HW}, c_{HWB}	0.59	−0.14	0.81	$c_{H\widetilde{W}}, c_{H\widetilde{W}B}$	±1.13	±0.39	0.80
c_{HB}, c_{HWB}	1.74	2.24	0.82	$c_{H\widetilde{B}}, c_{H\widetilde{W}B}$	0.00	0.00	0.79
c_{HW}, c_{HG}	0.54	−0.001	0.81	$c_{H\widetilde{W}}, c_{H\widetilde{G}}$	±0.56	0.00	0.79
c_{HB}, c_{HG}	−0.04	−0.001	0.78	$c_{H\widetilde{B}}, c_{H\widetilde{G}}$	0.00	0.00	1.00
c_{HWB}, c_{HG}	−0.02	−0.001	0.79	$c_{H\widetilde{W}B}, c_{H\widetilde{G}}$	0.00	0.00	0.79
c_{uH}, c_{HG}	−5.7, 17.7	−0.001	0.80	$c_{\widetilde{u}H}, c_{H\widetilde{G}}$	±21.21	0.00	0.80

smallest p-value is observed for $c_{\widetilde{u}H}$ with $p = 0.48$, which corresponds to deviation from the SM of 0.7σ. Thus, indicating no evidence for new physics.

In addition, possible correlations between the BSM coupling parameters are explored by fitting two Wilson coefficients at a time. No mixtures of $C\mathcal{P}$-even and $C\mathcal{P}$-odd operators are probed since the corresponding interference terms are vanishing as shown in Sections 6.1, 6.2 and 6.3.2, for the production, decay, and acceptance parameterizations, respectively. Thus, no non-trivial correlations between these parameters are expected. The two-dimensional contours of the test statistic at 95 % C. L. for the scalar parameter combinations are shown in the left panels of Figures 6.32, 6.31, and 6.33, while the pseudoscalar combinations are shown in the right panels. The best-fit points of these scans and their respective p-values are summarized in Table 6.19. All observed best-fit values agree with the SM prediction and are consistent with the one-dimensional results.

The anti-correlation between c_{HW} ($c_{H\widetilde{W}}$) and c_{HB} ($c_{H\widetilde{B}}$) originates from the parameterization of the signal acceptance. This can be seen clearly by comparing the expected signal yields for the $\sigma \cdot \mathrm{BR}$ and $\sigma \cdot \mathrm{BR} \cdot \mathcal{A}$ parameterizations in the gg2H-0j-p_T^H-High bin in Figures 6.18(a) and 6.18(d), respectively. The non-ellipsoidal shape is also caused by the acceptance parameterization. The "V"-shaped correlation for large absolute values of c_{HW} and $c_{H\widetilde{W}}$ are mostly caused by the qq2Hqq processes (see Figures 6.20(a) and D.25(a)). The same reasoning can also be applied to the other contours shown in Figure 6.32.

Similar "V"-shaped correlations are observed for parameter combinations that include c_{HG} and $c_{H\widetilde{G}}$ as shown in Figure 6.31. They result from BSM effects in the ggF production vertex, the Higgs boson decay vertex, and the signal acceptances. This loosens the constraint on $c_{H\widetilde{G}}$ if the absolute values of $c_{H\widetilde{W}}$, $c_{H\widetilde{B}}$ or $c_{H\widetilde{W}B}$ are increased. Similar arguments hold in the $C\mathcal{P}$-even case. However, while the contours for the pseudoscalar parameters are symmetrical around the $c_{H\widetilde{G}}$ axis, the corresponding ones for the scalar parameters are one-sided. This results from the large linear terms that contribute to ggF production cross-section for $C\mathcal{P}$-even operators. Due to the complex interplay between these parameters, additional islands in the parameter space are still allowed at 95 % C. L. for some parameter combinations.

The correlation between the c_{HG} ($c_{H\widetilde{G}}$) and c_{uH} ($c_{\widetilde{u}H}$) is caused by the ttH production vertex. This correlation has negligible impact on the measurement of c_{HG} and $c_{H\widetilde{G}}$ because they are already tightly constrained by the ggF vertex. The constraints on c_{uH} are tighter than the constraints on $c_{\widetilde{u}H}$ because of the additional linear terms and the larger quadratic terms in the parameterization of the production cross-section.

Table 6.20: The observed one-dimensional 95 % C. L. limits for the BSM coupling parameters of the SMEFT obtained in different Higgs boson decay channels at ATLAS. All other parameters are set to zero.

BSM coupling	139 fb^{-1}				36.1 fb^{-1}
parameter	$H \to ZZ^* \to 4\ell$	$H \to \gamma\gamma$	$H \to b\bar{b}$		$H \to WW^*$
			VH	VH (high-p_T^V)	$+H \to WW$
c_{HW}	$[-3.4, 2.1]$	$[-8.3, 8.3] \times 10^{-4}$	$[-0.97, 0.31]$	$[-0.87, 0.38]$	$[-3.6, 5.4]$
c_{HB}	$[-0.62, 0.59]$	$[-2.4, 2.4] \times 10^{-4}$	-	-	$[-9.4, 9.4]$
c_{HWB}	$[-1.06, 0.99]$	$[4.2, 4.2] \times 10^{-4}$	$[-1.1, 1.9]$	$[-7.1, 3.3]$	$[-8.0, 7.8]$
c_{HG}	$[-8.3, 6.8] \times 10^{-3}$	$[-6.1, 4.7] \times 10^{-4}$	-	-	$[-7.4, 15.5] \times 10^{-3}$
c_{uH}	$[-18, 30]$	-	-	-	$[-5.7, 2.6]$
$c_{H\widetilde{W}}$	$[-2.4, 2.4]$	$[1.5, 1.4] \times 10^{-4}$	-	-	-
$c_{H\widetilde{B}}$	$[-0.56, 0.56]$	$[-3.7, 3.7] \times 10^{-4}$	-	-	-
$c_{H\widetilde{W}B}$	$[-1.03, 1.03]$	$[-1.2, 1.1] \times 10^{-4}$	-	-	-
$c_{H\widetilde{G}}$	$[-2.9, 2.9] \times 10^{-2}$	$[-2.0, 2.0] \times 10^{-4}$	-	-	-
$c_{\widetilde{u}H}$	$[-50, 50]$	-	-	-	-

6.9 Comparison to other Decay Channels

The tensor structure of the Higgs boson interaction is also probed in other Higgs boson decays using the framework of the SMEFT. At ATLAS, results are available in $H \to \gamma\gamma$ decays, from a combined analysis of $H \to WW^*$ and $H \to WW$ decays [464], and in associated production of a Higgs boson decaying into b quarks with a vector boson [465, 466]. In addition, a combined interpretation of several search channels has already been published [467]. Since these analyses are performed in different decay channels, they target different interaction vertices, and thus, different BSM coupling modifiers. In this section, only the parameters that are equivalent to the ones interesting for the $H \to ZZ^* \to 4\ell$ decay channel are discussed.

Table 6.20 compares the 95 % C. L. intervals of the different analyses. The measurement in the $H \to \gamma\gamma$ decay channel is about one order of magnitude more sensitive for c_{HG} and $c_{H\widetilde{G}}$ compared to the interpretation performed in this thesis because of the larger amount of reconstructed Higgs boson candidates in $H \to \gamma\gamma$ decays. For the other probed BSM coupling parameters, the $H \to ZZ^* \to 4\ell$ analysis is about four orders of magnitude less sensitive. This is mainly related to the strong BSM dependence of the detector acceptance (see Figure 6.17), which significantly decreases the sensitivity of the measurement, and on the other hand, to the smaller number of reconstructed events containing Higgs boson candidates. The constraints obtained from the combined $H \to WW^*$ and $H \to WW$ analysis are weaker for most $C\mathcal{P}$-even parameter, because the measurement is performed on the reduced data set with only 36.1 fb^{-1}. However, the constraint on c_{uH} is significantly stronger. In addition to these parameters, the analysis also probes many other $C\mathcal{P}$-even BSM coupling parameters of the SMEFT, but no results on the $C\mathcal{P}$-odd are given. In the $H \to b\bar{b}$ decay channel, two separate analyses are conducted. Both target Higgs bosons produced in VH production, but one specifically targets vector bosons with large transverse momentum. Only the most sensitive parameters are studied explicitly. The relevant ones for this thesis are c_{HW} and c_{HWB}. For c_{HW}, the obtained limits are about a factor of 3 – 5 stronger than the constraints from the $H \to 4\ell$ analysis. For c_{HWB}, the constraint from the high-p_T^V analysis is significantly weaker, while the other analysis is only slightly less sensitive than the analysis in the four-lepton decay channel.

Since these measurements are not sensitive enough to constrain all coefficients in a simultaneous maximum likelihood fit, a second fitting procedure using principal component decomposition is performed. This approach provides a set of linear combinations of Wilson coefficients, called eigenvector combinations,

which are fitted simultaneously. The same approach is used in the ATLAS combination. Since these results are given in different basis representations, they are not directly comparable to the intervals given above. Results on the $C\mathcal{P}$-odd parameters are only available in the $H \to \gamma\gamma$ decay channel. Thus, no comparison with other analyses is possible.

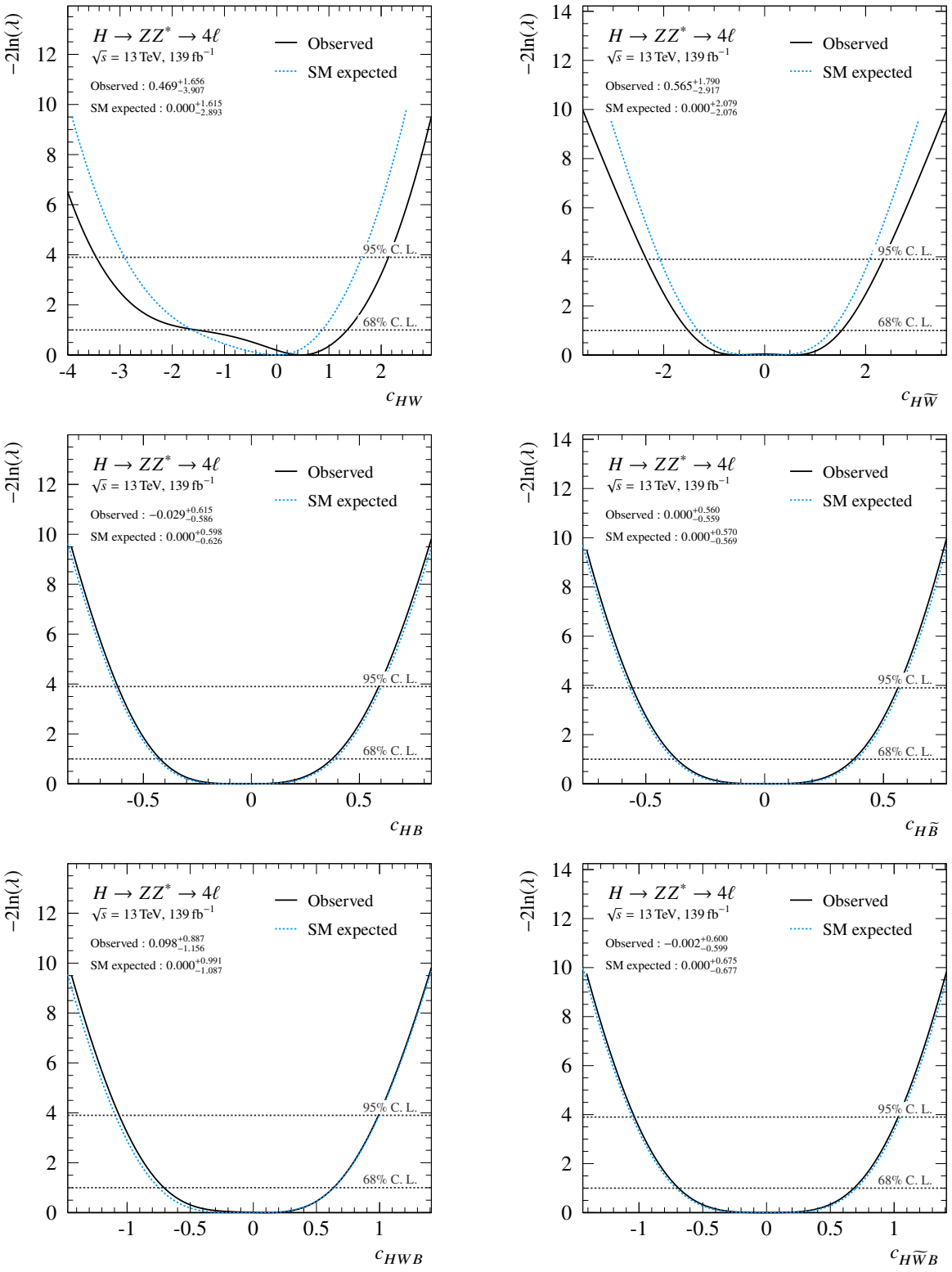

Figure 6.30: The one-dimensional fit results for the observed (black solid) and SM expected (blue dashed) statistical scans of the $\mathcal{CP}$-even BSM coupling parameters c_{HW}, c_{HB} and c_{HWB} (*left panels*), and $c_{H\widetilde{W}}$, $c_{H\widetilde{B}}$ and $c_{H\widetilde{W}B}$ (*right panels*) for an integrated luminosity of 139 fb[1] at $\sqrt{s}$ = 13 TeV. The 68 % and 95 % C. L. regions for the scanned parameter are indicated by dashed horizontal lines. Note that except for the fitted parameter, all other Wilson coefficients are set to zero.

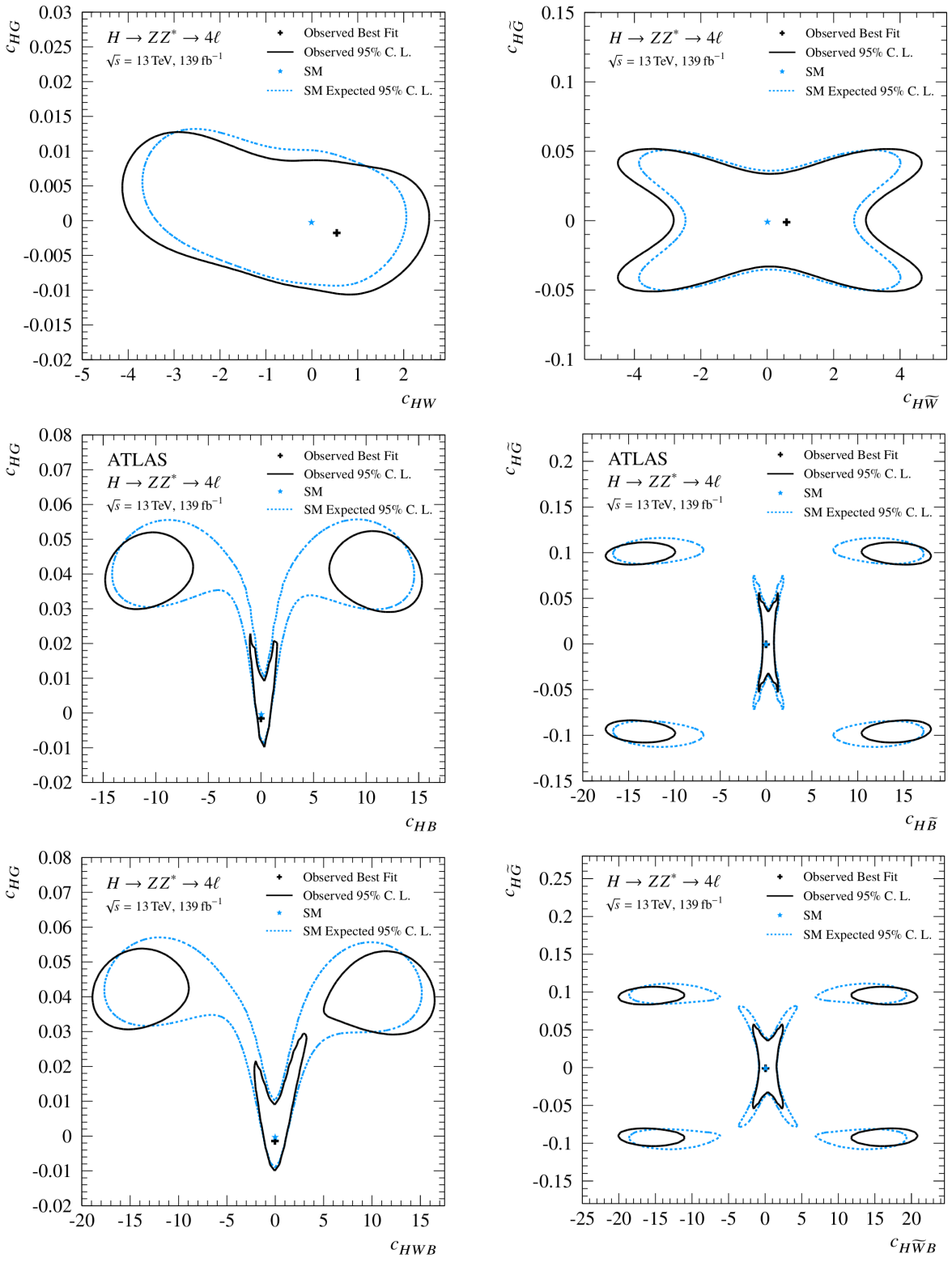

Figure 6.31: The two-dimensional fit results for the observed (black solid) and SM expected (blue dashed) likelihood contours at 95 % C. L. for different combinations of $C\mathcal{P}$-even parameter that involve the BSM coupling parameter c_{HG} and one of the parameters c_{HW}, c_{HB} and c_{HWB} each (*left panels*), and for different combinations of $C\mathcal{P}$-odd parameters that involve the BSM coupling parameter $c_{H\widetilde{G}}$ and one of the parameters $c_{H\widetilde{W}}$, $c_{H\widetilde{B}}$ and $c_{H\widetilde{W}B}$, each (*right panels*). Note that except for the fitted parameters, all other Wilson coefficients are set to zero.

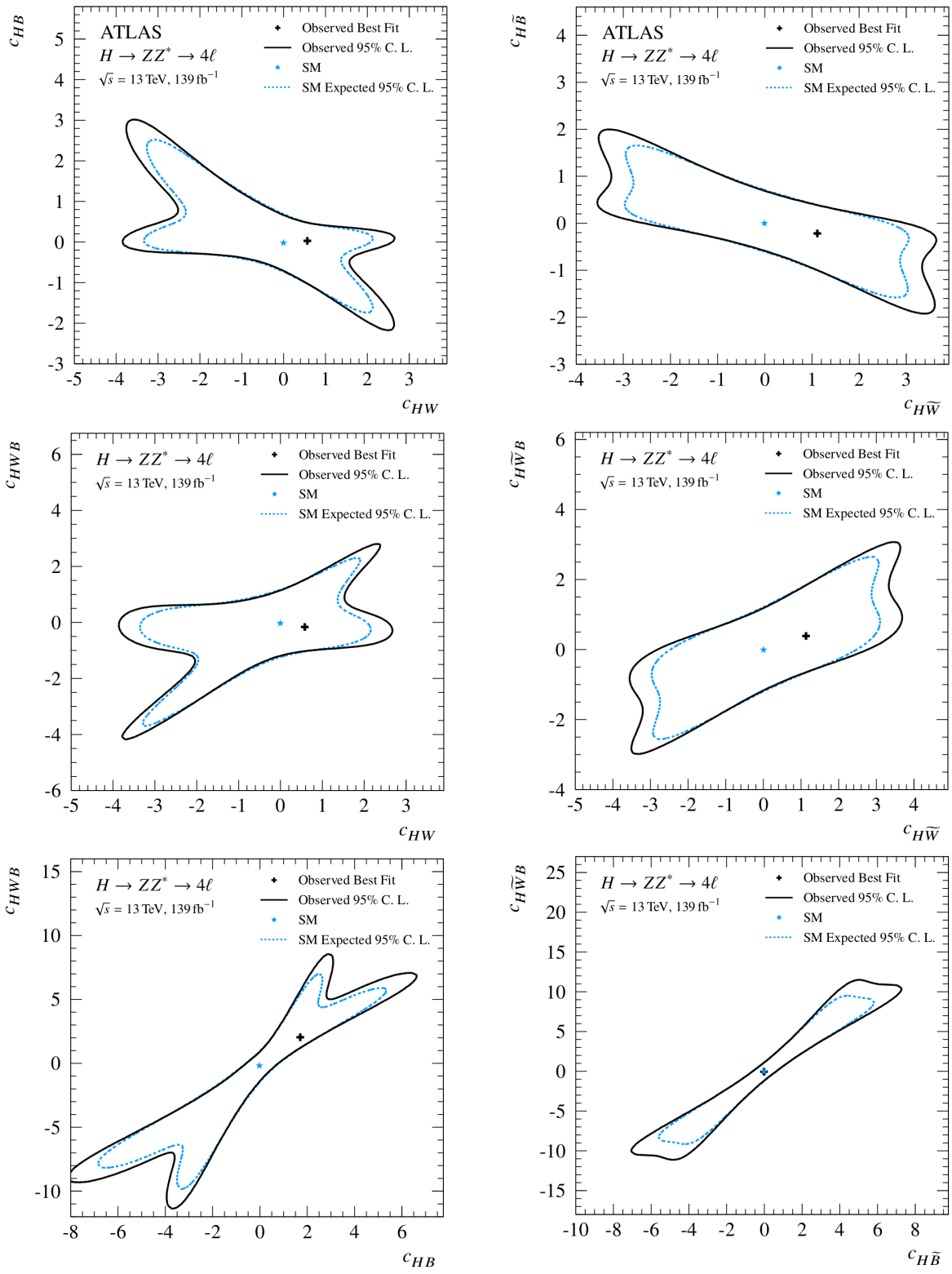

Figure 6.32: The two-dimensional fit results for the observed (black solid) and SM expected (blue dashed) likelihood contours at 95 % C. L. for different combinations of the $C\mathcal{P}$-even parameters c_{HW}, c_{HB} and c_{HWB} (*left panels*), and for different combinations of the $C\mathcal{P}$-odd parameters $c_{H\widetilde{W}}$, $c_{H\widetilde{B}}$ and $c_{H\widetilde{W}B}$ (*right panels*) for an integrated luminosity of 139 fb[1] at $\sqrt{s} = 13$ TeV. Note that except for the fitted parameters, all other BSM coupling parameters are set to zero.

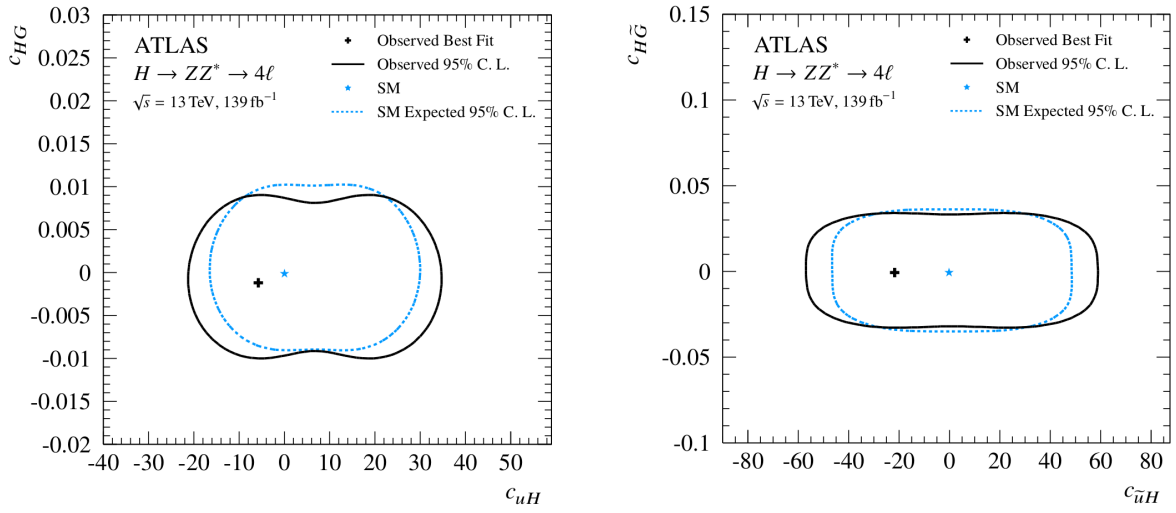

(a) (b)

Figure 6.33: The two-dimensional fit results for the observed (black solid) and SM expected (blue dashed) likelihood contours at 95 % C. L. of the parameters (a) $c_{uH} - c_{HG}$ and (b) $c_{\widetilde{u}H} - c_{H\widetilde{G}}$. Note that except for the fitted parameters, all other BSM coupling parameters are set to zero.

CHAPTER 7

Indirect Constraints on Possible $\mathcal{CP}$ Admixtures from Rate Measurements

In this chapter, the scope of possible $\mathcal{CP}$-violation in the Higgs sector and deviations from the SM couplings are explored. The studies are based on the *indirect approach* to probe the $\mathcal{CP}$ properties of the Higgs boson[1]. Constraints on possible $\mathcal{CP}$ admixtures are imposed by fitting a general $\mathcal{CP}$-violating model to the measured Higgs signal rates published by the LHC collaborations.

In Section 7.1, constraints on possible $\mathcal{CP}$ mixing in the top-Yukawa coupling [258] are set using `HiggsSignals` (introduced in Section 4). Different levels of complexity in the model assumptions are investigated, and the most general case considers modifications to the ggF, ZH and ttH production cross-sections and the $H \to \gamma\gamma$ decay rate. In Section 7.2, constraints on possible Higgs $\mathcal{CP}$ admixtures are set using the formalism introduced in Section 2.4.2.2. This parameterization describes the couplings of a general $\mathcal{CP}$-mixed state to the SM particles. It is consistent with a large variety of theoretical models consisting only of singlet and doublet Higgs fields. In its most general form, it also considers $\mathcal{CP}$-odd contributions from higher-dimensional interaction operators in the couplings to gauge bosons. Different model assumptions are investigated. The fits are performed with `HiggsSignals` using the LHC Run-1 and Run-2 Higgs signal measurements published by the LHC experiments. The same model is used in Section 7.3 to find constraints using the full likelihood function of the $H \to ZZ^* \to 4\ell$ analysis in ATLAS with 139 fb^{-1} of proton-proton collisions at a cms energy of 13 TeV.

7.1 Constraints on $\mathcal{CP}$-Mixing in the Top-Yukawa Coupling

The model used for the study presented in this section is described in Section 2.4.2.3. It is based on the Higgs characterization (HC) model but only considers possible CP-violating effects in the top quark sector. The model dependence of the $tt\phi$ coupling is studied by successively allowing for BSM contributions to the HVV and the effective $H\gamma\gamma$ and Hgg couplings. Four different model parameterizations are investigated. While model 1 has only two free parameters, c_t and $\tilde{c}_t$, the most general model (model 4) contains five free parameters: $c_t, \tilde{c}_t, c_V, c_g$, and c_γ. The study is performed with `HiggsSignals` using 81 LHC Run-2 measurements and 20 Run-1 measurements. The former input is listed in Tables B.1, B.2, and B.3, and the latter is described in Section 4.3.3.

The χ^2 evaluation for the different input formats in `HiggsSignals` is described in Section 4.3.2. It is assumed that the theoretical uncertainties of the Higgs boson production and decay rates and their correlations are the same as in the SM. The 1σ, 2σ, and 3σ C. L. regions for two-dimensional $\Delta\chi^2$ profiles assuming the Gaussian limit approximation correspond to $\Delta\chi^2 \leq 2.3$, 6.18, and 11.83, respectively.

[1] The difference between direct and indirect $\mathcal{CP}$ probes are discussed in Section 2.3.

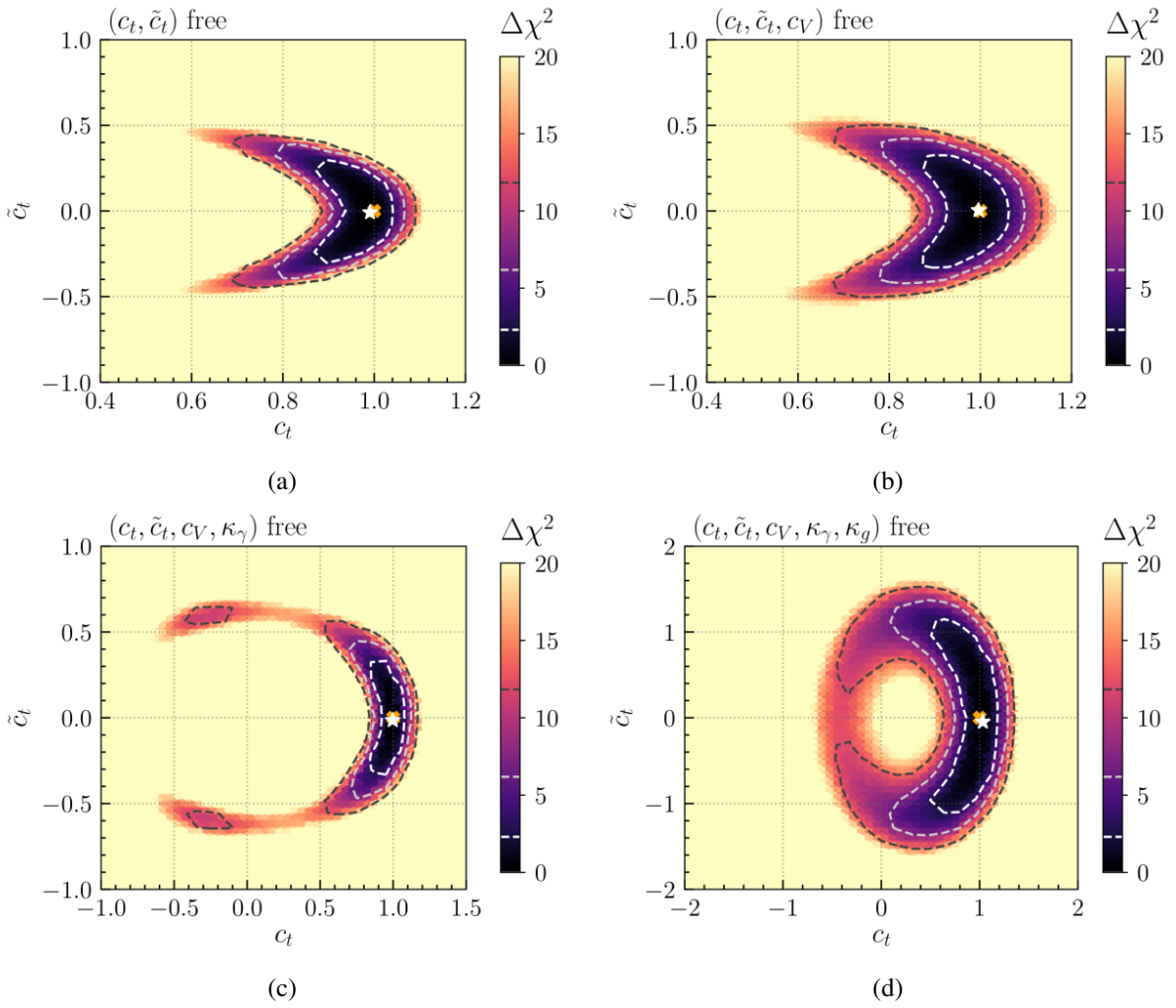

Figure 7.1: Fit results in the $(c_t, \tilde{c}_t)$ parameter plane for (a) model 1, (b) model 2, (c) model 3, and (d) model 4 using the available Higgs signal rate measurements from the LHC. The color corresponds to the $\Delta\chi^2$ value of the global fit and the 1σ, 2σ, and 3σ C. L. regions are shown as white, light-gray, and dark-gray dashed contours, respectively. The best-fit point and the SM prediction are marked by a white star and an orange cross, respectively. Note the larger scale required to display the bottom plots.

Figure 7.1 shows the fit results for the different model parameterizations. The two-dimensional $\Delta\chi^2$ profiles are shown in color and the 1σ, 2σ, and 3σ C. L. regions are indicated by white, light-gray, and dark-gray dashed lines, respectively. All four model parametrizations feature a best-fit point which is remarkably close to the SM prediction. The minimal χ^2 improves only insignificantly compared to the SM χ^2, despite the up to five additional free parameters.

In the first three model parameterizations (model 1, 2 and 3) the effective scale factor, κ_g, is derived as a function of c_t and $\tilde{c}_t$ assuming $c_g = \tilde{c}_g = 0$ in Equation 2.118. In model 1 and model 2, the favored region is constrained to positive values of c_t because the preferred value of the derived scale factor for the effective photon coupling, κ_γ, (see Equation 2.119 for $c_\gamma = \tilde{c}_\gamma = 0$) is close to +1. The favored region for model 2 (see Figure 7.1(b)) is slightly larger than the corresponding region for model 1 (see Figure 7.1(a)) because of the additional freedom in the Higgs-vector boson coupling, c_V, which influences the Higgs boson partial decay width into two photons. Since model 3 treats κ_γ as a free parameter, the lower bound

on c_t is weakend as shown in Figure 7.1(c). In this case, two local minima in the $\Delta\chi^2$ profile appear at $(c_t, \tilde{c}_t) \approx (-0.3, \pm 0.6)$, which are compatible with the data at the 3σ level. In these regions, the ggF and the combined top-quark associated signal strengths are SM-like. However, since the $gg \to ZH$ production is strongly enhanced in this region, it is excluded at 2σ level.

In model 4, both κ_g and κ_γ are treated as free parameters. In this case, the allowed region in the $(c_t, \tilde{c}_t)$ plane is largely extended as shown in Figure 7.1(d) (note the enlarged scale on both axes). Since the ggF production cross-section is now calculated by an individual parameter, the fit is no longer constrained to the allowed parameter space near the region where $\kappa_g = \kappa_g(c_t, \tilde{c}_t) \approx 1$. In this case, the $gg \to ZH$ and the top-quark associated production modes become more important and impose constraints on the $(c_t, \tilde{c}_t)$ parameter plane. Since these constraints are much weaker than before, the allowed region in c_t and $\tilde{c}_t$ is significantly enlarged allowing even vanishing values of c_t at the 2σ level.

The effects from the kinematic shape modifications in the $pp \to ZH$ channel induced by $\mathcal{CP}$-violating effects play a minor role in this discussion. Their impact is most pronounced in the regions of large $\tilde{c}_t$ and small c_t, as well as for negative c_t values if $\tilde{c}_t$ is small (see Figure E.1).

The constraints presented above can also be interpreted in terms of the $\mathcal{CP}$-violating phase, α_{tt}, in the top-Yukawa coupling. For model 1, 2 and 3, the constraints are similar, with $|\alpha_{tt}| \lessapprox 22.5° - 27°$ at the 2σ level. The second minima in model 3 (see Figure 7.1(c)) appear around $|\alpha_{tt}| \approx 110°$. In model 4, the $\mathcal{CP}$-violating phase is constrained to $|\alpha_{tt}| \lessapprox 72°$. Thus, in a general BSM model the constraints are still rather weak. For the differnet model assumptions they correspond to $\cos\alpha_{tt} \gtrapprox 0.89 - 0.92$ and $\cos\alpha_{tt} \gtrapprox 0.31$, respectively.

7.2 $\mathcal{CP}$-Mixing Constraints in Global Interpretations

In this section, $\mathcal{CP}$ violation in the Higgs sector is constrained using the latest LHC Run-1 and Run-2 Higgs signal measurements published by the ATLAS and CMS collaborations. The general model setup is described in Section 2.4.2.2, and the fits are performed with `HiggsSignals`.

For an efficient sampling of the parameter space, the scans are performed with an adaptive Metropolis (AM) algorithm [468] with flat prior probability distributions using the Markov-Chain Monte Carlo (MCMC) python package PyMC [469]. Appropriate initial values for the MCMC chains are found using the maximum a posteriori estimate (MAP) class of PyMC. The scans contain around 10^6-10^9 points, depending on the dimensionality of the parameter space. For each scan, several independent Markov chains are run simultaneously, featuring a typical length of 10^5-10^6 points. The results are presented in the pure frequentist interpretation based on the global χ^2 derived from `HiggsSignals`. The 1σ, 2σ, and 3σ C. L. regions for two-dimensional $\Delta\chi^2$ profiles assuming the Gaussian limit approximation correspond to $\Delta\chi^2 \leq 2.3$, 6.18 and 11.83, respectively.

Throughout this section, a bar on top of a coupling parameter indicates that the parameter is a derived quantity. Different benchmark parameterizations with increasing complexity are investigated.

7.2.1 Common Pseudoscalar Coupling Scale Factor for Fermions

The first model parameterization (model I) that is investigated in this section features only two free parameters, $\cos\alpha$ and κ_f^p. The first one parameterizes the mixing of a $\mathcal{CP}$-even (H) and $\mathcal{CP}$-odd (A) Higgs boson, and the second one is a common coupling modifier for fermions parameterizing the pseudoscalar Yukawa couplings. The $\mathcal{CP}$-even Higgs couplings are assumed to be identical to the SM couplings, i. e. $\kappa_W^s = \kappa_Z^s = \kappa_f^s = 1$. Furthermore, it is assumed that there are no decays of the general Higgs state, $\phi = H\cos\alpha + A\sin\alpha$, into states of new physics (NP), i. e. $\mathrm{BR}(\phi \to \mathrm{NP}) = 0$.

Figure 7.2 shows the fit results as one- and two-dimensional $\Delta\chi^2$ profiles. The allowed range for

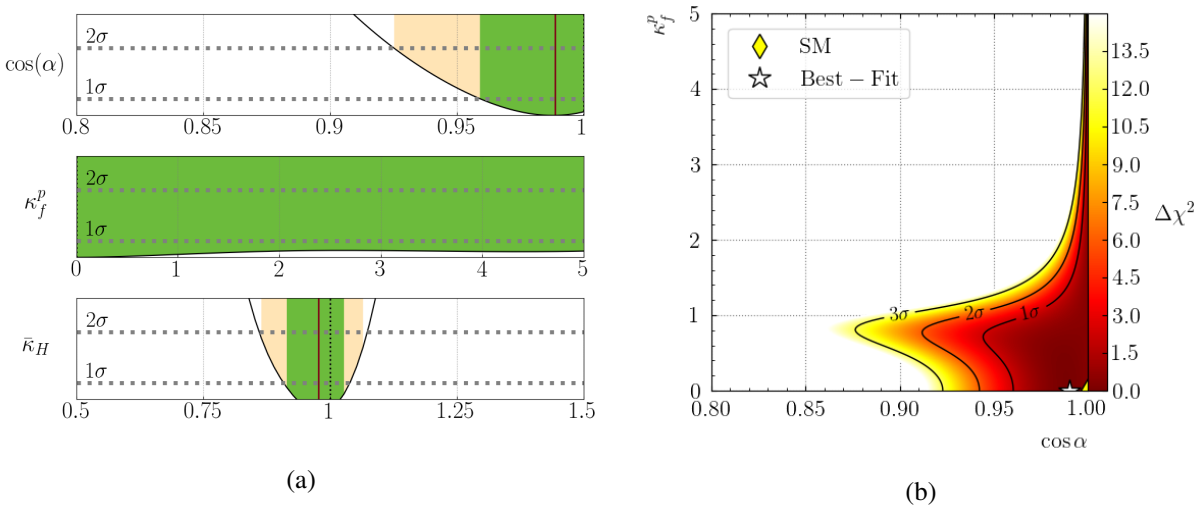

Figure 7.2: The (a) one-dimensional and (b) two-dimensional $\Delta\chi^2$ profiles for the free parameters $\cos\alpha$ and κ_f^p of model I of the general $C\mathcal{P}$-admixture parameterization. $\bar{\kappa}_H$ is the derived scale factor for the total width of the Higgs boson calculated from the model parameters.

Table 7.1: The best-fit values and the 68 % and 95 % C. L. regions for the fit parameters obtained from the one-dimensional $\Delta\chi^2$ profiles in the $(\cos\alpha, \kappa_f^p)$ fit.

Fit parameter	best-fit value	68 % C. L.	95 % C. L.
$\cos(\alpha)$	0.99	[0.97, 1.00]	[0.94, 1.00]
κ_f^p	0.0	-	-
$\bar{\kappa}_H$	0.98	[0.90, 1.04]	[0.87, 1.08]

possible $C\mathcal{P}$ admixtures is tightly constrained since the $C\mathcal{P}$-even couplings to SM particles are set to their SM values. The corresponding 68 % (95 %) C. L. region is defined by $\cos\alpha \geq 0.96$ (0.93). This limit corresponds to $\alpha \leq 15.9°$ (21.6°). The χ^2 distribution of the pseudoscalar coupling parameter is almost flat since the best-fit point is found very close to the SM limit. This means that any arbitrary large coupling parameter can be compensated with an arbitrarily small value of $\sin\alpha$. While the fit slightly prefers a vanishing value for κ_f^p, no constraint at 1σ C. L. is obtained. The fit results are summarized in Table 7.1.

The best-fit point features a goodness-of-fit of $\chi^2_{\text{min}}/\text{ndf} = 83.7/97$ which corresponds to a p-value of 83.0 %. There are some caveats in the interpretation of the goodness-of-fit, which become particularly important in case the p-value approaches the α level of the statistical test. One of them is related to the fact that the p-value depends on the statistical consistency between different separate measurement channels (see Section 4.4). Since all fits considered in this section are based on the same dataset, the p-value will be quoted in the following.

7.2.2 Probing Custodial Symmetry

In model II, the custodial global SU(2) symmetry is probed by introducing individual scale factors for the $C\mathcal{P}$-even Higgs couplings to W and Z bosons. In this model, the Yukawa couplings are scaled by generation-independent coupling scale factors κ_t, κ_b and κ_τ, and the Higgs-photon and Higgs-gluon

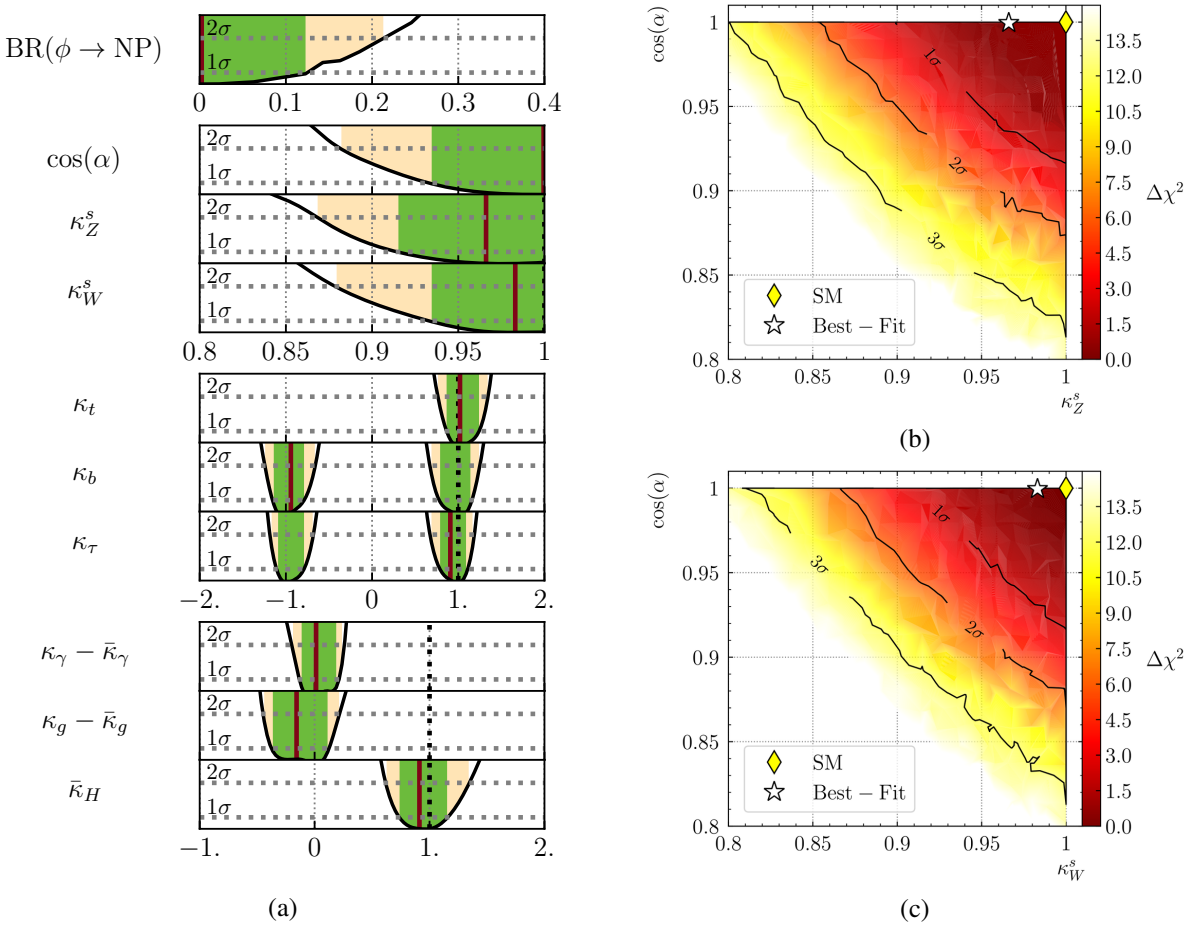

Figure 7.3: The fit results for model II(a) (i. e. assuming $\kappa_{W,Z}^s \leq 1$) of the general $C\mathcal{P}$-admixture parameterization. (a) The one-dimensional $\Delta\chi^2$ profiles for the free parameters of model II. The derived scale factors for the Higgs boson couplings to photons and gluons, $\bar{\kappa}_\gamma$ and $\bar{\kappa}_g$, are subtracted from the free fit values, κ_γ and κ_g, respectively. $\bar{\kappa}_H$ is the derived scale factor for the total width the Higgs boson calculated from the model parameters. (b) The two-dimensional $\Delta\chi^2$ profile in the $(\kappa_Z^s, \cos\alpha)$ plane and (c) the corresponding profile in the $(\kappa_W^s, \cos\alpha)$ plane.

couplings are treated as free quantities parameterized by κ_γ and κ_g, respectively. Furthermore, the branching ratio into states of new physics is an additional fit parameter BR($\phi \to$ NP).

Three different fit setups are investigated. In each fit, a different constraint is used to overcome the degeneracy induced by the unknown total width of the Higgs boson (see Section 2.4.1). Since the $W - Z$ boson interference term in the VBF production channel is neglected, the corresponding scale factors are assumed to be positive without loss of information.

The fit results for model II(a) (assuming that $\kappa_{W,Z}^s \leq 1$) are shown in Figure 7.3. The best-fit point is consistent with the SM limit and it features $\chi^2_{\text{min}}/\text{ndf} = 82.5/90$, corresponding to a p-value of 70.0 %. The best-fit values and the 68 % and 95 % C. L. ranges of the one-dimensional $\Delta\chi^2$ profiles are listed in Table 7.2. For the $C\mathcal{P}$-mixing parameter, these limits are $\cos\alpha \geq 0.93$ (i. e. $\alpha \leq 21.9°$) and $\cos\alpha \geq 0.89$ (i. e. $\alpha \leq 27.1°$), respectively. No significant difference between the Higgs coupling to Z and W bosons is observed. The two-dimensional profiles in the $(\kappa_Z^s, \cos\alpha)$ and $(\kappa_W^s, \cos\alpha)$ planes, shown in Figure 7.3(b) and 7.3(c), respectively, feature similar correlations. The corresponding profiles for the remaining parameter combinations are summarized in Figure E.2.

The top-Yukawa scale factor κ_t is constrained to positive values because of the $\kappa_t \kappa_W^s$ interference terms

Table 7.2: The best-fit values and 68 % and 95 % C. L. regions for the fit parameters of model II(a) obtained from the one-dimensional $\Delta\chi^2$ profiles. For κ_b, κ_τ, κ_γ, and κ_g only absolute values are given.

Fit parameter	best-fit value	68 % C. L.	95 % C. L.
$\cos(\alpha)$	1.0	[0.93, 1.00]	[0.89, 1.00]
κ_Z^s	0.96	[0.95, 1.00]	[0.86, 1.00]
κ_W^s	0.98	[0.95, 1.00]	[0.90, 1.00]
κ_t	1.02	[0.86, 1.24]	[0.76, 1.34]
$\lvert\kappa_b\rvert$	0.94	[0.79, 1.14]	[0.69, 1.21]
$\lvert\kappa_\tau\rvert$	0.91	[0.79, 1.09]	[0.69, 1.07]
$\lvert\kappa_\gamma\rvert$	0.98	[0.90, 1.13]	[0.84, 1.17]
$\lvert\kappa_g\rvert$	0.97	[0.80, 1.16]	[0.76, 1.24]
BR($\phi \to$ NP)	0.00	[0.00, 0.12]	[0.00, 0.21]
$\kappa_\gamma - \bar{\kappa}_\gamma$	0.01	[−0.14, 0.21]	[−0.19, 0.26]
$\kappa_g - \bar{\kappa}_g$	−0.16	[−0.36, 0.11]	[−0.44, 0.21]
$\bar{\kappa}_H$	0.91	[0.74, 1.15]	[0.61, 1.33]

in $Z\phi$, $tW\phi$ and $t\phi$ production. Since the corresponding terms for the bottom quark are very small (and therefore neglected), the profile of κ_b is symmetric with respect to the sign of the coupling parameter. Both the derived and the free fit parameters of the Higgs-photon and Higgs-gluon couplings are consistent with the SM coupling strength (see Table 7.2). Therefore, only the difference is shown in Figure 7.3(a).

The tight constraints on $\cos\alpha$ observed for model II(a) result from the assumption $\kappa_{W,Z}^s \leq 1$, which is valid in any scalar singlet and doublet extension of the SM. In the following, this constraint is subsequently loosened. In model II(b) it is loosened to $\kappa_{W,Z}^s \cos\alpha \leq 1$. This constraint still breaks the degeneracy induced by the total width by limiting the VBF, ZH and WH Higgs production channels. In contrast to that, in model II(c) the degeneracy is broken by taking into account an additional χ^2 contribution arising from constraints of the latest invisible Higgs search performed by ATLAS [256], which limits the allowed range of $\kappa_{W,Z}^s \cos\alpha$ and κ_t by assuming BR($\phi \to$ NP) = BR($\phi \to$ inv.).

Figure 7.4 shows the fit results obtained for both models in the $(\kappa_Z^s, \cos\alpha)$ plane. In both cases no physical constraint on $\cos\alpha$ is found. The artifical constraint $\cos\alpha \gtrapprox 0.1$ results from the fact that the allowed range of κ_Z^s (and κ_W^s) is limited to $[0, 10]$ in the fit setup. Since the fit prefers values of $\kappa_{Z,W}^s \cos\alpha \approx 1$, the smallest "allowed" value for the mixing parameter is $\cos\alpha \approx 0.1$. The model setup for model II(b) strictly requires that the mixing parameter is constrained to $\cos\alpha < 1/\kappa_{Z,W}^s$ (see Figure 7.4(a)). This constraint is loosened in model II(c), resulting in a slightly wider profile (see Figure 7.4(b)). The corresponding profiles in the $(\cos\alpha, \kappa_W^s)$ plane, depicted in Figure E.4, share the same properties.

The one-dimensional $\Delta\chi^2$ profiles of model II(b) and model II(c) are summarized in Figure E.3, and the corresponding best-fit point and the 68 % and 95 % C. L. ranges are listed in Table E.1. In both models, the best-fit point features a goodness-of-fit of $\chi^2_{\text{min}}/\text{ndf} = 82.4/90$, corresponding to a p-value of 70.3 %.

The fit results for all three constraints discussed in this section agree with the assumption of custodial symmetry. Therefore, $\kappa_W^s = \kappa_Z^s \equiv \kappa_V^s$ is assumed in the following.

7.2.3 Probing the Yukawa Couplings and the Effects of Dimension-Five Operators

In this section, model III and model IV of the general $C\mathcal{P}$-admixture parameterization are studied. In model III, the $C\mathcal{P}$ properties of the Yukawa couplings are investigated more carefully. To that end,

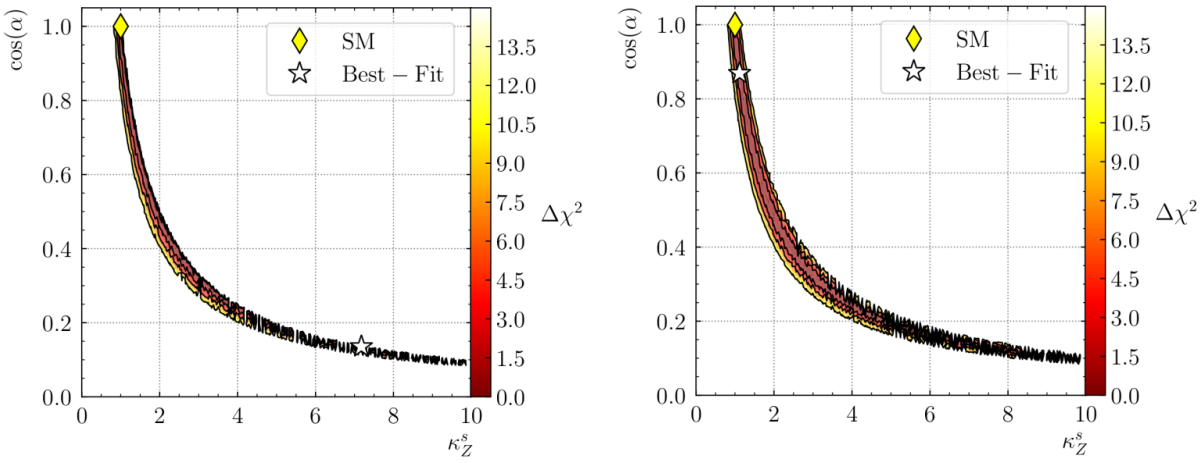

Figure 7.4: The two-dimensional projections of the $\Delta\chi^2$ profile for (a) model II(b) and (b) model II(c) of the general $C\mathcal{P}$-admixture parameterization in the $(\kappa_Z^s, \cos\alpha)$ plane. The black solid lines indicate the 1σ, 1σ, and 3σ C. L. contours. The corresponding labels are suppressed for clarity reasons.

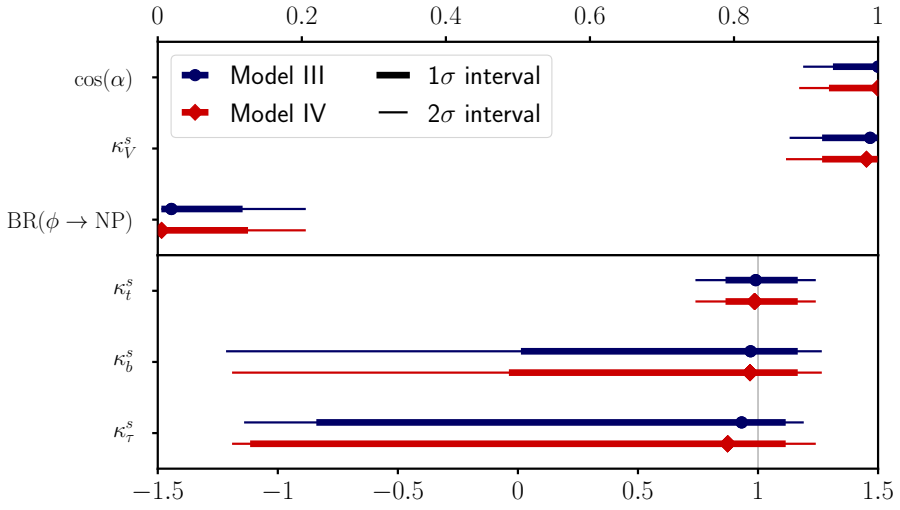

Figure 7.5: The fit results for the parameters $\cos\alpha$, κ_V^s, BR($\phi \to$ NP), κ_t^s, κ_b^s, and κ_τ^s of model III (blue) and IV (red) of the general $C\mathcal{P}$-admixture parameterization. The $C\mathcal{P}$-odd coupling parameters (including the Wilson coefficients c_G, c_B and c_W) are not shown, since the corresponding one-dimensional $\Delta\chi^2$ profiles are flat.

generation-independent scalar and pseudoscalar scale factors for up-type quarks (κ_t^s and κ_t^p), down-type quarks (κ_b^s and κ_b^p) and leptons (κ_τ^s and κ_τ^p), are introduced. The $C\mathcal{P}$-even Higgs couplings to W and Z bosons are described by a common coupling factor, κ_V^s, and the branching ratio of the Higgs boson into states of new physics is a free parameter in the fit. In model IV, the effects of $C\mathcal{P}$-odd dimension-five operators describing additional modifications to the Higgs-gauge boson couplings are studied. Thus, the three BSM coupling parameters c_G, c_B and c_W are introduced. Since such operators are not allowed in 2HDM-like models at tree-level, they are assumed to be loop-suppressed, and their impact is expected to be very small. To constrain the total width of the Higgs boson $\kappa_V^s \leq 1$ is assumed. The free parameters of both models are listed in Table 2.8.

Figure 7.5 compares the fit results of model III and model IV. Shown are only $\cos\alpha$, BR($\phi \to$ NP)

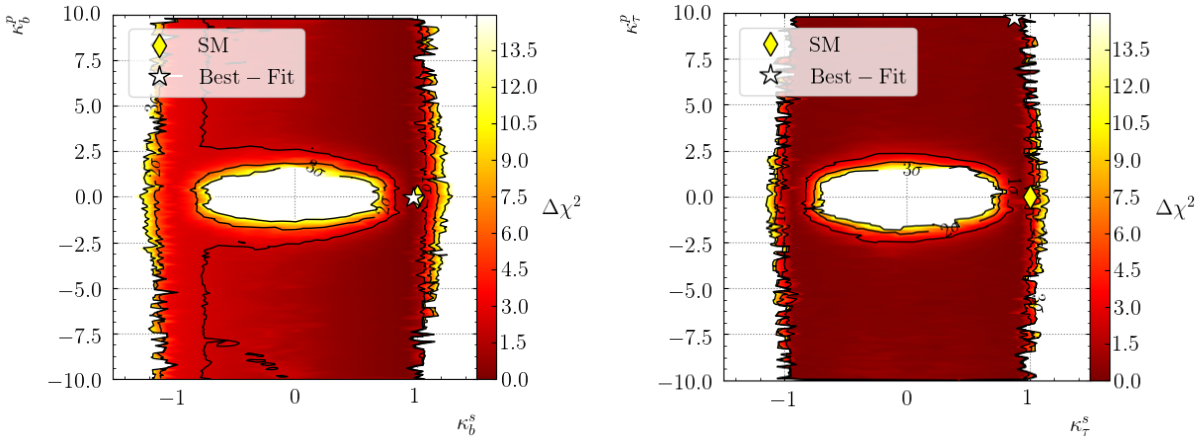

Figure 7.6: The two-dimensional $\Delta\chi^2$ profile for model IV of the general $C\mathcal{P}$-admixture parameterization in the (a) (κ_b^s, κ_b^p) and (b) $(\kappa_\tau^s, \kappa_\tau^p)$ plane.

and the $C\mathcal{P}$-even coupling parameters. The best-fit point for model III (IV) features a goodness-of-fit of $\chi^2_{\text{min}}/\text{ndf} = 83.0/89$ (83.0/86) corresponding to a p-value of 65.9 % (57.2 %). Since the best-fit points of both models are compatible with the SM prediction, no constraints on the $C\mathcal{P}$-odd parameters are found. This statements includes the Wilson coefficients c_G, c_B and c_W in model IV, since the EFT is assumed to be perturbative[1]. For that reason, the corresponding results are hidden in Figure 7.5. However, they are shown as one-dimensional $\Delta\chi^2$ profiles in Figure E.6 for completeness. Despite the additional freedom of the Wilson coefficients, the allowed range of the $C\mathcal{P}$-mixing parameter in model III and model IV is comparable. The corresponding 1σ (2σ) C. L. limits are $\cos\alpha \geq 0.94$ (0.90) and $\cos\alpha \geq 0.93$ (0.89), respectively. The reason for this is the fact that the $C\mathcal{P}$-odd contributions to the $H \to WW$ (see Equation 2.101) and the $H \to ZZ$ (see Equation 2.102) decays are loop suppressed, and their natural size is very small. Therefore, the Wilson coefficients have to be extended far beyond the regime where the EFT is perturbative in order to significantly impact the sensitivity on $\cos\alpha$.

As shown in Figure 7.5, negative values for κ_t^s are disfavored. This is due to its influence on the Higgs-photon effective coupling in the convention $\kappa_V^s > 0$. In contrast, negative values of κ_b^s (κ_τ^s) are still consistent with the measurements within 95 % (68 %) C. L. because of their small influence on the loop-induced Higgs couplings to gluons and photons. While the sign discrimination of κ_τ^s is very weak, the sign degeneracy of κ_b^s is broken. This is explained by the sensitivity of the Higgs-gluon coupling scale factor to the relative sign of κ_t^s and κ_b^s. For κ_b^s and κ_τ^s even vanishing values are consistent with the measurements due to the presence of the corresponding $C\mathcal{P}$-odd parameters κ_b^p and κ_τ^p in the fit setups. In case that $\kappa_b^s \to 0$ ($\kappa_\tau^s \to 0$), κ_b^p (κ_τ^p) provides the required Higgs boson production (decay) rate. Thus, either the scalar or the pseudoscalar parameter is allowed to vanish but not both simultaneously, as shown in Figure 7.6. The best-fit values and the one-dimensional 68 % and 95 % C. L. limits for the sensitive parameters of model III and model IV are listed in Table 7.3.

The correlation between the various parameters of model III and model IV are shown as two-dimensional $\Delta\chi^2$ profiles in Figures E.7 and E.8, respectively.

[1] In a perturbative EFT, the Wilson coefficients c_i are required to be $-4\pi \leq c_i \leq 4\pi$.

Table 7.3: The best-fit values, and 68 % and 95 % C. L. regions for $\cos\alpha$, BR($\phi \to$ NP), and the$C\mathcal{P}$-even fit parameters of model III and model IV obtained from the corresponding one-dimensional $\Delta\chi^2$ profiles.

Parameter	model III			model IV		
	best-fit	68 % C. L.	95 % C. L.	best-fit	68 % C. L.	95 % C. L.
$\cos(\alpha)$	1.00	[0.94, 1.00]	[0.90, 1.00]	1.00	[0.93, 1.00]	[0.89, 1.00]
κ_V^s	0.99	[0.92, 1.00]	[0.88, 1.00]	0.98	[0.92, 1.00]	[0.87, 1.00]
κ_t^s	0.99	[0.86, 1.16]	[0.74, 1.24]	0.99	[0.87, 1.17]	[0.62, 1.12]
κ_b^s	0.97	[0.01, 1.17]	[−1.21, 1.27]	0.97	[−0.03, 1.17]	[−1.19, 1.27]
κ_τ^s	0.93	[−0.84, 1.11]	[−1.14, 1.19]	0.87	[−1.12, 1.11]	[−1.19, 1.24]
BR($\phi \to$ NP)	0.02	[0.00, 0.12]	[0.00, 0.21]	0.01	[0.00, 0.13]	[0.00, 0.21]
$\bar{\kappa}_H$	0.94	[0.74, 1.18]	[0.42, 1.11]	0.93	[0.73, 1.18]	[0.60, 1.32]

7.2.4 Summary

To conclude, limits are set on possible $C\mathcal{P}$-admixtures using a general parameterization that is consistent with 2HDM-type models. In particular, it is assumed that the $C\mathcal{P}$-odd state A does not couple to weak gauge bosons at tree level and that κ_V^s is restricted $0 \leq \kappa_V^s \leq 1$. Both assumptions are compatible with a wide range of theoretical models, in particular with all scalar singlet and doublet extensions of the SM. In these models, effective AVV couplings are loop suppressed and can only be realized through higher-dimensional interaction operators. In general, these operators will impact the sensitivity on $\cos\alpha$ if their contributions are large enough. However, by requiring that new physics is perturbative, they can be constrained to $|c_i| < 4\pi$. In this case, the loop suppression of the operators significantly limits their contributions to the measured Higgs signal rates.

In the most complex model, the mixing parameter is constrained to $\cos\alpha \geq 0.89$ ($\Leftrightarrow \alpha \leq 27.4°$) at 95 % C. L. This means that the observed Higgs boson is at most 34 % $C\mathcal{P}$-odd. At this point, it is important to stress the fact that the obtained limits have to be taken with a grain of salt. Despite the large number of data points that are considered in these fits, it is not possible to guarantee that the parameter space is sufficiently sampled. In case of model IV, 12 free parameters are considered. If any parameter would have been sampled on a one-dimensional grid consisting of only 10 parameter values, the full twelve-dimensional space would already contain 10^{12} points. For a more realistic sampling on a finer grid, the number of points increases exponentially. Efficient sampling is achieved using the Metropolis-Hastings algorithm ("random walk") provided by the pyMC package. Independent chains with randomly chosen initial positions are run in parallel. The number of chains has been set based on the requirement that the one-dimensional $\Delta\chi^2$ profiles approach a quadratic functional dependence. However, even in this case, some allowed islands in the parameter space may be missed. Some of the drawbacks of the presented approach are the rather slow convergence and the fact that the same parameter region may be sampled several times, which reduces the efficiency of the sampling. Therefore, it is worth to further investigate more elaborate sampling techniques.

7.3 Constraints from the $H \to 4\ell$ Decay Channel at ATLAS

In this section, the parameterization of the previous section is used to constrain the $C\mathcal{P}$ mixing parameter α using only the cross-section measurement in the $H \to ZZ^* \to 4\ell$ decay channel at ATLAS (see Section 5). This measurement is performed using the complete Run-2 dataset of proton-proton collisions

collected by the ATLAS detector ($\sqrt{s} = 13\,\text{TeV}$ and $L = 139\,\text{fb}^{-}1$). The simplest model (model I) and the most complex model (model IV) of the general $C\mathcal{P}$-admixture parameterization listed in Table 2.8 are investigated. Since this study is performed within the ATLAS collaboration, the full likelihood function is known. Thus, it does not have to be approximated as in the previous sections. The statistical model is described in the following.

7.3.1 Statistical Treatment

The $C\mathcal{P}$-admixture parameterization is described in Section 2.4.2.2. For the statistical interpretation, the expected event rates in the Stage 0 particle-level production bins p are expressed in terms of signal strength modifiers,

$$\mu^{p}(\boldsymbol{x}) = \frac{\sigma^{p}(\boldsymbol{x}) \cdot \text{BR}^{4\ell}(\boldsymbol{x})}{\sigma^{p}_{\text{SM}} \cdot \text{BR}^{4\ell}_{\text{SM}}}\,, \tag{7.1}$$

which scale the corresponding SM prediction as a function of the model parameters, $\boldsymbol{x}$, listed in Table 2.8. The signal strengths $\mu^{p}(\boldsymbol{x})$ are incorporated into the statistical analysis model by replacing the SM expected signals, $S_{i,j}(\boldsymbol{\sigma}, \boldsymbol{\theta})$ (see Section 5.7), with $\mu^{p}(\boldsymbol{c}) \cdot S_{i,j}(\boldsymbol{\sigma}, \boldsymbol{\theta})$. BSM effects in the acceptances, a^{p}, and the reconstruction efficiencies, $\epsilon^{p}_{i,j}$, are expected to be negligible, and thus not taken into account. The likelihood function is given by

$$\mathcal{L}(\boldsymbol{\sigma}, \boldsymbol{\theta}) = \prod_{j}^{N_{\text{categories}}} \prod_{i}^{N_{\text{bins}}} P\left(N_{i,j} | \mu^{p}(\boldsymbol{x}) \cdot L \cdot \boldsymbol{\sigma} \cdot \text{BR} + B_{i,j}(\boldsymbol{\theta})\right) \times \prod_{m}^{N_{\text{nuisance}}} C_{m}(\boldsymbol{\theta})\,. \tag{7.2}$$

Note that BSM contributions to the background predictions $B_{i,j}(\boldsymbol{\theta})$ are neglected. Constraints on the model parameters are obtained using the profile likelihood ratio (Equation 5.2) discussed in Section 5.7.

7.3.2 Common Pseudoscalar Coupling Parameter for Fermions

The first model that is investigated is model I. It contains only two free parameters, $\cos\alpha$ and κ^{p}_{f}. The first one parameterizes the mixing of a $C\mathcal{P}$-even and $C\mathcal{P}$-odd state (see Equation 2.91), and the second one is a common coupling parameter for fermions parameterizing the pseudoscalar Yukawa couplings. All other parameters are set to their SM values.

Figure 7.7 shows the fit results for model I. The observed (black solid line) and expected (blue dashed line) one-dimensional $-2\ln(\lambda)$ profiles for $\cos\alpha$ are displayed in Figure 7.7(a). The lower limit on the measured 68 % (95 %) C. I. is 0.94 (0.85), and it is significantly narrower than the corresponding SM expectation. This is explained by the enhanced yields in the VBF and VH production bins (see Figure 5.9(a)), which are very sensitive to $\cos\alpha$. Since the best-fit point is found in the SM limit, any arbitrarily large value of κ^{p}_{f} can always be compensated by an arbitrarily small value of $\sin\alpha \to 0$, i. e. no limits for κ^{p}_{f} are found. This can also be seen in Figure 7.7(b). Here, a unconstrained direction along κ^{p}_{f} is found for $\cos\alpha \to 1$. However, for an $C\mathcal{P}$ admixture with a sizable $C\mathcal{P}$-odd component like $\cos\alpha \approx 0.75$, constraints on κ^{p}_{f} can be imposed. The preferred value of κ^{f}_{p} is close to one in this case.

7.3.3 General Parameterization Including $C\mathcal{P}$-odd Dimension-Five Operators

In this section, model IV of the general $C\mathcal{P}$-admixture parameterization is investigated. It has 12 free parameters (see Table 2.8), which are all allowed to float free in the fit. The degeneracy induced by the unknown total width of the Higgs boson is resolved by assuming $0 \leq \kappa^{s}_{V} \leq 1$.

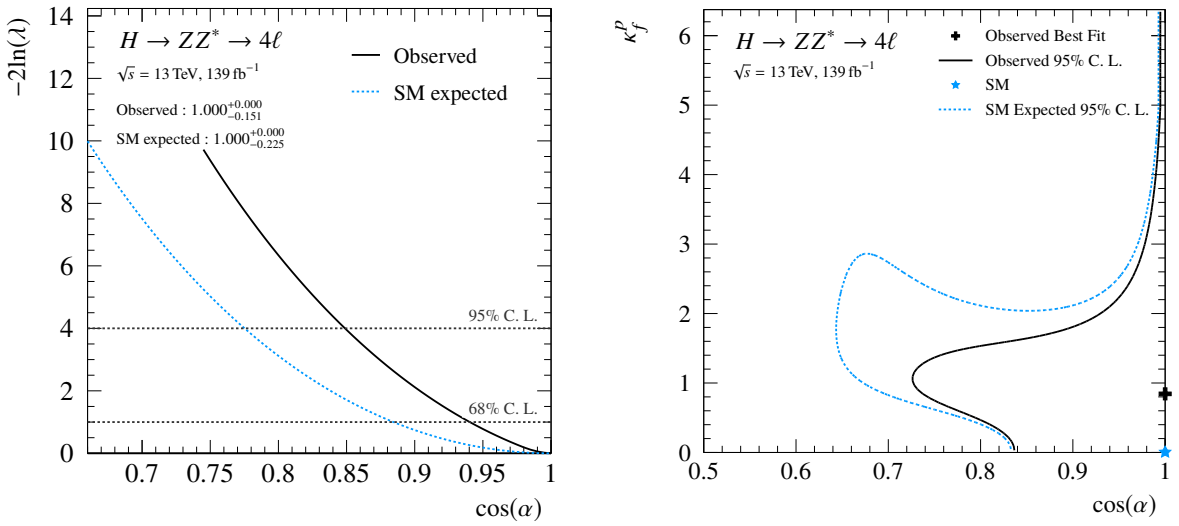

(a) (b)

Figure 7.7: The fit result for the free parameters of model I of the $C\mathcal{P}$-admixture parameterization obtained in the $H \to ZZ^* \to 4\ell$ decay channel at ATLAS using an integrated luminosity of 139 fb^1 of pp collisions at a cms energy of $\sqrt{s}$ = 13 TeV. (a) The one-dimensional projections of the observed (black solid) and SM expected (blue dashed) $-2\ln(\lambda)$ profiles for $\cos\alpha$. The 68 % and 95 % C. L. regions are indicated by dashed horizontal lines. (b) The two-dimensional contours at 95 % C. L. in the $(\cos\alpha, \kappa_f^P)$ plane. The observed and SM expected best-fit points are indicated by black and blue stars, respectively.

Table 7.4: The observed best-fit values for the parameters of model IV of the general $C\mathcal{P}$-admixture parameterization together with the observed and expected confidence intervals at 68 % and 95 % C. L. for an integrated luminosity of 139 fb^1 at $\sqrt{s}$ = 13 TeV. All parameters of the model are allowed to float free in the fit.

Parameter	Best-fit		observed		SM expected	
	value	p-value	68 % C. L.	95 % C. L.	68 % C. L.	95 % C. L.
BR($\phi \to$ NP)	0.0		[0.00, 0.67]	[0.00, 0.75]	[0.00, 0.73]	[0.00, 0.81]
$\cos\alpha$	1.00		[0.58, 1.00]	[0.50, 1.00]	[0.52, 1.00]	[0.44, 1.00]
κ_V^s	1.00		[0.58, 1.00]	[0.50, 1.00]	[0.52, 1.00]	[0.44, 1.00]
κ_t^s	0.86		[−1.05, 1.05]	[−1.36, 1.36]	[−1.29, 1.29]	[−1.84, 1.84]
κ_b^s	0.87		[−1.08, 1.12]	[−1.47, 1.50]	[−1.41, 1.41]	[−2.06, 2.06]
κ_τ^s	0.00		[−3.4, 3.4]	[−4.5, 4.5]	[−4.3, 4.3]	[−6.2, 6.2]

Figure 7.8 shows the one-dimensional projections of the fit result for some of the sensitive parameters of model IV. These are $\cos\alpha$, BR($\phi \to$ NP), κ_V^s, and κ_t^s. The corresponding profiles for κ_b^s and κ_τ^s are shown in Figure E.9. The expected 68 % (95 %) C. L. limit on possible $C\mathcal{P}$ admixtures is $\cos\alpha \geq 0.52$ (0.44). This constraint is much weaker than the one of model I because of the additional freedom in the scalar fermionic couplings. Since no constraints are found for the pseudoscalar coupling parameters (including the Wilson coefficients c_G, c_W, and c_B), the corresponding profiles are not shown. As explained in the previous section, this is expected since the best-fit value for $\cos\alpha$ is consistent with the SM prediction.

However, the $C\mathcal{P}$-odd parameters are not completely free, as can be seen in the two-dimensional profiles shown in Figure E.10. For $C\mathcal{P}$ admixtures with a sizable pseudoscalar component, A, an upper

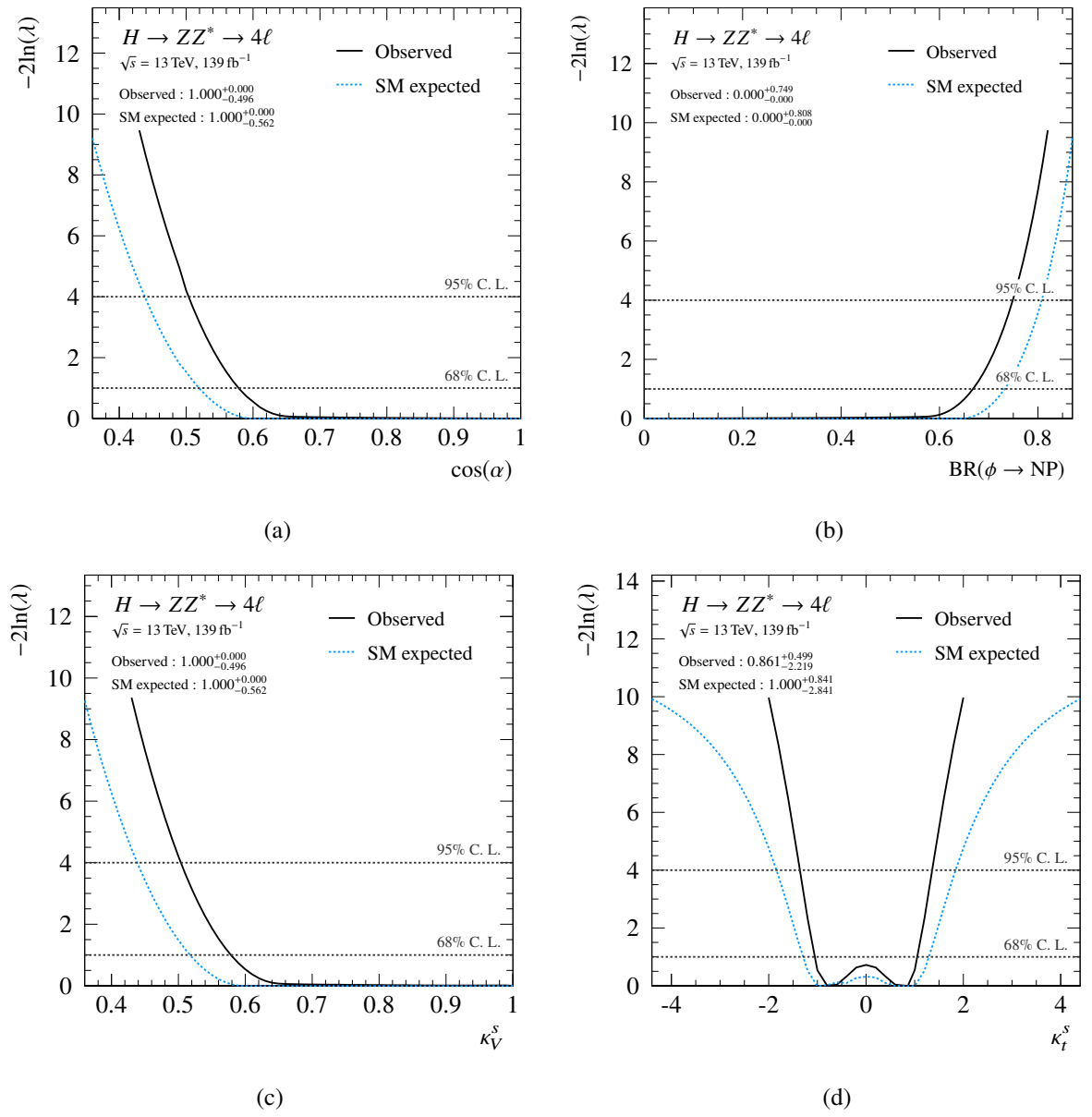

Figure 7.8: The one-dimensional projections of the observed (black solid) and SM expected (blue dashed) fit result for the parameter (a) $\cos\alpha$, (b) BR($\phi \to$ NP), (c) κ_V^s, and (d) κ_t^s of model IV of the general $\mathcal{CP}$-admixture parameterization for an integrated luminosity of 139 fb^1 of pp collisions at a cms energy of $\sqrt{s}$ = 13 TeV. The 68 % and 95 % C. I. are indicated by dashed horizontal lines. All fit parameters are allowed to float free in the fit.

limit on the pseudoscalar coupling parameters can be set.

To conclude, the obtained exclusion on the $\mathcal{CP}$-mixing parameter at 95 % C. L. is $\cos\alpha \geq 0.44$ ($\Rightarrow \alpha \leq 64°$). According to this study, the observed Higgs boson is at most 67 % $\mathcal{CP}$-odd. This constraint is much weaker than the constraints obtained in Section 7.2.3, because it is obtained in a single channel. In contrast, the `HiggsSignals` constraints are obtained from a global fit to the ATLAS and CMS data, including several Higgs signal measurements in different production and decay channels.

CHAPTER 8

Summary and Conclusion

The Higgs boson discovered by ATLAS and CMS in 2012 was the last missing particle predicted by the Standard Model (SM). The measurements of its coupling, spin, and $\mathcal{CP}$ properties conducted so far are consistent with the SM prediction. However, the measurement precision does not exclude many well-motivated beyond the SM (BSM) theories. For instance, it is still possible that the Higgs boson is a $\mathcal{CP}$ admixture, which introduces an additional source of $\mathcal{CP}$ violation as required by baryogenesis.

In this dissertation, the $\mathcal{CP}$ nature of the Higgs boson is probed using different Higgs boson interpretation frameworks. The studies presented can roughly be divided into three categories. The first ones are performed in the $H \to \tau\tau$ decay channel at ATLAS, aiming to improve the energy scale of hadronically decaying tau leptons. The second kind of studies is performed in the $H \to ZZ^* \to 4\ell$ decay channel at ATLAS comprising performance test for particle-flow (PFlow) jets and the study of $\mathcal{CP}$-even and $\mathcal{CP}$-odd admixtures to the SM Higgs boson using the Standard Model Effective Field Theory (SMEFT). The third category encompasses phenomenological studies conducted with the public computer code `HiggsSignals`. First, various performance tests of `HiggsSignals` are conducted, and second, the program is used to probe the $\mathcal{CP}$ nature of the Higgs boson in the context of different model assumptions.

The key ingredients for the measurement of the $\mathcal{CP}$-mixing angle in the tau-Yukawa coupling are the identification of the tau decay mode and the precise reconstruction of the energy of the tau decay products [221]. For Run 2 of the LHC, both have been significantly improved using the PFlow concept. The new PFlow-based reconstruction outperforms the baseline method for tau leptons with $p_T \lessapprox 140\,\text{GeV}$ but deteriorates quickly as the energy is increased. To overcome this problem, the Combined tau energy scale (TES) has been developed. It is the core-weighted average of both methods corrected for the non-Gaussian outliers of the PFlow-based reconstruction. This approach cuts down the resolution of low-energetic taus by up to 25 % (70 %) in decays with (without) neutral pions. The tau energy is further improved by employing a multivariate analysis (MVA) technique. This method uses the Combined TES alongside other calorimeter and substructure-based information in a boosted decision tree regression. Since the objects obtained with the MVA regression are not consistent tau leptons, a method has been developed to correct the energy of neutral pions in 1p1n, 1pXn, and 3pXn decays. The corresponding improvement of the neutral pion p_T resolution is about 20 %, 30 %, and 60 %, respectively.

The Run 2 cross-section measurement in the $H \to ZZ^* \to 4\ell$ decay channel at ATLAS uses an integrated luminosity of $139\,\text{fb}^{-1}$ of proton-proton collisions at a center-of-mass energy of 13 TeV. For this measurement, the jet reconstruction has been moved to PFlow, which improves the jet-related variables by about 2-3 % in the central detector region. However, this improvement is mitigated by high pileup in the forward region due to the lack of a forward jet-vertex-tagger cut for PFlow jets. To compensate for this, a forward transverse momentum cut is employed, which significantly reduces the number of pile-up jets. The expected performance of PFlow jets in the cross-section measurement is similar to the EMTopo jet collection. The largest improvements are found in the VH-Had and sideband bins with about 2-5 %.

The measurement of the tensor structure of the Higgs boson couplings in the $H \to ZZ^* \to 4\ell$ decay channel at ATLAS is performed with the full Run 2 dataset. BSM contributions to the Higgs boson couplings to weak vector bosons, gluons, and top quarks are modeled using the SMEFT. The $C\mathcal{P}$-odd ($C\mathcal{P}$-even) SMEFT parameters describing the HVV vertex are $c_{H\widetilde{W}}$, $c_{H\widetilde{B}}$, $c_{H\widetilde{W}B}$ (c_{HW}, c_{HB}, c_{HWB}), while the parameters for the Hgg and Htt vertices are $c_{H\widetilde{G}}$ (c_{HG}) and $c_{\widetilde{u}H}$ (c_{uH}), respectively. To probe these parameters, cross-sections have been measured in exclusive regions of phase space at particle level, and fitted with the SMEFT prediction. Constraints have been obtained under the assumption that only one parameter floats freely, while the others are set to zero. The most stringent ones are set on the BSM coupling parameters to gluons with $|c_{H\widetilde{G}}| < 0.029$ and $-0.0083 < c_{HG} < 0.0068$ at 95 % C. L. The limit on the $C\mathcal{P}$-odd parameter is significantly weaker due to the missing linear terms in the cross-section expansion. The constraints on the $C\mathcal{P}$-odd BSM couplings parameters to weak vector bosons are $|c_{H\widetilde{W}}| < 2.4$, $|c_{H\widetilde{B}}| < 0.56$, and $| < c_{H\widetilde{W}B}| < 1.03$. The corresponding limits on the $C\mathcal{P}$-even parameters are slightly weaker, $-3.4 < c_{HW} < 2.1$, $-0.62 < c_{HB} < 0.59$, and $-1.06 < c_{HWB} < 0.99$. In addition, correlations between the BSM coupling parameters are probed by fitting two parameters simultaneously. The largest correlations for the $C\mathcal{P}$-odd ($C\mathcal{P}$-even) parameters are observed for $c_{H\widetilde{W}B}$ vs. $c_{H\widetilde{B}}$ (c_{HWB} vs. c_{HB}). If all parameters are allowed to float freely in the fit, no constraints are found due to the limited sensitivity of the measurement. Therefore, in a general model, large BSM couplings are still possible, including sizable $C\mathcal{P}$-odd contributions. The given constraints are the first limits on the SMEFT parameters in the $H \to ZZ^* \to 4\ell$ decay channel. For a conclusive picture they have to be combined with the measurements in other Higgs boson decay modes.

`HiggsSignals` provides a quick and convenient framework to confront arbitrary Higgs sectors with Higgs signal measurements. For Run 2 of the LHC, the input scheme of `HiggsSignals` has been expanded to handle measurements provided in terms of simplified template cross-sections (STXSs). Several performance tests of `HiggsSignals` using the new STXS and the Run 1 signal strength measurements have been performed. It is shown that excellent agreement with official results is achieved if the experimental collaborations provide the necessary information.

While the SM Higgs boson is a $C\mathcal{P}$-even particle, the discovered resonance may be a mixed $C\mathcal{P}$ state. To probe the size of a potential $C\mathcal{P}$ admixture, different model setups are investigated with `HiggsSignals`. The experimental input for these studies comprises all relevant inclusive and differential Higgs boson measurements provided by the ATLAS and CMS collaborations. The first model setup targets the $C\mathcal{P}$ nature of the top-Yukawa interaction. The model dependence of the constraint is probed by successively allowing for new physics contributions to the Higgs boson couplings to weak vector bosons, photons, and gluons. In the most restricted BSM scenario, the upper limit on a $C\mathcal{P}$-violating phase is found to be $\alpha_{tt} \lessapprox 22.5°$ at 95 % C. L., while it is much less constrained in the most general model ($\alpha_{tt} \lessapprox 72°$).

The second model setup parameterizes the Higgs boson as an arbitrary admixture of $C\mathcal{P}$-even and $C\mathcal{P}$-odd components as described by the two-Higgs-doublet model (2HDM). In this context, no couplings of the pseudoscalar component to weak gauge bosons are allowed at tree-level, and they can only be induced through loop corrections of heavy new fields. This fact is used to set constraints on the $C\mathcal{P}$ mixing angle α for different model parameterizations. The simplest model contains only two free parameters, α and a common coupling modifier of the $C\mathcal{P}$-odd state to fermions. All other parameters are set to their SM values. In this case, the mixing angle is constrained to $\alpha \leq 21.6°$. The second model realization probes the custodial SU(2) symmetry. No significant differences between the scalar coupling scale factor to W and Z bosons, κ_W^s and κ_Z^s, respectively, are found, which motivates the use of a common modifier $\kappa_V^s \equiv \kappa_W^s = \kappa_Z^s$. Constraints on $\cos\alpha$ are set in case $\kappa_V^s \leq 1$. This assumption is valid for the 2HDM if the orthogonal Higgs state is much heavier than the observed Higgs boson. In the most general model, the effects of higher-dimensional interaction operators are studied. Under the assumption that new physics is perturbative, their impact is very small and the constraint on the mixing parameter is set to $\alpha \leq 27.4°$. This implies that in the context of 2HDM-type models the Higgs boson is at least 66 % $C\mathcal{P}$-even.

Bibliography

[1] F. Englert and R. Brout, *Broken Symmetry and the Mass of Gauge Vector Mesons*, Phys. Rev. Lett. **13** (9 1964) 321, URL: https://link.aps.org/doi/10.1103/PhysRevLett.13.321 (cit. on pp. 1, 4, 9).

[2] P. W. Higgs, *Broken Symmetries and the Masses of Gauge Bosons*, Phys. Rev. Lett. **13** (16 1964) 508, URL: https://link.aps.org/doi/10.1103/PhysRevLett.13.508 (cit. on pp. 1, 4, 9).

[3] P. Higgs, *Broken symmetries, massless particles and gauge fields*, Physics Letters **12** (1964) 132, ISSN: 0031-9163, URL: http://www.sciencedirect.com/science/article/pii/0031916364911369 (cit. on pp. 1, 4, 9).

[4] G. Aad et al., *Observation of a new particle in the search for the Standard Model Higgs boson with the ATLAS detector at the LHC*, Phys. Lett. B **716** (2012) 1, arXiv: 1207.7214 [hep-ex] (cit. on pp. 1, 4, 14, 79).

[5] S. Chatrchyan et al., *Observation of a New Boson at a Mass of 125 GeV with the CMS Experiment at the LHC*, Phys. Lett. B **716** (2012) 30, arXiv: 1207.7235 [hep-ex] (cit. on pp. 1, 4, 14, 79).

[6] L. H. Ryder, *Quantum Field Theory*, 2nd ed., Cambridge University Press, 1996 (cit. on p. 3).

[7] M. Schwartz, *Quantum Field Theory and the Standard Model*, (2014) (cit. on p. 3).

[8] M. Peskin and D. Schroeder, *An Introduction To Quantum Field Theory*, Frontiers in Physics, Avalon Publishing, 1995 (cit. on p. 3).

[9] D. Griffiths, *Introduction to Elementary Particles*, Physics textbook, Wiley, 2008, ISBN: 9783527406012 (cit. on p. 3).

[10] A. Einstein, *Die Grundlage der allgemeinen Relativitätstheorie*, Annalen der Physik **354** (1916) 769, eprint: https://onlinelibrary.wiley.com/doi/pdf/10.1002/andp.19163540702, URL: https://onlinelibrary.wiley.com/doi/abs/10.1002/andp.19163540702 (cit. on p. 3).

[11] S. L. Glashow, *Partial-symmetries of weak interactions*, Nuclear Physics **22** (1961) 579, ISSN: 0029-5582, URL: http://www.sciencedirect.com/science/article/pii/0029558261904692 (cit. on pp. 3, 6).

[12] S. Weinberg, *A Model of Leptons*, Phys. Rev. Lett. **19** (21 1967) 1264, URL: https://link.aps.org/doi/10.1103/PhysRevLett.19.1264 (cit. on pp. 3, 6).

[13] A. Salam, *Weak and Electromagnetic Interactions*, Conf. Proc. C **680519** (1968) 367 (cit. on pp. 3, 6).

[14] E. Fermi, *Zur Quantelung des idealen einatomigen Gases*, Zeitschrift für Physik **36** (1926) 902 (cit. on p. 3).

[15] S. Bose, *Plancks Gesetz und Lichtquantenhypothese*, Zeitschrift für Physik **26** (1924) 178 (cit. on p. 3).

[16] N. M. et al., *Standard Model of Elementary Particles, modified version, 2014*, [Online; accessed 20-October-2020], URL: https://commons.wikimedia.org/wiki/File:Standard_Model_of_Elementary_Particles_modified_version.svg#/media/File:Standard_Model_of_Elementary_Particles_afr.svg (cit. on p. 4).

[17] H. Fritzsch, M. Gell-Mann and H. Leutwyler, *Advantages of the Color Octet Gluon Picture*, Phys. Lett. B **47** (1973) 365 (cit. on pp. 4, 8).

[18] D. J. Gross and F. Wilczek, *Ultraviolet Behavior of Non-Abelian Gauge Theories*, Phys. Rev. Lett. **30** (26 1973) 1343, URL: https://link.aps.org/doi/10.1103/PhysRevLett.30.1343 (cit. on p. 4).

[19] H. D. Politzer, *Reliable Perturbative Results for Strong Interactions?*, Phys. Rev. Lett. **30** (26 1973) 1346, URL: https://link.aps.org/doi/10.1103/PhysRevLett.30.1346 (cit. on pp. 4, 9).

[20] D. J. Gross and F. Wilczek, *Asymptotically Free Gauge Theories. I*, Phys. Rev. D **8** (10 1973) 3633, URL: https://link.aps.org/doi/10.1103/PhysRevD.8.3633 (cit. on pp. 4, 9).

[21] M. Gell-Mann, *A Schematic Model of Baryons and Mesons*, Phys. Lett. **8** (1964) 214 (cit. on pp. 4, 8).

[22] W. E. Lamb and R. C. Retherford, *Fine Structure of the Hydrogen Atom by a Microwave Method*, Phys. Rev. **72** (3 1947) 241, URL: https://link.aps.org/doi/10.1103/PhysRev.72.241 (cit. on p. 6).

[23] J. Schwinger, *On Quantum-Electrodynamics and the Magnetic Moment of the Electron*, Phys. Rev. **73** (4 1948) 416, URL: https://link.aps.org/doi/10.1103/PhysRev.73.416 (cit. on p. 6).

[24] T. Aoyama et al., *Tenth-Order QED Contribution to the Electron $g-2$ and an Improved Value of the Fine Structure Constant*, Phys. Rev. Lett. **109** (11 2012) 111807, URL: https://link.aps.org/doi/10.1103/PhysRevLett.109.111807 (cit. on p. 6).

[25] T. Aoyama et al., *Tenth-Order Electron Anomalous Magnetic Moment — Contribution of Diagrams without Closed Lepton Loops*, Phys. Rev. D **91** (2015) 033006, [Erratum: Phys.Rev.D 96, 019901 (2017)], arXiv: 1412.8284 [hep-ph] (cit. on p. 6).

[26] D. Hanneke, S. Hoogerheide and G. Gabrielse, *Cavity Control of a Single-Electron Quantum Cyclotron: Measuring the Electron Magnetic Moment*, Phys. Rev. A **83** (2011) 052122, arXiv: 1009.4831 [physics.atom-ph] (cit. on p. 6).

[27] M. Thomson, *Modern Particle Physics*, Cambridge University Press, 2013 (cit. on p. 6).

[28] H. Becquerel, *Sur les radiations émises par phosphorescence*, Comptes Rendus **122** (1896) 420 (cit. on p. 6).

[29] H. Becquerel, *Sur les radiations invisibles émises par les corps phosphorescents*, Comptes Rendus **122** (1896) 501 (cit. on p. 6).

[30] E. Rutherford, *Radioactive Transformations*, Archibald Constable & Co., Ltd., 1906 (cit. on p. 6).

[31] G. Gamow, *Zur Quantentheorie des Atomkernes*, Zeitschrift für Physik **51** (1928) 204 (cit. on p. 6).

[32] E. Fermi, *Versuch einer Theorie der -Strahlen. I*, Zeitschrift für Physik **88** (1934) 161 (cit. on p. 6).

[33] C. N. Yang and R. L. Mills, *Conservation of Isotopic Spin and Isotopic Gauge Invariance*, Phys. Rev. **96** (1 1954) 191, URL: https://link.aps.org/doi/10.1103/PhysRev.96.191 (cit. on p. 6).

[34] G. Arnison et al., *Experimental Observation of Isolated Large Transverse Energy Electrons with Associated Missing Energy at s**(1/2) = 540-GeV*, Phys. Lett. B **122** (1983) 103 (cit. on p. 7).

[35] G. A. et al., *Experimental observation of lepton pairs of invariant mass around 95 GeV/c2 at the CERN SPS collider*, Physics Letters B **126** (1983) 398, ISSN: 0370-2693, URL: http://www.sciencedirect.com/science/article/pii/0370269383901880 (cit. on p. 7).

[36] H. Yukawa, *On the Interaction of Elementary Particles I*, Proc. Phys. Math. Soc. Jap. **17** (1935) 48 (cit. on p. 8).

[37] C. M. G. Lattes et al., *PROCESSES INVOLVING CHARGED MESONS*, Nature **159** (1947) 694 (cit. on p. 8).

[38] G. Rochester and C. Butler, *Evidence for the Existence of New Unstable Elementary Particles*, Nature **160** (1947) 855 (cit. on p. 8).

[39] V. D. Hopper and S. Biswas, *Evidence Concerning the Existence of the New Unstable Elementary Neutral Particle*, Phys. Rev. **80** (6 1950) 1099, URL: https://link.aps.org/doi/10.1103/PhysRev.80.1099 (cit. on p. 8).

[40] R. Armenteros et al., *LVI. The properties of charged V-particles*, The London, Edinburgh, and Dublin Philosophical Magazine and Journal of Science **43** (1952) 597, eprint: https://doi.org/10.1080/14786440608520216, URL: https://doi.org/10.1080/14786440608520216 (cit. on p. 8).

[41] G. Zweig, "An SU(3) model for strong interaction symmetry and its breaking. Version 2", *DEVELOPMENTS IN THE QUARK THEORY OF HADRONS. VOL. 1. 1964 - 1978*, ed. by D. Lichtenberg and S. P. Rosen, 1964 22 (cit. on p. 8).

[42] M. Gell-Mann and Y. Ne'eman, *The Eightfold way: a review with a collection of reprints*, (1964) (cit. on p. 8).

[43] M. Y. Han and Y. Nambu, *Three-Triplet Model with Double* SU(3) *Symmetry*, Phys. Rev. **139** (4B 1965) B1006, URL: https://link.aps.org/doi/10.1103/PhysRev.139.B1006 (cit. on p. 8).

[44] C. Bouchiat, J. Iliopoulos and P. Meyer, *An anomaly-free version of Weinberg's model*, Physics Letters B **38** (1972) 519, ISSN: 0370-2693, URL: http://www.sciencedirect.com/science/article/pii/0370269372905321 (cit. on p. 8).

[45] S. Bethke, *The 2009 World Average of alpha(s)*, Eur. Phys. J. C **64** (2009) 689, ed. by D. H. Beck, D. Haidt and J. W. Negele, arXiv: 0908.1135 [hep-ph] (cit. on p. 9).

[46] J. Ellis, "Higgs Physics", *2013 European School of High-Energy Physics*, 2015 117, arXiv: 1312.5672 [hep-ph] (cit. on p. 10).

[47] J. Goldstone, *Field Theories with Superconductor Solutions*, Nuovo Cim. **19** (1961) 154 (cit. on p. 11).

[48] J. Goldstone, A. Salam and S. Weinberg, *Broken Symmetries*, Phys. Rev. **127** (3 1962) 965, URL: https://link.aps.org/doi/10.1103/PhysRev.127.965 (cit. on p. 11).

[49] Y. Nambu and G. Jona-Lasinio, *Dynamical Model of Elementary Particles Based on an Analogy with Superconductivity. I*, Phys. Rev. **122** (1 1961) 345, URL: https://link.aps.org/doi/10.1103/PhysRev.122.345 (cit. on p. 11).

[50] Y. Nambu and G. Jona-Lasinio, *Dynamical Model of Elementary Particles Based on an Analogy with Superconductivity. II*, Phys. Rev. **124** (1 1961) 246, URL: https://link.aps.org/doi/10.1103/PhysRev.124.246 (cit. on p. 11).

[51] D. Webber et al., *Measurement of the Positive Muon Lifetime and Determination of the Fermi Constant to Part-per-Million Precision*, Phys. Rev. Lett. **106** (2011) 041803, arXiv: 1010.0991 [hep-ex] (cit. on p. 12).

[52] V. Tishchenko et al., *Detailed Report of the MuLan Measurement of the Positive Muon Lifetime and Determination of the Fermi Constant*, Phys. Rev. D **87** (2013) 052003, arXiv: 1211.0960 [hep-ex] (cit. on p. 12).

[53] J. Erler and P. Langacker, *Electroweak model and constraints on new physics*, The European Physical Journal C - Particles and Fields **15** (2000) 95 (cit. on p. 12).

[54] P. Zyla et al., *Review of Particle Physics*, PTEP **2020** (2020) 083C01 (cit. on pp. 12, 14, 59, 60, 64, 73, 97).

[55] N. Cabibbo, *Unitary Symmetry and Leptonic Decays*, Phys. Rev. Lett. **10** (12 1963) 531, URL: https://link.aps.org/doi/10.1103/PhysRevLett.10.531 (cit. on p. 13).

[56] M. Kobayashi and T. Maskawa, *CP-Violation in the Renormalizable Theory of Weak Interaction*, Progress of Theoretical Physics **49** (1973) 652, ISSN: 0033-068X, eprint: https://academic.oup.com/ptp/article-pdf/49/2/652/5257692/49-2-652.pdf, URL: https://doi.org/10.1143/PTP.49.652 (cit. on p. 13).

[57] B. Pontecorvo, *Neutrino Experiments and the Problem of Conservation of Leptonic Charge*, Sov. Phys. JETP **26** (1968) 984 (cit. on p. 13).

[58] B. Pontecorvo, *Mesonium and anti-mesonium*, Sov. Phys. JETP **6** (1957) 429 (cit. on p. 13).

[59] Z. Maki, M. Nakagawa and S. Sakata, *Remarks on the Unified Model of Elementary Particles*, Progress of Theoretical Physics **28** (1962) 870, ISSN: 0033-068X, eprint: https://academic.oup.com/ptp/article-pdf/28/5/870/5258750/28-5-870.pdf, URL: https://doi.org/10.1143/PTP.28.870 (cit. on p. 13).

[60] Y. Fukuda et al., *Evidence for Oscillation of Atmospheric Neutrinos*, Phys. Rev. Lett. **81** (8 1998) 1562, URL: https://link.aps.org/doi/10.1103/PhysRevLett.81.1562 (cit. on p. 13).

[61] Q. R. Ahmad et al., *Measurement of the Rate of $\nu_e + d \rightarrow p + p + e^-$ Interactions Produced by ^8B Solar Neutrinos at the Sudbury Neutrino Observatory*, Phys. Rev. Lett. **87** (7 2001) 071301, URL: https://link.aps.org/doi/10.1103/PhysRevLett.87.071301 (cit. on p. 13).

[62] Q. R. Ahmad et al., *Direct Evidence for Neutrino Flavor Transformation from Neutral-Current Interactions in the Sudbury Neutrino Observatory*, Phys. Rev. Lett. **89** (1 2002) 011301, URL: https://link.aps.org/doi/10.1103/PhysRevLett.89.011301 (cit. on pp. 13, 19).

[63] Y. Fukuda et al., *Measurement of the flux and zenith angle distribution of upward through going muons by Super-Kamiokande*, Phys. Rev. Lett. **82** (1999) 2644, arXiv: hep-ex/9812014 (cit. on pp. 13, 19).

[64] Y. Fukuda et al., *Measurements of the solar neutrino flux from Super-Kamiokande's first 300 days*, Phys. Rev. Lett. **81** (1998) 1158, [Erratum: Phys.Rev.Lett. 81, 4279 (1998)], arXiv: hep-ex/9805021 (cit. on pp. 13, 19).

[65] M. Apollonio et al., *Search for neutrino oscillations on a long baseline at the CHOOZ nuclear power station*, Eur. Phys. J. C **27** (2003) 331, arXiv: hep-ex/0301017 (cit. on pp. 13, 19).

[66] D. Michael et al., *Observation of muon neutrino disappearance with the MINOS detectors and the NuMI neutrino beam*, Phys. Rev. Lett. **97** (2006) 191801, arXiv: hep-ex/0607088 (cit. on pp. 13, 19).

[67] K. Abe et al., *Indication of Electron Neutrino Appearance from an Accelerator-produced Off-axis Muon Neutrino Beam*, Phys. Rev. Lett. **107** (2011) 041801, arXiv: 1106.2822 [hep-ex] (cit. on pp. 13, 19).

[68] F. An et al., *Observation of electron-antineutrino disappearance at Daya Bay*, Phys. Rev. Lett. **108** (2012) 171803, arXiv: 1203.1669 [hep-ex] (cit. on pp. 13, 19).

[69] N. Palanque-Delabrouille et al., *Neutrino masses and cosmology with Lyman-alpha forest power spectrum*, JCAP **11** (2015) 011, arXiv: 1506.05976 [astro-ph.CO] (cit. on pp. 13, 19).

[70] M. Gell-Mann, P. Ramond and R. Slansky, *Complex Spinors and Unified Theories*, Conf. Proc. C **790927** (1979) 315, arXiv: 1306.4669 [hep-th] (cit. on pp. 13, 19).

[71] O. Sawada and A. Sugamoto, eds., *Proceedings: Workshop on the Unified Theories and the Baryon Number in the Universe: Tsukuba, Japan, February 13-14, 1979*, Natl.Lab.High Energy Phys., 1979 (cit. on pp. 13, 19).

[72] R. N. Mohapatra and G. Senjanovic, *Neutrino Mass and Spontaneous Parity Nonconservation*, Phys. Rev. Lett. **44** (1980) 912 (cit. on pp. 13, 19).

[73] R. D. Ball et al., *Parton distributions for the LHC run II*, Journal of High Energy Physics **2015** (2015), ISSN: 1029-8479, URL: http://dx.doi.org/10.1007/JHEP04(2015)040 (cit. on pp. 14, 102).

[74] *LHC Higgs Cross Section Working Group*, [Online; accessed 20-October-2020], URL: https://twiki.cern.ch/twiki/bin/view/LHCPhysics/LHCHXSWG (cit. on pp. 16–19, 47).

[75] J. R. Ellis, M. K. Gaillard and D. V. Nanopoulos, *A Phenomenological Profile of the Higgs Boson*, Nucl. Phys. B **106** (1976) 292 (cit. on p. 17).

[76] L. Resnick, M. K. Sundaresan and P. J. S. Watson, *Is There a Light Scalar Boson?*, Phys. Rev. D **8** (1 1973) 172, URL: https://link.aps.org/doi/10.1103/PhysRevD.8.172 (cit. on p. 17).

[77] M. Aaboud et al., *Observation of $H \to b\bar{b}$ decays and VH production with the ATLAS detector*, Phys. Lett. B **786** (2018) 59, arXiv: 1808.08238 [hep-ex] (cit. on p. 17).

[78] A. M. Sirunyan et al., *Observation of Higgs boson decay to bottom quarks*, Phys. Rev. Lett. **121** (2018) 121801, arXiv: 1808.08242 [hep-ex] (cit. on p. 17).

[79] B. T. Cleveland et al.,
Measurement of the Solar Electron Neutrino Flux with the Homestake Chlorine Detector,
The Astrophysical Journal **496** (1998) 505, URL: https://doi.org/10.1086%2F305343
(cit. on p. 19).

[80] M. Gonzalez-Garcia and M. Maltoni, *Phenomenology with Massive Neutrinos*,
Phys. Rept. **460** (2008) 1, arXiv: 0704.1800 [hep-ph] (cit. on p. 19).

[81] S. F. King, *Neutrino mass*, Contemporary Physics **48** (2007) 195, ISSN: 1366-5812,
URL: http://dx.doi.org/10.1080/00107510701770539 (cit. on p. 19).

[82] F. Borzumati et al., *Neutrino masses and mixing in supersymmetric models without R parity*,
Phys. Lett. B **384** (1996) 123, arXiv: hep-ph/9606251 (cit. on p. 19).

[83] Y. Grossman and H. E. Haber, *Sneutrino mixing phenomena*, Phys. Rev. Lett. **78** (1997) 3438,
arXiv: hep-ph/9702421 (cit. on p. 19).

[84] Y. Grossman and H. E. Haber,
(S)neutrino properties in R-parity violating supersymmetry. 1. CP conserving phenomena,
Phys. Rev. D **59** (1999) 093008, arXiv: hep-ph/9810536 (cit. on p. 19).

[85] Y. Grossman and H. E. Haber,
"Neutrino masses and sneutrino mixing in R-parity violating supersymmetry", 1999,
arXiv: hep-ph/9906310 (cit. on p. 19).

[86] S. Davidson and M. Losada, *Neutrino masses in the R(p) violating MSSM*, JHEP **05** (2000) 021,
arXiv: hep-ph/0005080 (cit. on p. 19).

[87] M. Hirsch et al., *Neutrino masses and mixings from supersymmetry with bilinear R parity violation: A Theory for solar and atmospheric neutrino oscillations*,
Phys. Rev. D **62** (2000) 113008, [Erratum: Phys.Rev.D 65, 119901 (2002)],
arXiv: hep-ph/0004115 (cit. on p. 19).

[88] A. G. Cohen, D. B. Kaplan and A. E. Nelson, *Weak scale baryogenesis*,
Physics Letters B **245** (1990) 561, ISSN: 0370-2693,
URL: http://www.sciencedirect.com/science/article/pii/0370269390906908
(cit. on p. 19).

[89] A. G. Cohen, D. Kaplan and A. Nelson, *Progress in electroweak baryogenesis*,
Ann. Rev. Nucl. Part. Sci. **43** (1993) 27, arXiv: hep-ph/9302210 (cit. on p. 19).

[90] G. W. Anderson and L. J. Hall, *Electroweak phase transition and baryogenesis*,
Phys. Rev. D **45** (8 1992) 2685,
URL: https://link.aps.org/doi/10.1103/PhysRevD.45.2685 (cit. on p. 19).

[91] V. Rubakov and M. Shaposhnikov,
Electroweak baryon number nonconservation in the early universe and in high-energy collisions,
Usp. Fiz. Nauk **166** (1996) 493, arXiv: hep-ph/9603208 (cit. on p. 19).

[92] T. Konstandin, *Quantum Transport and Electroweak Baryogenesis*, Phys. Usp. **56** (2013) 747,
arXiv: 1302.6713 [hep-ph] (cit. on p. 19).

[93] D. E. Morrissey and M. J. Ramsey-Musolf, *Electroweak baryogenesis*,
New J. Phys. **14** (2012) 125003, arXiv: 1206.2942 [hep-ph] (cit. on p. 19).

[94] A. Sakharov, *Violation of CP Invariance, C asymmetry, and baryon asymmetry of the universe*,
Sov. Phys. Usp. **34** (1991) 392 (cit. on p. 19).

[95] W. Bernreuther, *CP violation and baryogenesis*, Lect. Notes Phys. **591** (2002) 237, arXiv: hep-ph/0205279 (cit. on p. 20).

[96] N. Manton, *Topology in the Weinberg-Salam Theory*, Phys. Rev. D **28** (1983) 2019 (cit. on p. 20).

[97] F. R. Klinkhamer and N. Manton, *A Saddle Point Solution in the Weinberg-Salam Theory*, Phys. Rev. D **30** (1984) 2212 (cit. on p. 20).

[98] A. Strumia, "Baryogenesis via leptogenesis", *Les Houches Summer School on Theoretical Physics: Session 84: Particle Physics Beyond the Standard Model*, 2006 655, arXiv: hep-ph/0608347 (cit. on p. 20).

[99] A. Bochkarev and M. Shaposhnikov, *Electroweak Production of Baryon Asymmetry and Upper Bounds on the Higgs and Top Masses*, Mod. Phys. Lett. A **2** (1987) 417 (cit. on p. 20).

[100] K. Kajantie et al., *The Electroweak phase transition: A Nonperturbative analysis*, Nucl. Phys. B **466** (1996) 189, arXiv: hep-lat/9510020 (cit. on p. 20).

[101] M. Gavela et al., *Standard model CP violation and baryon asymmetry*, Mod. Phys. Lett. A **9** (1994) 795, arXiv: hep-ph/9312215 (cit. on p. 20).

[102] P. Huet and E. Sather, *Electroweak baryogenesis and standard model CP violation*, Phys. Rev. D **51** (1995) 379, arXiv: hep-ph/9404302 (cit. on p. 20).

[103] M. Gavela et al., *Standard model CP violation and baryon asymmetry. Part 2: Finite temperature*, Nucl. Phys. B **430** (1994) 382, arXiv: hep-ph/9406289 (cit. on p. 20).

[104] M. Milgrom, *A Modification of the Newtonian dynamics as a possible alternative to the hidden mass hypothesis*, Astrophys. J. **270** (1983) 365 (cit. on p. 20).

[105] E. P. Verlinde, *Emergent Gravity and the Dark Universe*, SciPost Phys. **2** (2017) 016, arXiv: 1611.02269 [hep-th] (cit. on p. 20).

[106] J. Kapteyn, *First Attempt at a Theory of the Arrangement and Motion of the Sidereal System*, Astrophys. J. **55** (1922) 302 (cit. on p. 21).

[107] F. Zwicky, *Die Rotverschiebung von extragalaktischen Nebeln*, Helv. Phys. Acta **6** (1933) 110 (cit. on p. 21).

[108] J. R. Ellis et al., *Supersymmetric Relics from the Big Bang*, Nucl. Phys. B **238** (1984) 453, ed. by M. Srednicki (cit. on p. 21).

[109] M. Drees and M. M. Nojiri, *The Neutralino relic density in minimal $N = 1$ supergravity*, Phys. Rev. D **47** (1993) 376, arXiv: hep-ph/9207234 (cit. on p. 21).

[110] C. Csaki, *The Minimal supersymmetric standard model (MSSM)*, Mod. Phys. Lett. A **11** (1996) 599, arXiv: hep-ph/9606414 (cit. on pp. 21, 23).

[111] J. M. Cline et al., *Update on scalar singlet dark matter*, Phys. Rev. D **88** (2013) 055025, [Erratum: Phys.Rev.D 92, 039906 (2015)], arXiv: 1306.4710 [hep-ph] (cit. on p. 21).

[112] L. Lopez Honorez and C. E. Yaguna, *The inert doublet model of dark matter revisited*, JHEP **09** (2010) 046, arXiv: 1003.3125 [hep-ph] (cit. on p. 21).

[113] L. Covi et al., *Axinos as dark matter*, JHEP **05** (2001) 033, arXiv: hep-ph/0101009 (cit. on p. 21).

[114] J. E. Kim and G. Carosi, *Axions and the Strong CP Problem*, Rev. Mod. Phys. **82** (2010) 557, [Erratum: Rev.Mod.Phys. 91, 049902 (2019)], arXiv: 0807.3125 [hep-ph] (cit. on p. 21).

[115] G. Servant and T. M. Tait, *Is the lightest Kaluza-Klein particle a viable dark matter candidate?*, Nucl. Phys. B **650** (2003) 391, arXiv: hep-ph/0206071 (cit. on p. 21).

[116] H.-C. Cheng, J. L. Feng and K. T. Matchev, *Kaluza-Klein dark matter*, Phys. Rev. Lett. **89** (2002) 211301, arXiv: hep-ph/0207125 (cit. on p. 21).

[117] D. Hooper and S. Profumo, *Dark Matter and Collider Phenomenology of Universal Extra Dimensions*, Phys. Rept. **453** (2007) 29, arXiv: hep-ph/0701197 (cit. on p. 21).

[118] J. March-Russell et al., *Heavy Dark Matter Through the Higgs Portal*, JHEP **07** (2008) 058, arXiv: 0801.3440 [hep-ph] (cit. on p. 21).

[119] J. L. Feng, H. Tu and H.-B. Yu, *Thermal Relics in Hidden Sectors*, JCAP **10** (2008) 043, arXiv: 0808.2318 [hep-ph] (cit. on p. 21).

[120] J. L. Feng et al., *Hidden Charged Dark Matter*, JCAP **07** (2009) 004, arXiv: 0905.3039 [hep-ph] (cit. on p. 21).

[121] T. Cohen et al., *Asymmetric Dark Matter from a GeV Hidden Sector*, Phys. Rev. D **82** (2010) 056001, arXiv: 1005.1655 [hep-ph] (cit. on p. 21).

[122] S. Perlmutter et al., *Measurements of Ω and Λ from 42 high redshift supernovae*, Astrophys. J. **517** (1999) 565, arXiv: astro-ph/9812133 (cit. on p. 21).

[123] S. M. Carroll, *The Cosmological constant*, Living Rev. Rel. **4** (2001) 1, arXiv: astro-ph/0004075 (cit. on p. 21).

[124] N. Aghanim et al., *Planck 2018 results. VI. Cosmological parameters*, Astron. Astrophys. **641** (2020) A6, arXiv: 1807.06209 [astro-ph.CO] (cit. on p. 21).

[125] H. Georgi and S. Glashow, *Unity of All Elementary Particle Forces*, Phys. Rev. Lett. **32** (1974) 438 (cit. on p. 21).

[126] P. Langacker, *Grand Unified Theories*, eConf **C810824** (1981) 823, ed. by W. Pfeil (cit. on p. 21).

[127] P. Langacker, *Grand Unified Theories and Proton Decay*, Phys. Rept. **72** (1981) 185 (cit. on p. 21).

[128] S. Dimopoulos, S. Raby and F. Wilczek, *Supersymmetry and the Scale of Unification*, Phys. Rev. D **24** (1981) 1681 (cit. on p. 21).

[129] J. R. Ellis, S. Kelley and D. V. Nanopoulos, *Precision LEP data, supersymmetric GUTs and string unification*, Phys. Lett. B **249** (1990) 441 (cit. on p. 21).

[130] U. Amaldi, W. de Boer and H. Furstenau, *Comparison of grand unified theories with electroweak and strong coupling constants measured at LEP*, Phys. Lett. B **260** (1991) 447 (cit. on p. 21).

[131] S. R. Wadia, *String Theory: A Framework for Quantum Gravity and Various Applications*, (2008), arXiv: 0809.1036 [gr-qc] (cit. on p. 21).

[132] M. Blau and S. Theisen, *String theory as a theory of quantum gravity: A status report*, Gen. Rel. Grav. **41** (2009) 743 (cit. on p. 21).

[133] L. E. Ibanez, *The Second string (phenomenology) revolution*, Class. Quant. Grav. **17** (2000) 1117, ed. by O. Lechtenfeld et al., arXiv: hep-ph/9911499 (cit. on p. 21).

[134] S. B. Giddings, *Is string theory a theory of quantum gravity?*, Found. Phys. **43** (2013) 115, arXiv: 1105.6359 [hep-th] (cit. on p. 21).

[135] C. Rovelli and L. Smolin, *Knot Theory and Quantum Gravity*, Phys. Rev. Lett. **61** (10 1988) 1155, URL: https://link.aps.org/doi/10.1103/PhysRevLett.61.1155 (cit. on p. 21).

[136] C. Rovelli and L. Smolin, *Loop Space Representation of Quantum General Relativity*, Nucl. Phys. B **331** (1990) 80 (cit. on p. 21).

[137] T. Thiemann, *Loop Quantum Gravity: An Inside View*, Lect. Notes Phys. **721** (2007) 185, arXiv: hep-th/0608210 (cit. on p. 21).

[138] M. Drees, "An Introduction to supersymmetry", *Inauguration Conference of the Asia Pacific Center for Theoretical Physics (APCTP)*, 1996, arXiv: hep-ph/9611409 (cit. on pp. 22, 28).

[139] R. K. Kaul and P. Majumdar, *Cancellation of Quadratically Divergent Mass Corrections in Globally Supersymmetric Spontaneously Broken Gauge Theories*, Nucl. Phys. B **199** (1982) 36 (cit. on p. 22).

[140] N. Arkani-Hamed, S. Dimopoulos and G. Dvali, *Phenomenology, astrophysics and cosmology of theories with submillimeter dimensions and TeV scale quantum gravity*, Phys. Rev. D **59** (1999) 086004, arXiv: hep-ph/9807344 (cit. on p. 23).

[141] I. Antoniadis et al., *New dimensions at a millimeter to a Fermi and superstrings at a TeV*, Phys. Lett. B **436** (1998) 257, arXiv: hep-ph/9804398 (cit. on p. 23).

[142] N. Arkani-Hamed, S. Dimopoulos and G. Dvali, *The Hierarchy problem and new dimensions at a millimeter*, Phys. Lett. B **429** (1998) 263, arXiv: hep-ph/9803315 (cit. on p. 23).

[143] E. Farhi and L. Susskind, *Technicolor*, Phys. Rept. **74** (1981) 277 (cit. on p. 23).

[144] D. B. Kaplan, H. Georgi and S. Dimopoulos, *Composite Higgs Scalars*, Phys. Lett. B **136** (1984) 187 (cit. on p. 23).

[145] M. J. Dugan, H. Georgi and D. B. Kaplan, *Anatomy of a Composite Higgs Model*, Nucl. Phys. B **254** (1985) 299 (cit. on p. 23).

[146] C. T. Hill, *Topcolor assisted technicolor*, Phys. Lett. B **345** (1995) 483, arXiv: hep-ph/9411426 (cit. on p. 23).

[147] I. P. Ivanov, *Building and testing models with extended Higgs sectors*, Prog. Part. Nucl. Phys. **95** (2017) 160, arXiv: 1702.03776 [hep-ph] (cit. on p. 23).

[148] G. C. Branco, L. Lavoura and J. P. Silva, *CP Violation*, vol. 103, 1999 (cit. on p. 23).

[149] A. M. Teixeira, "The Next-to-Minimal Supersymmetric Standard Model: An Overview", *46th Rencontres de Moriond on Electroweak Interactions and Unified Theories*, 2011 79, arXiv: 1106.2103 [hep-ph] (cit. on p. 23).

[150] U. Ellwanger, C. Hugonie and A. M. Teixeira, *The Next-to-Minimal Supersymmetric Standard Model*, Phys. Rept. **496** (2010) 1, arXiv: 0910.1785 [hep-ph] (cit. on p. 23).

[151] G. Branco, P. Parada and M. Rebelo, *A Common origin for all CP violations*, (2003), arXiv: hep-ph/0307119 (cit. on p. 23).

[152] V. Barger et al., *Complex Singlet Extension of the Standard Model*, Phys. Rev. D **79** (2009) 015018, arXiv: 0811.0393 [hep-ph] (cit. on p. 23).

[153] M. Mühlleitner et al., *Phenomenological Comparison of Models with Extended Higgs Sectors*, JHEP **08** (2017) 132, arXiv: 1703.07750 [hep-ph] (cit. on p. 23).

[154] N. Darvishi and M. Krawczyk, *CP violation in the extension of SM with a complex singlet scalar and vector quarks*, (2016), arXiv: 1603.00598 [hep-ph] (cit. on p. 23).

[155] I. F. Ginzburg and M. Krawczyk, *Symmetries of two Higgs doublet model and CP violation*, Phys. Rev. D **72** (2005) 115013, arXiv: hep-ph/0408011 (cit. on p. 23).

[156] J. F. Gunion and H. E. Haber, *Conditions for CP-violation in the general two-Higgs-doublet model*, Phys. Rev. D **72** (2005) 095002, arXiv: hep-ph/0506227 (cit. on p. 23).

[157] G. Branco et al., *Theory and phenomenology of two-Higgs-doublet models*, Phys. Rept. **516** (2012) 1, arXiv: 1106.0034 [hep-ph] (cit. on p. 23).

[158] J. F. Gunion et al., *The Higgs Hunter's Guide*, vol. 80, 2000 (cit. on p. 23).

[159] E. Accomando et al., *Workshop on CP Studies and Non-Standard Higgs Physics*, (2006), arXiv: hep-ph/0608079 (cit. on pp. 23, 29).

[160] T. Ibrahim, *Mixing of the CP even and the CP odd Higgs bosons and the EDM constraints*, Phys. Rev. D **64** (2001) 035009, arXiv: hep-ph/0102218 (cit. on p. 23).

[161] S. Patel et al., *$C\!\!\!/P$-violating Effects on MSSM Higgs Searches*, Acta Phys. Polon. Supp. **11** (2018) 223, arXiv: 1801.05331 [hep-ph] (cit. on p. 23).

[162] E. Graverini, *Flavour anomalies: a review*, J. Phys. Conf. Ser. **1137** (2019) 012025, ed. by F. Bar ao et al., arXiv: 1807.11373 [hep-ex] (cit. on p. 24).

[163] Y. Amhis et al., *Averages of b-hadron, c-hadron, and τ-lepton properties as of summer 2016*, Eur. Phys. J. C **77** (2017) 895, arXiv: 1612.07233 [hep-ex] (cit. on p. 24).

[164] V. Khachatryan et al., *Observation of the rare $B_s^0 \to \mu^+\mu^-$ decay from the combined analysis of CMS and LHCb data*, Nature **522** (2015) 68, arXiv: 1411.4413 [hep-ex] (cit. on p. 24).

[165] R. Aaij et al., *Measurement of the $B_s^0 \to \mu^+\mu^-$ branching fraction and effective lifetime and search for $B^0 \to \mu^+\mu^-$ decays*, Phys. Rev. Lett. **118** (2017) 191801, arXiv: 1703.05747 [hep-ex] (cit. on p. 24).

[166] J. F. Gunion, A. Mendez and F. I. Olness, *Is the Left-right Higgs Sector Observable?*, Int. J. Mod. Phys. A **2** (1987) 1085 (cit. on p. 24).

[167] N. G. Deshpande et al., *Left-right-symmetric electroweak models with triplet Higgs field*, Phys. Rev. D **44** (3 1991) 837, URL: https://link.aps.org/doi/10.1103/PhysRevD.44.837 (cit. on p. 24).

[168] I. F. Ginzburg, M. Krawczyk and P. Osland, "Two Higgs doublet models with CP violation", *International Workshop on Linear Colliders (LCWS 2002)*, 2002 703, arXiv: hep-ph/0211371 (cit. on p. 24).

[169] R. Haag, J. T. Lopuszanski and M. Sohnius,
All Possible Generators of Supersymmetries of the s Matrix, Nucl. Phys. B **88** (1975) 257 (cit. on p. 26).

[170] S. Dimopoulos and D. W. Sutter, *The Supersymmetric flavor problem*, Nucl. Phys. B **452** (1995) 496, arXiv: hep-ph/9504415 (cit. on p. 27).

[171] S. Jager, *Supersymmetry beyond minimal flavour violation*, Eur. Phys. J. C **59** (2009) 497, arXiv: 0808.2044 [hep-ph] (cit. on p. 27).

[172] F. Gabbiani et al., *A Complete analysis of FCNC and CP constraints in general SUSY extensions of the standard model*, Nucl. Phys. B **477** (1996) 321, arXiv: hep-ph/9604387 (cit. on p. 27).

[173] H. E. Haber, "Introductory low-energy supersymmetry",
Theoretical Advanced Study Institute (TASI 92): From Black Holes and Strings to Particles, 1993 589, arXiv: hep-ph/9306207 (cit. on p. 27).

[174] J. Gunion and H. E. Haber,
Higgs Bosons in Supersymmetric Models. 2. Implications for Phenomenology,
Nucl. Phys. B **278** (1986) 449, ed. by S. Loken, [Erratum: Nucl.Phys.B 402, 569–569 (1993)] (cit. on p. 27).

[175] C. Patrignani et al., *Review of Particle Physics*, Chin. Phys. C **40** (2016) 100001 (cit. on p. 28).

[176] D. A. Demir et al., *Electric dipole moments in the MSSM at large tan beta*,
Nucl. Phys. B **680** (2004) 339, arXiv: hep-ph/0311314 (cit. on p. 29).

[177] D. Chang, W.-Y. Keung and A. Pilaftsis,
New two loop contribution to electric dipole moment in supersymmetric theories,
Phys. Rev. Lett. **82** (1999) 900, [Erratum: Phys.Rev.Lett. 83, 3972 (1999)],
arXiv: hep-ph/9811202 (cit. on p. 29).

[178] A. Pilaftsis, *Higgs boson two loop contributions to electric dipole moments in the MSSM*,
Phys. Lett. B **471** (1999) 174, arXiv: hep-ph/9909485 (cit. on p. 29).

[179] W. Hollik et al.,
One loop MSSM contribution to the weak magnetic dipole moments of heavy fermions,
Phys. Lett. B **416** (1998) 345, arXiv: hep-ph/9707437 (cit. on p. 29).

[180] W. Hollik et al., *Weak electric dipole moments of heavy fermions in the MSSM*,
Phys. Lett. B **425** (1998) 322, arXiv: hep-ph/9711322 (cit. on p. 29).

[181] O. Lebedev et al., *Probing CP violation with the deuteron electric dipole moment*,
Phys. Rev. D **70** (2004) 016003, arXiv: hep-ph/0402023 (cit. on p. 29).

[182] Y. Li, S. Profumo and M. Ramsey-Musolf, *A Comprehensive Analysis of Electric Dipole Moment Constraints on CP-violating Phases in the MSSM*, JHEP **08** (2010) 062,
arXiv: 1006.1440 [hep-ph] (cit. on p. 29).

[183] J. Ellis and D. S. Hwang, *Does the 'Higgs' have Spin Zero?*, JHEP **09** (2012) 071,
arXiv: 1202.6660 [hep-ph] (cit. on p. 30).

[184] J. Ellis et al., *Distinguishing 'Higgs' spin hypotheses using $\gamma\gamma$ and WW^* decays*,
Eur. Phys. J. C **73** (2013) 2488, arXiv: 1210.5229 [hep-ph] (cit. on p. 30).

[185] S. Choi et al., *Identifying the Higgs spin and parity in decays to Z pairs*,
Phys. Lett. B **553** (2003) 61, arXiv: hep-ph/0210077 (cit. on p. 30).

[186] R. Boughezal, T. J. LeCompte and F. Petriello,
Single-variable asymmetries for measuring the 'Higgs' boson spin and CP properties, (2012), arXiv: 1208.4311 [hep-ph] (cit. on p. 30).

[187] S. Choi, M. Muhlleitner and P. Zerwas,
Theoretical Basis of Higgs-Spin Analysis in $H \to \gamma\gamma$ and $Z\gamma$ Decays,
Phys. Lett. B **718** (2013) 1031, arXiv: 1209.5268 [hep-ph] (cit. on p. 30).

[188] A. De Rujula et al., *Higgs Look-Alikes at the LHC*, Phys. Rev. D **82** (2010) 013003, arXiv: 1001.5300 [hep-ph] (cit. on p. 30).

[189] Y. Gao et al., *Spin Determination of Single-Produced Resonances at Hadron Colliders*, Phys. Rev. D **81** (2010) 075022, arXiv: 1001.3396 [hep-ph] (cit. on p. 30).

[190] C. Buszello et al., *Prospective analysis of spin- and CP-sensitive variables in H —> Z Z —> l(1)+ l(1)- l(2)+ l(2)- at the LHC*, Eur. Phys. J. C **32** (2004) 209, arXiv: hep-ph/0212396 (cit. on p. 30).

[191] S. Bolognesi et al., *On the spin and parity of a single-produced resonance at the LHC*, Phys. Rev. D **86** (2012) 095031, arXiv: 1208.4018 [hep-ph] (cit. on p. 30).

[192] A. Alves,
Is the New Resonance Spin 0 or 2? Taking a Step Forward in the Higgs Boson Discovery, Phys. Rev. D **86** (2012) 113010, arXiv: 1209.1037 [hep-ph] (cit. on p. 30).

[193] J. P. Skittrall, *Production of a Z boson and a photon via a Randall-Sundrum-type graviton at the Large Hadron Collider*, Eur. Phys. J. C **60** (2009) 291, arXiv: 0809.4383 [hep-ph] (cit. on p. 30).

[194] A. Freitas and P. Schwaller, *Multi-Photon Signals from Composite Models at LHC*, JHEP **01** (2011) 022, arXiv: 1010.2528 [hep-ph] (cit. on p. 30).

[195] T. Plehn, D. L. Rainwater and D. Zeppenfeld,
Determining the Structure of Higgs Couplings at the LHC, Phys. Rev. Lett. **88** (2002) 051801, arXiv: hep-ph/0105325 (cit. on p. 30).

[196] V. Hankele et al., *Anomalous Higgs boson couplings in vector boson fusion at the CERN LHC*, Phys. Rev. D **74** (2006) 095001, arXiv: hep-ph/0609075 (cit. on p. 30).

[197] G. Klamke and D. Zeppenfeld,
Higgs plus two jet production via gluon fusion as a signal at the CERN LHC,
JHEP **04** (2007) 052, arXiv: hep-ph/0703202 (cit. on p. 30).

[198] F. Campanario and M. Kubocz, *Higgs boson CP-properties of the gluonic contributions in Higgs plus three jet production via gluon fusion at the LHC*,
Journal of High Energy Physics **2014** (2014) (cit. on p. 30).

[199] C. Englert, M. Spannowsky and M. Takeuchi,
Measuring Higgs CP and couplings with hadronic event shapes, JHEP **06** (2012) 108, arXiv: 1203.5788 [hep-ph] (cit. on p. 30).

[200] S. Berge, W. Bernreuther and J. Ziethe, *Determining the CP Parity of Higgs Bosons via Their τ Decay Channels at the Large Hadron Collider*, Phys. Rev. Lett. **100** (17 2008) 171605,
URL: https://link.aps.org/doi/10.1103/PhysRevLett.100.171605 (cit. on p. 30).

[201] S. Berge et al.,
How to pin down the CP quantum numbers of a Higgs boson in its τ decays at the LHC,
Phys. Rev. D **84** (11 2011) 116003,
URL: https://link.aps.org/doi/10.1103/PhysRevD.84.116003 (cit. on p. 30).

[202] S. Berge, W. Bernreuther and S. Kirchner,
Determination of the Higgs CP-mixing angle in the tau decay channels,
Nuclear and Particle Physics Proceedings **273-275** (2016) 841, 37th International Conference on High Energy Physics (ICHEP), ISSN: 2405-6014,
URL: http://www.sciencedirect.com/science/article/pii/S2405601415006185
(cit. on p. 30).

[203] J. Ellis et al., *Disentangling Higgs-Top Couplings in Associated Production*, JHEP **04** (2014) 004, arXiv: 1312.5736 [hep-ph] (cit. on p. 30).

[204] D. A. Faroughy et al., *Probing the CP nature of the top quark Yukawa at hadron colliders*, JHEP **02** (2020) 085, arXiv: 1909.00007 [hep-ph] (cit. on p. 30).

[205] B. Bortolato et al., *Optimized probes of CP-odd effects in the $t\bar{t}h$ process at hadron colliders*, (2020), arXiv: 2006.13110 [hep-ph] (cit. on p. 30).

[206] G. Aad et al., *Evidence for the spin-0 nature of the Higgs boson using ATLAS data*, Phys. Lett. B **726** (2013) 120, arXiv: 1307.1432 [hep-ex] (cit. on p. 30).

[207] V. Khachatryan et al., *Constraints on the spin-parity and anomalous HVV couplings of the Higgs boson in proton collisions at 7 and 8 TeV*, Phys. Rev. D **92** (2015) 012004, arXiv: 1411.3441 [hep-ex] (cit. on p. 30).

[208] G. Aad et al.,
Study of the spin and parity of the Higgs boson in diboson decays with the ATLAS detector,
Eur. Phys. J. C **75** (2015) 476, [Erratum: Eur.Phys.J.C 76, 152 (2016)],
arXiv: 1506.05669 [hep-ex] (cit. on p. 30).

[209] M. Aaboud et al., *Measurement of the Higgs boson coupling properties in the $H \to ZZ^* \to 4\ell$ decay channel at $\sqrt{s} = 13$ TeV with the ATLAS detector*, JHEP **03** (2018) 095, arXiv: 1712.02304 [hep-ex] (cit. on p. 30).

[210] A. M. Sirunyan et al., *Measurements of the Higgs boson width and anomalous HVV couplings from on-shell and off-shell production in the four-lepton final state*, Phys. Rev. D **99** (2019) 112003, arXiv: 1901.00174 [hep-ex] (cit. on p. 30).

[211] V. Khachatryan et al., *Combined search for anomalous pseudoscalar HVV couplings in VH($H \to b\bar{b}$) production and $H \to VV$ decay*, Phys. Lett. B **759** (2016) 672, arXiv: 1602.04305 [hep-ex] (cit. on p. 30).

[212] A. M. Sirunyan et al., *Constraints on anomalous HVV couplings from the production of Higgs bosons decaying to τ lepton pairs*, Phys. Rev. D **100** (2019) 112002, arXiv: 1903.06973 [hep-ex] (cit. on p. 30).

[213] G. Aad et al., *Test of CP invariance in vector-boson fusion production of the Higgs boson in the $H \to \tau\tau$ channel in proton–proton collisions at $\sqrt{s} = 13$ TeV with the ATLAS detector*, Phys. Lett. B **805** (2020) 135426, arXiv: 2002.05315 [hep-ex] (cit. on p. 30).

[214] G. Aad et al., *Test of CP Invariance in vector-boson fusion production of the Higgs boson using the Optimal Observable method in the ditau decay channel with the ATLAS detector*, Eur. Phys. J. C **76** (2016) 658, arXiv: 1602.04516 [hep-ex] (cit. on p. 30).

[215] A. Freitas and P. Schwaller, *Higgs CP Properties From Early LHC Data*, Phys. Rev. D **87** (2013) 055014, arXiv: 1211.1980 [hep-ph] (cit. on pp. 30, 38, 40, 41).

[216] A. Djouadi and G. Moreau, *The couplings of the Higgs boson and its CP properties from fits of the signal strengths and their ratios at the 7+8 TeV LHC*, Eur. Phys. J. C **73** (2013) 2512, arXiv: 1303.6591 [hep-ph] (cit. on p. 30).

[217] F. Boudjema et al., *Lab-frame observables for probing the top-Higgs interaction*, Phys. Rev. D **92** (2015) 015019, arXiv: 1501.03157 [hep-ph] (cit. on p. 30).

[218] G. Aad et al., *CP Properties of Higgs Boson Interactions with Top Quarks in the $t\bar{t}H$ and tH Processes Using $H \to \gamma\gamma$ with the ATLAS Detector*, Phys. Rev. Lett. **125** (2020) 061802, arXiv: 2004.04545 [hep-ex] (cit. on p. 31).

[219] A. M. Sirunyan et al., *Measurements of $\mathrm{t\bar{t}}H$ Production and the CP Structure of the Yukawa Interaction between the Higgs Boson and Top Quark in the Diphoton Decay Channel*, Phys. Rev. Lett. **125** (2020) 061801, arXiv: 2003.10866 [hep-ex] (cit. on pp. 31, 236).

[220] *Analysis of the CP structure of the Yukawa coupling between the Higgs boson and τ leptons in proton-proton collisions at $\sqrt{s} = 13$ TeV*, (2020) (cit. on p. 31).

[221] M. C. Hansen, *Studies into measuring the Higgs CP-state in $H \to \tau\tau$ decays at ATLAS*, PhD thesis: Bonn U., 2020 (cit. on pp. 31, 177).

[222] D. Stockinger, *The Muon Magnetic Moment and Supersymmetry*, J. Phys. G **34** (2007) R45, arXiv: hep-ph/0609168 (cit. on p. 31).

[223] J. Brod, U. Haisch and J. Zupan, *Constraints on CP-violating Higgs couplings to the third generation*, JHEP **11** (2013) 180, arXiv: 1310.1385 [hep-ph] (cit. on p. 31).

[224] V. Andreev et al., *Improved limit on the electric dipole moment of the electron*, Nature **562** (2018) 355 (cit. on p. 31).

[225] C. Abel et al., *Measurement of the permanent electric dipole moment of the neutron*, Phys. Rev. Lett. **124** (2020) 081803, arXiv: 2001.11966 [hep-ex] (cit. on p. 31).

[226] Y. Chien et al., *Direct and indirect constraints on CP-violating Higgs-quark and Higgs-gluon interactions*, JHEP **02** (2016) 011, arXiv: 1510.00725 [hep-ph] (cit. on p. 32).

[227] V. Cirigliano et al., *Constraining the top-Higgs sector of the Standard Model Effective Field Theory*, Phys. Rev. D **94** (2016) 034031, arXiv: 1605.04311 [hep-ph] (cit. on p. 32).

[228] G. Panico, A. Pomarol and M. Riembau, *EFT approach to the electron Electric Dipole Moment at the two-loop level*, JHEP **04** (2019) 090, arXiv: 1810.09413 [hep-ph] (cit. on p. 32).

[229] LHC Higgs Cross Section Working Group, S. Heinemeyer, C. Mariotti, G. Passarino, R. Tanaka (Eds), *Handbook of LHC Higgs Cross Sections: 3. Higgs Properties*, CERN-2013-004 (2013), arXiv: 1307.1347 [hep-ph] (cit. on pp. 32, 102).

[230] B. A. Dobrescu and J. D. Lykken, *Coupling spans of the Higgs-like boson*, JHEP **02** (2013) 073, arXiv: 1210.3342 [hep-ph] (cit. on p. 33).

[231] D. Zeppenfeld et al., *Measuring Higgs boson couplings at the CERN LHC*, Phys. Rev. D **62** (2000) 013009, arXiv: hep-ph/0002036 (cit. on p. 33).

[232] M. Duhrssen et al., "Determination of Higgs-boson couplings at the LHC", *Proceedings, 39th Rencontres de Moriond, 04 Electroweak interactions and unified theories: La Thuile, Aosta, Italy, Mar 21-28, 2004*, 2004 131, arXiv: hep-ph/0407190 [hep-ph], URL: http://inspirehep.net/record/654651/files/arXiv:hep-ph_0407190.pdf (cit. on p. 33).

[233] M. Duhrssen et al., *Extracting Higgs boson couplings from CERN LHC data*, Phys. Rev. **D70** (2004) 113009, arXiv: hep-ph/0406323 [hep-ph] (cit. on p. 33).

[234] A. Falkowski, S. Rychkov and A. Urbano, *What if the Higgs couplings to W and Z bosons are larger than in the Standard Model?*, JHEP **04** (2012) 073, arXiv: 1202.1532 [hep-ph] (cit. on p. 33).

[235] H. Georgi, *Effective Field Theory*, Annual Review of Nuclear and Particle Science **43** (1993) 209, eprint: https://doi.org/10.1146/annurev.ns.43.120193.001233, URL: https://doi.org/10.1146/annurev.ns.43.120193.001233 (cit. on p. 34).

[236] J. Bardeen, L. N. Cooper and J. R. Schrieffer, *Microscopic Theory of Superconductivity*, Phys. Rev. **106** (1 1957) 162, URL: https://link.aps.org/doi/10.1103/PhysRev.106.162 (cit. on p. 34).

[237] E. Fermi, *Versuch einer Theorie der SS-Strahlen. I*, Zeitschrift für Physik **88** (1 1934) 161, URL: https://doi.org/10.1007/BF01351864 (cit. on p. 34).

[238] C. S. Wu et al., *Experimental Test of Parity Conservation in Beta Decay*, Phys. Rev. **105** (4 1957) 1413, URL: https://link.aps.org/doi/10.1103/PhysRev.105.1413 (cit. on p. 35).

[239] M. Goldhaber, L. Grodzins and A. W. Sunyar, *Helicity of Neutrinos*, Phys. Rev. **109** (3 1958) 1015, URL: https://link.aps.org/doi/10.1103/PhysRev.109.1015 (cit. on p. 35).

[240] T. Appelquist and J. Carazzone, *Infrared Singularities and Massive Fields*, Phys. Rev. D **11** (1975) 2856 (cit. on p. 35).

[241] B. Grzadkowski et al., *Dimension-Six Terms in the Standard Model Lagrangian*, JHEP **10** (2010) 085, arXiv: 1008.4884 [hep-ph] (cit. on p. 36).

[242] L. Lehman, *Extending the Standard Model Effective Field Theory with the Complete Set of Dimension-7 Operators*, Phys. Rev. D **90** (2014) 125023, arXiv: 1410.4193 [hep-ph] (cit. on p. 36).

[243] C. W. Murphy, *Dimension-8 operators in the Standard Model Eective Field Theory*, JHEP **10** (2020) 174, arXiv: 2005.00059 [hep-ph] (cit. on p. 36).

[244] H.-L. Li et al., *Complete Set of Dimension-9 Operators in the Standard Model Effective Field Theory*, (2020), arXiv: 2007.07899 [hep-ph] (cit. on p. 36).

[245] B. Henning et al., *2, 84, 30, 993, 560, 15456, 11962, 261485, ...: Higher dimension operators in the SM EFT*, JHEP **08** (2017) 016, [Erratum: JHEP 09, 019 (2019)], arXiv: 1512.03433 [hep-ph] (cit. on p. 36).

[246] A. Baldini et al., *Search for the lepton flavour violating decay $\mu^+ \to e^+\gamma$ with the full dataset of the MEG experiment*, Eur. Phys. J. C **76** (2016) 434, arXiv: 1605.05081 [hep-ex] (cit. on p. 36).

[247] N. Quintero, *Constraints on lepton number violating short-range interactions from $|\Delta L| = 2$ processes*, Phys. Lett. B **764** (2017) 60, arXiv: 1606.03477 [hep-ph] (cit. on p. 36).

[248] F. F. Deppisch et al., *Falsifying High-Scale Baryogenesis with Neutrinoless Double Beta Decay and Lepton Flavor Violation*, Phys. Rev. D **92** (2015) 036005, arXiv: 1503.04825 [hep-ph] (cit. on p. 36).

[249] I. Brivio, Y. Jiang and M. Trott, *The SMEFTsim package, theory and tools*, JHEP **12** (2017) 070, arXiv: 1709.06492 [hep-ph] (cit. on pp. 36–38).

[250] R. Alonso et al., *Renormalization Group Evolution of the Standard Model Dimension Six Operators III: Gauge Coupling Dependence and Phenomenology*, JHEP **04** (2014) 159, arXiv: 1312.2014 [hep-ph] (cit. on p. 37).

[251] J. Gunion and H. E. Haber, *Higgs Bosons in Supersymmetric Models. 1.*, Nucl. Phys. B **272** (1986) 1, [Erratum: Nucl.Phys.B 402, 567–569 (1993)] (cit. on p. 40).

[252] M. Spira, *QCD effects in Higgs physics*, Fortsch. Phys. **46** (1998) 203, arXiv: hep-ph/9705337 (cit. on p. 40).

[253] R. Hempfling, *Yukawa coupling unification with supersymmetric threshold corrections*, Phys. Rev. D **49** (1994) 6168 (cit. on p. 42).

[254] L. J. Hall, R. Rattazzi and U. Sarid, *The Top quark mass in supersymmetric SO(10) unification*, Phys. Rev. D **50** (1994) 7048, arXiv: hep-ph/9306309 (cit. on p. 42).

[255] M. Carena et al., *Electroweak symmetry breaking and bottom - top Yukawa unification*, Nucl. Phys. B **426** (1994) 269, arXiv: hep-ph/9402253 (cit. on p. 42).

[256] *Combination of searches for invisible Higgs boson decays with the ATLAS experiment*, (2020) (cit. on pp. 42, 170).

[257] P. Artoisenet et al., *A framework for Higgs characterisation*, JHEP **11** (2013) 043, arXiv: 1306.6464 [hep-ph] (cit. on pp. 43, 44).

[258] H. Bahl et al., *Indirect $\mathcal{CP}$ probes of the Higgs-top-quark interaction: current LHC constraints and future opportunities*, (2020), arXiv: 2007.08542 [hep-ph] (cit. on pp. 43, 81, 165).

[259] A. V. Gritsan et al., *New features in the JHU generator framework: constraining Higgs boson properties from on-shell and off-shell production*, Phys. Rev. D **102** (2020) 056022, arXiv: 2002.09888 [hep-ph] (cit. on p. 43).

[260] F. Demartin et al., *Higgs characterisation at NLO in QCD: CP properties of the top-quark Yukawa interaction*, Eur. Phys. J. C **74** (2014) 3065, arXiv: 1407.5089 [hep-ph] (cit. on p. 43).

[261] *LHC Design Report Vol.1: The LHC Main Ring*, (2004), ed. by O. S. Bruning et al. (cit. on p. 45).

[262] *LHC Design Report. 2. The LHC infrastructure and general services*, (2004), ed. by O. Buning et al. (cit. on p. 45).

[263] *LHC Design Report. 3. The LHC injector chain*, (2004), ed. by M. Benedikt et al. (cit. on p. 45).

[264] E. Mobs, *The CERN accelerator complex - August 2018. Complexe des accélérateurs du CERN - Août 2018*, (2018), General Photo, URL: http://cds.cern.ch/record/2636343 (cit. on p. 46).

[265] K. Schindl, *The PS booster as preinjector for LHC*, Part. Accel. **58** (1997) 63, ed. by O. S. Bruning and E. Keil (cit. on p. 45).

[266] R. Cappi, *The PS in the LHC injector chain*, Part. Accel. **58** (1997) 79, ed. by O. S. Bruning and E. Keil (cit. on p. 45).

[267] P. Collier et al., *The SPS as injector for LHC: Conceptual design*, (1997) (cit. on p. 45).

[268] *LEP Design Report Vol.1: The LEP Injector Chain*, (1983) (cit. on p. 47).

[269] *LEP Design Report: Vol.2. The LEP Main Ring*, (1984) (cit. on p. 47).

[270] *LEP Design Report: Vol.3: LEP2*, (1996), ed. by C. Wyss (cit. on p. 47).

[271] *Luminosity determination in pp collisions at* $\sqrt{s} = 13$ *TeV using the ATLAS detector at the LHC*, (2019) (cit. on pp. 47, 110).

[272] *The ATLAS experiment - public results*, Accessed on 01/11/2020, URL: https://twiki.cern.ch/twiki/bin/view/AtlasPublic/LuminosityPublicResultsRun2#Luminosity%5C_Plots%5C_for%5C_multiple%5C_Ru (cit. on p. 47).

[273] F. Cafagna, *Latest results for Proton-proton Cross Section Measurements with the TOTEM experiment at LHC.*, PoS **ICRC2019** (2020) 207 (cit. on p. 47).

[274] G. Aad et al., *The ATLAS Experiment at the CERN Large Hadron Collider*, JINST **3** (2008) S08003 (cit. on pp. 48, 51–54).

[275] S. Chatrchyan et al., *The CMS Experiment at the CERN LHC*, JINST **3** (2008) S08004 (cit. on p. 48).

[276] K. Aamodt et al., *The ALICE experiment at the CERN LHC*, JINST **3** (2008) S08002 (cit. on p. 48).

[277] J. Alves A.Augusto et al., *The LHCb Detector at the LHC*, JINST **3** (2008) S08005 (cit. on p. 48).

[278] J. Pequenao, "Computer generated image of the whole ATLAS detector", 2008, URL: https://cds.cern.ch/record/1095924 (cit. on p. 48).

[279] G. Aad et al., *Performance of the ATLAS Trigger System in 2010*, Eur. Phys. J. C **72** (2012) 1849, arXiv: 1110.1530 [hep-ex] (cit. on p. 50).

[280] *2015 start-up trigger menu and initial performance assessment of the ATLAS trigger using Run-2 data*, tech. rep. ATL-DAQ-PUB-2016-001, CERN, 2016, URL: https://cds.cern.ch/record/2136007 (cit. on p. 50).

[281] *ATLAS inner detector: Technical design report. Vol. 1*, (1997) (cit. on p. 50).

[282] *ATLAS inner detector: Technical design report. Vol. 2*, (1997) (cit. on p. 50).

[283] M. Backhaus, *The upgraded Pixel Detector of the ATLAS Experiment for Run 2 at the Large Hadron Collider*, Nucl. Instrum. Meth. A **831** (2016) 65, ed. by Y. Unno et al. (cit. on p. 50).

[284] K. Potamianos, *The upgraded Pixel detector and the commissioning of the Inner Detector tracking of the ATLAS experiment for Run-2 at the Large Hadron Collider*, PoS **EPS-HEP2015** (2015) 261, arXiv: 1608.07850 [physics.ins-det] (cit. on p. 50).

[285] M. Capeans et al., *ATLAS Insertable B-Layer Technical Design Report*, (2010) (cit. on p. 50).

[286] A. Ahmad et al., *The Silicon microstrip sensors of the ATLAS semiconductor tracker*, Nucl. Instrum. Meth. A **578** (2007) 98 (cit. on p. 51).

[287] E. Abat et al., *The ATLAS Transition Radiation Tracker (TRT) proportional drift tube: Design and performance*, JINST **3** (2008) P02013 (cit. on p. 51).

[288] J. Pequenao, "Computer Generated image of the ATLAS calorimeter", 2008, URL: https://cds.cern.ch/record/1095927 (cit. on p. 52).

[289] *ATLAS tile calorimeter: Technical design report*, (1996) (cit. on p. 51).

[290] *ATLAS liquid argon calorimeter: Technical design report*, (1996) (cit. on p. 51).

[291] *ATLAS muon spectrometer: Technical design report*, (1997) (cit. on p. 54).

[292] J. Pequenao and P. Schaffner,
"How ATLAS detects particles: diagram of particle paths in the detector", 2013,
URL: https://cds.cern.ch/record/1505342 (cit. on p. 54).

[293] *Electron efficiency measurements with the ATLAS detector using the 2015 LHC proton-proton collision data*, (2016), URL: https://cds.cern.ch/record/2157687 (cit. on pp. 55, 56).

[294] *Electron identification measurements in ATLAS using $\sqrt{s} = 13$ TeV data with 50 ns bunch spacing*, (2015), URL: https://cds.cern.ch/record/2048202 (cit. on pp. 55, 56).

[295] M. Aaboud et al., *Electron reconstruction and identification in the ATLAS experiment using the 2015 and 2016 LHC proton-proton collision data at $\sqrt{s} = 13$ TeV*, Eur. Phys. J. C **79** (2019) 639, arXiv: 1902.04655 [physics.ins-det] (cit. on pp. 55, 56).

[296] *Electron and photon reconstruction and performance in ATLAS using a dynamical, topological cell clustering-based approach*, (2017), URL: https://cds.cern.ch/record/2298955 (cit. on pp. 55, 105).

[297] G. Aad et al.,
Topological cell clustering in the ATLAS calorimeters and its performance in LHC Run 1,
Eur. Phys. J. C **77** (2017) 490, arXiv: 1603.02934 [hep-ex] (cit. on pp. 55, 104).

[298] A. Salzburger, *Optimisation of the ATLAS Track Reconstruction Software for Run-2*,
J. Phys. Conf. Ser. **664** (2015) 072042 (cit. on p. 55).

[299] T. Cornelissen et al., *Concepts, Design and Implementation of the ATLAS New Tracking (NEWT)*, (2007), URL: http://cds.cern.ch/record/1020106 (cit. on p. 55).

[300] R. Fruhwirth, *Application of Kalman filtering to track and vertex fitting*,
Nucl. Instrum. Meth. A **262** (1987) 444 (cit. on p. 55).

[301] *Improved electron reconstruction in ATLAS using the Gaussian Sum Filter-based model for bremsstrahlung*, (2012), URL: https://cds.cern.ch/record/1449796 (cit. on p. 55).

[302] M. Aaboud et al., *Electron and photon energy calibration with the ATLAS detector using 20152016 LHC proton-proton collision data*, JINST **14** (2019) P03017,
arXiv: 1812.03848 [hep-ex] (cit. on p. 56).

[303] G. Aad et al., *Measurement of the muon reconstruction performance of the ATLAS detector using 2011 and 2012 LHC protonproton collision data*, Eur. Phys. J. C **74** (2014) 3130,
arXiv: 1407.3935 [hep-ex] (cit. on p. 57).

[304] G. Aad et al., *Muon reconstruction performance of the ATLAS detector in protonproton collision data at $\sqrt{s}$ =13 TeV*, Eur. Phys. J. C **76** (2016) 292, arXiv: 1603.05598 [hep-ex]
(cit. on pp. 57, 104, 105).

[305] *ATLAS Muon Combined Performance with 2017 and 2016 dataset*, Accessed on 05/12/2020,
URL: https://atlas.web.cern.ch/Atlas/GROUPS/PHYSICS/PLOTS/MUON-2017-002/index.html (cit. on p. 58).

[306] R. Atkin, *Review of jet reconstruction algorithms*,
J. Phys. Conf. Ser. **645** (2015) 012008, ed. by A. S. Cornell and B. Mellado (cit. on p. 58).

[307] S. D. Ellis and D. E. Soper, *Successive combination jet algorithm for hadron collisions*,
Phys. Rev. D **48** (1993) 3160, arXiv: hep-ph/9305266 (cit. on p. 58).

[308] M. Cacciari, G. P. Salam and G. Soyez, *The anti-k_t jet clustering algorithm*, JHEP **04** (2008) 063,
arXiv: 0802.1189 [hep-ph] (cit. on pp. 58, 104).

[309] M. Aaboud et al., *Jet energy scale measurements and their systematic uncertainties in proton-proton collisions at $\sqrt{s}$ = 13 TeV with the ATLAS detector*, Phys. Rev. D **96** (2017) 072002, arXiv: 1703.09665 [hep-ex] (cit. on p. 59).

[310] *Tagging and suppression of pileup jets*, (2014) (cit. on pp. 59, 104).

[311] G. Aad et al., *Performance of pile-up mitigation techniques for jets in pp collisions at $\sqrt{s}$ = 8 TeV using the ATLAS detector*, Eur. Phys. J. C **76** (2016) 581, arXiv: 1510.03823 [hep-ex] (cit. on pp. 59, 104).

[312] M. Aaboud et al., *Measurements of b-jet tagging efficiency with the ATLAS detector using $t\bar{t}$ events at $\sqrt{s}$ = 13 TeV*, JHEP **08** (2018) 089, arXiv: 1805.01845 [hep-ex] (cit. on pp. 59, 104).

[313] *Expected performance of the ATLAS b-tagging algorithms in Run-2*, (2015) (cit. on p. 59).

[314] *Reconstruction, Energy Calibration, and Identification of Hadronically Decaying Tau Leptons in the ATLAS Experiment for Run-2 of the LHC*, (2015) (cit. on p. 60).

[315] *Measurement of the tau lepton reconstruction and identification performance in the ATLAS experiment using pp collisions at $\sqrt{s}$ = 13 TeV*, (2017) (cit. on pp. 60, 70, 71).

[316] G. Aad et al., *Reconstruction of hadronic decay products of tau leptons with the ATLAS experiment*, Eur. Phys. J. C **76** (2016) 295, arXiv: 1512.05955 [hep-ex] (cit. on pp. 61, 62, 64).

[317] M. Aaboud et al., *Jet reconstruction and performance using particle flow with the ATLAS Detector*, Eur. Phys. J. C **77** (2017) 466, arXiv: 1703.10485 [hep-ex] (cit. on pp. 61, 62, 104).

[318] G. Aad et al., *Jet energy scale and resolution measured in proton-proton collisions at $\sqrt{s}$ = 13 TeV with the ATLAS detector*, (2020), arXiv: 2007.02645 [hep-ex] (cit. on p. 63).

[319] P. Bechtle et al., *HiggsSignals: Confronting arbitrary Higgs sectors with measurements at the Tevatron and the LHC*, Eur. Phys. J. **C74** (2014) 2711, arXiv: 1305.1933 [hep-ph] (cit. on p. 79).

[320] P. Bechtle et al., *HiggsSignals-2: Probing new physics with precision Higgs measurements in the LHC 13 TeV era*, (2020), arXiv: 2012.09197 [hep-ph] (cit. on pp. 79, 82, 85).

[321] P. Bechtle et al., *HiggsBounds: Confronting Arbitrary Higgs Sectors with Exclusion Bounds from LEP and the Tevatron*, Comput. Phys. Commun. **181** (2010) 138, arXiv: 0811.4169 [hep-ph] (cit. on p. 79).

[322] P. Bechtle et al., *HiggsBounds 2.0.0: Confronting Neutral and Charged Higgs Sector Predictions with Exclusion Bounds from LEP and the Tevatron*, Comput. Phys. Commun. **182** (2011) 2605, arXiv: 1102.1898 [hep-ph] (cit. on p. 79).

[323] P. Bechtle et al., *Recent Developments in HiggsBounds and a Preview of HiggsSignals*, PoS **CHARGED2012** (2012) 024, ed. by R. Enberg and A. Ferrari, arXiv: 1301.2345 [hep-ph] (cit. on p. 79).

[324] P. Bechtle et al., HiggsBounds – 4*: Improved Tests of Extended Higgs Sectors against Exclusion Bounds from LEP, the Tevatron and the LHC*, Eur. Phys. J. **C74** (2014) 2693, arXiv: 1311.0055 [hep-ph] (cit. on p. 79).

[325] P. Bechtle et al., *Applying Exclusion Likelihoods from LHC Searches to Extended Higgs Sectors*, Eur. Phys. J. **C75** (2015) 421, arXiv: 1507.06706 [hep-ph] (cit. on p. 79).

[326] P. Bechtle et al., *HiggsBounds-5: Testing Higgs Sectors in the LHC 13 TeV Era*, (2020), arXiv: 2006.06007 [hep-ph] (cit. on pp. 79–81).

[327] *HiggsBounds online documentation*, URL: https://higgsbounds.gitlab.io/higgsbounds/ (cit. on p. 79).

[328] O. Brein, R. V. Harlander and T. J. Zirke, *vh@nnlo - Higgs Strahlung at hadron colliders*, Comput. Phys. Commun. **184** (2013) 998, arXiv: 1210.5347 [hep-ph] (cit. on pp. 81, 102).

[329] R. V. Harlander et al., *vh@nnlo-v2: New physics in Higgs Strahlung*, JHEP **05** (2018) 089, arXiv: 1802.04817 [hep-ph] (cit. on pp. 81, 102).

[330] J. Alwall et al., *The automated computation of tree-level and next-to-leading order differential cross sections, and their matching to parton shower simulations*, JHEP **07** (2014) 079, arXiv: 1405.0301 [hep-ph] (cit. on pp. 81, 101, 117, 119).

[331] M. Wiesemann et al., *Higgs production in association with bottom quarks*, JHEP **02** (2015) 132, arXiv: 1409.5301 [hep-ph] (cit. on pp. 81, 101, 117).

[332] T. Sjöstrand, S. Mrenna and P. Z. Skands, *A brief introduction to PYTHIA 8.1*, Comput. Phys. Commun. **178** (2008) 852, arXiv: 0710.3820 [hep-ph] (cit. on pp. 81, 102, 117, 119).

[333] G. Aad et al., *Measurements of the Higgs boson production and decay rates and constraints on its couplings from a combined ATLAS and CMS analysis of the LHC pp collision data at $\sqrt{s}$ = 7 and 8 TeV*, JHEP **08** (2016) 045, arXiv: 1606.02266 [hep-ex] (cit. on pp. 82, 83, 86, 87, 89).

[334] G. Aad et al., *Combined Measurement of the Higgs Boson Mass in pp Collisions at $\sqrt{s}$ = 7 and 8 TeV with the ATLAS and CMS Experiments*, Phys. Rev. Lett. **114** (2015) 191803, arXiv: 1503.07589 [hep-ex] (cit. on pp. 82, 83).

[335] *HiggsSignals online documentation*, URL: https://higgsbounds.gitlab.io/higgssignals/ (cit. on p. 83).

[336] LHC Higgs Cross Section Working Group, D. de Florian et al. (Eds), *Handbook of LHC Higgs Cross Sections: 4. Deciphering the Nature of the Higgs Sector*, CERN-2017-002 (2017), arXiv: 1610.07922 [hep-ph] (cit. on pp. 84, 102).

[337] P. Bechtle et al., *Killing the cMSSM softly*, Eur. Phys. J. **C76** (2016) 96, arXiv: 1508.05951 [hep-ph] (cit. on pp. 85, 87).

[338] J. Neyman and E. S. Pearson, *On the Problem of the Most Efficient Tests of Statistical Hypotheses*, Phil. Trans. Roy. Soc. Lond. A **231** (1933) 289 (cit. on p. 86).

[339] G. Aad et al., *Measurement of Higgs boson production in the diphoton decay channel in pp collisions at center-of-mass energies of 7 and 8 TeV with the ATLAS detector*, Phys. Rev. **D90** (2014) 112015, arXiv: 1408.7084 [hep-ex] (cit. on p. 87).

[340] G. Aad et al., *Evidence for the Higgs-boson Yukawa coupling to tau leptons with the ATLAS detector*, JHEP **04** (2015) 117, arXiv: 1501.04943 [hep-ex] (cit. on p. 87).

[341] G. Aad et al., *Observation and measurement of Higgs boson decays to WW^* with the ATLAS detector*, Phys. Rev. **D92** (2015) 012006, arXiv: 1412.2641 [hep-ex] (cit. on p. 87).

[342] G. Aad et al., *Measurements of Higgs boson production and couplings in the four-lepton channel in pp collisions at center-of-mass energies of 7 and 8 TeV with the ATLAS detector*, Phys. Rev. **D91** (2015) 012006, arXiv: 1408.5191 [hep-ex] (cit. on p. 87).

[343] G. Aad et al., *Search for the Standard Model Higgs boson produced in association with top quarks and decaying into $b\bar{b}$ in pp collisions at $\sqrt{s} = 8$ TeV with the ATLAS detector*, Eur. Phys. J. **C75** (2015) 349, arXiv: 1503.05066 [hep-ex] (cit. on p. 87).

[344] T. A. collaboration, *Study of the Higgs boson decaying to WW^* produced in association with a weak boson with the ATLAS detector at the LHC*, (2015) (cit. on p. 87).

[345] S. Chatrchyan et al., *Measurement of Higgs boson production and properties in the WW decay channel with leptonic final states*, JHEP **01** (2014) 096, arXiv: 1312.1129 [hep-ex] (cit. on p. 87).

[346] *VH with $H \to WW \to \ell\nu\ell\nu$ and $V \to jj$*, tech. rep. CMS-PAS-HIG-13-017, CERN, 2013, URL: https://cds.cern.ch/record/1560844 (cit. on p. 87).

[347] V. Khachatryan et al., *Observation of the diphoton decay of the Higgs boson and measurement of its properties*, Eur. Phys. J. **C74** (2014) 3076, arXiv: 1407.0558 [hep-ex] (cit. on p. 87).

[348] S. Chatrchyan et al., *Evidence for the 125 GeV Higgs boson decaying to a pair of τ leptons*, JHEP **05** (2014) 104, arXiv: 1401.5041 [hep-ex] (cit. on p. 87).

[349] *Precise determination of the mass of the Higgs boson and studies of the compatibility of its couplings with the standard model*, (2014) (cit. on p. 87).

[350] S. Chatrchyan et al., *Measurement of the properties of a Higgs boson in the four-lepton final state*, Phys. Rev. **D89** (2014) 092007, arXiv: 1312.5353 [hep-ex] (cit. on p. 87).

[351] V. Khachatryan et al., *Search for the associated production of the Higgs boson with a top-quark pair*, JHEP **09** (2014) 087, [Erratum: JHEP10,106(2014)], arXiv: 1408.1682 [hep-ex] (cit. on p. 87).

[352] C. Collaboration, *Search for the standard model Higgs boson produced in association with W or Z bosons, and decaying to bottom quarks for LHCp 2013*, (2013) (cit. on p. 87).

[353] *Search for the Standard-Model Higgs boson decaying to tau pairs in proton-proton collisions at sqrt(s) = 7 and 8 TeV*, (2013) (cit. on p. 87).

[354] G. Aad et al., *Measurements of the Higgs boson production and decay rates and coupling strengths using pp collision data at $\sqrt{s} = 7$ and 8 TeV in the ATLAS experiment*, Eur. Phys. J. **C76** (2016) 6, arXiv: 1507.04548 [hep-ex] (cit. on p. 90).

[355] V. Khachatryan et al., *Precise determination of the mass of the Higgs boson and tests of compatibility of its couplings with the standard model predictions using proton collisions at 7 and 8 TeV*, Eur. Phys. J. **C75** (2015) 212, arXiv: 1412.8662 [hep-ex] (cit. on p. 90).

[356] *Higgs to WW measurements with* 15.2 fb^{-1} *of 13 TeV proton-proton collisions*, tech. rep. CMS-PAS-HIG-16-021, CERN, 2017, URL: https://cds.cern.ch/record/2273908 (cit. on pp. 91, 92).

[357] A. M. Sirunyan et al., *Measurements of properties of the Higgs boson decaying to a W boson pair in pp collisions at $\sqrt{s} = 13$ TeV*, Phys. Lett. B **791** (2019) 96, arXiv: 1806.05246 [hep-ex] (cit. on p. 92).

[358] *Measurements of differential Higgs boson production cross sections in the leptonic WW decay mode at* $\sqrt{s}$ = 13 TeV, tech. rep. CMS-PAS-HIG-19-002, CERN, 2019, URL: http://cds.cern.ch/record/2691268 (cit. on p. 92).

[359] G. Aad et al., *Higgs boson production cross-section measurements and their EFT interpretation in the* 4ℓ *decay channel at* $\sqrt{s}$ *=13 TeV with the ATLAS detector*, Eur. Phys. J. C **80** (2020) 957, arXiv: 2004.03447 [hep-ex] (cit. on pp. 93, 106, 107, 135, 235).

[360] LHC Higgs Cross Section Working Group 1 (ggF subgroup), (), 16th March 2017, URL: http://dgillber.web.cern.ch/dgillber/ggF_uncertainty_2017/corr2017.pdf (cit. on p. 93).

[361] *Measurement of Higgs boson production and decay to the* $\tau\tau$ *final state*, tech. rep. CMS-PAS-HIG-18-032, CERN, 2019, URL: https://cds.cern.ch/record/2668685 (cit. on pp. 93, 94).

[362] G. Aad et al., *Combined measurements of Higgs boson production and decay using up to* 80 fb^{-1} *of proton-proton collision data at* $\sqrt{s}$ *= 13 TeV collected with the ATLAS experiment*, Phys. Rev. D **101** (2020) 012002, arXiv: 1909.02845 [hep-ex] (cit. on p. 94).

[363] Particle Data Group, K. Nakamura et al., *Review of Particle Physics*, J. Phys. G **37** (2010) 075021, URL: http://pdg.lbl.gov (cit. on p. 97).

[364] *LHC Higgs Cross Section Working Group*, URL: https://twiki.cern.ch/twiki/bin/view/LHCPhysics/LHCHXSWG (cit. on p. 98).

[365] M. Pivk and F. Le Diberder, *: A statistical tool to unfold data distributions*, Nuclear Instruments and Methods in Physics Research Section A: Accelerators, Spectrometers, Detectors and Associated Equipment **555** (2005) 356, ISSN: 0168-9002, URL: http://dx.doi.org/10.1016/j.nima.2005.08.106 (cit. on p. 100).

[366] S. Agostinelli et al., *GEANT4–a simulation toolkit*, Nucl. Instrum. Meth. A **506** (2003) 250, URL: http://www.sciencedirect.com/science/article/pii/S0168900203013688 (cit. on p. 101).

[367] G. Aad et al., *The ATLAS Simulation Infrastructure*, The European Physical Journal C **70** (2010) 823, ISSN: 1434-6052, URL: http://dx.doi.org/10.1140/epjc/s10052-010-1429-9 (cit. on p. 101).

[368] P. Nason, *A New method for combining NLO QCD with shower Monte Carlo algorithms*, JHEP **11** (2004) 040, arXiv: hep-ph/0409146 (cit. on p. 101).

[369] S. Frixione, P. Nason and C. Oleari, *Matching NLO QCD computations with parton shower simulations: the POWHEG method*, JHEP **11** (2007) 070, arXiv: 0709.2092 [hep-ph] (cit. on p. 101).

[370] S. Alioli et al., *A general framework for implementing NLO calculations in shower Monte Carlo programs: the POWHEG BOX*, JHEP **06** (2010) 043, arXiv: 1002.2581 [hep-ph] (cit. on p. 101).

[371] J. Butterworth et al., *PDF4LHC recommendations for LHC Run II*, J. Phys. G **43** (2016) 023001, arXiv: 1510.03865 [hep-ph] (cit. on pp. 101, 112).

[372] K. Hamilton, P. Nason and G. Zanderighi, *MINLO: multi-scale improved NLO*, Journal of High Energy Physics **2012** (2012), ISSN: 1029-8479, URL: http://dx.doi.org/10.1007/JHEP10(2012)155 (cit. on p. 101).

[373] J. M. Campbell et al., *NLO Higgs Boson Production Plus One and Two Jets Using the POWHEG BOX, MadGraph4 and MCFM*, JHEP **07** (2012) 092, arXiv: 1202.5475 [hep-ph] (cit. on p. 101).

[374] K. Hamilton et al., *Merging H/W/Z + 0 and 1 jet at NLO with no merging scale: a path to parton shower + NNLO matching*, Journal of High Energy Physics **2013** (2013), ISSN: 1029-8479, URL: http://dx.doi.org/10.1007/JHEP05(2013)082 (cit. on p. 101).

[375] E. Bagnaschi et al., *Higgs production via gluon fusion in the POWHEG approach in the SM and in the MSSM*, Journal of High Energy Physics **2012** (2012), ISSN: 1029-8479, URL: http://dx.doi.org/10.1007/JHEP02(2012)088 (cit. on p. 101).

[376] M. Aaboud et al., *Measurements of Higgs boson properties in the diphoton decay channel with 36 fb^{-1} of pp collision data at $\sqrt{s}$ = 13 TeV with the ATLAS detector*, (2018), arXiv: 1802.04146 [hep-ex] (cit. on pp. 101, 117).

[377] M. Grazzini, *NNLO predictions for the Higgs boson signal in the $H \to WW \to l\nu l\nu$ and $H \to ZZ \to 4l$ decay channels*, JHEP **02** (2008) 043, arXiv: 0801.3232 [hep-ph] (cit. on p. 101).

[378] G. Bozzi et al., *Transverse-momentum resummation and the spectrum of the Higgs boson at the LHC*, Nucl. Phys. **B737** (2006) 73, arXiv: hep-ph/0508068 [hep-ph] (cit. on pp. 101, 102).

[379] D. de Florian et al., *Transverse-momentum resummation: Higgs boson production at the Tevatron and the LHC*, JHEP **11** (2011) 064, arXiv: 1109.2109 [hep-ph] (cit. on pp. 101, 102).

[380] P. Nason and C. Oleari, *NLO Higgs boson production via vector-boson fusion matched with shower in POWHEG*, JHEP **02** (2010) 037, arXiv: 0911.5299 [hep-ph] (cit. on p. 101).

[381] G. Luisoni et al., *$HW^{\pm}$/HZ + 0 and 1 jet at NLO with the POWHEG BOX interfaced to GoSam and their merging within MiNLO*, JHEP **10** (2013) 083, arXiv: 1306.2542 [hep-ph] (cit. on p. 101).

[382] H. B. Hartanto et al., *Higgs boson production in association with top quarks in the POWHEG BOX*, Phys. Rev. D **91** (9 2015) 094003, URL: https://link.aps.org/doi/10.1103/PhysRevD.91.094003 (cit. on p. 101).

[383] G. Cullen et al., *Automated one-loop calculations with GoSam*, The European Physical Journal C **72** (2012), ISSN: 1434-6052, URL: http://dx.doi.org/10.1140/epjc/s10052-012-1889-1 (cit. on p. 101).

[384] H.-L. Lai et al., *New parton distributions for collider physics*, Phys. Rev. D **82** (2010) 074024, arXiv: 1007.2241 [hep-ph] (cit. on p. 101).

[385] G. Aad et al., *Measurement of the Z/ * boson transverse momentum distribution in pp collisions at $\sqrt{s}$ = 7 TeV with the ATLAS detector*, Journal of High Energy Physics **2014** (2014), ISSN: 1029-8479, URL: http://dx.doi.org/10.1007/JHEP09(2014)145 (cit. on p. 102).

[386] *ATLAS Pythia 8 tunes to 7 TeV datas*, tech. rep. ATL-PHYS-PUB-2014-021, CERN, 2014, URL: https://cds.cern.ch/record/1966419 (cit. on p. 102).

[387] LHC Higgs Cross Section Working Group, S. Dittmaier, C. Mariotti, G. Passarino, R. Tanaka (Eds), *Handbook of LHC Higgs Cross Sections: 1. Inclusive Observables*, CERN-2011-002 (2011), arXiv: 1101.0593 [hep-ph] (cit. on p. 102).

[388] LHC Higgs Cross Section Working Group, S. Dittmaier, C. Mariotti, G. Passarino, R. Tanaka (Eds), *Handbook of LHC Higgs Cross Sections: 2. Differential Distributions*, CERN-2012-002 (2012), arXiv: 1201.3084 [hep-ph] (cit. on p. 102).

[389] A. Djouadi, J. Kalinowski and M. Spira, *HDECAY: a program for Higgs boson decays in the Standard Model and its supersymmetric extension*, Computer Physics Communications **108** (1998) 56, ISSN: 0010-4655, URL: http://dx.doi.org/10.1016/S0010-4655(97)00123-9 (cit. on p. 102).

[390] A. Djouadi, M. Muhlleitner and M. Spira, *Decays of supersymmetric particles: The Program SUSY-HIT (SUspect-SdecaY-Hdecay-InTerface)*, Acta Phys. Polon. B **38** (2007) 635, ed. by K. Fialkowski and B. Muryn, arXiv: hep-ph/0609292 (cit. on p. 102).

[391] S. Dulat et al., *New parton distribution functions from a global analysis of quantum chromodynamics*, Physical Review D **93** (2016), ISSN: 2470-0029, URL: http://dx.doi.org/10.1103/PhysRevD.93.033006 (cit. on p. 102).

[392] L. A. Harland-Lang et al., *Parton distributions in the LHC era: MMHT 2014 PDFs*, The European Physical Journal C **75** (2015), ISSN: 1434-6052, URL: http://dx.doi.org/10.1140/epjc/s10052-015-3397-6 (cit. on p. 102).

[393] A. Bredenstein et al., *Precise predictions for the Higgs-boson decayHWW/ZZ4leptons*, Physical Review D **74** (2006), ISSN: 1550-2368, URL: http://dx.doi.org/10.1103/PhysRevD.74.013004 (cit. on p. 102).

[394] A. Bredenstein et al., *Radiative corrections to the semileptonic and hadronic Higgs-boson decays HWW/ZZ4 fermions*, Journal of High Energy Physics **2007** (2007) 080, ISSN: 1029-847, URL: http://dx.doi.org/10.1088/1126-6708/2007/02/080 (cit. on p. 102).

[395] F. Demartin et al., *Higgs production in association with a single top quark at the LHC*, Eur. Phys. J. C **75** (2015) 267, arXiv: 1504.00611 [hep-ph] (cit. on p. 102).

[396] F. Demartin et al., *tWH associated production at the LHC*, Eur. Phys. J. C **77** (2017) 34, arXiv: 1607.05862 [hep-ph] (cit. on p. 102).

[397] U. Aglietti et al., *Two loop light fermion contribution to Higgs production and decays*, Phys. Lett. B **595** (2004) 432, arXiv: hep-ph/0404071 (cit. on p. 102).

[398] M. Bonetti, K. Melnikov and L. Tancredi, *Higher order corrections to mixed QCD-EW contributions to Higgs boson production in gluon fusion*, Phys. Rev. D **97** (2018) 056017, [Erratum: Phys.Rev.D 97, 099906 (2018)], arXiv: 1801.10403 [hep-ph] (cit. on p. 102).

[399] S. Actis et al., *NNLO Computational Techniques: The Cases H —> gamma gamma and H —> g g*, Nucl. Phys. B **811** (2009) 182, arXiv: 0809.3667 [hep-ph] (cit. on p. 102).

[400] S. Actis et al., *NLO electroweak corrections to Higgs boson production at hadron colliders*, Phys. Lett. B **670** (2008) 12, arXiv: 0809.1301 [hep-ph] (cit. on p. 102).

[401] A. Pak, M. Rogal and M. Steinhauser,
Finite top quark mass effects in NNLO Higgs boson production at LHC, JHEP **02** (2010) 025, arXiv: 0911.4662 [hep-ph] (cit. on p. 102).

[402] R. V. Harlander et al.,
Higgs production in gluon fusion at next-to-next-to-leading order QCD for finite top mass, Eur. Phys. J. C **66** (2010) 359, arXiv: 0912.2104 [hep-ph] (cit. on p. 102).

[403] R. V. Harlander and K. J. Ozeren,
Top mass effects in Higgs production at next-to-next-to-leading order QCD: Virtual corrections, Phys. Lett. B **679** (2009) 467, arXiv: 0907.2997 [hep-ph] (cit. on p. 102).

[404] R. V. Harlander and K. J. Ozeren,
Finite top mass effects for hadronic Higgs production at next-to-next-to-leading order, JHEP **11** (2009) 088, arXiv: 0909.3420 [hep-ph] (cit. on p. 102).

[405] F. Dulat, A. Lazopoulos and B. Mistlberger, *iHixs 2 Inclusive Higgs cross sections*, Comput. Phys. Commun. **233** (2018) 243, arXiv: 1802.00827 [hep-ph] (cit. on p. 102).

[406] C. Anastasiou et al., *Higgs Boson Gluon-Fusion Production in QCD at Three Loops*, Phys. Rev. Lett. **114** (2015) 212001, arXiv: 1503.06056 [hep-ph] (cit. on p. 102).

[407] C. Anastasiou et al.,
High precision determination of the gluon fusion Higgs boson cross-section at the LHC, JHEP **05** (2016) 058, arXiv: 1602.00695 [hep-ph] (cit. on p. 102).

[408] M. Ciccolini, A. Denner and S. Dittmaier, *Strong and electroweak corrections to the production of Higgs + 2-jets via weak interactions at the LHC*, Phys. Rev. Lett. **99** (2007) 161803, arXiv: 0707.0381 [hep-ph] (cit. on p. 102).

[409] M. Ciccolini, A. Denner and S. Dittmaier,
Electroweak and QCD corrections to Higgs production via vector-boson fusion at the LHC, Phys. Rev. D **77** (2008) 013002, arXiv: 0710.4749 [hep-ph] (cit. on p. 102).

[410] P. Bolzoni et al., *Higgs production via vector-boson fusion at NNLO in QCD*, Phys. Rev. Lett. **105** (2010) 011801, arXiv: 1003.4451 [hep-ph] (cit. on p. 102).

[411] O. Brein, A. Djouadi and R. Harlander,
NNLO QCD corrections to the Higgs-strahlung processes at hadron colliders, Phys. Lett. B **579** (2004) 149, arXiv: hep-ph/0307206 (cit. on p. 102).

[412] O. Brein et al., *Top-Quark Mediated Effects in Hadronic Higgs-Strahlung*, Eur. Phys. J. C **72** (2012) 1868, arXiv: 1111.0761 [hep-ph] (cit. on p. 102).

[413] A. Denner et al., *Electroweak corrections to Higgs-strahlung off W/Z bosons at the Tevatron and the LHC with HAWK*, JHEP **03** (2012) 075, arXiv: 1112.5142 [hep-ph] (cit. on p. 102).

[414] L. Altenkamp et al., *Gluon-induced Higgs-strahlung at next-to-leading order QCD*, JHEP **02** (2013) 078, arXiv: 1211.5015 [hep-ph] (cit. on p. 102).

[415] R. V. Harlander et al., *Soft gluon resummation for gluon-induced Higgs Strahlung*, JHEP **11** (2014) 082, arXiv: 1410.0217 [hep-ph] (cit. on p. 102).

[416] A. Denner et al., *HAWK 2.0: A Monte Carlo program for Higgs production in vector-boson fusion and Higgs strahlung at hadron colliders*, Comput. Phys. Commun. **195** (2015) 161, arXiv: 1412.5390 [hep-ph] (cit. on p. 102).

[417] M.L. Ciccolini, S. Dittmaier and M. Krämer,
Electroweak radiative corrections to associated WH and ZH production at hadron colliders,
Phys. Rev. D **68** (2003) 073003, arXiv: hep-ph/0306234 (cit. on p. 102).

[418] W. Beenakker et al., *NLO QCD corrections to $t\bar{t}H$ production in hadron collisions*,
Nucl. Phys. B **653** (2003) 151, arXiv: hep-ph/0211352 (cit. on p. 102).

[419] S. Dawson et al.,
Associated Higgs production with top quarks at the large hadron collider: NLO QCD corrections,
Phys. Rev. D **68** (2003) 034022, arXiv: hep-ph/0305087 (cit. on p. 102).

[420] Y. Zhang et al.,
QCD NLO and EW NLO corrections to $t\bar{t}H$ production with top quark decays at hadron collider,
Phys. Lett. B **738** (2014) 1, arXiv: 1407.1110 [hep-ph] (cit. on p. 102).

[421] S. Frixione et al.,
Electroweak and QCD corrections to top-pair hadroproduction in association with heavy bosons,
JHEP **06** (2015) 184, arXiv: 1504.03446 [hep-ph] (cit. on p. 102).

[422] S. Dawson et al., *Exclusive Higgs boson production with bottom quarks at hadron colliders*,
Phys. Rev. D **69** (2004) 074027, arXiv: hep-ph/0311067 (cit. on p. 102).

[423] S. Dittmaier, M. Krämer and M. Spira,
Higgs radiation off bottom quarks at the Tevatron and the CERN LHC,
Phys. Rev. D **70** (2004) 074010, arXiv: hep-ph/0309204 (cit. on p. 102).

[424] R. Harlander, M. Kramer and M. Schumacher, *Bottom-quark associated Higgs-boson production: reconciling the four- and five-flavour scheme approach*, (2011), arXiv: 1112.3478 [hep-ph]
(cit. on p. 102).

[425] A. Bredenstein et al., *Precision calculations for the Higgs decays H —> ZZ/WW —> 4 leptons*,
Nucl. Phys. B Proc. Suppl. **160** (2006) 131, ed. by J. Blumlein, S. Moch and T. Riemann,
arXiv: hep-ph/0607060 (cit. on p. 102).

[426] S. Boselli et al., *Higgs boson decay into four leptons at NLOPS electroweak accuracy*,
JHEP **06** (2015) 023, arXiv: 1503.07394 [hep-ph] (cit. on p. 102).

[427] K. Hamilton et al., *NNLOPS simulation of Higgs boson production*, JHEP **10** (2013) 222,
arXiv: 1309.0017 [hep-ph] (cit. on p. 102).

[428] T. Gleisberg et al., *Event generation with SHERPA 1.1*, JHEP **02** (2009) 007,
arXiv: 0811.4622 [hep-ph] (cit. on p. 102).

[429] T. Gleisberg and S. Hoeche, *Comix, a new matrix element generator*, JHEP **12** (2008) 039,
arXiv: 0808.3674 [hep-ph] (cit. on pp. 102, 103).

[430] F. Cascioli, P. Maierhofer and S. Pozzorini, *Scattering Amplitudes with Open Loops*,
Phys. Rev. Lett. **108** (2012) 111601, arXiv: 1111.5206 [hep-ph] (cit. on pp. 102, 103).

[431] E. Bothmann et al., *Event Generation with Sherpa 2.2*, SciPost Phys. **7** (2019) 034,
arXiv: 1905.09127 [hep-ph] (cit. on p. 102).

[432] B. Biedermann et al.,
Electroweak corrections to $pp \to \mu^+\mu^- e^+ e^- + X$ at the LHC: a Higgs background study,
Phys. Rev. Lett. **116** (2016) 161803, arXiv: 1601.07787 [hep-ph] (cit. on p. 102).

[433] B. Biedermann et al., *Next-to-leading-order electroweak corrections to the production of four charged leptons at the LHC*, JHEP **01** (2017) 033, arXiv: 1611.05338 [hep-ph]
(cit. on p. 102).

[434] M. Bonvini et al., *Signal-background interference effects for $ggHW^+W^-$ beyond leading order*, Phys. Rev. D **88** (2013) 034032, arXiv: 1304.3053 [hep-ph] (cit. on p. 102).

[435] C. S. Li et al., *Soft gluon resummation in the signal-background interference process of $gg(\to h) \to ZZ$*, JHEP **08** (2015) 065, arXiv: 1504.02388 [hep-ph] (cit. on p. 102).

[436] K. Melnikov and M. Dowling, *Production of two Z-bosons in gluon fusion in the heavy top quark approximation*, Phys. Lett. B **744** (2015) 43, arXiv: 1503.01274 [hep-ph] (cit. on p. 102).

[437] F. Caola et al., *QCD corrections to ZZ production in gluon fusion at the LHC*, Phys. Rev. D **92** (2015) 094028, arXiv: 1509.06734 [hep-ph] (cit. on p. 103).

[438] F. Caola et al., *QCD corrections to W^+W^- production through gluon fusion*, Phys. Lett. B **754** (2016) 275, arXiv: 1511.08617 [hep-ph] (cit. on p. 103).

[439] J. M. Campbell et al., *Two loop correction to interference in $gg \to ZZ$*, JHEP **08** (2016) 011, arXiv: 1605.01380 [hep-ph] (cit. on p. 103).

[440] S. Schumann and F. Krauss, *A Parton shower algorithm based on Catani-Seymour dipole factorisation*, JHEP **03** (2008) 038, arXiv: 0709.1027 [hep-ph] (cit. on p. 103).

[441] S. Hoeche et al., *QCD matrix elements + parton showers: The NLO case*, JHEP **04** (2013) 027, arXiv: 1207.5030 [hep-ph] (cit. on p. 103).

[442] P. Nason and G. Zanderighi, *W^+W^- , WZ and ZZ production in the POWHEG-BOX-V2*, Eur. Phys. J. C **74** (2014) 2702, arXiv: 1311.1365 [hep-ph] (cit. on p. 103).

[443] G. Aad et al., *Electron and photon performance measurements with the ATLAS detector using the 20152017 LHC proton-proton collision data*, JINST **14** (2019) P12006, arXiv: 1908.00005 [hep-ex] (cit. on p. 104).

[444] M. Cacciari, G. P. Salam and G. Soyez, *FastJet User Manual*, Eur. Phys. J. C **72** (2012) 1896, arXiv: 1111.6097 [hep-ph] (cit. on p. 104).

[445] M. Aaboud et al., *Measurement of the Higgs boson mass in the $H \to ZZ^* \to 4\ell$ and $H \to \gamma\gamma$ channels with $\sqrt{s} = 13$ TeV pp collisions using the ATLAS detector*, Phys. Lett. B **784** (2018) 345, arXiv: 1806.00242 [hep-ex] (cit. on p. 104).

[446] *Measurements of the Higgs boson production, fiducial and differential cross sections in the 4ℓ decay channel at $\sqrt{s} = 13$ TeV with the ATLAS detector*, (2018) (cit. on p. 104).

[447] *Optimisation and performance studies of the ATLAS b-tagging algorithms for the 2017-18 LHC run*, (2017) (cit. on p. 104).

[448] G. Aad et al., *ATLAS b-jet identification performance and efficiency measurement with $t\bar{t}$ events in pp collisions at $\sqrt{s} = 13$ TeV*, Eur. Phys. J. C **79** (2019) 970, arXiv: 1907.05120 [hep-ex] (cit. on p. 104).

[449] M. Aaboud et al., *Measurement of the Inelastic Proton-Proton Cross Section at $\sqrt{s} = 13$ TeV with the ATLAS Detector at the LHC*, Phys. Rev. Lett. **117** (2016) 182002, arXiv: 1606.02625 [hep-ex] (cit. on p. 110).

[450] I. W. Stewart et al., *Jet p_T resummation in Higgs production at $NNLL' + NNLO$*, Phys. Rev. D **89** (2014) 054001, arXiv: 1307.1808 [hep-ph] (cit. on p. 112).

[451] X. Liu and F. Petriello,
Reducing theoretical uncertainties for exclusive Higgs-boson plus one-jet production at the LHC,
Phys. Rev. D **87** (2013) 094027, arXiv: 1303.4405 [hep-ph] (cit. on p. 112).

[452] R. Boughezal et al., *Combining Resummed Higgs Predictions Across Jet Bins*,
Phys. Rev. D **89** (2014) 074044, arXiv: 1312.4535 [hep-ph] (cit. on p. 112).

[453] J. Bellm et al., *Herwig 7.0/Herwig++ 3.0 release note*, Eur. Phys. J. C **76** (2016) 196,
arXiv: 1512.01178 [hep-ph] (cit. on p. 112).

[454] G. Cowan et al., *Asymptotic formulae for likelihood-based tests of new physics*,
Eur. Phys. J. C **71** (2011) 1554, [Erratum: Eur.Phys.J.C 73, 2501 (2013)],
arXiv: 1007.1727 [physics.data-an] (cit. on p. 113).

[455] J. Ellis et al., *Updated global SMEFT fit to Higgs, diboson and electroweak data*,
Journal of High Energy Physics **2018** (2018), ISSN: 1029-8479,
URL: http://dx.doi.org/10.1007/JHEP06(2018)146 (cit. on p. 116).

[456] A. Azatov et al., *Helicity selection rules and noninterference for BSM amplitudes*,
Physical Review D **95** (2017), ISSN: 2470-0029,
URL: http://dx.doi.org/10.1103/PhysRevD.95.065014 (cit. on pp. 116, 117).

[457] *Test of CP invariance in vector-boson fusion production of the Higgs boson using the Optimal Observable method in the ditau decay channel with the ATLAS detector*,
The European Physical Journal C **76** (2016), ISSN: 1434-6052 (cit. on p. 116).

[458] D. Zanzi,
Measurement of the Higgs Boson Couplings and CP Structure Using Tau Leptons at the LHC,
Nuclear and Particle Physics Proceedings **287-288** (2017) 115, The 14th International Workshop on Tau Lepton Physics, ISSN: 2405-6014,
URL: http://www.sciencedirect.com/science/article/pii/S2405601417301177
(cit. on p. 116).

[459] V. M. Walbrecht, *Measurement of the Higgs Boson Coupling Structure in Decays to Four Leptons with the ATLAS Detector*, PhD Thesis: University of Munich, 2020, URL: https://publications.mppmu.mpg.de/?action=search&language=en&mpi=MPP-2020-2
(cit. on pp. 116, 135, 136, 148, 152, 153, 271).

[460] I. Brivio, Y. Jiang and M. Trott, *The SMEFTsim package, theory and tools*,
Journal of High Energy Physics **2017** (2017), ISSN: 1029-8479,
URL: http://dx.doi.org/10.1007/JHEP12(2017)070 (cit. on p. 117).

[461] *Standard Model Effective Field Theory The SMEFTsim package*, accessed November 27, 2019,
URL: https://feynrules.irmp.ucl.ac.be/wiki/SMEFT (cit. on p. 117).

[462] B. Grzadkowski et al., *Dimension-six terms in the Standard Model Lagrangian*,
Journal of High Energy Physics **2010** (2010), ISSN: 1029-8479,
URL: http://dx.doi.org/10.1007/JHEP10(2010)085 (cit. on p. 117).

[463] S. Catani et al., *Longitudinally invariant K_t clustering algorithms for hadron hadron collisions*,
Nucl. Phys. **B406** (1993) 187 (cit. on p. 119).

[464] *Combined effective field theory interpretation of $H \to WW^*$ and WW measurements using ATLAS data*, tech. rep., All figures including auxiliary figures are available at https://atlas.web.cern.ch/Atlas/GROUPS/PHYSICS/PUBNOTES/ATL-PHYS-PUB-2021-010:
CERN, 2021, URL: http://cds.cern.ch/record/2758785 (cit. on p. 159).

[465] G. Aad et al., *Measurements of WH and ZH production in the $H \to b\bar{b}$ decay channel in pp collisions at 13 TeV with the ATLAS detector*, Eur. Phys. J. C **81** (2021) 178, arXiv: 2007.02873 [hep-ex] (cit. on pp. 159, 235).

[466] G. Aad et al., *Measurement of the associated production of a Higgs boson decaying into b-quarks with a vector boson at high transverse momentum in pp collisions at $\sqrt{s}$ = 13 TeV with the ATLAS detector*, Phys. Lett. B **816** (2021) 136204, arXiv: 2008.02508 [hep-ex] (cit. on p. 159).

[467] *Interpretations of the combined measurement of Higgs boson production and decay*, (2020) (cit. on p. 159).

[468] H. Haario, E. Saksman and J. Tamminen, *An adaptive Metropolis algorithm*, English, Bernoulli **7** (2001) 223, ISSN: 1350-7265 (cit. on p. 167).

[469] A. Patil, D. Huard and C. J. Fonnesbeck, *PyMC: Bayesian Stochastic Modelling in Python*, Journal of Statistical Software, Articles **35** (2010) 1, ISSN: 1548-7660, URL: https://www.jstatsoft.org/v035/i04 (cit. on p. 167).

[470] M. Aaboud et al., *Measurements of gluon-gluon fusion and vector-boson fusion Higgs boson production cross-sections in the $H \to WW^* \to e\nu\mu\nu$ decay channel in pp collisions at $\sqrt{s}$ = 13 TeV with the ATLAS detector*, Phys. Lett. **B789** (2019) 508, arXiv: 1808.09054 [hep-ex] (cit. on p. 235).

[471] *Measurements and interpretations of Higgs-boson fiducial cross sections in the diphoton decay channel using 139 fb1 of pp collision data at $\sqrt{s}$ = 13 TeV with the ATLAS detector*, (2019) (cit. on p. 235).

[472] M. Aaboud et al., *Cross-section measurements of the Higgs boson decaying into a pair of τ-leptons in proton-proton collisions at $\sqrt{s}$ = 13 TeV with the ATLAS detector*, Phys. Rev. **D99** (2019) 072001, arXiv: 1811.08856 [hep-ex] (cit. on p. 235).

[473] G. Aad et al., *Measurement of the production cross section for a Higgs boson in association with a vector boson in the $H \to WW^* \to \ell\nu\ell\nu$ channel in pp collisions at $\sqrt{s}$ = 13 TeV with the ATLAS detector*, Phys. Lett. **B798** (2019) 134949, arXiv: 1903.10052 [hep-ex] (cit. on p. 235).

[474] M. Aaboud et al., *Search for Higgs bosons produced via vector-boson fusion and decaying into bottom quark pairs in $\sqrt{s}$ = 13 TeV pp collisions with the ATLAS detector*, Phys. Rev. **D98** (2018) 052003, arXiv: 1807.08639 [hep-ex] (cit. on p. 236).

[475] M. Aaboud et al., *Search for the Standard Model Higgs boson produced in association with top quarks and decaying into a $b\bar{b}$ pair in pp collisions at $\sqrt{s}$ = 13 TeV with the ATLAS detector*, Submitted to: Phys. Rev. D (2017), arXiv: 1712.08895 [hep-ex] (cit. on p. 236).

[476] *Analysis of $t\bar{t}H$ and $t\bar{t}W$ production in multilepton final states with the ATLAS detector*, (2019) (cit. on p. 236).

[477] A. M. Sirunyan et al., *Search for the Higgs boson decaying to two muons in proton-proton collisions at $\sqrt{s}$ = 13 TeV*, Phys. Rev. Lett. **122** (2019) 021801, arXiv: 1807.06325 [hep-ex] (cit. on p. 236).

[478] A. M. Sirunyan et al., *Evidence for the Higgs boson decay to a bottom quark-antiquark pair*, Phys. Lett. **B780** (2018) 501, arXiv: 1709.07497 [hep-ex] (cit. on p. 236).

[479] A. M. Sirunyan et al., *Inclusive search for a highly boosted Higgs boson decaying to a bottom quark-antiquark pair*, Phys. Rev. Lett. **120** (2018) 071802, arXiv: 1709.05543 [hep-ex] (cit. on p. 236).

[480] A. M. Sirunyan et al., *Search for* $\mathrm{t\bar{t}H}$ *production in the* $\mathrm{H} \to \mathrm{b\bar{b}}$ *decay channel with leptonic* $\mathrm{t\bar{t}}$ *decays in proton-proton collisions at* $\sqrt{s} = 13$ *TeV*, JHEP **03** (2019) 026, arXiv: 1804.03682 [hep-ex] (cit. on p. 236).

[481] C. Collaboration, *Measurement of* $\mathrm{t\bar{t}H}$ *production in the* $\mathrm{H} \to \mathrm{b\bar{b}}$ *decay channel in* $41.5\,\mathrm{fb}^{-1}$ *of proton-proton collision data at* $\sqrt{s} = 13\,\mathrm{TeV}$, (2019) (cit. on p. 236).

[482] A. M. Sirunyan et al., *Evidence for associated production of a Higgs boson with a top quark pair in final states with electrons, muons, and hadronically decaying* τ *leptons at* $\sqrt{s} = 13$ *TeV*, JHEP **08** (2018) 066, arXiv: 1803.05485 [hep-ex] (cit. on p. 236).

[483] C. Collaboration, *Measurement of the associated production of a Higgs boson with a top quark pair in final states with electrons, muons and hadronically decaying* τ *leptons in data recorded in 2017 at* $\sqrt{s} = 13$ TeV, (2018) (cit. on p. 236).

[484] A. M. Sirunyan et al., *Measurement of the inclusive and differential Higgs boson production cross sections in the leptonic WW decay mode at* $\sqrt{s} = 13$ *TeV*, (2020), arXiv: 2007.01984 [hep-ex] (cit. on p. 236).

[485] C. Collaboration, *Measurements of properties of the Higgs boson in the four-lepton final state in proton-proton collisions at* $\sqrt{s} = 13$ TeV, (2019) (cit. on p. 236).

[486] C. Collaboration, *Measurements of Higgs boson production via gluon fusion and vector boson fusion in the diphoton decay channel at* $\sqrt{s} = 13$ *TeV*, (2019) (cit. on p. 236).

[487] C. Collaboration, *Measurement of Higgs boson production and decay to the* $\tau\tau$ *final state*, (2019) (cit. on p. 236).

APPENDIX A

Energy Reconstruction of Hadronic Tau Leptons

A.1 Gaussian fits to the Core Energy Resolutions

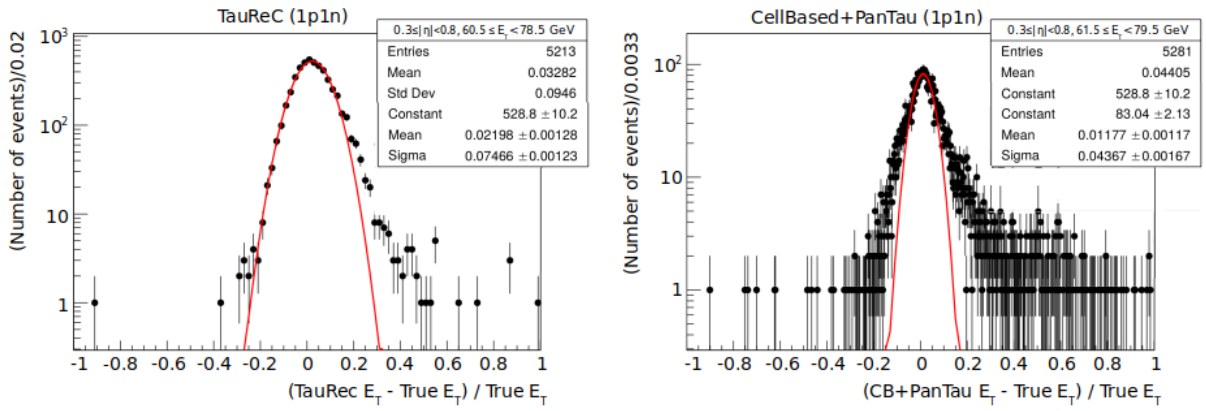

(a) (b)

Figure A.1: Example fits to the core of the energy resolution of hadronic tau leptons obtained from (a) the TauRec and (b) the CellBased+PanTau reconstruction algorithm for reconstructed 1p1n decays with $0.3 \leq |\eta| < 0.8$. The E_T bins for the TauRec ($60.5\,\text{GeV} \leq E_T < 78.5\,\text{GeV}$) and CellBased+PanTau ($61.5\,\text{GeV} \leq E_T < 79.5\,\text{GeV}$) algorithms differ slightly because the bins are defined based such that they contain similar statistics. The scale on the y-axis is logarithmic. The simulated data points are shown in black and the gaussian fit to the core region is shown in red. Additional information about the distribution (three upper entries) and the gaussian fit parameters (three lower entries) are displayed in the box.

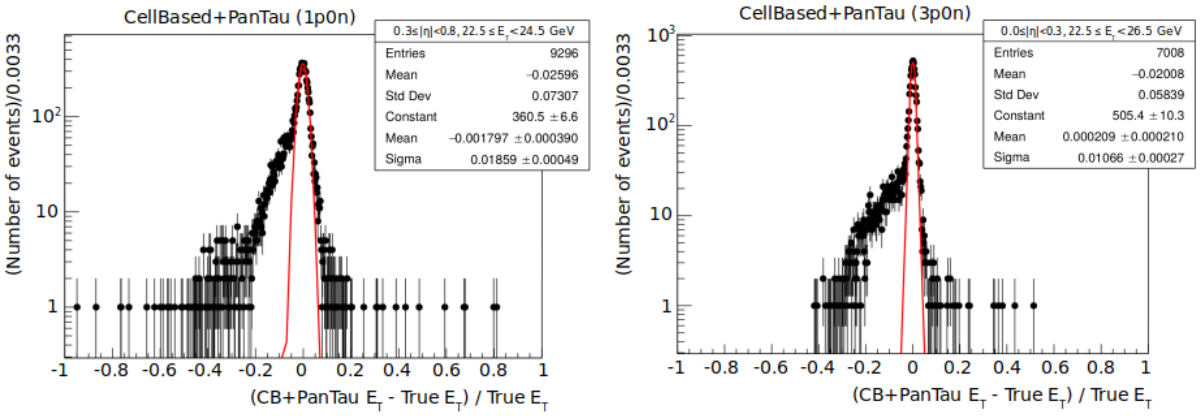

(a) (b)

Figure A.2: Example fits to the core of the energy resolution of hadronic tau leptons obtained from the Cell-Based+PanTau reconstruction algorithm for reconstructed (a) 1p0n and (b) 3p0n decays with $0.3 \leq |\eta| < 0.8$. The corresponding E_T bins are $60.5\,\text{GeV} \leq E_T < 78.5\,\text{GeV}$ and $61.5\,\text{GeV} \leq E_T < 79.5\,\text{GeV}$, respectively. The scale on the y-axis is logarithmic. The simulated data points are shown in black and the gaussian fit to the core region is shown in red. Additional information about the distribution (three upper entries) and the gaussian fit parameters (three lower entries) are displayed in the box.

A.1.1 Extracted Mean Values of Core Resolutions

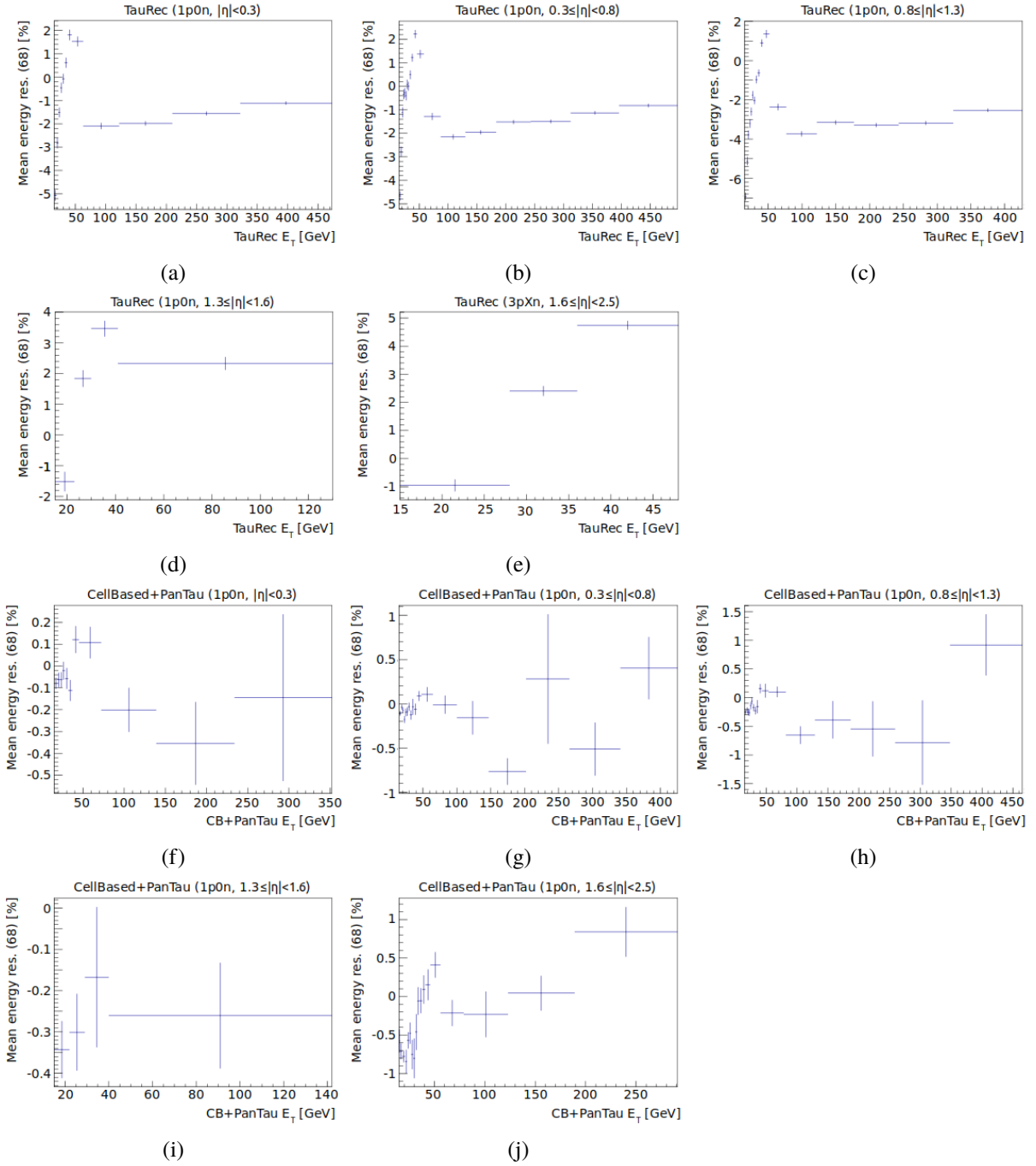

Figure A.3: The (a) - (e) TauRec and (f) - (j) CellBased+PanTau mean values extracted from the Gaussian fits to the core region of the energy resolution, binned in the reconstructed transverse energy E_T, for different η bins in the 1p0n decay mode.

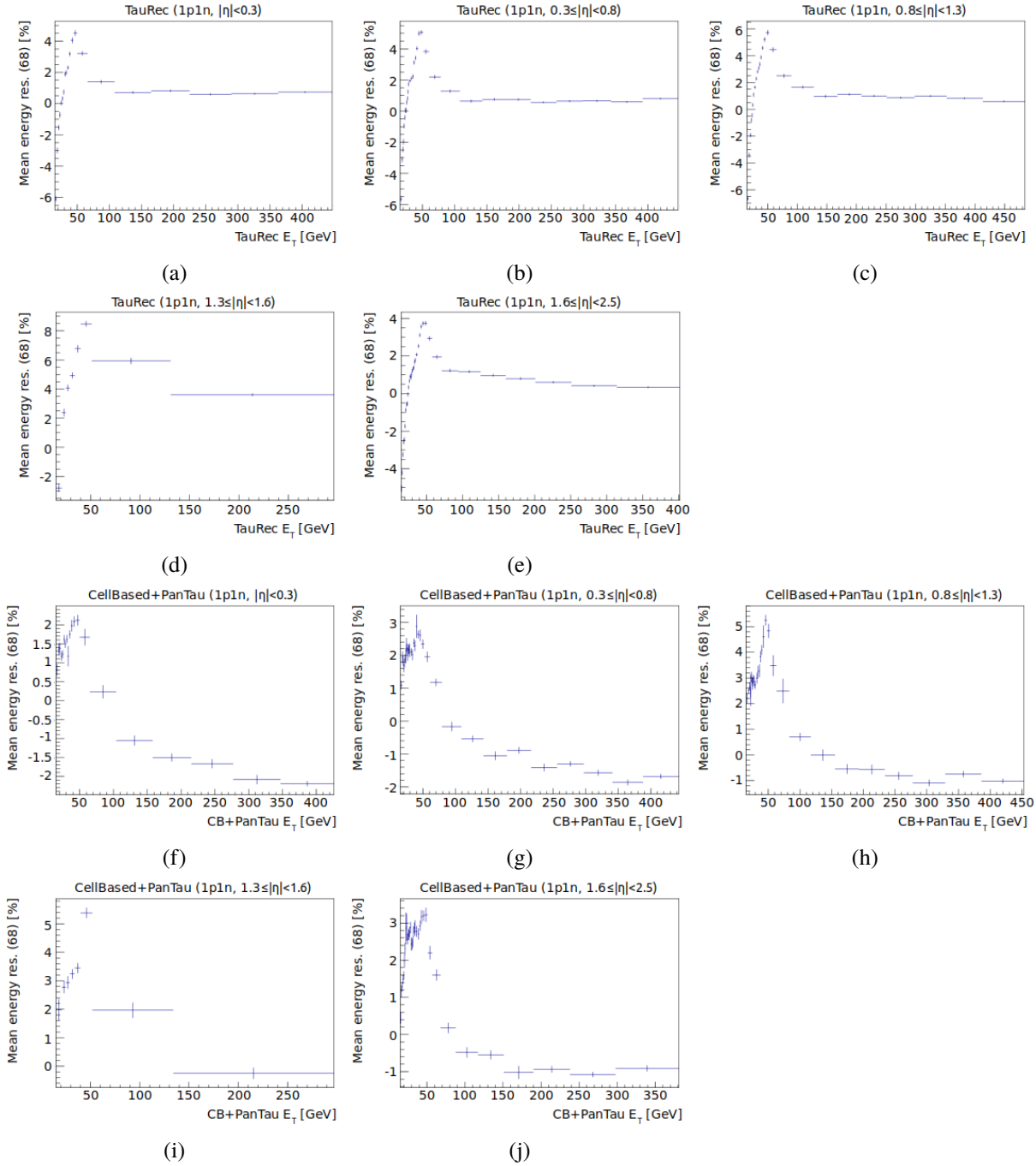

Figure A.4: The (a) - (e) TauRec and (f) - (j) CellBased+PanTau mean values extracted from the Gaussian fits to the core region of the energy resolution, binned in the reconstructed transverse energy E_T, for different η bins in the 1p1n decay mode.

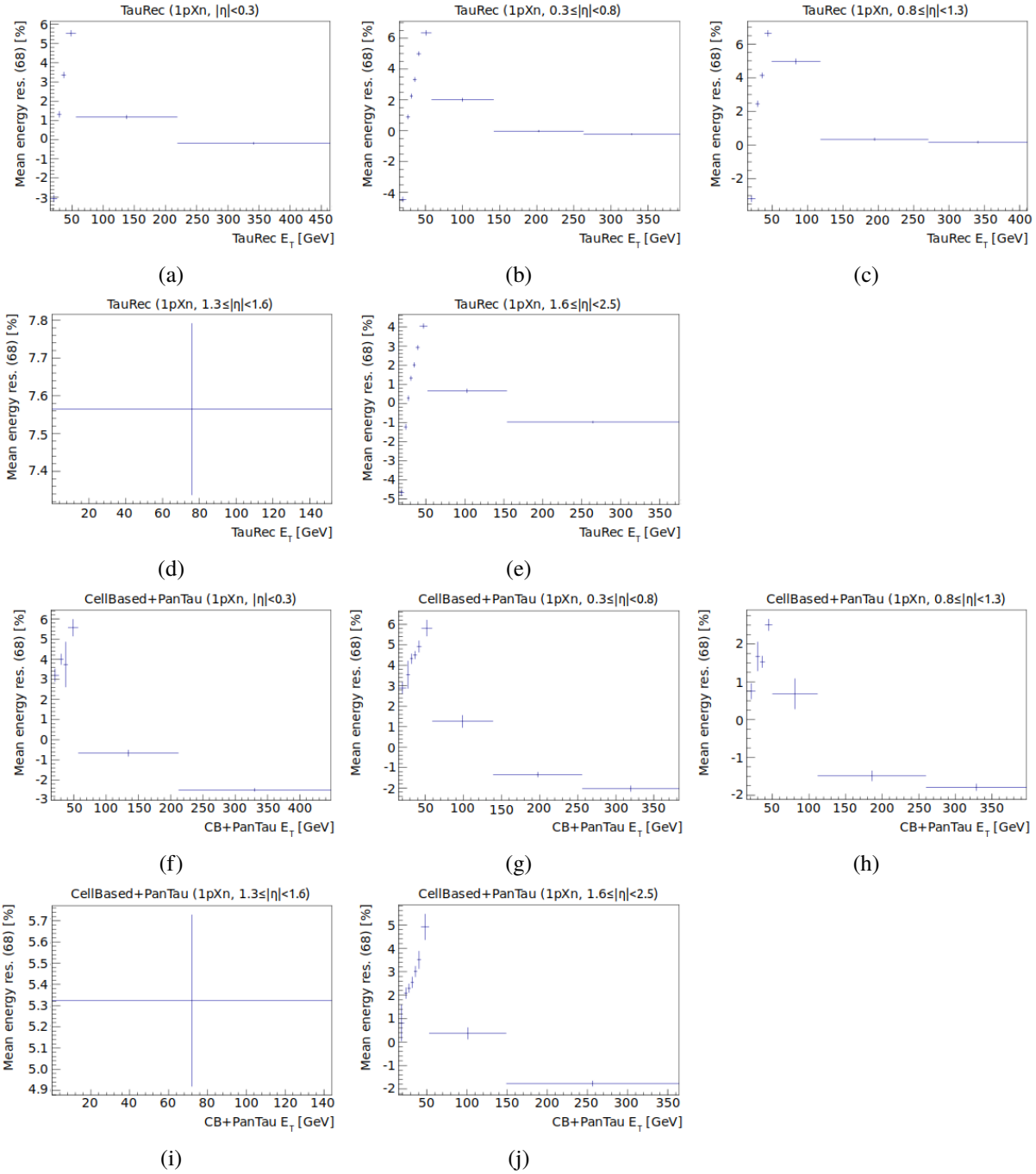

Figure A.5: The (a) - (e) TauRec and (f) - (j) CellBased+PanTau mean values extracted from the Gaussian fits to the core region of the energy resolution, binned in the reconstructed transverse energy E_T, for different η bins in the 1pXn decay mode.

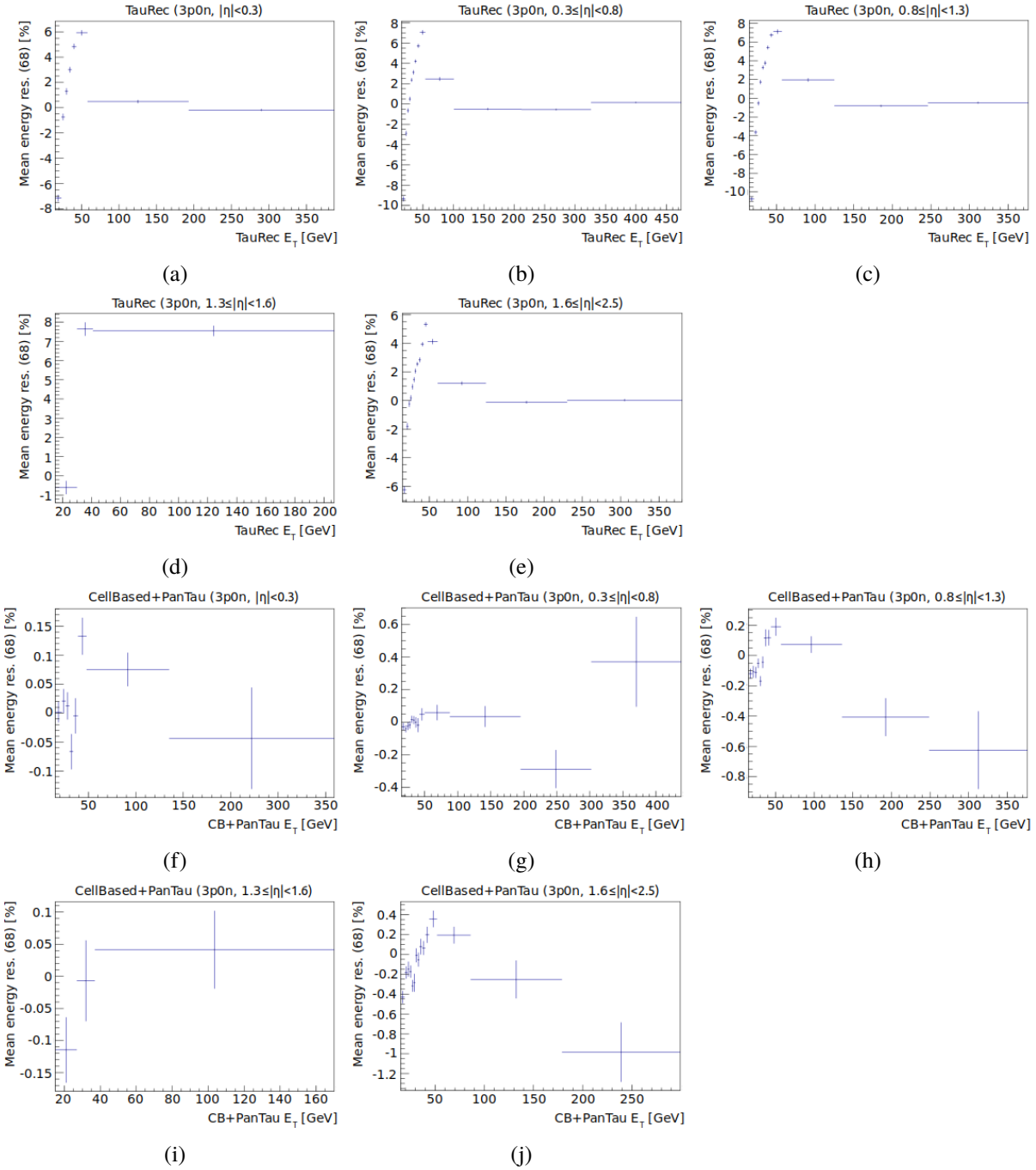

Figure A.6: The (a) - (e) TauRec and (f) - (j) CellBased+PanTau mean values extracted from the Gaussian fits to the core region of the energy resolution, binned in the reconstructed transverse energy E_T, for different η bins in the 3p0n decay mode.

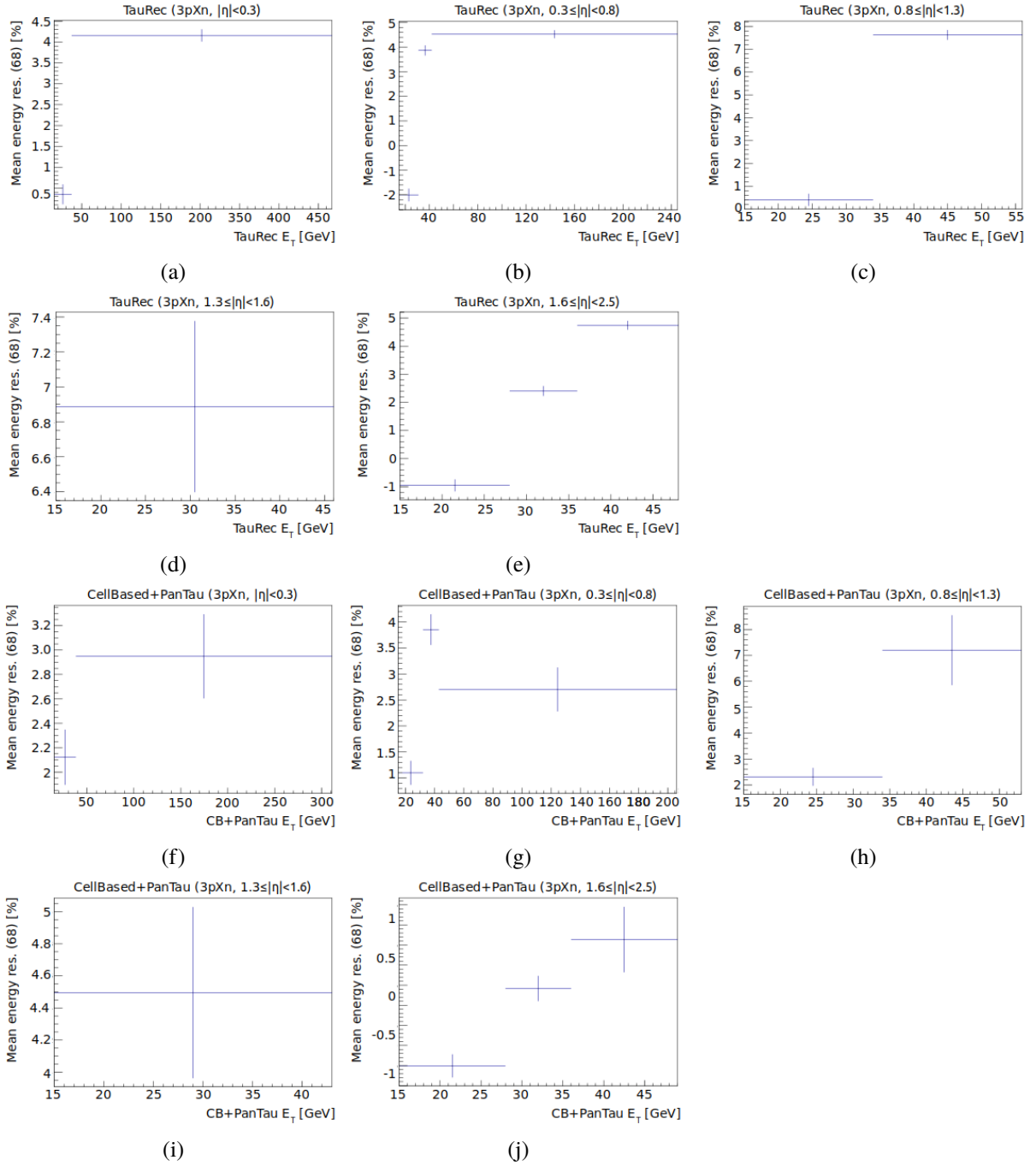

Figure A.7: The (a) - (e) TauRec and (f) - (j) CellBased+PanTau mean values extracted from the Gaussian fits to the core region of the energy resolution, binned in the reconstructed transverse energy E_T, for different η bins in the 3pXn decay mode.

A.1.2 Extracted Widths of Core Resolutions

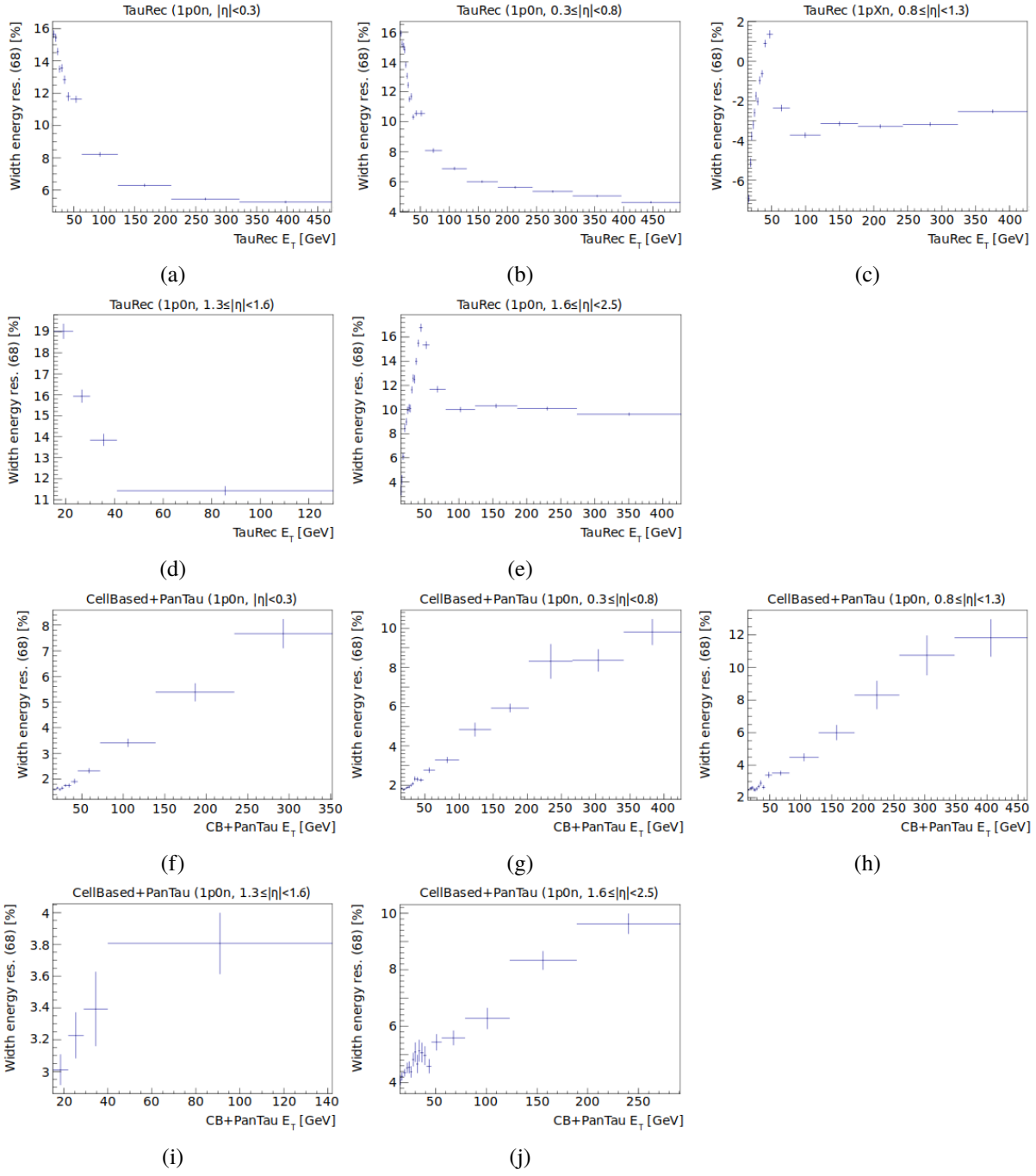

Figure A.8: The (a) - (e) TauRec and (f) - (j) CellBased+PanTau width values extracted from the Gaussian fits to the core region of the energy resolution, binned in the reconstructed transverse energy E_T, for different η bins in the 1p0n decay mode.

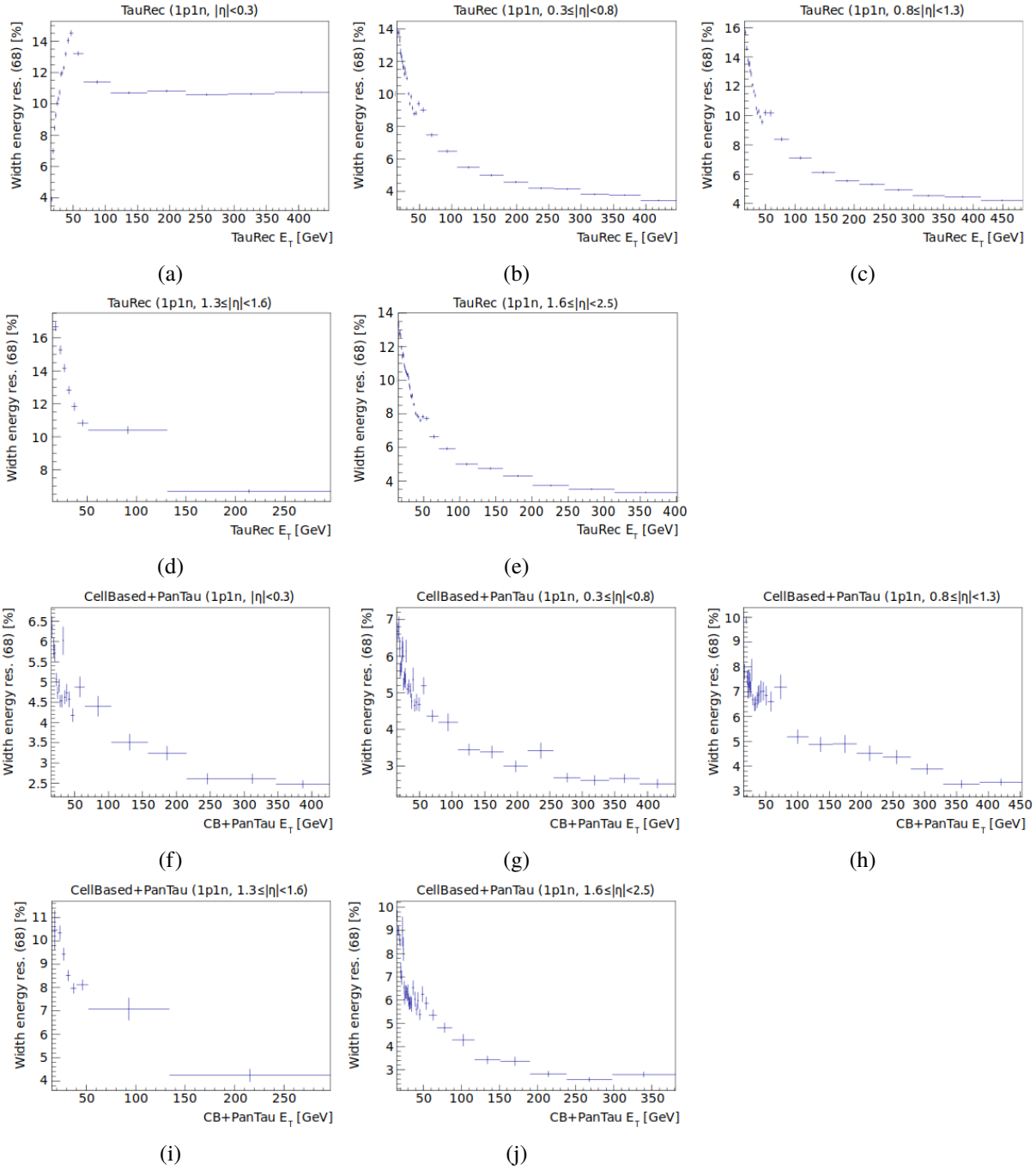

Figure A.9: The (a) - (e) TauRec and (f) - (j) CellBased+PanTau width values extracted from the Gaussian fits to the core region of the energy resolution, binned in the reconstructed transverse energy E_T, for different η bins in the 1p1n decay mode.

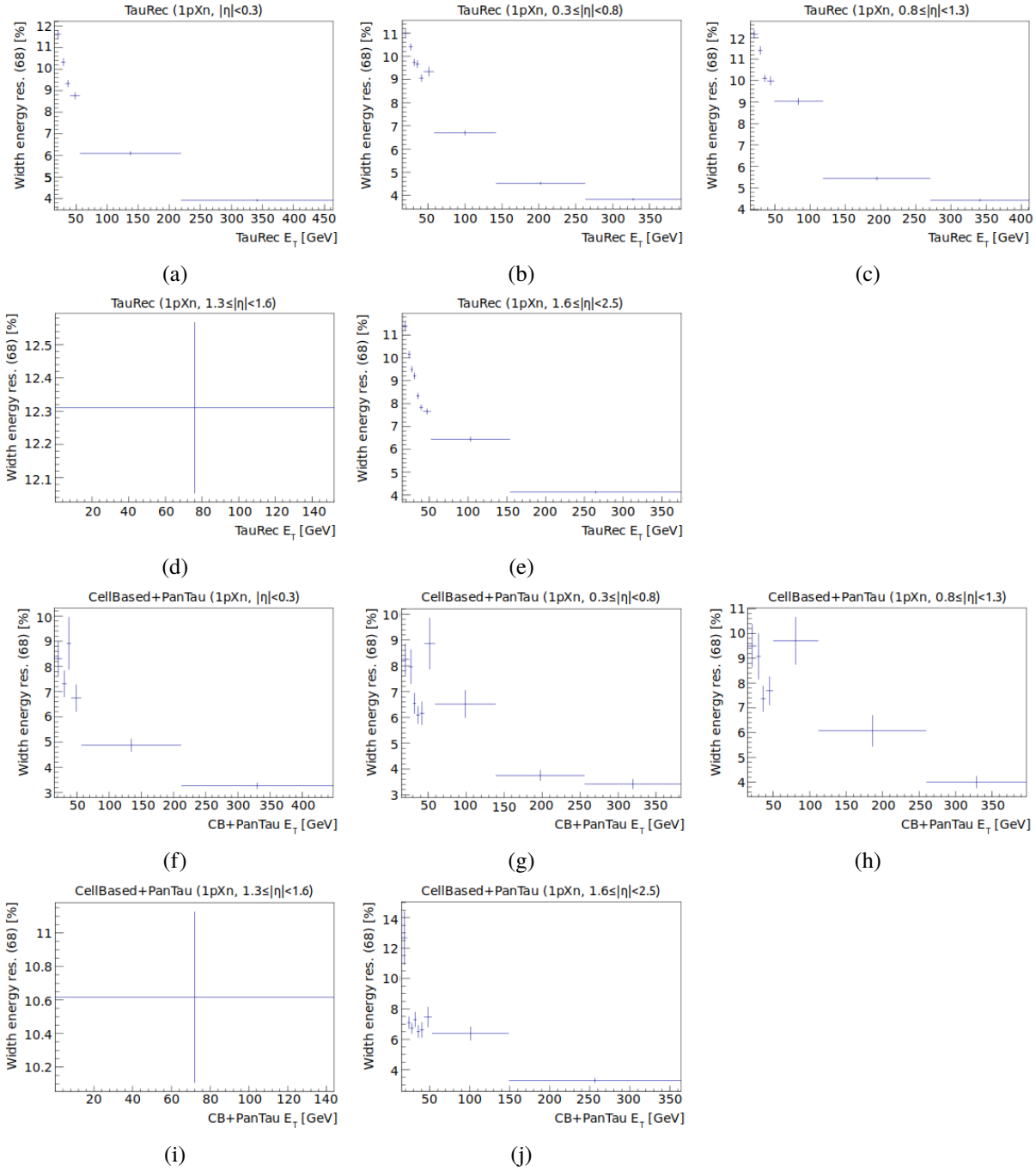

Figure A.10: The (a) - (e) TauRec and (f) - (j) CellBased+PanTau width values extracted from the Gaussian fits to the core region of the energy resolution, binned in the reconstructed transverse energy E_T, for different η bins in the 1pXn decay mode.

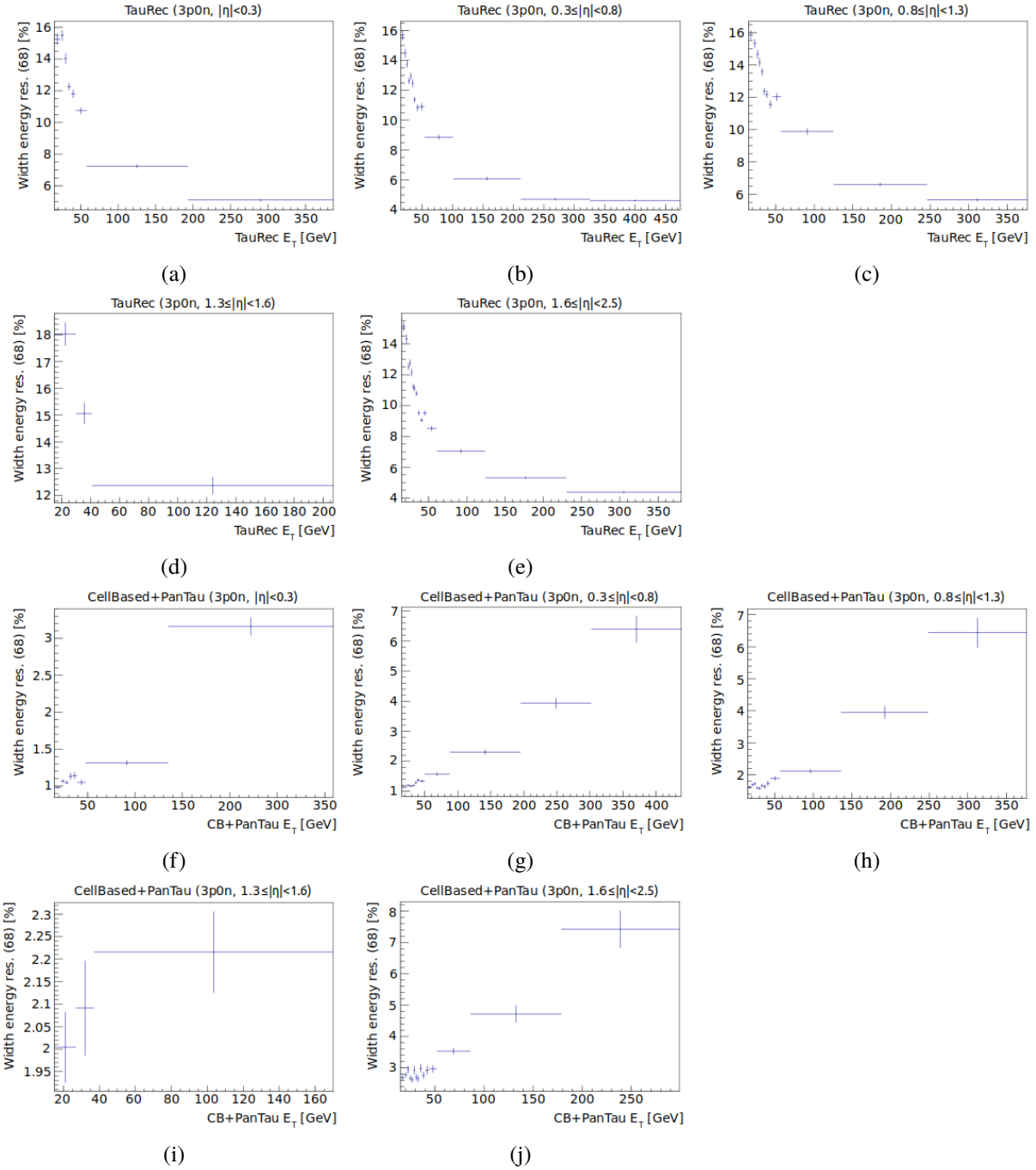

Figure A.11: The (a) - (e) TauRec and (f) - (j) CellBased+PanTau width values extracted from the Gaussian fits to the core region of the energy resolution, binned in the reconstructed transverse energy E_T, for different η bins in the 3p0n decay mode.

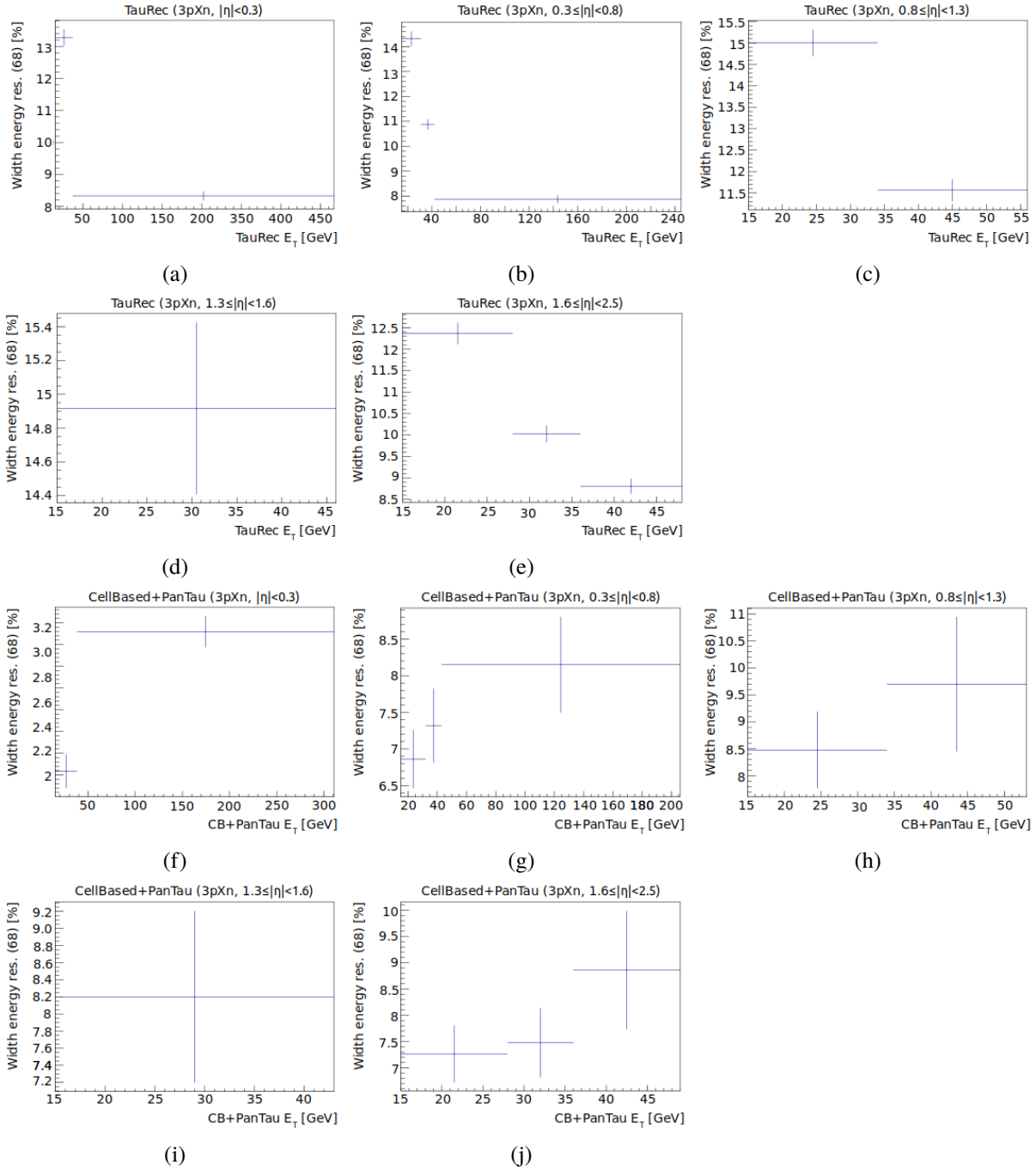

Figure A.12: The (a) - (e) TauRec and (f) - (j) CellBased+PanTau width values extracted from the Gaussian fits to the core region of the energy resolution, binned in the reconstructed transverse energy E_T, for different η bins in the 3pXn decay mode.

A.2 Compatibility Condition

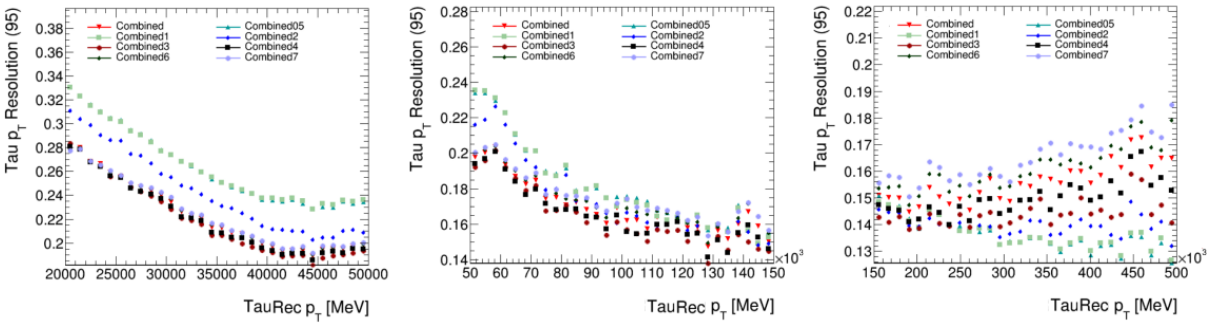

(a) (b) (c)

Figure A.13: The tail resolution (95 % quantiles) of the Combined energy reconstruction for different values of the compatibility constant N as a function of the reconstructed TauRec p_T. Shown are (a) the low-p_T region, (b) the mid-p_T region and (c) the high-p_T region. The value of N is added to the name "Combined" in the legend of each subfigure. The "Combined" method without the additional N value refers to the baseline choice ($N = 5$).

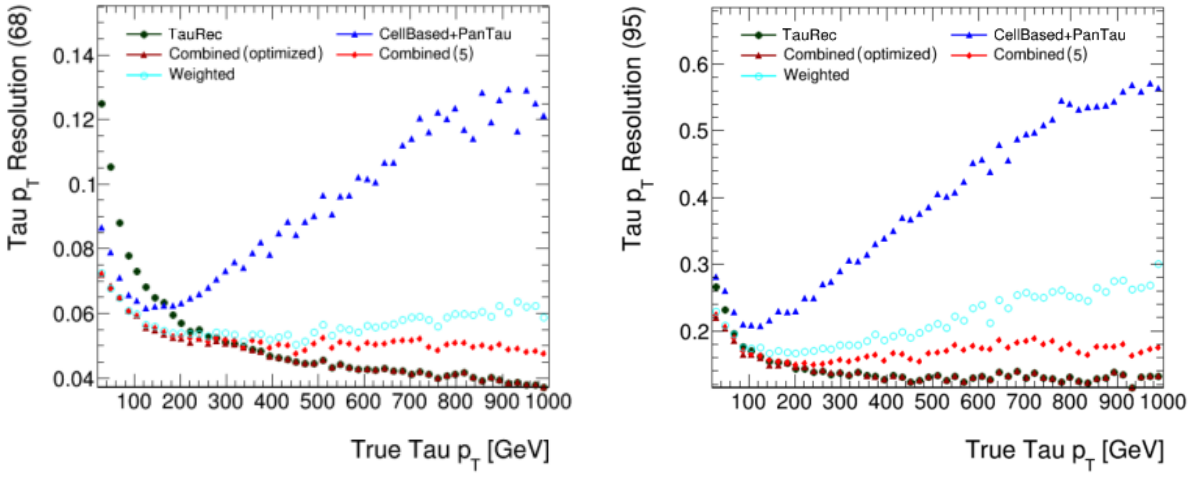

(a) (b)

Figure A.14: The (a) 68 % and (b) 95 % quantiles of the Combined energy resolutions for the baseline compatibility condition ($N = 5$) and the optimized compatibility condition as a function true tau p_T. The TauRec, the CellBased+PanTau and the Weighted resolutions are added for comparison.

A.3 Summary of Energy Resolution Plots

This Section provides additional information about the performance of the Combined and MVA-based energy reconstruction methods depending on the decay mode of hadronic tau leptons. Only the visible part of the tau lepton is considered, i. e. the final state neutrino is neglected. The considered decay modes are 1p0n, 1p1n, 1pXn, 3p0n, and 3pXn as defined in Table 3.1. The performance is separately shown for reconstructed (classified by the PanTau algorithm) and true (generated by the event simulation) tau lepton decays.

A.3.1 1p0n Decays

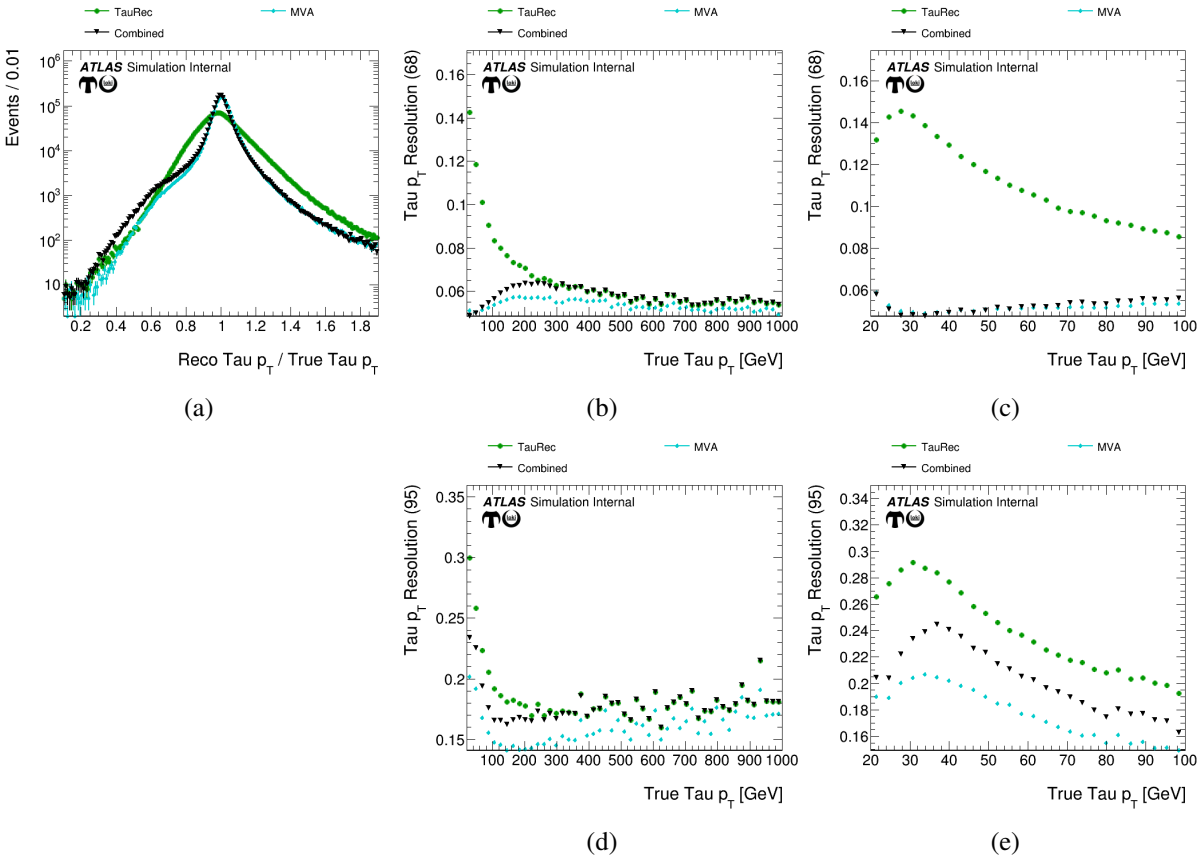

Figure A.15: Transverse momentum p_T resolution for true 1p0n hadronic tau decays obtained with the TauRec, the Combined and the MVA-based energy reconstruction methods. (a) The responses of the reconstructed (Reco) p_T normalized to the simulated (True) p_T. (b) The core resolution as a function of the true p_T for $p_T < 1\,\text{TeV}$ and (c) for $p_T < 100\,\text{GeV}$. (d) and (e) show the corresponding tail resolutions.

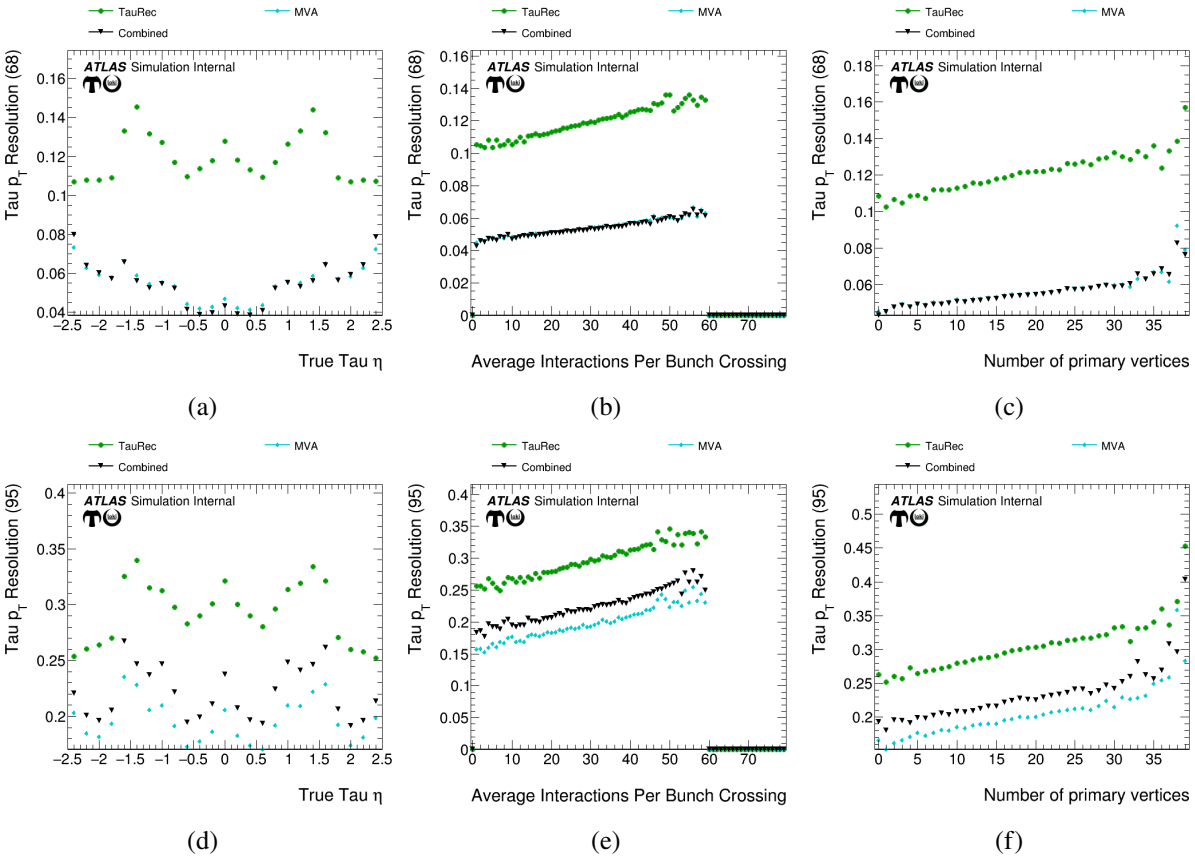

Figure A.16: Transverse momentum p_T resolution for true 1p0n hadronic tau decays obtained with the TauRec, the Combined and the MVA-based energy reconstruction methods. The core resolution vs. (a) the simulated pseudorapidity of the tau lepton η, (b) the average number of interactions per bunch crossing and (c) the number of primary vertices. (d), (e) and (f) show the corresponding tail resolutions.

A.3.2 1p1n Decays

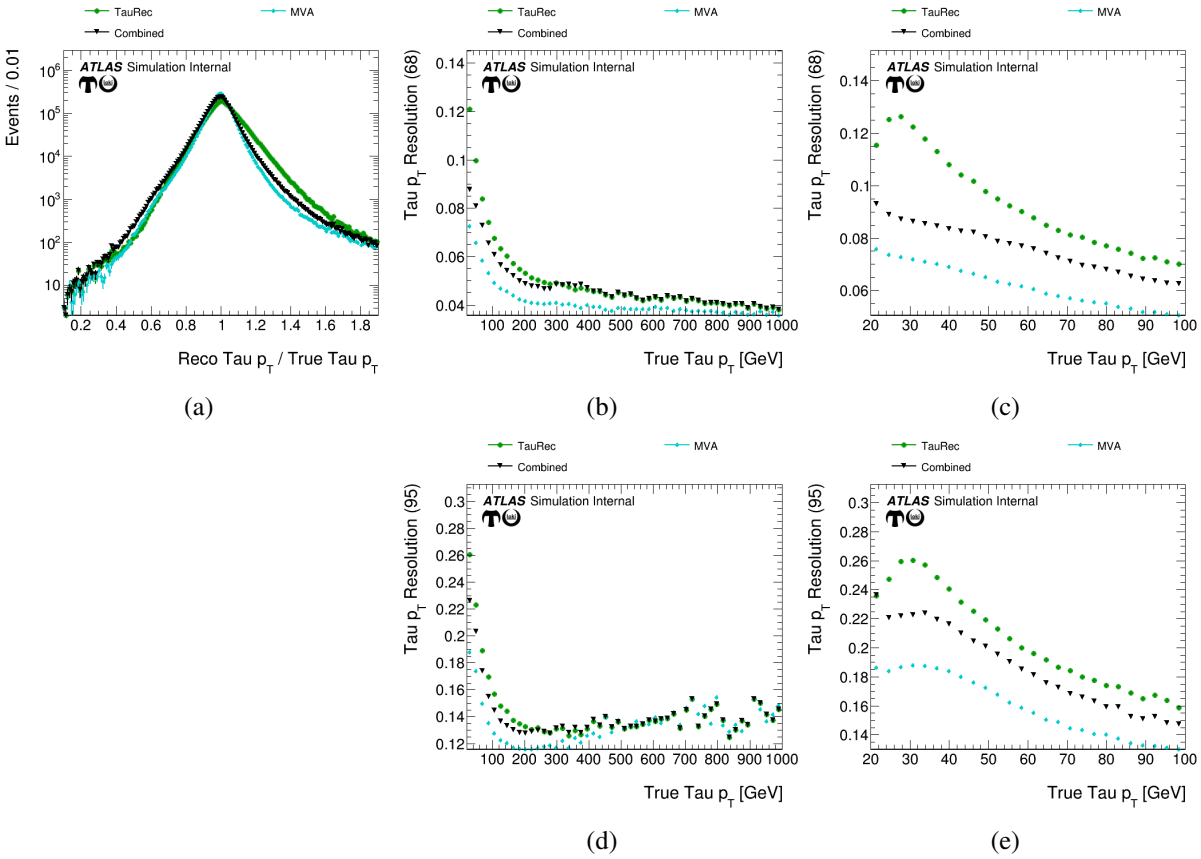

(a) (b) (c) (d) (e)

Figure A.17: Transverse momentum p_T resolution for true 1p1n hadronic tau decays obtained with the TauRec, the Combined and the MVA-based energy reconstruction methods. (a) The responses of the reconstructed (Reco) p_T normalized to the simulated (True) p_T. (b) The core resolution as a function of the true p_T for $p_T < 1$ TeV and (c) for $p_T < 100$ GeV. (d) and (e) show the corresponding tail resolutions.

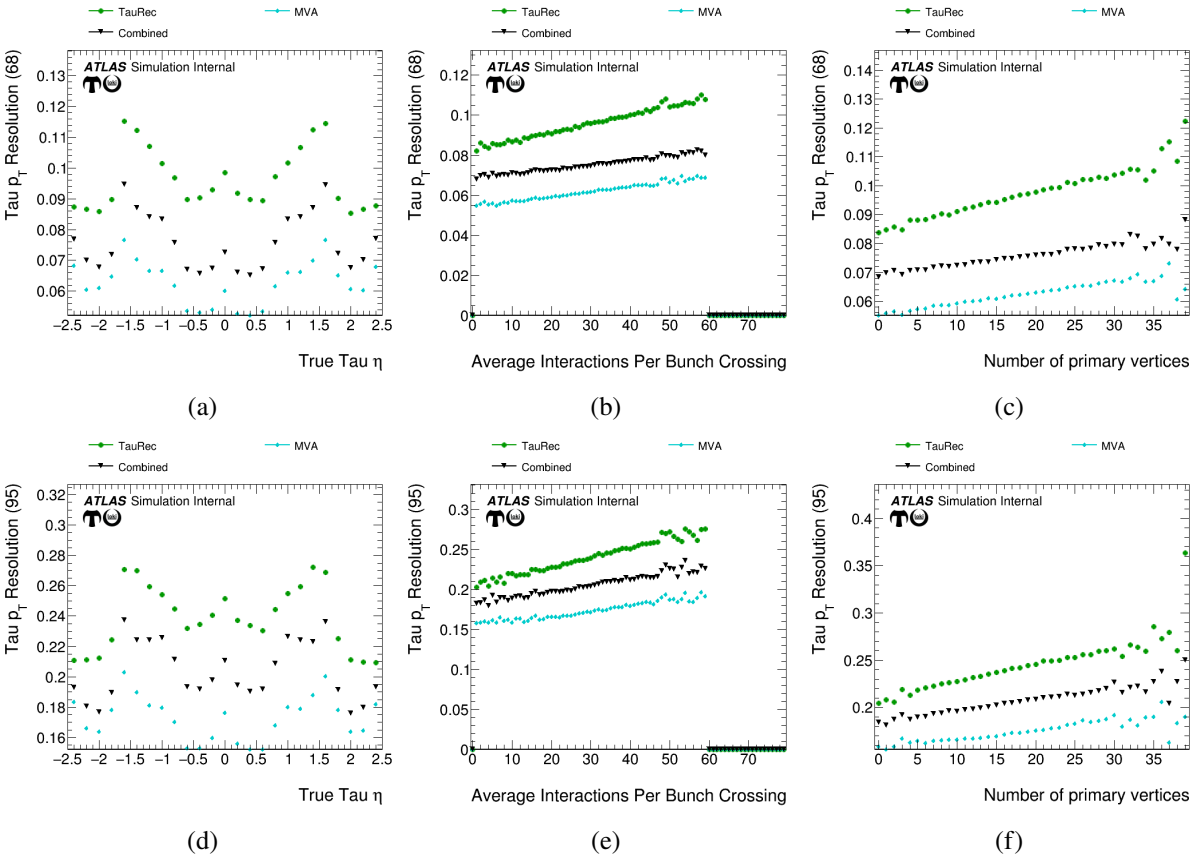

Figure A.18: Transverse momentum p_T resolution for true 1p1n hadronic tau decays obtained with the TauRec, the Combined and the MVA-based energy reconstruction methods. The core resolution vs. (a) the simulated pseudorapidity of the tau lepton η, (b) the average number of interactions per bunch crossing and (c) the number of primary vertices. (d), (e) and (f) show the corresponding tail resolutions.

A.3.3 1pXn Decays

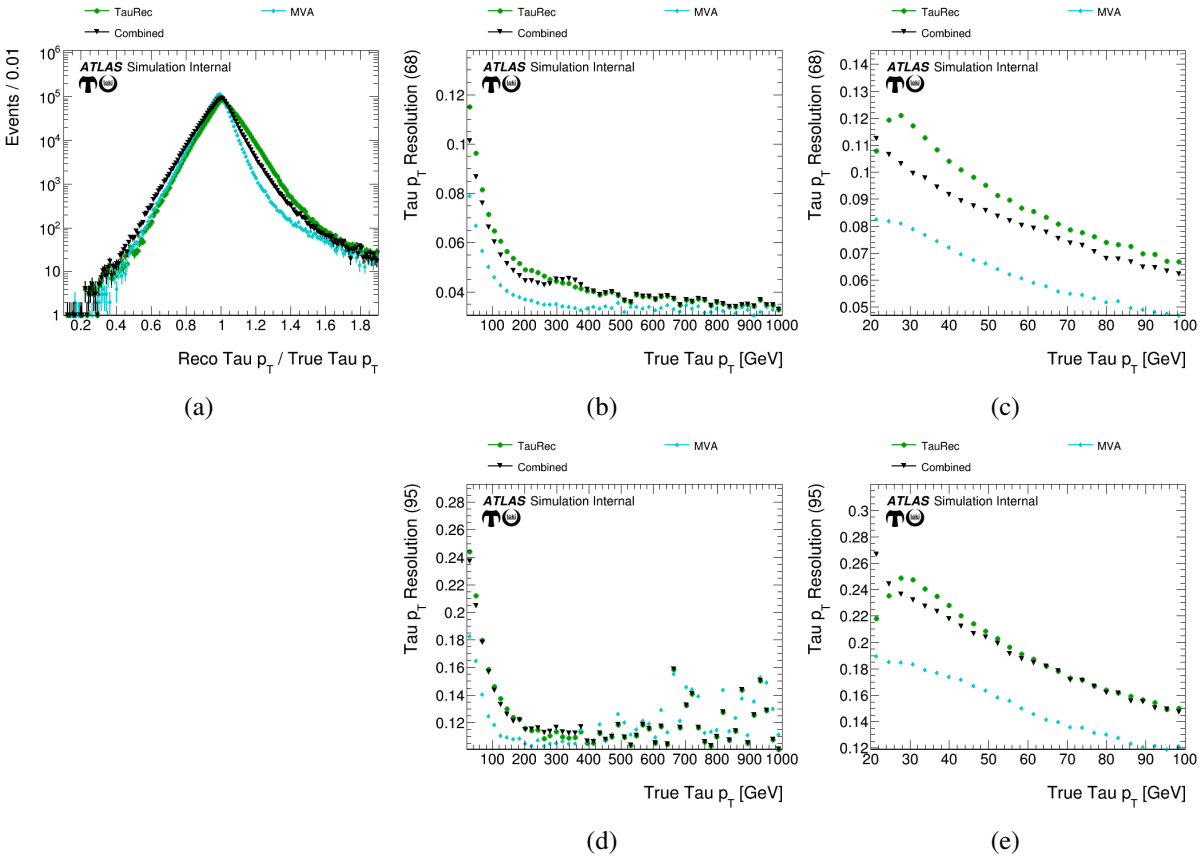

Figure A.19: Transverse momentum p_T resolution for true 1pXn hadronic tau decays obtained with the TauRec, the Combined and the MVA-based energy reconstruction methods. (a) The responses of the reconstructed (Reco) p_T normalized to the simulated (True) p_T. (b) The core resolution as a function of the true p_T for $p_T < 1$ TeV and (c) for $p_T < 100$ GeV. (d) and (e) show the corresponding tail resolutions.

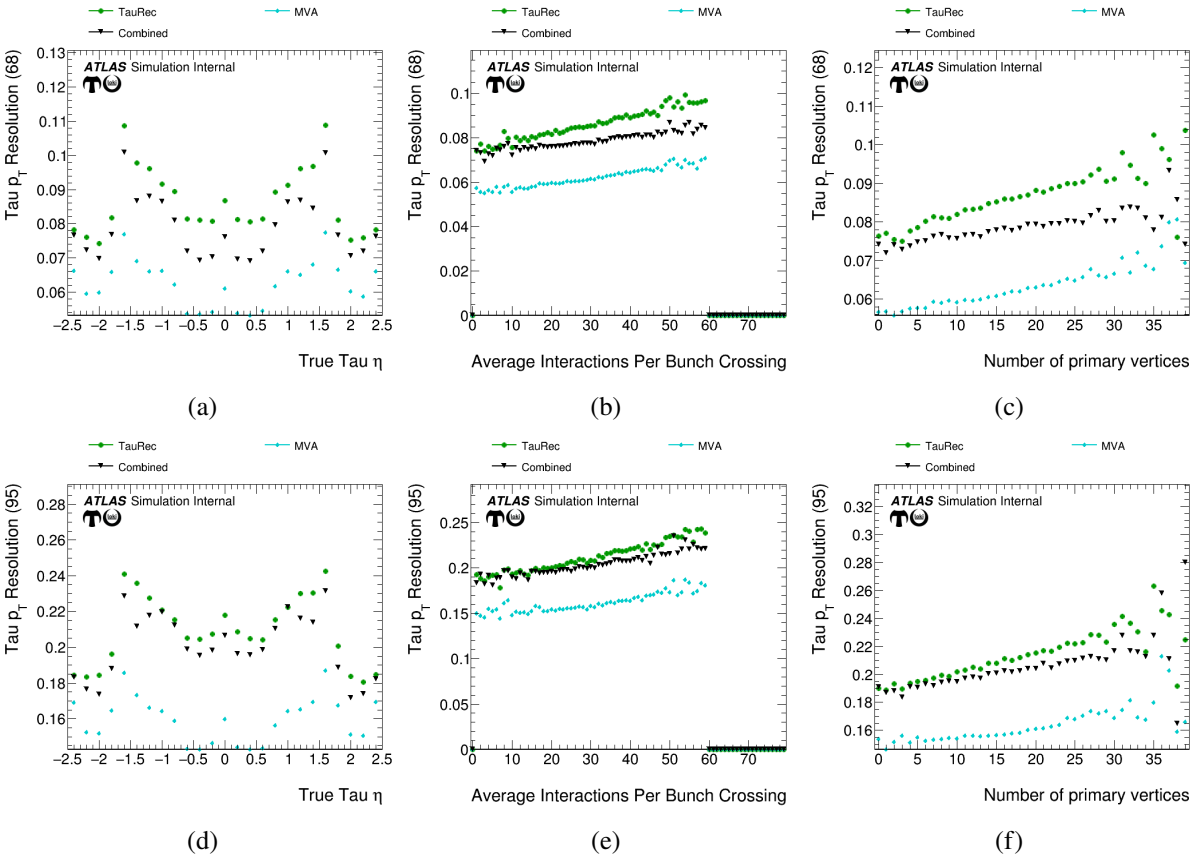

Figure A.20: Transverse momentum p_T resolution for true 1pXn hadronic tau decays obtained with the TauRec, the Combined and the MVA-based energy reconstruction methods. The core resolution vs. (a) the simulated pseudorapidity of the tau lepton η, (b) the average number of interactions per bunch crossing and (c) the number of primary vertices. (d), (e) and (f) show the corresponding tail resolutions.

A.3.4 3p0n Decays

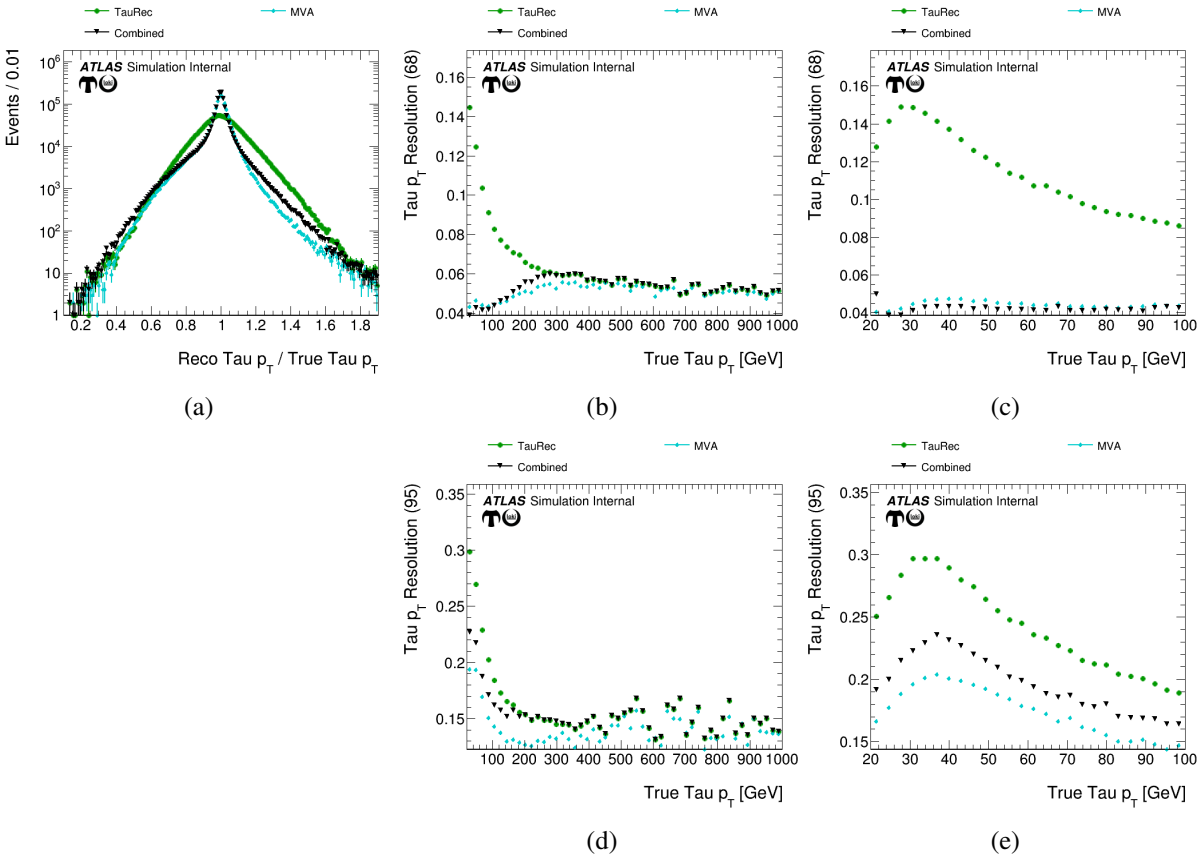

Figure A.21: Transverse momentum p_T resolution for true 3p0n hadronic tau decays obtained with the TauRec, the Combined and the MVA-based energy reconstruction methods. (a) The responses of the reconstructed (Reco) p_T normalized to the simulated (True) p_T. (b) The core resolution as a function of the true p_T for $p_T < 1$ TeV and (c) for $p_T < 100$ GeV. (d) and (e) show the corresponding tail resolutions.

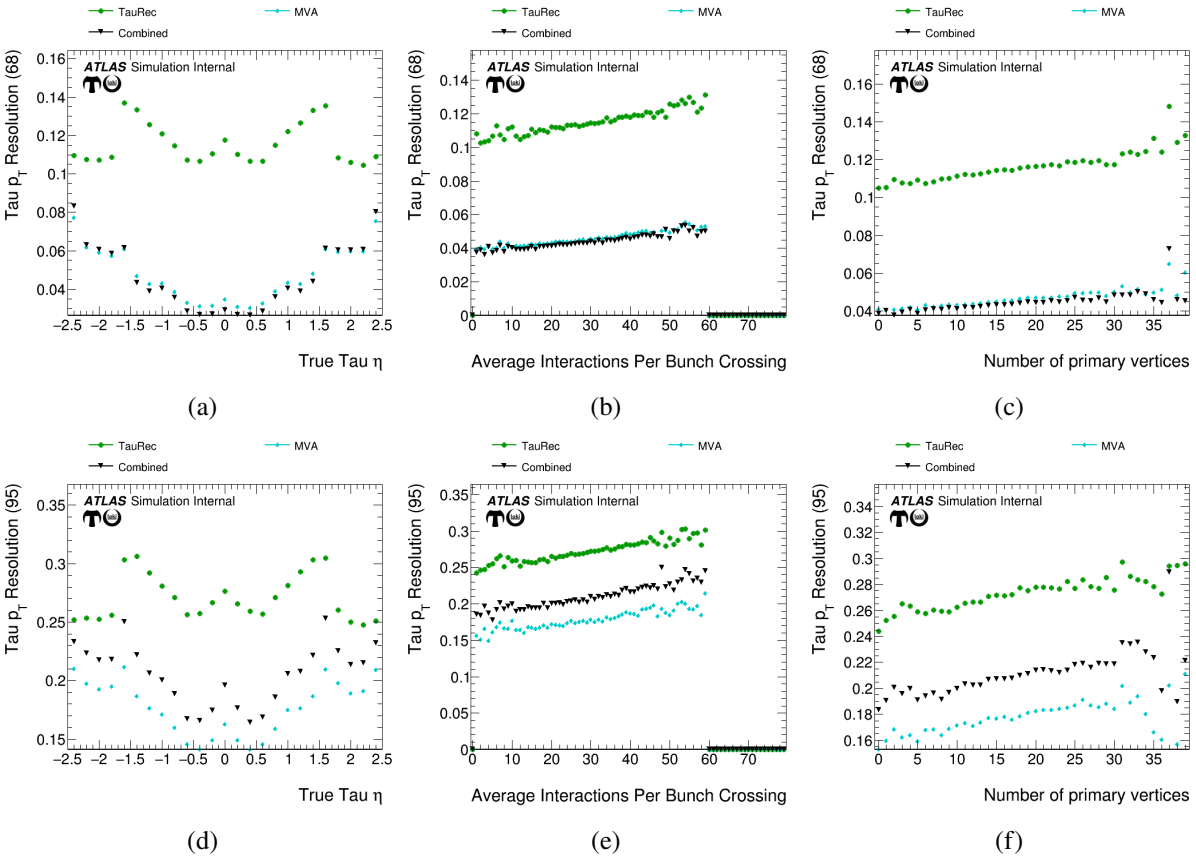

Figure A.22: Transverse momentum p_T resolution for true 3p0n hadronic tau decays obtained with the TauRec, the Combined and the MVA-based energy reconstruction methods. The core resolution vs. (a) the simulated pseudorapidity of the tau lepton η, (b) the average number of interactions per bunch crossing and (c) the number of primary vertices. (d), (e) and (f) show the corresponding tail resolutions.

A.3.5 3pXn Decays

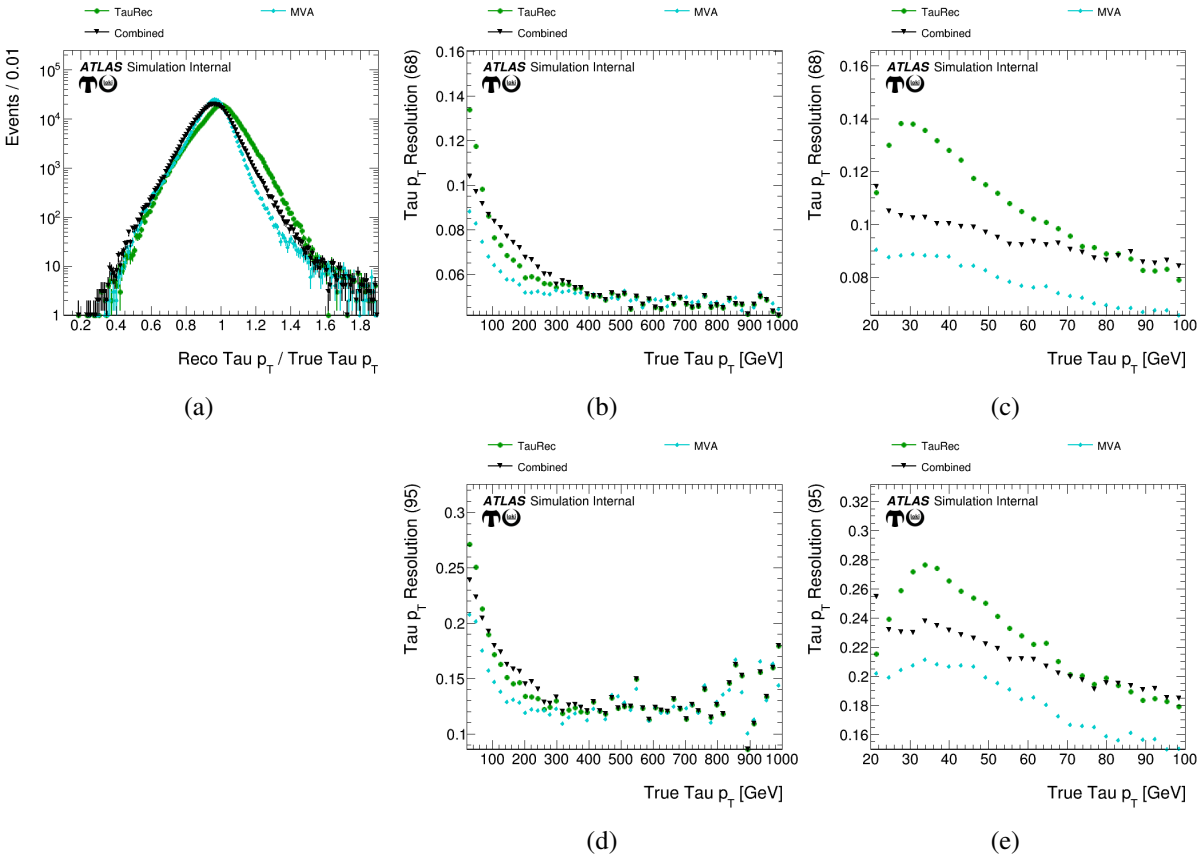

Figure A.23: Transverse momentum p_T resolution for true 3pXn hadronic tau decays obtained with the TauRec, the Combined and the MVA-based energy reconstruction methods. (a) The responses of the reconstructed (Reco) p_T normalized to the simulated (True) p_T. (b) The core resolution as a function of the true p_T for $p_T < 1$ TeV and (c) for $p_T < 100$ GeV. (d) and (e) show the corresponding tail resolutions.

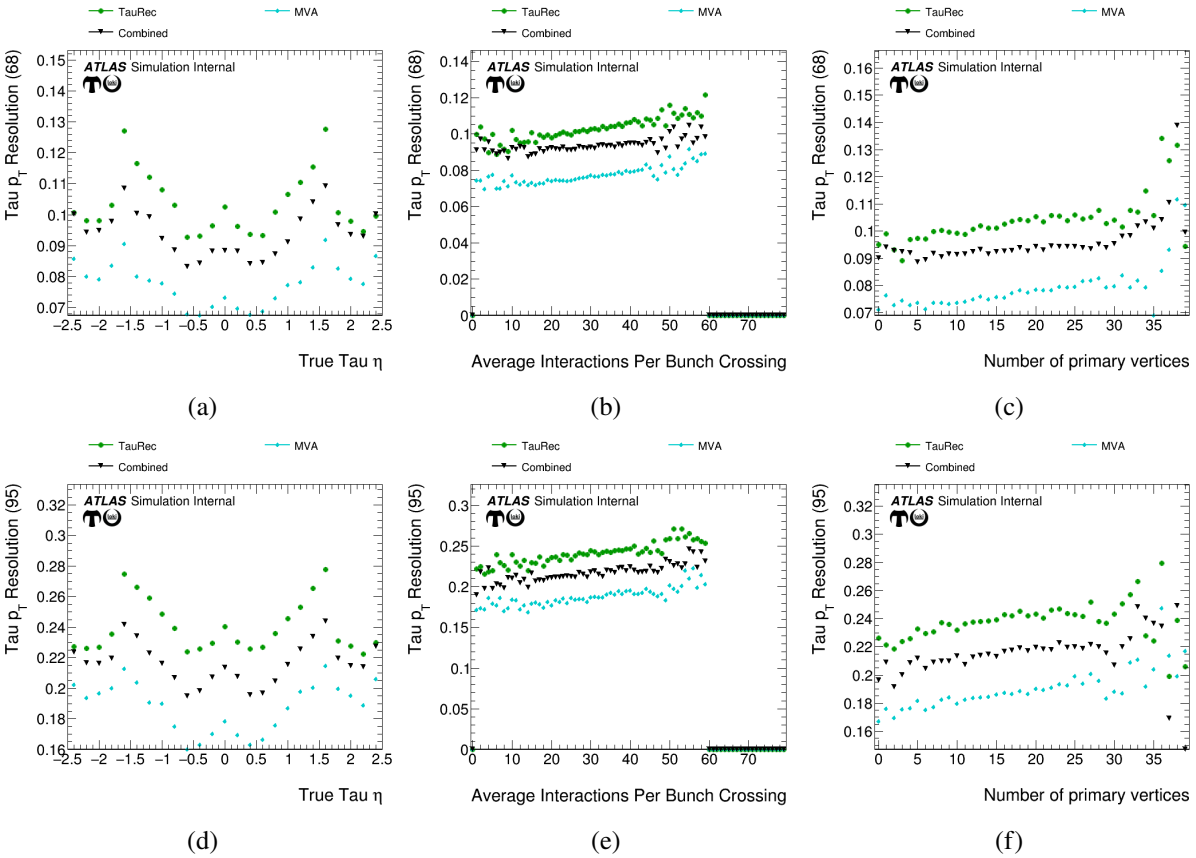

Figure A.24: Transverse momentum p_T resolution for true 3pXn hadronic tau decays obtained with the TauRec, the Combined and the MVA-based energy reconstruction methods. The core resolution vs. (a) the simulated pseudorapidity of the tau lepton η, (b) the average number of interactions per bunch crossing and (c) the number of primary vertices. (d), (e) and (f) show the corresponding tail resolutions.

A.4 Neutral Pion Correction

A.4.1 True==Reco 1p1n decay

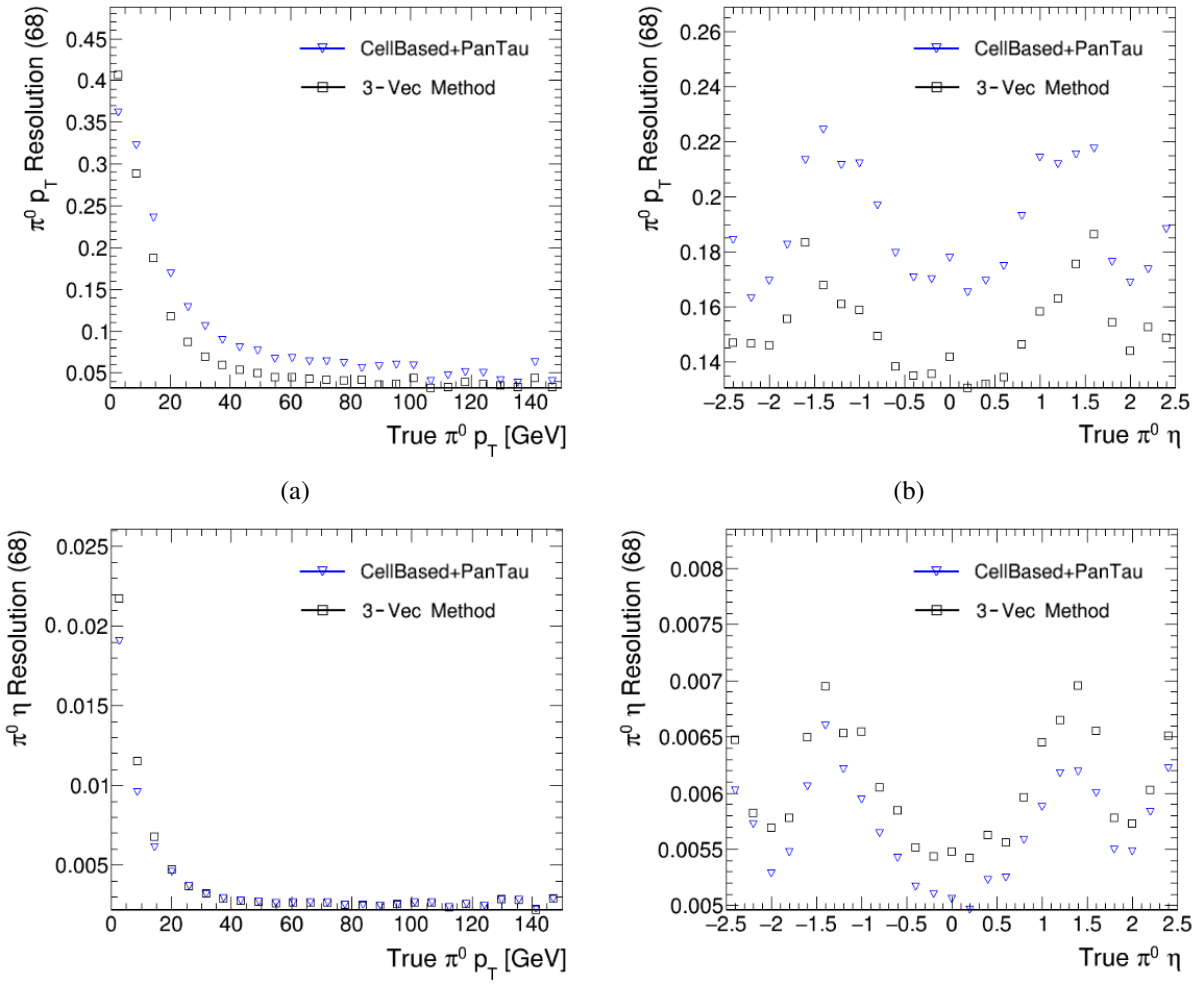

Figure A.25: The neutral pion transverse momentum (upper panels) and pseudorapidity (lower panels) core resolutions for correctly classified 1p1n decays. Compared are the baseline (CellBased+PanTau) and the 3-vector corrected resolutions as a function of (a,c) the generated transverse momentum, and (b,d) the generated pseudorapidity of the neutral pion.

A.4.2 True==Reco 1PXN Decays

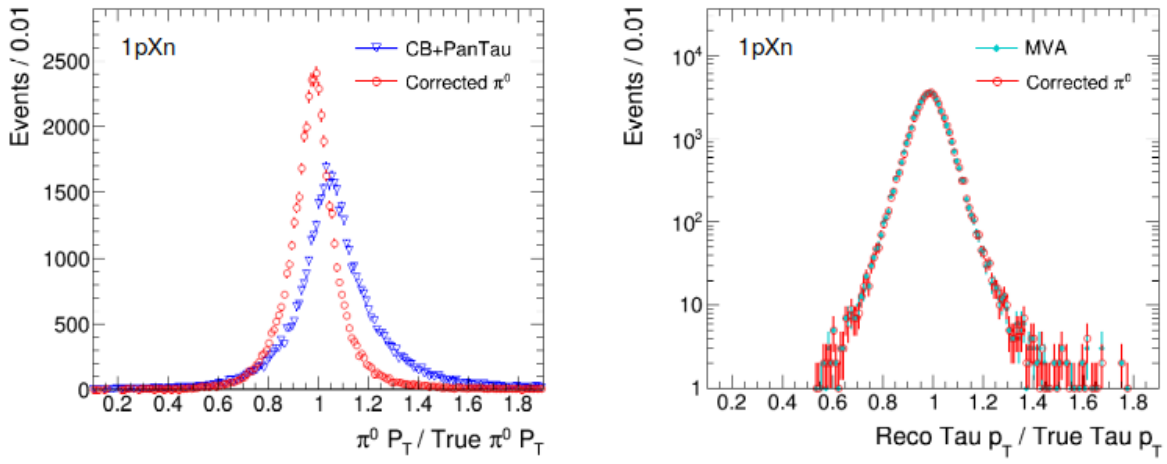

(a) (b)

Figure A.26: The responses of the reconstructed (Reco) transverse momenta of (a) neutral pions and (b) hadronic tau leptons in 1pXn decays obtained from the baseline and the π^0-corrected reconstruction methods normalized to the corresponding simulated (True) transverse momenta for correctly classified (i. e. True == Reco) decays.

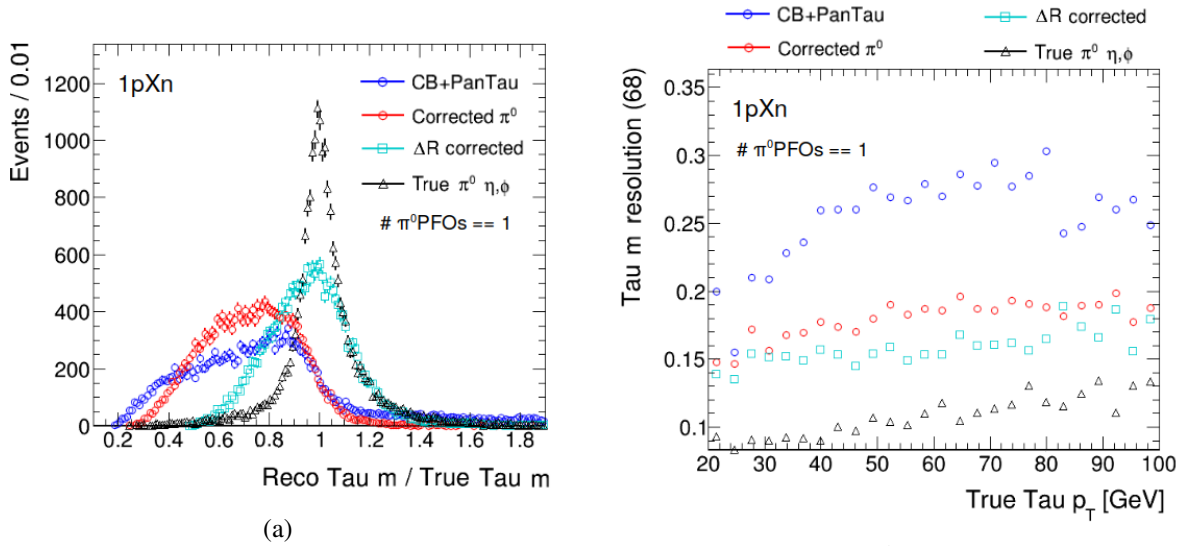

(a) (b)

Figure A.27: (a) The invariant mass response of reconstructed (Reco) $\tau_{\text{had-vis}}$ normalized to the corresponding simulated (True) invariant mass for 1pXn decays with one reconstructed neutral particle flow objects (PFOs) and (b) the corresponding core resolution for transverse tau lepton momenta $p_T < 100\,\text{GeV}$. The results of the CellBased+PanTau, the π^0-corrected and the ΔR-corrected reconstruction methods are compared to the invariant mass response with the simulated π^0 angles. Only correctly classified decays are considered.

A.4.3 True==Reco 3PXN decay

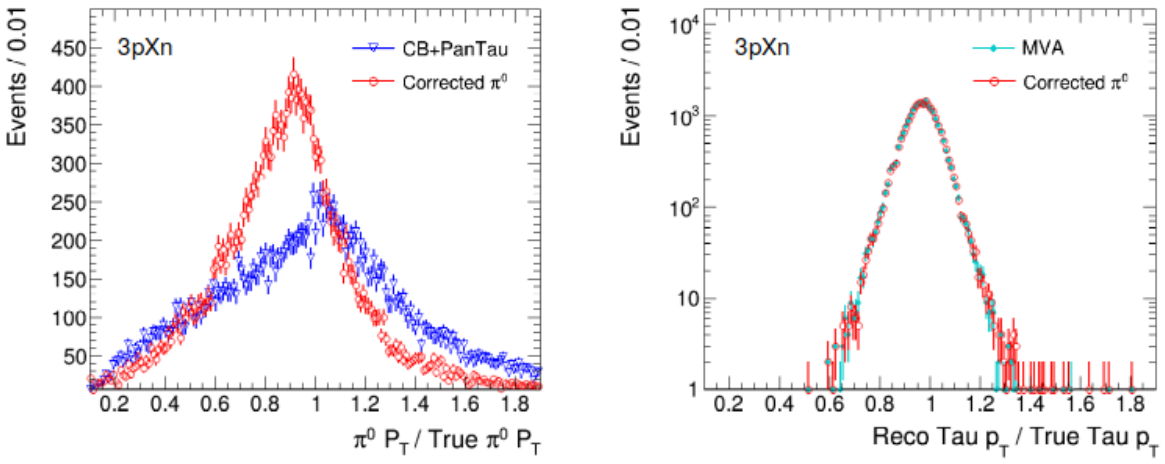

(a) (b)

Figure A.28: The responses of the reconstructed (Reco) transverse momenta of (a) neutral pions and (b) hadronic tau leptons in 3pXn decays obtained from the baseline and the π^0-corrected reconstruction methods normalized to the corresponding simulated (True) transverse momenta for correctly classified (i. e. True == Reco) decays.

APPENDIX B

Experimental Input in HiggsSignals

Tables B.1, B.2, and B.3 list all LHC Run-2 Higgs signal measurements from ATLAS and CMS.

Table B.1: ATLAS Higgs STXS measurements from LHC Run-2 included in the observable set LHC13_Apr2020.

		σ_{obs} [pb]	σ_{SM} [pb]	
$gg \to H, H \to W^+W^-$	36.1	$11.4^{+2.2}_{-2.1}$	10.4 ± 0.6	[470]
VBF, $H \to W^+W^-$	36.1	$0.50^{+0.29}_{-0.28}$	0.81 ± 0.02	[470]
VBF, $H \to ZZ$ ($p_{T,H}$ high)	139.0	$0.0005^{+0.0079}_{-0.0048}$	0.00420 ± 0.00018	[359]
VBF, $H \to ZZ$ ($p_{T,H}$ low)	139.0	$0.15^{+0.064}_{-0.052}$	$0.1076^{+0.0024}_{-0.0035}$	[359]
V(had)$H, H \to ZZ$	139.0	0.021 ± 0.035	$0.0138^{+0.0004}_{-0.0006}$	[359]
V(lep)$H, H \to ZZ$	139.0	$0.022^{+0.028}_{-0.018}$	0.0164 ± 0.0004	[359]
$gg \to H, H \to ZZ$ ($p_{T,H}$ high)	139.0	$0.038^{+0.021}_{-0.016}$	0.015 ± 0.004	[359]
$gg \to H, H \to ZZ$ ($0j$, $p_{T,H}$ high)	139.0	0.630 ± 0.110	0.55 ± 0.04	[359]
$gg \to H, H \to ZZ$ ($0j$, $p_{T,H}$ low)	139.0	0.17 ± 0.055	0.176 ± 0.025	[359]
$gg \to H, H \to ZZ$ ($1j$, $p_{T,H}$ high)	139.0	$0.009^{+0.016}_{-0.012}$	0.020 ± 0.004	[359]
$gg \to H, H \to ZZ$ ($1j$, $p_{T,H}$ low)	139.0	0.05 ± 0.08	0.172 ± 0.025	[359]
$gg \to H, H \to ZZ$ ($1j$, $p_{T,H}$ med.)	139.0	0.17 ± 0.05	0.119 ± 0.018	[359]
$gg \to H, H \to ZZ$ ($2j$)	139.0	0.040 ± 0.075	0.127 ± 0.027	[359]
$t\bar{t}H, H \to ZZ$	139.0	$0.025^{+0.022}_{-0.013}$	$0.0154^{+0.0010}_{-0.0013}$	[359]
$gg \to H, H \to \gamma\gamma$ ($0j$)	139.0	0.039 ± 0.006	$0.0382^{+0.0019}_{-0.0018}$	[471]
$gg \to H, H \to \gamma\gamma$ ($1j$)	139.0	$0.0162^{+0.0031}_{-0.0022}$	$0.0194^{+0.0018}_{-0.0019}$	[471]
$gg \to H, H \to \gamma\gamma$ ($2j$, $\Delta\Phi_{jj} \in [-\pi, -\frac{\pi}{2}]$)	139.0	0.0023 ± 0.0007	0.0024 ± 0.0002	[471]
$gg \to H, H \to \gamma\gamma$ ($2j$, $\Delta\Phi_{jj} \in [-\frac{\pi}{2}, 0]$)	139.0	0.0011 ± 0.0004	0.0020 ± 0.0002	[471]
$gg \to H, H \to \gamma\gamma$ ($2j$, $\Delta\Phi_{jj} \in [0, \frac{\pi}{2}]$)	139.0	0.0014 ± 0.0004	0.0020 ± 0.0002	[471]
$gg \to H, H \to \gamma\gamma$ ($2j$, $\Delta\Phi_{jj} \in [\frac{\pi}{2}, \pi]$)	139.0	0.0021 ± 0.0007	0.0024 ± 0.0002	[471]
$t\bar{t}H, H \to \gamma\gamma$	139.0	$1.59^{+0.43}_{-0.39}$	$1.15^{+0.09}_{-0.12}$	[471]
VBF, $H \to \tau^+\tau^-$	36.1	$0.28^{+0.14}_{-0.13}$	0.237 ± 0.006	[472]
$gg \to H, H \to \tau^+\tau^-$	36.1	$3.10^{+1.90}_{-1.60}$	3.05 ± 0.13	[472]
$WH, H \to W^+W^-$	36.1	$0.67^{+0.36}_{-0.30}$	0.293 ± 0.007	[473]
$ZH, H \to W^+W^-$	36.1	$0.54^{+0.34}_{-0.25}$	0.189 ± 0.007	[473]
$WH, H \to b\bar{b}$ ($p_{T,V} \in [150, 250]$ GeV)	139.0	0.0190 ± 0.0121	0.0240 ± 0.0011	[465]
$WH, H \to b\bar{b}$ ($p_{T,V} \geq 250$ GeV)	139.0	0.0072 ± 0.0022	0.0071 ± 0.0030	[465]
$ZH, H \to b\bar{b}$ ($p_{T,V} \in [75, 150]$ GeV)	139.0	0.0425 ± 0.0359	0.0506 ± 0.0041	[465]
$ZH, H \to b\bar{b}$ ($p_{T,V} \in [150, 250]$ GeV)	139.0	0.0205 ± 0.0062	0.0188 ± 0.0024	[465]
$ZH, H \to b\bar{b}$ ($p_{T,V} \geq 250$ GeV)	139.0	0.0054 ± 0.0017	0.0049 ± 0.0005	[465]

Table B.2: ATLAS Higgs rate measurements from LHC Run-2 included in the observable set LHC13_Apr2020.

Channel	Luminosity [fb^{-1}]	Signal strength μ	Ref.
VBF, $H \to b\bar{b}$	30.6	$3.0^{+1.7}_{-1.8}$	[474]
$t\bar{t}H$, $H \to b\bar{b}$ (1ℓ)	36.1	$0.67^{+0.71}_{-0.69}$	[475]
$t\bar{t}H$, $H \to b\bar{b}$ (2ℓ)	36.1	$0.11^{+1.36}_{-1.41}$	[475]
$t\bar{t}H$, multilepton ($2\ell ss$)	79.9	$0.38^{+0.57}_{-0.54}$	[476]
$t\bar{t}H$, multilepton (3ℓ)	79.9	$0.93^{+0.58}_{-0.52}$	[476]
$t\bar{t}H$, multilepton (4ℓ)	79.9	$0.52^{+0.93}_{-0.72}$	[476]
$t\bar{t}H$, multilepton ($1\ell + 2\tau_h$)	79.9	$0.30^{+1.01}_{-0.90}$	[476]
$t\bar{t}H$, multilepton ($2\ell + 1\tau_h$)	79.9	$0.49^{+0.94}_{-0.82}$	[476]
$t\bar{t}H$, multilepton ($3\ell + 1\tau_h$)	79.9	$0.43^{+1.10}_{-0.85}$	[476]

Table B.3: CMS Higgs rate measurements from LHC Run-2 included in the observable set LHC13_Apr2020.

Channel	Luminosity [fb^{-1}]	Signal strength μ	Ref.
$pp \to H$, $H \to \mu^+\mu^-$	35.9	$1.0^{+1.1}_{-1.1}$	[477]
WH, $H \to b\bar{b}$	35.9	$1.7^{+0.7}_{-0.7}$	[478]
ZH, $H \to b\bar{b}$	35.9	$0.9^{+0.5}_{-0.5}$	[478]
$pp \to H$ (boosted), $H \to b\bar{b}$	35.9	$2.3^{+1.8}_{-1.6}$	[479]
$t\bar{t}H$, $H \to b\bar{b}$ (1ℓ)	35.9 $\oplus$ 41.5	$0.84^{+0.52}_{-0.50} \oplus 1.84^{+0.62}_{-0.56}$	[480, 481]
$t\bar{t}H$, $H \to b\bar{b}$ (2ℓ)	35.9 $\oplus$ 41.5	$-0.24^{+1.21}_{-1.12} \oplus 1.62^{+0.90}_{-0.85}$	[480, 481]
$t\bar{t}H$, $H \to b\bar{b}$ (hadronic)	41.5	$-1.69^{+1.43}_{-1.47}$	[480]
$t\bar{t}H$, multilepton ($1\ell + 2\tau_h$)	35.9 $\oplus$ 41.5	$-1.52^{+1.76}_{-1.72} \oplus 1.4^{+1.24}_{-1.14}$	[482, 483]
$t\bar{t}H$, multilepton ($2\ell ss + 1\tau_h$)	35.9 $\oplus$ 41.5	$0.94^{+0.80}_{-0.67} \oplus 1.13^{+1.03}_{-1.11}$	[482, 483]
$t\bar{t}H$, multilepton ($2\ell ss$)	35.9 $\oplus$ 41.5	$1.61^{+0.58}_{-0.51} \oplus 0.87^{+0.62}_{-0.55}$	[482, 483]
$t\bar{t}H$, multilepton ($3\ell + 1\tau_h$)	35.9 $\oplus$ 41.5	$1.34^{+1.42}_{-1.07} \oplus -0.96^{+1.96}_{-1.33}$	[482, 483]
$t\bar{t}H$, multilepton (3ℓ)	35.9 $\oplus$ 41.5	$0.82^{+0.77}_{-0.71} \oplus 0.29^{+0.82}_{-0.62}$	[482, 483]
$t\bar{t}H$, multilepton (4ℓ)	35.9 $\oplus$ 41.5	$0.57^{+2.29}_{-1.57} \oplus 0.99^{+3.31}_{-1.69}$	[482, 483]
		σ_{obs} [pb]	σ_{SM} [pb]	
$gg \to H$, $H \to W^+W^-$ ($0j$)	137.0	$0.0423^{+0.0063}_{-0.0059}$	$0.0457^{+0.0029}_{-0.0018}$	[484]
$gg \to H$, $H \to W^+W^-$ ($1j$)	137.0	$0.0240^{+0.0057}_{-0.0051}$	$0.0217^{+0.0023}_{-0.0022}$	[484]
$gg \to H$, $H \to W^+W^-$ ($2j$)	137.0	$0.0151^{+0.0051}_{-0.0046}$	$0.0100^{+0.0020}_{-0.0011}$	[484]
$gg \to H$, $H \to W^+W^-$ ($3j$)	137.0	$0.0050^{+0.0045}_{-0.0042}$	$0.0033^{+0.0002}_{-0.0004}$	[484]
$gg \to H$, $H \to W^+W^-$ ($4j$)	137.0	$0.0064^{+0.0039}_{-0.0e034}$	$0.0018^{+0.0001}_{-0.0002}$	[484]
VBF, $H \to ZZ$	137.1	$0.279^{+0.211}_{-0.162}$	0.450 ± 0.010	[485]
$gg/b\bar{b} \to H$, $H \to ZZ$	137.1	5.328 ± 0.611	$5.550^{+0.600}_{-0.650}$	[485]
VH, $H \to ZZ$	137.1	$0.305^{+0.243}_{-0.194}$	0.270 ± 0.010	[485]
$t\bar{t}H, tH$, $H \to ZZ$	137.1	0.0078 ± 0.0552	$0.060^{+0.011}_{-0.012}$	[485]
$gg \to H$, $H \to \gamma\gamma$ ($0j$)	77.4	0.072 ± 0.0122	$0.0610^{+0.0037}_{-0.0031}$	[486]
$gg \to H$, $H \to \gamma\gamma$ ($1j$, $p_{T,H}$ high)	77.4	$0.0029^{+0.0017}_{-0.0012}$	0.0017 ± 0.0002	[486]
$gg \to H$, $H \to \gamma\gamma$ ($1j$, $p_{T,H}$ low)	77.4	$0.021^{+0.0090}_{-0.0075}$	0.015 ± 0.0015	[486]
$gg \to H$, $H \to \gamma\gamma$ ($1j$, $p_{T,H}$ med.)	77.4	0.0076 ± 0.0040	0.010 ± 0.001	[486]
$gg \to H$, $H \to \gamma\gamma$ ($2j$)	77.4	$0.0084^{+0.0066}_{-0.0055}$	0.011 ± 0.002	[486]
$gg \to H$, $H \to \gamma\gamma$ (BSM)	77.4	0.0029 ± 0.00104	0.0013 ± 0.0003	[486]
VBF, $H \to \gamma\gamma$	77.4	$0.0091^{+0.0044}_{-0.0033}$	0.0011 ± 0.002	[486]
$t\bar{t}H$, $H \to \gamma\gamma$	137.0	$0.00156^{+0.00034}_{-0.00032}$	$0.0013^{+0.00008}_{-0.00011}$	[219]
V(had)H, $H \to \tau^+\tau^-$	77.4	$-0.0433^{+0.057}_{-0.054}$	0.037 ± 0.001	[487]
VBF, $H \to \tau^+\tau^-$	77.4	$0.114^{+0.034}_{-0.033}$	0.114 ± 0.009	[487]
$gg \to H$, $H \to \tau^+\tau^-$ ($0j$)	77.4	$-0.680^{+1.292}_{-1.275}$	1.70 ± 0.10	[487]
$gg \to H$, $H \to \tau^+\tau^-$ ($1j$, $p_{T,H}$ high)	77.4	$0.108^{+0.071}_{-0.061}$	0.060 ± 0.010	[487]
$gg \to H$, $H \to \tau^+\tau^-$ ($1j$, $p_{T,H}$ low)	77.4	$-0.139^{+0.562}_{-0.570}$	0.410 ± 0.060	[487]
$gg \to H$, $H \to \tau^+\tau^-$ ($1j$, $p_{T,H}$ med.)	77.4	$0.353^{+0.437}_{-0.420}$	0.280 ± 0.040	[487]
$gg \to H$, $H \to \tau^+\tau^-$ ($2j$)	77.4	$0.0987^{+0.1911}_{-0.1806}$	0.210 ± 0.050	[487]
$gg \to H$, $H \to \tau^+\tau^-$ ($1j$, $p_T^{j_1} > 200\,\text{GeV}$)	77.4	$0.0199^{+0.0145}_{-0.0148}$	0.0141 ± 0.0004	[487]
$gg \to H$, $H \to \tau^+\tau^-$ (Rest)	77.4	$-0.195^{+0.506}_{-0.491}$	0.184 ± 0.005	[487]

APPENDIX C

Higgs Boson Cross-section Measurement in the $H \to ZZ^* \to 4\ell$ Decay Channel at ATLAS

C.1 Event Selection

Table C.1: Summary of the event selection requirements. The two lepton pairs in the quadruplets are denoted as m_{12} and m_{34}.

Reconstruction of the final state particles		
Data quality:	All components of the detector have be operating correctly	
	At least one collision vertex with at least two jets, where $p_T^j > 500\,\text{MeV}$	
Trigger system	Combination of single-lepton, dilepton and trilepton triggers	
Selection of the final state particles		
Electrons:	*Loose* likelihood identification criteria, $E_T > 7\,\text{GeV}$, $\lvert\eta\rvert < 2.47$	
	Interaction point constraint: $\lvert z_0 \cdot \sin\theta\rvert < 0.5\,\text{mm}$ (if ID track is available)	
Muons	*Loose* likelihood identification criteria, $p_T > 5\,\text{GeV}$, $\lvert\eta\rvert < 2.7$	
	If calorimeter tagged:	$p_T > 15\,\text{GeV}$, $\lvert\eta\rvert < 0.1$
	If segmented tagged:	$\lvert\eta\rvert < 0.1$, $p_T > 5\,\text{GeV}$
	If stand-alone:	$2.5 < \lvert\eta\rvert < 2.7$, $p_T > 5\,\text{GeV}$
Jets	Anti-k_T jets ($R = 0.4$), $p_T > 30\,\text{GeV}$ and $\lvert\eta\rvert < 4.5$	
	Jets with $p_T < 60\,\text{GeV}$ and $\lvert\eta\rvert < 2.4$ are required to pass the pile-up jet rejection at the 92 % working point (JVT score > 0.59).	
	Jets with $p_T < 50\,\text{GeV}$ and $\lvert\eta\rvert > 2.5$ are required to pass the forward pile-up jet rejection at the 90 % working point	
	If b-tagged:	`MV2_c10` algorithm
Overlap removal	Jets within $\Delta R < 0.2$ ($\Delta R < 0.1$) of an electron (a muon) are removed	
Lepton Quadruplets		
Quadruplet:	All combinations of two same-flavor and opposite-charge lepton pairs	
Leptons:	p_T thresholds for three leading leptons: 20, 15 and 10 GeV	
	At most one calorimeter-tagged or stand-alone muon	
	Contribution from the other leptons of the quadruplet is subtracted	
Lepton pairs:	Leading di-lepton pair: $50 < m_{12} < 106\,\text{GeV}$	
	Sub-leading di-lepton pair: $m_{\text{threshold}} < m_{34} < 115\,\text{GeV}$	
	$\Delta R(\ell, \ell') > 0.10$ for all leptons in the quadruplet	
	Remove quadruplet if alternative same-flavour opposite-charge	
	$m_{\ell\ell} > 5\,\text{GeV}$	
	Keep all quadruplets passing the above selection	
Lepton isolation:	All leptons: $I_{\text{track}} + 0.4 \cdot I_{\text{calo}} < 0.16$	
Impact parameter	For electrons:	$d_0/\sigma_{d_0} < 5$
Significance:	For muons:	$d_0/\sigma_{d_0} < 3$
Common vertex:	$\chi^2/\text{ndof} < 5$ for 4μ and < 9 for others decay channels	
Higgs boson candidate		
Best quadruplet:	Select quadruplet with m_{12} closest to m_Z from one decay final state	
	Order priority: 4μ, $2e2\mu$, $2\mu2e$ and $4e$	
	If at least one additional lepton with $p_T > 12\,\text{GeV}$ select	
	the quadruplet with the highest matrix-element value	
Higgs mass window:	Correct for final state radiation	
	Four lepton invariant mass:	Signal region $115 < m_{4\ell} < 130\,\text{GeV}$
		Sideband region $130 < m_{4\ell} < 160\,\text{GeV}$

C.2 Performance Studies for PFlow Jets

Table C.2: Comparison of Asimov results for the variables $N_{\text{b-jets}}$, $p_T^{\text{lead. jet}}$, $p_T^{\text{sub. lead. jet}}$, m_{jj}, $\Delta\eta_{jj}$ and $\Delta\phi_{jj}$ using response matrix unfolding for MC datasets using EMTopo and PFlow jets. Only statistical errors are considered.

POI	σ_{inj} [fb]	EMTopo		PFlow	
		σ_{fit} [fb]	Rel. Error	σ_{fit} [fb]	Rel. Error
		$N_{\text{b-jets}}$			
$\sigma(N_{\text{b-jets}} = 0)$	3.3	$3.3^{+0.302}_{-0.291}$	$^{+9.16\%}_{-8.81\%}$	$3.3^{+0.303}_{-0.291}$	$^{+9.17\%}_{-8.83\%}$
$\sigma(N_{\text{b-jets}} \geq 1)$	0.113	$0.113^{+0.107}_{-0.0845}$	$^{+94.6\%}_{-75.0\%}$	$0.113^{+0.107}_{-0.086}$	$^{+95.4\%}_{-76.4\%}$
		$p_T^{\text{lead. jet}}$			
$\sigma(N_{\text{jets}} = 0)$	1.86	$1.86^{+0.27}_{-0.257}$	$^{+14.6\%}_{-13.9\%}$	$1.86^{+0.27}_{-0.257}$	$^{+14.6\%}_{-13.8\%}$
$\sigma(30\,\text{GeV} \leq p_T^{\text{lead. jet}} < 60\,\text{GeV})$	0.792	$0.792^{+0.213}_{-0.199}$	$^{+26.8\%}_{-25.1\%}$	$0.792^{+0.212}_{-0.198}$	$^{+26.8\%}_{-25.0\%}$
$\sigma(60\,\text{GeV} \leq p_T^{\text{lead. jet}} < 120\,\text{GeV})$	0.532	$0.532^{+0.139}_{-0.126}$	$^{+26.1\%}_{-23.7\%}$	$0.532^{+0.140}_{-0.127}$	$^{+26.3\%}_{-23.9\%}$
$\sigma(120\,\text{GeV} \leq p_T^{\text{lead. jet}} < 350\,\text{GeV})$	0.223	$0.223^{+0.078}_{-0.0671}$	$^{+35.0\%}_{-30.1\%}$	$0.223^{+0.0784}_{-0.0674}$	$^{+35.2\%}_{-30.3\%}$
		$p_T^{\text{sub. lead. jet}}$			
$\sigma(N_{\text{jets}} < 2)$	2.81	$2.81^{+0.298}_{-0.287}$	$^{+10.6\%}_{-10.2\%}$	$2.81^{+0.299}_{-0.287}$	$^{+10.6\%}_{-10.2\%}$
$\sigma(30\,\text{GeV} \leq p_T^{\text{sub. lead. jet}} < 60\,\text{GeV})$	0.416	$0.416^{+0.151}_{-0.137}$	$^{+36.4\%}_{-32.9\%}$	$0.416^{+0.151}_{-0.137}$	$^{+36.2\%}_{-32.9\%}$
$\sigma(60\,\text{GeV} \leq p_T^{\text{sub. lead. jet}} < 120\,\text{GeV})$	0.156	$0.156^{+0.0802}_{-0.0671}$	$^{+51.4\%}_{-43.0\%}$	$0.156^{+0.0805}_{-0.0676}$	$^{+51.6\%}_{-43.3\%}$
$\sigma(120\,\text{GeV} \leq p_T^{\text{sub. lead. jet}} < 350\,\text{GeV})$	0.0313	$0.0313^{+0.040}_{-0.0257}$	$^{+128.0\%}_{-82.1\%}$	$0.0313^{+0.0401}_{-0.0258}$	$^{+128.0\%}_{-82.6\%}$
		m_{jj}			
$\sigma(N_{\text{jets}} < 2)$	2.81	$2.81^{+0.295}_{-0.285}$	$^{+10.5\%}_{-10.1\%}$	$2.81^{+0.296}_{-0.285}$	$^{+10.5\%}_{-10.2\%}$
$\sigma(\leq m_{jj} < 120\,\text{GeV})$	0.196	$0.196^{+0.116}_{-0.1}$	$^{+59.2\%}_{-43.1\%}$	$0.196^{+0.114}_{-0.0986}$	$^{+58.0\%}_{-50.4\%}$
$\sigma(120\,\text{GeV} \leq m_{jj} < 450\,\text{GeV})$	0.269	$0.269^{+0.116}_{-0.101}$	$^{+43.1\%}_{-37.0\%}$	$0.269^{+0.116}_{-0.101}$	$^{+43.0\%}_{-37.7\%}$
$\sigma(120\,\text{GeV} \leq m_{jj} < 350\,\text{GeV})$	0.138	$0.138^{+0.0673}_{-0.0553}$	$^{+48.9\%}_{-40.2\%}$	$0.138^{+0.0686}_{-0.0569}$	$^{+49.9\%}_{-41.4\%}$
		$\Delta\eta_{jj}$			
$\sigma(N_{\text{jets}} < 2)$	2.81	$2.81^{+0.295}_{-0.284}$	$^{+10.5\%}_{-10.1\%}$	$2.81^{+0.296}_{-0.285}$	$^{+10.5\%}_{-10.1\%}$
$\sigma(\Delta\eta_{jj} < 1.0)$	0.199	$0.199^{+0.102}_{-0.0881}$	$^{+51.6\%}_{-44.4\%}$	$0.199^{+0.101}_{-0.0874}$	$^{+51.0\%}_{-44.0\%}$
$\sigma(1.0 \leq \Delta\eta_{jj} < 2.5)$	0.176	$0.176^{+0.0972}_{-0.0822}$	$^{+55.1\%}_{-46.6\%}$	$0.176^{+0.0957}_{-0.0812}$	$^{+54.3\%}_{-46.1\%}$
$\sigma(2.5 \leq \Delta\eta_{jj} < 9.0)$	0.229	$0.229^{+0.0916}_{-0.0791}$	$^{+39.9\%}_{-34.5\%}$	$0.229^{+0.0928}_{-0.0807}$	$^{+40.4\%}_{-35.2\%}$
		$\Delta\phi_{jj}$			
$\sigma(N_{\text{jets}} < 2)$	2.81	$2.81^{+0.294}_{-0.284}$	$^{+10.5\%}_{-10.1\%}$	$2.81^{+0.295}_{-0.284}$	$^{+10.5\%}_{-10.1\%}$
$\sigma(\Delta\phi_{jj} < 1/2\pi)$	0.140	$0.140^{+0.0795}_{-0.0661}$	$^{+56.6\%}_{-47.1\%}$	$0.140^{+0.0784}_{-0.0656}$	$^{+55.9\%}_{-46.7\%}$
$\sigma(1/2\pi \leq \Delta\phi_{jj} < \pi)$	0.162	$0.162^{+0.0965}_{-0.0813}$	$^{+59.7\%}_{-50.3\%}$	$0.162^{+0.0955}_{-0.0808}$	$^{+59.1\%}_{-50.0\%}$
$\sigma(\pi \leq \Delta\phi_{jj} < 3/2\pi)$	0.161	$0.161^{+0.095}_{-0.0797}$	$^{+58.8\%}_{-49.4\%}$	$0.161^{+0.0946}_{-0.0798}$	$^{+58.6\%}_{-49.5\%}$
$\sigma(3/2\pi \leq \Delta\phi_{jj} < 2\pi)$	0.141	$0.141^{+0.0758}_{-0.0626}$	$^{+53.7\%}_{-44.4\%}$	$0.141^{+0.0748}_{-0.0622}$	$^{+53.1\%}_{-44.1\%}$

C.2.1 Checks on the Reduced Jet Phase Space

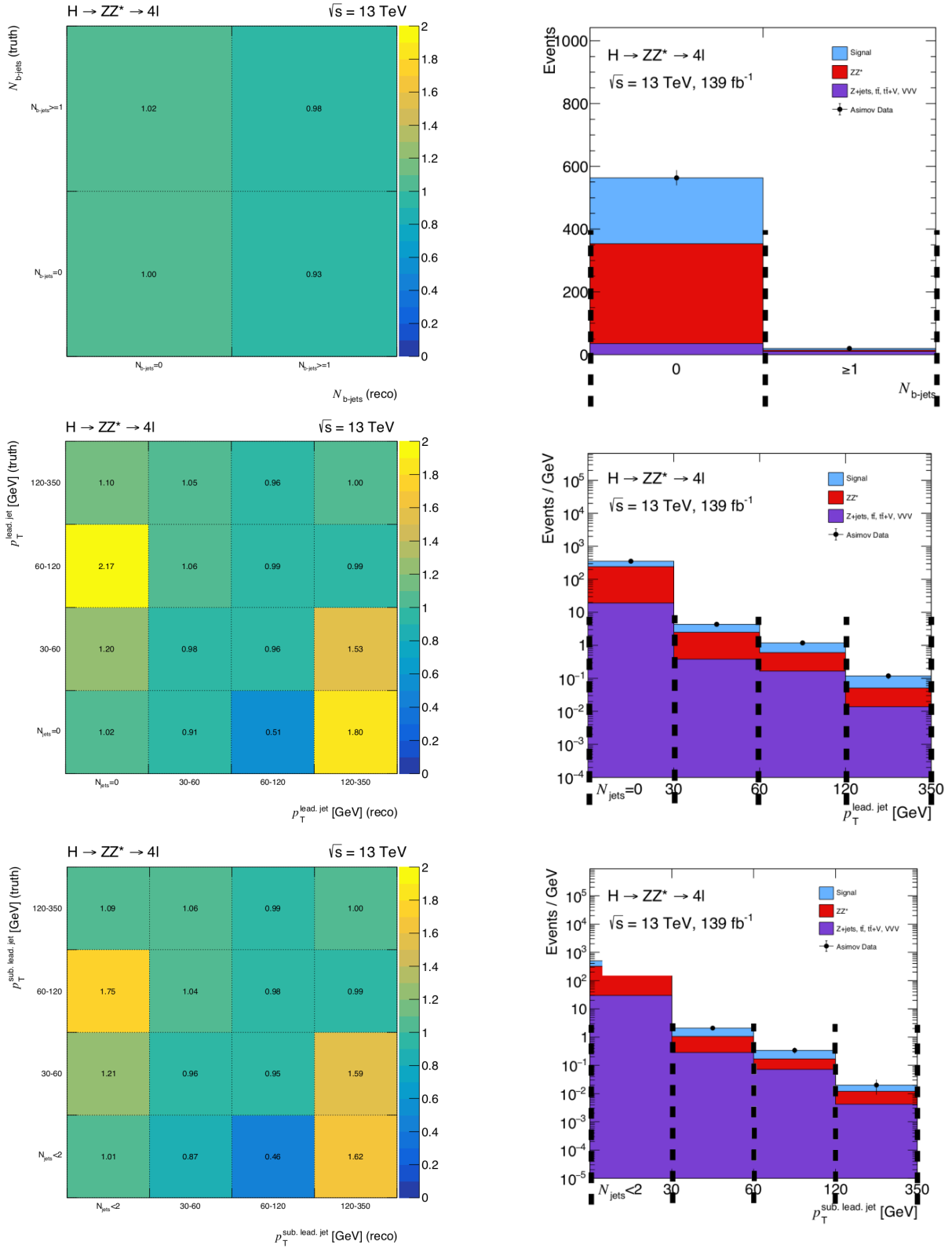

Figure C.1: The (top-left panel) $N_{\text{b-jets}}$, (middle-left panel) $p_T^{\text{lead. jet}}$ and (bottom-left panel) $p_T^{\text{sub. lead. jet}}$ ratio of response matrices for EMTopo jets derived using simulated datasets divided by the corresponding matrices for PFlow jets. The corresponding Asimov results the different distributions for the PFlow dataset are shown in the right panels. The corresponding results for the EMTopo dataset is not shown.

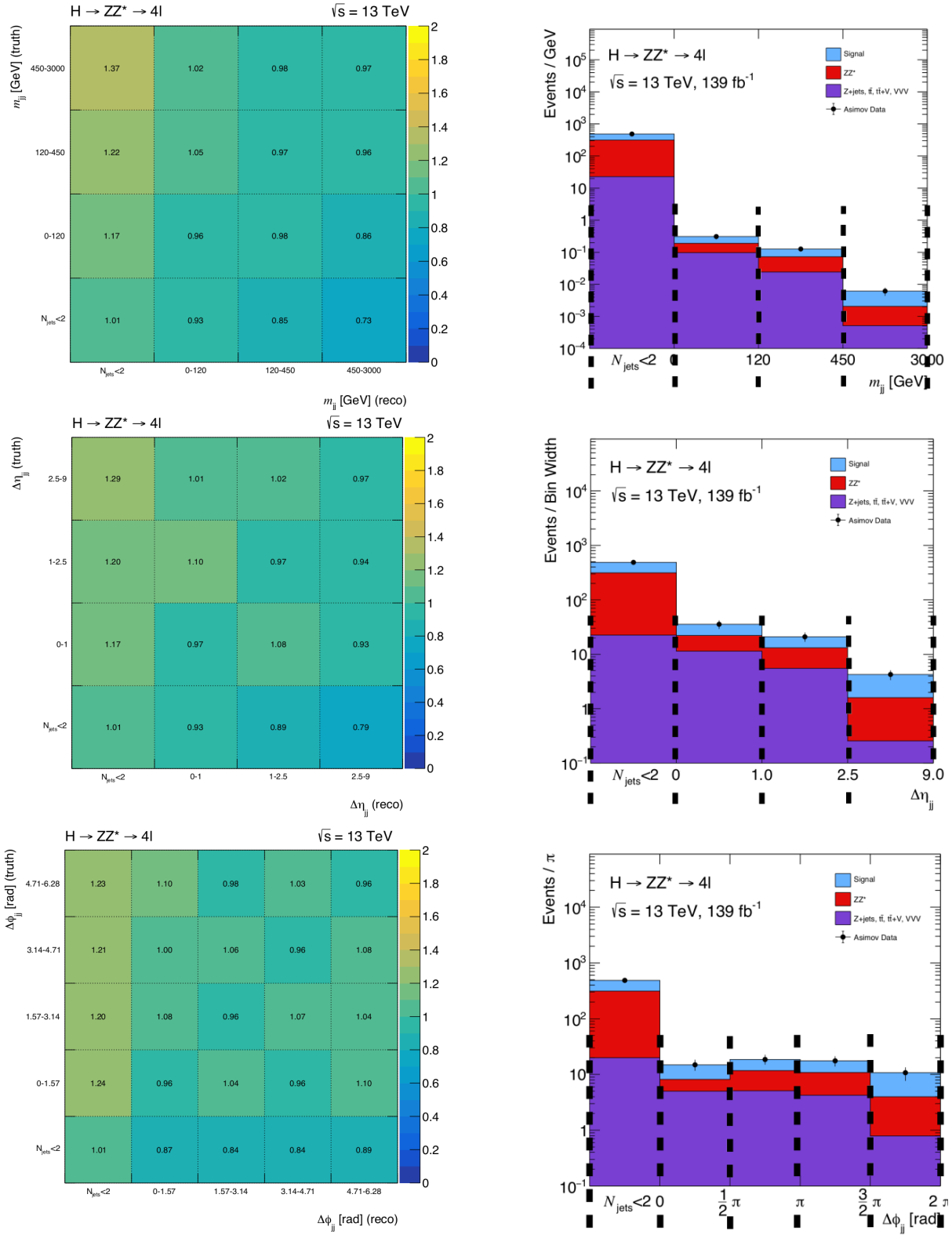

Figure C.2: The (top-left panel) m_{jj}, (middle-left panel) $\Delta\eta_{jj}$ and (bottom-left panel) $\Delta\phi_{jj}$ ratio of response matrices for EMTopo jets derived using simulated datasets divided by the corresponding matrices for PFlow jets. The corresponding Asimov results for the different distributions for the PFlow dataset are shown in the right panels. The corresponding results for the EMTopo dataset is not shown.

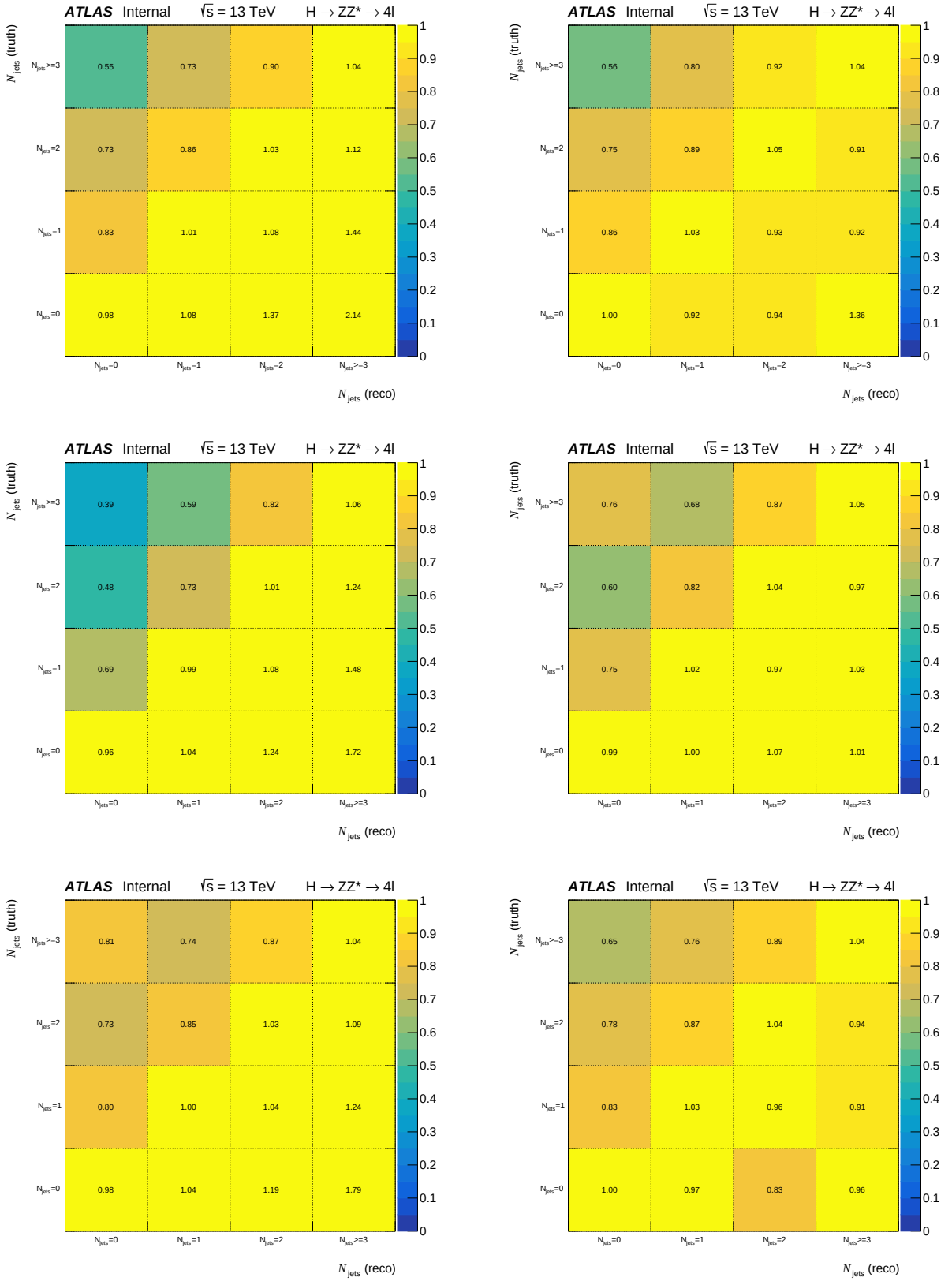

Figure C.3: The N_{jets} ratio of response matrices for PFlow jets derived using simulated (top panels) $ggH + bbH$, (middle panels) VBF and (lower panels) VH events divided by the corresponding matrices for EMTopo jets for (left panels) all jets and (right panels) for central jets ($|\eta| < 2.5$).

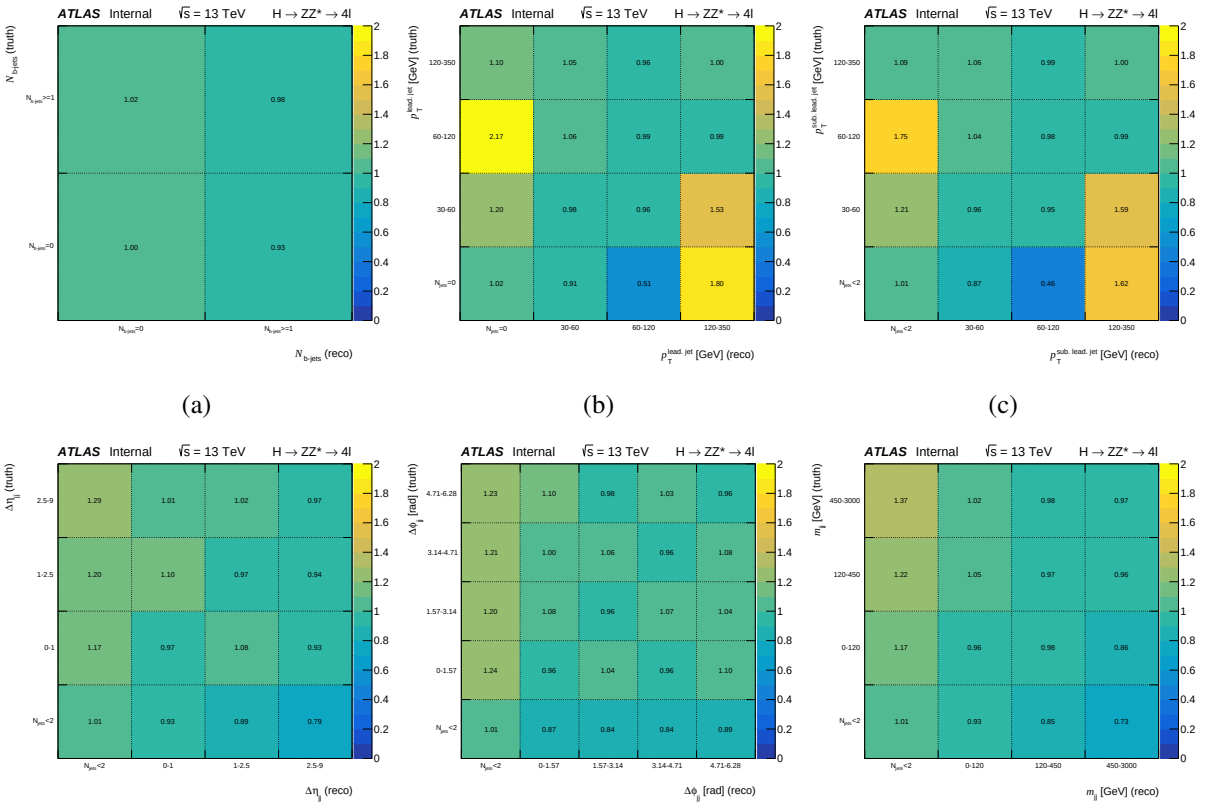

Figure C.4: Ratio of response matrices derived using simulation datasets with EMTopo jets divided by response matrices derived using simulation datasets with PFlow jets for the variables (a) $N_{b-\text{jets}}$, (b) $p_T^{\text{lead. jet}}$, (c) $p_T^{\text{sublead. jet}}$, (d) η_{jj}, (e)
$varphi_{jj}$ and (f) m_{jj}.

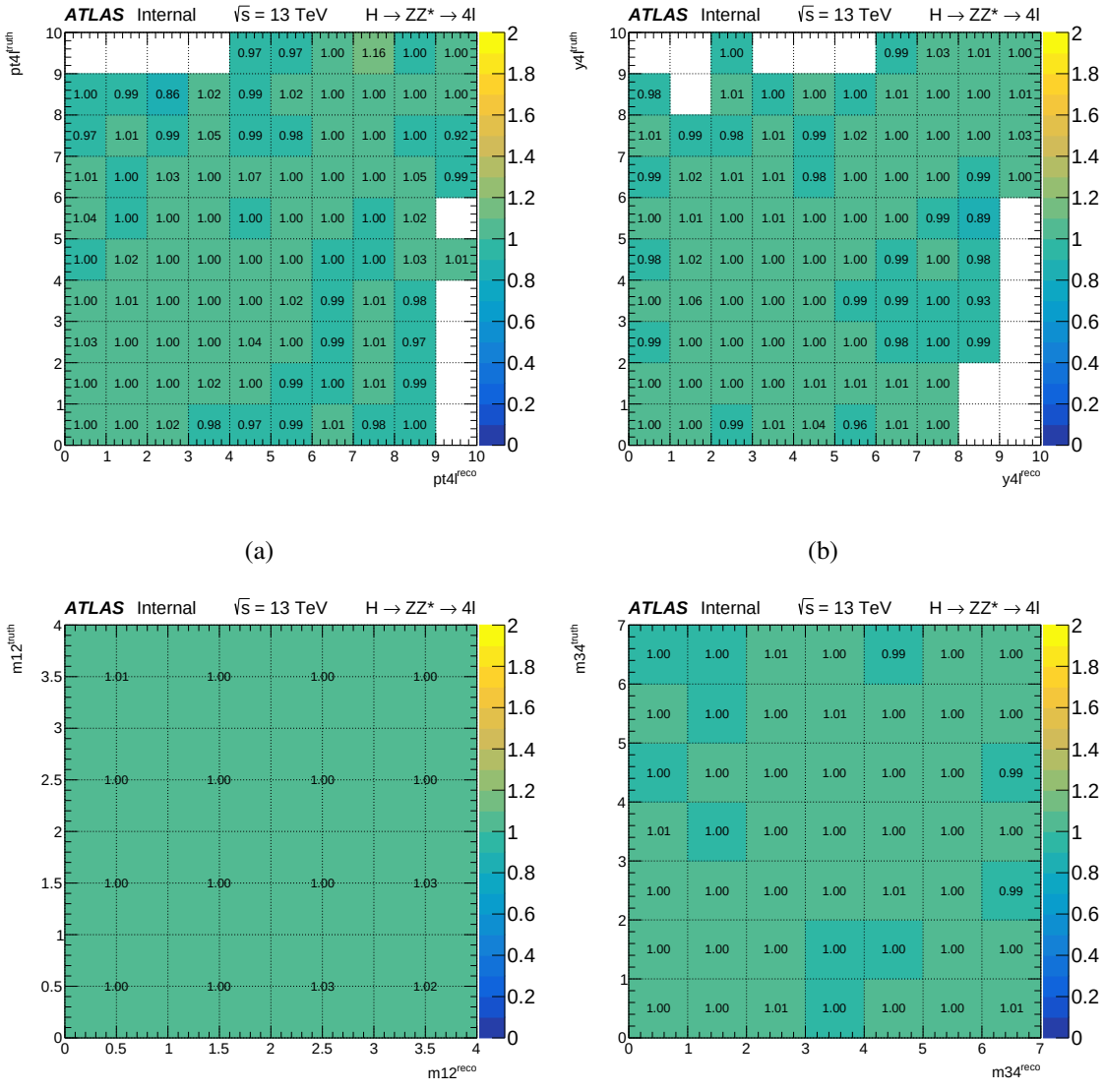

Figure C.5: Ratio of response matrices derived using simulation datasets with EMTopo jets divided by response matrices derived using simulation datasets with PFlow jets. Four sample Higgs variables are provided: (a) $p_{T,4\ell}$, (b) $|y_{4\ell}$, (c) m_{12}, and (d) m_{34}.

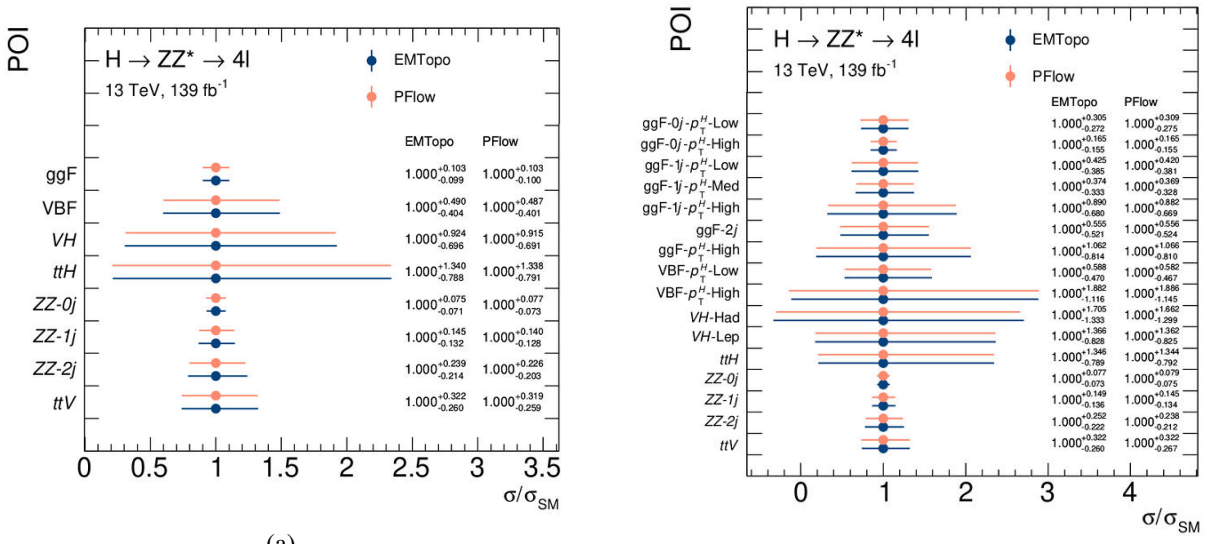

(a) (b)

Figure C.6: The expected stat-only uncertainty on the (a) Stage 0 and (b) Reduced Stage 1.1 parameters of interest (POI) using the PFlow and the EMTopo jet collections.

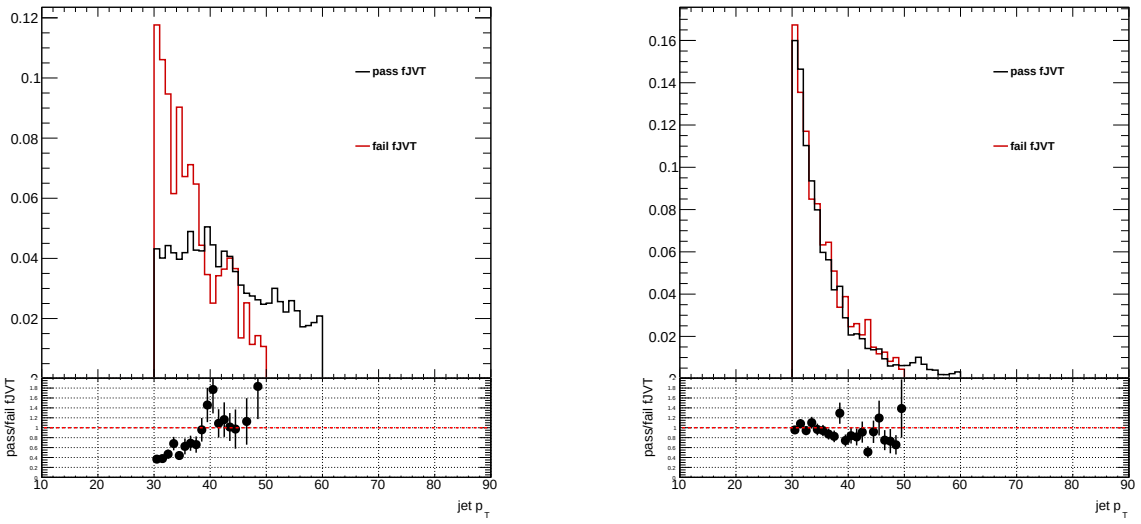

(a) (b)

Figure C.7: (a) The p_T distribution for hard scatter jets which pass and fail the fJVT cut and (b) the p_T distribution for pileup jets which pass and fail the fJVT cut. Even with the fJVT cut applied, pileup jets remain within the distribution.

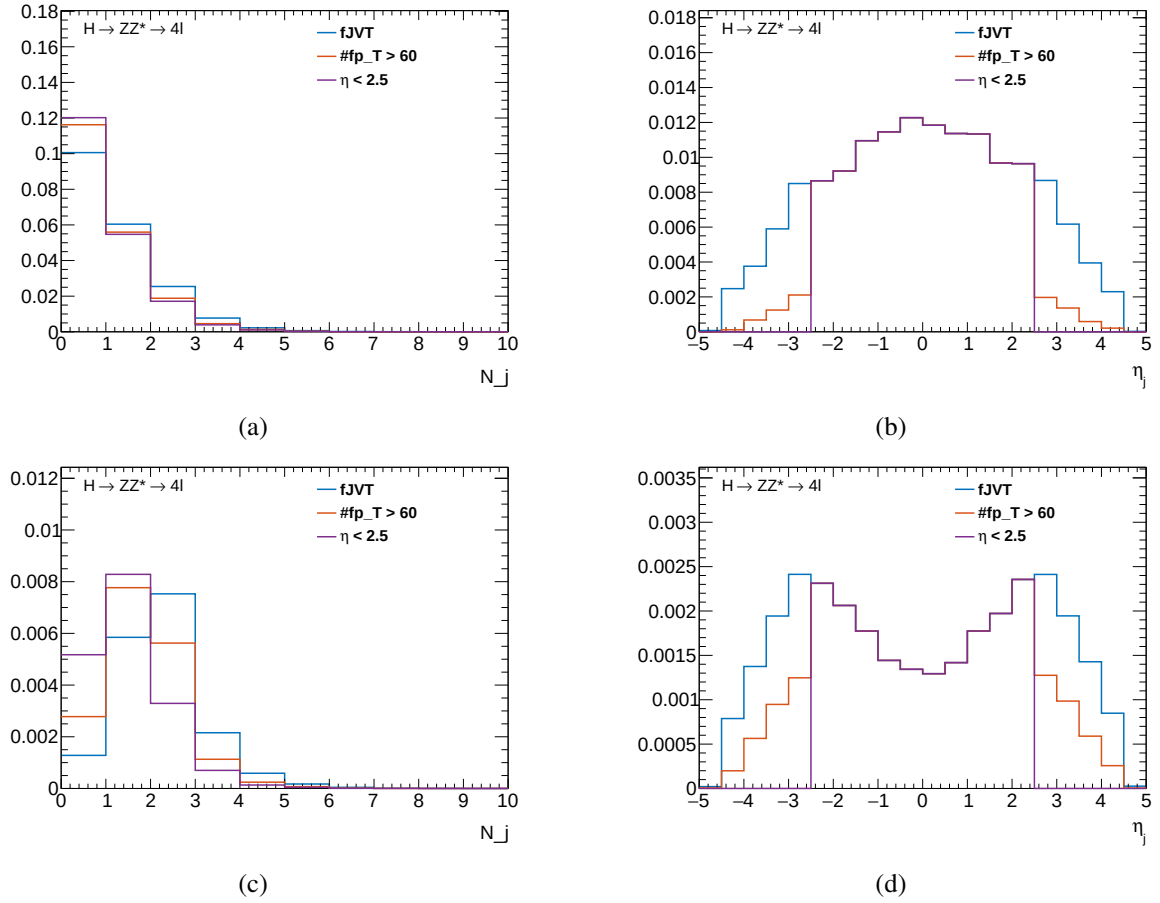

Figure C.8: The (a) ggH N_{jet}, (b) ggH η_j, (c) VBF N_{jet} and (d) VBF η_j distribution for the three forward jet cut scenarios. These distributions correspond to events with $\mu > 50$.

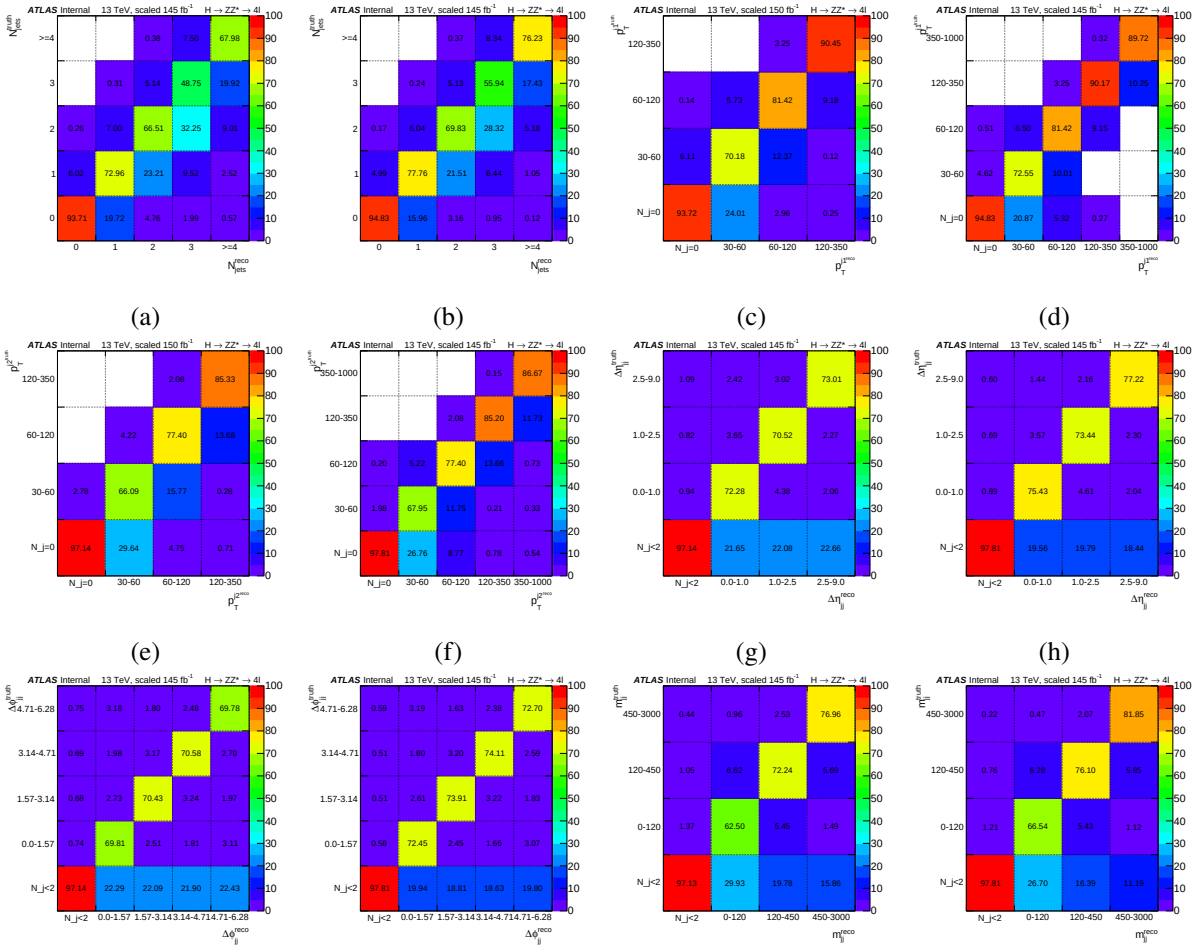

Figure C.9: Comparison of migration matrices for nominal jet selection vs. restricted jet phase space for the fpT scenario.

C.3 Results

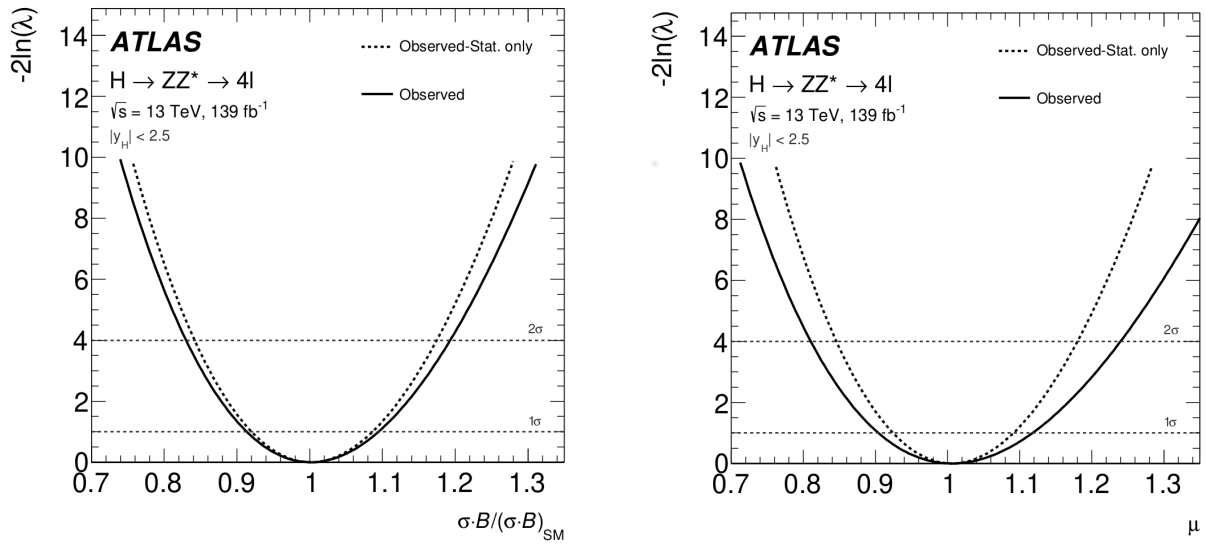

(a) (b)

Figure C.10: Observed profile likelihood as a function of (a) $\sigma \cdot B(H \to ZZ^*)$ normalized by the SM expectation and (b) the inclusive signal strength μ. Both scans are shown with (solid line) and without (dashed line) systematic uncertainties.

APPENDIX D

EFT Interpretation in the $H \to ZZ^* \to 4\ell$ Decay Channel at ATLAS

D.1 Generated BSM Signal Samples

Table D.1: Configuration and MADGRAPH5_aMC@NLO syntax for the generated BSM signal samples in the ggF+bbH production mode. The Wilson coefficients not listed in table are set to zero ($c_{HW} = c_{H\widetilde{W}} = c_{HB} = c_{H\widetilde{B}} = c_{HWB} = c_{H\widetilde{W}B} = c_{uH} = c_{\widetilde{u}H} = 0$). INT - c_i denotes the SM-BSM interaction term for the BSM parameter c_i, BSM - c_i the pure BSM term for the parameter c_i and BSM - c_i, c_j the mixed BSM term for parameters c_i and c_j.

Cross-section term	Syntax	c_{HG}	$c_{H\widetilde{G}}$
SM	NP^2==0	0	0
INT - c_{HG}	NP^2==1	1	0
INT - $c_{H\widetilde{G}}$	NP^2==1	0	1
BSM - c_{HG}	NP^2==2	1	0
BSM - $c_{H\widetilde{G}}$	NP^2==2	0	1
BSM - c_{HG}, $c_{H\widetilde{G}}$	NP^2==2	1	1

Table D.2: Configuration and MADGRAPH5_aMC@NLO syntax for the generated BSM signal samples in the WH-Lep production mode. The Wilson coefficients not listed in table are set to zero ($c_{HB} = c_{H\widetilde{B}} = c_{HWB} = c_{H\widetilde{W}B} = c_{HG} = c_{H\widetilde{G}} = c_{uH} = c_{\widetilde{u}H} = 0$). INT - c_i denotes the SM-BSM interaction term for the BSM parameter c_i, BSM - c_i the pure BSM term for the parameter c_i and BSM - c_i, c_j the mixed BSM term for parameters c_i and c_j.

Cross-section term	Syntax	c_{HW}	$c_{H\widetilde{W}}$
SM	NP^2==0	0	0
INT - c_{HW}	NP^2==1	1	0
INT - $c_{H\widetilde{W}}$	NP^2==1	0	1
BSM - c_{HW}	NP^2==2	1	0
BSM - $c_{H\widetilde{W}}$	NP^2==2	0	1
BSM - c_{HW}, $c_{H\widetilde{W}}$	NP^2==2	1	1

Table D.3: Configuration and MADGRAPH5_aMC@NLO syntax for the generated BSM signal samples in the VBF+VH-Had and ZH-Lep production modes. The Wilson coefficients not listed in table are set to zero ($c_{HG} = c_{H\widetilde{G}} = c_{uH} = c_{\widetilde{u}H} = 0$). INT - c_i denotes the SM-BSM interaction term for the BSM parameter c_i, BSM - c_i the pure BSM term for the parameter c_i and BSM - c_i, c_j the mixed BSM term for parameters c_i and c_j.

Cross-section term	Syntax	c_{HW}	$c_{H\widetilde{W}}$	c_{HB}	$c_{H\widetilde{B}}$	c_{HWB}	$c_{H\widetilde{W}B}$
SM	NP^2==0	0	0	0	0	0	0
INT - c_{HW}	NP^2==1	1	0	0	0	0	0
INT - $c_{H\widetilde{W}}$	NP^2==1	0	1	0	0	0	0
INT - c_{HB}	NP^2==1	0	0	1	0	0	0
INT - $c_{H\widetilde{B}}$	NP^2==1	0	0	0	1	0	0
INT - c_{HWB}	NP^2==1	0	0	0	0	1	0
INT - $c_{H\widetilde{W}B}$	NP^2==1	0	0	0	0	0	1
BSM - c_{HW}	NP^2==2	1	0	0	0	0	0
BSM - $c_{H\widetilde{W}}$	NP^2==2	0	1	0	0	0	0
BSM - c_{HB}	NP^2==2	0	0	1	0	0	0
BSM - $c_{H\widetilde{B}}$	NP^2==2	0	0	0	1	0	0
BSM - c_{HWB}	NP^2==2	0	0	0	0	1	0
BSM - $c_{H\widetilde{W}B}$	NP^2==2	0	0	0	0	0	1
BSM - c_{HW}, $c_{H\widetilde{W}}$	NP^2==2	1	1	0	0	0	0
BSM - c_{HW}, $c_{H\widetilde{B}}$	NP^2==2	1	0	0	1	0	0
BSM - c_{HW}, $c_{H\widetilde{W}B}$	NP^2==2	1	1	0	0	0	1
BSM - c_{HB}, $c_{H\widetilde{W}}$	NP^2==2	0	1	1	0	0	0
BSM - c_{HB}, $c_{H\widetilde{B}}$	NP^2==2	0	0	1	1	0	0
BSM - c_{HB}, $c_{H\widetilde{W}B}$	NP^2==2	0	0	1	0	0	1
BSM - c_{HWB}, $c_{H\widetilde{W}}$	NP^2==2	0	1	0	0	1	0
BSM - c_{HWB}, $c_{H\widetilde{B}}$	NP^2==2	0	0	0	1	1	0
BSM - c_{HWB}, $c_{H\widetilde{W}B}$	NP^2==2	0	0	0	0	1	1

Table D.4: Configuration and MADGRAPH5_aMC@NLO syntax for the generated BSM signal samples in the ttH, $tHjb$ and tHW production modes. The Wilson coefficients not listed in table are set to zero ($c_{HW} = c_{H\widetilde{W}} = c_{HB} = c_{H\widetilde{B}} = c_{HWB} = c_{H\widetilde{W}B} = 0$). INT - c_i denotes the SM-BSM interaction term for the BSM parameter c_i, BSM - c_i the pure BSM term for the parameter c_i and BSM - c_i, c_j the mixed BSM term for parameters c_i and c_j.

Cross-section term	Syntax	c_{uH}	$c_{\widetilde{u}H}$	c_{HG}	$c_{H\widetilde{G}}$
SM	NP^2==0	0	0	0	0
INT - c_{uH}	NP^2==1	1	0	0	0
INT - $c_{\widetilde{u}H}$	NP^2==1	0	1	0	0
INT - c_{HG}	NP^2==1	0	0	1	0
INT - $c_{H\widetilde{G}}$	NP^2==1	0	0	0	1
BSM - c_{uH}	NP^2==2	1	0	0	0
BSM - $c_{\widetilde{u}H}$	NP^2==2	0	1	0	0
BSM - c_{HG}	NP^2==2	0	0	1	0
BSM - $c_{H\widetilde{G}}$	NP^2==2	0	0	0	1
BSM - c_{uH}, $c_{\widetilde{u}H}$	NP^2==2	1	1	0	0
BSM - c_{uH}, $c_{H\widetilde{G}}$	NP^2==2	1	0	0	1
BSM - c_{HG}, $c_{\widetilde{u}H}$	NP^2==2	0	1	1	0
BSM - c_{HG}, $c_{H\widetilde{G}}$	NP^2==2	0	0	1	1

D.2 Particle-level Production Processes

D.2.1 gg2H Production

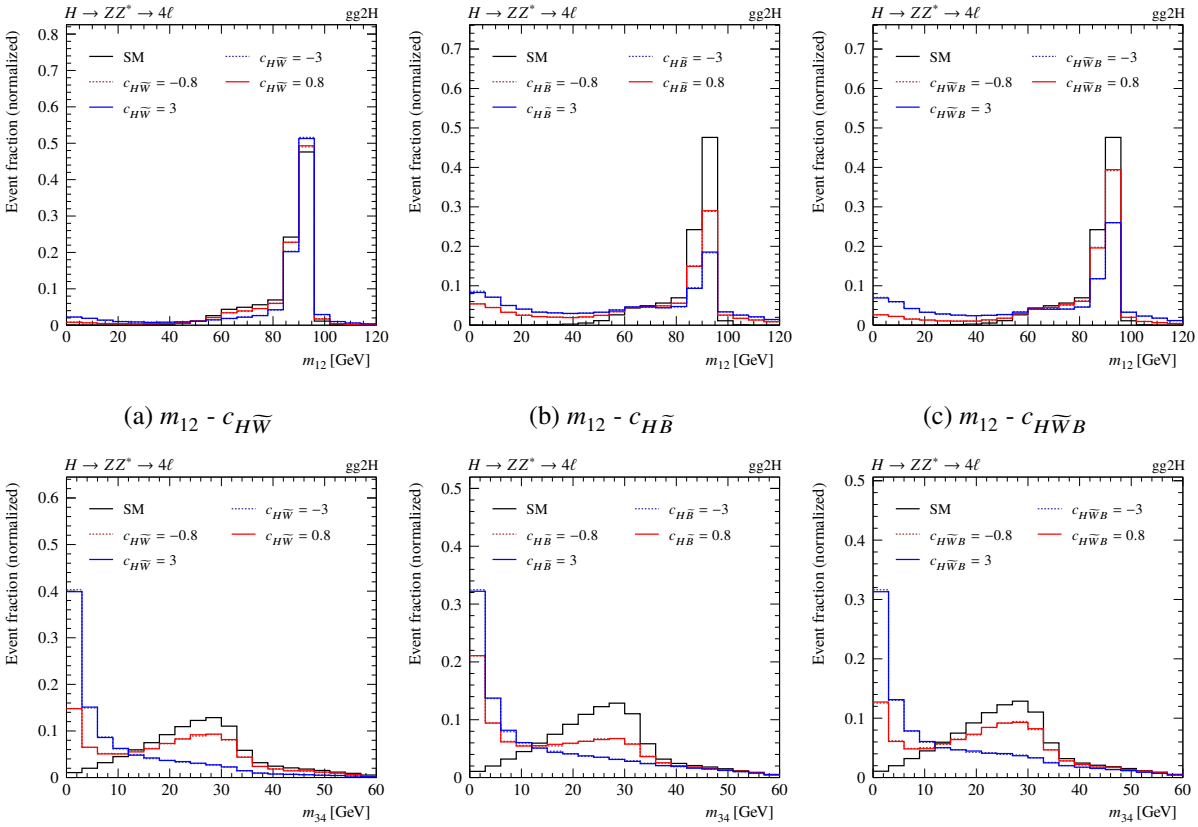

(a) m_{12} - $c_{H\widetilde{W}}$ (b) m_{12} - $c_{H\widetilde{B}}$ (c) m_{12} - $c_{H\widetilde{W}B}$

(d) m_{34} - $c_{H\widetilde{W}}$ (e) m_{34} - $c_{H\widetilde{B}}$ (f) m_{34} - $c_{H\widetilde{W}B}$

Figure D.1: The SM expected invariant mass spectrum m_{12} of the on-shell produced Z boson (top panels), and m_{34} of the off-shell produced Z boson (bottom panels), together with specific BSM scenarios featuring different values of the $\mathcal{CP}$-odd BSM coupling parameters. All other Wilson coefficients are set to zero.

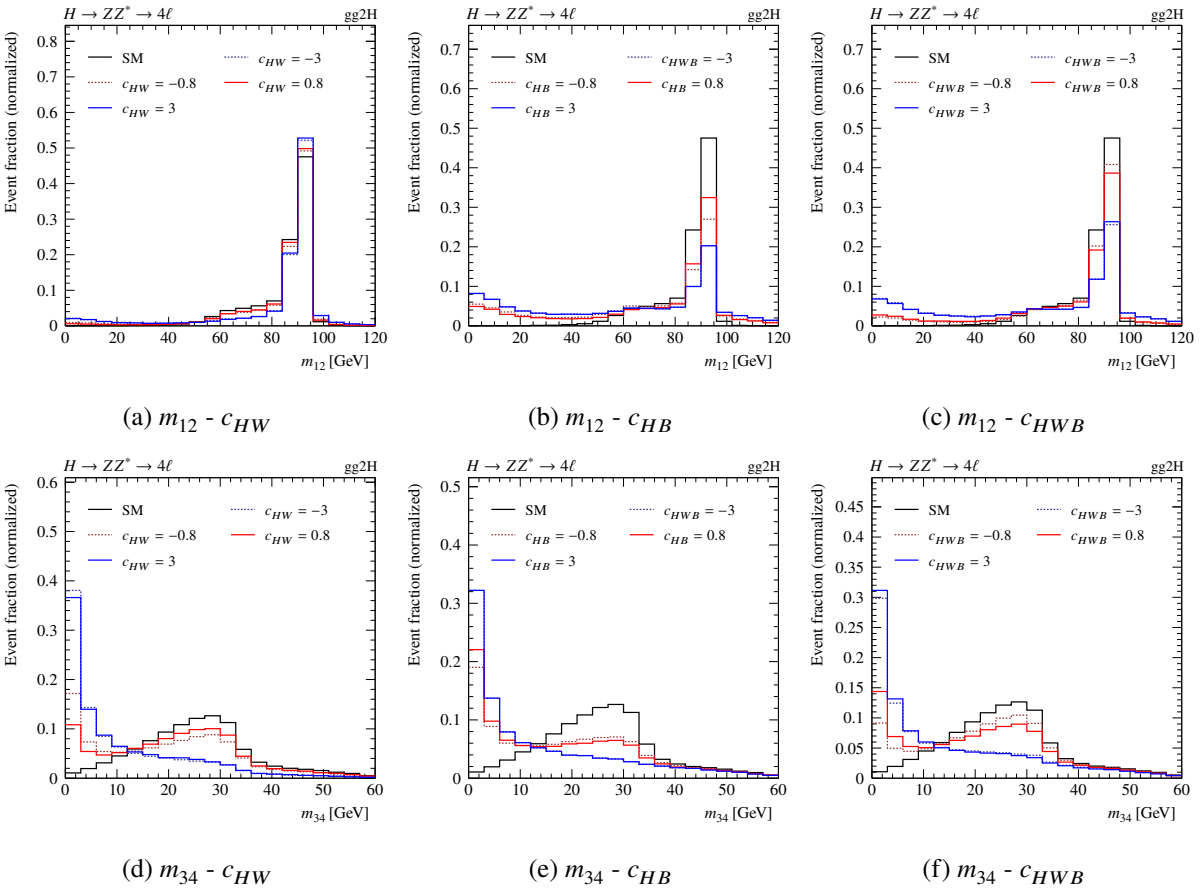

(a) m_{12} - c_{HW} (b) m_{12} - c_{HB} (c) m_{12} - c_{HWB}

(d) m_{34} - c_{HW} (e) m_{34} - c_{HB} (f) m_{34} - c_{HWB}

Figure D.2: The SM expected invariant mass spectrum m_{12} of the on-shell produced Z boson (top panels), and m_{34} of the off-shell produced Z boson (bottom panels), together with specific BSM scenarios featuring different values of the $C\mathcal{P}$-odd BSM coupling parameters. All other Wilson coefficients are set to zero.

D.2.2 qq2Hqq Production

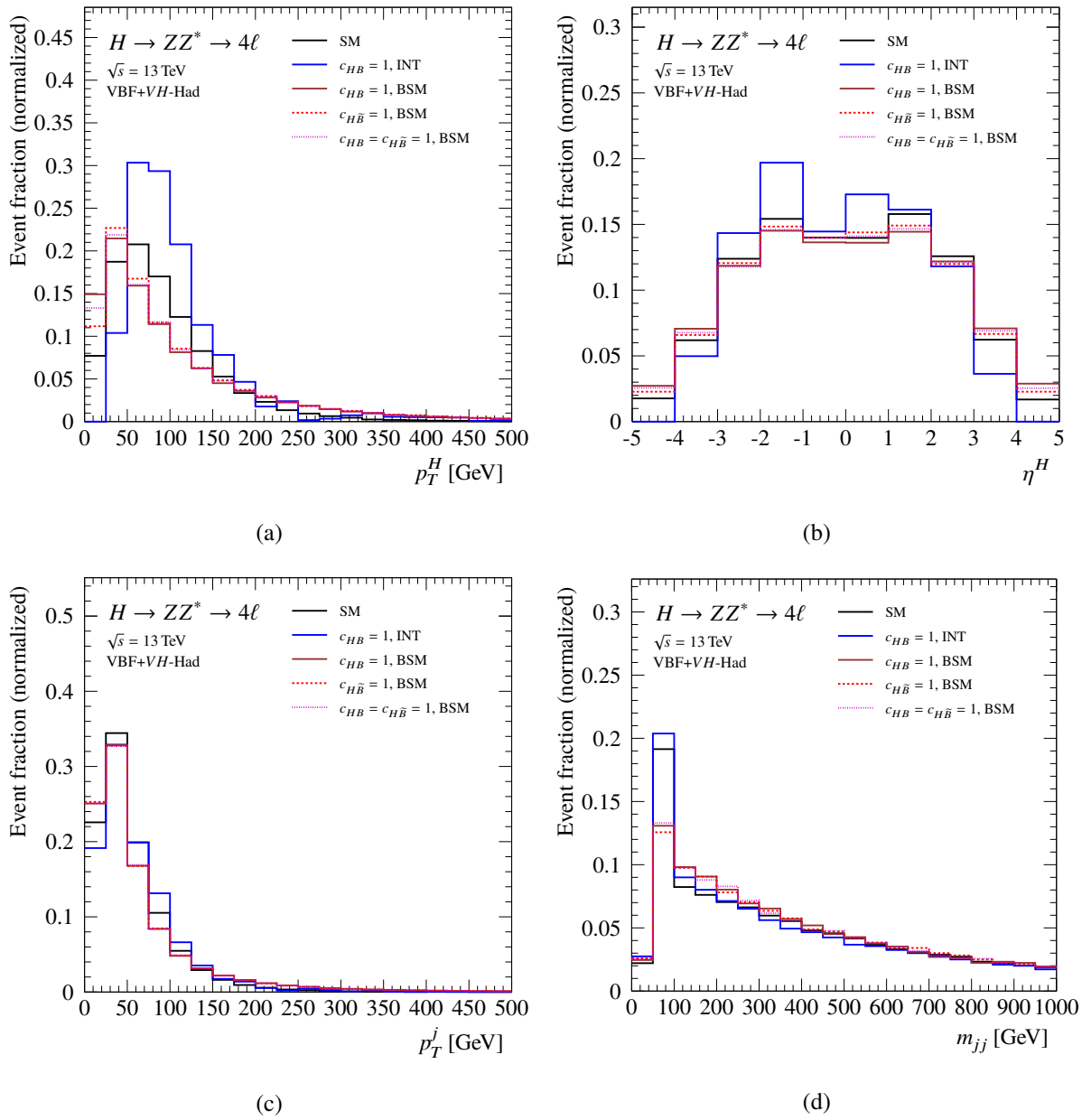

Figure D.3: The simulated distributions of (a) the Higgs boson transverse momentum p_T^H, (b) the pseudorapidity of the Higgs boson η^H, (c) the jet transverse momentum p_T^j and (d) the dijet invariant mass m_{jj} in the VBF+VH-Had production mode. Shown are the SM, the c_{HB} interference and the pure BSM terms for c_{HB} and $c_{H\tilde{B}}$. All distributions are normalized to unit area.

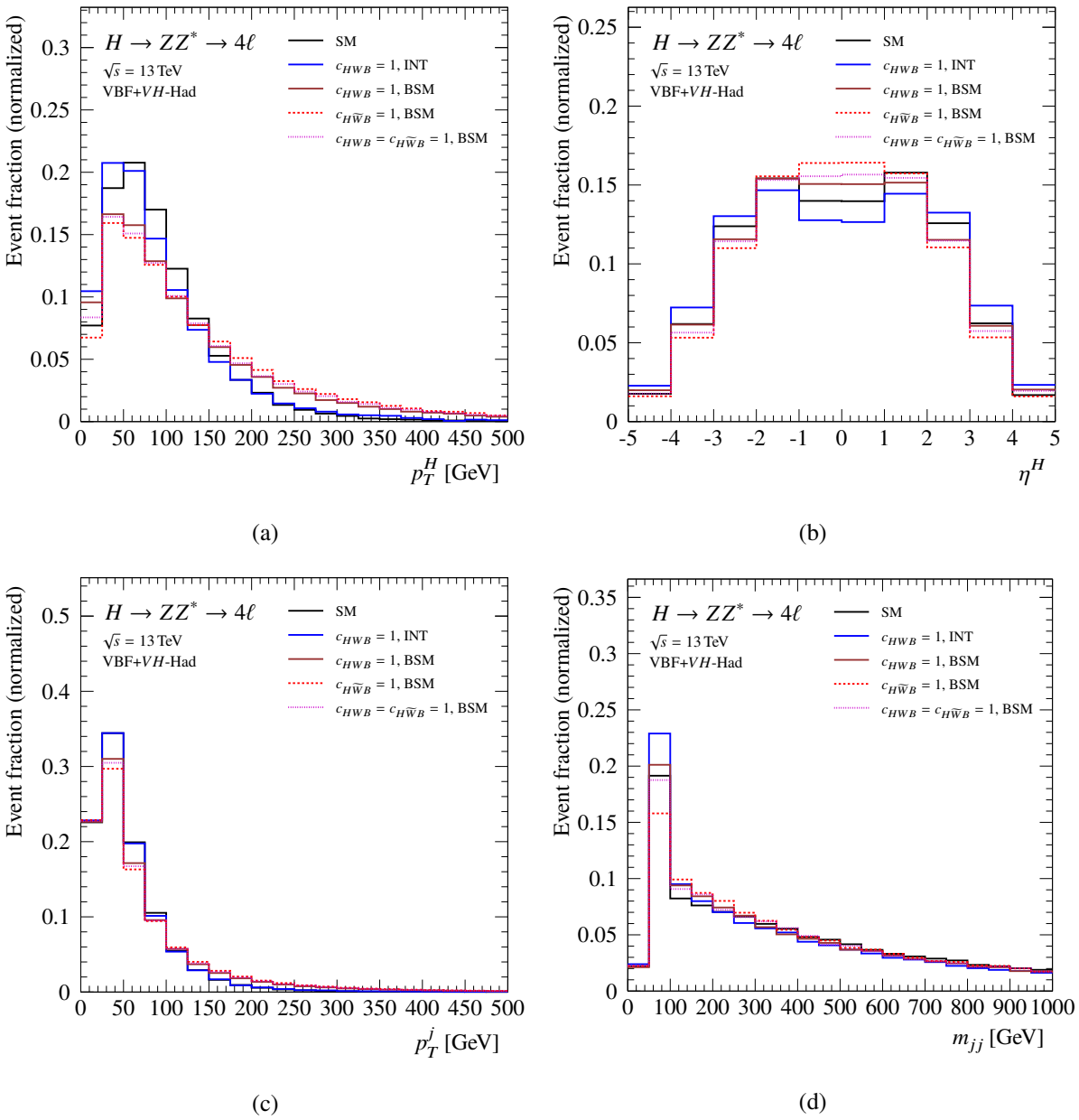

Figure D.4: The simulated distributions of (a) the Higgs boson transverse momentum p_T^H, (b) the pseudorapidity of the Higgs boson η^H, (c) the jet transverse momentum p_T^j and (d) the dijet invariant mass m_{jj} in the VBF+VH-Had production mode. Shown are the SM, the c_{HWB} interference and the pure BSM terms for c_{HWB} and $c_{H\widetilde{W}B}$. All distributions are normalized to unit area.

D.2.3 VH Production

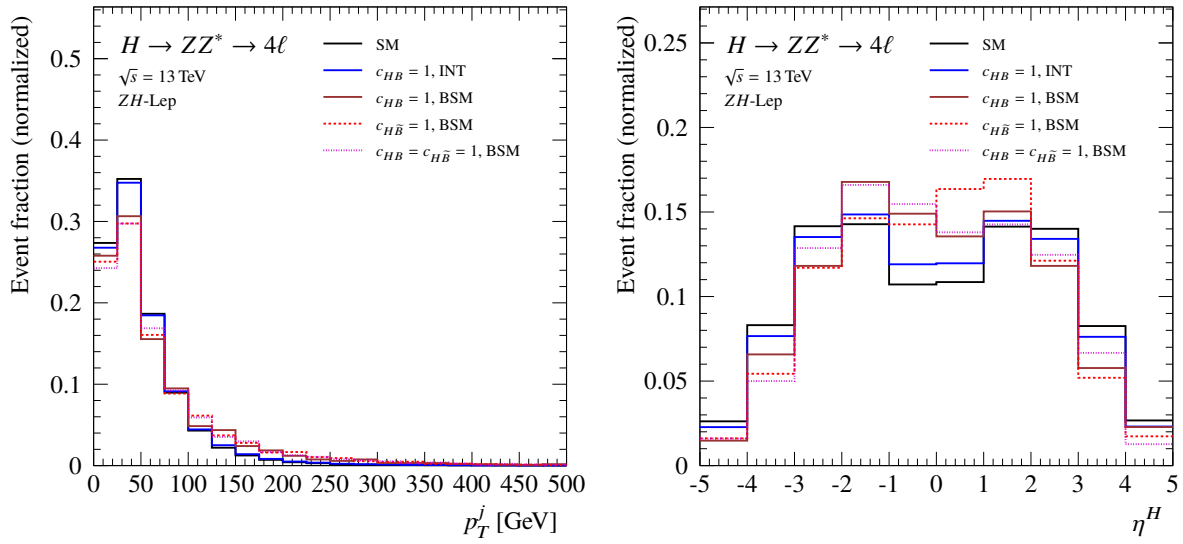

(a) (b)

Figure D.5: The simulated distributions of (a) the jet transverse momentum p_T^j and (b) the pseudorapidity of the Higgs boson η^H in the ZH-Lep production mode. Shown are the SM, the c_{HB} interference and the pure BSM terms for c_{HB} and $c_{H\widetilde{B}}$. All distributions are normalized to unit area.

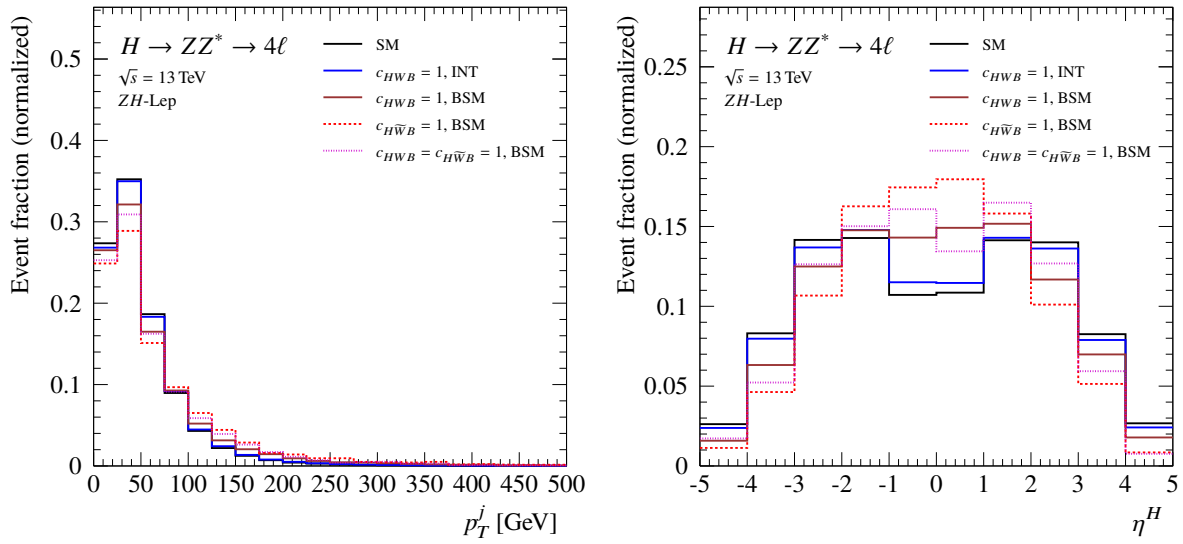

(a) (b)

Figure D.6: The simulated distributions of (a) the jet transverse momentum p_T^j and (b) the pseudorapidity of the Higgs boson η^H in the ZH-Lep production mode. Shown are the SM, the c_{HWB} interference and the pure BSM terms for c_{HWB} and $c_{H\widetilde{W}B}$. All distributions are normalized to unit area.

D.2.4 ttH+tH Production

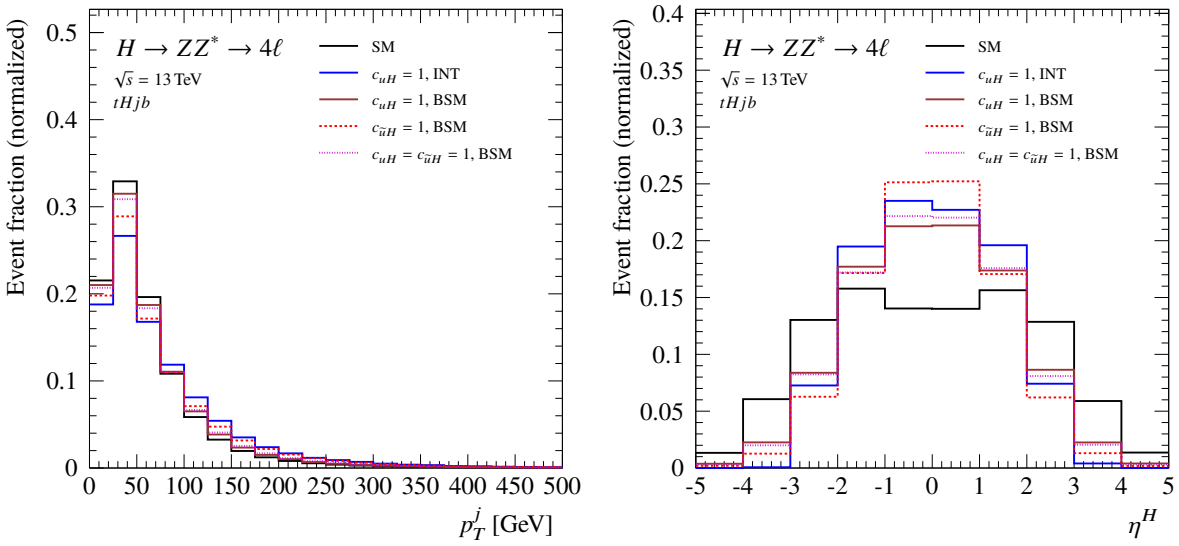

(a) (b)

Figure D.7: The simulated distributions of (a) the jet transverse momentum p_T^j and (b) the pseudorapidity of the Higgs boson η^H in the $tHjb$ production mode. Shown are the SM, the c_{uH} interference and the pure BSM terms for c_{uH} and $c_{\tilde{u}H}$. All distributions are normalized to unit area.

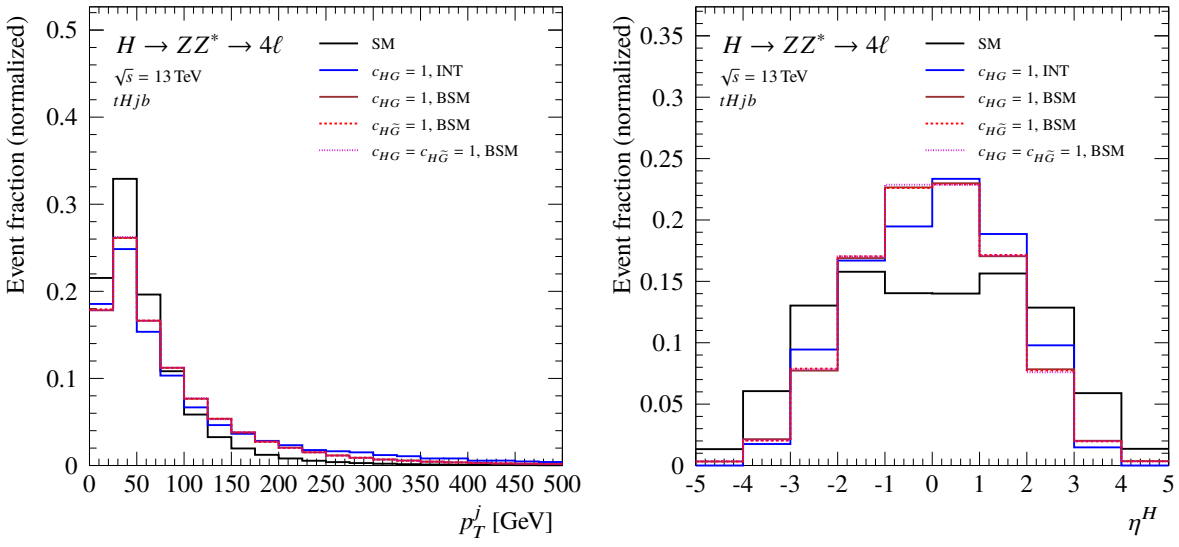

(a) (b)

Figure D.8: The simulated distributions of (a) the jet transverse momentum p_T^j and (b) the pseudorapidity of the Higgs boson η^H in the $tHjb$ production mode. Shown are the SM, the c_{HG} interference and the pure BSM terms for c_{HG} and $c_{H\tilde{G}}$. All distributions are normalized to unit area.

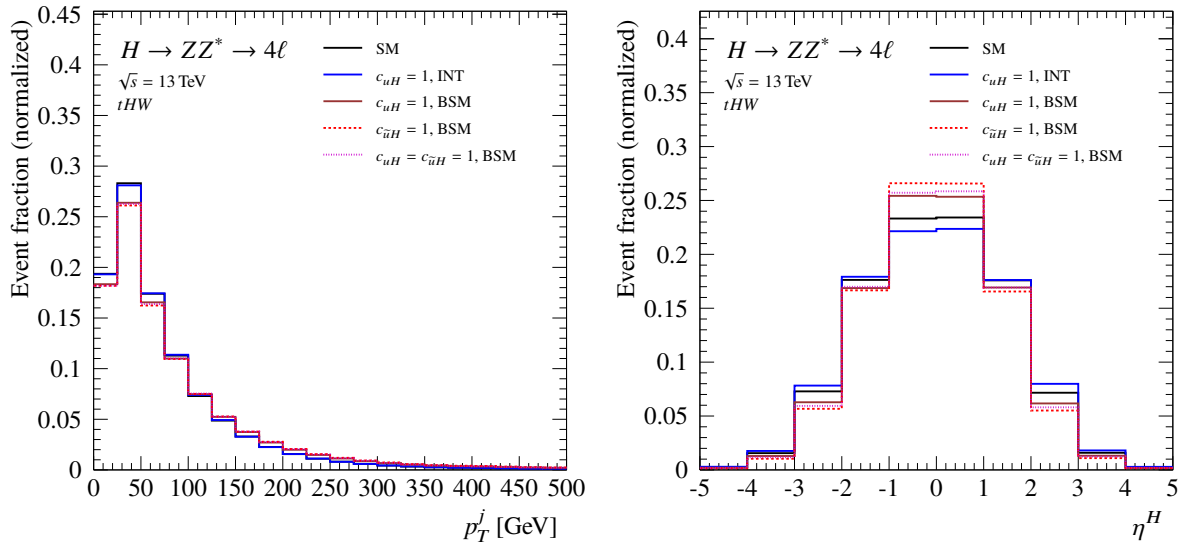

(a) (b)

Figure D.9: The simulated distributions of (a) the jet transverse momentum p_T^j and (b) the pseudorapidity of the Higgs boson η^H in the tHW production mode. Shown are the SM, the c_{uH} interference and the pure BSM terms for c_{uH} and $c_{\tilde{u}H}$. All distributions are normalized to unit area.

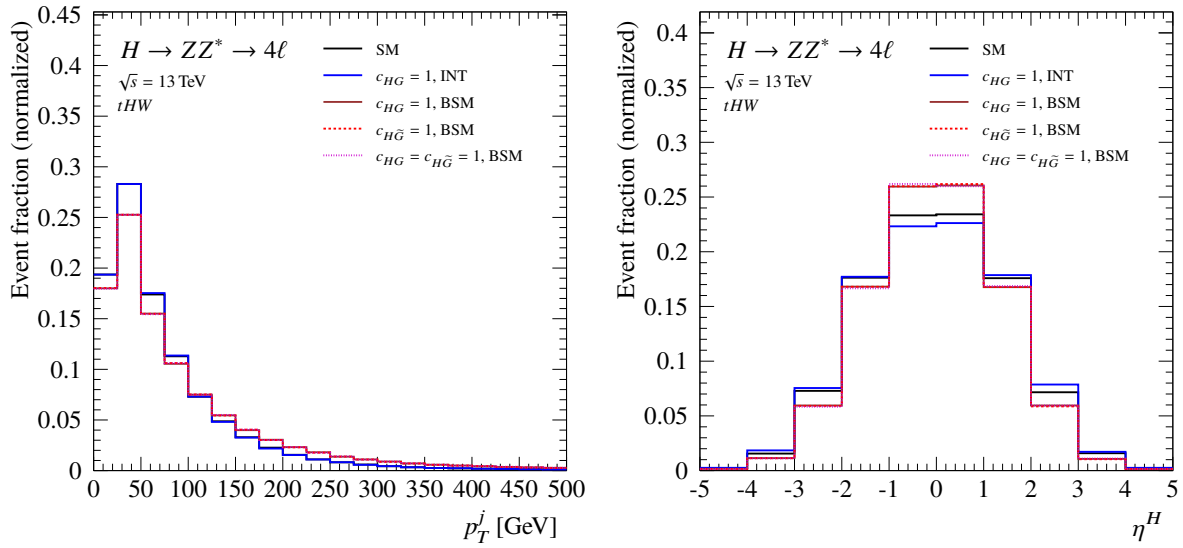

(a) (b)

Figure D.10: The simulated distributions of (a) the jet transverse momentum p_T^j and (b) the pseudorapidity of the Higgs boson η^H in the tHW production mode. Shown are the SM, the c_{HG} interference and the pure BSM terms for c_{HG} and $c_{H\tilde{G}}$. All distributions are normalized to unit area.

D.2.5 Validation of the Production Cross-Section Parameterization

In Section 6.5.2 not all of the relevant validation results are discussed. Specifically, none of the $C\mathcal{P}$-even validations and not all of the $C\mathcal{P}$-odd validations in the VH-Lep bin. Figure D.12 shows the scalar validation results for the gg2H, qq2Hqq and VH-Lep production bins. The remaining $C\mathcal{P}$-even/-odd validations are summarized in Figure D.11.

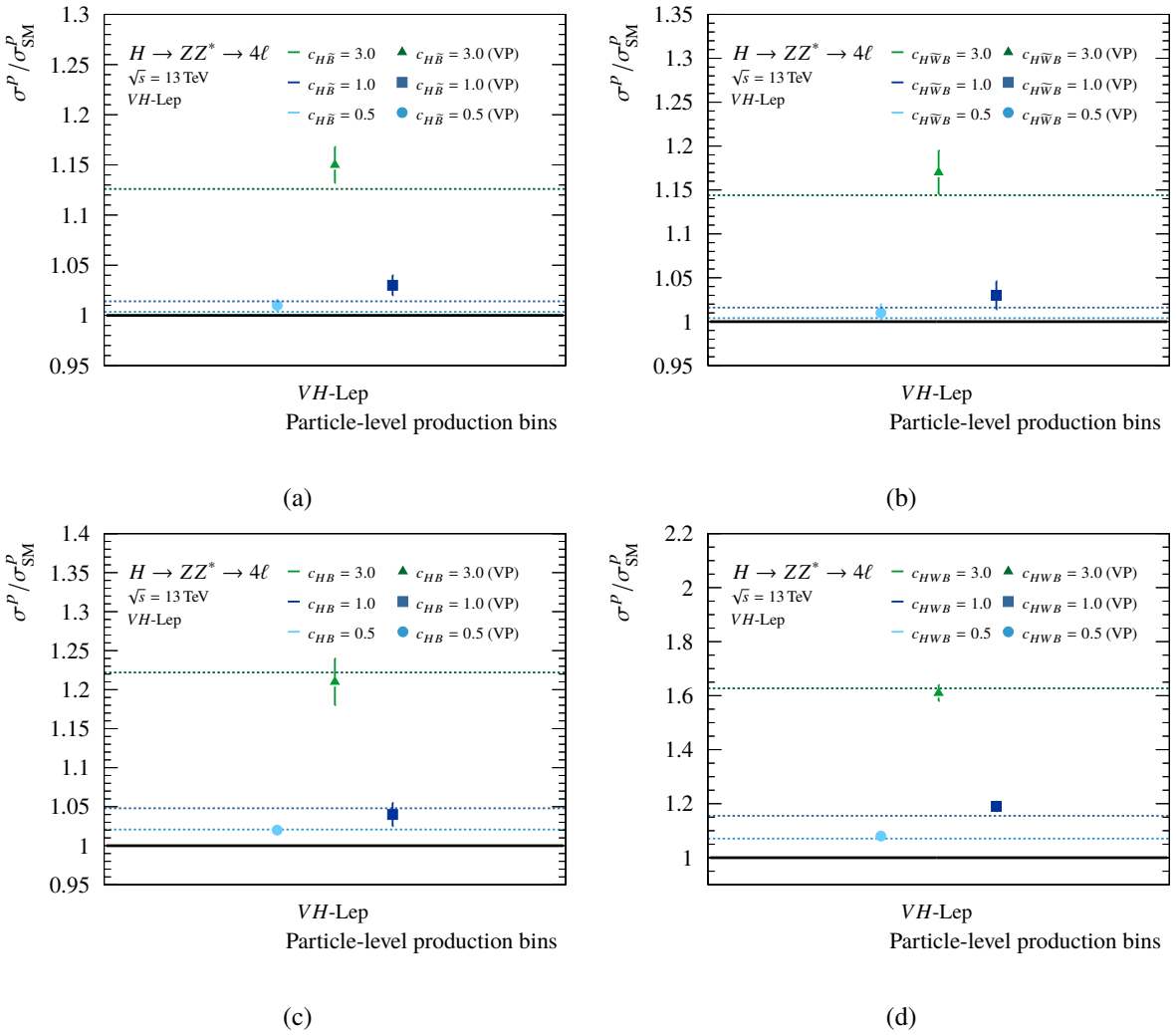

Figure D.11: Comparison of the relative cross-section σ/σ_{SM} for the (a) $c_{H\widetilde{B}}$, (b) $c_{H\widetilde{W}B}$ (c) c_{HB} and (d) c_{HWB} in the VH-Lep particle production bin of the Reduced Stage 1.1 scheme for different values of the BSM coupling parameters. Compared are the predicted cross-sections from the EFT parameterization (dotted line) and the cross-section from generated validation Monte Carlo samples (points).

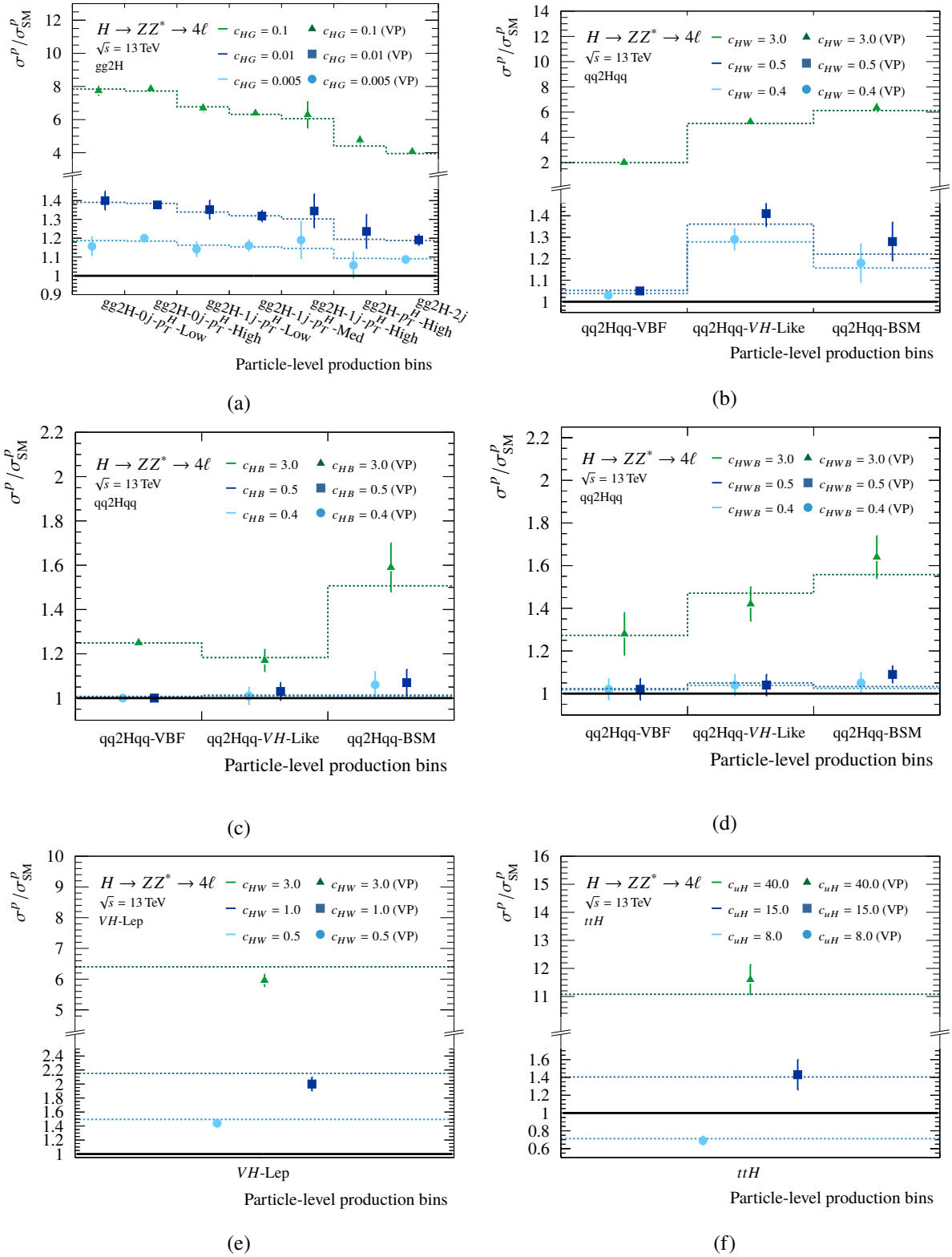

Figure D.12: Comparison of the relative cross-section σ/σ_{SM} for each particle-level production bin of the Reduced Stage 1.1 scheme for different values of the $C\mathcal{P}$-even BSM coupling parameters. Compared are the predicted cross-sections from the EFT parameterization (dotted line) and the cross-section from generated validation Monte Carlo samples (points) for (a) gg2H, (b)-(d) qq2Hqq, (e) VH-Lep and (f) ttH production.

D.3 Generated BSM Samples for the Acceptance Parameterization

D.3.1 gg2H Production

Table D.5: Simulated gg2H truth level samples with different values of the $C\mathcal{P}$-odd BSM couplings parameters $c_{H\widetilde{W}}$, $c_{H\widetilde{B}}$ and $c_{H\widetilde{W}B}$. The corresponding acceptance scale factors are given by $f(\boldsymbol{c}) = {}^{A_{BSM}}/_{A_{SM}}$.

$c_{H\widetilde{W}}$	$c_{H\widetilde{B}}$	$c_{H\widetilde{W}B}$	$f(\boldsymbol{c})$	$c_{H\widetilde{W}}$	$c_{H\widetilde{B}}$	$c_{H\widetilde{W}B}$	$f(\boldsymbol{c})$	$c_{H\widetilde{W}}$	$c_{H\widetilde{B}}$	$c_{H\widetilde{W}B}$	$f(\boldsymbol{c})$
−3	0	0	0.236	−0.3	0	−0.3	0.984	0	−3	−3	0.168
−2	0	0	0.351	−0.3	−0.3	0	0.805	−3	0	−3	0.456
−0.8	0	0	0.731	−0.3	−0.3	0.3	0.675	−3	−3	0	0.151
−0.5	0	0	0.874	0	−0.3	0.3	0.741	−3	−3	3	0.136
−0.3	0	0	0.954	−0.3	0	0.3	0.823	0	−3	3	0.145
0	0	0	1	−0.3	0.3	−0.3	0.77	−3	0	3	0.15
0.3	0	0	0.951	0	0.3	−0.3	0.745	−3	3	−3	0.144
0.5	0	0	0.869	−0.3	0.3	0	0.805	0	3	−3	0.142
0.8	0	0	0.73	−0.3	0.3	0.3	0.774	−3	3	0	0.147
2	0	0	0.354	0	0.3	0.3	0.875	−3	3	3	0.137
3	0	0	0.236	0.3	−0.3	−0.3	0.775	0	3	3	0.165
5	0	0	0.165	0.3	0	−0.3	0.823	3	−3	−3	0.142
10	0	0	0.127	0.3	−0.3	0	0.807	3	0	−3	0.152
0	−3	0	0.16	0.3	−0.3	0.3	0.768	3	−3	0	0.151
0	−2	0	0.199	0.3	0	0.3	0.984	3	−3	3	0.143
0	−0.8	0	0.464	0.3	0.3	−0.3	0.679	3	0	3	0.458
0	−0.5	0	0.664	0.3	0.3	0	0.805	3	3	−3	0.137
0	−0.3	0	0.847	0.3	0.3	0.3	0.906	3	3	0	0.152
0	0.3	0	0.845	−0.8	−0.8	−0.8	0.594	3	3	3	0.185
0	0.5	0	0.666	0	−0.8	−0.8	0.509	−10	−10	−10	0.125
0	0.8	0	0.467	−0.8	0	−0.8	0.909	0	−10	−10	0.124
0	2	0	0.198	−0.8	−0.8	0	0.413	−10	0	−10	0.171
0	3	0	0.156	−0.8	−0.8	0.8	0.287	−10	−10	0	0.126
0	5	0	0.133	0	−0.8	0.8	0.345	−10	−10	10	0.121
0	10	0	0.124	−0.8	0	0.8	0.437	0	−10	10	0.125
0	0	−3	0.225	−0.8	0.8	−0.8	0.367	−10	0	10	0.118
0	0	−2	0.335	0	0.8	−0.8	0.342	−10	10	−10	0.12
0	0	−0.8	0.709	−0.8	0.8	0	0.411	0	10	−10	0.124
0	0	−0.5	0.86	−0.8	0.8	0.8	0.368	−10	10	0	0.122
0	0	−0.3	0.944	0	0.8	0.8	0.513	−10	10	10	0.118
0	0	0.3	0.943	0.8	−0.8	−0.8	0.368	0	10	10	0.124
0	0	0.5	0.857	0.8	0	−0.8	0.439	10	−10	−10	0.117
0	0	0.8	0.708	0.8	−0.8	0	0.413	10	0	−10	0.117
0	0	2	0.331	0.8	−0.8	0.8	0.37	10	−10	0	0.119
0	0	3	0.223	0.8	0	0.8	0.91	10	−10	10	0.125
0	0	5	0.165	0.8	0.8	−0.8	0.288	10	0	10	0.169
0	0	10	0.13	0.8	0.8	0	0.409	10	10	−10	0.121
−0.3	−0.3	−0.3	0.911	0.8	0.8	0.8	0.606	10	10	0	0.123
0	−0.3	−0.3	0.876	−3	−3	−3	0.186	10	10	10	0.125

Table D.6: Simulated gg2H truth level samples with different values for the $C\mathcal{P}$-even and $C\mathcal{P}$-odd BSM couplings parameters. The corresponding acceptance scale factors are given by $f = {}^{A_{BSM}}/_{A_{SM}}$.

c_{HW}	$c_{H\widetilde{W}}$	f	c_{HB}	$c_{H\widetilde{B}}$	f	c_{HWB}	$c_{H\widetilde{W}B}$	f
0.4	0.0	0.97	0.4	0.0	0.76	0.4	0.0	0.86
0.5	0.0	0.94	0.5	0.0	0.67	0.4	0.0	0.82
1.0	0.0	0.71	1.0	0.0	0.38	1.0	0.0	0.59
3.0	0.0	0.29	3.0	0.0	0.17	3.0	0.0	0.24
0.0	0.4	0.91	0.0	0.4	0.75	0.0	0.4	0.91
0.0	0.5	0.87	0.0	0.5	0.67	0.0	0.5	0.86
0.0	1.0	0.66	0.0	1.0	0.38	0.0	1.0	0.63
0.0	3.0	0.24	0.0	3.0	0.16	0.0	3.0	0.23
0.4	0.4	0.88	0.4	0.4	0.62	0.4	0.4	0.80
0.5	0.5	0.82	0.5	0.5	0.52	0.5	0.5	0.73
1.0	1.0	0.54	1.0	1.0	0.27	1.0	1.0	0.47
3.0	3.0	0.22	3.0	3.0	0.14	3.0	3.0	0.18

D.3.2 qq2Hqq Production

Table D.7: Fit parameters for the three-dimensional parameterization of the signal acceptance for the $C\mathcal{P}$-odd Wilson coefficients $c_{H\widetilde{W}}$, $c_{H\widetilde{B}}$ and $c_{H\widetilde{W}B}$ using the qq2Hqq production mode.

Parameter	Fit result	Parameter	Fit result
$\widetilde{\alpha}_0$	0.143 ± 0.001	$\delta_{H\widetilde{W}}$	2.265 ± 0.023
$\widetilde{\alpha}_1$	1.745 ± 0.009	$\delta_{H\widetilde{B}}$	8.662 ± 0.004
$\widetilde{\alpha}_2$	3.575 ± 0.040	$\delta_{H\widetilde{W}B}$	2.773 ± 0.001
$\beta_{H\widetilde{W}}$	-0.001 ± 0.001	$\delta_{(H\widetilde{W},H\widetilde{B})}$	-0.003 ± 0.008
$\beta_{H\widetilde{B}}$	-0.001 ± 0.001	$\delta_{(H\widetilde{W},H\widetilde{W}B)}$	-4.507 ± 0.055
$\beta_{H\widetilde{W}B}$	0.001 ± 0.001	$\delta_{(H\widetilde{B},H\widetilde{W}B)}$	-4.546 ± 0.085
		$\delta_{(H\widetilde{W},H\widetilde{B},H\widetilde{W}B)}$	0.595 ± 0.052

Table D.8: Simulated qq2Hqq truth level samples with different values for the $\mathcal{CP}$-odd BSM couplings parameters $c_{H\widetilde{W}}$, $c_{H\widetilde{B}}$ and $c_{H\widetilde{W}B}$. The corresponding acceptance scale factors are given by $f(\boldsymbol{c}) = {}^{A_{BSM}}/_{A_{SM}}$.

$c_{H\widetilde{W}}$	$c_{H\widetilde{B}}$	$c_{H\widetilde{W}B}$	$f(\boldsymbol{c})$	$c_{H\widetilde{W}}$	$c_{H\widetilde{B}}$	$c_{H\widetilde{W}B}$	$f(\boldsymbol{c})$	$c_{H\widetilde{W}}$	$c_{H\widetilde{B}}$	$c_{H\widetilde{W}B}$	$f(\boldsymbol{c})$
−3	0	0	0.27	−0.3	0	−0.3	0.984	0	−3	−3	0.181
−2	0	0	0.382	−0.3	−0.3	0	0.819	−3	0	−3	0.507
−0.8	0	0	0.741	−0.3	−0.3	0.3	0.687	−3	−3	0	0.166
−0.5	0 gg2H	0	0.871	0	−0.3	0.3	0.756	−3	−3	3	0.151
−0.3	0	0	0.942	−0.3	0	0.3	0.831	0	−3	3	0.152
0	0	0	0.995	−0.3	0.3	−0.3	0.769	−3	0	3	0.173
0.3	0	0	0.948	0	0.3	−0.3	0.756	−3	3	−3	0.166
0.5	0	0	0.877	−0.3	0.3	0	0.809	0	3	−3	0.153
0.8	0	0	0.744	−0.3	0.3	0.3	0.777	−3	3	0	0.174
2	0	0	0.38	0	0.3	0.3	0.878	−3	3	3	0.168
3	0	0	0.271	0.3	−0.3	−0.3	0.777	0	3	3	0.179
5	0	0	0.2	0.3	0	−0.3	0.827	3	−3	−3	0.168
10	0	0	0.171	0.3	−0.3	0	0.812	3	0	−3	0.175
0	−3	0	0.167	0.3	−0.3	0.3	0.779	3	−3	0	0.175
0	−2	0	0.211	0.3	0	0.3	0.981	3	−3	3	0.168
0	−0.8	0	0.48	0.3	0.3	−0.3	0.691	3	0	3	0.506
0	−0.5	0	0.68	0.3	0.3	0	0.815	3	3	−3	0.15
0	−0.3	0	0.844	0.3	0.3	0.3	0.913	3	3	0	0.171
0	0.3	0	0.85	−0.8	−0.8	−0.8	0.614	3	3	3	0.218
0	0.5	0	0.679	0	−0.8	−0.8	0.527	−10	−10	−10	0.162
0	0.8	0	0.481	−0.8	0	−0.8	0.914	0	−10	−10	0.148
0	2	0	0.214	−0.8	−0.8	0	0.433	−10	0	−10	0.219
0	3	0	0.17	−0.8	−0.8	0.8	0.305	−10	−10	0	0.149
0	5	0	0.144	0	−0.8	0.8	0.359	−10	−10	10	0.142
0	10	0	0.131	−0.8	0	0.8	0.455	0	−10	10	0.135
0	0	−3	0.245	−0.8	0.8	−0.8	0.385	−10	0	10	0.153
0	0	−2	0.349	0	0.8	−0.8	0.362	−10	10	−10	0.152
0	0	−0.8	0.725	−0.8	0.8	0	0.426	0	10	−10	0.128
0	0	−0.5	0.861	−0.8	0.8	0.8	0.384	−10	10	0	0.158
0	0	−0.3	0.938	0	0.8	0.8	0.526	−10	10	10	0.159
0	0	0.3	0.945	0.8	−0.8	−0.8	0.38	0	10	10	0.146
0	0	0.5	0.864	0.8	0	−0.8	0.457	10	−10	−10	0.163
0	0	0.8	0.719	0.8	−0.8	0	0.429	10	0	−10	0.151
0	0	2	0.349	0.8	−0.8	0.8	0.389	10	−10	0	0.158
0	0	3	0.241	0.8	0	0.8	0.91	10	−10	10	0.151
0	0	5	0.173	0.8	0.8	−0.8	0.306	10	0	10	0.219
0	0	10	0.148	0.8	0.8	0	0.433	10	10	−10	0.142
−0.3	−0.3	−0.3	0.915	0.8	0.8	0.8	0.622	10	10	0	0.147
0	−0.3	−0.3	0.873	−3	−3	−3	0.218	10	10	10	0.163

Table D.9: Simulated qq2Hqq truth level samples with different values for the $\mathcal{CP}$-even BSM couplings parameters c_{HW}, c_{HB} and c_{HWB}. The corresponding acceptance scale factors are given by $f(\boldsymbol{c}) = {}^{A_{BSM}}/_{A_{SM}}$.

c_{HW}	c_{HB}	c_{HWB}	$f(\boldsymbol{c})$	c_{HW}	c_{HB}	c_{HWB}	$f(\boldsymbol{c})$	c_{HW}	c_{HB}	c_{HWB}	$f(\boldsymbol{c})$
−3	0	0	0.303	−0.3	0	−0.3	0.984	0	−3	−3	0.215
−2	0	0	0.391	−0.3	−0.3	0	0.792	−3	0	−3	0.59
−0.8	0	0	0.698	−0.3	−0.3	0.3	0.666	−3	−3	0	0.189
−0.5	0	0	0.831	0	−0.3	0.3	0.736	−3	−3	3	0.166
−0.3	0	0	0.914	−0.3	0	0.3	0.787	0	−3	3	0.171
0	0	0	1	−0.3	0.3	−0.3	0.785	−3	0	3	0.195
0.3	0	0	0.986	0	0.3	−0.3	0.779	−3	3	−3	0.207
0.5	0	0	0.923	−0.3	0.3	0	0.788	0	3	−3	0.164
0.8	0	0	0.799	−0.3	0.3	0.3	0.734	−3	3	0	0.215
2	0	0	0.414	0	0.3	0.3	0.84	−3	3	3	0.196
3	0	0	0.308	0.3	−0.3	−0.3	0.825	0	3	3	0.188
5	0	0	0.238	0.3	0	−0.3	0.892	3	−3	−3	0.207
10	0	0	0.21	0.3	−0.3	0	0.836	3	0	−3	0.191
0	−3	0	0.199	0.3	−0.3	0.3	0.776	3	−3	0	0.223
0	−2	0	0.243	0.3	0	0.3	0.974	3	−3	3	0.208
0	−0.8	0	0.496	0.3	0.3	−0.3	0.727	3	0	3	0.549
0	−0.5	0	0.684	0.3	0.3	0	0.841	3	3	−3	0.154
0	−0.3	0	0.849	0.3	0.3	0.3	0.902	3	3	0	0.167
0	0.3	0	0.848	−0.8	−0.8	−0.8	0.631	3	3	3	0.198
0	0.5	0	0.677	0	−0.8	−0.8	0.575	−10	−10	−10	0.172
0	0.8	0	0.473	−0.8	0	−0.8	0.923	0	−10	−10	0.176
0	2	0	0.215	−0.8	−0.8	0	0.439	−10	0	−10	0.386
0	3	0	0.179	−0.8	−0.8	0.8	0.318	−10	−10	0	0.156
0	5	0	0.161	0	−0.8	0.8	0.372	−10	−10	10	0.148
0	10	0	0.153	−0.8	0	0.8	0.44	0	−10	10	0.151
0	0	−3	0.271	−0.8	0.8	−0.8	0.403	−10	0	10	0.17
0	0	−2	0.393	0	0.8	−0.8	0.371	−10	10	−10	0.189
0	0	−0.8	0.792	−0.8	0.8	0	0.428	0	10	−10	0.147
0	0	−0.5	0.925	−0.8	0.8	0.8	0.374	−10	10	0	0.201
0	0	−0.3	0.984	0	0.8	0.8	0.494	−10	10	10	0.191
0	0	0.3	0.906	0.8	−0.8	−0.8	0.437	0	10	10	0.159
0	0	0.5	0.815	0.8	0	−0.8	0.498	10	−10	−10	0.192
0	0	0.8	0.682	0.8	−0.8	0	0.467	10	0	−10	0.168
0	0	2	0.343	0.8	−0.8	0.8	0.416	10	−10	0	0.201
0	0	3	0.246	0.8	0	0.8	0.906	10	−10	10	0.19
0	0	5	0.186	0.8	0.8	−0.8	0.315	10	0	10	0.364
0	0	10	0.155	0.8	0.8	0	0.427	10	10	−10	0.151
−0.3	−0.3	−0.3	0.911	0.8	0.8	0.8	0.596	10	10	0	0.15
0	−0.3	−0.3	0.906	−3	−3	−3	0.247	10	10	10	0.156

D.4 Projections of the $C\mathcal{P}$-Odd Signal Model

In this section one- and two-dimensional projections of the $C\mathcal{P}$-odd signal model are given for the various event categories of the Reduced-Stage-1.1 STXS scheme.

gg2H production:

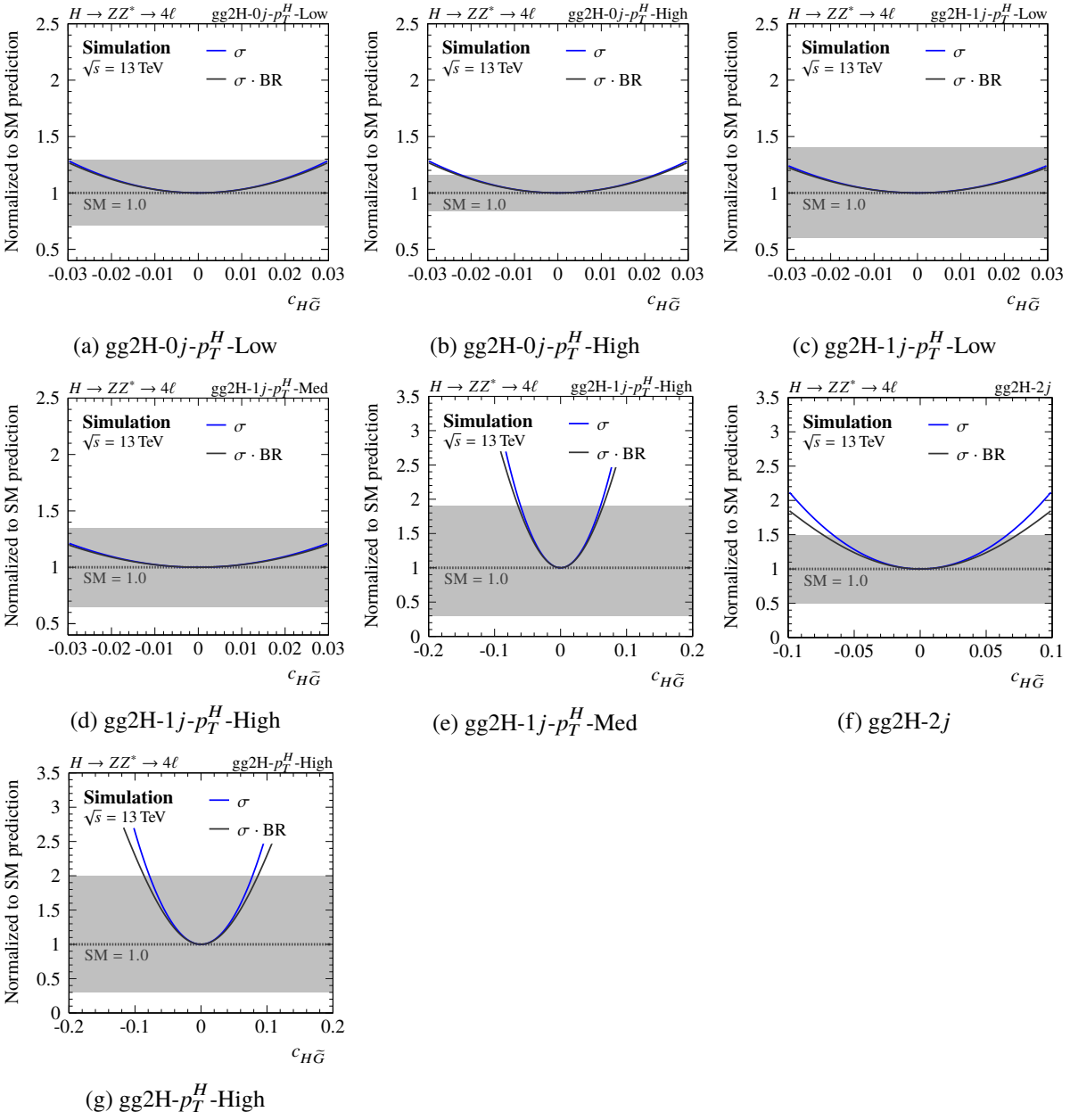

(a) gg2H-0j-p_T^H-Low (b) gg2H-0j-p_T^H-High (c) gg2H-1j-p_T^H-Low

(d) gg2H-1j-p_T^H-High (e) gg2H-1j-p_T^H-Med (f) gg2H-2j

(g) gg2H-p_T^H-High

Figure D.13: The one-dimensional projection of the expected event yield relative to the SM prediction onto the axis of the Wilson coefficient $c_{H\tilde{G}}$ in the gg2H bins of the Reduced-Stage-1.1 scheme. The gray bands indicate the expected 68 % C. L. interval from the cross-section analysis.

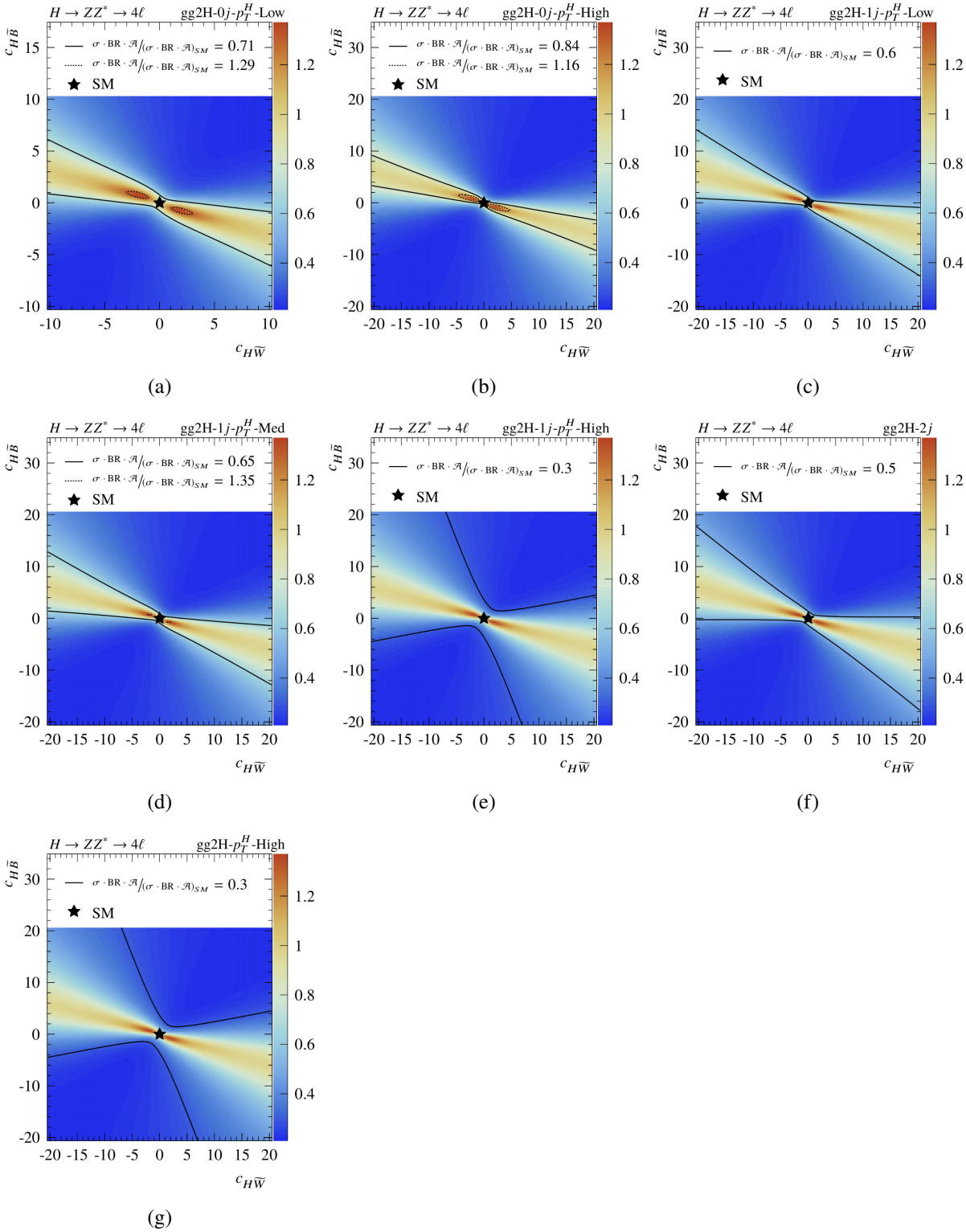

Figure D.14: The two-dimensional projections of the expected event yield relative to the SM prediction onto the $c_{H\widetilde{W}}$-$c_{H\widetilde{B}}$ plane for the full signal model in the various gg2H production bins of the Reduced-Stage-1.1 scheme. The black solid (dashed) contours indicate the lower (upper) limit of the expected 68 % C. L. interval from the cross-section analysis.

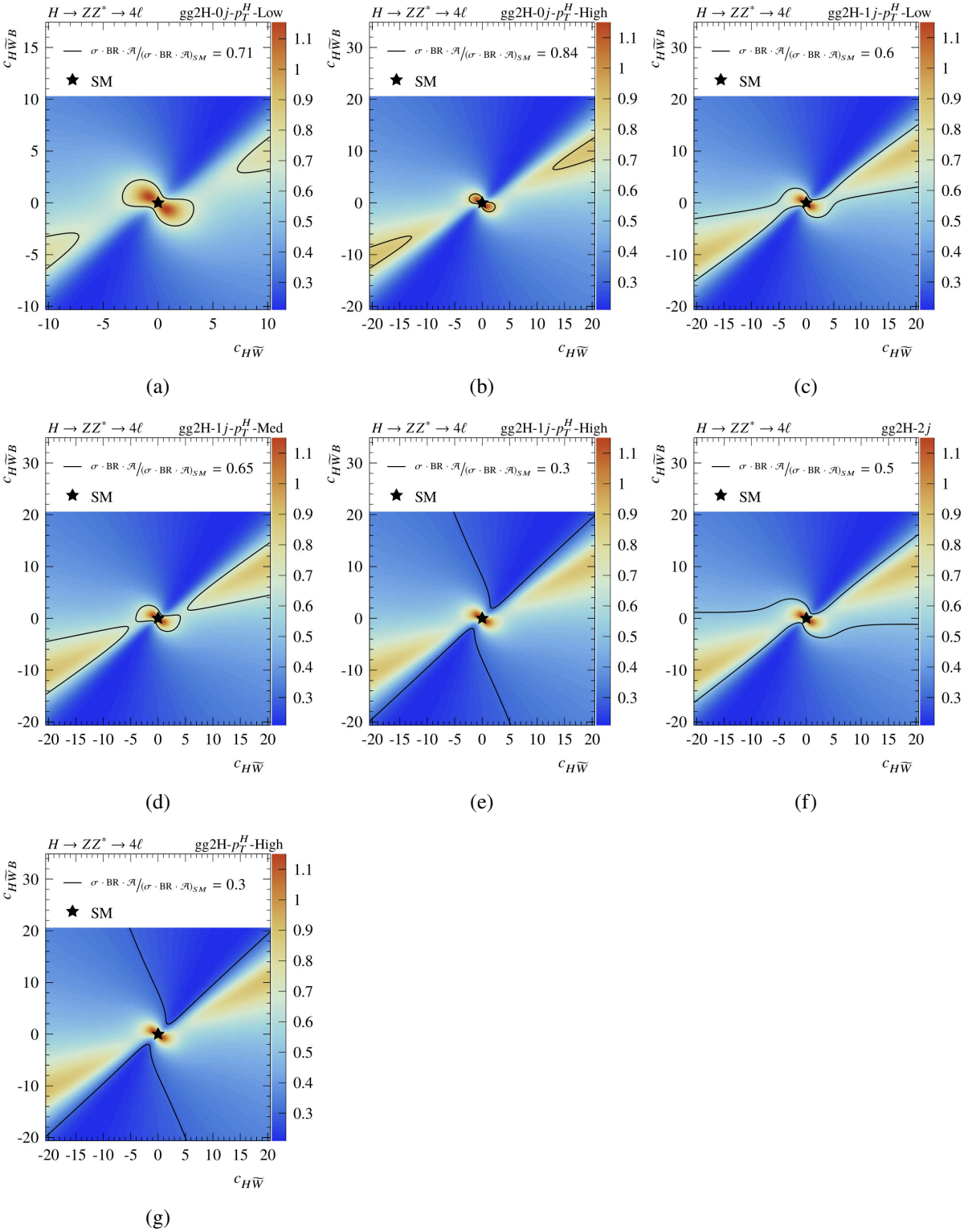

Figure D.15: The two-dimensional projections of the expected event yield relative to the SM prediction onto the $c_{H\widetilde{W}}$-$c_{H\widetilde{W}B}$ plane for the full signal model in the various gg2H production bins of the Reduced-Stage-1.1 scheme. The black solid (dashed) contours indicate the lower (upper) limit of the expected 68 % C. L. interval from the cross-section analysis.

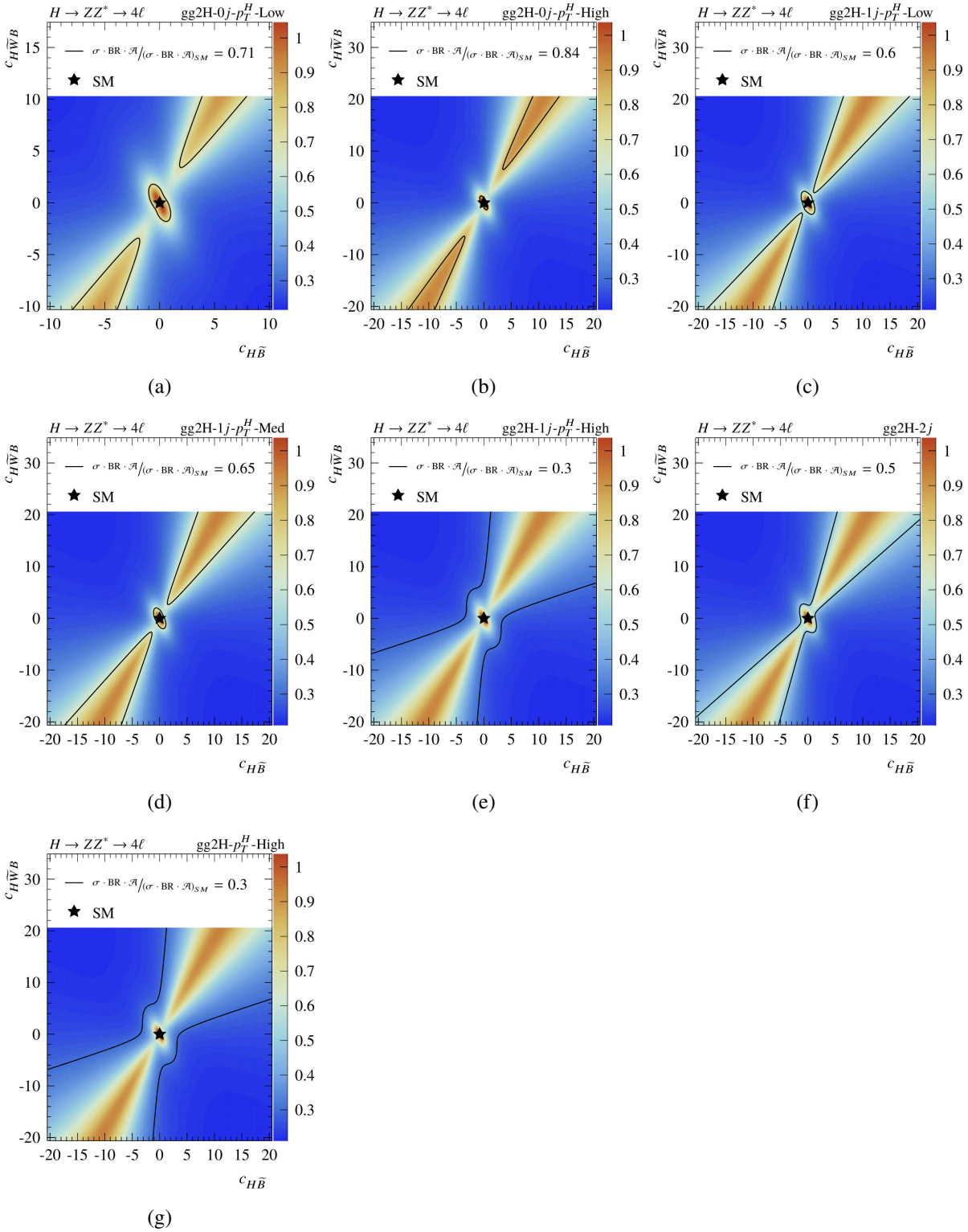

Figure D.16: The two-dimensional projections of the expected event yield relative to the SM prediction onto the $c_{H\widetilde{B}}$-$c_{H\widetilde{W}B}$ plane for the full signal model in the various gg2H production bins of the Reduced-Stage-1.1 scheme. The black solid (dashed) contours indicate the lower (upper) limit of the expected 68 % C. L. interval from the cross-section analysis.

qq2Hqq production:

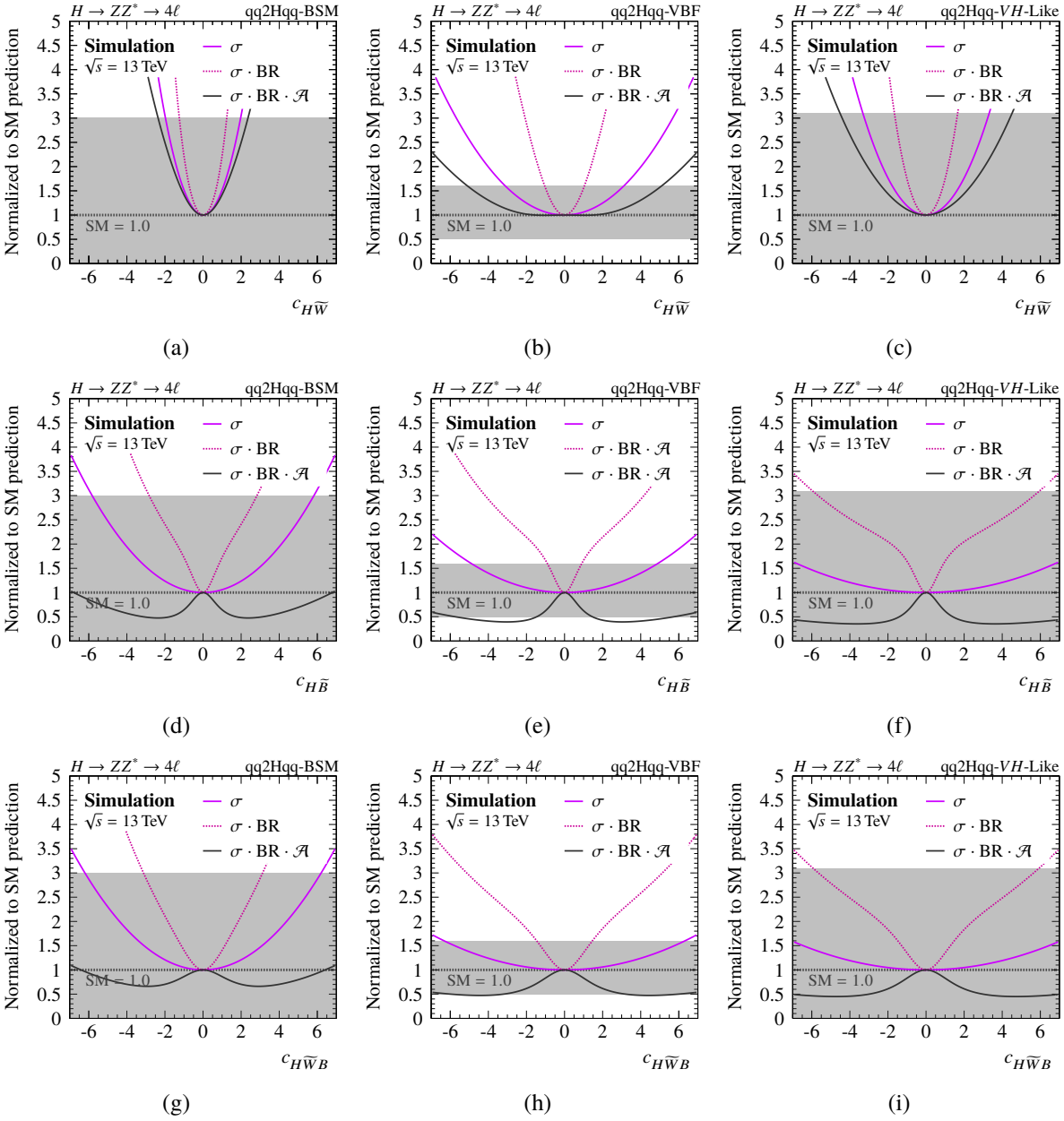

Figure D.17: The one-dimensional projection of the expected event yield relative to the SM prediction onto the Wilson coefficient (top) $c_{H\widetilde{W}}$, (middle) $c_{H\widetilde{B}}$ and (bottom) $c_{H\widetilde{W}B}$ in the qq2Hqq production bin of the Reduced-Stage-1.1 scheme. The gray bands indicate the expected 68 % C. L. interval from the cross-section analysis.

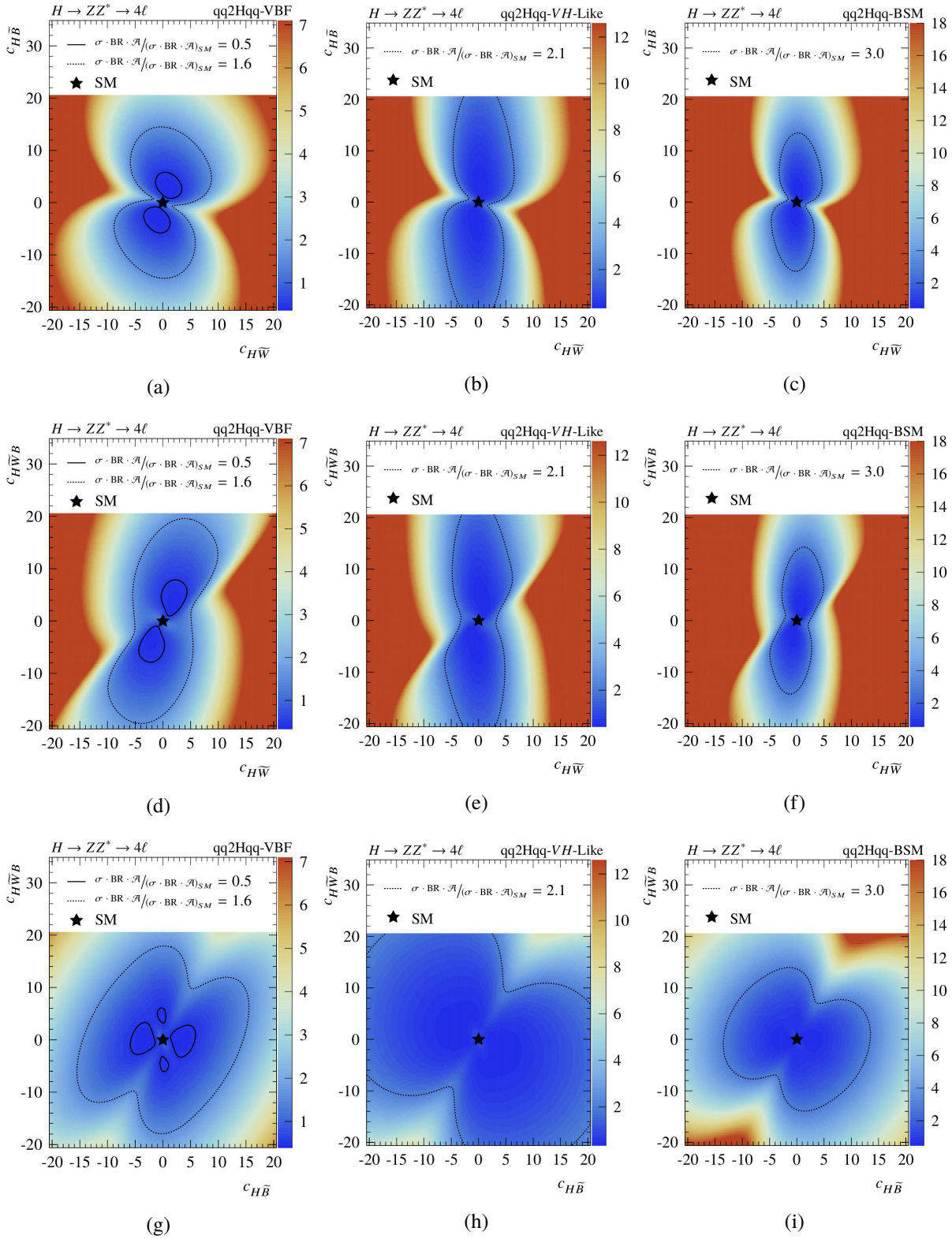

Figure D.18: The two-dimensional projections of the expected event yield relative to the SM prediction onto the (top) $c_{H\widetilde{W}}$-$c_{H\widetilde{B}}$ (middle) $c_{H\widetilde{W}}$-$c_{H\widetilde{W}B}$ and (bottom) $c_{H\widetilde{W}B}$-$c_{H\widetilde{B}}$ plane for the full signal model in the qq2Hqq particle-level production bins of the Reduced-Stage-1.1 scheme. The black solid (dashed) contours indicate the lower (upper) limit of the expected 68 % C. L. interval from the cross-section analysis.

D.5 EFT Parameterization with $C\mathcal{P}$-Even Operators

This section comprises additional information on the parameterization of the EFT signal model in the $C\mathcal{P}$-even BSM scenario. This information are based on the work of Verena Maria Walbrecht and can be found in Reference [459].

D.5.1 The Complete EFT Signal Model

In the $C\mathcal{P}$-even scenario, the full EFT signal model for each particle-level production bin p is found by multiplying the equations for the production cross-section $\sigma^p(\boldsymbol{c})$, the decay branching ratio $\mathrm{BR}^{4\ell}(\boldsymbol{c})$ and the signal acceptance $\mathcal{A}^p(\boldsymbol{c})$. The latter is given by a three-dimensional Lorenztian function $f(\boldsymbol{c})$.

$$f(\boldsymbol{c}) = \alpha_0 + \frac{(\alpha_1)^2}{\alpha_2 + \sum\limits_i \delta_i \cdot (c_i + \beta_i)^2 + \sum\limits_{i,j\geq j} \delta_{(i,j)} \cdot c_i c_j + \delta_{\substack{(i,j,k)\\ i<j<k}} \cdot c_i c_j c_k}. \tag{D.1}$$

The corresponding fit parameters are summarized in Table D.10.

Table D.10: Fit parameters for the three-dimensional parameterization signal acceptance for the $C\mathcal{P}$-even Wilson coefficients c_{HW}, c_{HB} and c_{HWB}.

Parameter	Fit result	Parameter	Fit result
α_0	0.153 ± 0.003	δ_{HW}	0.614 ± 0.027
α_1	0.874 ± 0.010	δ_{HB}	2.294 ± 0.033
α_2	0.881 ± 0.019	δ_{HWB}	0.703 ± 0.029
β_{HW}	-0.133 ± 0.012	$\delta_{(HW,HB)}$	-1.210 ± 0.040
β_{HB}	-0.005 ± 0.005	$\delta_{(HW,HWB)}$	-1.220 ± 0.060
β_{HWB}	0.120 ± 0.011	$\delta_{(HB,HWB)}$	0.080 ± 0.070
		$\delta_{(HW,HB,HWB)}$	0.050 ± 0.060

Thus, the final parameterization for complete EFT signal model in the $C\mathcal{P}$-even scenario reads

$$\begin{aligned}\left(\sigma^p \cdot \mathrm{BR}^{4\ell} \cdot \mathcal{A}^p\right)(\boldsymbol{c}) = &\left(\sigma^{p,\texttt{(N)NLO}} \cdot \mathrm{BR}^{4\ell,\texttt{NLO}} \cdot \mathcal{A}^p\right)_{SM} \\ &\cdot \left(1 + \sum_i A_i^p c_i + \sum_{i,j\geq i} B_{ij}^p c_i c_j\right) \cdot \frac{1 + \sum\limits_i A_i^{4\ell} c_i + \sum\limits_{i,j\geq i} B_{ij}^{4\ell} c_i c_j}{1 + \sum\limits_i A_i^{\mathrm{tot}} c_i + \sum\limits_{i,j\geq i} B_{ij}^{\mathrm{tot}} c_i c_j} \\ &\cdot \left(\alpha_0 + \frac{(\alpha_1)^2}{\alpha_2 + \sum\limits_i \delta_i \cdot (c_i + \beta_i)^2 + \sum\limits_{i,j\geq i} \delta_{(i,j)} \cdot c_i c_j + \delta_{\substack{(i,j,k)\\ i>j>k}} \cdot c_i c_j c_k}\right).\end{aligned} \tag{D.2}$$

D.5.2 Projections of the $C\mathcal{P}$-Even Signal Model

gg2H production:

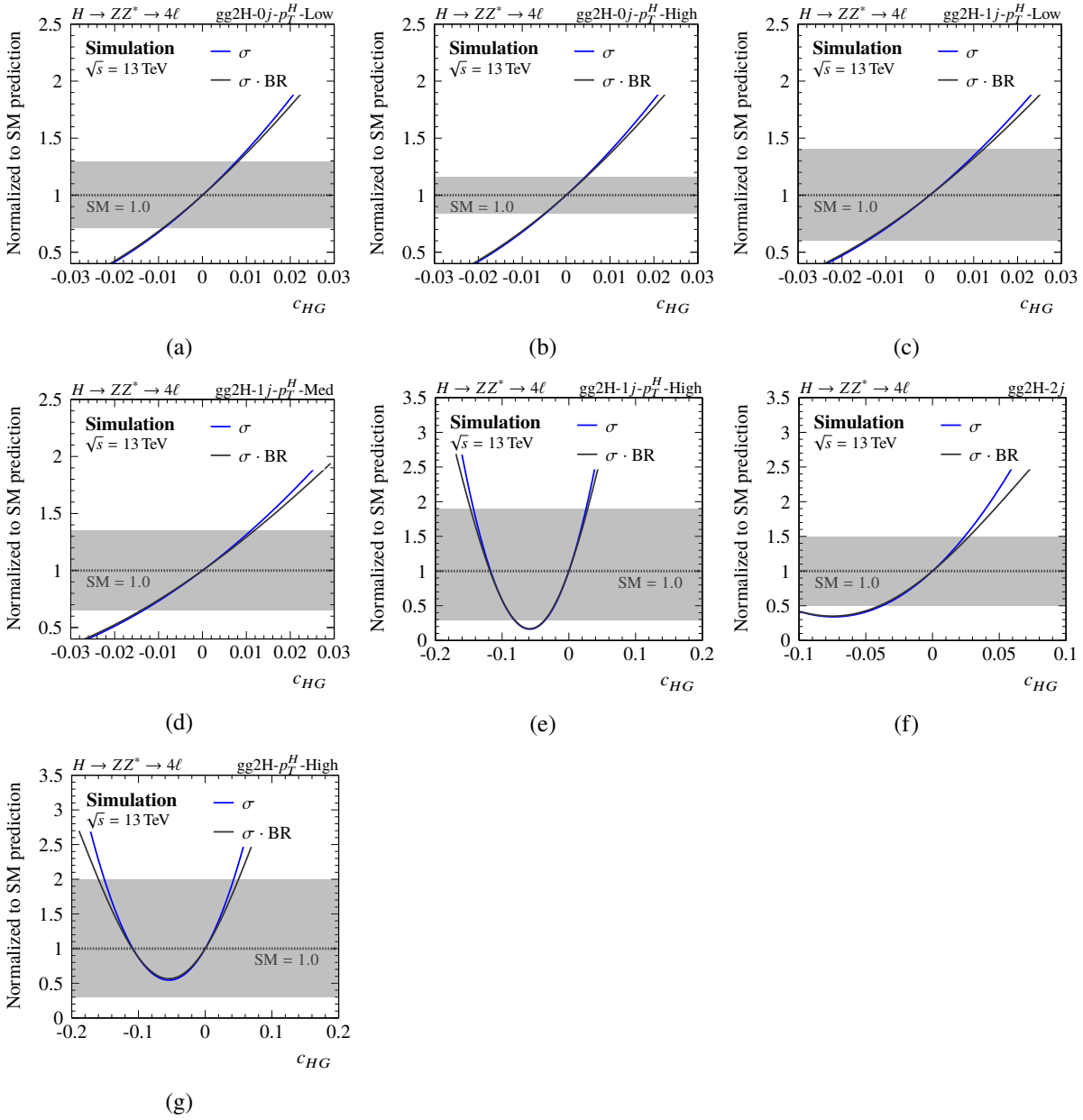

Figure D.19: The one-dimensional projection of the expected event yield relative to the SM prediction onto the c_{HG} axis in the various gg2H particle-level production bins of the Reduced-Stage-1.1 scheme. The gray bands indicate the expected 68 % C. L. interval from the cross-section analysis.

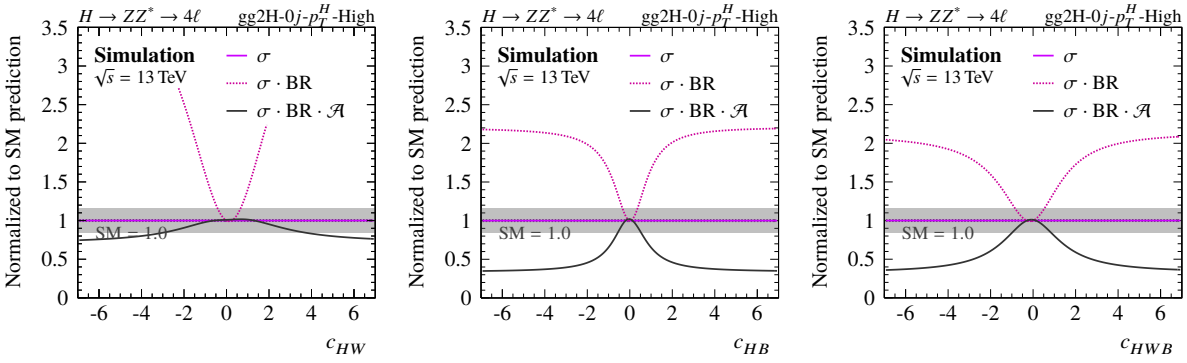

(a) (b) (c)

Figure D.20: The one-dimensional projection of the expected event yield relative to the SM prediction onto the Wilson coefficient (a) c_{HW}, (b) c_{HB} and (c) c_{HWB} in the gg2H-0j-p_T^H-High production bin of the Reduced-Stage-1.1 scheme. The gray band indicates the expected 68 % C. L. interval from the cross-section analysis.

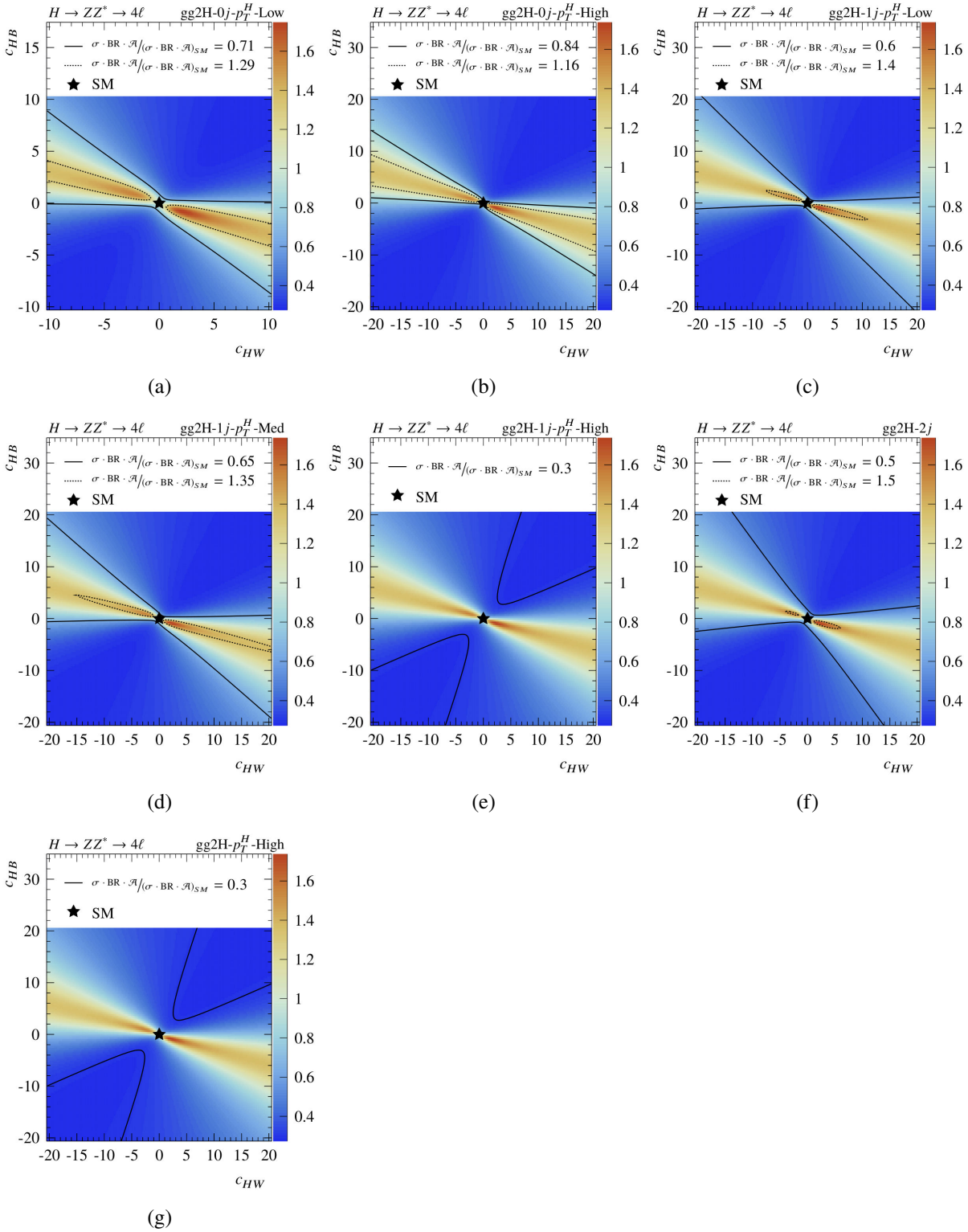

Figure D.21: The two-dimensional projections of the expected event yield relative to the SM prediction onto the c_{HW}-c_{HB} plane for the full signal model in the various gg2H production bins of the Reduced-Stage-1.1 scheme. The red (blue) contours indicate the upper (lower) limit of the expected 68 % C. L. interval from the cross-section analysis in the respective bin.

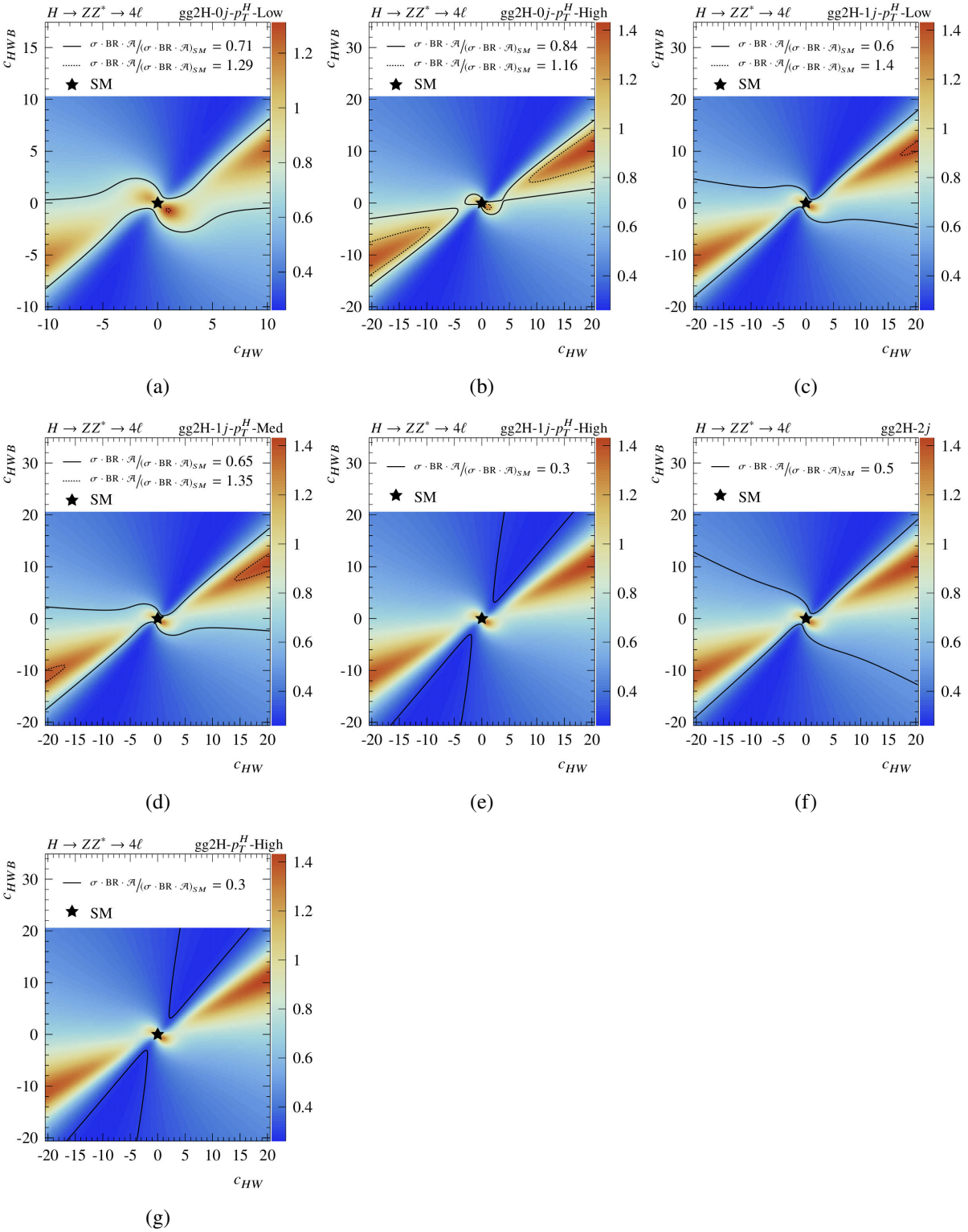

Figure D.22: The two-dimensional projections of the expected event yield relative to the SM prediction onto the c_{HW}-c_{HWB} plane for the full signal model in the various gg2H production bins of the Reduced-Stage-1.1 scheme. The red (blue) contours indicate the upper (lower) limit of the expected 68 % C. L. interval from the cross-section analysis in the respective bin.

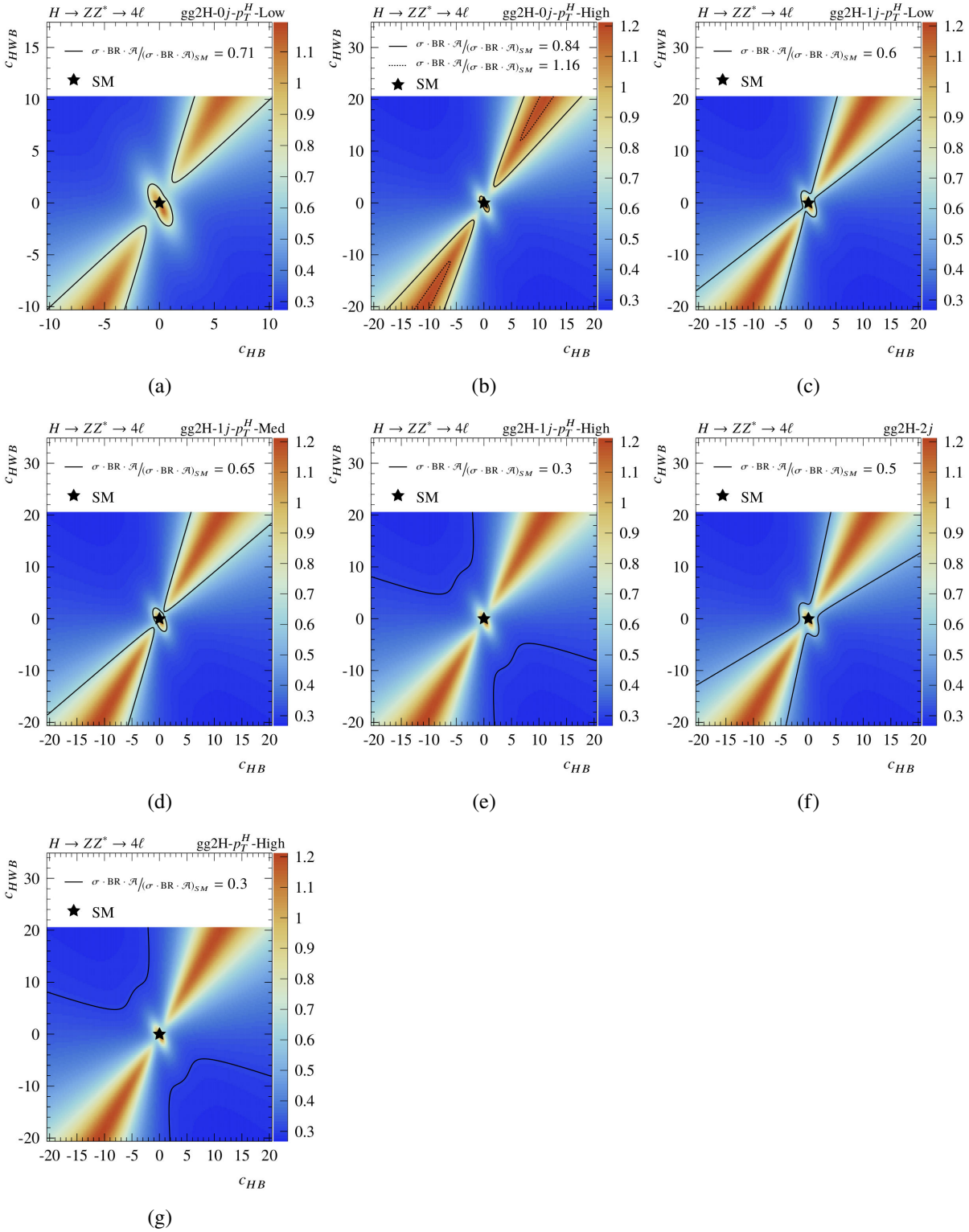

Figure D.23: The two-dimensional projections of the expected event yield relative to the SM prediction onto the c_{HB}-c_{HWB} plane for the full signal model in the various gg2H production bins of the Reduced-Stage-1.1 scheme. The red (blue) contours indicate the upper (lower) limit of the expected 68 % C. L. interval from the cross-section analysis in the respective bin.

qq2Hqq and VH-Lep production:

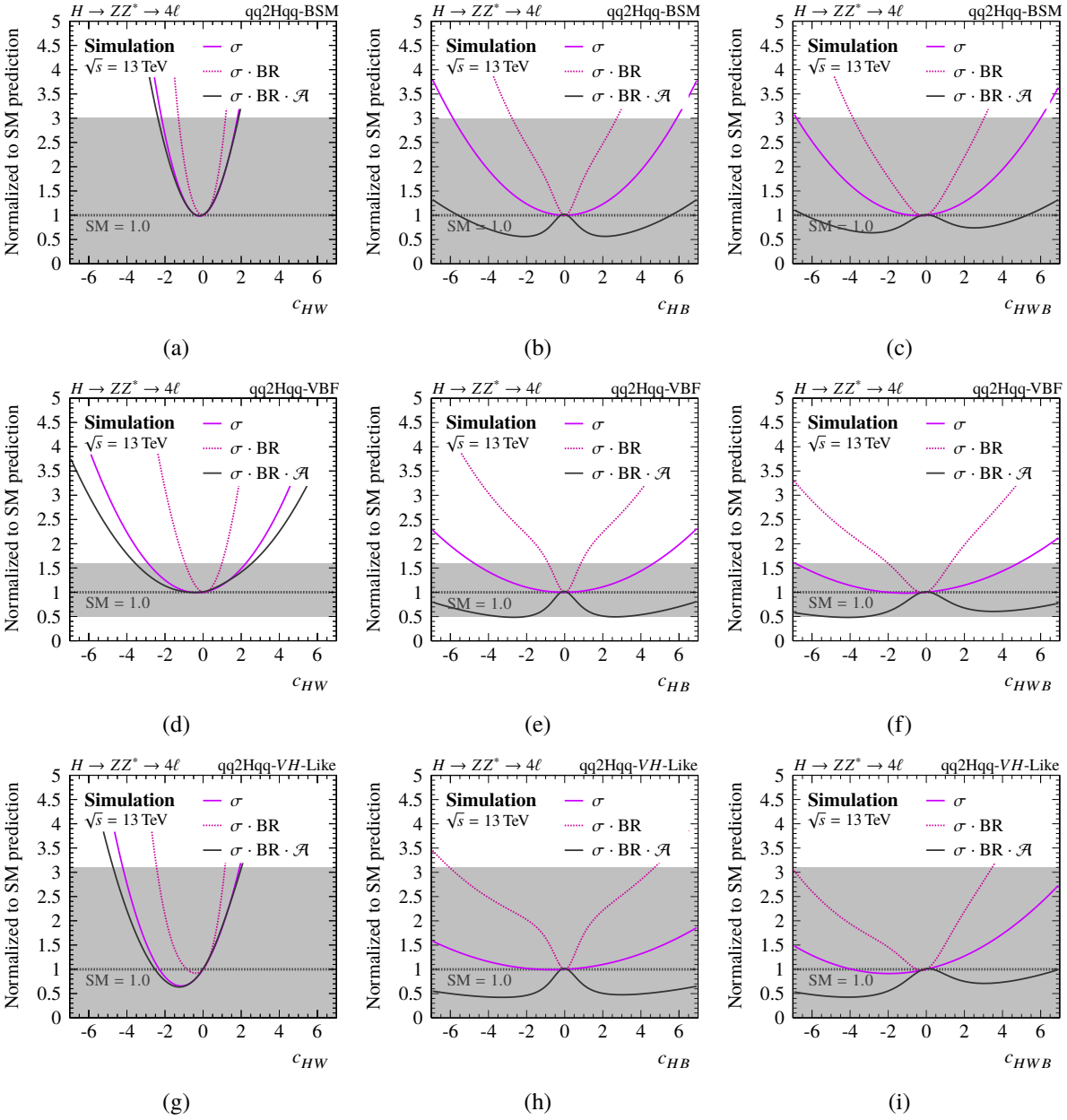

Figure D.24: The one-dimensional projection of the expected event yield relative to the SM prediction onto the Wilson coefficient (a) $c_{H\widetilde{W}}$, (b) $c_{H\widetilde{B}}$ and (c) $c_{H\widetilde{W}B}$ in the qq2Hqq particle-level production bins of the Reduced-Stage-1.1 scheme. The gray band indicates the expected 68 % C. L. interval from the cross-section analysis.

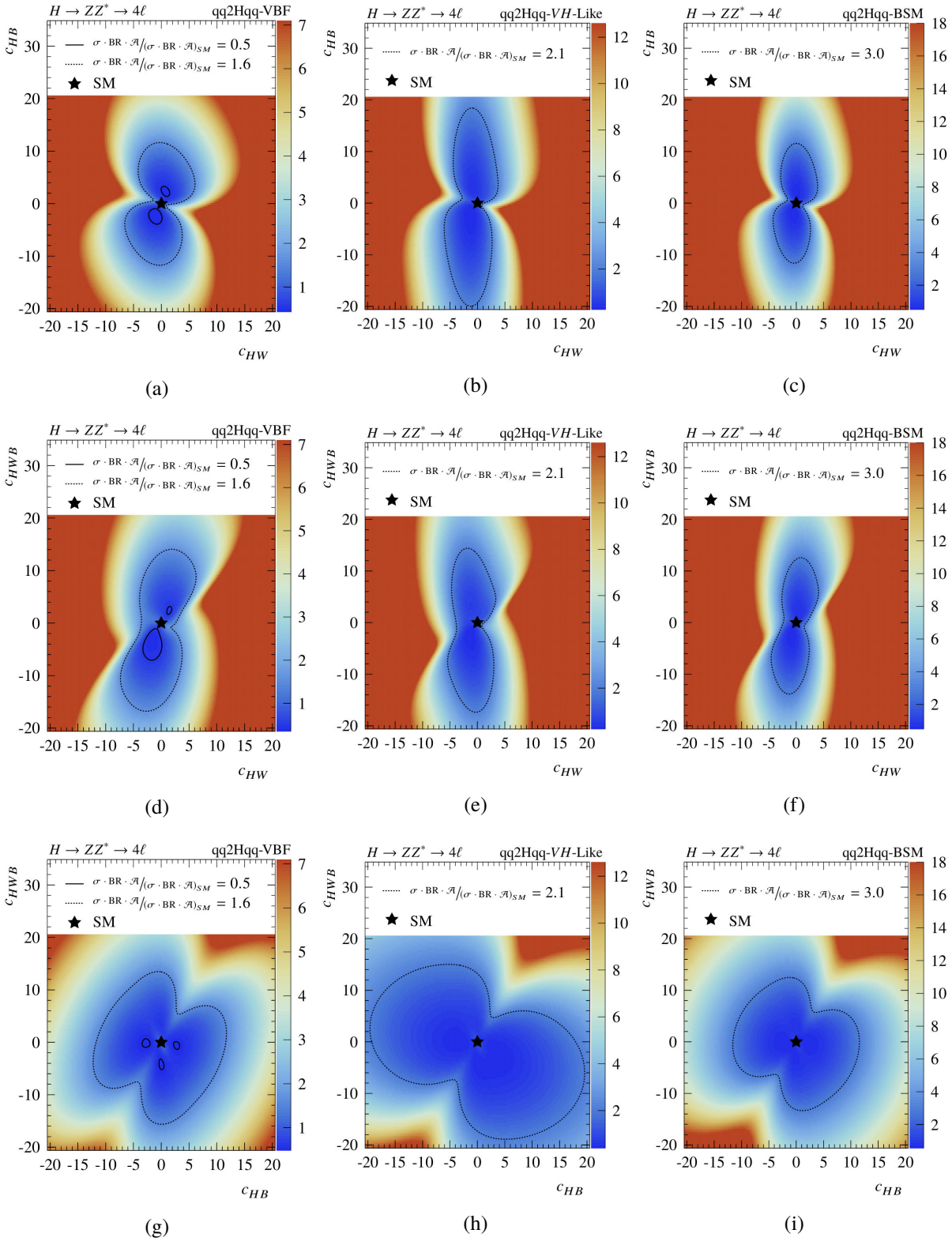

Figure D.25: The two-dimensional projections of the expected event yield relative to the SM prediction onto the (top) c_{HW}-c_{HB} (middle) c_{HW}-c_{HWB} and (bottom) c_{HB}-c_{HWB} plane for the full signal model in the qq2Hqq particle-level production bins of the Reduced-Stage-1.1 scheme. The red (blue) contours indicate the upper (lower) limit of the expected 68 % C. L. interval from the cross-section analysis in the respective bin.

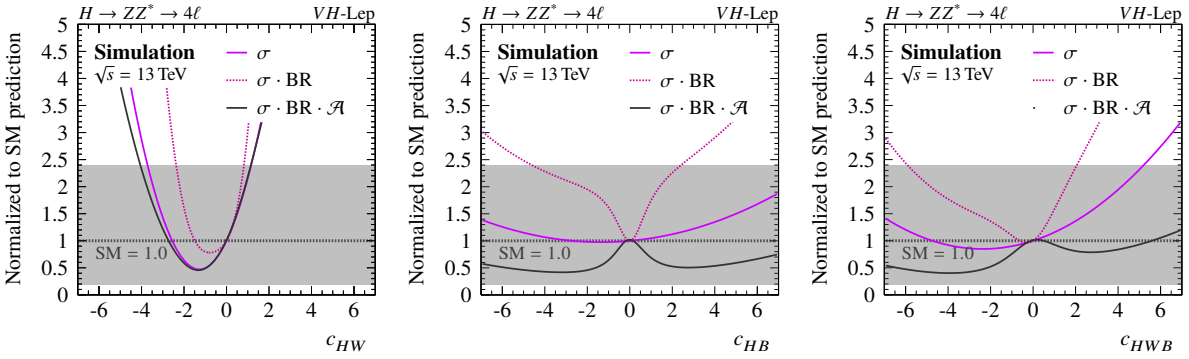

(a) (b) (c)

Figure D.26: The one-dimensional projection of the expected event yield relative to the SM prediction onto the Wilson coefficient (a) c_{HW}, (b) c_{HB} and (c) c_{HWB} in the VH-Lep particle-level production bin of the Reduced-Stage-1.1 scheme. The gray band indicates the expected 68 % C. L. interval from the cross-section analysis.

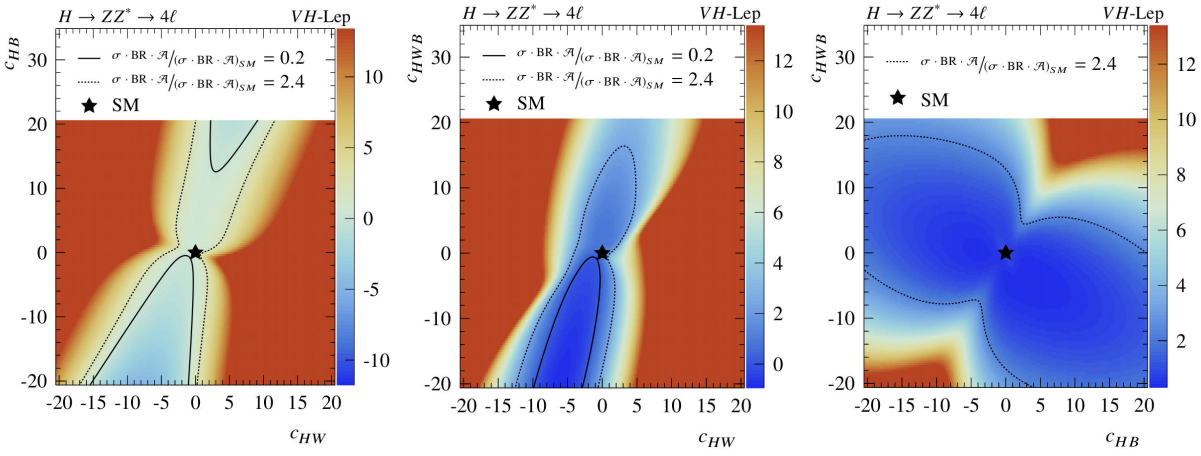

(a) (b) (c)

Figure D.27: The two-dimensional projections of the expected event yield relative to the SM prediction onto the (a) c_{HW}-c_{HB} (b) c_{HW}-c_{HWB} and (c) c_{HB}-c_{HWB} plane for the full signal model in the VH-Lep particle-level production bin of the Reduced-Stage-1.1 scheme. The red (blue) contours indicate the upper (lower) limit of the expected 68 % C. L. interval from the cross-section analysis in the respective bin.

***ttH* production:**

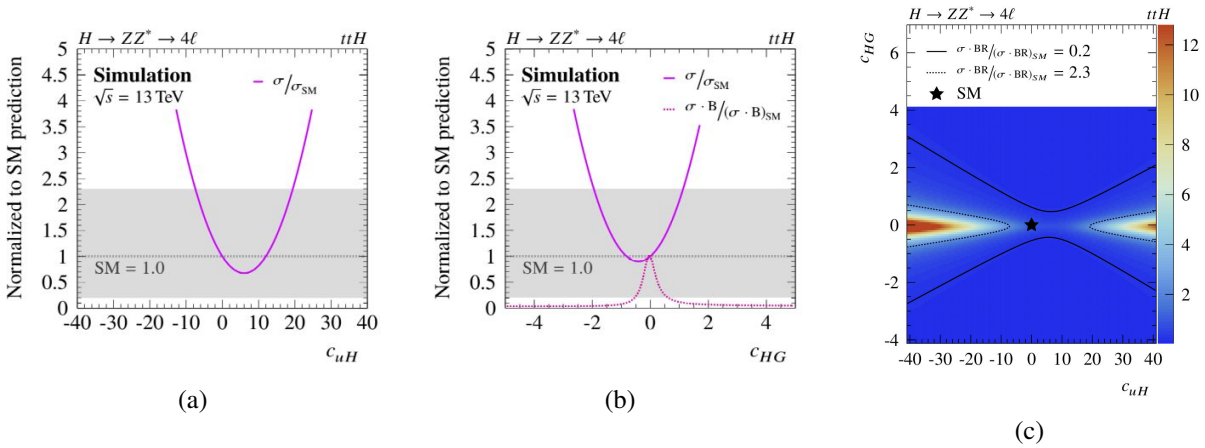

(a) (b) (c)

Figure D.28: The projections of the expected event yield relative to the SM prediction onto the (a) c_{uH} axis, (b) c_{HG} axis and (c) c_{uH}-c_{HG} plane in the ttH particle-level production bin of the Reduced-Stage-1.1 scheme. The gray band (red and blue contours) indicate(s) the expected 68 % C. L. interval from the cross-section analysis in the one-dimensional (two-dimensional) projections.

D.6 Systematic Uncertainties

D.6.1 QCD Scale Variations

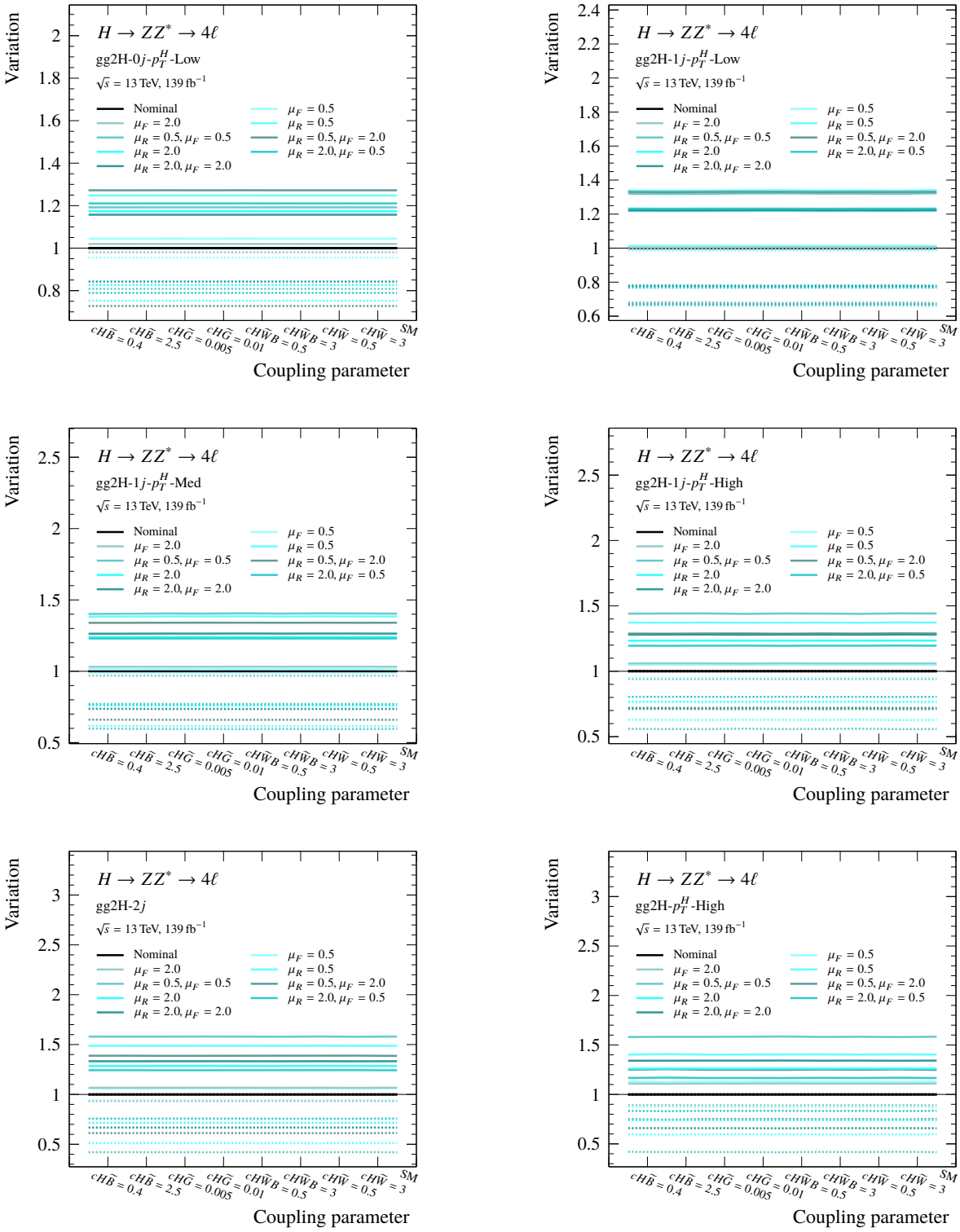

Figure D.29: QCD scale uncertainties in the gg2H production bins for different values of $C\mathcal{P}$-odd BSM coupling parameters.

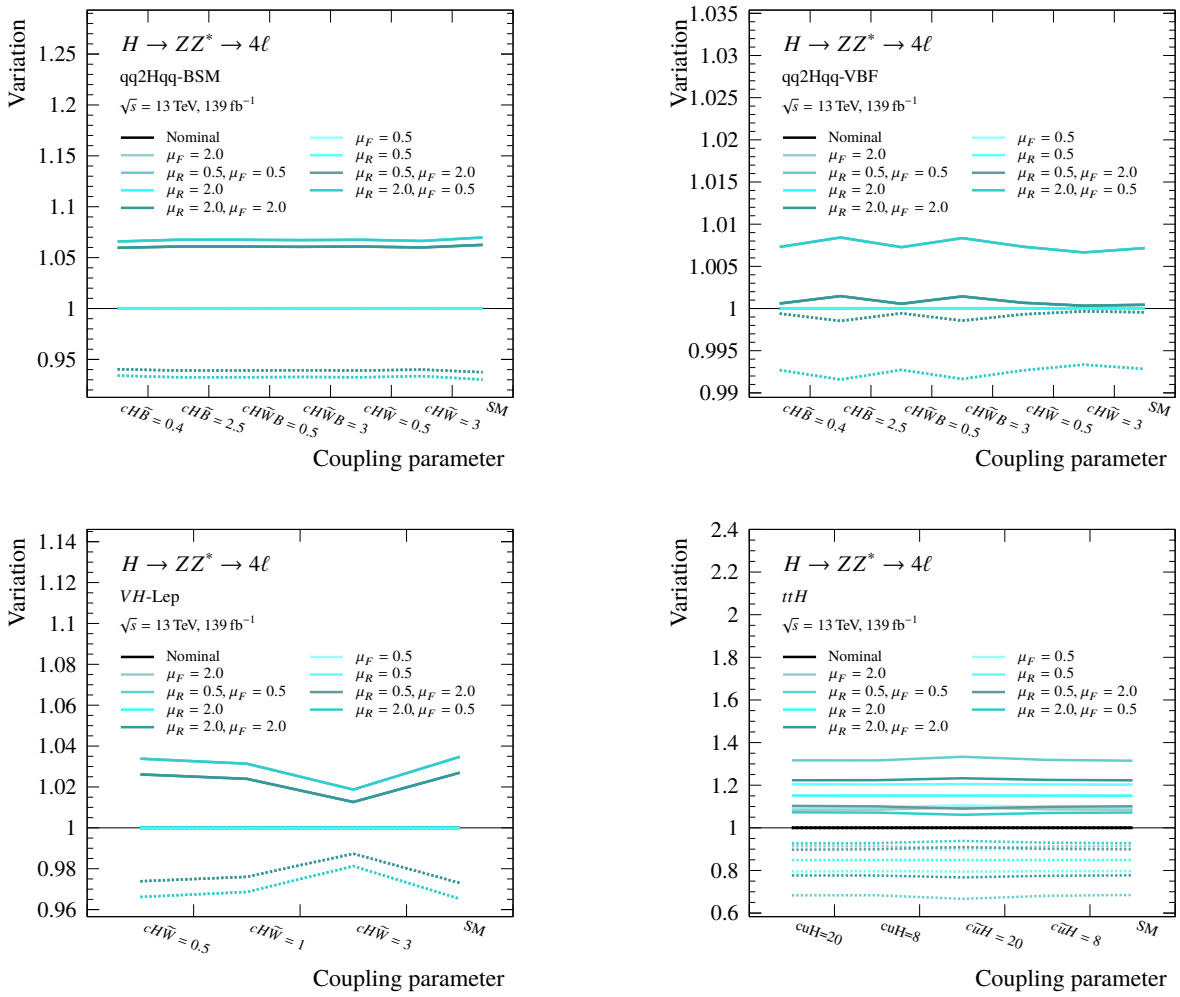

Figure D.30: QCD scale uncertainties in the qq2Hqq, VH-Lep and ttH production bins for different values of $C\mathcal{P}$-odd BSM coupling parameters.

D.6.2 PDF Variations

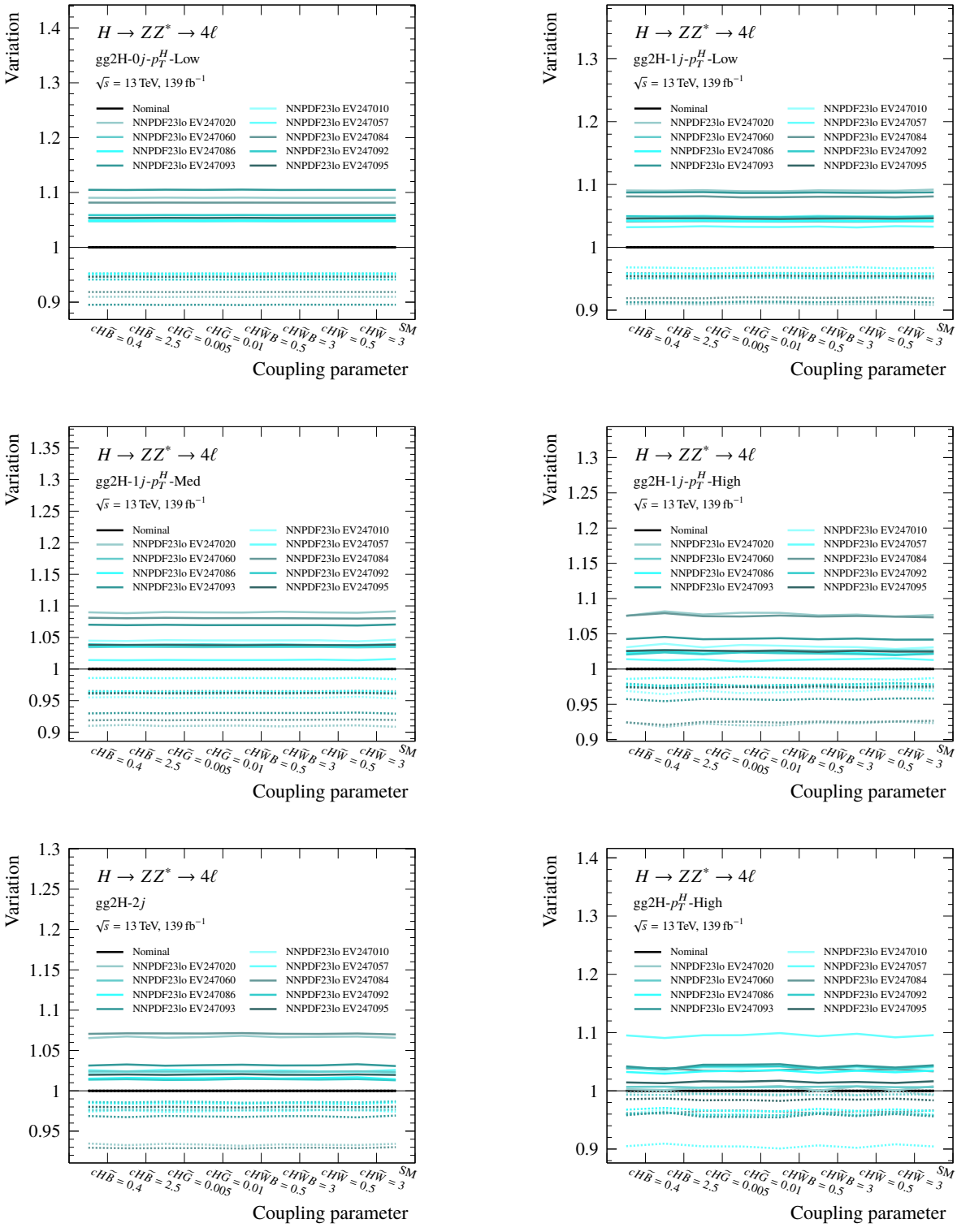

Figure D.31: PDF variation uncertainties in the gg2H production bins for different values of $C\mathcal{P}$-odd BSM coupling parameters..

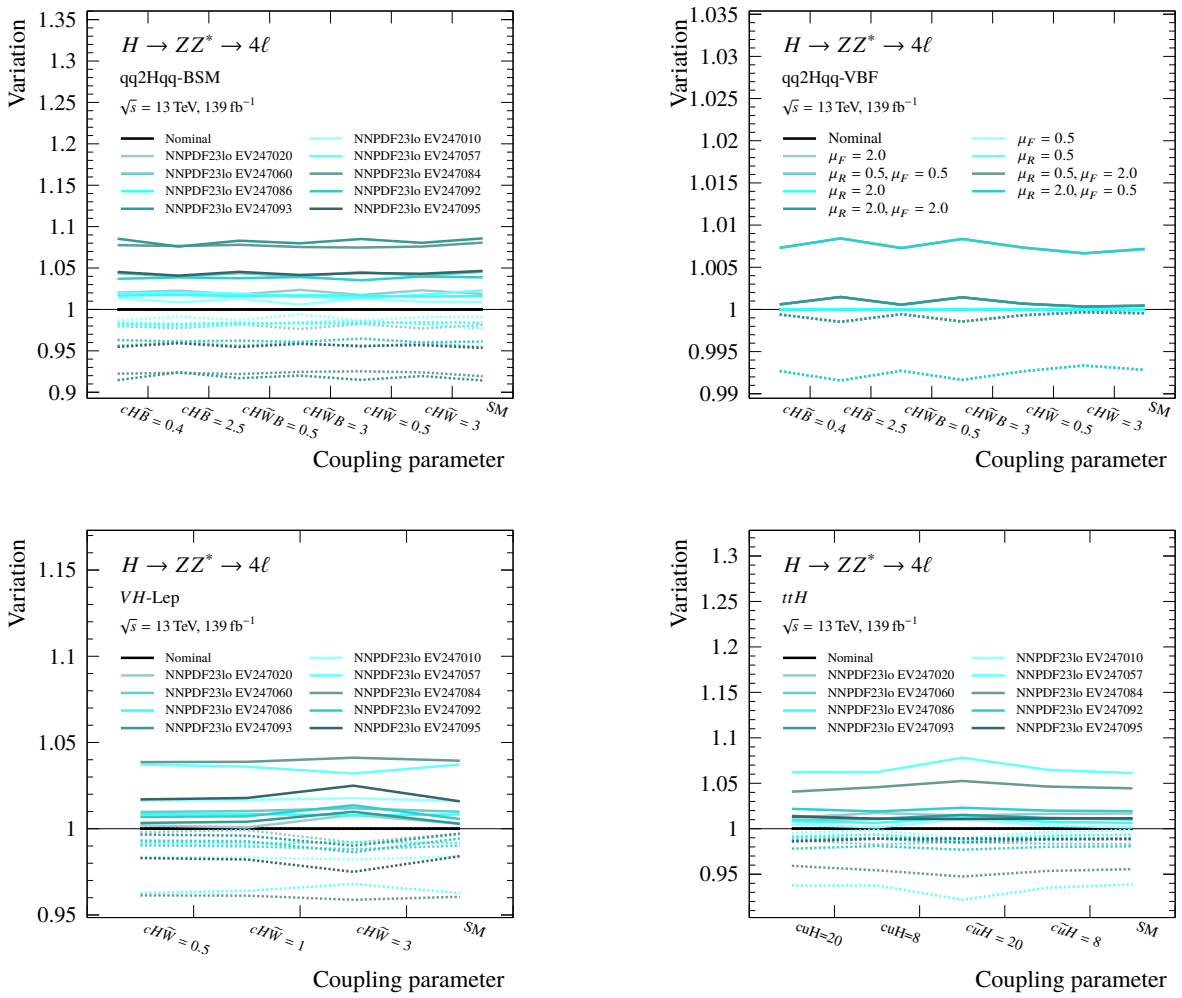

Figure D.32: PDF variation uncertainties in the qq2Hqq, VH-Lep and ttH production bins for different values of $C\mathcal{P}$-odd BSM coupling parameters.

APPENDIX E

Indirect Constraints on Possible $\mathcal{CP}$ Admixtures from Rate Measurements

E.1 Constraints on $\mathcal{CP}$-Mixing in the Top-Yukawa Coupling

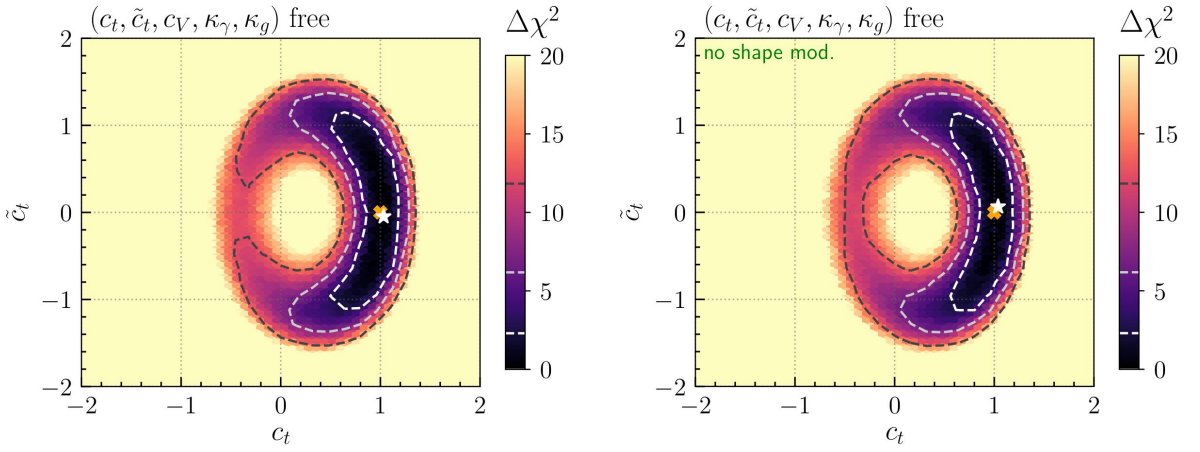

(a) (b)

Figure E.1: Fit results in the $(c_t\,,\,\tilde{c}_t)$ parameter plane for model 4 if Higgs-p_T-shape modifications in the $gg \to ZH$ production process due to a modified top-Yukawa coupling are (a) included and (b) excluded. The color corresponds to the $\Delta\chi^2$ value of the global fit and the 1σ , 2σ , and 3σ C. L. regions are shown as white, light-gray and dark-gray dashed contours, respectively. The best-fit point and the SM case are marked by a white star and an orange cross, respectively. Note the larger scale required to display the bottom plots.

E.2 Constraints from Global Fits

E.3 Model II

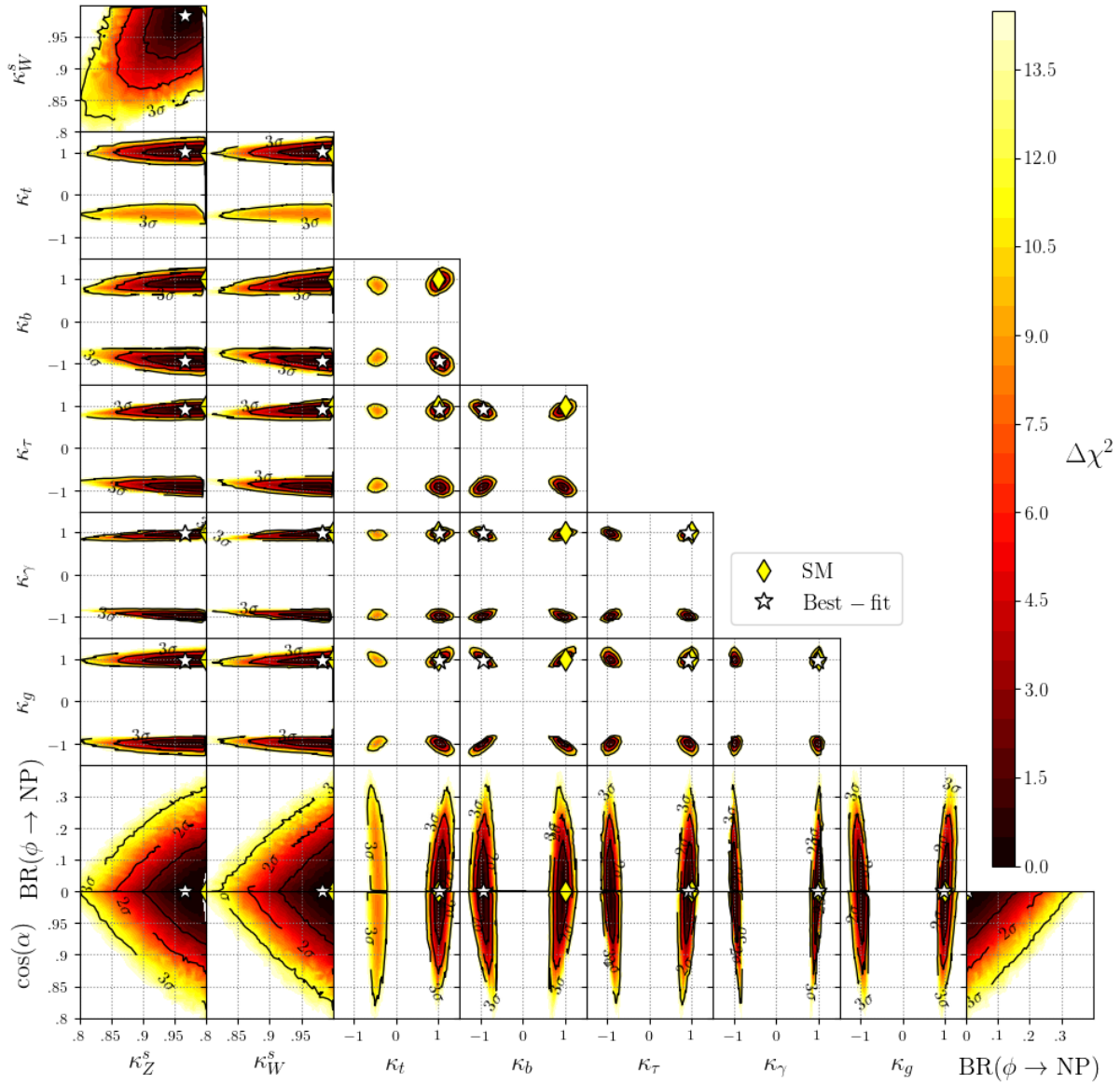

Figure E.2: The two-dimensional $\Delta\chi^2$ profiles for the parameters of model II(a) assuming $\kappa_{W,Z}^s \leq 1$.

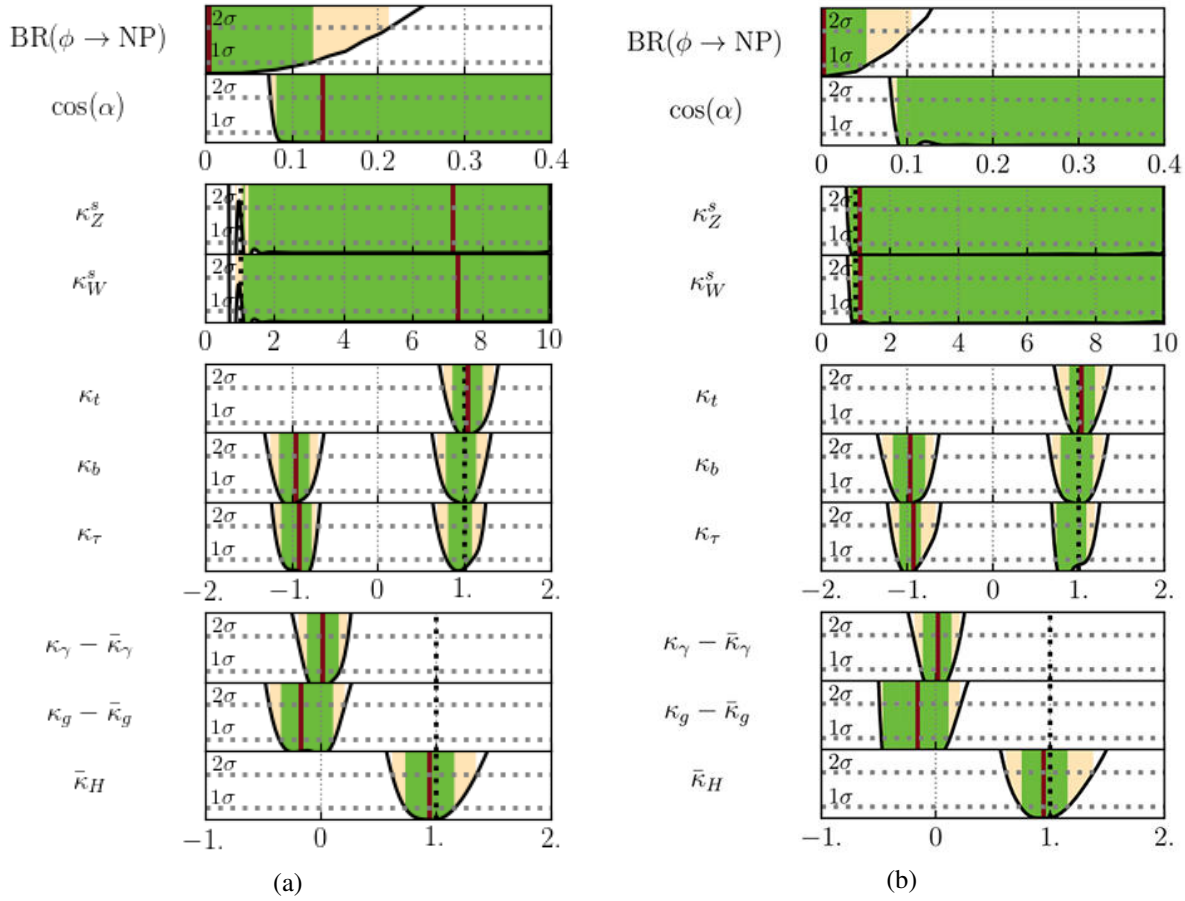

Figure E.3: The one-dimensional $\Delta\chi^2$ profiles for the fit parameters of (a) model II(b) and (b) model II(c) of the general $C\mathcal{P}$-admixture parameterization. The derived scale factors for the Higgs boson couplings to photons and gluons, $\bar{\kappa}_\gamma$ and $\bar{\kappa}_g$, are subtracted from the free fit values, κ_γ and κ_g, respectively. $\bar{\kappa}_H$ is the derived scale factor for the total width the Higgs boson calculated from the model parameters.

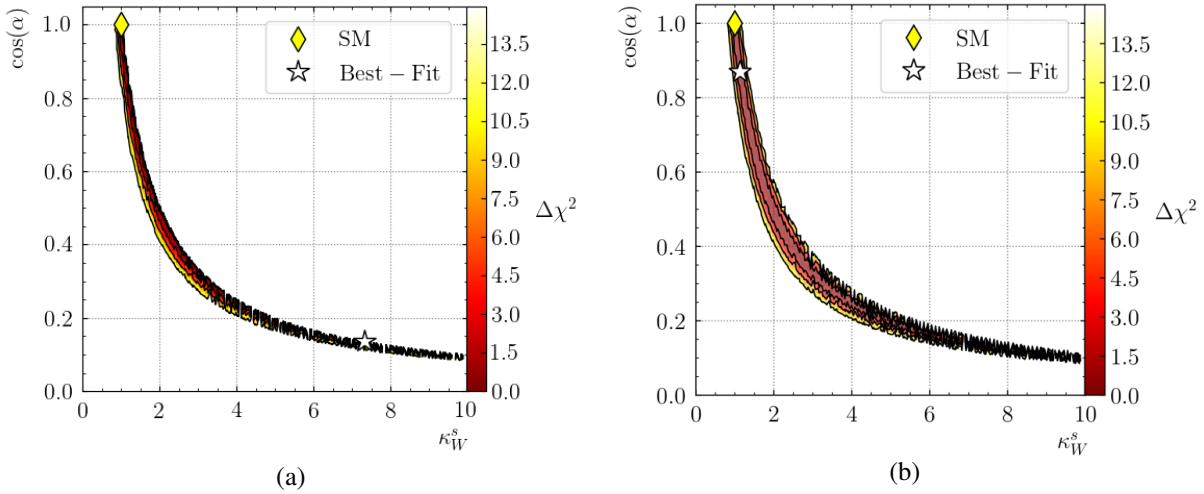

Figure E.4: The two-dimensional $\Delta\chi^2$ profile for (a) model II(b) and (b) model II(c) of the general $C\mathcal{P}$-admixture parameterization in the (κ_W^s , cos α) plane.

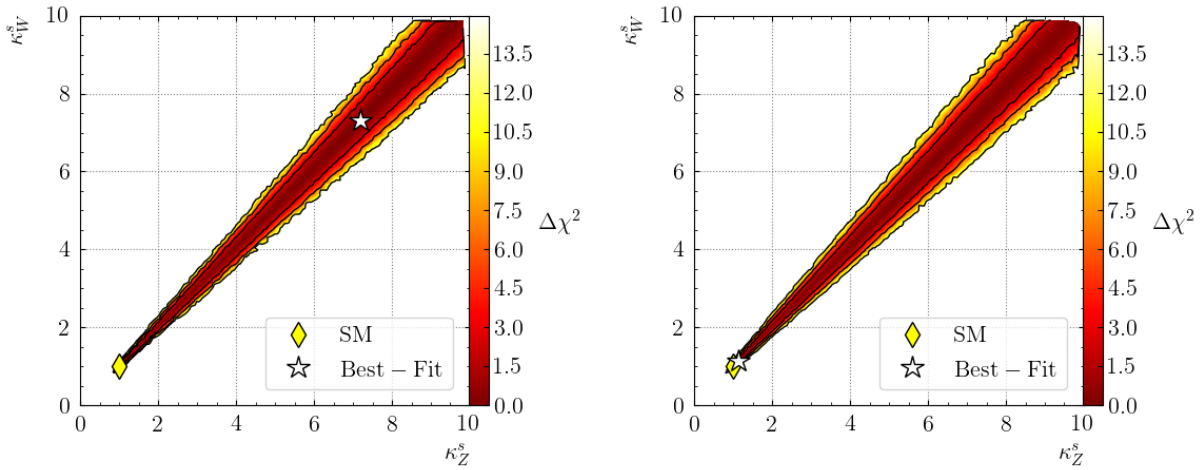

(a) (b)

Figure E.5: The two-dimensional $\Delta\chi^2$ profile for (a) model II(b) and (b) model II(c) of the general $C\mathcal{P}$-admixture parameterization in the $(\kappa_Z^s\,,\kappa_W^s)$ plane.

Table E.1: The best-fit values and 68 % and 95 % C. L. regions for the fit parameters of model II(b) and model II(c) obtained from the one-dimensional $\Delta\chi^2$ profiles. For $\kappa_b\,,\kappa_\tau\,,\kappa_\gamma$ and κ_g only absolute values are given.

Parameter	Model II(b)			Model II(c)		
	best-fit	68 % C. L.	95 % C. L.	best-fit	68 % C. L.	95 % C. L.
$\cos(\alpha)$	0.14	$^{+0.86}_{-0.05}$	$^{+0.86}_{-0.06}$	0.87	$^{+0.23}_{-0.78}$	$^{+0.23}_{-0.79}$
κ_Z^s	7.18	$^{+2.82}_{-6.29}$	$^{+2.82}_{-6.49}$	1.12	$^{+8.88}_{-0.29}$	$^{+8.88}_{-0.37}$
κ_W^s	7.31	$^{+2.69}_{-6.62}$	$^{+2.69}_{-6.62}$	1.14	$^{+8.86}_{-0.28}$	$^{+8.86}_{-0.34}$
κ_t	1.04	$^{+0.20}_{-0.17}$	$^{+0.3}_{-0.27}$	1.03	$^{+0.16}_{-0.17}$	$^{+0.28}_{-0.27}$
$\lvert\kappa_b\rvert$	0.96	$^{+0.21}_{-0.20}$	$^{+0.31}_{-0.3}$	0.96	$^{+0.20}_{-0.20}$	$^{+0.33}_{-0.3}$
$\lvert\kappa_\tau\rvert$	0.92	$^{+0.20}_{-0.10}$	$^{+0.23}_{-0.12}$	0.92	$^{+0.19}_{-0.11}$	$^{+0.27}_{-0.16}$
$\lvert\kappa_\gamma\rvert$	0.98	$^{+0.16}_{-0.12}$	$^{+0.21}_{-0.18}$	0.98	$^{+0.16}_{-0.18}$	$^{+0.21}_{-0.20}$
$\lvert\kappa_g\rvert$	0.98	$^{+0.21}_{-0.19}$	$^{+0.29}_{-0.25}$	0.98	$^{+0.21}_{-0.19}$	$^{+0.29}_{-0.25}$
BR($\phi \to$ NP)	0.0	$^{+0.12}_{-0.0}$	$^{+0.21}_{-0.0}$	0.0	$^{+0.05}_{-0.0}$	$^{+0.1}_{-0.0}$
$\kappa_\gamma - \bar{\kappa}_\gamma$	0.02	$^{+0.15}_{-0.15}$	$^{+0.22}_{-0.23}$	0.02	$^{+0.12}_{-0.16}$	$^{+0.19}_{-0.21}$
$\kappa_g - \bar{\kappa}_g$	−0.17	$^{+0.3}_{-0.2}$	$^{+0.38}_{-0.27}$	−0.16	$^{+-0.13}_{-0.31}$	$^{+0.37}_{-0.33}$
$\bar{\kappa}_H$	0.94	$^{+0.22}_{-0.2}$	$^{+0.42}_{-0.32}$	0.94	$^{+0.21}_{-0.2}$	$^{+0.44}_{-0.33}$

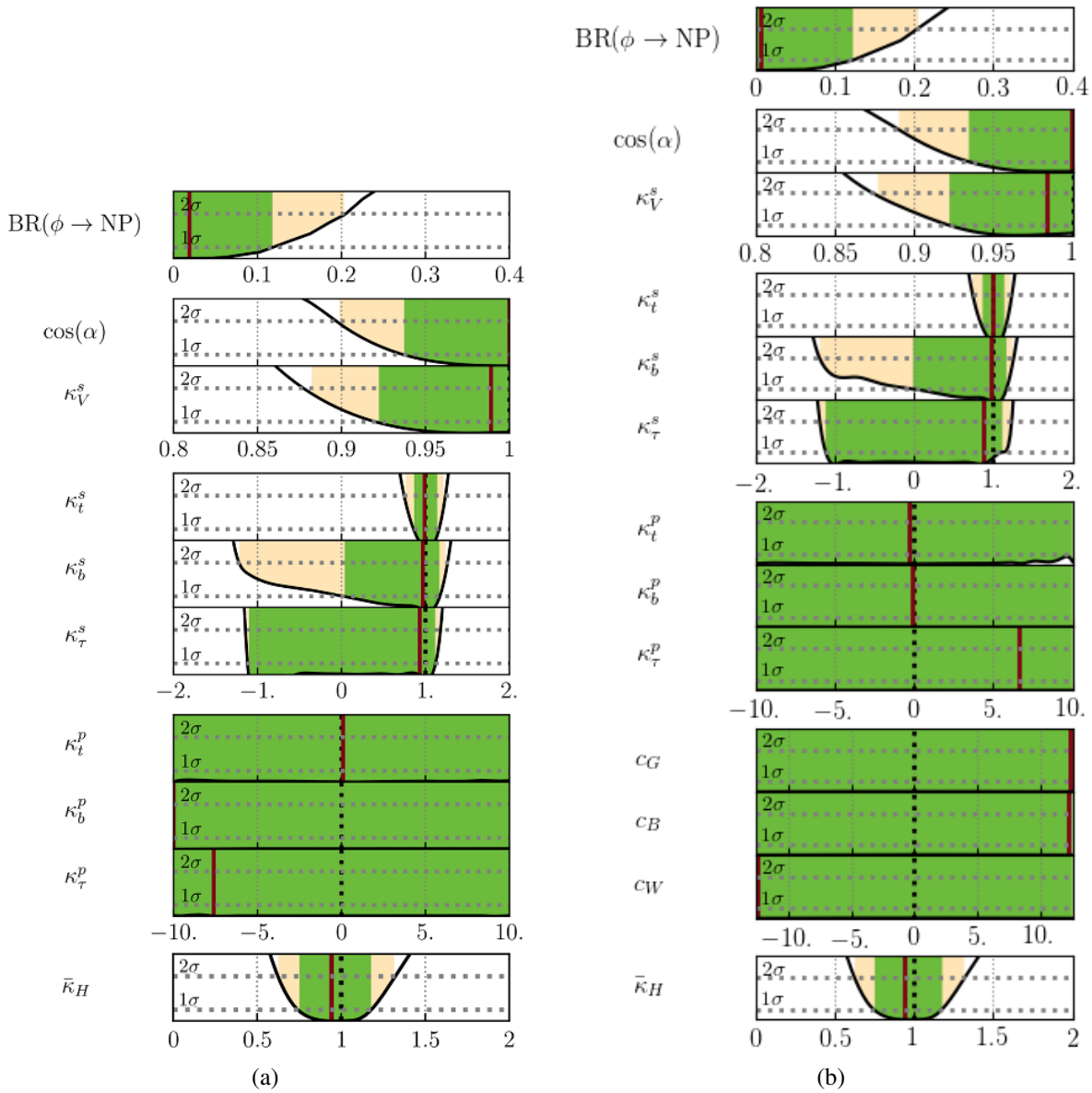

Figure E.6: The one-dimensional $\Delta\chi^2$ profiles for the sensitive parameters of (a) model III and (b) model IV of the general $C\mathcal{P}$-admixture parameterization. $\bar{\kappa}_H$ is the derived scale factor for the total width the Higgs boson calculated from the model parameters.

E.4 Model III and Model IV

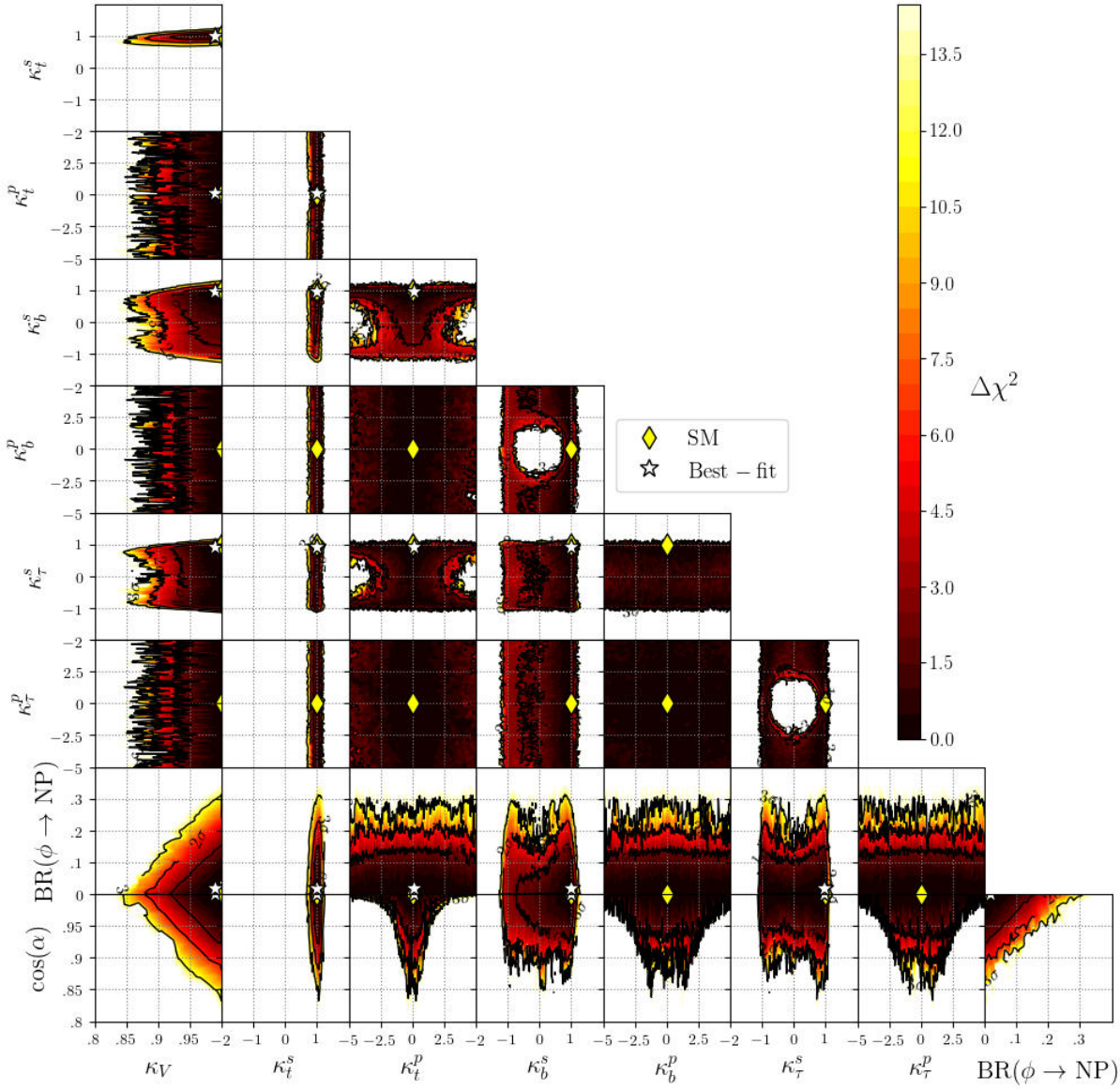

Figure E.7: The two-dimensional $\Delta\chi^2$ profiles for the free parameters of model III of the general $C\mathcal{P}$-admixture parameterization.

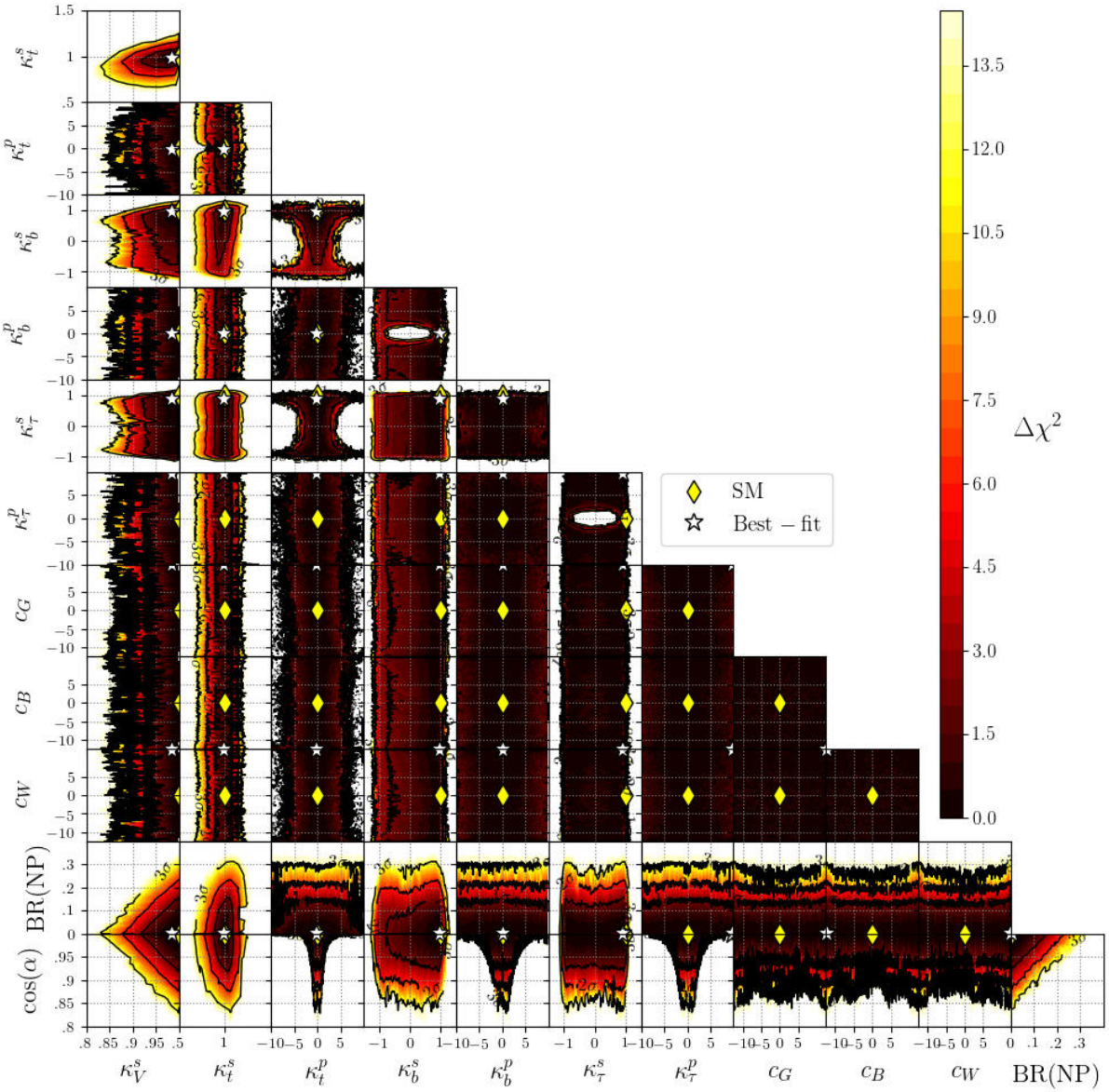

Figure E.8: The two-dimensional $\Delta\chi^2$ profiles for the free parameters of model IV of the general $C\mathcal{P}$-admixture parameterization.

E.5 Constraints from the $H \to 4\ell$ Decay Channel at ATLAS

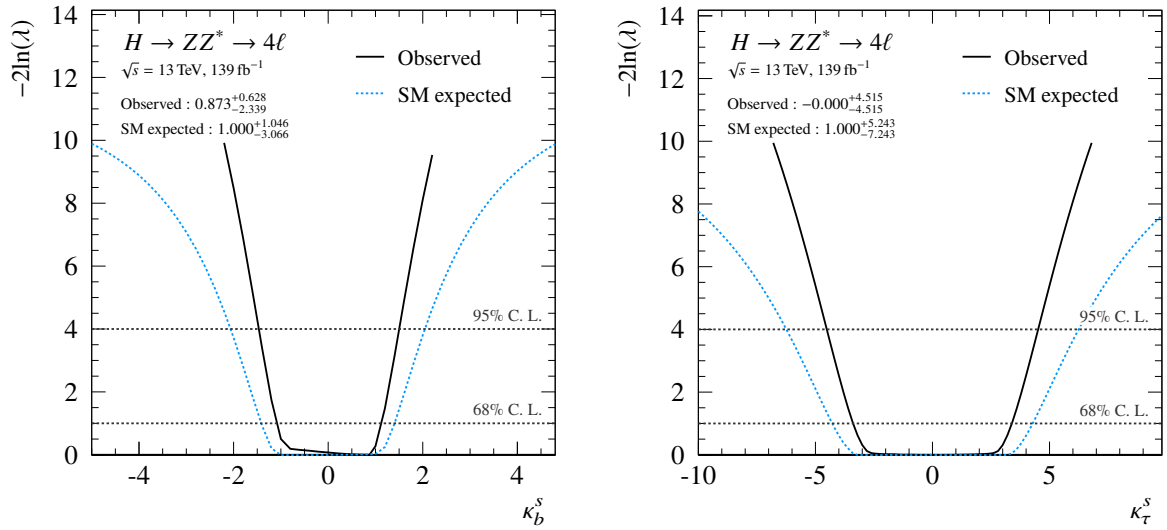

Figure E.9: The one-dimensional projections of the observed (black solid) and SM expected (blue dashed) fit result for the parameter (a) κ_b^s and (b) κ_τ^s of model IV of the general $\mathcal{CP}$-admixture parameterization for an integrated luminosity of 139 fb^1 of proton-proton collision data at a cms energy of $\sqrt{s} = 13$ TeV. The 68 % and 95 % C. I. are indicated by dashed horizontal lines. All fit parameters are allowed to float free in the fit.

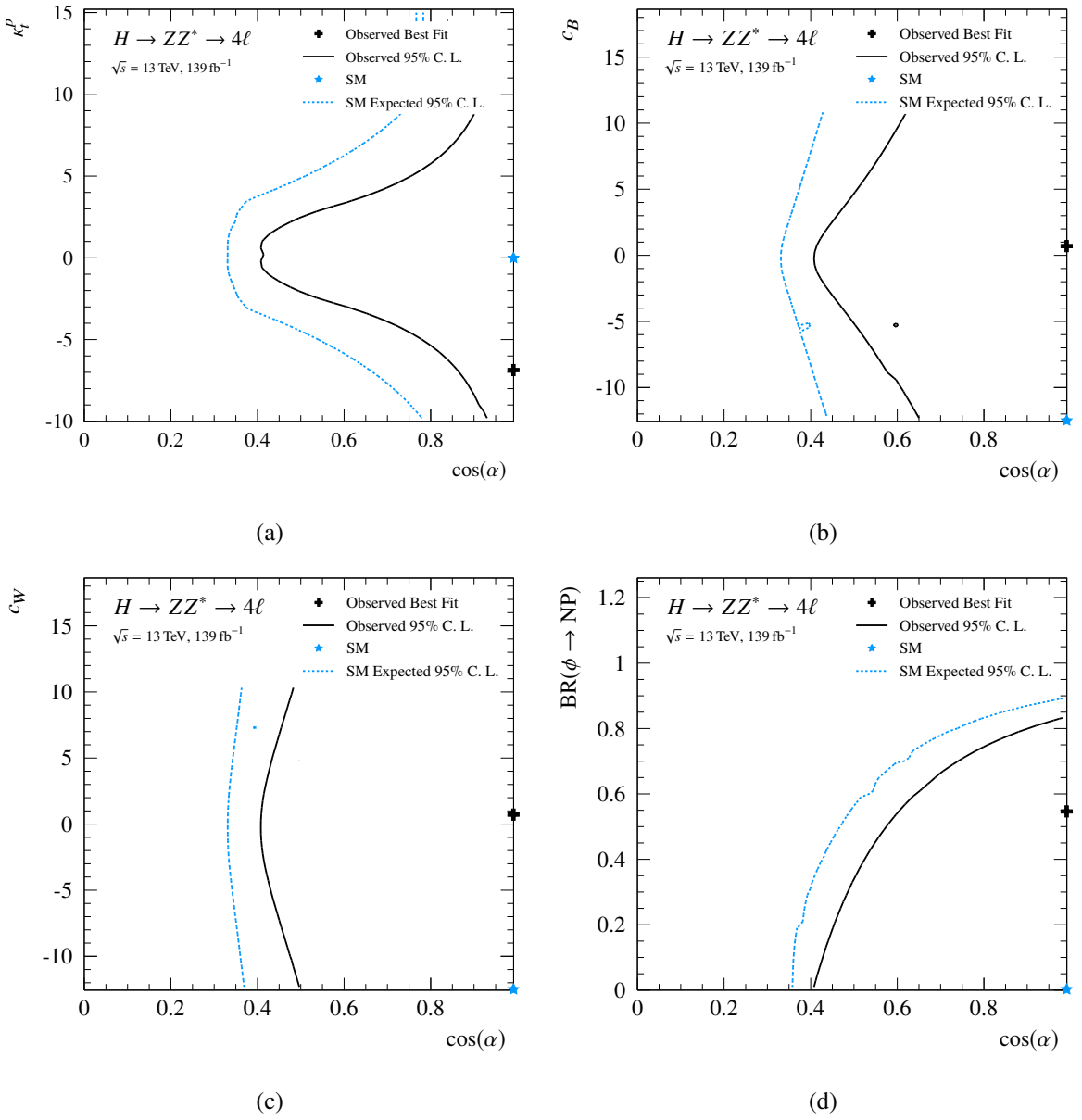

Figure E.10: Two-dimensional projections of the observed (black solid) and SM expected (blue dashed) fit result for the parameter planes (a) κ_t^P vs. $\cos\alpha$, (b) c_B vs. $\cos\alpha$, (c) c_W vs. $\cos\alpha$ and (d) BR($\phi \to$ NP) vs. $\cos\alpha$ of model IV of the general $C\mathcal{P}$-admixture parameterization for an integrated luminosity of 139 fb^1 of proton-proton collision data at a cms energy of $\sqrt{s} = 13$ TeV.

List of Figures

2.1 The particle content of the SM. . . . 4
2.2 The Feynman diagrams for the simplified QCD Lagrangian. . . . 9
2.3 Illustration of the Higgs potential. . . . 10
2.4 Illustration of the Higgs boson couplings. . . . 13
2.5 Parton distribution functions. . . . 14
2.6 Feynman diagrams for ggF and VBF SM Higgs boson production. . . . 15
2.7 Feynman diagrams for associated SM Higgs production with a weak gauge boson. . . . 15
2.8 Feynman diagrams for $t\bar{t}H$ and $b\bar{b}H$ production in the SM. . . . 15
2.9 Feynman diagrams for tHb, tHW, and tHq production in the SM. . . . 16
2.10 The SM Higgs boson production cross-sections for the main production modes. . . . 17
2.11 The SM Higgs boson decay width and the decay branching ratios. . . . 18
2.12 Feynman diagrams for SM Higgs boson decays into fermions and weak gauge bosons. . . . 18
2.13 Feynman diagrams for the SM Higgs boson decays into gauge bosons. . . . 19
2.14 One-loop corrections to the Higgs boson mass. . . . 22
2.15 The Feynman diagram for the charged current interaction in the SM and in the Fermi Theory. 34
2.16 Tree-level Feynman diagrams for different Higgs boson production processes in the SMEFT. 38

3.1 The accelerator complex at CERN. . . . 46
3.2 The integrated luminosity at ATLAS over time. . . . 47
3.3 Cut-away view of the ATLAS detector. . . . 48
3.4 Cut-away view of the ATLAS Inner Detector system. . . . 51
3.5 Cut-away view of the ATLAS calorimeter. . . . 52
3.6 Cut-away view of the ATLAS muon system. . . . 53
3.7 The signatures of different particles in the ATLAS detector [292]. . . . 54
3.8 The electron identification efficiencies in ALTAS. . . . 56
3.9 The muon identification efficiency in ATLAS. . . . 58
3.10 The resolution of the ATLAS calorimeter and tracking detector. . . . 61
3.11 Comparison of the energy resolution for EMTopo and PFlow jets. . . . 63
3.12 The tau decay mode classification of CB+PanTau. . . . 64
3.13 The transverse momentum resolutions of TauRec and CB+PanTau. . . . 65
3.14 Example fits of TauRec and CB+PanTau in reconstructed 1p1n decays. . . . 67
3.15 The TauRec and CB+PanTau mean values for reconstructed 1p1n decays with $\eta < 0.3$. . . . 68
3.16 The resolutions of the TauRec, CB+PanTau and Weighted TES. . . . 69
3.17 The optimal values for the compatibility condition as a function of p_T. . . . 70
3.18 The resolutions of the TauRec, CB+PanTau, Combined and MVA TES. . . . 72
3.19 The responses of the reconstructed tau p_T obtained from the TauRec, CB+PanTau and MVA-based energy reconstruction methods. . . . 73
3.20 Illustration of the neutral pion three-momentum correction in 1p1n decays. . . . 74
3.21 Kinematic variables of neutral pions and tau leptons in 1p1n decays. . . . 75
3.22 The invariant mass of reconstructed $\tau_{\text{had-vis}}$ in 1p1n decays. . . . 75

3.23 Illustration of the neutral pion three-momentum correction in Xn decays. 76
3.24 The invariant mass of reconstructed $\tau_{\text{had-vis}}$ in Xn decays. 77
3.25 The ΔR separation between the simulated neutral pions in 1pXn decays. 77
3.26 The invariant mass of reconstructed $\tau_{\text{had-vis}}$ in 1pXn decays. 78

4.1 Reproduction of ATLAS and CMS Run-1 results in the κ-Framework with `HiggsSignals`. 88
4.2 Reproduction of ATLAS and CMS Run-1 results using ratios of κ factors with `HiggsSignals`. 89
4.3 Reproduction of ATLAS and CMS Run-1 results using ratios of cross-sections and branching fractions with `HiggsSignals`. 90
4.4 Reproduction of individual ATLAS and CMS Run-1 results using ratios of cross-sections and branching fractions with `HiggsSignals`. 91
4.5 The `HiggsSignals` fit results for fermionic and bosonic production modes using CMS measurements in the $H \to W^+W^-$ channel. 92
4.6 `HiggsSignals` performance tests in the (κ_V, κ_F) parameter plane using the ATLAS STXS measurement in the $H \to ZZ^* \to 4\ell$ decay channel with 139 fb^{-1} [359]. 93
4.7 `HiggsSignals` performance tests using the CMS STXS measurements in the $H \to \tau\tau$ decay channel with 77 fb^{-1} [361]. 94
4.8 `HiggsSignals` performance tests using the STXS measurements of the ATLAS Run-2 Higgs combination with 80 fb^{-1}. 95

5.1 Tree-level Feynman diagram of the Higgs boson decay into four light leptons. 98
5.2 Feynman diagrams for non-resonant ZZ^* production. 99
5.3 Feynman diagrams for the minor processes of the irreducible background. 99
5.4 Feynman diagrams for the main processes of the reducible background. 100
5.5 The particle-level bins of the STXS scheme. 106
5.6 The SM expected signal composition. 107
5.7 The N_{jets} response matrices for EMTopo/PFlow jets and the Asimov results for PFlow jets. 108
5.8 Differences in the unfolding of the ggH and VBF samples. 110
5.9 The measured cross-sections and correlations in the $H \to ZZ^* \to 4\ell$ decay channel. . . 114

6.1 Simulated kinematic distributions of the Higgs boson and jets in gg2H production. . . . 122
6.2 The one-dimensional dependence of $\sigma/\sigma_{\text{SM}}$ on c_{HG} and $c_{H\widetilde{G}}$ in the gg2H STXS bins. . 124
6.3 Simulated kinematic distributions of the Higgs boson and jets in VBF+VH-Had production. 125
6.4 The one-dimensional dependence of $\sigma/\sigma_{\text{SM}}$ in the qq2Hqq STXS bins on the BSM parameters c_{HW}, c_{HB}, c_{HWB}, $c_{H\widetilde{W}}$, $c_{H\widetilde{B}}$, and (f) $c_{H\widetilde{W}B}$. 126
6.5 Simulated kinematic distributions of the Higgs boson and jets in ZH-Lep production. . . 127
6.6 Simulated kinematic distributions of the Higgs boson and jets in WH-Lep production. . . 127
6.7 The one-dimensional dependence of $\sigma/\sigma_{\text{SM}}$ in the VH-Lep STXS bin on the BSM parameters c_{HW}, c_{HB}, c_{HWB}, $c_{H\widetilde{W}}$, $c_{H\widetilde{B}}$, and $c_{H\widetilde{W}B}$. 129
6.8 Simulated kinematic distributions of the Higgs boson and jets in ttH production. 130
6.9 Simulated kinematic distributions of the Higgs boson and jets in ttH production. 130
6.10 The one-dimensional dependence of $\sigma/\sigma_{\text{SM}}$ in the ttH STXS bin on the BSM parameters c_{uH} and $c_{\widetilde{u}H}$. 131
6.11 The one-dimensional dependence of $\text{BR}^{4\ell}/\text{BR}^{4\ell}_{\text{SM}}$ on the relevant BSM coefficients. 135
6.12 The SM and SMEFT invariant mass spectra of the on-shell and off-shell produced Z bosons. 137
6.13 The SM and SMEFT invariant mass spectra of the on-shell and off-shell produced Z bosons. 138
6.14 Two-dimensional projections of the $C\mathcal{P}$-even acceptance correction. 140
6.15 One-dimensional projections of the $C\mathcal{P}$-even and $C\mathcal{P}$-odd acceptance correction. . . . 141

6.16 One-dimensional projections of the yield onto the BSM parameters c_{HG} and $c_{H\widetilde{G}}$ in the gg2H-0j-p_T^H-High and gg2H-p_T^H-High production bins. . . . 143
6.17 One-dimensional projections of the yield onto the BSM parameters $c_{H\widetilde{W}}$, $c_{H\widetilde{B}}$, and $c_{H\widetilde{W}B}$ in the gg2H-0j-p_T^H-High bin. . . . 144
6.18 Two-dimensional projections of the yield onto different parameter planes in the gg2H-0j-p_T^H-High bin. . . . 145
6.19 One-dimensional projections of the yield onto the BSM parameters $c_{H\widetilde{W}}$, $c_{H\widetilde{B}}$, and $c_{H\widetilde{W}B}$ in the qq2Hqq-VBF and VH-Lep bins. . . . 146
6.20 Two-dimensional projections of the yield onto different parameter planes in the qq2Hqq-VBF and VH-Lep bins. . . . 147
6.21 One-dimensional projections of the yield onto the BSM parameters $c_{H\widetilde{G}}$ and $c_{\widetilde{u}H}$ in the ttH bin. . . . 148
6.22 One-dimensional projections of the $C\mathcal{P}$-odd and $C\mathcal{P}$-even acceptance correction in gg2H and qq2Hqq production. . . . 149
6.23 Comparison of $\sigma/\sigma_{\mathrm{SM}}$ for different particle-level bins. . . . 151
6.24 Comparison between the expected $p_T^{4\ell}$ distributions of the SM SMEFT LO predictions and the SM (N)NLO predictions. . . . 152
6.25 Comparison between the reconstruction efficiencies in the SM and different BSM scenarios. 153
6.26 BSM effects in the systematic uncertainties in the gg2H bins. . . . 154
6.27 The measured signal yield ratio in each particle-level production bin. . . . 155
6.28 The observed best-fit values for the SMEFT coupling parameters. . . . 156
6.29 The one-dimensional fit results for the BSM parameters c_{HG} and c_{uH}. . . . 157
6.30 The one-dimensional fit results for the BSM parameters c_{HW}, c_{HB}, c_{HWB}, $c_{H\widetilde{W}}$, $c_{H\widetilde{B}}$, and $c_{H\widetilde{W}B}$. . . . 161
6.31 The two-dimensional fit results for different BSM parameter combinations. . . . 162
6.32 The two-dimensional fit results for different BSM parameter combinations. . . . 163
6.33 The two-dimensional fit results for different BSM parameter combinations. . . . 164

7.1 Fit results in the $(c_t, \tilde{c}_t)$ parameter plane for different models. . . . 166
7.2 The $\Delta\chi^2$ profiles for the parameters of model I of the $C\mathcal{P}$-admixture parameterization. . . . 168
7.3 The fit results for the parameters of model II. . . . 169
7.4 Two-dimensional projections of the fit results for model II. . . . 171
7.5 The fit results for the parameters of model III and IV. . . . 171
7.6 Two-dimensional projections of the fit results for model IV. . . . 172
7.7 The fit results for model I in ATLAS. . . . 175
7.8 The fit results for model IV in ATLAS. . . . 176

A.1 Example fits for TauRec and CB+PanTau in 1p1n decays with $0.3 \leq |\eta| < 0.8$. . . . 209
A.2 Example fits for CB+PanTau in 1p0n and 3p0n decays with $0.3 \leq |\eta| < 0.8$. . . . 210
A.3 The TauRec and CB+PanTau mean values extracted from the Gaussian fits in 1p0n decays. 211
A.4 The TauRec and CB+PanTau mean values extracted from the Gaussian fits in 1p1n decays. 212
A.5 The TauRec and CB+PanTau mean values extracted from the Gaussian fits in 1pXn decays. 213
A.6 The TauRec and CB+PanTau mean values extracted from the Gaussian fits in 3p0n decays. 214
A.7 The TauRec and CB+PanTau mean values extracted from the Gaussian fits in 3pXn decays. 215
A.8 The TauRec and CB+PanTau widths extracted from the Gaussian fits in 1p0n decays. . . 216
A.9 The TauRec and CB+PanTau widths extracted from the Gaussian fits in 1p1n decays. . . 217
A.10 The TauRec and CB+PanTau widths extracted from the Gaussian fits in 1pXn decays. . . 218
A.11 The TauRec and CB+PanTau widths extracted from the Gaussian fits in 3p0n decays. . . 219

A.12 The TauRec and CB+PanTau widths extracted from the Gaussian fits in 3pXn decays. . . 220
A.13 The tail resolution of the Combined TES for different compatibility conditions as a function of p_T. Shown are (a) the low-p_T region, (b) the mid-p_T region and (c) the high-p_T region. . . . 221
A.14 The Combined TES resolution using the baseline and the optimized compatibility condition. 221
A.15 The tau p_T resolution of the TauRec, Combined and MVA TES for 1p0n decays. 222
A.16 The tau p_T resolution of the TauRec, Combined MVA TES for 1p0n decays as a function of different variables. . . . 223
A.17 The tau p_T resolution of the TauRec, Combined MVA TES for 1p1n decays. 224
A.18 The tau p_T resolution of the TauRec, Combined MVA TES for 1p1n decays as a function of different variables. . . . 225
A.19 The tau p_T resolution of the TauRec, Combined MVA TES for 1pXn decays. 226
A.20 The tau p_T resolution of the TauRec, Combined MVA TES for 1pXn decays as a function of different variables. . . . 227
A.21 The tau p_T resolution of the TauRec, Combined MVA TES for 3p0n decays. 228
A.22 The tau p_T resolution of the TauRec, Combined MVA TES for 3p0n decays as a function of different variables. . . . 229
A.23 The tau p_T resolution of the TauRec, Combined MVA TES for 3pXn decays. 230
A.24 The tau p_T resolution of the TauRec, Combined MVA TES for 3pXn decays as a function of different variables. . . . 231
A.25 Kinematic distributions of neutral pions obtained from CB+PanTau and the 3-Vec method in 1p1n decays. . . . 232
A.26 p_T responses of neutral pions in 1pXn decays. . . . 233
A.27 Invariant mass responses of different reconstruction methods in 1pXn decays. . . . 233
A.28 p_T responses of neutral pions in 3pXn decays. . . . 234

C.1 Response matrices for EMTopo/PFlow for different variables. . . . 240
C.2 Response matrices for EMTopo/PFlow for dijet variables. . . . 241
C.3 The response matrices of N_{jets} for PFlow/EMTopo derived using simulated $ggH + bbH$, VBF, and VH events. . . . 242
C.4 The response matrices of different jet variables for EMTopo/PFlow. . . . 243
C.5 Response matrices EMTopo/PFlow jets for different variables. . . . 244
C.6 The statistical uncertainty on STXS POIs using PFlow and EMTopo jets. . . . 245
C.7 p_T distributions for hard scatter/pile-up jets which pass and fail the fJVT cut. . . . 245
C.8 Kinematic jet distributions in ggH and VBF production for the three forward jet cut scenarios. . . . 246
C.9 Migration matrices for nominal jet selection vs. restricted jet phase space. . . . 247
C.10 Observed profile likelihood as a function of $\sigma \cdot B(H \to ZZ^*)$ and μ. . . . 248

D.1 The SM and SMEFT invariant mass spectra of the on-shell and off-shell produced Z bosons. 252
D.2 The SM and SMEFT invariant mass spectra of the on-shell and off-shell produced Z bosons. 253
D.3 Kinematic distributions of the Higgs boson and jets in VBF+VH-Had production. . . . 254
D.4 Kinematic distributions of the Higgs boson and jets in VBF+VH-Had production. . . . 255
D.5 The p_T^j and η^H distributions in the ZH-Lep production. . . . 256
D.6 The p_T^j and η^H distributions in ZH-Lep production. . . . 256
D.7 The p_T^j and η^H distributions in $tHjb$ production. . . . 257
D.8 The p_T^j and η^H distributions in $tHjb$ production. . . . 257

D.9 The p_T^j and η^H distributions in tHW production. . . . 258
D.10 The p_T^j and η^H distributions in tHW production. . . . 258
D.11 The $\sigma/\sigma_{\text{SM}}$ ratio for $c_{H\tilde{B}}$ $c_{H\widetilde{W}B}$, c_{HB}, and c_{HWB} in the VH-Lep particle production bin. . 259
D.12 The dependence of $\sigma/\sigma_{\text{SM}}$ on the $C\mathcal{P}$-even BSM coupling parameters for each STXS bin. . 260
D.13 The one-dimensional projection of the yield onto the BSM parameter $c_{H\widetilde{G}}$ in the gg2H bins. 265
D.14 The two-dimensional projections of the yield onto the $c_{H\widetilde{W}}$-$c_{H\tilde{B}}$ plane in various gg2H production bins. . . . 266
D.15 The two-dimensional projections of the yield onto the $c_{H\widetilde{W}}$-$c_{H\widetilde{W}B}$ plane in various gg2H production bins. . . . 267
D.16 The two-dimensional projections of the yield onto the $c_{H\tilde{B}}$-$c_{H\widetilde{W}B}$ plane in various gg2H production bins. . . . 268
D.17 The one-dimensional projection of the yield onto the BSM parameters $c_{H\widetilde{W}}$, $c_{H\tilde{B}}$, and $c_{H\widetilde{W}B}$ in the qq2Hqq bins. . . . 269
D.18 The two-dimensional projections of the yield onto different BSM parameter planes in the qq2Hqq bins. . . . 270
D.19 The one-dimensional projection of the yield onto c_{HG} in the different gg2H bins. . . . 272
D.20 The one-dimensional projection of the yield onto the BSM parameters c_{HW} c_{HB}, and c_{HWB} in the gg2H-0j-p_T^H-High bin. . . . 273
D.21 The two-dimensional projections of yield onto the c_{HW}-c_{HB} plane in the different gg2H production bins. . . . 274
D.22 The two-dimensional projections of yield onto the c_{HW}-c_{HWB} plane in the different gg2H production bins. . . . 275
D.23 The two-dimensional projections of yield onto the c_{HB}-c_{HWB} plane in the different gg2H production bins. . . . 276
D.24 The one-dimensional projection of the yield onto the BSM parameters $c_{H\widetilde{W}}$, $c_{H\tilde{B}}$, and $c_{H\widetilde{W}B}$ in the qq2Hqq bins. . . . 277
D.25 The two-dimensional projections of the yield onto different parameter planes in the qq2Hqq bins. . . . 278
D.26 The one-dimensional projection of the yieldonto the Wilson coefficient c_{HW}, c_{HB}, and c_{HWB} in the VH-Lep bin. . . . 279
D.27 The two-dimensional projections of the yield onto the different BSM parameters planes in the VH-Lep bin. . . . 279
D.28 The projections of the yield in the ttH bin. . . . 280
D.29 QCD scale uncertainties in the gg2H production bins. . . . 281
D.30 QCD scale uncertainties in the qq2Hqq, VH-Lep and ttH production bins. . . . 282
D.31 PDF variation uncertainties in the gg2H production bins. . . . 283
D.32 PDF variation uncertainties in the qq2Hqq, VH-Lep and ttH production bins. . . . 284

E.1 Fit results in the $(c_t\,,\,\tilde{c}_t)$ parameter plane of model 4 taking Higgs-p_T-shape modifications into account. . . . 285
E.2 The two-dimensional $\Delta\chi^2$ profiles for the parameters of model II(a). . . . 286
E.3 The one-dimensional $\Delta\chi^2$ profiles for the fit parameters of, model II(b) and model II(c). . 287
E.4 The two-dimensional $\Delta\chi^2$ profile for model II(b) and model II(c). . . . 287
E.5 The two-dimensional $\Delta\chi^2$ profile for model II(b) and model II(c). . . . 288
E.6 The one-dimensional $\Delta\chi^2$ profiles for the sensitive parameters of model III and model IV. 289
E.7 The two-dimensional $\Delta\chi^2$ profiles for the parameters of model III. . . . 290
E.8 The two-dimensional $\Delta\chi^2$ profiles for the parameters of model IV. . . . 291
E.9 The one-dimensional projections of the fit result onto κ_b^s and κ_τ^s of model IV. . . . 292

E.10 Two-dimensional projections of the fit result onto different parameter planes. 293

List of Tables

2.1 The electroweak multiplets and their quantum numbers. . . . 7
2.2 The cross-sections of the dominant SM Higgs boson production modes. . . . 16
2.3 The branching ratios of the dominant SM Higgs boson decay modes. . . . 19
2.4 The effective Yukawa couplings of the Higgs boson in the C2HDM. . . . 26
2.5 The chiral supermultiplets of the MSSM. . . . 27
2.6 The gauge supermultiplets of the MSSM. . . . 28
2.7 The SMEFT operators in the $U(3)^5$ symmetry limit. . . . 37
2.8 Overview of the considered models in the Higgs $C\mathcal{P}$-mixing scenario. . . . 43

3.1 Summary of the main τ^- decay modes. . . . 60
3.2 Summary of reconstructed decay modes, η and E_T bins. . . . 66

5.1 The integrated luminosity for Run-2 of the LHC. . . . 101
5.2 The SM Higgs boson production cross-sections of different production processes. . . . 102
5.3 Comparison of Asimov results for N_{jets} using EMTopo and PFlow jets. . . . 108
5.4 Proportion of hard scatter, pile-up, and out-of-time jets. . . . 109
5.5 The impact of systematic uncertainties on the cross-section measurement. . . . 111

6.1 MADGRAPH5_aMC@NLO syntax and BSM dependence of the cross-section. . . . 118
6.2 Cross-section EFT parameterization with two BSM coupling parameters. . . . 118
6.3 MADGRAPH5_aMC@NLO syntax and the number of samples for the parameterization of the Higgs boson production cross-sections. . . . 120
6.4 Inclusive cross-section terms for all production modes. . . . 121
6.5 Percentage of ggF+bbH events in the gg2H STXS bins. . . . 123
6.6 Percentage of VBF+VH-Had events in the qq2Hqq STXS bins. . . . 124
6.7 Percentage of ZH-Lep and WH-Lep events in the VH-Lep STXS bin. . . . 128
6.8 Percentage of ttH, $tHjb$ and tHW events in the ttH STXS bin. . . . 131
6.9 EFT parameterization of the production cross-section ratio. . . . 132
6.10 MADGRAPH5_aMC@NLO syntax and BSM dependence of the Higgs decay widths. . . . 132
6.11 MADGRAPH5_aMC@NLO syntax and the number of samples for parameterization of the Higgs boson decay branching ratio into four-lepton final states. . . . 133
6.12 SM and SMEFT Higgs boson decay widths. . . . 134
6.13 SMEFT parameterization of the Higgs boson branching ratio into four-lepton final states. 134
6.14 Fit parameters for the $C\mathcal{P}$-odd signal acceptance. . . . 140
6.15 Fit parameters of the two-dimensional acceptance parameterization in gg2H production. . 141
6.16 The acceptance correction for different $C\mathcal{P}$-even BSM points in gg2H, qq2Hqq, ZH-Lep, WH-Lep and ttH production. . . . 150
6.17 The acceptance correction for different $C\mathcal{P}$-odd BSM points in gg2H, qq2Hqq, ZH-Lep, WH-Lep and ttH production. . . . 150
6.18 The best-fit values of the SMEFT coupling parameters. . . . 156
6.19 The observed best-fit points from the two-dimensional likelihood scans. . . . 158

6.20 The one-dimensional limits for the SMEFT parameters obtained in different Higgs boson decay channels at ATLAS. . . . 159

7.1 The fit results for the parameters of model I. . . . 168
7.2 The fit results for the parameters of model II. . . . 170
7.3 The fit results for model III and model IV. . . . 173
7.4 The fit results for model IV in ATLAS. . . . 175

B.1 Run-2 Higgs boson measurements (STXS) from ATLAS. . . . 235
B.2 Run-2 Higgs boson measurements (rate) from ATLAS. . . . 236
B.3 Run-2 Higgs boson measurements from CMS. . . . 236

C.1 Summary of the event selection requirements. . . . 238
C.2 Comparison of Asimov results for different variables using matrix unfolding. . . . 239

D.1 Configuration and MADGRAPH5_aMC@NLO syntax for the generated BSM signal samples in the ggF+bbH production mode. . . . 249
D.2 Configuration and MADGRAPH5_aMC@NLO syntax for the generated BSM signal samples in the WH-Lep production mode. . . . 249
D.3 Configuration and MADGRAPH5_aMC@NLO syntax for the generated BSM signal samples in the VBF+VH-Had and ZH-Lep production modes. . . . 250
D.4 Configuration and MADGRAPH5_aMC@NLO syntax for the generated BSM signal samples in the ttH, $tHjb$ and tHW production modes. . . . 251
D.5 The acceptance of simulated gg2H samples with different values of the $C\mathcal{P}$-odd BSM parameters. . . . 261
D.6 The acceptance of simulated gg2H samples with different values of the $C\mathcal{P}$-even and $C\mathcal{P}$-odd BSM parameters. . . . 262
D.7 Fit parameters of the signal acceptance for the $C\mathcal{P}$-odd Wilson coefficients in the qq2Hqq production mode. . . . 262
D.8 The acceptance of simulated qq2Hqq samples with different values of the $C\mathcal{P}$-odd BSM parameters. . . . 263
D.9 The acceptance of simulated qq2Hqq samples with different values of the $C\mathcal{P}$-even BSM parameters. . . . 264
D.10 Fit parameters for the $C\mathcal{P}$-even signals acceptance. . . . 271

E.1 The fit results for the fit parameters of model II(b) and model II(c). . . . 288

Acknowledgements

First of all, I would like to thank Klaus Desch for providing me with the opportunity to do my PhD in his research group and for supervision. In addition, I am grateful for his advice and support over the years, and the insightful suggestions he provided. The same holds for Philip Bechtle, who has been a great discussion partner, who always had a good idea ready. He always motivated and supported me, even with problems beyond physics. I also want to thank Peter Wagner, who helped me to get started with ATLAS in the first place, and for the scientific exchange.

I would like to thank all my collaborators that I had the pleasure to work with during my PhD. I am very grateful to Tim Stefaniak for getting me into `HiggsSignals`. Also for his support, and the countless scientific discussions about theoretical particle physics. Moreover, I am grateful for the collaboration and discussions with Georg Weiglein and Sven Heinemeyer. I also want to thank Jonas Wittbrodt for the discussions about extended Higgs sectors. I am grateful to Syed Abidi, Verena Walbrecht, Bianca Ciungu, and Laurelle Veloce for their support when I got into the $H \to ZZ^* \to 4\ell$ analysis at ATLAS, and also for the scientific discussions that followed afterwards. In addition, I want to thank Ian Brock, Christian Grefe, Michael Hübner, Will Davey, Terry Chan, and Rongkun Wang for many fruitful discussions. I want to thank Ilaria Brivio and Pedro Schwaller for insightful discussions about BSM Higgs physics and effective field theories.

Good research can only be performed in a pleasant and productive environment. Therefore, I want to thank all current and former members of office 0.030 (and 0.029) for the great time we spent together (at work and after work), namely Peter, Maike, Lara, Michael, Martin, Alina, Henrik, Florian, Hoang, Lena, Dominik, and Marco. I am also really grateful for all the amazing people I got to meet at schools and workshops. Special thanks to Marco, Alina, Lena, Alexander, and Lars for feedback on my thesis.

I also want to thank Florian Bernlochner for being the second assessor of my thesis, and Herbert Dreiner and Andreas Hense for also reviewing my thesis.

Last but not least, I owe a debt of gratitude to the support by my parents, and I want to thank my brothers and friends for reminding me about the beautiful things in life besides physics.